Progress in Nanotechnology

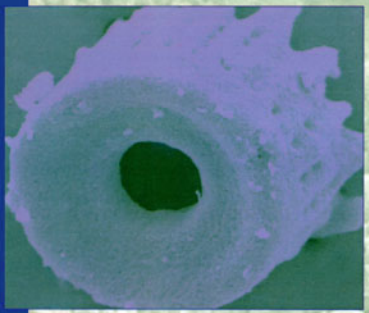

Progress

in

Nanotechnology

Published by
The American Ceramic Society
735 Ceramic Place
Westerville, Ohio 43081 USA
www.ceramics.org

COVER PHOTOS: Top right: "SEM micrograph of SiC-based fibers, prepared from a (TEOS/phenolic)-based sol, after pyrolysis at 1100°C" is courtesy of Chang-An Wang, Michael D. Sacks, Greg A. Staab, and Zhe Cheng, and appears as figure 4 in their paper "Solution-Based Processing of Nanocrystalline SiC," which begins on page 283.

Left center: "Secondary electron images of a) Aulacoseira diatom frustule after reactive conversion (900°C, 4 h, Mg(g) into MgO" is courtesy of Ken H. Sandhage, Matthew B. Dickerson, Philip M. Huseman, Frank M. Zalar, Mark C. Carroll, Michelle R. Rondon, and Eryn C. Sandhage, and appears as figure 2a in their paper "A Novel Hybrid Route to Chemically-Tailored, Three-Dimensional Oxide Nanostructures: The Basic (Bioclastic and Shape-Preserving Inorganic Conversion) Process," which begins on page 255.

Bottom right: "Sintered zirconia tube shaped by EPD of a powder mixture of nanosized and micrometer-sized zirconia particles from an aqueous suspension" is courtesy of Jan Tabellion and Rolf Clasen, and appears as figure 8 in their paper "Advanced Ceramic or Glass Components and Composites by Electrophoretic Deposition/Impregnation Using Nanosized Particles," which begins on page 227.

Background: "Silica green body with functionally graded density and pore size...(left) with nanosized fumed silica particles" is courtesy of Jan Tabellion and Rolf Clasen, and appears as figure 9 in their paper "Advanced Ceramic or Glass Components and Composites by Electrophoretic Deposition/Impregnation Using Nanosized Particles," which begins on page 227.

For information on ordering titles published by The American Ceramic Society, or to request a publications catalog, please contact our Customer Service Department at 614-794-5890 (phone), 614-794-5892 (fax), <customersrvc@acers.org> (e-mail), or write to Customer Service Department, 735 Ceramic Place, Westerville, OH 43081, USA.

Printed in the United States of America.

4 3 2 1–05 04 03 02

ISBN 1-57498-168-4

www.ceramics.org

www.ceramicbulletin.org

www.ceramicjournal.org

CONTENTS

CERAMIC TRANSACTIONS

CERAMIC ENGINEERING AND SCIENCE PROCEEDINGS (CESP)

INTRODUCTION

The fields of nanoscale science, engineering, and technology, more widely known as nanotechnology, have experienced quite an explosion of interest, both scientific and industrial, over the past decade.

Many believe nanotechnology has the potential for becoming the next materials revolution. The U.S. National Science and Technology Council created the National Nanotechnology Initiative (NNI) in 2000. NNI became the top science and technology priority for the U.S. government with an initial 2001 budget of $495 million. For FY2003, the President's budget requested about $710 million for federal investment in nanotechnology, a 17% increase over FY2002. According to one market analysis*, the world market for nanoparticles reached $492.5 million in 2000 and is expected to climb to $900.1 million in 2005.

The ceramics/materials community's interest in nanotechnology is fueled by the unique properties that can be obtained. Nanostructured materials with enhanced electrical, mechanical, magnetic, and optical properties have been developed. These enhanced properties open the door for many exciting applications.

Current applications of nanomaterials include abrasives, catalysts, coatings, magnetic recording media, magnetic fluid seals, ceramic membranes, sunscreens, adhesives, MRI contrast agents, and reinforcements/fillers. Applications in biomaterials, cutting tools, gas sensors, solid oxide fuel cells, structural ceramics, thick films, wear-resistant coatings, FED phosphors and emitters, and transparent functional films will likely become common.

The American Ceramic Society (ACerS) proudly contributes to the "nano-revolution" by organizing and sponsoring forums for information exchange and disseminating information through its various periodicals and books.

This new book is a compilation of articles and papers previously published by ACerS. The articles originated from the *Journal of the American Ceramic Society*, the *American Ceramic Society Bulletin*, *Ceramic Engineering and Science Proceedings*, and *Ceramic Transactions*. We hope this collection of papers on current research and development, manufacturing, and marketing data will provide a reference resource for those involved in this new and exciting field of nanotechnology.

**Business Communication Co. Inc., Norwalk, Conn.*

This page intentionally left blank

AMERICAN CERAMIC SOCIETY BULLETIN

This page intentionally left blank

MARKET ANALYSIS OF

Nanostructured Materials

The world market for nanoparticles is expected to increase markedly during the next several years.

Mindy N. Rittner
Business Communications Co. Inc., Norwalk, Conn.

Nano terminology has become trendy, popular and representative of all that is high-tech in the materials world. Literally, nano represents 0.000000001, or 10–9, an extremely small quantity with enormous implications for the miniaturization-driven technology of the twenty-first century.

Within the past two decades, a variety of terms sharing the prefix nano, such as nanoparticle, nanomaterial, nanophase and nanostructured, has emerged to describe certain materials, technologies and even businesses. In fact, several firms listed on the NASDAQ stock exchange use the prefix nano in their company names. Although not yet a household word, it is indeed well-known within and increasingly vital to the advanced materials community and high-technology business sector.

Generally speaking, nanoterminology is aptly used to describe materials that are characterized by structural features ranging in size from ~0.000000001 (1×10^{-9}) to 0.0000001 (100×10^{-9}) meter (m)—that is, 1 to 100 nanometers (nm).

This nanostructuring may exist in one, two or three dimensions. For example, a thin film of 10 nm in thickness is nanostructured in one dimension, a whisker or fiber of 25 nm in diameter and 1000 nm (1 micrometer (μm)) in length is nanostructured in two dimensions, and a roughly spherical crystal or grain of 30 nm in diameter is nanostructured in three dimensions.

It is this latter type of material—three-dimensionally nanostructured materials, or nanoparticulate materials—that is the primary focus of this article. For comparison, conventional particles typically have dimensions in the range of 10–100 μm (10^{-5}–10^{-4} m).

Commercial Products

Nanoparticles are available commercially in the form of dry powders or liquid dispersions. The latter is obtained by

combining nanoparticles with an aqueous or organic liquid to form a suspension or paste. It may be necessary to use chemical additives (surfactants, dispersants) to obtain a uniform and stable dispersion of particles. With further processing steps, nanostructured powders and dispersions can be used to fabricate coatings, components or devices that may or may not retain the nanostructure of the particulate raw materials.

Currently, the most commercially important nanoparticulate materials are simple metal oxides, such as silica (SiO_2), titania (TiO_2), alumina (Al_2O_3), iron oxide (Fe_3O_4, Fe_2O_3), zinc oxide (ZnO), ceria (CeO_2) and zirconia (ZrO_2). Also of increasing importance are the mixed oxides, indium tin oxide (In_2O_3–SnO_2 or ITO) and antimony tin oxide (Sb_2O_3–SnO_2 or ATO), as well as titanates, in particular barium titanate ($BaTiO_3$). Silica and iron oxide nanoparticles have a commercial history spanning half a century or more, while nanocrystalline titania, zinc oxide, ceria, ITO, and other oxides have more recently entered the marketplace.

Other types of nanoparticles, including various complex oxides, metals, semiconductors and nonoxide ceramics, also are under development and are available from some companies in small- or pilot-scale quantities primarily. With the exception of semiconducting oxides, such as titania and ITO, semiconductor nanocrystals are not yet used in large-scale commercial applications. The technology to produce and utilize nanocrystalline semiconductors, often called quantum dots, is relatively new and rapidly developing.

A technological problem limiting the use of metal nanoparticles in some applications is their high reactivity. It is difficult to produce, transfer and store metal nanopowders without particle contamination and, in some cases, safety hazards (because of the pyrophoricity of the high-surface-area particles).

Nanoparticle Pricing

Despite progress in scaling up production and reducing costs, nanoparticles remain relatively expensive materials. Mass-produced nanopowders typically range in cost from tens of dollars to several hundred dollars per kilogram, depending on the production volume, material type, powder characteristics (e.g., particle size, size distribution, purity), manufacturing method and postsynthesis processing treatments.

Custom-processed nanopowders or developmental quantities of material may be priced in the tens-of-dollars-per-gram range or higher (which translates into tens of thousands of dollars per kilogram and higher). Nanoparticles and dispersions produced for pharmaceutical applications may be priced even higher.

Market Analysis—Background

In 1997, Business Communications Co. (BCC) published a seminal technical-market study, *Opportunities in Nanostructured Materials*, that defined the scope of the nanomaterials industry for the first time. The report identified the 1996 U.S. market for nanoparticles at $41.3 million and forecast a $148.6 U.S. market for 2001, corresponding to a 29.2% average annual growth rate (AAGR) from 1996 through 2001.

Since that first report was published, the industry has witnessed many changes: new entrants into the business; production scale-up efforts; new commercialization strategies; and technological advancements. As a result of these developments, BCC opted to take another look at the industry and reevaluate the existing and potential markets for nanoparticulate materials.

The culmination of that research is a comprehensive, three-volume series of reports on which this article is based: GB-201A, *Opportunities in Nanostructured Materials: Electronic, Magnetic, and Optoelectronic Applications*, published May, 2001; GB-201B, *Opportunities in Nanostructured Materials: Biomedical, Pharmaceutical, and Cosmetic Applications*, published August, 2001; and GB-201C, *Opportunities in Nanostructured Materials: Energy, Catalytic, and Structural*

Current and Emerging Applications for Nanoparticles Covered in Three-Volume Series

Electronic, optoelectronic, magnetic applications	Biomedical, pharmaceutical, cosmetic applications	Energy, catalytic, structural applications
Chemical–mechanical polishing supports	Antimicrobials	Automotive catalyst
Electroconductive coatings	Biodetection and labeling	Ceramic membranes
Magnetic fluid seals	Biomagnetic separations	Fuel cells
Magnetic-recording media	Drug delivery	Photocatalysts
Multilayer ceramic capacitors	MRI contrast agents	Propellants
Optical fibers	Orthopedics	Scratch-resistant coatings
Phosphors	Sunscreens	Structural ceramics
Quantum optical devices		Thermal spray coatings
Solar cells		

Source: Business Communications Co. Inc.

Applications, published December, 2001. The reports describe 24 different current and emerging applications for nanoparticles.

In each report, the market data and forecasts are presented in terms of the value (constant U.S. dollars, US$) and volume (kg) of nanoparticles consumed. For use in some applications, nanoparticles are further processed into a coating or consolidated into a dense component. However, for the sake of consistency, the market figures specifically represent the value of the powders or dispersions themselves, as opposed to higher-value-added products, such as coatings or fabricated parts.

The information and data contained in the three-volume series of reports were derived from primary and secondary sources. More than 150 industry participants—executives, engineers, managers, researchers and salespeople from companies and research institutions involved in the development, production and/or use of nanostructured materials—were interviewed during the studies.

Other information was obtained from an exhaustive review of the patent literature and government databases, as well as scientific, trade and business journals, and company literature. BCC newsletters, reports and conference proceedings provided additional information.

Market Analysis—Major Results

The total world market for nanoparticulate materials reached $492.5 million in 2000 and is expected to be $900.1 million in 2005, corresponding to a 12.8% AAGR during the next five years.

Electronic, magnetic and optoelectronic applications for nanoparticles accounted for more than two-thirds, or 67.6%, of the 2000 market. Biomedical, pharmaceutical and cosmetic applications accounted for almost one-fifth, or 19.7% of the total market. Energy, catalytic and structural applications accounted for the remaining 12.7%. By 2005, the market shares are forecasted to shift to 74.2%, 16.1% and 9.8%, respectively. In 2000, the most important applications in terms of revenues generated were chemical–mechanical polishing (CMP), magnetic recording tapes, sunscreens, automotive catalyst supports, biolabeling, electroconductive coatings and optical fibers.

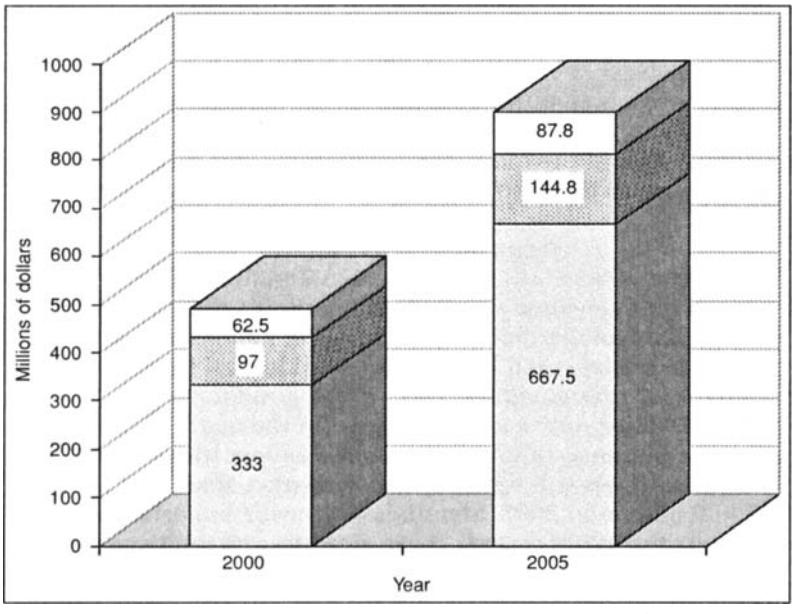

Nanoparticle world market by application area. Total 2000 market was $492.5 million. Total 2005 market expected to be $900.1 million. ((■) energy, catalytic and structural applications; (▨) biomedical, pharmaceutical and cosmetic applications; and (■) electronic, magnetic and optoelectronic applications). Source: Business Communications Co. Inc.

Electronic, Magnetic, Optoelectronic Applications

The world market for nanoparticulate materials in electronic, magnetic and optoelectronic applications was $333 million, or 67.6% of the total market, in 2000. This figure represents the value of nanoparticles consumed to produce CMP slurries, electroconductive coatings, magnetic fluid seals, magnetic tape coatings, optical fibers, passive electronic devices, phosphors, quantum optical devices and solar cells.

Because of growth in the already-substantial CMP market, as well as the emergence of several on-the-verge applications, BCC projects that the world market for nanoparticles in electronic, magnetic and optoelectronic applications will reach $667.5 million, corresponding to a 14.9% AAGR in terms of value from 2000 to 2005, and 74.2% of the projected world market.

Simple oxides, such as silica and alumina, will continue to account for the majority of the market. However, complex oxides are expected to increase their market share while demand for metallic nanoparticles will be strongly affected by sluggishness in the magnetic recording industry.

Biomedical, Pharmaceutical, Cosmetic Applications

The world market for nanoparticulate materials in biomedical, pharmaceutical and cosmetic applications

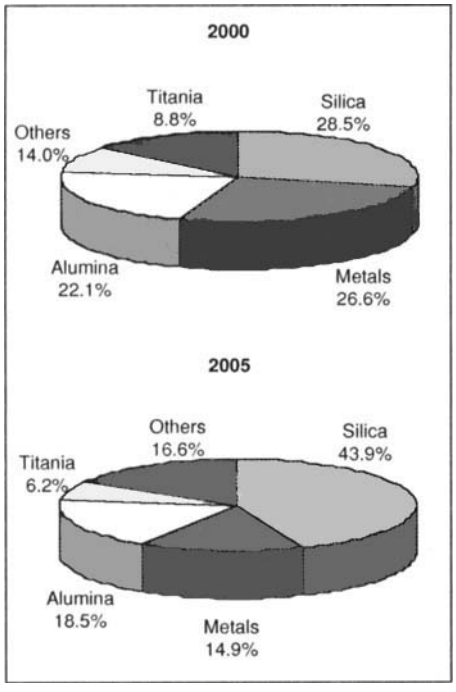

Shares of the world market for nanoparticles by material type. Total 2000 market was $492.5 million. Total 2005 market expected to be $900.1 million. Source: Business Communications Co. Inc.

was $97.0 million, or 19.7% of the total market, in 2000. This figure represents the value of inorganic nanoparticles used as or to produce antimicrobial agents, biological labels for research and diagnostics, biomagnetic separations media, carriers for drug delivery, magnetic resonance imaging (MRI) contrast media, orthopedic materials and sunscreens. More than 90% of this market can be attributed to two applications, sunscreens and biolabels, that have been undergoing development and commercialization for a decade or more.

Among the most important factors influencing growth in the various market segments is competition from alternative materials and technologies. BCC projects that the world market for nanoparticles in biomedical, pharmaceutical and cosmetic applications will increase at an 8.3% AAGR during the next five years, reaching $144.8 million (16.1% of the total projected market) in 2005. The sun-protection market has the greatest near-term revenue potential, while drug-carrier applications will be slowest to penetrate the market.

Energy, Catalytic, Structural Applications

The world market for nanoparticulate materials in energy, catalytic and structural applications reached $62.5 million (12.7% of the total market) in 2000 mainly because of world efforts to clean up the environment. This figure represents the value of inorganic nanoparticles used as or to produce automotive catalyst supports, ceramic membranes, fuel cells, photocatalysts, propellants and explosives, scratch-resistant coatings, structural ceramics, and thermal spray coatings.

These market segments are a diverse mix of mostly new nanoparticle applications combined with one established use: automotive catalysts. Decades old, but responding to greater environmental consciousness and more stringent emissions standards worldwide, the automotive catalyst market is experiencing changes in catalyst materials and engineering.

During the 1990s, companies had mixed success in using nanoparticles to fabricate dense ceramic components. However, two particular structural ceramic products have made headway into the marketplace. Also, the promising photocatalyst market for nanocrystals is beginning to generate revenues mainly because of development projects and new product introductions by companies in Japan and Europe. The U.S. Navy has increased interest in thermal spray applications for nanoparticulate feedstock, and progress also has been made in exploiting the characteristics and properties of nanocrystals in ceramic membrane, fuel cell, propellant and scratch-resistant-coating applications.

BCC projects that the wold market for nanoparticulate materials in energy, catalysis and structural applications will be $87.8 million (9.8% of the total projected market) by 2005, corresponding to an AAGR of 7.0% during the forecast period.

Segmentation by Material Type

86% of the 2000 world market—$423.7 million—is due to applications that consume silica, alumina, titania and specific types of metallic nanoparticles. Other types of nanoparticles, primarily simple oxides, such as ceria, zinc oxide, and iron oxide, account for the remaining 14%, or $68.8 million.

There will be only a slight decrease in the market dominance of silica, alumina, titania and metallic nanoparticles in 2005. These materials will retain an 83.4% market share and generate $750.9 million in 2005. Materials of growing importance during the next five years include ceria, zirconia and multicomponent oxides. ■

$PbTiO_3$ Nanosized Ceramics

Lead titanate powders have been prepared using the sol–gel method with lead lactate as the lead precursor.

D.S. Yu and J.C. Han
Center for Composite Materials, Harbin Institute of Technology, Harbin, P.R. China

Liu Ba
Harbin University of Science & Technology, Harbin, P.R. China

Lead titanate ($PbTiO_3$) is an important ferroelectric ceramic. It has a high Curie temperature, high pyroelectric coefficient, low dielectric constant and high spontaneous polarization. $PbTiO_3$ has been widely used for capacitors, ultrasonic transducers, thermistors, optical electronic devices and satellite detection systems.

Nanometer-sized $PbTiO_3$ crystals can be prepared using chemical coprecipitation,[1] sol–gel,[2,3] hydrothermal[4] and traditional solid reaction methods. Sol–gel processing offers significant advantages,[5] including high purity, chemical homogeneity and controlled particle size. Compared with other methods, the sol–gel process provides lower reaction temperature and better control of molecular-level properties.

One of the major disadvantages of the sol–gel process is the high cost of the alkoxide reagents. Alkoxide reagents are used in organic compounds to increase the stability of multicomponent systems, increasing the stability of the multicomponent systems when the use of constituent alkoxides becomes difficult or produces poisonous gas. $TiCl_4$ and $Pb(NO_3)_2$ have been used as precursors. However, chloride ions are difficult to remove, even at high temperature.

Another disadvantage of the sol–gel process is that the precursor solution is extremely moisture sensitive. Therefore, the purpose of this study is to decrease the cost of the alkoxide reagents and to increase the stability of solidification and gelation.

During the study, we discovered that hydroxylic acids effectively lower the synthesis temperature for nanometer-sized $PbTiO_3$ crystal preparation. Therefore, lead lactate ($Pb(CH_3CHOHCOO)_2$, PbL_2) was used as the lead precursor and was formed from the reaction between lead oxide (PbO) and lactic acid ($CH_3CHOHCOOH$), with viscous lactic acid as the solvent. The system lead lactate–lactic acid–ethanol–titanium butoxide was selected as the precursor for the sol–gel processing of $PbTiO_3$.

Lead lactate and titanium butoxide ($Ti(OC_4H_9)_4$) were used as starting materials. Bright-yellow, crystalline $PbTiO_3$ was obtained, and it had a particle size of ~60 nm.

IR spectra of lactic acid, PbL_2 dissolved in lactic acid, $Ti(OC_4H_9)$, and a mixture of $Ti(OC_4H_9)_4$ and PbL_2 (precursor

liquid) were measured. A new band vibration at ~441.6 cm^{-1} (υ(Ti–O)) was found. The $Ti(OC_4H_9)_4$ and the lactic acid reacted and interlinked with each other. The IR absorption of υ(Ti–O) changed from higher frequency (~581.2 cm^{-1}, 600°C) to lower frequency (~579.3 cm^{-1}, 900°C) with increased temperature. This conformed with the red-transfer phenomenon. The two bands at ~3338.6 and 1624 cm^{-1} were assigned to stretching vibration of free water or alcohol.

TG-DTA curves showed a weight loss of ~25% accompanied by a sharp exothermic peaks at ~306°C. This was attributed to the combustion of the original moiety in the gel. The small exothermal peaks at ~52 and 160°C were caused by the heat of melting gel and vaporizing lactic acid and alcohol. Another small exothermal peak at ~416°C was attributed to the heat of crystallization of $PbTiO_3$. The formation of phase-pure tetragonal $PbTiO_3$ was confirmed by XRD results.

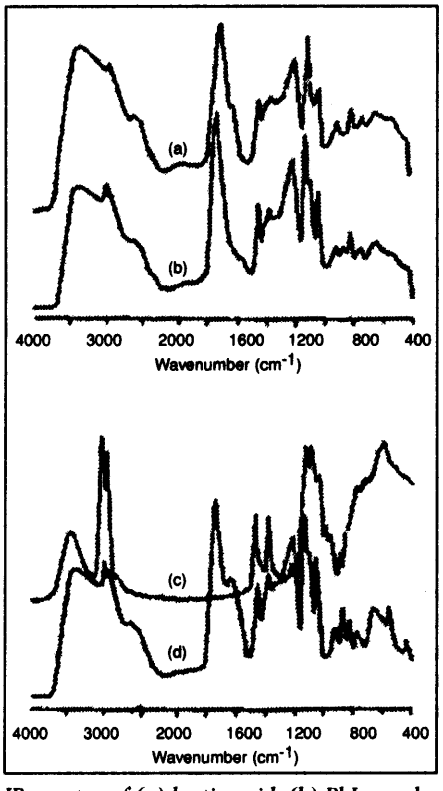

IR spectra of (a) lactic acid, (b) PbL_2 and lactic acid, (c) $Ti(OC_4H_9)_4$ and (d) precursor liquid.

XRD patterns were obtained of products prepared at various temperatures. Calcined materials were present in the PbO phase at 400°C. A phase-pure tetragonal-perovskite-type material was formed at 420°C. Sharper XRD peak patterns resulted from higher preparation temperatures. Particle sizes were determined from the half-widths of the XRD peaks on the (111) interface using the Debye–Scherrer equation. The result was supported by a TEM micrograph of the particle.

SRS patterns of $PbTiO_3$ particles prepared under various temperatures showed that lower treatment temperature produced higher SRS values. SRS also showed that cubic-phase nanometer-sized $PbTiO_3$ existed at room temperature. SEM showed that the size of particles was ~50 nm.

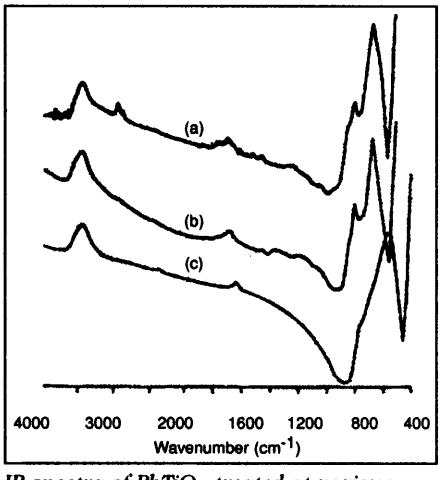

IR spectra of $PbTiO_3$ treated at various temperatures: (a) 600, (b) 750 and (c) 900°C.

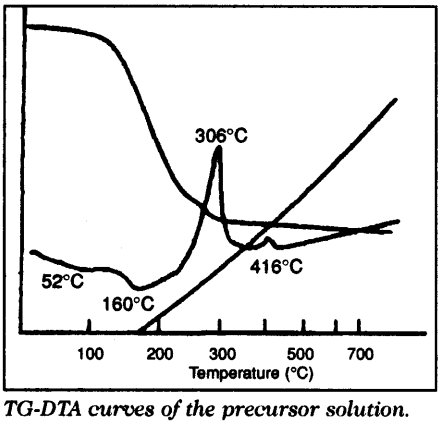

TG-DTA curves of the precursor solution.

Nanometer-sized $PbTiO_3$ can be easily synthesized using self-combustion techniques and dry gel. ■

References

[1]G.R. Fox, J.H. Adair and R.E. Newnham, *J. Mater. Sci.*, **25**, 3634 (1990).

[2]V. Kumar et al., *Am. Ceram. Soc. Bull.*, **79** [10] 2775 (1996).

[3]J.B. Blum and S.R. Gurkovich, *J. Mater. Sci.*, **20**, 4479 (1985).

[4]H. Cheng, J. Ma and Z. Zhao, *J. Am Ceram. Soc.*, **75** [5] 1125 (1992).

[5]D.R. Ulrich, *J. Non-Cryst. Solids*, **100**, 174 (1998).

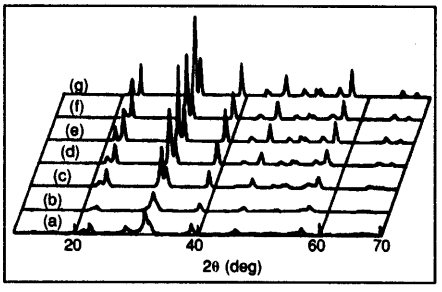

XRD pattern of $PbTiO_3$ powders treated at (a) 400, (b) 420, (c) 450, (d) 500, (e) 600, (f) 700 and (g) 800°C.

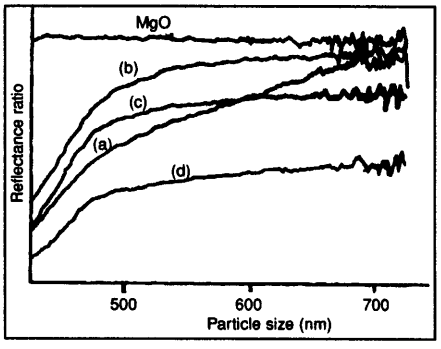

SRS curves of powders treated at (a) 400, (b) 420, (c) 450 and (d) 500°C.

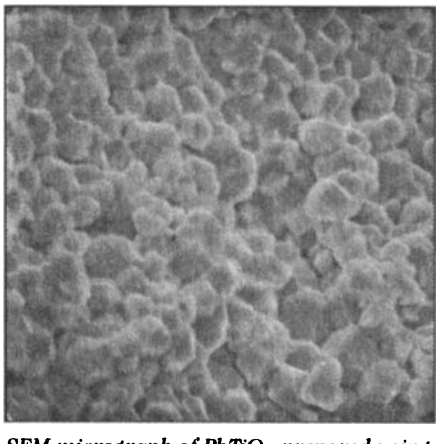

SEM micrograph of $PbTiO_3$ prepared using new sol–gel method.

Exciting new applications are being discovered for nanosized materials that are produced by the electroexplosion of wire.

Nanosized Alumina Fibers

Frederick Tepper
Argonide Corp.,
Sanford, Fla.

Marat Lerner
Design Technology Center,
Russian Academy of Sciences,
Tomsk, Russia

David Ginley
National Renewable Energy Laboratory,
Golden, Colo.

The growth of nanotechnology is being accompanied by a widening of processes for producing ceramic and metallic nanopowders. We produce nanosized metal powders by the electroexplosion of wire (EEW). Wire is fed into an argon-filled reactor, and it is subjected to a high-current, high-voltage microsecond pulse to cause it to explode.

The metal clusters that are formed are collected and either immersed into a hydrocarbon liquid (hexane, kerosene or mineral oil), passivated with a unimolecular organic film or coated with an oxide veneer. Any elemental metal or alloy that is available in the form of ductile wire can be used as a feed material.

The process can be modified to produce metal oxides or nitrides by explosion of the wire in an active gas. We have produced 15 different metals, several oxides and aluminum nitride in quantities ranging from a single kilogram to several hundred kilograms in the case of aluminum metal.

The principal current uses for the nanometals include:

- Nano-aluminum (Alex®) that is used in rocket propellants, pyrotechnics and explosives;
- Nano-copper that is used in thick-film pastes; and
- Nano-copper that is used as a lubricant additive.

Materials with aspect ratios other than spherical (fiber, flake, etc.) and with dimensions of microns and greater are used for a variety of purposes but mostly for reinforcement of polymeric, metallic and ceramic matrices. Until now, and with the possible exception of fullerenes, such forms with nanodimensions have not been available other than in laboratory quantities.

Formulation and Characterization of Nano-alumina Fibers

We now produce (in kilogram quantities) discontinuous alumina fibers (whiskers) ~2–4 nm in diameter and aspect ratios in the tens to hundreds. This form of alumina currently is produced using two process versions. Both versions result in fibers that are relatively comparable in diameter (~2–4 nm) and appear to have aspect ratios greater than ~20, although many of the fibers are hundreds of nanometers long. To put this into dimensional perspective, the fibers seem to be about the size of or smaller than DNA molecules and carbon tubes.

The fibers are produced by a sol–gel process variation, with subsequent heat treatment to a cut-off temperature. Version A has been developed to maximize surface area (450–600 m^2/g), using heat treatment to 300°C. Version B results in a lesser surface area, using a heat treatment to 450°C.

XRD results show that version A is a mixture of aluminum hydroxide and boehmite (AlOOH), and that version B is amorphous alumina. FTIR data confirm that version A contains hydroxide and that version B is principally devoid of combined water. Version B seems to be less agglomerated, although artifacts in focusing could have caused the opaque regions observed in electron micrographs of version A.

Our studies are now directed at determination of the chemistry and crystallographic structure that results during heat treatment up to ~1200°C. We do not know whether there is a distinction between versions A and B after this level of heat treatment, but we hope to answer this question through ongoing R&D.

Applications

The unusual (and unexpected) fibrous nature of nanosized alumina suggests many important applications.

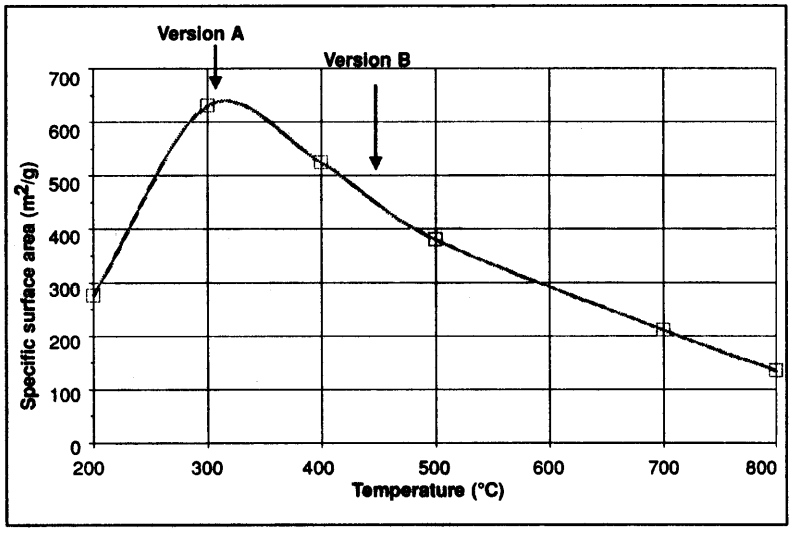

Specific surface area of nano-alumina fibers.

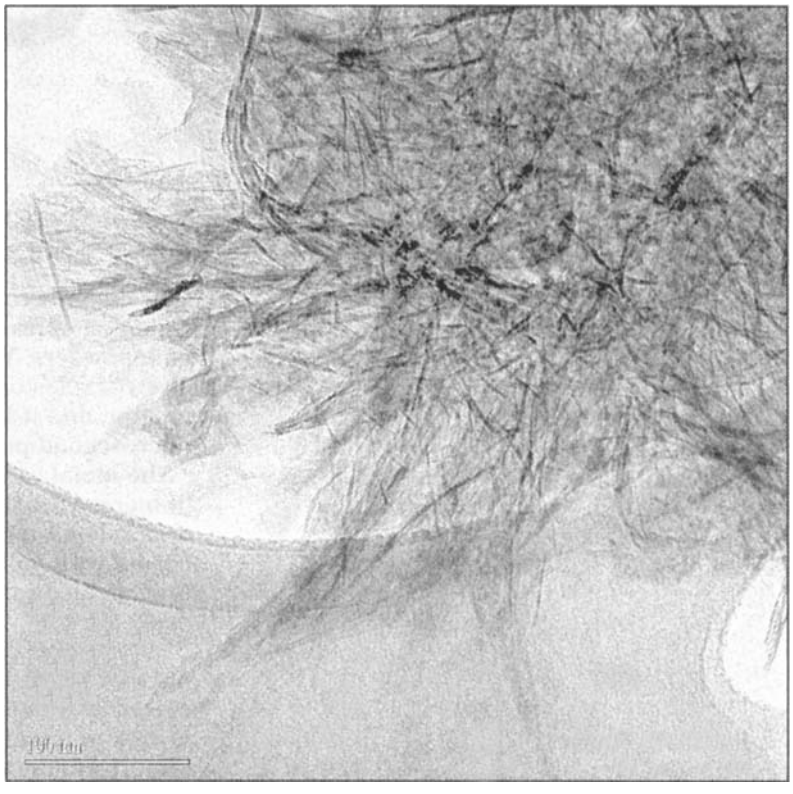

TEM micrograph of nano-alumina fibers (version A). Note absence of particles. The scale is 100 nm long.

Ceramic Substrates, Ceramic Filters and Membranes. Nanosized particles are known for their ability to sinter at temperatures far lower those of micron-sized particles. This suggests their use as sintering aids. When the fibers are heated from ~400 to 900°C, they lose ~75% of their surface area, suggesting that the sintering process is well underway.

Preforms containing the fibers can be made by mulching and filtering them through a cellulose ultrafilter. The green strength

of such mats is sufficient for handling and subsequent sintering, even without an organic binder. Green strength and green density also can be improved by cold pressing the mat. We plan to develop data on pressureless sintering of such fibrous mats, with the intent of using them as an ultrafilter, gas-separating membrane and electronic substrate.

Alumina is used as a substrate for hybrid circuits. Another application is in low-temperature, cofired ceramic multilayer circuits (LTCC), where up to eight layers of gold conductor circuit are arranged between alumina layers formed from flexible, cofired ceramic tape.

Copper is a preferred conductor, but it has not yet been adapted for LTCC use, partly because the cofired firing temperature is too high. Decreasing the sintering temperature of cofired ceramic tape by including alumina nanofibers and minimizing or eliminating the organic binders in the tape might allow copper to be used.

The interstices (pores) produced by cold pressing these fibers are likely to be less than ~10 nm. Subsequent sintering would shrink such pores further and provide some structural rigidity to the ceramic member. The net result would be membranes with pores smaller than ~5 nm, which would be effective for filtering viruses (70–1000 nm in diameter) and bacteria. Further sintering could produce open pore structures <2 nm, making these membranes potential gas separators.

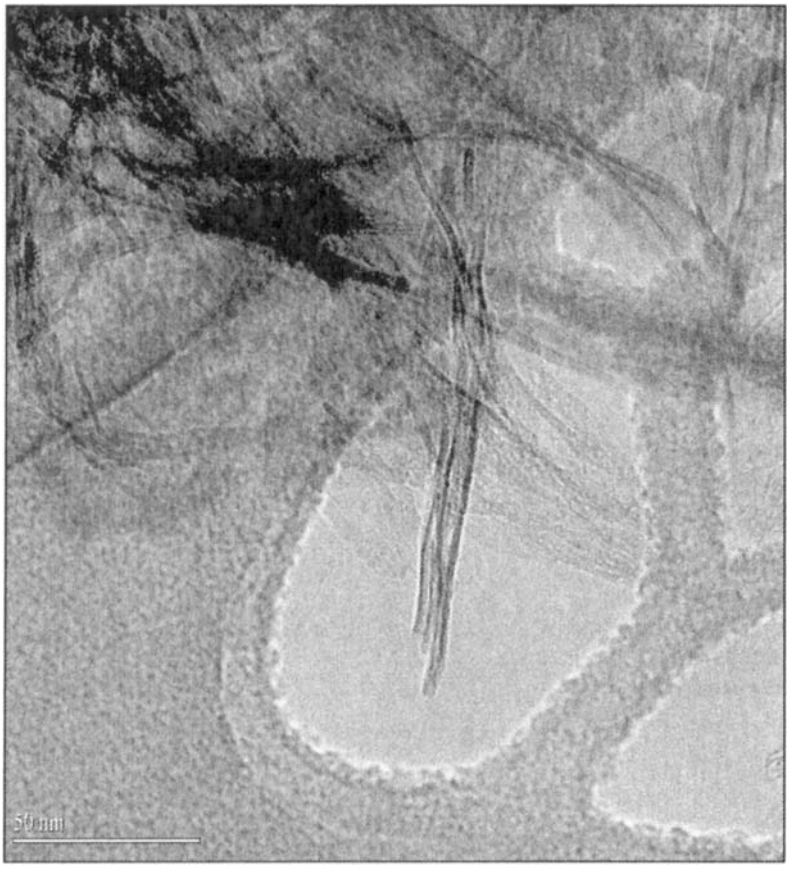

TEM micrograph of nano-alumina fibers (version A). Note fibers in focus in the lower foreground. The scale is 50 nm long.

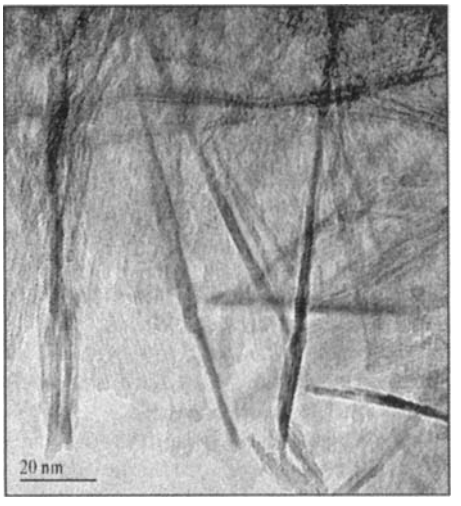

TEM micrograph of nano-alumina fibers (version B). Note fibers in focus in the lower foreground. The scale is 20 nm long.

TEM micrograph of nano-alumina fibers (version B). Note absence of particles. The scale is 100 nm long.

Strengthening of Composites. Ceramic fibers can be used for reinforcing composites where the matrix is a ceramic (CMCs), metal (MMCs) or plastic. Conventional wisdom suggests that smaller-diameter fibers have a greater strengthening benefit than larger-diameter fibers. However, using these fibers in CMCs is problematic, because alumina fibers have poor creep resistance.

Moreover, alumina fibers are likely to dissolve into the solid matrix during firing. Dispersing fibers into metallic matrices also is expected to be difficult. However, many of these forming problems might be circumvented in the case of plastic matrices.

Catalysis. Alumina is used as a catalyst and, preferably, as a catalyst substrate. The high surface area and unusual chemisorption properties of the alumina fibers suggest that they might be more catalytically active than conventional alumina.

Chemisorption of Metals. Alumina fibers are good absorbents for removal of trace metal ions from water. The absorption kinetics is rapid in removing heavy metals from an influent concentration of ppm to an effluent concentration of ppb. The sorbent can be regenerated by back-washing with mild acid or base. Applications of chemisorpton include filtration of hazardous plating wastes.

Biological and Biomedical. Version A alumina fibers are biologically active as an effective platform for the growth of bacteria and animal cells. Bacteria are effectively filtered from water and thrive on the fibers. Version B alumina fibers have yet to be evaluated in that regard.

Nanoceramic and Nanometal. Composites of nanofibers and our nanometals might lead to novel high-tensile-strength structures and surface coatings.

Nanocopper can be sintered to fully dense, low electrical resistivity (~2 mW·cm), thick films at 500°C. The potential for combining low-sintering-temperature substrates using nanofibers with low-temperature sintering of nanocopper might produce a low-cost and highly effective LTCC process.

Argonide—History and Capability

Argonide was founded in 1994 to commercialize materials technologies developed in the former Soviet Union.

The practice of exploding wire began in 1774. In the 1970s, a group in Tomsk innovated the EEW process by exploding wire in inert- or hydrogen-gas atmospheres within a chamber. In the mid 1990s, Argonide invested in this technology in exchange for exclusive sales and manufacturing rights.

In 2000, the U.S. Department of Energy provided additional funds to support this project. The project involves three U.S. National Laboratories—National Renewable Energy Laboratory (NREL), Los Alamos National Laboratory and Kansas City Operations. Our nanopowders have received *R&D Magazine's* "Best 100 New Products" award for 2000.

Approximately 60 Russian scientists are involved in nanometal R&D. Recently, the R&D effort was increased to focus on nanoceramics and, in particular, ceramic fibers. NREL provides analytical and electron microscopy support for some of the characterization studies.

Argonide's internal R&D program complements the Russian effort. We also have received SBIR awards, including a NASA Phase 2 Study on nano-aluminum as an additive and accelerant for kerosene rocket fuel.

Nanometals and nanofibers are stocked in kilogram quantities. Powders are produced in either Tomsk or Florida. The process that had been semicontinuous is now being modified for continuous operation, where wire is fed externally and powders are withdrawn on a continuous basis. ■

A New Flame Process for Producing Nanopowders

Nanophase powders (<100 nm, i.e., 0.1 μm) offer a number of interesting and attractive properties that differ from those associated with larger particles. The market for these powders is growing rapidly.

G. S. Tompa and G. Skandan
Nanopowder Enterprises Inc.
Piscataway, N.J.

N. Glumac and B. H. Kear
Rutgers University
Piscataway, N.J.

The market for nanopowders has increased dramatically in recent years with the growth of applications in the cosmetics and chemical mechanical polishing (CMP) industries. Other applications include luminescent materials, chemical gas sensors, multilayer ceramic capacitors and heat transfer fluids.

Since established technologies are beginning to use nanopowders instead of coarser particles, the market is growing rapidly. New applications are evolving that exploit the unique properties of these materials.

Processing Technology

A number of nanopowder processing technologies have evolved over the past two decades, including wet chemical synthesis, spray pyrolysis, sol-gel processing and vapor phase condensation. Commercial high-quality nanopowder production has focused on two techniques—precipitation from liquid solution and dry vapor phase condensation.

In order to produce loosely agglomerated particles, wet chemical processes generally require the use of a surface coating. In some applications, the coating may be a desirable feature. For most applications, however, a coating complicates subsequent processing because the coating becomes a processing contaminant.

A major step in the forming of loosely agglomerated particles is the introduction of the inert gas condensation (IGC) process. This process utilizes evaporation in a low-pressure atmosphere.

The next innovation came about through scaled commercial processes, where methods for achieving high evaporation rates were developed.

In addressing the challenge of high-rate production of nanopowders, chemical precursors were used as starting material, and a combustion flame provided the thermochemical energy required to pyrolyze the precursors. Specifically, the authors have invented and patented a low-pressure chemical vapor condensation (CVC) process that lends itself to large-scale production. The powders are sold under the trade name Nanomyte™.

In the combustion flame-chemical vapor condensation (CF-CVC) process, a stable flat flame is generated by burning a fuel/oxygen mixture at low pressure. Chemical precursors, introduced along with combustibles, experience rapid thermal decomposition in the hot zone of the flame.

Since the temperature profile, gas phase residence time and precursor concentration are uniform across the entire surface of the burner, the effect is to generate a beam of essentially monodispersed nanoparticles. Pyrolysis occurs in the thin combustion layer.

Clusters are formed and nanoparticles condense as the temperature of the gas falls sharply. These unique conditions are achievable only in the low-pressure flat flame and enable fully pyrolyzed nanoparticles to be produced with a narrow particle size distribution.

It should be noted that, unlike the physical

evaporation process that requires several kilowatts of power per individual evaporation station, the CF-CVC process is energy efficient, requiring no high power source.

CF-CVC Modeling

A key to the successful development of the CF-CVC process is detailed prior modeling not only of the combustion region but also the whole assembly. Several process parameters affect the controlled formation of a narrow distribution of nonagglomerated particles.

In-situ laser diagnostics and computer simulation of the process has allowed each of these issues to be addressed. Scaling methodologies have been developed and implemented that have consistently and predictably scaled the production rate. The key to the process is uniformity in all of these parameters at all locations across the entire surface of the burner.

Particle Collection

The process of collecting nanoparticles is straightforward. It draws upon pre-existing technology and an advantageous thermodynamic attribute of nanoparticles that are dispersed in a low-pressure gas. A nanoparticle suspended in a gas stream is thermodynamically driven away from a hot surface by a natural process called thermophoresis.

Fortunately, this same thermophoretic process also drives nanoparticles to a cold surface. By properly designing the reactors and maintaining the required temperature gradients, the particles can be driven from the hot burners to the cold reactor wall where they are simply scraped off into a hopper.

Materials Produced

One of the main advantages of the CF-CVC production route is that there are many economical precursors for oxide nanoparticle production that are gaseous or can be transported as vapors into the combustion region. Furthermore, since several reactant sources can be networked together to flow into the burner, the process can produce nanocomposite powders.

The net effect is a simple, versatile low-cost production technology for any oxide whose components have chemical precursors that can be vaporized. The CF-CVC process has been used to produce an array of oxide powders.

Nanomyte™ Oxides Routinely Produced by Combustion Flame	
SiO_2	SrO
Al_2O_3	$BaTiO_3$
TiO_2	ZnO
SnO_2	CuO
Y_2O_3	

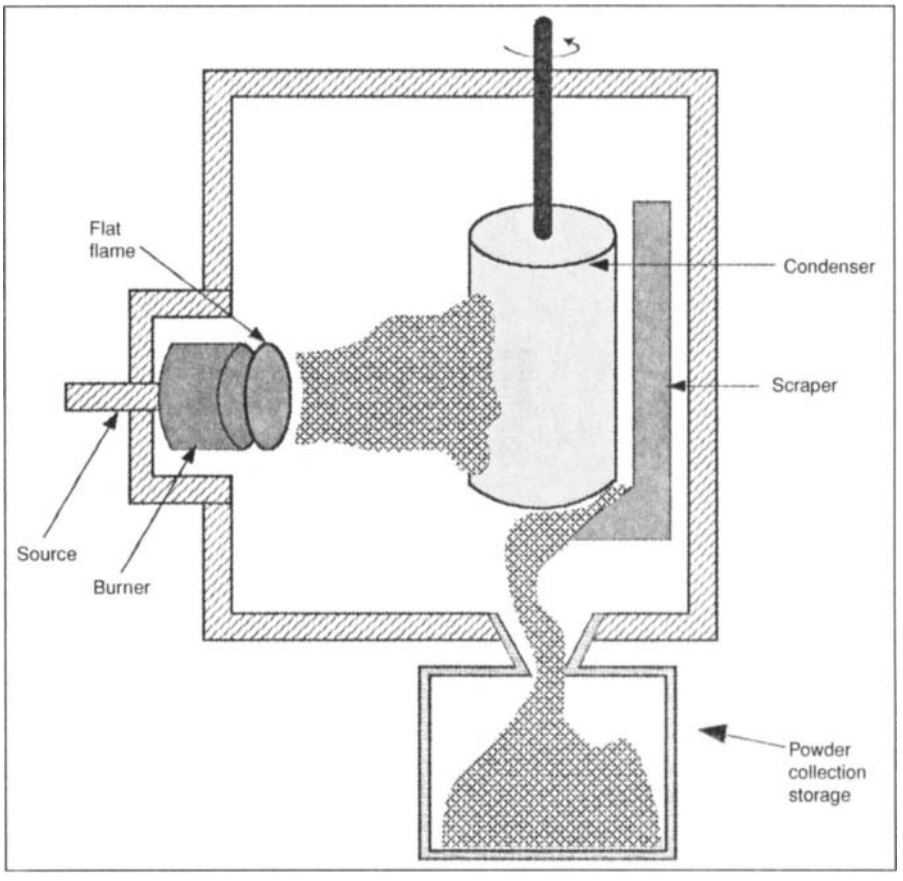

Schematic of the combustion flame-chemical vapor condensation (CF-CVC) process.

High-Purity Process

No process-related contaminants are introduced during the process. All chemical reactions occur in the gas phase, thus eliminating the possibility of incorporating contaminants.

Reaction byproducts are volatile and pumped away as part of the exhaust. The flame temperature and residence time are optimized to allow complete pyrolysis of the precursor species so that no residue from the precursor is entrained in the nanoparticles.

Process Efficiency

The combustion flame method of powder production is an efficient process with theoretical efficiencies approaching 100%. This is because the entire precursor delivered into the combustion zone is pyrolyzed and condensed into nanoparticles. In addition, the reactor design allows all the powder to be collected.

The simple system configuration readily lends itself to computer control, further ensuring that the system is continuously operating in an optimized state. In practice, the efficiency is ~95%.

Size and Agglomeration

The mean particle size can easily be controlled within a range of 3–75 nm by varying parameters (e.g., flame temperature, the rate at which precursor is

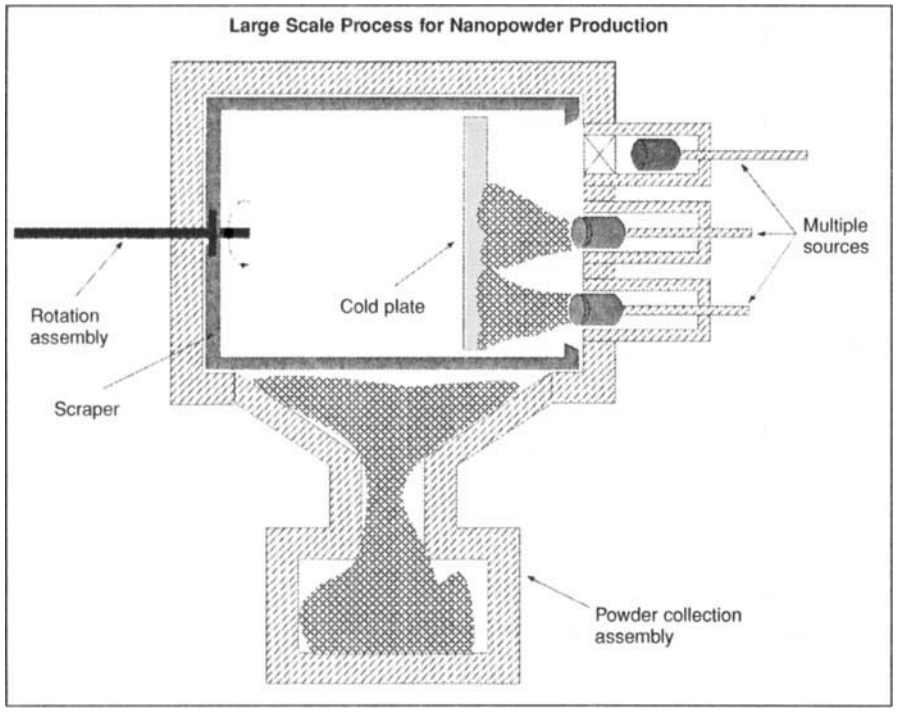

Schematic of a production tool utilizing multiple burners that can be independently cycled on or off line, thereby maintaining maximum yield.

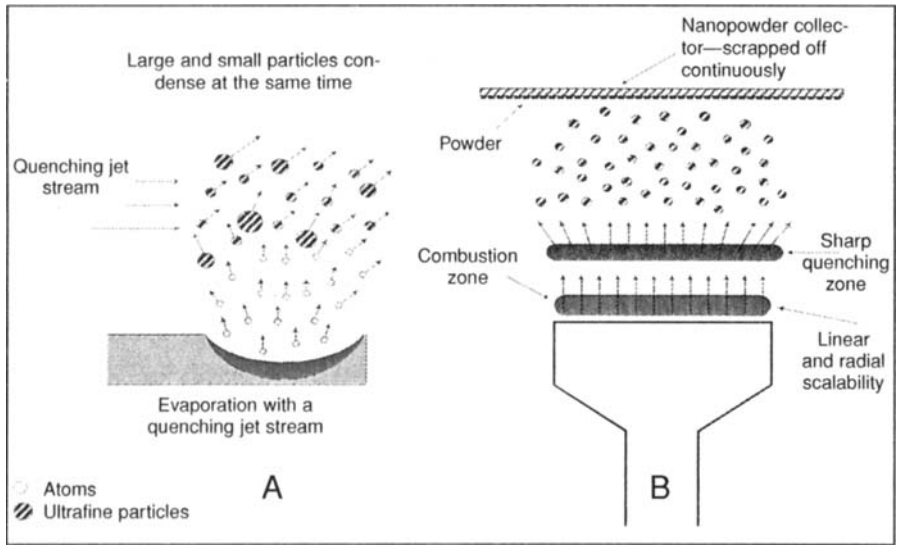

Comparison of particle formation mechanisms in: A) thermal evaporation and B) CF-CVC processes. The linearity of the flat flame leads to a narrow particle size distribution.

NEI Nanoparticle Attributes and Applications

Attribute	Application
Narrow particle size distribution	Ultra-smooth, scratch-free surfaces in chemical mechanical polishing (CMP)
High surface area	Chemical gas sensors, catalysts, purifiers
Low temperature sinterability	Ultrafine grain size in sintered products
Small particle size	Maximize UV-scattering
Loosely agglomerated	Functional fillers in a polymeric matrix; high suspension fluids

delivered to the combustion zone and pressure in the chamber). Nanopowder Enterprises Inc.'s (NEI) efforts, however, are focused on the ≤20-nm range. These parameters have been optimized using sophisticated on-line diagnostics and process modeling.

For a given particle size, the concentration of precursor in the gas phase, flow rates and chamber pressure are adjusted to maximize particle formation while minimizing formed particle collisions. The rarefied atmosphere, combined with the rapid quenching of the process, minimizes particle agglomeration.

All of the nanoparticles follow the same reaction pathway with the same residence time across the entire combustion reaction zone. They all grow to the same size and are then quenched simultaneously. These process attributes lead to nanoparticles that have a narrow particle size distribution.

Scaling

Unlike the thermally intense evaporation method of producing oxide nanoparticles, the NEI process is easily scaled while maintaining uniformity and narrow size distribution.

Any thermally driven evaporation process will have a hot zone. The only way to expand this zone is to add heat. Adding heat uniformly is difficult.

Additionally, a vapor concentration gradient develops from the hottest point outward. Adding a particle-quenching gaseous jet stream helps only slightly.

In the flat-flame configuration, there is perfect lateral symmetry. Moving horizontally, all reactions see exactly the same chemistry.

Moving outward from the face of the burner, the process proceeds in three steps:

- The reactants pyrolyze while traversing the combustion zone a few mm thick, starting a few mm from the burner surface. (Once through the combustion layer, no further heat is added to the now condensing particles.)
- Particles quench as they condense and begin to disperse in the expanding and cooling combustion flow.
- Finally, nonagglomerated nano-

particles collect on a moving cold finger or on the reactor wall.

The beauty of the process is that a flat burner is naturally scaleable in a linear or radial fashion. In fact, scaling rules are simple. Essentially, one need only to maintain a constant flux over ever-increasing areas. Linear or radial scaling has an additional benefit—it lessens the effect of the flame edge on size distribution. To date, NEI has successfully scaled its burner to five times its original size.

For practical purposes, it is desirable to achieve a balance between the size and number of burners in a given system, as well as the number of systems. Large-scale production, using 20 or 50 small systems, is not economical.

Although an optimum number of systems is somewhat arbitrary, NEI has determined that using four reasonably sized (burners less than two times the present size) and a few operational burners at a time is sufficient to produce ~100 kg per day.

It is important to note that required gas flows for further scaling or use of multiple burners is well within the range of commercially-available pumping systems.

Production Costs

An analysis of present and projected costs has been made for CF-CVC production of nanoparticles along with projected scaling of the process. Conservative assumptions for large-scale production of the technology were made based upon demonstrated results. All estimated costs and production volumes were standardized to what could be produced if the system(s) were operated three shifts a day, two hundred days a year and amortized over a five-year period.

Previous time periods are a matter of record. From 1994–96, research dollars were spent on the development of CVC technology at Rutgers University. The authors are co-inventors of the technology and NEI has exclusive worldwide rights to the technology. From 1996–97, invested contract funds were extrapolated for a three-shift operation. From 1997–98, contract funding was used as the cost base with an extrapolation to include the cost of three-shift operation.

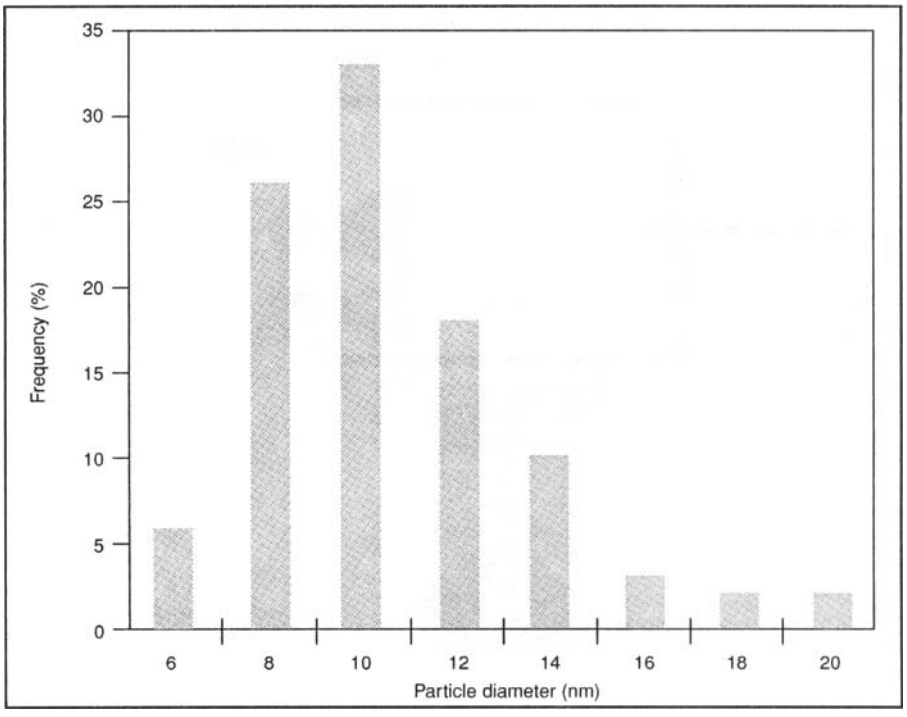

A typical particle size distribution for Nanomyte™ TiO_2.

Cost estimates for pilot production (1998–99) and full-scale production (1999–2001) include:

- Minimal scaling of burner dimensions (1.6 times the present size);
- Multiple burners per system;
- Use of multiple systems;
- Amortization of system costs;
- Modest improvements in up-time (<25%);
- Utilization of semi-automated reactors;
- Use of technician operators;
- Quoted volume discounts on precursors;
- Appropriate facility/overhead costing.

There is a dramatic decrease in price with quantity of material produced. As in all large-scale chemical processes, the equipment and operations overhead reduces to pennies per gram of material processed. The key factor, then, is the cost of the starting precursor materials. If the starting precursor cost is $0.02 per gram, then, in quantity, the process will add at most $0.02 per gram—a relatively small factor.

Finally, the authors believe their estimation process has been conservative enough that when actual scaling is carried out, additional operations overhead will be further reduced. This will lessen the projected cost to tens of dollars per kilogram.

Applications

Nanocrystalline materials offer a high surface or interfacial area and exhibit dramatic changes in properties:

- Enhanced sinterability at low temperature;
- Improved UV scattering;
- High hardness and wear resistance;
- Enhanced gas sensitivity;
- Smaller particle size in colloidal suspensions (allowing higher concentrations);
- Superior magnetic or dielectric strength;
- Enhanced optoelectronic properties.

Nanoparticles are ideally suited to forming slurries for CMP planarization and to forming base particles for sunscreens, other cosmetic applications, suspensions for heat transfer fluids and coatings (dip coatings or electrolytic processes).

They also are suited to forming bulk structures in applications (e.g., high-performance cutting tools, high surface area supports for catalysts, heat sinks and chemical gas sensors).

Each of these applications has specific powder requirements in terms of chemical composition, morphology,

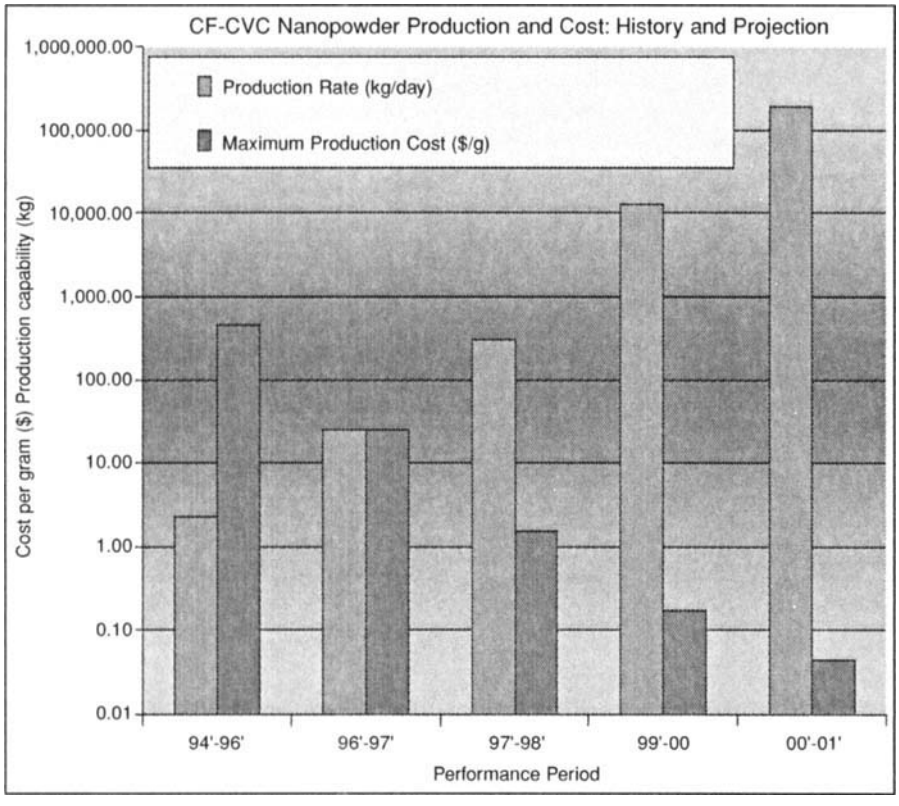

Scaling of powder production and corresponding reduction in cost.

NEI's Nanopowders

Example Industries

Aerospace	Automotive	Chemical	Consumer goods
Energy	Electrical	Medical	Optical
Catalyst	Cutting tool	Display	Electronics

Example Industries

Electonic Cu	IR Window Al_2O_3	Sensor SnO_2	Catalyst host Al_2O_3
Phosphor Y_2O_3:Eu	Abrasive Al_2O_3, SiO_2	Cosmetic TiO_2	Dielectric $BaTiO_3$

Typical Contamination Levels Formed in Nanomyte™ SiO_2

Element	Amount (ppm)	Element	Amount (ppm)
Calcium	<10	Manganese	<1
Cadmium	<1	Molybdenum	<10
Chromium	<2	Nickel	<2
Cobalt	<2	Potassium	63
Copper	11	Sodium	<10
Iron	4.9	Vanadium	<10
Lead	<5	Zinc	<2
Magnesium	<10	Zirconium	<16

crystallinity, extent of agglomeration, etc. NEI's technology is catering to all of these markets. ■

Acknowledgments

NEI greatly appreciates initial support from ONR and ongoing funding from BMDO and DoE.

Bibliography

H. Gleiter, *Progress in Mat. Sci.*, **33** 4 (1990).

Q. Ford, *Ceramic Industry*, **31** (1998).

G. Skandan, B. H. Kear, W. Chang and H. Hahn, U.S. Patent No. 5,514,350.

W. Chang, G. Skandan, H. Hahn, S. C. Danforth and B. H. Kear, *Nanostructured Mat.*, **4** 507 (1994).

J. J. Wu and R. C. Flagan, *J. Appl. Phys.*, **61** [4] 1365 (1987).

This page intentionally left blank

Journal of the American Ceramic Society

This page intentionally left blank

journal

Structure and Properties of Advanced Nitrides and Electronic Nitrides

J. Am. Ceram. Soc., 85 [1] 105–108 (2002)

Carbon Nitride-Related Nanomaterials from Chemical Vapor Deposition: Structure and Properties

E. G. Wang

Institute of Physics and International Center for Quantum Structures, Chinese Academy of Sciences, Beijing 100080, China

Nanoscale-sized carbon nitride-related materials exhibit a wealth of interesting structural, electronic, and optical property behaviors. Chemical vapor deposition technology allows almost unlimited freedom to produce films with compositions and structures approaching the nanometer scale among light elements. Aligned polymerized carbon nitride (CN) nanobells have been grown on a large scale and provide excellent field electron emission properties, as described by a side-emission mechanism. Separation of single CN nanobells and fabrication of heterojunctions between CN nanobells and pure carbon nanotubes have been achieved. Boron carbonitride (BCN) nanofibers with controlled orientation and composition have been synthesized; these nanofibers show strong blue-violet photoluminescense at room temperature. Recent progress also has been made on nitrogen-containing diamond, CN, and BCN films. The purpose of this paper is to survey the work that has been conducted and to detail the level of understanding that has been attained in the research on nitride-related materials.

I. Introduction

For more than ten years, a large amount of work worldwide has been directed toward obtaining an understanding of the new, covalently bonded nanomaterials made from nitrogen and other light elements, because of their novel microstructures and extraordinary combination of physical and chemical properties.[1–3] One example of such nanomaterials is carbon nitride (CN), which should have high hardness and toughness, oxidation resistance, chemical stability, high adherence, and high thermal conductivity. In addition, because of the structural similarity between graphite and *h*-BN, solid solutions of boron carbonitride (BCN) with a graphite-like structure have been proposed and prepared.[4] Theoretical calculation and experimental study indicate that the BCN compounds possess semiconducting properties intermediate between those of semimetallic graphite and insulating *h*-BN.[5,6] The importance of this phenomenon is that the electric properties of BCN compounds can be controlled by varying the atomic composition and atomic arrangement of the compounds.[7] The synthesis and characterization of CN and BCN nanotubes have also attracted considerable attention.[8–13] This paper describes recent progress on the study of nitride-related nanomaterials prepared by chemical vapor deposition (CVD).

I. Tanaka—contributing editor

Manuscript No. 187822. Received March 28, 2001; approved September 6, 2001.
Supported by the Chinese Academy of Sciences, the Chinese Natural Science Foundation, and the National Key Project on Basic Research (G2000067103).
Presented at Symposium A4, "Structure and Properties of Advanced Nitrides and Electronic Nitrides," at the 103rd Annual Meeting of the American Ceramic Society, Indianapolis, IN, April 22–25, 2001.

II. Polymerized Carbon Nitride Nanobells

Carbon nanotubes were first studied by Iijima[14] in 1991. However, for practical applications, a uniformly doped nanotube remains a challenge. Polymerized CN nanobells (CN-NBs) are prepared from methane and nitrogen source gases by microwave plasma (MWP) CVD.[8] Mesoporous silica plates containing catalytic iron and nickel nanoparticles are used as substrates, because these nanoparticles are essential for both the initial nucleation and the subsequent growth of carbon nanotubes. The X-ray photoelectron spectra of the specimens indicate covalently bonded C–N, resulting from nitrogen doping into the carbon network. The C 1*s* spectrum presents a main peak at 285.4 eV and a distinct shoulder at 286.9 eV. The first peak is characteristic of graphitic carbon, and the second peak indicates that the carbon atoms are bonded by nitrogen. The N 1*s* peak is located at 400.9 eV, which confirms the presence of nitrogen atoms in a graphite-like structure.[15] The presence of nitrogen in individual nanotubes is also detected by spatially resolved electron energy loss spectroscopy (EELS), and a level of nitrogen doping as high as 10% is found. EELS experiments are performed on a dedicated scanning transmission electron microscope (Model VG-HB501, VG Microscopes, West Sussex, U.K.), operating at 100 kV, with a probe <1 nm in diameter, which allows chemical analysis on a nanometer scale.

High-resolution transmission electron microscopy (HRTEM) images reveal that the CN nanotubes are linearly polymerized nanobells with one end closed by a hemifullerence cap and the other left open (Fig. 1). The atomic layers in the walls of the CN-NBs are parallel to each other, with an interplanar spacing of ~0.34 nm. However, unlike the diameter of a carbon nanotube, that of a nanobell increases continuously from the top to the bottom; i.e., no part of the walls is parallel to the axis of the nanobell. The formation of such a conical structure probably results from an excess of pentagons near the upper (or closed) end of the bell, but, in addition, all of the graphitic sheets apparently stop growing when their open edges extend a certain distance from the center of the catalytic particles. Because the nanotube is built of nanobells, its outer longitudinal surface no longer terminates with a single graphitic layer, as in a normal carbon nanotube. Instead, the outside surface consists of apparently open ends of graphitic sheets. This novel surface structure undoubtedly plays a major role in determining the unusual physical properties of these nanobells.

The typical field electron emission characteristics, i.e., both the spatial distribution of emission sites and the total emission current–voltage (*I–V*) characteristic of the specimens, have been investigated by the transparent anode imaging technique.[16] A quite low threshold field of 1.0 V/mm is observed, which is considerably lower than the value of 1.5 V/mm from pure multiwall carbon nanotubes.[17] The highest current density detected from the specimens is ~200 mA/cm^2 for an applied field of 5–6 V/mm. The relative fluctuation from a specimen at a current density of 150 mA/cm^2 is 1.3% during a test period of 200 s, and no significant degradation of the current density is observed over 100 h. In our samples, whether before or after emission testing, neither graphite flakes nor open-top nanotubes are detected. Therefore, one of the

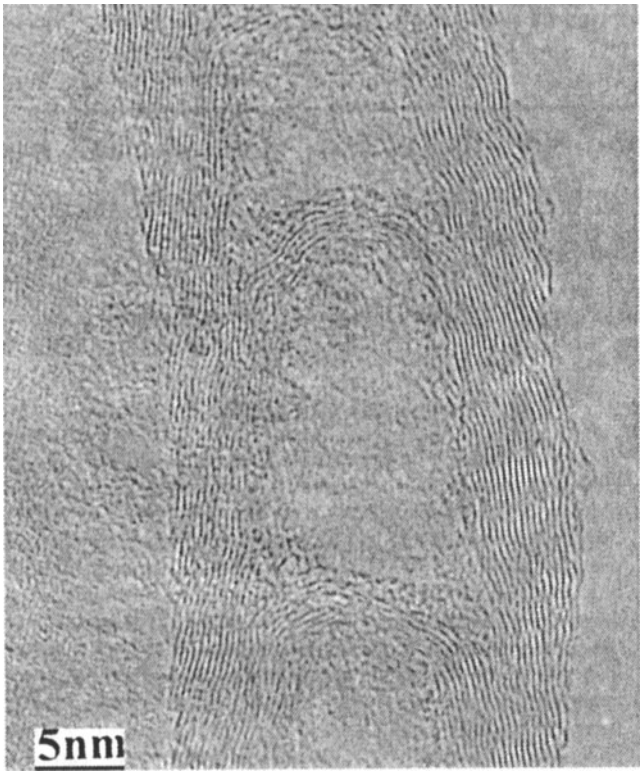

Fig. 1. Typical HRTEM image of the polymerized CN nanobells.

possible field emission mechanisms of the highest current density observed is that of electrons emitted from the sides of the nanotubes. More precisely, the emission sites appear to be the open ends of the nanobells.

Direct control of the length of carbon nanotubes on a nanometer scale is extremely difficult. Therefore, nanotubes containing polymerized nanobells are good precursors for short nanotubes. Two methods, hydrogen-gas plasma treatment followed by grinding, and oxidation with acidified potassium permanganate, have been successfully used for this purpose. The length of these very short nanotubes can be controlled to give a wide range of sizes. The shortest nanotubes are composed of only a single nanobell, measuring ~15 nm in both diameter and length. Furthermore, a heterojunction between a CN nanotube with polymerized nanobells and a pure carbon cylindrical nanotube has been synthesized by MWPCVD in a continuous growth process.[10] Because the CN tubules are thought to be metallic, whereas the carbon nanotubes are either metallic or semiconducting, such nanotube junctions may exhibit metal–metal or metal–semiconductor contact behaviors.

III. Boron Carbonitride Nanofibers

Previous studies only present some BCN nanotubes/nanofibers in random orientation, with tangly distribution and low yields, a situation that hampers both fundamental and applied studies of BCN nanotubes. Large-area, highly oriented BCN nanofibers (BCN-NFs) are first synthesized directly on polycrystalline nickel substrates by bias-assisted hot-filament (HF) CVD.[11] The diameters of the BCN tubes are in the range 50–200 nm, and the average density of the nanofibers is estimated to be $\sim 10^8/mm^2$. The orientation of the BCN-NFs can be controlled by applied negative bias.[18] Only random growth is obtained without using the bias.

HRTEM is used to determine the interior and wall structures of the BCN-NFs. The HRTEM results definitely show that the nanofiber is a multiwalled, centrally hollow tube. A distinct feature of the BCN-NFs is many small graphitic spines that stand on the surface of the fibers, making the fibers cactus-like, as shown in Fig. 2. The EELS measurements of *K*-edge absorption for boron, carbon, and nitrogen are used to determine the chemical composition of the nanofibers. Typical ionization edges are observed at ~188, 284, and 401 eV, which correspond to the characteristic *K*-shell ionization edges of boron, carbon, and nitrogen, respectively. Each core-edge fine structure consists of a sharp π^* peak and a well-resolved σ^* band characteristic of sp^2 hybridization. This conformation attests that the three atomic species are arranged in planes of graphite-like hexagonal rings.

Strong blue-violet photoluminescence (PL) from the large-scale, highly aligned BCN-NFs at room temperature is clearly observed by the naked eye. Room-temperature PL experiments are conducted using an He–Cd laser, with a wavelength, λ_{exc}, of 325 nm, as the excitation source. The laser spot on the sample is ~0.1 mm^2, with a maximum power of 25 mW. The PL peak wavelength shifts within the range 470–390 nm when the chemical composition of the nanofibers is changed. Defects in the nanofibers are unavoidable so far into the CVD process, resulting in broadened PL spectra.[12] We have also studied the field emission behavior of BCN-NFs. An emission current of 0.26 nA can be detected at an applied electric field intensity of 1.8 V/μm, regarded as the threshold electric field. A maximum emission current of 0.92 mA is obtained at an electric field of 8.6 V/μm, and the corresponding maximum emission current density is ~120 mA/cm^2.

IV. Nitrogen-Containing Diamond Films Composed of Size-Controlled Nanoparticles

Very recently, nitrogen-containing diamond films with uniform size-controlled nanoparticles have been obtained by hydrogen addition to an N_2/CH_4 precursor in MWPCVD.[19] The film microstructure, including the diamond grain size and the content of the graphite impurities, can be well controlled by the deposition parameters.[20] As the hydrogen-gas flow rate is increased, the diamond grain size increases, from 8 to 20 nm (5 sccm (standard cubic centimeters per minute) H_2), and then to 50 nm (10 sccm H_2). In the meantime, the graphite phase significantly decreases; nearly pure nanocrystalline diamond films are revealed in TEM images. In fact, with increasing hydrogen-gas concentration, the films change color significantly, from deep black to gray, and then become transparent under visible light. Thus, pure nanocrystalline diamond films with controllable grain size can be obtained by varying the hydrogen-gas concentration during growth.

X-ray diffractometry (XRD) images and Raman spectra also confirm these results. When the hydrogen-gas flow rate is increased from 0 to 10 sccm, the average diamond grain size increases from 8 to 50 nm. This value is highly consistent with that estimated from the TEM images. The evolution of the Raman

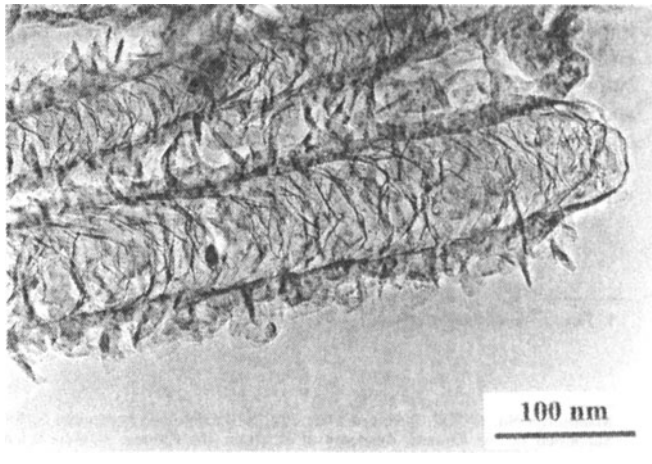

Fig. 2. Typical TEM image of BCN nanofibers, showing a cactus-like structure.

spectra with increasing hydrogen-gas flow rate is as follows: First, the relative strength of the 1332 cm^{-1} diamond peak to the graphite bands (G-band at 1560 cm^{-1} and D-band at 1350 cm^{-1}) increases significantly as the hydrogen-gas flow rate increases, which indicates that the graphite content has greatly decreased. Second, the peak at 1150 cm^{-1}, indicative of nanosized diamond crystallites, disappears in the films grown with higher hydrogen-gas concentrations, of 7.5 and 10.0 sccm. Secondary ion mass spectroscopy (Model IMS 4f, Cameca Instruments, Courbevoie Cedex, France), with 10 keV positive cesium ions, indicates that the doped nitrogen concentrations are $\sim 10^{21}$ cm^{-3} for all of the films.

To explain why nanocrystalline diamond films are easily obtained in an N_2/CH_4 environment, whereas polycrystalline diamond films usually are obtained with traditional hydrogen-gas/hydrocarbon precursors, we propose a surface stable growth model. In fact, atomic hydrogen plays two key roles in the deposition of CVD-grown diamond films. Hydrogen can selectively etch off a nondiamond phase to produce pure diamond; at the same time, the terminated hydrogen on the diamond surface also plays a role in stabilizing the diamond growing surface. Thus, with the aid of atomic hydrogen, new diamond easily forms on the existing diamond surface, leading to the easy growth of large diamond particles. Conversely, in an N_2/CH_4 environment, we believe that atomic nitrogen does not stabilize the diamond growing surface. Thus, diamond growth occurs from a new diamond seed and leads to the easy growth of nanocrystalline diamond films. When hydrogen gas is introduced to the gas mixture, the surface-stabilizing mechanism is introduced simultaneously. The amount of additional hydrogen gas determines the stability of the growing surface and, thus, the diamond grain size. At the same time, selective etching of the nondiamond phase of the atomic hydrogen results in the deposition of pure nanocrystalline diamond films.

A graphite/nanodiamond mixed-phase model has been proposed to study the field electron emission (FEE) mechanism of nanocrystalline diamond films.[19] In such a model, graphite works as a conduction channel from the back contact metal to the film surface. The diamond on the surface has a relatively low, or even negative, electron affinity. Thus, electrons first tunnel through the diamond edges and then emit from the diamond surface. Two main factors control the FEE properties under this process: (1) the diamond grain size and (2) the graphite content in the film. Because electrons from the diamond/graphite interface must tunnel through the diamond to the vacuum, the diamond grain size is a critical factor in determining the tunneling probability. When the diamond grains are large, electrons can only emit from regions close to the edge, which must be thin enough for electrons to tunnel through. On the other hand, when the diamond grains are small, electrons can effectively emit from the larger area or even from whole diamond particles, greatly increasing the emission site density. The graphite content is another critical factor, because emission occurs from the diamond/graphite interface. When the graphite content is high enough to fill the gaps between the diamond grains, decreasing the graphite content increases the diamond/graphite interface area and, thus, enhances electron emission. However, when the graphite content is decreased to a critical value that is not enough to fill the gaps, the diamond/graphite interface area decreases, and the field emission properties are destroyed. When the graphite phase is further decreased, it can no longer form a conducting channel through the film, and the emission properties rapidly degrade. Novel FEE properties can be obtained by optimizing the deposition parameters.

V. Carbon Nitride Films

Ever since the theoretical prediction by Cohen[21] in 1985, tremendous experimental effort has been applied to synthesizing carbon nitrides by many of the more readily available techniques.[2] Nearly pure CN films, which are composed of α-C_3N_4, β-C_3N_4, and other unknown CN phases, have been prepared on silicon and nickel substrates.[22,23] Well-faceted nanocrystallites, consisting entirely of a CN network on nickel substrates, have been obtained in sizes from tens of nanometers to several micrometers. The experimental lattice constants[23] of α-C_3N_4 (a = 6.38 Å, c = 4.648 Å) and β-C_3N_4 (a = 6.24 Å, c = 2.36 Å) with relative N/C ratios of 1.20–1.60, on nickel, are in good agreement with *ab initio* calculations,[24,25] varying by less than 1.3% and 2.5%, respectively.

For these samples, micro-Raman spectroscopy measurements have been performed. The spectra show several sharp lines in the spectral range from 500 to 1600 cm^{-1}, which are not related to the formation of other compounds of the participating materials, but rather to the formation of C_3N_4. A comparison of the theoretically calculated vibrational densities of states with calculations made using Hookes's law enables correlation of the measured phonon features with C_3N_4 phonon modes.[26]

The successful synthesis of mixed-phase CN films has prompted us to consider the possibility of achieving a specific C_3N_4-phase film and the necessary experimental parameters of such a film. Our first attempts to control the methane concentration and to add a fraction of hydrogen were intended to reveal the influence of these parameters on the growth mechanism.[27,28] By applying a selected-growth parameter through bias-assisted HFCVD, we have obtained a group of CN films with a relatively higher concentration of the unknown CN phases. Some columns with a prismatic tetrahedron morphology are observed. Based on XRD and TEM results, the lattice parameters for the new tetragonal CN phase are determined to be a = 5.56 Å and c = 2.75 Å. The N/C ratio of the new tetrahedral phase is ~0.8–1.0, as determined by energy-dispersive X-ray (EDX) analysis.[29] A monoclinic CN structure for some relatively larger grains with irregular surface morphologies also has been identified in the CVD-grown films.[30] Combined with the TEM results, further XRD tests identify a new, monoclinic CN structure, with the lattice parameters a = 5.065 Å, b = 11.5 Å, c = 2.801 Å and β = 96°. EDX analysis shows that the N/C ratio of this new phase is 0.5–1.0.

VI. Conclusions

Covalently bonded nanomaterials from nitrogen and other light elements, including SiCN[31] and BCN[7,32] films, compose an interesting, challenging, and technologically important material system, which is important for basic research and also has potential for industrial application. Over the past decade, the physics/materials-science community has witnessed a flood of studies specifically addressing the novel formation mechanism, as well as the physical and chemical properties, of these nanomaterials. Our ever-increasing understanding of this class of systems has been greatly facilitated by the use of modern growth-and-analysis technologies and also by comparison of theoretical calculations.

Acknowledgments

It is a pleasure to thank my co-workers, especially X. D. Bai, X. C. Ma, J. Yu, Y. Chen, K. H. Wu, J. D. Guo, G. C. Xu, S. Liu, L. P. Guo, Z. Gong, W. Zhou, D. A. Jefferson, R. D. Tilley, N. S. Xu, J. Yuan, T. Werninghaus, D. R. T. Zahn, X. Jiang, and Z. L. Wang, for their contributions to this work.

References

[1]E. G. Wang, "New Development in Covalently Bonded Carbon-Nitride and Related Materials," *Adv. Mater.*, **11**, 1129 (1999).

[2](a)E. G. Wang, "Research on Carbon Nitrides," *Prog. Mater. Sci.*, **41**, 241 (1997). (b)E. G. Wang, Y. Chen, and L. P. Guo, "Synthesis and Characterization of Pure Crystalline C-N Film," *Phys. Scr.*, **T46**, 108 (1997).

[3]S. Veprek, "The Search for Novel, Superhard Materials," *J. Vac. Sci. Technol.*, **A17**, 2401 (1999).

[4]J. Yu and E. G. Wang, "Turbostratic B-C-N Film and Its Field Emitting Behavior," *Appl. Phys. Lett.*, **74**, 2948 (1999).

[5]A. Y. Liu, R. M. Wentzcovitch, and M. L. Cohen, "Atomic Arrangement and Electronic Structure of BC_2N Semiconductor," *Phys. Rev. B: Solid State*, **B39**, 1760 (1989).

[6]M. O. Watanabe, S. Itoh, T. Sasaki, and K. Mizushima, "Visible-Light-Emitting Layered BC_2N Semiconductor," *Phys. Rev. Lett.*, **77**, 187 (1996).

[7]J. Yu, E. G. Wang, and G. C. Xu, "Synthesis and Characterization of B-C-N Compounds on Molybdenum," *J. Mater. Res.*, **14**, 1137 (1999).

[8]X. C. Ma, E. G. Wang, W. Zhou, D. A. Jefferson, J. Chen, S. Deng, and N. Xu, "Polymerized Carbon Nitrogen Nanobells and Their Field Emission," *Appl. Phys. Lett.*, **75**, 3105 (1999).

[9]X. C. Ma, E. G. Wang, R. D. Tilley, D. A. Jefferson, and W. Zhou, "Size-Controlled Short Nanotubes: Growth and Formation Mechanism," *Appl. Phys. Lett.*, **77**, 4136 (2000).

[10]X. C. Ma and E. G. Wang, "CN_x/Carbon Nanotube Junctions Synthesized by Microwave Chemical Vapor Deposition," *Appl. Phys. Lett.*, **78**, 978 (2001).

[11]X. D. Bai, J. D. Guo, J. Yu, E. G. Wang, J. Yuan, and W. Zhou, "Synthesis and Field Emission Behavior of Highly Oriented Boron Carbonitride Nanofibers," *Appl. Phys. Lett.*, **76**, 2624 (2000).

[12]X. D. Bai, E. G. Wang, J. Yu, and H. Yang, "Blue-Violet PL from Large-Scale Highly Aligned BCN Nanofibers," *Appl. Phys. Lett.*, **77**, 67 (2000).

[13]J. Yu, J. Ahn, S. F. Yoon, Q. Zhong, B. Gan, K. Chew, M. B. Yu, X. D. Bai, and E. G. Wang, "Turbostratic Boron Carbonitride Films Produced by Bias-Assisted HFCVD," *Appl. Phys. Lett.*, **77**, 1949 (2000).

[14]S. Iijima, "Helical Microtubules of Graphitic Carbon," *Nature (London)*, **354**, 56 (1991).

[15]J. Casanovas, J. M. Ricart, J. Rubio, F. Illas, and J. M. JimenezMateos, "Origin of the Large N 1*s* Binding Energy in X-ray Photoelectron Spectra of Calcined Carbonaceous Materials," *J. Am. Chem. Soc.*, **118**, 8071 (1996).

[16]R. V. Latham, K. H. Bayliss, and B. M. Cox, "Spatially Correlated Breakdown Events Initiated by Field Electron Emission in Vacuum and High-Pressure SF6," *J. Phys. C: Solid State Phys.*, **19**, 219 (1986).

[17]O. M. Kuttel, O. Groening, C. Emmenegger, and L. Schlapbach, "Electron Field Emission from Phase Pure Nanotube Films Grown in a Methane/Hydrogen Plasma," *Appl. Phys. Lett.*, **73**, 2113 (1998).

[18]J. Yu, X. D. Bai, J. Ahn, S. F. Yoon, and E. G. Wang, "Highly Oriented Rich Boron B-C-N Nanotubes by Bias-Assisted Hot Filament Chemical Vapor Deposition," *Chem. Phys. Lett.*, **323**, 529 (2000).

[19]K. Wu, E. G. Wang, Z. X. Cao, Z. L. Wang, and X. Jiang, "Microstructure and Its Effect on Field Electron Emission of Uniform Size-Controlled Nanocrystalline Diamond Films," *J. Appl. Phys.*, **88**, 2967 (2000).

[20]K. Wu, E. G. Wang, J. Chen, and N. S. Xu, "Nitrogen-Incorporated Distorted Nanocrystalline Diamond Films: Structure and Field Emission Properties," *J. Vac. Sci. Technol.*, **B17**, 1059 (1999).

[21]M. L. Cohen, "Calculation of Bulk Moduli of Diamond and Zinc-Blende Solids," *Phys. Rev. B: Solid State*, **B32**, 7988 (1985).

[22]Y. Chen, L. P. Guo, F. Chen, and E. G. Wang, "Synthesis and Characterization of C_3N_4 Crystal on Silicon," *J. Phys.: Condens. Matter*, **8**, L685 (1996).

[23]Y. Chen, L. P. Guo, and E. G. Wang, "Experimental Evidence for α- and β-Phases of Pure Crystalline C_3N_4 in Films Deposited on Nickel Substrates," *Philos. Mag. Lett.*, **75**, 155 (1997).

[24]A. Y. Liu and M. L. Cohen, "Structural Properties and Electronic Structure of Low-Compressibility Materials: β-Si_3N_4 and Hypothetical β-C_3N_4," *Phys. Rev. B: Solid State*, **B41**, 10727 (1990).

[25]D. M. Teter and R. J. Hemley, "Low-Compressibility Carbon Nitrides," *Science*, **271**, 53 (1996).

[26]T. Werninghaus, D. R. Zahn, E. G. Wang, and Y. Chen, "Micro-Raman Spectroscopy Investigation of C_3N_4 Crystals Deposited on Nickel Substrates," *Diam. Relat. Mater.*, **7**, 52 (1998),

[27]Y. Chen, L. P. Guo, and E. G. Wang, "Effect on Selected-Phase Growth of Crystalline C-N Films by Controlling Nitrogen, Hydrogen, and Methane Mixture," *J. Mater. Sci. Lett.*, **16**, 594 (1997).

[28]Y. Chen, L. P. Guo, and E. G. Wang, "Effect of the Methane Concentration at the Growth of Prototypes C-N Films," *J. Cryst. Growth*, **179**, 515 (1997).

[29]L. P. Guo, Y. Chen, E. G. Wang, Z. X. Zhao, and L. Li, "Identification of a New Tetragonal C-N Phase," *J. Cryst. Growth*, **178**, 639 (1997).

[30]L. P. Guo, Y. Chen, E. G. Wang, Z. X. Zhao, and L. Li, "Identification of a New C-N Phase with Monoclinic Structure," *Chem. Phys. Lett.*, **268**, 26 (1997).

[31]Z. Gong, E. G. Wang, G. C. Xu, and Y. Chen, "Influence of Deposition Condition and Hydrogen on Amorphous-to-Polycrystalline SiCN Films," *Thin Solid Films*, **348**, 114 (1999).

[32]J. Yu and E. G. Wang, "Turbostratic B-C-N Film and Its Field Emitting Behavior," *Appl. Phys. Lett.*, **74**, 2948 (1999). □

journal

J. Am. Ceram. Soc., 85 [3] 554–64 (2002)

Effect of Ammonia Treatment on the Crystallization of Amorphous Silicon–Carbon–Nitrogen Ceramics Derived from Polymer Precursor Pyrolysis

Julin Wan,* Matthew J. Gasch,* and Amiya K. Mukherjee

Department of Chemical Engineering and Materials Science, University of California, Davis, California 95616

An effort was made toward modifying the Si_3N_4–SiC phase ratio in bulk nanocomposites obtained from polymer precursors. While pyrolyzing the polymer, flowing ammonia was introduced, to facilitate a chemical exchange, resulting in a different C/N ratio in the ceramic pyrolysis product. A prepyrolysis/binding/pyrolysis approach was used for sample consolidation. Comparison was made between the crystallization behavior of the pyrolysis-derived ceramic powders and consolidated bulk samples. A profound enhancement in crystallization tendency was observed in the consolidated samples whose nitrogen content was increased by ammonia treatment. A mechanism based on the particle/binder interface energy was proposed to account for this observation.

I. Introduction

RESEARCH into the possibility of producing three-dimensional non-oxide engineering ceramics—especially nanocomposites based on silicon nitride (Si_3N_4)—from the pyrolysis of polymer precursors has intensified over the past two decades.[1–3] The increased emphasis on this processing method comes from the possibility of obtaining consolidated covalent ceramics at lower temperature and without liquid-phase sintering, thus offering a potential way to achieve good high-temperature properties. Pyrolysis of a polymer proceeds via the destruction of the polymer macromolecular network, leaving behind an amorphous ceramic skeleton.[4,5] Two methods have been developed to make crack-free bulk ceramics from the pyrolysis of polymer precursors. One method is the compaction of cross-linked infusible polymer powders, via cold isostatic pressing (CIPing) or warm pressing, followed by pyrolysis at a slow heating rate.[3,6] This approach produces ceramics with a substantial amount of open porosity. The other approach is a hybrid method that is based on prepyrolysis and binding.[7–9] In this approach, polymer powder is pyrolyzed to an appropriate extent and, before being compacted, liquid polymer precursor is added as a binder during compaction. Using this second method, much less gas generation and volume shrinkage are observed. Furthermore, samples contain less open porosity and a larger viable material size is obtainable. Therefore, the prepyrolysis/binding method is considered to be the preferred route for the prospective industrial production of bulk covalent ceramics from polymer precursors.

The bulk amorphous ceramics can further be crystallized into silicon nitride/silicon carbide (Si_3N_4–SiC) nanocomposites. For Si_3N_4–SiC composites, the grain size, the grain-boundary conditions, and the phase ratio between Si_3N_4 and SiC are major factors that affect the properties of the material under service conditions.[10] One advantage of using a polymer precursor as the starting material is that the chemistry of the pyrolysis product—and, thus, the microstructure of the final nanocomposite—can readily be changed, using the reactions of the polymer precursor, e.g., by controlling the environment of the pyrolysis.[1,11,12] For polysilazane precursors, amorphous Si-C-N ceramics are produced if pyrolysis is performed in a nitrogen atmosphere, whereas the pyrolysis product is a binary siliconitride (Si-N) material when pyrolyzed in ammonia (NH_3). However, very little effort has been devoted to the adjustment of bulk ceramics other than powders. Galusek *et al.*[13] made an attempt to adjust the carbon content of amorphous Si-C-N bulk ceramics derived from a poly(hydridomethyl)silazane precursor. In their work, polymer powders were compacted by CIPing, and the compacts were pyrolyzed in NH_3 or NH_3/argon gas mixtures. This procedure, although proven to be effective in increasing the nitrogen content in the amorphous ceramics, produces materials with very low density (only ~2.0 g/cm^3) and a large volume of open porosity. Their sample size is also limited by the tendency of cracking of specimens due to severe gas evolution. Another intrinsic limitation of their approach is that an inhomogeneous nitrogen content is likely to result between the surface and interior of the compacted samples. Furthermore, no information about the crystallization behavior, as a result of the ammonia treatment, was provided.

In the present paper, the hybrid method of prepyrolysis and binding was used to consolidate bulk ceramics. An ammonia treatment was introduced before the compacting operation. Materials with higher density, less tendency for cracking, and equally effective chemical adjustment, in comparison with the reported results, were achieved. Heat treatment of the bulk ceramics was conducted up to temperatures above the crystallization temperature, to provide a detailed picture of the effect of ammonia treatment on the crystallization behavior of the Si-C-N ceramics.

II. Experimental Procedure

All experiments were performed with commercially available polyureasilazane precursor (Ceraset™ SN, purchased from Commodore Polymer Technologies, Columbus, OH) with the following empirical formula:

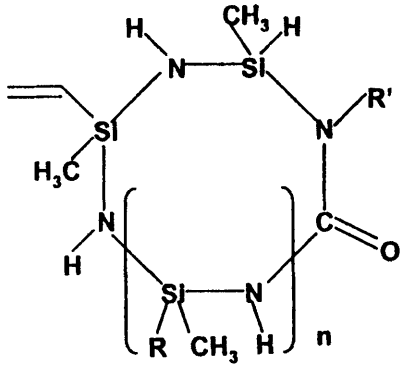

G. Grathwöhl—contributing editor

Manuscript No. 187955. Received February 12, 2001; approved August 29, 2001.
This research is sponsored by U.S. Office of Naval Research, under Grant No. N00014-00-1-0186.
*Member, American Ceramic Society.

where n = 1–20 and R = H or CH—CH_2. This polymer contains repeat units in which Si atoms are bonded in an alternating sequence to N atoms. With the addition of 0.5 wt% of dicumyl peroxide (98% pure, Aldrich Chemical Co., Inc., Milwaukee, WI) as a catalyst, the low-viscosity liquid polymer can be cross-linked to an infusible solid using hydrosilylation and vinyl polymerization.[14] The ceramic conversion rate on pyrolysis was ~75 wt% in nitrogen or argon.

The cross-linked polymer was crushed to a 200 mesh powder and subjected to ammonia treatment and a prepyrolysis nitrogen treatment. The polymer powder was placed into an alumina boat and heated at a rate of 10°C/min in a quartz tube furnace in flowing nitrogen (gas flow of 150 cm^3/min). When the predetermined ammonia treatment temperature (T_a) was attained, the flowing gas was switched from nitrogen to ammonia (150 cm^3/min), and the temperature was held at T_a for 1 h. After the ammonia treatment, the flowing gas was switched back to nitrogen and the temperature was increased to the prepyrolysis temperature (T_p). For the specimens discussed in this paper, T_a is in the range of 300°–800°C, whereas T_p is fixed at 800°C.

After the ammonia treatment and prepyrolysis, the powder was mechanically mixed with 25 wt% liquid Ceraset polymer. The mixture was placed into a stainless-steel die and degassed for 30 min under vacuum before being uniaxially pressed at 20–100 MPa into the form of pellets 12.5 mm in diameter. The pellets were further densified by CIPing at 400 MPa. Green bodies thus derived were subjected to pyrolysis in nitrogen at a pressure of 1.5 atm (~0.15 MPa), using a heating rate of 5°–25°C/h and a final pyrolysis temperature of 1450°C for 4 h.

To distinguish the effect of compacting state (powder or consolidated) on crystallization, powders with the same heat-treatment history (ammonia-treated at T_a, prepyrolyzed at T_p, and pyrolyzed at 1450°C) were subjected to the same crystallization heat treatments as the consolidated samples. Powder and consolidated specimens with the same thermal/chemical history were placed in a boron nitride (BN) crucible and heated at a rate of 10°C/min to 1550° or 1650°C for 2 h in a furnace filled with nitrogen (1.5 atm).

For comparison, polymer powders heat-treated in nitrogen were subjected to the same heat-treatment history and crystallization heat treatments as powders that had been heat-treated with ammonia. Then, Fourier transform infrared spectroscopy (FTIR) was conducted on all the powder samples, to follow the reactions that occur during the heat treatment in ammonia or nitrogen.

Powders pyrolyzed at 1450°C (with or without ammonia treatment), along with the powders after crystallization heat treatment, were analyzed via electron microprobe analysis (EPMA), to obtain semiquantitative information about the change in chemical composition. The silicon, carbon, nitrogen, and oxygen contents were analyzed; the hydrogen content was ignored here, because of its small amount (<1 wt%) in the fully pyrolyzed materials.

X-ray diffraction (XRD) analysis was conducted on both the ceramized powders and consolidated ceramics. For the consolidated ceramics, both the surface and the interior were examined via XRD. Disks 3 mm in diameter were cut from the consolidated samples and processed to create transmission electron microscopy (TEM) samples by the standard mechanical thinning, dimpling, and ion milling to perforation. Samples were also coated with a thin layer of carbon to prevent charging. TEM observations were conducted on a TEM microscope (Model CM12, Philips Research Laboratories, Eindhoven, The Netherlands) that was operated at an accelerating voltage of 100 kV.

III. Results

(1) *Fourier Transform Infrared Spectroscopy Analysis*

The FTIR spectra of the precursor powders pyrolyzed in nitrogen at different temperatures are shown in Fig. 1(a). The signals that were assignable to identified bonds were as follows: 3405 cm^{-1}, N—H stretching vibration; 2955 and 2900 cm^{-1}, C—H asymmetric and symmetric stretching; 2150 cm^{-1}, Si—H stretching; 1730 cm^{-1}, C=O stretching; 1640 cm^{-1}, C=C stretching; 1255 cm^{-1}, Si—CH_3 stretching band; and 1409 cm^{-1}, Si—CH=CH_2 deformation band.[15] The information from backbone vibrations can be obtained from the bands that are distributed and often overlap each other in the wavelength range of 800-1200 cm^{-1}. Signals from Si—NH—Si (Si—N), which exists in the original polymer network, are located at 1180 and 930 cm^{-1}.[16–19] Signals from the bond combination of Si—CH_2—Si (Si—C), which is the result of cross-linking reactions, can be found at 1035 and 800 cm^{-1}.[16,18,20] A very weak but distinct C—N stretching band was observed at 1390 cm^{-1}.[15]

As the pyrolysis temperature increased, the major events that could be observed via FTIR are the continuous decrease of the Si—H, C—H, Si—CH_3, and Si—CH=CH_2 bands. After pyrolysis at 1450°C, the Si—H band is completely eliminated. However, vibrations that correspond to N—H and even C—H still can be observed, which is indicative that hydrogen still exists within the Si-C-N ceramic network and is mostly bonded to N and C atoms rather than Si atoms. The skeletal vibrations of the Si—N and Si—C bonds completely overlap each other and form a broad band at 800–1200 cm^{-1}. The 1640 cm^{-1} band, which is assumed to be C=C stretching, persists to temperatures well above 800°C, showing higher stability of this bonding than that observed in other polymers in which the C=C bonds disappear at lower temperatures;[21] the reason for this phenomenon is not yet clear. The possibility exists that the 1640 cm^{-1} band does not correspond to the C=C stretching but, instead, corresponds to other more-stable groups, such as —C(=O)—N.[22]

After the heat treatment in ammonia (Fig. 1(b)), the Si—CH_3 band disappears at lower temperature (600°C) than when heat-treated in nitrogen (800°C). However, no bands characteristic of —NH_2 (i.e., the doublet band located at ~3400 cm^{-1})[15] were displayed by the FTIR analysis. The increase in nitrogen content due to ammonia treatment was demonstrated by the increase of the Si—NH—Si vibration at 1180 cm^{-1} in the FTIR spectra. Comparison between Figs. 1(b) and 1(a) shows that the increase in Si—NH—Si bonds is most profound at intermediate temperatures (~600°C). Also, the Si—H band disappears at lower temperature in ammonia (500°C) than when heat-treated in nitrogen (>800°C). However, when the ammonia treatment was conducted at higher temperatures (700° and 800°C, as in Fig. 1(b)), the intensity of the Si—H band increases.

(2) *Microprobe Analysis*

The chemical composition of the ammonia-treated and pyrolyzed ceramics, along with that of the samples heat-treated only in nitrogen, was characterized by EPMA; some of the results are shown in Table I. In accordance with the FTIR results, the introduction of nitrogen into the ceramics by ammonia treatment was most effective at temperatures of ~600°C. When heat-treated in ammonia at 600°C for 1 h, the carbon content can be reduced to ~50% of that in the ceramics not treated by ammonia (from ~44 at.% to ~22 at.%). Accordingly, the nitrogen content increased from ~23 at.% to 39 at.%. Both lower and higher ammonia treatment temperatures were featured by less increase in nitrogen content. The silicon content remained essentially the same, which indicates that no silicon-containing species were lost during the ammonia treatment.

EPMA also indicated a substantial amount of oxygen in the pyrolyzed ceramics. There are two sources of oxygen in the Ceraset polymer: (i) the intrinsic oxygen that is contained in the C(=O)—N groups in the original polymer network (less importantly, in the dicumyl peroxide catalyst) and (ii) the absorption of oxygen or water vapor when handled in air. Table I shows that a substantial increase in oxygen content resulted

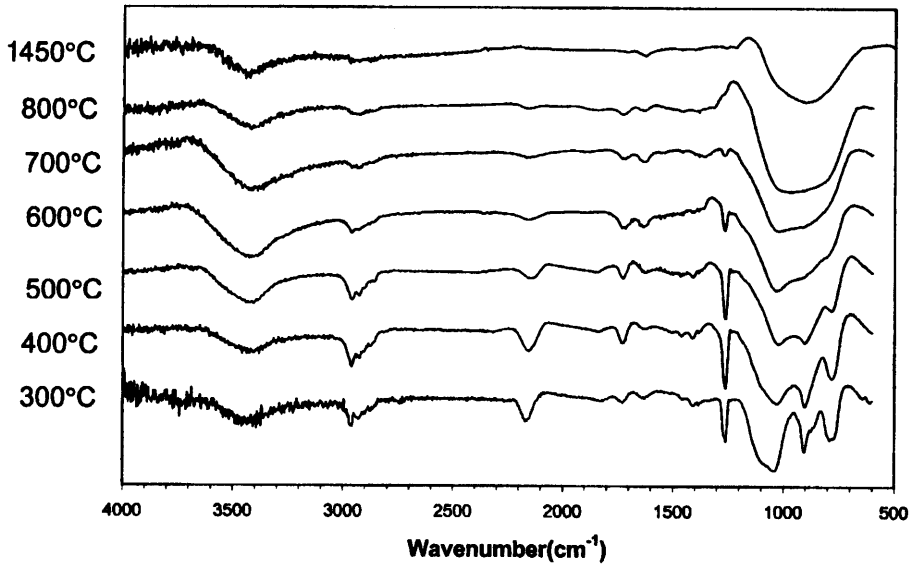

(a)

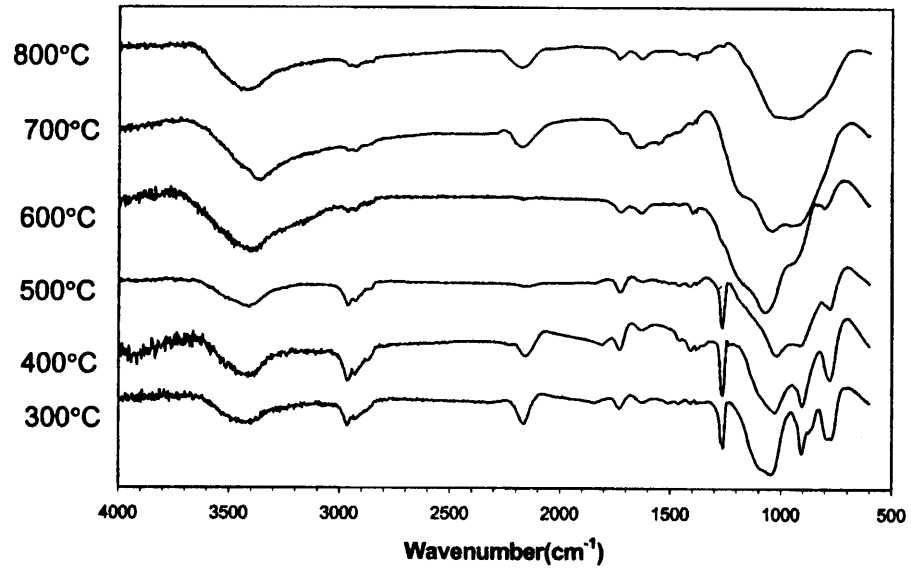

(b)

Fig. 1. FTIR spectra of the polymer precursor pyrolyzed at different temperatures ((a) in nitrogen and (b) in ammonia).

from ammonia treatment; thus, the oxygen source could be the oxygen gas impurity in the ammonia flowing gas (premium-grade, anhydrous, liquefied).

Crystallization heat treatment led to a slight decrease in nitrogen content and an increase in carbon content, because of the decomposition and release of nitrogen gas. The oxygen content was also reduced by the generation of CO and H_2O upon heat treatment at high temperatures.

(3) X-ray Diffraction Results

The crystallization of Ceraset-derived ceramics, pyrolyzed only in nitrogen, has been discussed in earlier publications.[7,8] Figures 2–4 summarize the XRD results of the powder and consolidated samples that were treated in ammonia at temperatures of 400°, 500°, and 600°C, respectively, pyrolyzed to 1450°C and crystallized at 1550° and 1650°C. Consolidated samples were analyzed both on the sample surface and inside the sample.

(A) Powder: For powder samples, ammonia treatment (i.e., difference in C/N ratio) did not seem to influence the starting temperature for crystallization. All the samples that were treated at 1450°C remained amorphous. Peaks that indicate the appearance of crystalline phases began to show up at ~1500°C. After heat treatment for 2 h at 1550°C, crystalline peaks could be observed on all the spectra, although the majority of the matrix remained amorphous. For all the powders subjected to ammonia (Figs. 2(a), 3(a), and 4(a)), most of the XRD peaks correspond to Si_3N_4. Both α- and β-Si_3N_4 were observed in the powders with the greater carbon contents (Figs. 2(a) and 3(a)), whereas for the powder with the least amount of carbon, only α-Si_3N_4 peaks are observed (Fig. 4(a)).

After heat treatment for 2 h in nitrogen at 1650°C, a high level of crystallinity is achieved, although the samples are not entirely crystalline. Interestingly, only after this high-temperature treatment does SiC start to manifest its presence in the XRD spectra and a distinct trend in regard to how the

Table I. Chemical Composition of Si-C-N Powders

Ammonia treatment	Final pyrolysis	Composition (at.%) C	N	O	Si	Nominal formula
None	1450°C/4 h/N_2	43.86	22.95	4.90	28.28	$Si_{1.00}C_{1.55}N_{0.81}O_{0.17}$
400°C/1 h	1450°C/4 h/N_2	42.66	26.77	2.99	27.58	$Si_{1.00}C_{1.55}N_{0.97}O_{0.11}$
500°C/1 h	1450°C/4 h/N_2	37.01	31.17	3.17	28.65	$Si_{1.00}C_{1.29}N_{1.09}O_{0.11}$
550°C/1 h	1450°C/4 h/N_2	24.14	38.79	9.27	27.8	$Si_{1.00}C_{0.87}N_{1.40}O_{0.33}$
600°C/1 h	1450°C/4 h/N_2	21.96	38.62	9.44	29.98	$Si_{1.00}C_{0.73}N_{1.29}O_{0.31}$
650°C/1 h	1450°C/4 h/N_2	26.53	37.67	8.75	27.05	$Si_{1.00}C_{0.98}N_{1.39}O_{0.32}$
700°C/1 h	1450°C/4 h/N_2	38.92	31.77	4.11	25.19	$Si_{1.00}C_{1.55}N_{1.26}O_{0.16}$
None	(1450°C/4 h + 1550°C/2 h)/N_2	47.22	21.25	1.29	30.24	$Si_{1.00}C_{1.56}N_{0.70}O_{0.04}$
None	(1450°C/4 h + 1650°C/2 h)/N_2	45.5	21.98	2.41	30.11	$Si_{1.00}C_{1.51}N_{0.73}O_{0.08}$
600°C/1 h	(1450°C/4 h + 1550°C/2 h)/N_2	24.27	40.38	5.93	29.42	$Si_{1.00}C_{0.82}N_{1.37}O_{0.20}$
600°C/1 h	(1450°C/4 h + 1650°C/2 h)/N_2	26.06	40.45	5.67	27.84	$Si_{1.00}C_{0.94}N_{1.45}O_{0.20}$

ammonia treatment temperature affects the Si_3N_4/SiC phase ratio becomes established. With the increase of ammonia treatment temperature from 300°C up to 600°C, the Si_3N_4 proportion increases until the only crystalline phase present, as demonstrated by XRD, is Si_3N_4. Further increases in the ammonia treatment temperature, to 700° and 800°C, decreases the proportion of Si_3N_4. Again, the powders with greater carbon content contain both α- and β-Si_3N_4, with α- Si_3N_4 having the larger proportion and seemingly larger grain size (sharper peaks). In the 600°C ammonia-treated sample (Fig. 4(a)), the crystalline phase is exclusively α-Si_3N_4.

(B) Bulk Materials: In considering the proportion of crystalline phase in the consolidated materials, one should recall that all the materials contain ~25 wt% binder in the green compacts. This binder was not subjected to ammonia treatment. If the pyrolysis of the polymer proceeds in the same way as if it were in powder form (ignoring the possible reaction between the prepyrolyzed powder and the binder, which might result in changes in chemistry and ceramic yield of the binder) after pyrolysis, the binder occupies ~18.7 wt% of a consolidated sample. The binder portions also have a greater carbon content than the ammonia-treated particles.

After heat treatment for 4 h in nitrogen at 1450°C, the 400°C ammonia-treated bulk material remains amorphous. In the 500°C ammonia-treated bulk material, however, primitive crystalline peaks begin to emerge over the amorphous background, which indicates easier crystallization in the bulk than the powder (compare Figs. 3(b) and (c) with Fig. 3(a)). The most profound difference between bulk and powder materials was observed in the 600°C ammonia-treated samples. The 1450°C/4 h powder, which was heat-treated in nitrogen, is amorphous (see Fig. 4(a)), whereas the bulk material after the same treatment is almost entirely crystalline (see Figs. 4(b) and (c)).

Increasing the heat-treatment temperature to 1550°C results in increased crystallinity in all the three types of bulk materials shown in Figs. 2–4. One distinct difference between the bulk and powder samples is noted: the peaks of bulk materials are much broader, which indicates that the grain size of the consolidated samples is smaller than that of the powders.

Heat treatment at 1650°C leads to advanced crystallinity, and, again, the grain size of the bulk materials is smaller than that of the corresponding powders; this observation is especially apparent for α-Si_3N_4. As expected, the proportion of SiC is somewhat higher in the bulk than in the powder form; this phenomenon is attributable to the greater carbon content, which is due to the existence of a binder phase in the consolidated ceramics. Interestingly, the consolidated state seems to favor the formation of β-Si_3N_4 over α-Si_3N_4. In the 400° and 500°C ammonia-treated samples, in which both α- and β-Si_3N_4 are observed in crystallized powders, the β/α ratio is obviously higher in the bulk samples (see Figs. 2(c) and 3(c)) than in the powders (see Figs. 2(a) and 3(a)). In the 600°C ammonia-treated samples, only α-Si_3N_4 was observed in the 1650°C/4 h heat-treated powder; however, both α- and β-Si_3N_4 can be observed via XRD in the consolidated sample, although α-Si_3N_4 still claims the dominant portion. A small amount of silicon oxynitride and free silicon can be observed in the 600°C ammonia-treated and consolidated samples (see Figs. 4(b) and (c)).

The XRD patterns of the surface of the consolidated samples (Figs. 2(b), 3(b), and 4(b)) resemble those obtained inside the materials (Figs. 2(c), 3(c), and 4(c)), with only a very slightly higher α-Si_3N_4 proportion, which is indicative of the homogeneity of the materials made using this processing method. This type of homogeneity cannot be achieved by treating consolidated polymer green bodies in ammonia, as attempted by Galusek *et al.*[13]

(4) Transmission Electron Microscopy

After pyrolysis, the ammonia-treated bulk samples show a structure of fully dense particles surrounded by a binder phase that contains nanometer-sized pores. This structure is typical of the hybrid prepyrolysis/binding/pyrolysis consolidation procedure, as reported elsewhere for ceramics produced using the same method without ammonia treatment.[23] An example of this structure is given in Fig. 5(a). In the green compacts, before pyrolysis, the binder phase fills the space between the prepyrolyzed particles. When the polymer is cross-linked, a liquid-phase-separation/volatile-evaporation process leaves behind a porous structure with nanometer-sized pores. In the cross-linked polymer that has no prepyrolyzed particles as filler, these nanometer-sized pores will close when pyrolyzed at 600°C; the process of pore closure is accompanied by generation of a gas phase and volume shrinkage. However, in the case of the binder-added green compact, the closing of pores and shrinkage of the binder phase is restricted by the particle phase, which has much less shrinkage during pyrolysis, because of prepyrolysis. This retarded closure of nanometer-sized pores provides escape channels for the gaseous pyrolysis products and prevents the samples from cracking, while leaving behind a porous binder phase after pyrolysis.

For the 400°C ammonia-treated, 1450°C/4 h pyrolyzed ceramics shown in Fig. 5(a), the selected-area diffraction (SAD) pattern of the particle phase (inset, Fig. 5(a)) gives essentially an amorphous pattern. Observation at higher magnification (Fig. 5(b)) shows that small SiC crystals (~5 nm), although present as a very small volume fraction, are distributed homogeneously within the particle phase. The binder phase is characterized by nanoporosity, as well as higher crystallinity and a larger grain size (~6–8 nm), in comparison to the particle phase. The crystalline phases in the binder have been characterized via SAD to be SiC and Si_3N_4. In the 600°C ammonia-treated, 1450°C/4 h pyrolyzed samples, both the particle and the binder phases are highly crystalline and the crystals are mostly α-Si_3N_4, with a grain size of ~60 nm (Fig. 6).

Heat treatment at higher temperatures (1650°C) leads to crystallization of the particle phase in the 400°C ammonia-treated specimen, as shown in Fig. 7(a). The particle phase and the binder phase both are composed of grains with an average size of ~25 nm. Although the particle phase can still be distinguished from the binder phase by their difference in porosity (the particle phase is dense, whereas the binder phase contains nanometer-sized pores), the boundary between these two phases is not visible anymore (compare Fig. 7(a) with Fig. 5(a)). The 600°C ammonia-treated sample, when subjected to a 1650°C heat treatment, has approximately the same microstructure as the 1450°C treated sample, with the exception that the grain size is larger (~80 nm) (see Fig. 7(b)). Figure 7(b) clearly shows the presence of intergranular nanopores, even in the particle phase.

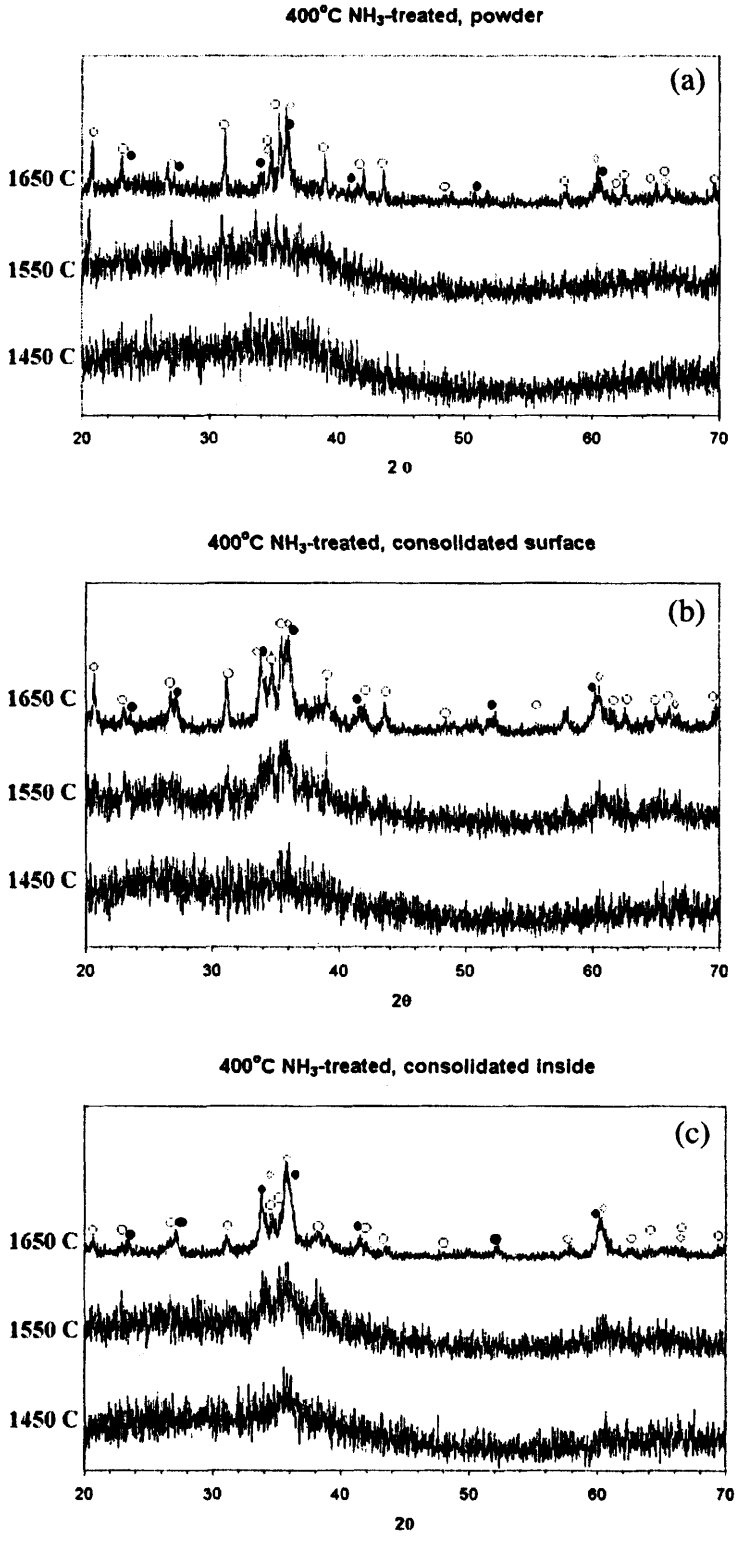

Fig. 2. XRD of (a) powder and consolidated samples ((b) surface and (c) inside), subjected to crystallization heat treatment at different temperatures in nitrogen; the powder sample, and the powder from which the consolidated samples were made, were heat-treated in ammonia for 1 h at 400°C. Legend is as follows: (○) α-Si_3N_4, (●) β-Si_3N_4, and (◇) SiC.

IV. Discussion

(1) Pyrolysis and Ammonia Treatment

Most of the carbon-containing functional groups were incorporated into the backbone of the polymer network through cross-linking reactions that involves carbon-containing functional groups and radical hydrogen (—H).[18,24,25] Upon pyrolysis in nitrogen or argon, the remaining functional groups might still undergo similar reactions that produce CH_4, C_2H_4, and H_2, which are the major gaseous pyrolysis products that are observed via mass spectroscopy.[7] These reactions result in a continuous decrease of the Si—H, C—H, Si—CH_3, and Si—CH=CH_2 FTIR bands with increasing pyrolysis temperature (see Fig. 1(a)). With further elimination of hydrogen and structural adjustment of the polymer skeleton, an amorphous Si-C-N ceramic network can be obtained.

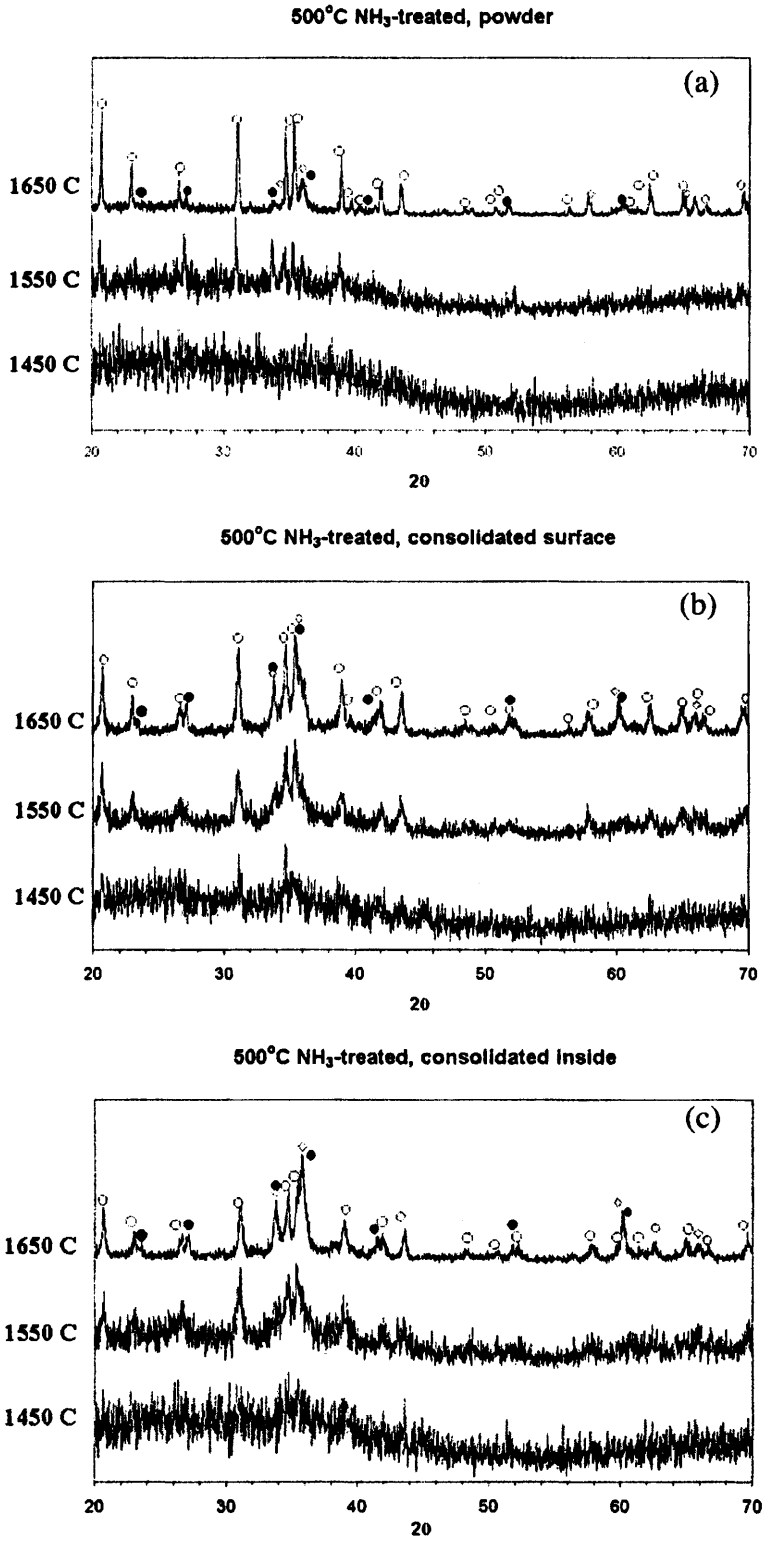

Fig. 3. XRD of (a) powder and consolidated samples ((b) surface and (c) inside), subjected to crystallization heat treatment at different temperatures in nitrogen; the powder sample, and the powder from which the consolidated samples were made, was heat-treated in ammonia for 1 h at 500°C. Legend is as follows: (○) α-Si_3N_4, (●) β-Si_3N_4, and (◇) SiC.

When ammonia is introduced into the pyrolysis environment, carbon-containing functional groups, e.g., —CH_3, are replaced by —NH_2 through the reaction[26]

$$\equiv Si\text{–}CH_3 + NH_3 \rightarrow \equiv Si\text{–}NH_2 + CH_4 \qquad (1)$$

which leads to the elimination of Si—CH_3 bands from the FTIR at lower temperatures (see Fig. 1(b)). The absence of —NH_2 signals from the FTIR spectra implies that the cross-linking reaction[27]

$$\equiv Si\text{–}NH_2 + CH_3\text{–}Si\equiv \rightarrow \equiv Si\text{–}NH\text{–}Si\equiv + CH_4 \qquad (2)$$

occurs simultaneously with reaction (1). These reactions are responsible for bringing nitrogen into the backbone of the polymer

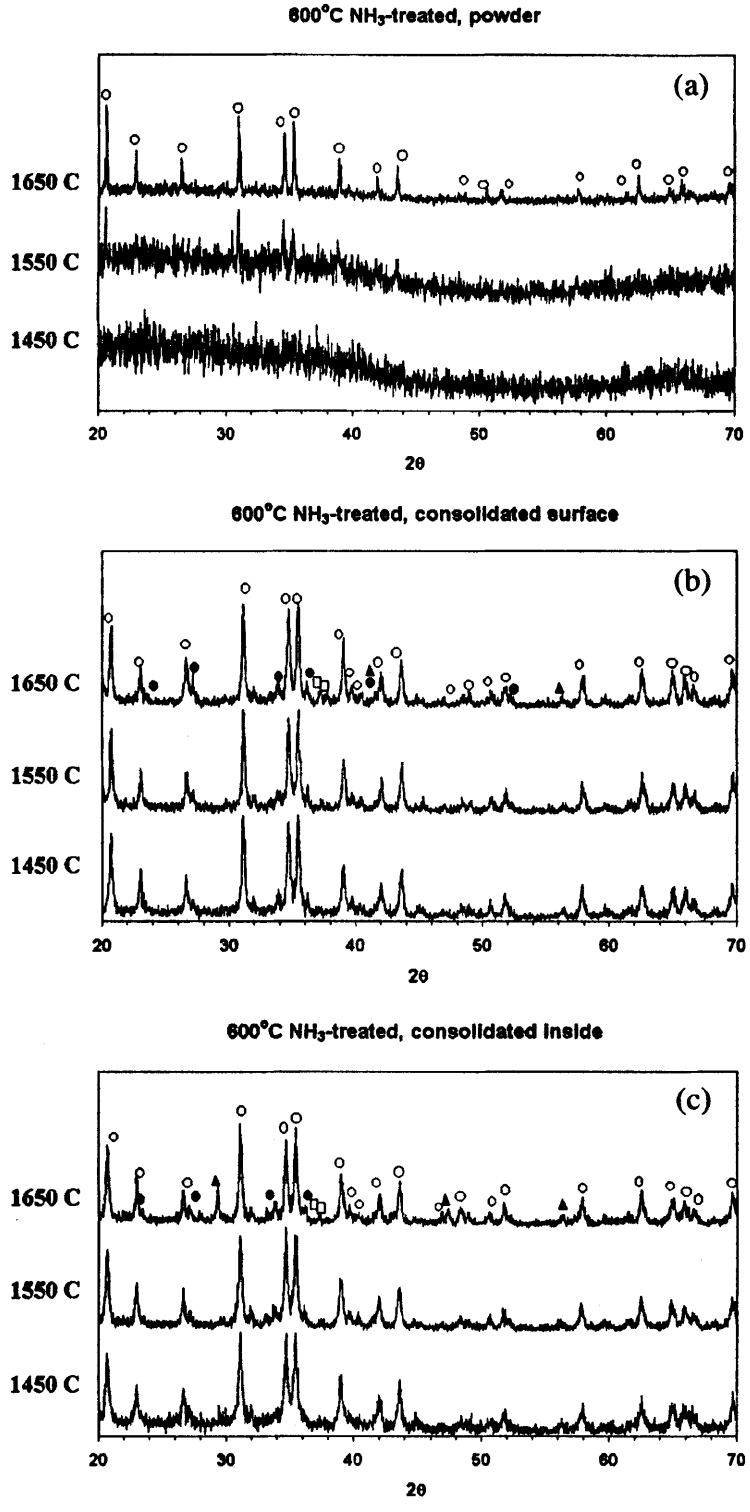

Fig. 4. XRD of (a) powder and consolidated samples ((b) surface and (c) inside), subjected to crystallization heat treatment at different temperatures in nitrogen; the powder sample, and the powder from which the consolidated samples were made, was heat-treated in ammonia for 1 h at 600°C. Legend is as follows: (○) α-Si_3N_4, (●) β-Si_3N_4, (◇) SiC, (□) Si_2N_2O, and (▲) silicon.

network and eventually increasing the nitrogen content in the ceramic.

At lower temperatures, because of insufficient thermal activation, reactions (4) and (5) proceed with slower speed and only result in a partial exchange of —CH_3 and —NH_2 functional groups within the limited reaction time (1 h); at higher temperatures (e.g., 800°C), cross-linking reactions that involve carbon-containing groups have already consumed most of the latent functional groups, such as —CH_3, during the heating to the ammonia treatment temperature (which was performed in nitrogen). A diminished population of these groups results in the limited introduction of nitrogen into the polymer network.

The presence of ammonia also results in reduced Si—H signals at lower temperature. This is likely due to the reaction[24]

$$\equiv Si\text{–}H + NH_3 \rightarrow \equiv Si\text{–}NH_2 + H_2 \quad (3)$$

which is followed by reaction (2) and contributes to the introduction of nitrogen into the polymer network. However,

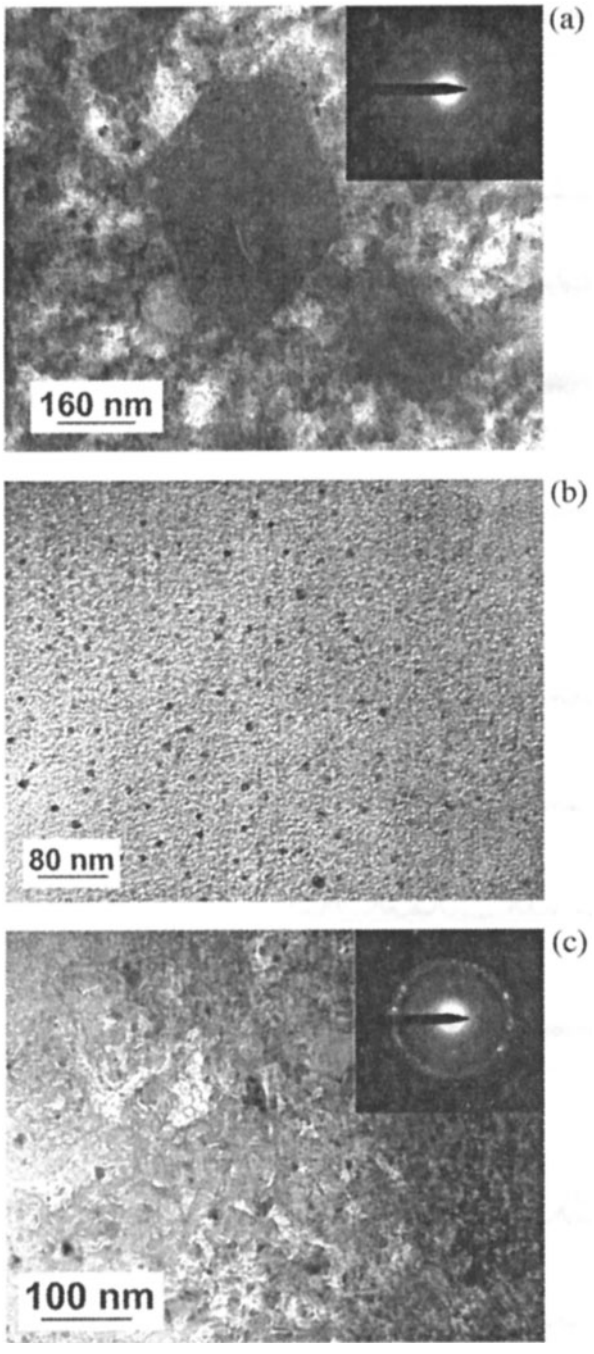

Fig. 5. Microstructure of the 400°C ammonia-treated, 1450°C pyrolyzed ceramics ((a) overall structure, composed of a dense particle phase and a porous binder phase; SAD (inset) of the particle phase shows an amorphous pattern; (b) higher-magnification image of the particle phase; small crystals of SiC can be observed in the amorphous matrix; and (c) higher-magnification image of the binder phase, showing nanoporosity; SAD (inset) reveals the increased crystallinity of both Si_3N_4 and SiC).

the fact that, at high ammonia treatment temperatures (700° and 800°C), the Si—H signal becomes stronger (than the 500°C and 600°C ammonia-treated samples) suggests that, at these temperatures, the effect of reaction (3) was suppressed by the active thermal cleavage of NH_3 molecules and the increase of free H atoms in the atmosphere.

As in the case of nitrogen introduction, the increase in oxygen content during ammonia treatment is also most profound at intermediate temperatures (550°–650°C). This phenomenon can be explained by the reactions between —H and carbon-containing

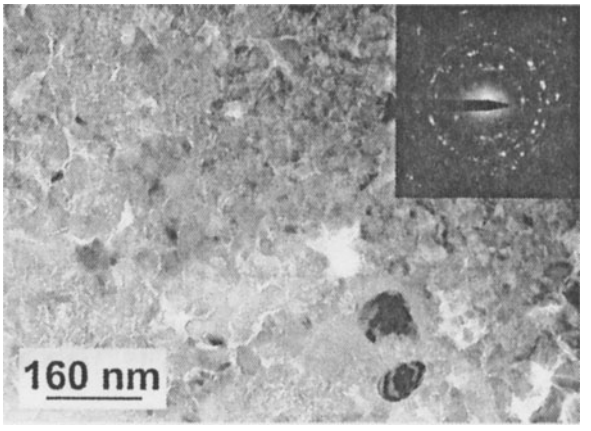

Fig. 6. Microstructure of the 600°C ammonia-treated, 1450°C pyrolyzed ceramics, showing higher crystallinity and a grain size larger than that of the 400°C ammonia-treated sample. Inset shows the SAD pattern for the ceramic.

groups with either oxygen or H_2O to produce ≡Si—OH.[28] Then, oxygen can enter the polymer backbone, via reactions (4) or (5):

$$\equiv Si\text{–}OH + CH_3\text{–}Si\equiv \rightarrow \equiv Si\text{–}O\text{–}Si\equiv + CH_4 \quad (4)$$

$$2\equiv Si\text{–}OH \rightarrow \equiv Si\text{–}O\text{–}Si\equiv + H_2O \quad (5)$$

The combined effect of thermal activation and the availability of latent functional groups again results in the maximum oxygen increase occurring at intermediate temperatures. The FTIR signals

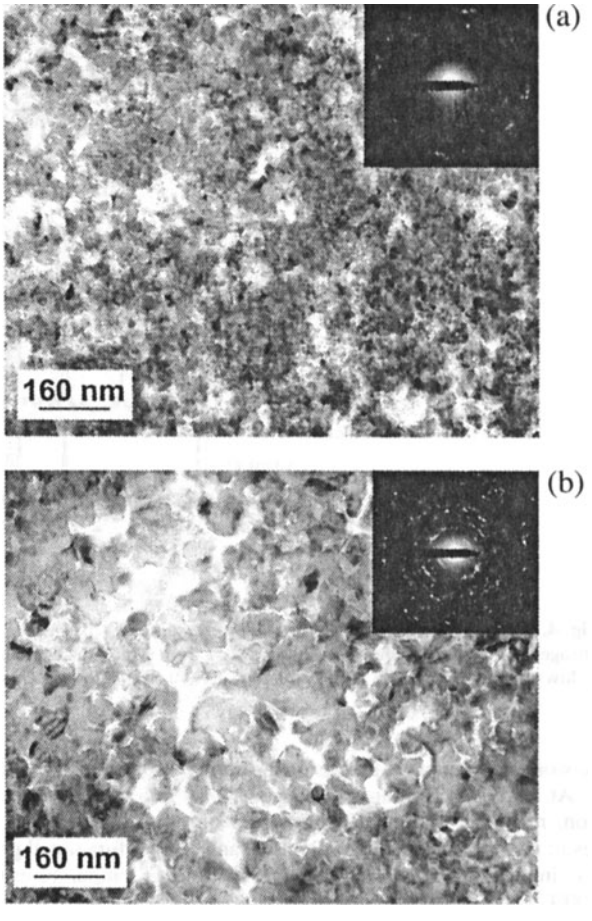

Fig. 7. Microstructure of ceramics crystallized at 1650°C in nitrogen, with ammonia heat treatment at different temperatures ((a) 400° and (b) 600°C). Inset in each shows the SAD pattern for the ceramic.

that are related to the Si—O bond (most of which are located in the 800–1200 cm^{-1} range) might be a factor that makes explanation of the spectra of Fig. 1 more problematic.[29,30]

(2) *Crystallization Behavior*

As discussed in earlier publications,[7,8,23] as well as in the works of other researchers,[31,32] the crystallization behavior of Si-C-N ceramics proceeds via two types of mechanisms: (i) heterogeneous crystallization at the surface (exterior surfaces and interior surfaces, such as pore walls) and (ii) homogeneous crystallization inside the amorphous ceramic network. The former happens earlier (at lower temperature) than the latter. In Si-C-N ceramics, within which oxygen is a substantial impurity, as in the case of the present work, gaseous species such as SiO, CO, N_2, and silicon vapor can be generated, because of amorphous phase degradation, when the material is heated to high temperatures. In an inert atmosphere such as argon, reactions between these gaseous phases—and between gaseous phases and free carbon at the surfaces—result in SiC formation on the surfaces:[32,33]

$$Si(g) + CO(g) \rightarrow SiC(s) + \tfrac{1}{2}O_2 \quad (6)$$

$$SiO(g) + CO(g) \rightarrow SiC(s) + O_2 \quad (7)$$

$$SiO(g) + 2C(s) \rightarrow SiC(s) + CO(g) \quad (8)$$

$$Si(g) + C(s) \rightarrow SiC(s) \quad (9)$$

When the crystallization heat treatment is performed in a nitrogen atmosphere, the dominant reactions might be

$$3Si(g) + 2N_2(g) \rightarrow Si_3N_4(s) \quad (10)$$

$$3SiO(g) + 2N_2(g) + 3CO(g) \rightarrow Si_3N_4(s) + 3CO_2(g) \quad (11)$$

which may result in the formation of Si_3N_4 whiskers at the surfaces.

In the amorphous bulk ceramics made by the prepyrolysis/binding/pyrolysis method, heterogeneous crystallization manifests in the binder phase before occurring in the particle phase. The abundance of nanometer-sized pores[34] provides the space for gaseous phase reactions to happen. For samples in which the particle phase was not treated by ammonia, the nanopores remain closed up to a temperature of 1450°C.[23] The low partial pressure of nitrogen gas results in the prevalence of SiC-forming reactions; therefore, only SiC crystals were observed in the binder phase of the 1450°C heat-treated bulk ceramics.

In bulk specimens made from ammonia-treated powders, both Si_3N_4 and SiC phases can be found in the binder phase, although the original chemistry of this binder phase is exactly the same as that in the materials without ammonia treatment. There might be several reasons to account for this disparity:

(1) Binder/powder reactions might occur, which change the chemistry of the binder phase and then lead to higher nitrogen content in the binder phase.

(2) Gas release from the ammonia-treated particle phase might result in increased nitrogen pressure in the pores.

(3) In the bulk specimens made from ammonia-treated particles, crystallization occurs at a lower temperature than in the materials not treated by ammonia, leading to more open pores, which might increase the opportunity for the nitrogen from the heat-treatment atmosphere to contribute to the gaseous phase.

Powder samples, in comparison with consolidated samples, should have more open surfaces; therefore, their crystallization behavior should reflect more of the characteristics of the gas-reaction-related heterogeneous crystallization. Indeed, the crystallized powder samples show larger grain sizes of α-Si_3N_4 than the consolidated materials, which, to a great extent, is the result of reactions (10) and (11). Unlike the crystallization in the consolidated specimens, which is dependent on the solid-state diffusion (which is slow in the Si_3N_4–SiC system, even at high temperatures), the gaseous phase reaction can facilitate fast grain growth and, therefore, larger grain size; even whiskers can be obtained.

One important point that was not expected from the comparison of the crystallization behavior of the ammonia-treated powders and bulk ceramics is that, in the bulk specimens, especially those with higher nitrogen content, crystallization occurs at much lower temperature than their powder counterparts. One would expect that the powders crystallize easier, because the gaseous-reaction-related mechanisms occur at lower temperatures than homogeneous crystallization. Perhaps the fact that ammonia-treated consolidated materials crystallize easier than ammonia-treated powders can be understood by considering the role of the particle/binder interface in accelerating the crystallization process in the particle phase.

It has been noticed that, in the consolidated specimens made via the prepyrolysis/binding/pyrolysis method, when the particle phase was not treated by ammonia, crystallization of the binder phases occurred inside the binder and no preferential crystallization was observed on the particle/binder interface. Kleebe and co-workers[9,31] also confirmed this finding. Crystallization of the particles proceeds homogeneously inside the particle phase, when it occurs at higher temperatures. The implication of this observation is that, in such cases, the particle/binder interface does not serve as an effective nucleation site for crystallization. Because of the identical chemistry of the particle phase and the binder phase, they have a low-energy interface, and such an interface is not able to provide a sufficient decrease in the nucleation energy barrier to favor crystallization. The particle/binder interface of a 400°C ammonia-treated specimen (Fig. 8(a)) shows that no crystallites are present to mark the interface region. This observation is an indication that, even in ammonia-treated samples, as long as the nitrogen introduction is not significant enough to result in a substantial difference in the chemistry of the particle and the binder phases, the interface energy remains low and no preferential crystallization can be observed at the interface region.

However, when the nitrogen introduction into the ceramics is more effective, which results in a sufficiently significant difference in the chemistry (C/N ratio) between that of the particle phase and that of the binder phase, crystallization of the material—or at least that of the particle phase—happens preferentially in the interface region. A typical example is given in Fig. 8(b), in which the interface region around a very large particle is shown. (Larger particles are retarded in crystallization. In the 600°C ammonia-treated sample, the regions that contain smaller particles are fully crystallized, as shown in Fig. 6, whereas the larger particles are only partially crystalline and, thus, provide an opportunity to observe the starting position of the crystallization process.) The binder phase is crystalline (it contains both Si_3N_4 and SiC, as indicated by SAD) and is highly porous, because of the restriction from the particle during pyrolysis. Within the particle, crystallization clearly seems to start from the interface and extends into the interior of the particle, which is still amorphous. Obviously, the particle/binder interface, which is supposed to have a higher-energy interface than that in Fig. 8(a), serves as the preferred nucleation site for the crystallization of the particle, because of its effectiveness in lowering the nucleation energy barrier. The crystals in the particle phase in Fig. 8(b) were determined to be α-Si_3N_4, according to SAD analysis.

Among the other effects of the ammonia heat treatment on the crystallization of bulk Si-C-N ceramics, the larger grain size in the high-nitrogen-content materials (e.g., 600°C, ammonia-treated) may be simply due to the smaller phase proportion of SiC and, therefore, lack of restriction to Si_3N_4 grain growth from it. The observation that higher nitrogen content favors α-Si_3N_4 formation over that of β-Si_3N_4, however, might be explained by the difference in oxygen content. Effective nitrogen introduction is accompanied by the increase in oxygen

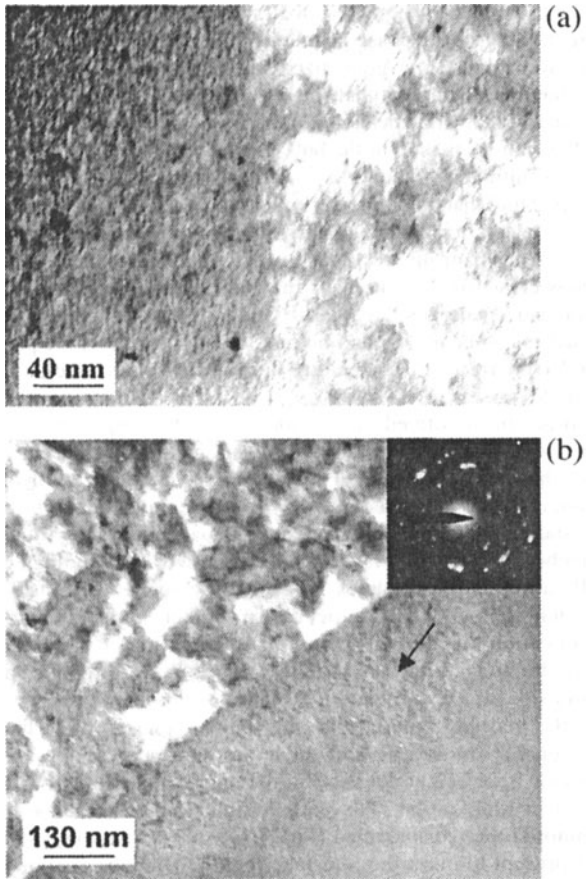

Fig. 8. Particle/binder interfaces in ammonia-treated samples ((a) 400° and (b) 600°C) after pyrolysis in nitrogen at 1450°C. Preferential crystallization was found at interface in the latter case but not in the former.

content, as shown by the chemical composition analysis in Table I. β-Si_3N_4 is the pure form of silicon nitride, which is made up of covalent SiN_4 tetrahedra joined in a three-dimensional network by sharing corners. In the structure of α-Si_3N_4, the literature reports that one O atom replaces every 30 N atoms in an array of these tetrahedra.[35] Therefore, α-Si_3N_4 can be understood as an oxygen-rich polytype of silicon nitride; the higher oxygen content in the high-nitrogen-content materials results in a smaller β/α ratio.

At temperatures where crystallization happens, oxygen has a tendency to leave the ceramic network in the form of SiO and CO species, as indicated by mass spectroscopy and by the composition information in Table I. Therefore, the bulk materials, in comparison with the powders, which are dependent more on gaseous phase reactions for crystallization, should contain less oxygen and, therefore, more β-Si_3N_4. This result is exactly what our experiments show. The 600°C ammonia-treated bulk material, after crystallization, contains 5–6 at.% oxygen, whereas the whiskers growing in the powder samples contain ~12–13 at.% oxygen. As predicted, the consolidated samples have a larger β/α ratio than the powder.

V. Conclusions

Crystallization of bulk Si-C-N(-O), consolidated by a prepyrolysis/binding/pyrolysis method, results in the formation of nanocrystalline composites of silicon nitride and silicon carbide. A prepyrolysis ammonia treatment at appropriate temperature can effectively change the phase proportion of the composite. A significant difference in crystallization behavior between powder samples and consolidated samples was observed in the ammonia-treated materials. Consolidated specimens crystallized at lower temperature than powder samples of the same processing history. Interaction between the binder phase and the particle phase in the consolidated materials, and gaseous-phase-reaction-related heterogeneous crystallization, were suggested to rationalize the observed phenomena.

Acknowledgments

The authors thank Dr. Vasudevan (their ONR program manager) and Dr. Kabacoff for overall project coordination.

References

[1]R. Riedel and W. Dressler, "Chemical Formation of Ceramics," *Ceram. Int.*, **22**, 233–39 (1996).

[2]J. Bill and F. Aldinger, "Progress in Material Synthesis," *Z. Metallkd.*, **87**, 829–40 (1996).

[3]E. Kroke, Y.-L. Li, C. Konetschny, E. Lecomte, C. Fasel, and R. Riedel, "Silazane Derived Ceramics and Related Materials," *Mater. Sci. Eng.*, **26**, 97–199 (2000).

[4]R. Riedel, "Advanced Ceramics from Inorganic Polymers"; pp. 1–50 in Materials Science and Technology, Vol. 17B: *A Comprehensive Treatment, Processing of Ceramics, Part II*. Edited by R. W. Cahn, P. Haasen, and E. J. Kramer. VCH, New York, 1996.

[5]J. Bill and F. Aldinger, "Precursor-Derived Covalent Ceramics"; pp. 33–51 in *Precursor-Derived Ceramics*. Edited by J. Bill, F. Wakai, and F. Aldinger. Wiley-VCH, Weinheim, Germany, 1999.

[6]J. Seitz and J. Bill, "Producton of Compact Polysilazane-Derived Si-C-N Ceramics by Plastic Forming," *J. Mater. Sci. Lett.*, **15**, 391–93 (1996).

[7]J. Wan, M. J. Gasch, and A. K. Mukherjee, "Silicon Carbonitride Ceramics Produced by Pyrolysis of Polymer Ceramic Precursor," *J. Mater. Res.*, **15** [8] 1657–60 (2000).

[8]J. Wan, M. J. Gasch, and A. K. Mukherjee, "Silicon Nitride/Silicon Carbide Nanocomposites Derived from Polymer Precursor Pyrolysis"; pp. 276–79 in *Proceedings of International Conference on Engineering and Technological Sciences 2000* (Beijing, China, 2000). Edited by J. Song and R. Yin. New World Press, Beijing, China, 2000.

[9]H.-J. Kleebe, D. Suttor, H. Müller, and G. Ziegler, "Decomposition–Crystallization of Polymer-Derived Si-C-N Ceramics," *J. Am. Ceram. Soc.*, **81** [11] 2971–77 (1998).

[10]M. Sternitzke, "Review: Structural Ceramic Nanocomposites," *J. Eur. Ceram. Soc.*, **17**, 1061–82 (1997).

[11]G. T. Burns and G. Chandra, "Pyrolysis of Preceramic Polymers in Ammonia: Preparation of Silicon Nitride Powders," *J. Am. Ceram. Soc.*, **72** [2] 333–37 (1989).

[12]R. Riedel and M. Seher, "Crystallization Behavior of Amorphous Silicon Nitride," *J. Eur. Ceram. Soc.*, **7**, 21–25 (1991).

[13]D. Galusek, S. Reschke, R. Riedel, W. Dressler, P. Sajgalik, Z. Lences, and J. Majling, "*In-Situ* Carbon Content Adjustment in Polysilazane Derived Amorphous SiCN Bulk Ceramics," *J. Eur. Ceram. Soc.*, **19**, 1911–21 (1999).

[14]J. M. Schwark and A. Lukaes, "Polysilazane Thermosets as Precursors for Silicon Carbide and Silicon Nitride"; pp. 43–54 in *Inorganic and Organometallic Polymers II: Advanced Materials and Intermediates*. Edited by P. Wisian-Neilson, H. R. Allcock, and K. J. Wynne. American Chemical Society, Division of Polymer Chemistry, and American Chemical Society, Washington, DC, 1994.

[15]D. Lin-Vien, N. B. Colthup, W. G. Fateley, and J. G. Grasselli, *The Handbook of Infrared and Raman Characteristic Frequencies of Organic Molecules*. Academic Press, Boston, MA, 1991.

[16]J. Lipowitz, "Structure and Properties of Ceramic Fibers Prepared from Organosilicon Polymers," *J. Inorg. Org. Polymers*, **1** [3] 277–97 (1991).

[17]T. Isoda, H. Kaya, H. Nishii, O. Funayama, T. Suzuki, and Y. Tashiro, "Perhydropolysilazane Precursors to Silicon Nitride Ceramics," *J. Inorg. Org. Polymers*, **2** [1] 151–59 (1992).

[18]J. Bill, J. Seitz, G. Thurn, J. Dürr, J. Canel, B. Z. Janos, A. Jalowiecki, D. Sauter, S. Schempp, H. P. Lamparter, J. Mayer, and F. Aldinger, "Structure Analysis and Properties of Si-C-N Ceramics Derived from Polysilazanes," *Phys. Status Solidi A*, **166**, 269–96 (1998).

[19]Y. S. Lee, H. Y. Lin, T. F. Lei, T. Y. Huang, T. C. Chang, and C. Y. Chang, "Comparison of N_2 and NH_3 Plasma Passivation Effects on Polycrystalline Silicon Thin-Film Transistors," *Jpn. J. Appl. Phys.*, **37**, 3900–903 (1998).

[20]J. Oh, H. Imai, H. Hirashima, and K. Tsukuma, "Direct Deposition of Silica Films Containing Organic Groups and Dyes from Silicon Alkoxide Solutions"; pp. 409–14 in Materials Research Society Symposium Proceedings, Vol. 435, *Better Ceramics through Chemistry VII: Organic/Inorganic Hybrid Materials*. Edited by B. K. Coltrain, C. Sanchez, D. W. Schaefer, and G. L. Wilkes. Materials Research Society, Pittsburgh, PA, 1996.

[21]X. Bao and M. J. Edirisinghe, "Different Strategies for the Synthesis of Silicon Carbide–Silicon Nitride Composites from Preceramic Precursors," *Composites: Part A*, **30**, 601–10 (1999).

[22]Y. Abe, T. Ozai, Y. Kuno, Y. Nagao, and T. Misono, "Synthesis and Properties of Oligo- and Polymethylsilazanes as a Precursor for Silicon Nitride," *J. Inorg. Org. Polymers*, **2** [1] 143–49 (1992).

[23]J. Wan, M. J. Gasch, and A. K. Mukherjee, "Consolidation and Crystallization of Si_3N_4/SiC Nanocomposites from Poly(urea–silazane) Ceramic Precursor," *J. Mater. Res.*, **16** [11] 3274–86 (2001).

[24]J. Seitz, J. Bill, N. Egger, and F. Aldinger, "Structural Investigation of Si/C/N-Ceramics from Polysilazane Precursors by Nuclear Magnetic Resonance," *J. Eur. Ceram. Soc.*, **16**, 885–91 (1996).

[25]D. Bahloul, M. Pereira, P. Goursat, N. S. Choong Kwet Yive, and R. J. P. Corriu, "Preparation of Silicon Carbonitrides from an Organic Polymer: I, Thermal Decomposition of the Cross-linked Polysilazane," *J. Am. Ceram. Soc.*, **76** [5] 1156–62 (1993).

[26]D. Seyferth, G. H. Wiseman, J. M. Schwark, Y. F. Yu, and C. A. Poutasse, "Organosilicon Polymers as Precursors for Silicon-Containing Ceramics: Recent Developments"; pp. 143–55 in *Inorganic and Organometallic Polymers*. Edited by M. Zeldin, K. J. Wynne, and H. R. Allcock. American Chemical Society, Washington, DC, 1988.

[27]M. Peuckert, T. Vaahs, and M. Brück, "Ceramics from Organometallic Polymers," *Adv. Mater.*, **2**, 398–404 (1990).

[28]H. Ichikawa, F. Machino, H. Teranishi, and T. Ishikawa, "Oxidation Reaction of Polycarbosilazane," *Adv. Chem. Ser.*, **224**, 619–77 (1990).

[29]Y. Yamashita and M. Kaziwara, "Application of Chrysotile-Derived Polymer to Microlithography," *J. Inorg. Org. Polymers*, **2** [1] 129–39 (1992).

[30]E. San Andrés, A. del Prado, F. L. Martínez, I. Mártil, D. Bravo, and F. J. López, "Rapid Thermal Annealing Effects on the Structural Properties and Density of Defects in SiO_2 and SiN_x:H Films Deposited by Electron Cyclotron Resonance," *J. Appl. Phys.*, **87** [3] 1187–92 (2000).

[31]H.-J. Kleebe, D. Suttor, and G. Ziegler, "Microsturcture Evolution and Crystallization Behavior of Polymer-Derived Si-C-N Monoliths; A TEM Study"; see Ref. 5, pp. 113–23.

[32]M. Monthioux and O. Delverdier, "Thermal Behavior of (Organosilicon) Polymer-Derived Ceramics, V: Main Facts and Trends," *J. Eur. Ceram. Soc.*, **16**, 721–37 (1996).

[33]D. Mocaer, Pailer, R. Naslain, R. Richard, C. Pillot, J. P. Dunogues, J. Delverdier, and O. M. Monthioux, "Si-C-N Ceramics with a High Microstructural Stability Elaborated from the Pyrolysis of New Polycarbosilazane Precursors. Part III. Effect of Pyrolysis Conditions on the Nature and Properties of Oxygen-Cured Derived Monofilaments," *J. Mater. Sci.*, **28**, 2639–53 (1993).

[34]H. J. Kleebe, "Microstructure and Stability of Polymer-Derived Ceramics: The Si-C-N System," *Phys. Status Solidi A*, **166**, 297–312 (1998).

[35]A. Jha, "Phase Equilibria in the Si-C-N-O System and the Kinetic Analysis of Silicon Carbide Whisker Growth," *J. Mater. Sci.*, **28**, 3069–79 (1993). □

This page intentionally left blank

J. Am. Ceram. Soc., 85 [3] 724–26 (2002)

journal

Novel Method to Prepare Electroconductive Titanium Nitride–Aluminum Oxide Nanocomposites

Jingguo Li, Lian Gao,*,† Jingkun Guo,* and Dongsheng Yan*

State Key Lab of High Performance Ceramics and Superfine Microstructure, Shanghai Institute of Ceramics, Chinese Academy of Sciences, Shanghai 200050, People's Republic of China

A novel method for the preparation of TiN–Al_2O_3 nanocomposites was developed. TiN–Al_2O_3 nanocomposite powders were prepared by the direct nitridation of TiO_2–Al_2O_3 nanocomposite powders that were derived from the simultaneous hydrolysis of tetra-butyl titanate and precipitation of aluminum nitrate. Dense sintered bodies of these TiN–Al_2O_3 nanocomposite powders were obtained by hot pressing at 1450°–1650°C and 30 MPa for 60 min. The resistivity of nanocomposite reaches a minimum (1.5×10^{-3} Ω·cm) at 25 vol% TiN additions. The percolation concentration of nanocomposite is ~10 vol% TiN.

I. Introduction

Recently, the properties of titanium nitride (TiN) particles reinforced with alumina or silicon nitride composites have been widely studied, because the addition of an electroconductive second phase to the matrix was reported not only to improve some mechanical properties but also to lower drastically the electrical resistivity.[1–5] If sintered Al_2O_3 bodies can be made electroconductive, the electrospark technique can be applied to manufacture complex components.[6–8] Moreover, such ceramics could have broader applications as heating elements, igniters, heat exchangers, wear-resistant materials, and cutting tools. The common method used to prepare these ceramic composites is to add a second phase directly into the matrix by ball milling. Such materials can sometimes exhibit poor characteristics, which result from an inadequate dispersion process and the lack of sinterability caused by the large volume fraction of inert dispersion required for the electroconductivity. Meanwhile, as the dispersed phases have generally less oxidation resistance than the matrix, an excess of the addition amount should be avoided. On the other hand, it is generally known that a minimum amount of dispersoids (20–30 vol%) must be added for electroconductivity. The electroconductivity of ceramic materials is strongly affected by the distribution of the electroconductive second phase. Thus, it is important to improve the preparation method to result in a better distribution of TiN particles. A preferable alternative is the *in situ* formation of the second phase so that optimum properties can be obtained.

The present paper reports a novel method to prepare TiN–Al_2O_3 nanocomposites by the *in situ* formation of the second phase (TiN). One of the most important advantages of an *in situ* composite method is causing the second phase to be homogeneously distributed in the matrix.

T. M. Besmann—contributing editor

Manuscript No. 187518. Received August 8, 2001; approved October 1, 2001.
*Member, American Ceramic Society.
†Author to whom correspondence should be addressed.

II. Experimental Procedures

Tetra-butyl titanate ($Ti(OC_4H_9)_4$), $Al(NO_3)_3 \cdot 9H_2O$ and NH_3 gas were selected as the raw materials. $Al(NO_3)_3$ and $Ti(OC_4H_9)_4$ were dissolved into anhydrous ethanol in the calculated proportion. The mixed solution was then dripped into the vigorously stirred, diluted NH_4OH solution with a pH of 9–10. After separation from the mother solution, precipitates were washed with distilled water and, finally, several times with anhydrous ethanol. The filtration cake was dried at 120°C and subsequently calcined at 450°C for 2 h in air to obtain TiO_2–γ-Al_2O_3 nanocomposite powders. Finally, TiO_2–γ-Al_2O_3 nanocomposite powders were put into a quartz crucible and nitrided at various temperatures for 5 h in the flow of NH_3 gas using a tube furnace. The flow rate of NH_3 gas was 1000 mL/min. The 5–25 vol% TiN–γ-Al_2O_3 nanocomposite powders produced were sintered by hot pressing at 1400°–1650°C and a pressure of 30 MPa for 60 min under a nitrogen-gas atmosphere.

The morphologies of the nanocomposite powders were observed by transmission electron microscopy (TEM; Model 2010CX, JEOL, Tokyo, Japan). The phase compositions of powders and sintered bodies were identified by X-ray diffraction (XRD; Model D/MAX rB, Rigaku Co., Tokyo, Japan). The density of the samples was measured using the water immersion technique. The microstructure was observed via scanning electron microscopy (SEM; Model LX-30 ESEM, Philips, Eindhoven, The Netherlands). The resistivity of the sintered bodies was measured with the four-probe method.

III. Results and Discussion

Figure 1 shows the XRD patterns of TiN–Al_2O_3 nanocomposite powder prepared at different nitridation temperatures for 5 h. When the TiO_2–Al_2O_3 nanocomposite powder was nitrided at 700° and 800°C for 5 h, the distinct peaks assigned to TiN(cubic), γ-Al_2O_3, TiO_2(anatase), and Ti_2O_3, which is an intermediate during the nitridation process, coexisted. This indicates that anatase TiO_2 nanoparticles were partially converted to TiN and to Ti_2O_3, whereas the nitridation reaction was not complete. When TiO_2–γ-Al_2O_3 nanocomposite powder was nitrided at 900°C for 5 h, the distinct peaks assigned to TiN(cubic) and γ-Al_2O_3 could be detected and no peaks of the other substance appeared. This indicates that the TiO_2 nanocomposite particle was completely converted to TiN at 900°C for 5 h in the flow of NH_3 gas. Because the nitridation reaction is a gas-solid phase reaction with a relatively slow rate, it is important to keep enough holding time and temperature so that TiO_2 nanoparticles are completely converted to TiN. We reported elsewhere[9] that pure anatase TiO_2 nanopowder could be completely nitrided at 800°C for 5 h. In the present study, some anatase TiO_2 nanoparticles were coated with γ-Al_2O_3 particles so that the nitridation reaction needed a higher temperature. Figure 2 shows a TEM micrograph of the TiN–Al_2O_3 nanocomposite powders prepared.

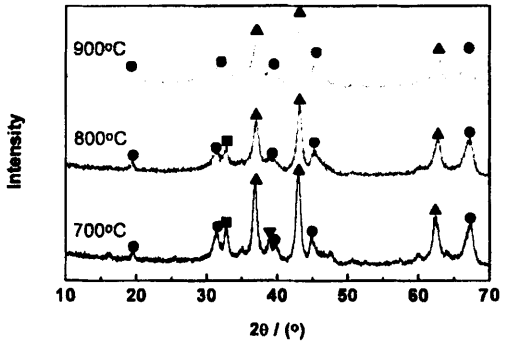

Fig. 1. XRD patterns of 20 vol% TiN–Al_2O_3 nanocomposite powders prepared at different nitridation temperatures for 5 h ((▲) TiN, (■) Ti_2O_3, (▼) TiO_2 (anatase), and (●) γ-Al_2O_3).

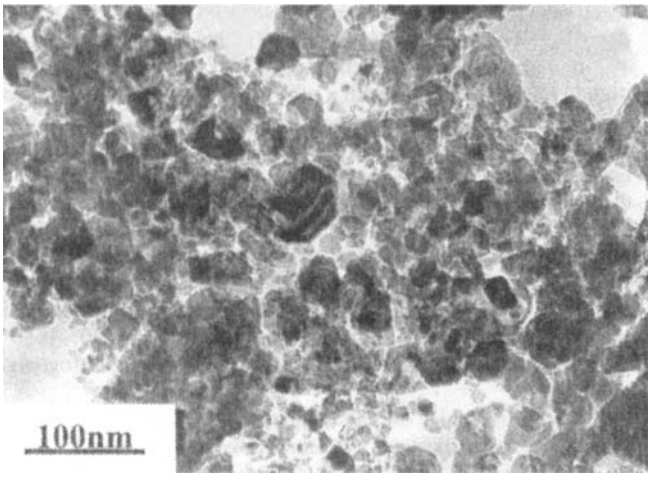

Fig. 2. TEM micrographs of 20 vol% TiN–Al_2O_3 nanocomposite powders.

The relative density of nanocomposites versus the sintering temperature is shown in Fig. 3, which demonstrates that nearly fully dense samples could be obtained by hot pressing at 1450°C for a 20 vol% TiN–Al_2O_3 nanocomposite. This densification temperature is lower than that of microcomposite powders reported by Z. S. Rak *et al.*[3] and A. Bellosi *et al.*[10] The result is that TiN–Al_2O_3 nanocomposite powders prepared by the *in situ* formation of second phase (TiN) have good sinterability.

Figure 4 shows the XRD patterns of a TiN–Al_2O_3 sintered body. XRD results revealed that prepared 20 vol% TiN–Al_2O_3 nanocomposites are composed of TiN (cubic) and α-Al_2O_3. The

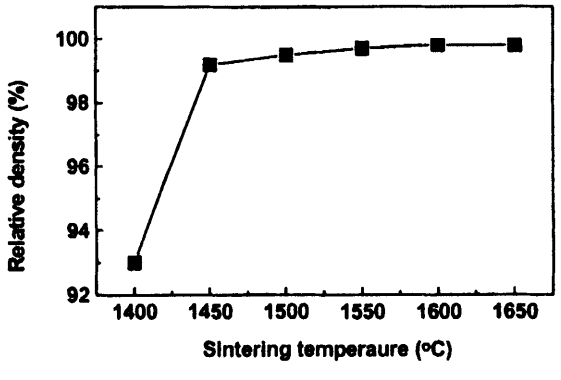

Fig. 3. Relative density versus the sintering temperature for 20 vol% TiN–Al_2O_3 nanocomposites by hot pressing sintering.

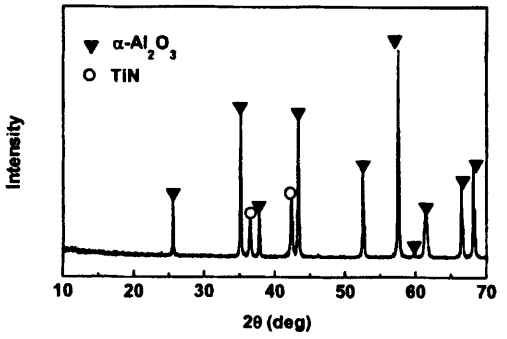

Fig. 4. XRD pattern of a 20 vol% TiN–Al_2O_3 sintered body.

results indicate that no chemical reaction occurs between the second phase and the matrix, but the initial γ-Al_2O_3 in the TiN–Al_2O_3 nanocomposite powder was converted to α-Al_2O_3 during the sintering process.

SEM micrographs of the fracture surface and backscatter of 10 vol% TiN–Al_2O_3 nanocomposites are shown in Fig. 5. It can be observed from Fig. 5(a) that the grains of the nanocomposite are very homogeneous. Figure 5(a) reveals that the fracture type of the nanocomposites is mainly intergranular. Figure 5(b) shows that TiN nanocomposite grains were uniformly dispersed in Al_2O_3 matrix.

Figure 6 shows the relationship between the TiN contents and the electrical resistivity of nanocomposites sintered at 1500°C with

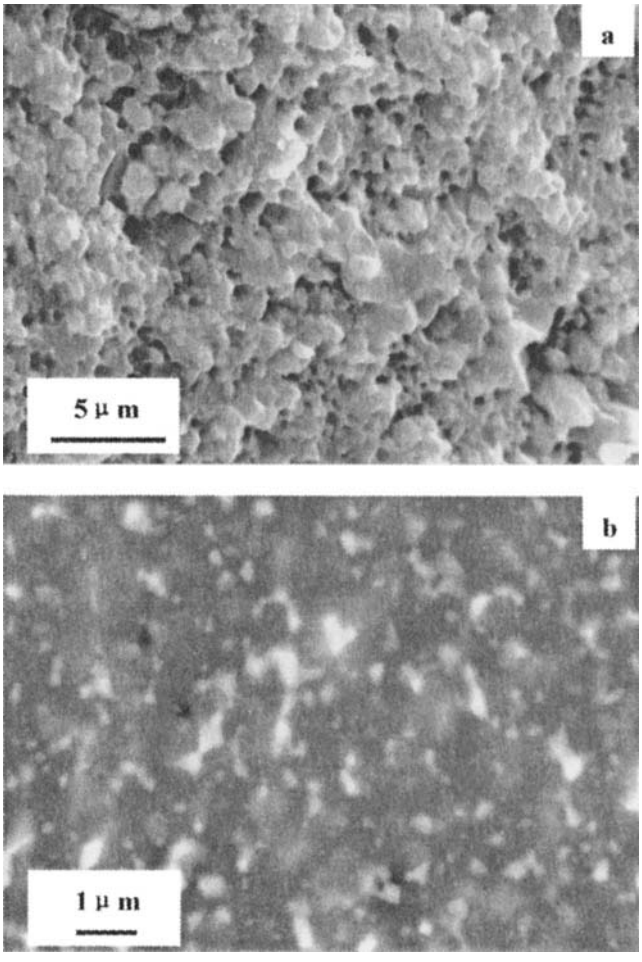

Fig. 5. SEM micrographs of 10 vol% TiN–Al_2O_3 nanocomposites ((a) fracture surface and (b) backscattered image). White areas are TiN particles.

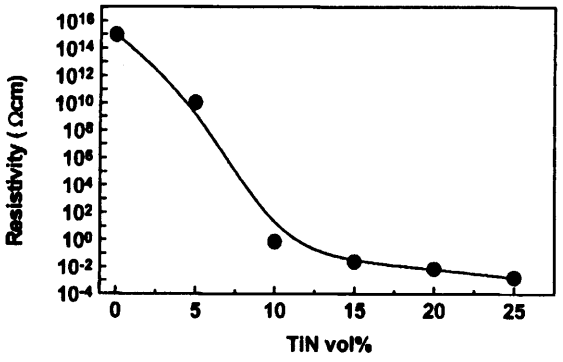

Fig. 6. Relationship between TiN contents and electrical resistivity of the nanocomposite sintered at 1500°C.

a pressure of 30 MPa for 60 min. The electrical resistivity of nanocomposites decreases with an increasing amount of TiN phase and reaches a minimum (1.5×10^{-3} Ω·cm) for the nanocomposite with 25 vol% TiN. The experimental results show that prepared TiN–Al_2O_3 nanocomposites have good electroconductivities, especially at low additions of TiN. The percolation concentration of nanocomposite is ~10 vol% TiN. This value is much lower than that reported for the microcomposites prepared by conventional methods.[3,4]

Because the mechanism of electrical conduction for TiN–Al_2O_3 composite materials is the formation of a network of the TiN electrical conductive phase within the Al_2O_3 matrix, the distribution of TiN particles is one of the most important factors of the electroconductivity.[11] From the backscattered SEM micrograph of 10 vol% TiN–Al_2O_3 nanocomposites shown in Fig. 5(b), it can be observed that the TiN particles in a sintered body were homogeneously dispersed in the matrix. Therefore, nanocomposites prepared by the *in situ* formation of a second phase (TiN) possess a high electroconductivity, which is confirmed by the results of electrical resistivity measurement.

IV. Conclusions

A TiN–Al_2O_3 nanocomposite powder has been successfully prepared using a novel method with *in situ* formation of a TiN second phase. Using these powders, dense TiN–Al_2O_3 nanocomposites have been sintered by hot pressing at a low sintering temperature. Experimental results indicate that the prepared nanocomposites have a good microstructure, a lower percolation concentration and a high electroconductivity. The results suggest that the present method is effective for the improvement of electroconductive TiN–Al_2O_3 nanocomposites.

References

[1]J. Mukerji and S. K. Biswas, "Synthesis, Properties and Oxidation of Alumina–Titanium Nitride Composites," *J. Am. Ceram. Soc.*, **73**, 142–45 (1990).

[2]Y. G. Gogotsi and F. Porz, "Mechanical Properties and Oxidation Behavior of Al_2O_3–TiN Composites," *J. Am. Ceram. Soc.*, **78**, 2251–59 (1992).

[3]Z. S. Rak and J. Czechowski, "Manufacture and Properties of Al_2O_3–TiN Particulate Composites," *J. Eur. Ceram. Soc.*, **18**, 373–80 (1998).

[4]A. Bellosi, G. D. Portu, and S. Guicciardi, "Preparation and Properties of Electroconductive Al_2O_3-based Composites," *J. Eur. Ceram. Soc.*, **10**, 307–15 (1992).

[5]A. Bellosi, S. Guicciardi, and A. Tampieri, "Development and Characterization of Electroconductive Si_3N_4–TiN Composites," *J. Eur. Ceram. Soc.*, **9**, 83–93 (1992).

[6]K. Tsugeki, T. Kato, Y. Koyanagi, K. Kusakabe, and K. Morooka, "Electroconductivity of Sintered Bodies of α-Al_2O_3–TiN Composite Prepared by CVD Reaction in a Fluidized Bed," *J. Mater. Sci.*, **28**, 3168–72 (1993).

[7]M. Ramulu, "EDM Sinker Cutting of Ceramic Particulate Composite, SiC–TiB_2," *Adv. Ceram. Mater.*, **3**, 324–27 (1998).

[8]N. F. Petrotes and A. M. Gadalla, "Electrical Discharge Machining of Advanced Ceramics," *Am. Ceram. Soc. Bull.*, **67**, 1048–52 (1998).

[9]J. G. Li, L. Gao, J. Sun, Q. H. Zhang, and J. K. Guo, "Synthesis of Nanocrystalline Titanium Nitride Powders by Direct Nitridation of Titanium Oxide," *J. Am. Ceram. Soc.* **84** [12] 3045–47 (2001).

[10]A. Bellosi, G. D. Portu, and S. Guicciardi, "Preparation and Properties of Electroconductive Al_2O_3-based Composites," *J. Eur. Ceram. Soc.*, **10**, 307–15 (1992).

[11]F. Lux, "Models Proposed to Explain the Electrical Conductivity of Mixtures Made of Conductive and Insulating Materials," *J. Mater. Sci.*, **28**, 285–301 (1993). □

This page intentionally left blank

journal

Glass and Optical Materials

J. Am. Ceram. Soc., 85 [5] 1057–60 (2002)

Near-Field Optical Characterization of Nanocomposite Materials

Lukas Novotny

The Institute of Optics, University of Rochester, Rochester, New York 14627

We present a near-field optical technique which makes use of the strongly enhanced optical field at a laser-illuminated metal tip. The enhanced field is used to locally excite the sample under investigation by multiphoton absorption. An optical scan image with spatial resolutions down to 20 nm is established by detecting the emitted fluorescence. The principle of the method is described and experimental results are demonstrated for samples of J-aggregates of PIC dye molecules. Ongoing experiments on nanocomposite, Er^{3+}-doped oxyfluoride glass-ceramics are discussed.

I. Introduction

NANOCOMPOSITE materials consist of nanoscale constituents which exhibit optical and electronic properties that differ from the corresponding macroscopic properties. There is a wide range of potential applications of nanocomposite materials. Among them are electrical and optical sensors, dispersions, coatings, and novel optical glasses. While there is a strong effort in the synthesis of nanostructures and nanocomposite materials, there is also a need to develop suitable techniques to probe the physical properties of these novel materials. In fact, the recent rapid advances in nanotechnology are due in large part to our newly acquired ability to measure and manipulate individual structures on the nanoscale. Among these techniques are scanning probe microscopes, optical tweezers, high-resolution electron microscopes, and others.

Currenly, there is a big effort to understand the physical and chemical properties of nanoscale systems. In the bottom-up approach one first intends to understand the building blocks on a nanometer scale before assembling them into a functional device. However, the properties of the building blocks can change once they are embedded into a macroscopic structure. This change is due to interactions between the building blocks and also interactions with the environment. In fact, one of the most interesting aspects of materials at the nanoscale involves properties dominated by collective phenomena. In some case, collective phenomena can bring about a large response to a small stimulus. To investigate such phenomena it is necessary to study the properties of single nanostructures in a complex environment. However, this requires instrumentation with high spatial resolution.

In this paper we describe a near-field optical technique for the characterization of nanocomposite materials. Using this technique, spectroscopic measurements with spatial resolutions of 20 nm have been demonstrated.[1] Here, we will first present experimental results for samples of J-aggregates of PIC dye molecules. These results demonstrate the principle and the capabilities of this near-field optical technique. We then discuss our current experiments on nanocomposite oxyfluoride glass-ceramics.[2]

R. K. Brow—contributing editor

Manuscript No. 187937. Received February 15, 2001; approved August 15, 2001.
Presented at the Fall Meeting of the Glass and Optical Materials Division, Oct. 1–4, 2000, Corning, NY.
This work was supported by the NSF Grant No. DMR-0078939.

II. Near-Field Optical Microscopy and Spectroscopy with Laser-Illuminated Metal Tips

Optical spectroscopy provides a wealth of information on structural and dynamical properties of materials. Combining optical spectroscopy with microscopy is especially desirable because the spectral features can be spatially resolved. In recent years a novel microscopy, called near-field optical microscopy,[3] has extended the range of optical measurements beyond the diffraction limit and stimulated interests in many disciplines, especially material sciences and biological sciences.[4] In the most widely adapted aperture approach,[5] light is sent down an aluminum-coated fiber tip of which the foremost end is left uncoated to form a small aperture. Unfortunately, only a tiny fraction of the light coupled into the fiber is emitted through the aperture because of the cutoff of propagation of the waveguide modes. The low light throughput and the finite skin depth of the metal are the limiting factors for resolution. Nowadays, it is doubted that an artifact-free resolution of 50 nm will be surpassed by the aperture technique. However, many applications in nanotechnology require higher spatial resolutions.

To overcome this limitation, we introduced a new apertureless technique.[6] It makes use of the strongly enhanced electric field close to a sharply pointed metal tip under laser illumination. Depending on the tip material and the polarization of the excitation, the energy density close to the metal tip can be 2 to 3 orders of magnitude larger than the energy density of the illuminating laser light. The field enhancement arises from a high surface charge density at the tip induced by the incident light polarized along the tip axis. In contrast, incident light with polarization perpendicular to the tip axis results in no field enhancement. Figure 1 shows the calculated field distribution and induced surface charge density when the gold tip is illuminated with the polarization along the tip axis. Notice that the field enhancement is *not* based on a surface plasmon resonance condition. Instead, it is generated by the quasi-electrostatic singularity at the tip (lightning rod effect).

The principle of the experimental setup is shown in Fig. 2. A laser beam is focused by a high numerical aperture objective onto the sample surface and the tip is laterally positioned into the focal spot. The laser wavelength and polarization are optimized to maximize the field enhancement at the metal tip. The enhanced fields near the tip form a local excitation source which allows for a highly confined optical interaction with the sample surface. This interaction gives rise to a spectroscopic response which is collected by the same objective lens and directed onto a confocal pinhole and a subsequent optical detector. To establish an optical image of the sample surface, the sample is laterally raster scanned while assigning to each point on the sample surface a corresponding spectroscopic signature. The metal tip is maintained within 0.5–2 nm above the sample surface by using a tuning-fork feedback mechanism.[7] A highly sensitive preamplification allows us to keep the interaction forces between tip and sample in the range of 10–100 pN. Forces in this range do not damage the soft metal tips. A phase-sensitive detection scheme[8] with a fast time response has been developed to circumvent the limitations imposed by the high Q factor (1600) of the tuning fork resonance. The vertical noise (electrical and mechanical) of the entire system is less than 0.1 nm (rms).

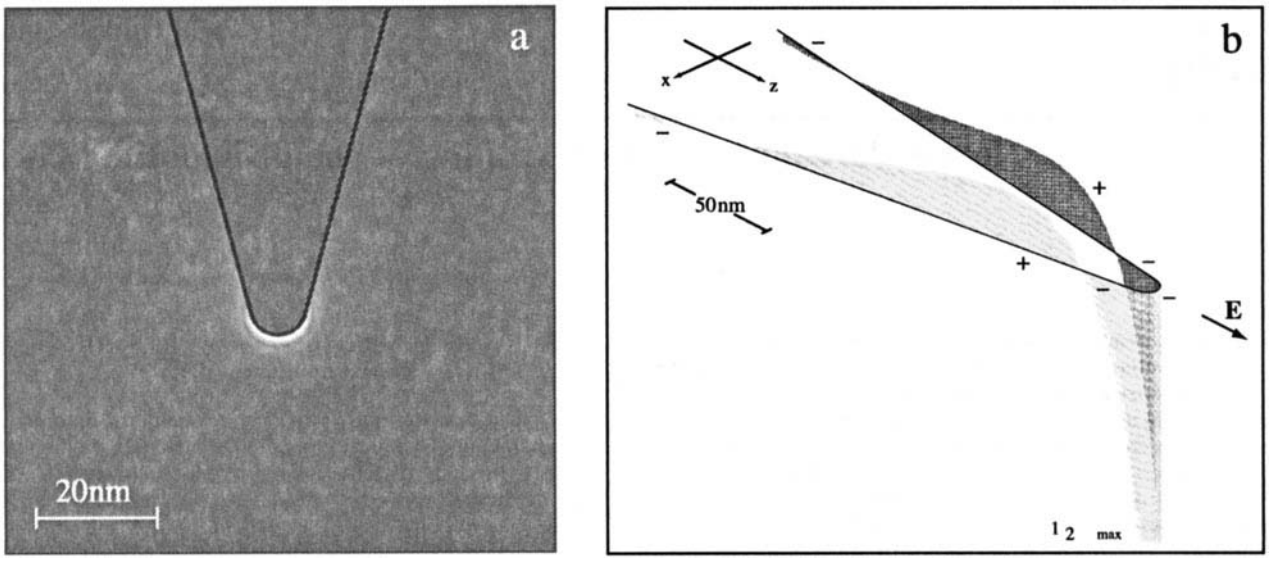

Fig. 1. (a) Calculated field distribution (E^2) near a gold tip illuminated by a plane wave polarized along the tip axis. The electric field is considerably enhanced beneath the tip. (b) Induced surface charge density. The surface charges form an oscillating standing wave. The large surface charge accumulation at the foremost part is responsible for the field enhancement. From Ref. 9.

The direct illumination of the sample surface gives rise to a far-field background signal. If we consider an optical interaction that is based on an nth-order nonlinear process and assume that only the sample surface is active, then the far-field background will be proportional to

$$S_{ff} \sim AI_0^n \tag{1}$$

where A is the illuminated surface area and I_0 is the laser intensity. The signal that we wish to detect and investigate (near-field signal) is excited by the enhanced field at the tip. If we designate the enhancement factor for the electric field intensity by f, then the near-field signal of interest is proportional to

$$S_{nf} \sim a(fI_0)^n \tag{2}$$

where a is a reduced area given by the tip size. If we require that the signal be stronger than the background ($S_{nf}/S_{ff} > 1$) and use realistic numbers for the areas ($a = (10\text{ nm})^2$, $A = (500\text{ nm})^2$), then we find that an enhancement factor of

$$f > \sqrt[n]{2500} \tag{3}$$

is required. For a first-order process ($n = 1$) such as scattering or fluorescence an enhancement factor of 3 to 4 orders of magnitude is required, which is beyond the calculated values. Therefore, the scheme is not applicable to first-order processes and it is necessary to involve higher-order nonlinear processes. For a second-order nonlinear process the required enhancement factor is only 50. This is the reason that our first experiments have been performed with two-photon excitation. Since the enhanced field is highly localized at the end of the tip, the achievable resolution is on the order of the tip diameter. Previous experiments with ultrasharp gold tips produced by focused ion beam milling demonstrated spectroscopic measurements with spatial resolutions on the order of 20 nm.[9] To date, this is the highest reported spatial resolution of a spectroscopic optical measurement.

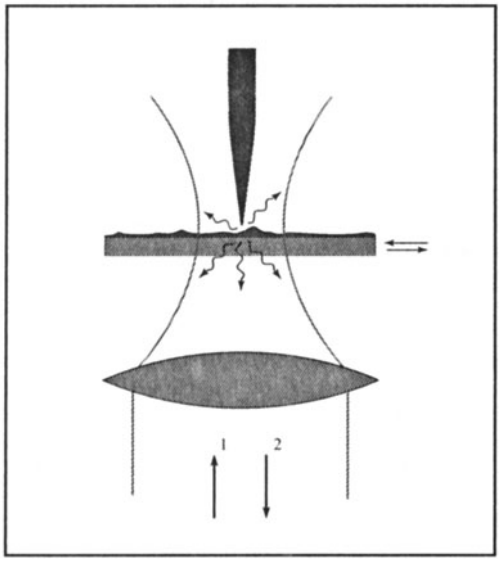

Fig. 2. Principle of the near-field optical technique. A laser beam is focused on a sample surface and a sharply pointed metal tip is held in close proximity above the surface. The enhanced fields at the tip locally interact with the sample surface, thereby exciting a spectroscopic response that is detected by the same objective and directed onto a detector.

III. Experiments on J-Aggregates Using Two-Photon Excitation

The enhanced field at the tip can be established only if the exciting laser light has an electric field component along the tip axis. Therefore, in an on-axis illumination as shown in Fig. 2 one would not expect a strong field enhancement. However, this is true only for a focused beam in the paraxial (weakly focused) approximation. For a beam focused by a lens with a high numerical aperture (NA) an appreciable longitudinal field is built up in the focus of the beam.[10] The longitudinal field is zero on the optical axis. In the focal plane it forms two distinct lobes aligned in the direction of the beam polarization. The strength of this longitudinal field increases with increasing NA of the focusing lens. For a strongly focused beam as encountered in our setup, the longitudinal field strength is only a factor of 5 weaker than the transverse field strength (cf. Fig. 3(c)). An image of the two longitudinal field lobes is shown in Fig. 3(a). To record these images we made use of the fact that the field enhancement is accompanied by increased second-harmonic generation at the metal tip surface. The light of a mode-locked titanium–sapphire (Ti:S) laser ($\lambda = 830$ nm) generating ≈150 fs laser pulses has been focused by an NA = 1.4 objective lens on the surface of a bare glass surface and a sharp gold tip was scanned line by line through the focus. An image was

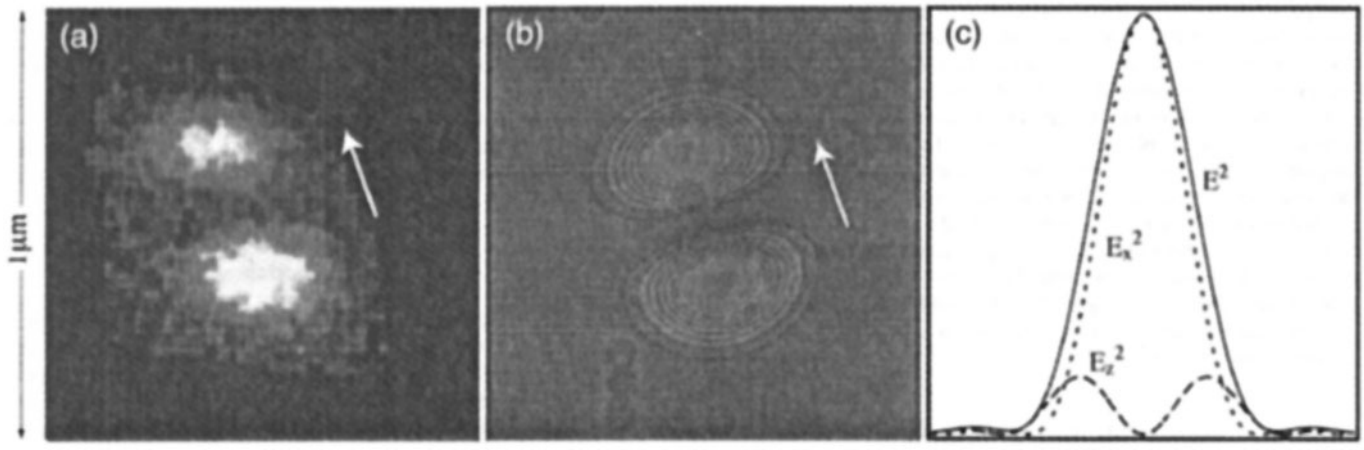

Fig. 3. Longitudinal field lobes in the focal plane of a strongly focused laser beam. The experimental image (a) has been measured by raster scanning the gold tip through the focal plane of the laser beam and recording the second-harmonic light generated at the surface of the tip. The two lobes are aligned in direction of the laser polarization in agreement with the calculated pattern (b). The arrows indicate the direction of polarization. (c) Longitudinal field strength (E_z^2), transverse field strength (E_x^2), and total field strength (E^2) as a function of the radial coordinate in the focal plane.

generated by recording the intensity of the generated second-harmonic light for each tip position. Figure 3(b) shows that the obtained image is in agreement with the calculated pattern. If the polarization of the laser beam is rotated by 90°, the two lobes rotate as well. Figure 3(c) depicts the longitudinal (E_z^2) and transverse (E_x^2) field strength as a function of the radial coordinate (along the polarization direction) in the focal plane.

To demonstrate the imaging properties of the field enhancement technique we chose a sample which simultaneously generates a near-field and a far-field image. This sample consists of single nanoscale PVS (poly(vinyl sulfate)) strands with J-aggregates of PIC (pseudoisocyanine) dye.[11] The gold tip has been positioned above a longitudinal field lobe in the laser focus and the sample with a single strand of J-aggregates was laterally scanned as schematically shown in Fig. 2. Both the focused Ti:S laser light and the enhanced field at the gold tip excite the J-aggregates by two-photon absorption. The emitted fluorescence is detected and used to establish an optical raster-scan image. Figure 4(a) shows the topographic (surface profile) image of a single strand of J-aggregates, and Fig. 4(b) shows the simultaneously recorded fluorescence image. The curves beneath the images show an arbitrary cross section. The size of the J-aggregate strand was chosen such that two distinct features can be recognized in the fluorescence image: (1) a broader shoulder due to fluorescence excited by the focused laser light and (2) a sharp peak which corresponds to the fluorescence excited by the enhanced field at the gold tip. Thus, the optical image is a superposition of a far-field image and a near-field image. The near-field peak disappears if the tip is retracted from the sample surface during the imaging process, but the far-field shoulder remains unaffected. Figure 4(c) shows

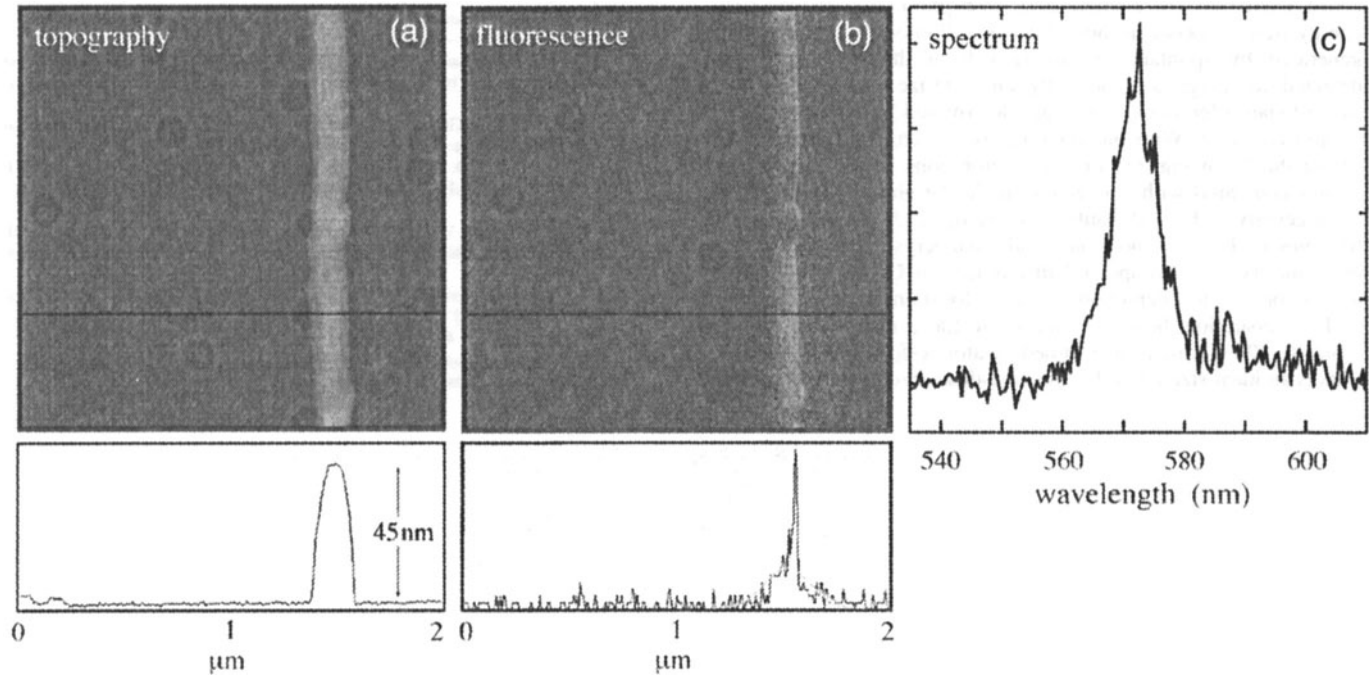

Fig. 4. Simultaneously recorded near-field and farfield image of a single PVC strand with J-aggregates of PIC dye: (a) topographic image; (b) two-photon excited fluorescence image. The sharp peak in the cross section is generated by the enhanced field at the laser illuminated tip (near-field image), whereas the broader Gaussian curve is generated directly by the focused laser light (far-field image). The near-field image is displaced from the center of the beam because of the off-axis location of the longitudinal field lobes (cf. Fig. 3(c)). (c) Spectrum of the emitted fluorescence.

the spectrum of the emitted fluorescence as determined by the PIC dye molecules. If the tip is retracted, the intensity of the spectrum drops because the near-field signal is lost. It can be clearly recognized that the near-field generated vertical line in Fig. 4(b) is slightly displaced from the center of the far-field image. The reason for this displacement is the off-axis location of the longitudinal field lobes. While the far-field image is generated by the total field strength (E^2 in Fig. 3(c)), the near-field image is excited by one of the two longitudinal field lobes (E_z^2 in Fig. 3(c)). Notice that only the surface of the J-aggregate strand contributes to the near-field signal. On the other hand, the entire thickness of the strand determines the strength of the far-field signal. Therefore, by imaging smaller strands it is possible to completely reject the far-field contribution.[12]

IV. Experiments on Nanocomposite Materials

While previous investigations on J-aggregates provided a good understanding and quantification of the field enhancement effect, our current research is focused on nanocomposite materials. One of the systems studied is rare-earth (RE) doped transparent oxyfluoride glass ceramics. These samples consist of a glass matrix with embedded LaF_3 nanocrystallites.[13] Because the phonon energy in LaF_3 is roughly a factor of 3 lower than in glass, phonon quenching of excited RE ions is smaller inside LaF_3 nanocrystallites than in the glass matrix. Therefore, the lifetime of excited RE ions inside LaF_3 nanocrystallites is higher than in the glass matrix and the stimulated emission cross section is increased. Thus, the optical properties of RE-doped oxyfluoride glass ceramics are controlled by the nanoscale fluoride crystal hosts, whereas the mechanical properties and the durability are determined by the oxide glass. Oxyfluoride glass ceramics are promising materials for fiber amplifiers and up-conversion devices.[14]

Our experiments are aimed at optically resolving individual LaF_3 nanocrystallites on the surface of a thin Er^{3+}-doped oxyfluoride glass ceramic sample. The erbium ions are excited from the $^4I_{15/2}$ state by the simultaneous absorption of two photons at $\lambda \approx$ 850 nm. This excitation scheme depends quadratically on the excitation intensity and therefore provides good suppression of the far-field background signal. The intermediate virtual level has to be sufficiently separated from the excited levels $^4I_{9/2}$ and $^4I_{11/2}$ to avoid excitation by excited-state absorption and excited-state energy transfer between individual ions. Photons at λ = 550 nm generated by spontaneous emission from the $^4S_{3/2}$ state are detected to image and optically characterize the sample. The excited-state lifetimes of Er^{3+} are determined by time-correlated photon counting. With our ongoing experiments we are investigating the following: (1) Er^{3+} concentrations in LaF_3 nanocrystallites compared with concentrations in the glass matrix, (2) the homogeneity of Er^{3+} dopants in the sample, (3) the excited-state lifetimes of Er^{3+} in individual LaF_3 nanocrystallites and in the glass matrix, and (4) spectral differences of Er^{3+} emission and absorption due to interactions with the local environment.

The separation between individual LaF_3 nanocrystallites is typically 30–60 nm as determined by atomic-force microscopy.[15] This is an ideal size range for the here-described near-field optical technique. It is important to use very thin samples and a confocal detection scheme to reduce the far-field background signal. To increase the signal-to-noise ratio it is also possible to apply a three-photon excitation scheme with excitation pulses at $\lambda \approx 1.25$ μm. The signal-to noise ratio can be further increased by illuminating the metal tip with a higher-order laser mode having a longitudinal field at its focus.[16] A convenient conversion scheme to produce such modes has been developed recently.[17]

V. Conclusions

We have described a near-field optical technique with optical spatial resolution down to 20 nm. This method is based on the field enhancement effect at laser-illuminated metal tips. Initial experiments on J-aggregates of PIC molecules demonstrate the principle of the technique. Ongoing experiments on nanocomposite glass ceramics are aimed at optically resolving individual LaF_3 nanocrystallites and measuring the concentration and lifetimes of Er^{3+} dopants.

Acknowledgments

I thank Professor S. Houde-Walter and G. Jones for prompting the experiments on oxyfluoride glass ceramics, and M. Dejneka for providing the samples.

References

[1]E. J. Sanchez, L. Novotny, and X. S. Xie, "Near-Field Fluorescence Microscopy Based on Two-Photon Excitation with Metal Tips," *Phys. Rev. Lett.*, **82**, 4014–17 (1999).

[2]L. Novotny, E. J. Sanchez, and X. S. Xie, "Near-Field Optical Spectroscopy Based on the Field Enhancement at Laser Illuminated Metal Tips," *Opt. Photonics News*, **10** [12] 24 (1999).

[3]"Progress Made in Near-Field Imaging with Light from a Sharp Tip," *Phys. Today*, [July] 18–20 (1999).

[4]M. J. Dejneka, "Transparent Oxyfluoride Glass Ceramics," *MRS Bull.*, [November] 57–62 (1998).

[5]D. W. Pohl, W. Denk, and M. Lanz, "Optical Stethoscopy: Image Recording with Resolution λ/20," *Appl. Phys. Lett.*, **44**, 651–653 (1984).

[6]A. Lewis, M. Isaacson, A. Harootunian, and A. Muray, "Development of a 500 Å Resolution Light Microscope," *Ultramicroscopy*, **13**, 227–31 (1984).

[7]For a recent review, see: B. Dunn, "Near-Field Scanning Optical Microscopy," *Chem. Rev.*, **99**, 2891–928 (1999).

[8]E. Betzig and J. K. Trautman, "Near-Field Optics: Microscopy, Spectroscopy, and Surface Modification beyond the Diffraction Limit," *Science*, **257**, 189–95 (1992).

[9]L. Novotny, R. X. Bian, and X. S. Xie, "Theory of Nanometric Optical Tweezers," *Phys. Rev. Lett.*, **79**, 645–48 (1997).

[10]L. Novotny, E. J. Sanchez, and X. S. Xie, "Near-Field Optical Imaging Using Metal Tips Illuminated by Higher-Order Hermite-Gaussian Beams," *Ultramicroscopy*, **71**, 21–29 (1998).

[11]K. Karrai and R. D. Grober, "Piezoelectric Tip-Sample Distance Control for Near Field Optical Microscopes," *Appl. Phys. Lett.*, **66**, 1842–44 (1995).

[12]A. G. T. Ruiter, K. O. van der Werf, J. A. Veerman, M. F. Garcia-Parajo, W. H. J. Rensen, and N. F. van Hulst, "Tuning Fork Shear-Force Feedback," *Ultramicroscopy*, **71**, 149–57 (1998).

[13]B. Richards, and E. Wolf, "Electromagnetic Diffraction in Optical Systems. II. Structure of the Image Field in an Aplanatic System," *Proc. R. Soc. London, A*, **253**, 358–79 (1959).

[14]D. A. Higgins, J. Kerimo, D. A. Vanden Bout, and P. F. Barbara, "A Molecular Yarn: Near-Field Optical Studies of Self-Assembled, Flexible, Fluorescent Fibers," *J. Am. Chem. Soc.*, **118**, 4049–58 (1996).

[15]K. S. Youngworth and T. G. Brown, "Focusing of High Numerical Aperture Cylindrical-Vector Beams," *Opt. Express*, **7**, 77–87 (2000). □

journal

J. Am. Ceram. Soc., 85 [5] 1127–32 (2002)

Morphological Control of Zirconia Nanoparticles through Combustion Aerosol Synthesis

Amit U. Limaye and Joseph J. Helble

Department of Chemical Engineering, University of Connecticut, Storrs, Connecticut 06269–3222

Ceramic oxide nanoparticles produced by flame-based processes are typically agglomerated, which can limit their use in some applications. In this paper, a novel combustion synthesis method that utilizes the spraying of combustible droplets into a premixed flame to produce nanoscale crystalline particles of agglomerated and unagglomerated morphologies is described. Although the same flame-based experimental setup is used in both cases, variation in peak flame temperatures results in a corresponding variation between fractallike agglomerates and single isolated spherical particles. TEM/ED analysis shows that both classes of particles are the tetragonal crystal phase of zirconia. In the case of the unagglomerated spherical particles, results indicate that each precursor solution droplet, which acts as the feed, produces multiple spherical ceramic nanoparticles with a number mean diameter of 90 nm. The use of an inertial impaction stage in the precursor feed line to eliminate large feed droplets leads to a decrease in the number mean diameter to 60 nm, suggesting that crystalline spherical nanoparticles can be produced in a continuous flame-based process through control of the feed droplet size.

I. Introduction

PARTICLES having features with dimensions ranging from a few to a few hundred nanometers are often referred to as nanoparticles. Nanoparticles of zirconia, which have a broad range of applications, including high-strength ceramics, thermal barrier coatings, paints, textiles, refractories, transformation-toughened ceramics, oxygen sensors, and fuel cells,[1–4] have been produced by a variety of techniques. Vapor deposition, mechanical milling, laser ablation, flame-based methods, spray pyrolysis, sol–gel, and microwave plasma synthesis have been used to produce ceramic particles ranging from a few nanometers to a few micrometers in size and of varied degrees of crystallinity.[5–9] Flame-based methods are of potential commercial importance, because they are relatively low cost and can be operated as continuous single-step processes.[10–24] Although very small particles (5–10 nm) can be produced by these methods, hard agglomerates are generally formed, resulting in "fractallike" branched structures that are undesirable in many applications. Attempts have been made to control agglomeration using electric fields,[22] but only moderate success has been achieved, with partial agglomeration always present. In addition, special burner and gas-flow configurations are often required in these processes,[12] because fuel–oxidizer mixing and flame structure affect the final particle morphology and size.[14,23]

In high-temperature synthesis methods, such as flame-based methods, the type of precursor also is important in determining the final particle characteristics. The use of solid,[13,16] liquid,[12,15,21] or gaseous[20,22–24] precursors for ceramic oxide particle production using flames or high-temperature furnaces[7,9] has been reported. Although the chlorides of silicon and titanium are relatively volatile and have been used as gaseous precursors for oxide particle formation, the low vapor pressure of zirconium chloride limits its use as a precursor. Consequently, liquid precursors, such as aqueous solutions or organometallic compounds of zirconium, have been used in flame[12,21] and spray-drying systems[7,25] for zirconia nanoparticle synthesis. Unagglomerated particles can be formed using liquid precursors with the final particle size governed by the precursor droplet size when a spray-drying furnace is used for processing.[7,25] Experimental trends observed in spray pyrolysis systems have been explained reasonably well by a model reported in the literature.[25] The model compares the rates of solute diffusion within the droplet and solvent vaporization from the droplet surface and explains their effect on the particle morphology. Large particles (micrometer scale) are formed, however, if dilute precursor concentrations are not used in these systems. Although typical flame-based processes produce agglomerated particles, unagglomerated particles also can be formed in a flame-based system using liquid precursors. The final particle sizes, however, are not directly dependent on the droplet sizes[12,21] in these systems, unlike in spray pyrolysis. The mechanism of particle formation when liquid precursors are used in flame-based systems is not yet fully understood. In processes using fine particles of metals as the precursor, it is suggested that the oxide particle growth occurs predominantly by vapor condensation,[16] whereas particle growth occurs by collision and coalescence when gaseous precursors are used.[19]

In this article, we present the results of a novel droplet combustion process for the synthesis of nanoparticles with controllable morphology and particle size. Using liquid precursors sprayed into a premixed methane–oxygen flame, we have eliminated the dependence of particle size on fuel–oxidizer mixing and flame structure. Details of the process are provided below.

II. Experimental Procedure

An experimental system was designed to provide flames of varying and controllable temperature profile, resulting in variable residence time of the combustion gases in the reactor. A schematic diagram of this experimental setup is shown in Fig. 1. A flat-flame, water-cooled, porous-plug stainless-steel burner (McKenna Products, Inc., Sebastopol, CA) was used as the heat source and the main component of the system. Methane, oxygen, and nitrogen were premixed within the burner, and the resulting two-dimensional flame was anchored on the porous plug. A shroud of nitrogen around the porous plug eliminated fluctuations in the flame caused by external disturbances. Ceramic precursors were introduced into the flame by spraying a combustible precursor solution through a feed tube located centrally in the burner. Zirconium(IV) *n*-butoxide (Strem Chemicals, Inc., Newburyport, MA) dissolved in 99.8% anhydrous butanol (Sigma Chemicals, Inc., St. Louis, MO) was used as the precursor feed stock. To prepare the feed solution, the zirconium(IV) *n*-butoxide was added to butanol with moderate stirring under nitrogen in a glove box to avoid reaction with water present in the air. The spray was

K. Bowman—contributing editor

Manuscript No. 187375. Received October 24, 2001; approved February 12, 2002.
Supported by the National Science Foundation under CAREER Grant No. CTS-9733234.

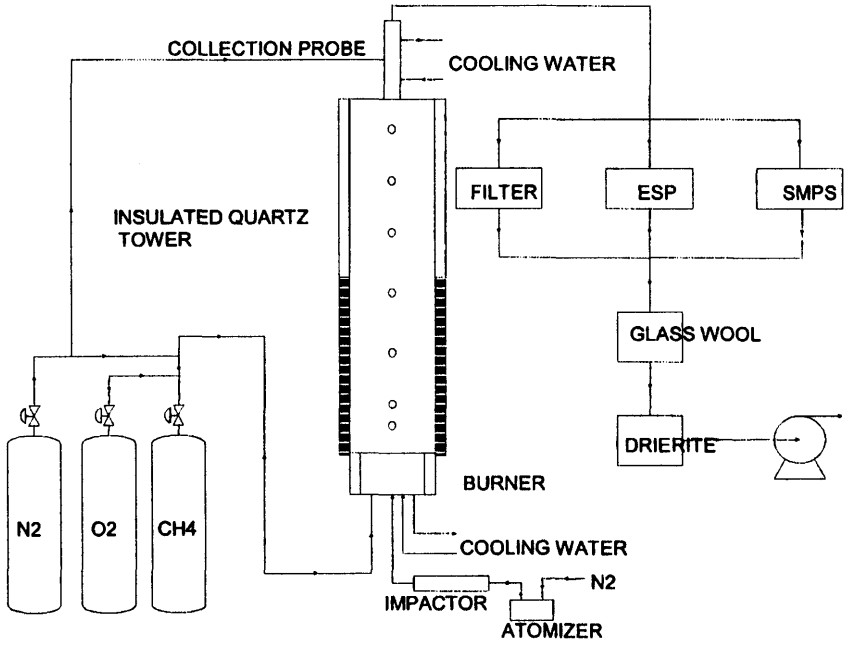

Fig. 1. Schematic diagram of experimental system used for the production of zirconia nanoparticles.

produced using a pressure-driven atomizer (Model 9302, TSI, Inc., St. Paul, MN) operating in the pressure range of 5–50 psi (34.5–345 kPa). The droplet size distribution output of the atomizer was characterized at various pressures using a phase doppler particle analyzer (PDPA; Aerometrics, Inc., Sunnyvale, CA) and was relatively independent of operating pressure over the entire range. The size distribution of the droplets produced by the atomizer had a number mean diameter ranging from 6 to 8 μm as the pressure increased from 5 to 50 psi (34.5–345 kPa). At an operating pressure of 10 psi (69 kPa) (used in most experiments in this study) a relatively small fraction of the droplets had a size >20 μm (~0.7%), thus indicating the absence of very large droplets in the spray.

A 1.0 m quartz tower placed downstream of the burner served to confine the products of combustion and to prevent entrainment of room air. The tower had sampling ports located axially every 15 cm along its height, providing access for thermophoretic sampling of particles at locations downstream of the flame. The entire tower was insulated to maintain high temperatures in the postcombustion region and avoid thermophoretic deposition of the particles on the tower walls. Fiberglass wrap was used to insulate the upper 50 cm of the tower. A steel shroud wrapped around the lower 50 cm of the tower insulated it against radiative losses while a castable insulating cement (McMaster, Inc.) insulated the outer surface of the shroud to minimize the heat loss from the shroud to the ambient air.

Particles were sampled by thermophoretic deposition on transmission electron microscopy (TEM) grids attached to the end of the thermophoretic sampling probe. A solenoid-controlled air-driven piston was used to introduce the probe through one of the tower axial sampling ports for 1000 repeated short-duration (700 ms) pulses to collect sufficient samples for analysis. A specially constructed, movable, water-cooled, nitrogen-quenched collection probe was also used to collect particles at the tower exit. The dilution was used to avoid the condensation of water vapor formed as a combustion product in the lines downstream of the reactor. Particles were then separated from the gas stream by deposition on a TEM grid located within a point-to-plane electrostatic precipitator (ESP; Intox Products, Inc., Albuquerque, NM). In some experiments, a scanning mobility particle sizer (SMPS; TSI, Inc., St. Paul, MN) was used to provide on-line measurement of particle-size distribution in the range of 18–900 nm. Particle morphology and crystallinity were subsequently analyzed using TEM (Model 420, Phillips, Amsterdam, The Netherlands) equipped for energy dispersive spectroscopy (EDS; EDAX, Inc., Stratford, CT).

III. Results and Discussion

To begin an experiment, the burner gases were ignited and the reactor was then allowed to attain a steady-state temperature profile by the heating of the reactor walls for 20–25 min. The precursor solution was then sprayed through the central feed tube using the atomizer. The premixed flame was run at an equivalence ratio of one (φ = 1.0) based on the methane and oxygen content. The relative contents of methane, oxygen, and nitrogen in the premixed gases were 1/2/13.2 on a molar basis, respectively, resulting in a calculated adiabatic flame temperature of 1710 K, assuming complete species chemical equilibrium. The linear velocity of the hot gases was calculated along the tower height and used to obtain the residence times of the gases in the tower. The temperature profile inside the reactor as measured using a K-type thermocouple and corrected for radiation effects is shown as the curve labeled "single" in Fig. 2. Figure 2 shows there was a rapid

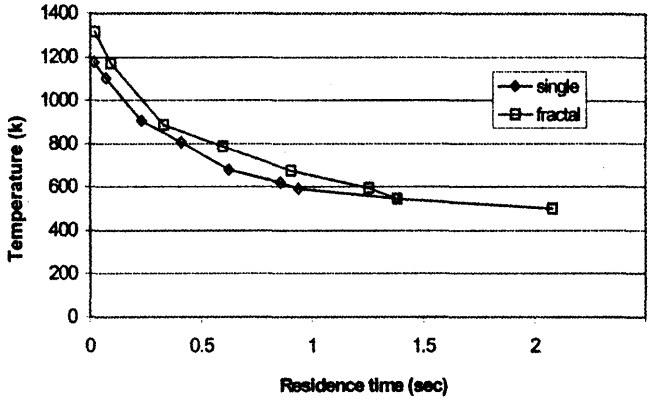

Fig. 2. Temperature in the reactor versus gas residence time showing the two operating conditions used for the production of agglomerated (fractal) and unagglomerated (single) particles.

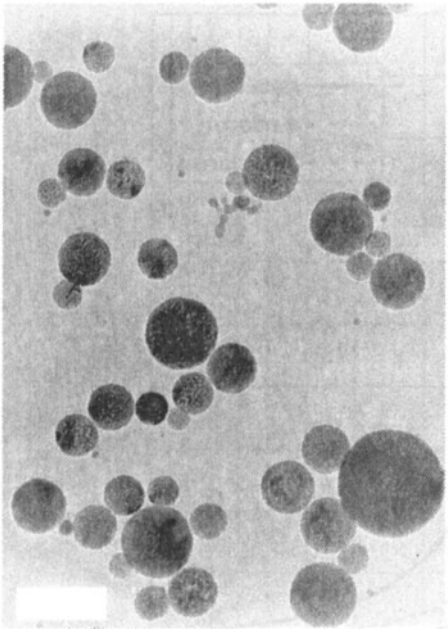

Fig. 3. Single, spherical unagglomerated particles obtained using a low-temperature flame (magnification is 88 600 times).

temperature decrease immediately after the flame. This was beneficial for inhibition of agglomeration resulting from interparticle collision in the postcombustion region, because colliding particles are less likely to coalesce at a low temperature.

For production of nanoparticles, a 0.047*M* solution of the precursor zirconium(IV) *n*-butoxide/butanol solution was sprayed into the core region of the flame using the atomizer operated at 10 psi (69 kPa). The calculated characteristic time required for the vaporization of a 10 μm droplet of butanol was 55 ms, whereas the calculated residence time of the gases in the flame zone was 20 ms. Consequently, particle formation was expected to occur within the flame and in the postcombustion region immediately downstream of the flame.

Nanoparticles were collected at intermediate locations (residence times of 400 and 850 ms) in the tower using the thermophoretic sampling probe. Particles were also collected at the exit of

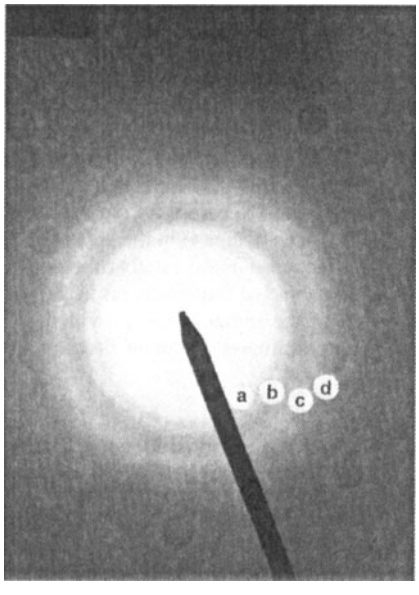

Fig. 4. Selected-area electron diffraction pattern for spherical particles shown in Fig. 3. Rings are labeled by the Miller indexes of diffracting planes: (a) (200), (b) (211), (c) (114), and (d) (312).

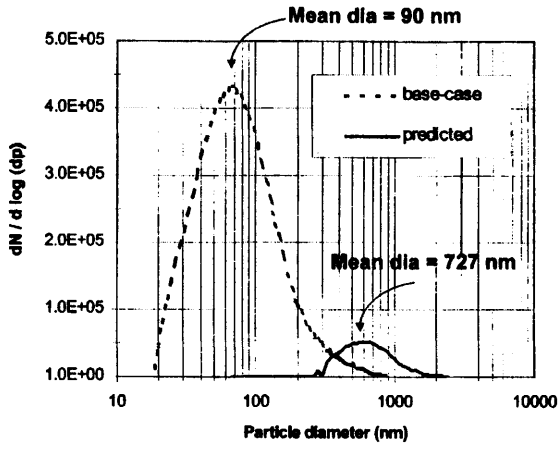

Fig. 5. Comparison of the measured PSD with that predicted from an assumption of a single particle produced per droplet.

the reactor (overall residence time of 1.4 s) using the collection probe and the ESP. The particles collected at these three locations were used to obtain information on the evolution of particle size and morphology as a function of residence time in the reactor. TEM was used to analyze particle morphology (size and shape) and crystallinity. A micrograph of particles collected at 400 ms residence time at a magnification of 88 600 is shown in Fig. 3. Isolated spherical particles were produced with no agglomeration observed. Selected area electron diffraction (SAD) study of these particles revealed they had the tetragonal crystal structure. A representative SAD pattern with the Miller indexes of the diffracting planes indicated on it is show in Fig. 4. Although the size distribution of the particles collected at the residence times of 400 and 850 ms was obtained using image analysis of TEM micrographs, the SMPS was used to obtain the particle-size distribution (PSD) of particles collected at the exit. This PSD, labeled "base case" in Fig. 5, indicated that the particle sizes were not uniform and varied over a wide range. The number mean diameter was 90 nm, but particles as large as 500 nm were also observed. The number mean diameter and the standard deviation for the PSD obtained for particles collected at all three locations are presented in Table I. The mean value and the standard deviation remained constant with increased residence time, indicating that there was no change in the particle size beyond a residence time of 400 ms. Although particle growth can occur by condensation of zirconia vapors or by coalescence of particles, the results indicated that the particle formation process was complete within 400 ms and subsequent particle growth did not occur. Particles collected at all three locations, as observed using TEM, had the same spherical shape with no agglomeration.

The present process of nanoparticle formation is similar to spray pyrolysis in that both processes use liquid precursors sprayed into a high-temperature region to form nanoparticles. In spray pyrolysis, however, each precursor droplet produces one particle, thereby making it possible to predict the final PSD as long as the precursor concentration in the solution and the size of the solution droplets are known. Because the concentration and size are known for our system, the PSD predicted by spray pyrolysis has been calculated and is shown as the curve labeled "predicted" in Fig. 5. Comparing

Table I. Comparison of Particle-Size Data Collected at Various Residence Times in the Reactor

Residence time (ms)	Number mean (nm)	Standard deviation (nm)	Particles >160 nm (%)
400	98	78	14
850	96	74	13
1400	90	80	11

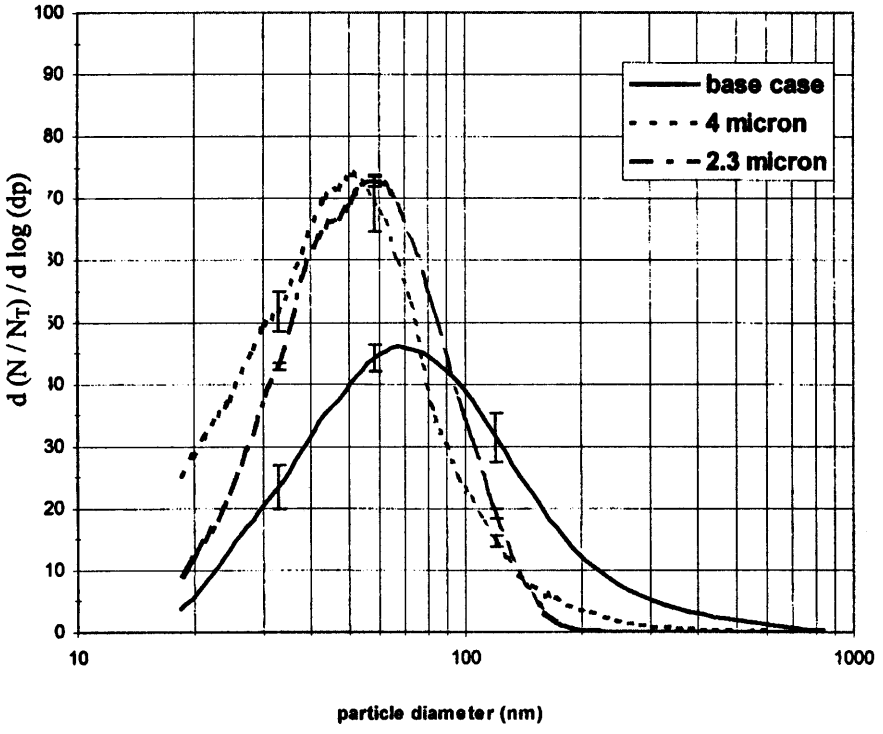

Fig. 6. PSD of zirconia nanoparticles obtained from experiments in which impactors were used to eliminate the large droplets in the feed stream. Each curve represents the average of four (base case) or five (impactor) experiments. Error bars represent standard deviation of the mean value of the normalized number distribution normalized by the total number count (N_T) at the indicated point.

the two curves in Fig. 5, it is apparent that spray pyrolysis would produce much larger particles (mean 727 nm) for the precursor concentration and droplet sizes used in this study. This clearly indicates that more than one ceramic nanoparticle results from each precursor droplet in combustion aerosol synthesis as developed in this study. This conclusion is of significance because it indicates that large droplets can be used to produce small particles without operating at the very low precursor concentrations required by spray pyrolysis. Such small particles are likely produced as a result of the competition between solvent vaporization and solute diffusion within the precursor droplets. If the evaporation rate is large compared with the solute diffusion rate, the local concentration of solute increases near the receding droplet surface, subsequently producing cenospheric particles rather than solid ones.[25] If the evaporation rate is much larger than the diffusion rate, however, regions of locally high solute concentration are expected to form. Nucleation occurs in these regions, producing isolated particles. This mechanism is possible in our system because of the much higher heating rates (10^4–10^5 K/s) compared with a typical spray pyrolysis process (10^3–10^4 K/s). Each droplet thus acts as a microreactor, producing many small particles.

Further examination of the curve labeled "base case" in Fig. 5 indicates that, although the number of small nanoparticles is high, large nanoparticles (200 nm or larger) are also present in the final PSD. This indicates that most of the mass of the sample is contributed by the larger particles. In general, size as well as morphology is of importance, and, in many applications, it is desired that the nanoparticles have a uniform size or narrow PSD. The presence of large particles in the base-case PSD suggests that they may be forming from the large droplets in the precursor spray. Therefore, an inertial impactor has been used to eliminate the large droplets from the precursor spray.[26] In the inertial impactor, the smaller droplets exit the impactor unaltered while the larger droplets in the spray are retained in the chamber. Droplets larger than a desired size are prevented from entering the flame. For this specific application, two single-stage impactors with different cut-point sizes (d_{50} = 4 and 2.3 μm) have been designed, constructed, and utilized to eliminate the large droplets from the spray. The final PSD of the zirconia nanoparticles obtained when the spray system is modified by the inclusion of the impactors is shown in Fig. 6. The curves labeled "impactor 4" and "impactor 2.3" indicate the final zirconia PSD obtained when the 4.0 and 2.3 μm impactors are used, respectively. The area under the three curves in Fig. 6 is not the same, because the samples are collected for a fixed time interval rather than for a fixed mass of particles. Choosing a particle size of 160 nm to describe the spread in the size distribution of the zirconia nanoparticles shows that the fraction of particles >160 nm decreases as impactors with subsequently smaller cut-point sizes are used. For example, 11% of the total number of particles is >160 nm when the feed is not manipulated using an inertial impactor (curve labeled "base case"), whereas the fraction of particles >160 nm is decreased to 2% when the 4 μm impactor is used. The use of the 2.3 μm impactor further decreases this fraction to 0.2%, implying that only two of every thousand particles are >160 nm. This, therefore, enables the transformation of the majority of the precursor mass into zirconia nanoparticles of small and relatively uniform size. The decreased polydispersity of the PSD is also indicated by the decrease in the standard deviation of the PSD from 80 nm for the base case to 27 nm for impactor 2.3. The decrease in the spread of the PSD is also accompanied by a decrease in the number mean diameter from 90 to 60 nm. A summary of the improvement in the nanoparticle size distribution on using the impactors is provided in Table II. This manipulation of the atomized precursor droplets has provided an

Table II. Effect of the Sprayed Droplet Size—Comparison of the Final Particle-Size Distribution

Feed conditions	Number mean (nm)	Standard deviation (nm)	Particles >160 nm (%)
Base case	90	80	11
4 μm cutoff impactor	64	40	2.0
2.3 μm cutoff impactor	63	27	0.2

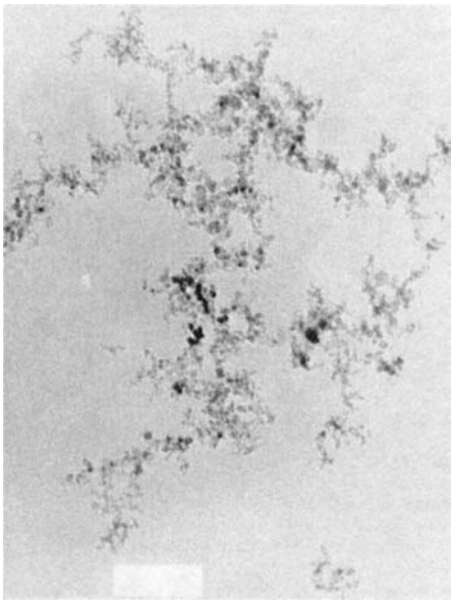

Fig. 7. Fractallike agglomerated particles obtained with a high-temperature flame (magnification of 88 600 times).

effective method of controlling the PSD in the combustion aerosol synthesis of crystalline ceramic nanoparticles.

Although the discussion thus far has been focused on crystalline spherical particles, agglomerated fractallike particles also can be produced using the same precursor and experimental setup. In general, production of agglomerated particles is facilitated by the vaporization of the precursors, as evidenced by numerous studies in the literature where gaseous or volatile precursors have been used.[14,20,22–24] It was speculated that an increase in the flame temperature would thus result in vaporization of the precursor, followed by subsequent reaction in the gas vapor phase to form zirconia nanoparticles. A higher-temperature premixed flame (φ = 1.0) was obtained by decreasing the nitrogen content such that the methane, oxygen, and nitrogen content of the premixed gases was 1/2/8.2 on a molar basis. Under these conditions, the calculated adiabatic flame temperature considering all species at chemical equilibrium was 2150 K. The radiation-corrected temperature profile is shown as the curve labeled "fractal" in Fig. 2. The particles produced under these conditions were composed of small individual primary particles that formed fractallike branched structures, as shown in Fig. 7. Although all the primary particles had comparable sizes of ~10 nm, the overall size of the agglomerated particles ranged from 100 nm to a few micrometers. Such open structures are characteristic of flame-based systems.[20,22–24]

The suggested mechanisms of competing vapor-phase and liquid-phase pathways, as applied to the work reported here, are shown schematically in Fig. 8. In both the cases, the first two steps are the same, regardless of whether particles of agglomerated or unagglomerated morphology are formed. In the liquid-phase pathway, the reaction of the precursors occurs in the liquid phase within each precursor droplet. Therefore, zirconium(IV) *n*-butoxide undergoes hydrolysis and/or oxidation within the confines of the sprayed liquid droplet. In contrast, in the vapor-phase pathway, the precursors vaporize/decompose in the high-temperature region and react in the vapor phase. The oxidized metal vapors then condense and form small particles that grow by coagulation. Consequently, hard fractallike agglomerates are more likely to form in materials with high vapor pressures in flame-based systems, because they vaporize more easily and react in the vapor phase to form oxide vapors.

In general, most nanoparticle synthesis processes require a postproduction step for crystallization of the final products and elimination of undesirable byproducts, such as chlorine and water.[8,9] Flame synthesis of nanoparticles eliminates this extra step, because calcination takes place within the process, resulting

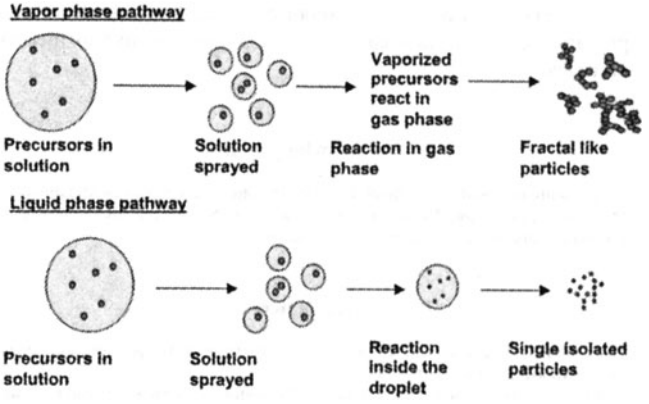

Fig. 8. Mechanisms of liquid- and vapor-phase pathways as applied to droplet combustion method of nanoparticle synthesis.

in a crystalline final product. Although the tetragonal phase of zirconia is not thermodynamically favored at room temperature, it is often found in materials with nanoscale structure, such as those produced in this work, because of the crystallite size effect.[27] This observation also has been made in this work. The crystallinity of the zirconia nanoparticles is determined using electron diffraction and is of the tetragonal phase structure irrespective of the particle morphology. The tetragonal phase is responsible for the unique quality of transformation toughening and is the desired phase of zirconia in applications requiring high fracture strength.[4]

IV. Summary and Conclusions

Combustion aerosol synthesis of zirconia nanoparticles with controllable morphology has been demonstrated in a single-step process for the first time. By varying the flame temperature and the temperature profile in the reactor, particles of either agglomerated or unagglomerated morphologies were synthesized. Although the experimental setup and the precursor loading were the same in both the cases, agglomerated particles resulted when higher flame temperatures were used. The high temperatures caused the zirconium(IV) *n*-butoxide precursor to vaporize/decompose and react in the gas phase to form zirconia particles, which grew by coagulation to form fractallike particles. In contrast, when the process of droplet to particle transformation occurred entirely in the liquid phase and at relatively low temperatures, single unagglomerated particles were formed. TEM analysis revealed that all the nanoparticles had the tetragonal-phase crystalline structure, regardless of the final particle morphology.

The final PSD, as obtained on spraying the precursors into the flame, was also polydisperse. Although all the particles were spherical and unagglomerated, the nonuniformity in their sizes was undesirable. Removal of large droplets through an inertial impactor caused a decrease in the number of large nanoparticles. When compared with the case where no impactor was used, the use of impactors increased the fraction of particles <160 nm from 89% to 99.8%. Good control on the unagglomerated PSD was thus obtained through control of the droplet size distribution.

The present process of droplet to particle conversion is compared with the spray pyrolysis method of particle synthesis. In spray pyrolysis, each particle forms from a single precursor droplet; however, the results from this work indicate that each precursor droplet results in multiple ceramic particles of varying sizes. This is attributed to the higher heating rates in a flame relative to a typical spray pyrolysis process. The formation of multiple particles per droplet is important, because it indicates that it is feasible to obtain small particles from large droplets. Spray pyrolysis suggests that small particles can be formed from large droplets only by operating at low precursor concentrations, and, thus, droplet size and the precursor concentration become controlling factors in the process. Although the restriction on the droplet

size is relaxed in the process reported here, a modest decrease in precursor concentration can further decrease the size of the final particles.

Acknowledgment

The authors would like to thank Dr. Donald Potter, Department of Metallurgy and Materials Engineering, University of Connecticut, Storrs, for his assistance and stimulating discussion regarding electron microscopy.

References

[1]H. Gleiter, "Materials with Ultrafine Microstructures: Retrospectives and Perspectives," *Nanostuct. Mater.*, **1**, 1–19 (1992).

[2]M. Gell, "Application Opportunities for Nanostructured Materials and Coatings," *Mater. Sci. Eng. A*, **A204**, 246–51 (1995).

[3]M. J. Mayo, J. R. Seidensticker, D. C. Hague, and A. H. Carim, "Surface Chemistry Effects on the Processing and the Superplastic Properties of Nanocrystalline Oxide Ceramics," *Nanostuct. Mater.*, **11** [2] 271–82 (1999).

[4]R. Stevens, "An Introduction to Zirconia," Pub. No. 113, Magnesium Elektron, Flemington, NJ, July 1986.

[5]T. D. Shen and C. C. Koch, "Formation and Hardening Effects in Nanocrystalline Ti–N Alloys Prepared by Mechanical Alloying," *Nanostuct. Mater.*, **5** [6] 615–29 (1995).

[6]R. J. Munz, T. Addona, and A.-C. da Cruz, "Application of Transferred Arcs to the Production of Nanoparticles," *Pure Appl. Chem.*, **71** [10] 1889–97 (1999).

[7]S. C. Zhang, G. Mulholland, and G. L. Messing, "Synthesis of ZrO_2 Nanoparticles by Spray Pyrolysis," *J. Mater. Synth. Proces.*, **4** [4] 227–33 (1996).

[8]L. L. Hench and J. K West, "The Sol–Gel Process," *Chem. Rev.*, **90** [1] 33–72 (1990).

[9]B. Xia, L. Duan, and Y. Xie, "ZrO_2 Nanopowders Prepared by Low-Temperature Vapor-Phase Hydrolysis," *J. Am. Ceram. Soc.*, **83** [5] 1077–80 (2000).

[10]D. E. Rosner, "Combustion Synthesis and Materials Processing," *Chem. Eng. Educ.*, [Fall] 228–35 (1997).

[11]Y. Chen, N. Glumac, B. H. Kear, and G. Skandan, "High Rate Synthesis of Nanophase Materials," *Nanostuct. Mater.*, **9**, 101–104 (1997).

[12]A. Kilian and T. F. Morse, "A Novel Aerosol Combustion Process for the High Rate Formation of Nanoscale Oxide Particles," *Aerosol Sci. Technol.*, **34**, 227–35 (2001).

[13]S. H. Ehrman and S. K. Friedlander, "Bimodal Distributions of Two Component Metal Oxide Aerosols," *Aerosol Sci. Technol.*, **30**, 259–72 (1999).

[14]S. E. Pratsinis, "Flame Aerosol Synthesis of Ceramic Powders," *Prog. Energy Combust. Sci.*, **24**, 197–219 (1998).

[15]J. Karthikeyan, C. C. Berndt, J. Tikkanen, J. Y. Wang, A. H. King, and H. Herman, "Nanomaterial Powders and Deposits Prepared by Flame Spray Processing of Liquid Precursors," *Nanostuct. Mater.*, **8** [1] 61–74 (1997).

[16]I. S. Altman, "On Condensation Growth of Oxide Particles During Gas-Phase Combustion of Metals," *Combust. Sci. Technol.*, **160**, 221–29 (2000).

[17]K. R. Venkatachari, D. Huang, S. P. Ostrander, W. A. Schulze, and G. C. Strangle, "Preparation of Nanocrystalline Yttria-Stabilized Zirconia," *J. Mater. Res.*, **10** [3] 756–61 (1995).

[18]G. D. Ulrich, "Flame Synthesis of Fine Particles" (special report), *Chem. Eng. News*, [Aug. 6] 22–29 (1984).

[19]B. W. Lee, J. I. Jeong, J. Y. Hwang, M. Choi, and S. H. Chung, "Analysis of Growth of Non-Spherical Silica Particles in a Counterflow Diffusion Flame Considering Chemical Reactions, Coagulation, and Coalescence," *J. Aerosol Sci.*, **32**, 165–85 (2001).

[20]O I. Arabi-Katbi, S. E. Pratsinis, P. W. Morrison Jr., and C. M. Megaridis, "Monitoring the Flame Synthesis of TiO_2 Particles by in-Situ FTIR Spectroscopy and Thermophoretic Sampling," *Combust. Flame*, **124**, 560–72 (2001).

[21]G. Saracco, F. Geobaldo, D. Mazza, and G. Baldi, "New Method of Catalyst Powder Manufacturing Based on Solvent Combustion," *J. Therm. Anal. Calorim.*, **56**, 1435–42 (1999).

[22]S. Vemury and S. E. Pratsinis, "Charging and Coagulation During Flame Synthesis of Silica," *J. Aerosol Sci.*, **27**, 951–66 (1996).

[23]S. E. Pratsinis, Z. Wenhua, and S. Vemury, "Role of Gas Mixing in the Flame Synthesis of Titania Powders," *Powder Technol.*, **86** [1] 87–93 (1996).

[24]H. D. Jang, "Generation of Silica Nanoparticles from Tetraethylorthosilicate (TEOS) Vapor in a Diffusion Flame," *Aerosol Sci. Technol.*, **30**, 477–88 (1999).

[25]S. C. Zhang and G. L. Messing, "Synthesis of Solid, Spherical Zirconia Particles by Spray Pyrolysis," *J. Am. Ceram. Soc.*, **73** [1] 61–67 (1990).

[26]W. C. Hinds, "Inertial Impaction"; pp. 121–28 in *Aerosol Technology: Properties, Behavior, and Measurement of Airborne Particles*, 2nd Ed. Wiley, New York, 1999.

[27]R. C. Garvie, "The Occurrence of Metastable Tetragonal Zirconia as a Crystallite Size Effect," *J. Phys. Chem.*, **69** [4] 1238–43 (1965). □

journal

J. Am. Ceram. Soc., 85 [5] 1318–20 (2002)

Preparation of a Bioactive Poly(methyl methacrylate)/Silica Nanocomposite

Sang-Hoon Rhee*,†

Korea Research Institute of Chemical Technology, Daejeon 305-600, Korea

Je-Yong Choi

Kyungpook National University, Daegu 700-422, Korea

The nanocomposite of a poly(methyl methacrylate)/silica containing calcium salt was synthesized through the sol–gel method. Methyl methacrylate was co-polymerized with 3-(trimethoxysilyl)propyl methacrylate and then co-condensed with tetraethyl orthosilicate and calcium nitrate tetrahydrate. Low crystalline hydroxycarbonate apatite was successfully formed on the surface after soaking in simulated body fluid for 1 week at 36.5°C. This study demonstrates that this nanocomposite may be used as a bioactive bone substitute or filler for poly(methyl methacrylate) bone cement.

I. Introduction

POLY(METHYL METHACRYLATE) (PMMA) is a representative material used as a bone cement because of its self-hardening property and excellent mechanical properties compared with other polymers. However, the application is almost restricted to bone cement because of its bio-inertness; no chemical or biological bonding occurs at the interface between the PMMA and bone, causing wear debris of PMMA from repeated interfacial movement.[1] This causes osteolysis and subsequent loosening of an implant.[2]

Many researchers, therefore, have attempted to give osteoconductivity to the PMMA bone cement by introducing bioactive ceramic fillers.[3–7] However, the interfacial strength between bioactive ceramic filler and the PMMA is of concern because of the lack of adhesion between the two phases, resulting in an early failure at the interface. In addition, the size of the ceramic filler used for this purpose is several tens of micrometers, so its distribution in the composite is inhomogeneous and exposure to the surface becomes small. This reduces the osteoconducting ability of PMMA with ceramic filler.

The improvement of the adhesion between the ceramic fillers and the PMMA could be achieved using a silane coupling agent;[5,6] however, the increase of bioactive ceramic fillers exposed on the surface could not be achieved through this method. Therefore, if the nanometer-sized bioactive ceramics can be dispersed homogeneously and bonded covalently to the PMMA at the molecular level, all problems are likely to be solved.

In the present investigation, a PMMA/silica nanocomposite made via the sol–gel reaction with methylmethacrylate (MMA), tetraethyl orthosilicate (TEOS), and 3-(trimethoxysilyl)propyl methacrylate (MSMA) as a coupling agent was re-examined with the main focus on its use as a bioactive bone substitute. Because of its superior mechanical properties of the nanocomposite, applications as a biomaterial have already been reported; there have been feasibility tests as filler for PMMA bone cement[8] and resin for dental applications.[9,10] However, these studies were not aimed at giving and using bioactivity, but simply using its superior mechanical properties to single PMMA.

In this study, a PMMA/silica nanocomposite was designed to produce the low crystalline hydroxy carbonate apatite (HCA) on its surface in the simulated body fluid (SBF) using the silanol group as a nucleation site and calcium salt as a promoter for the nucleation of HCA via the increase of ionic activity product.

II. Experimental Procedure

The trimethoxysilyl functionalized polymethylmethacrylate was prepared by free radical polymerization of 3-(trimethoxysilyl)propyl methacrylate (MSMA) with methyl methacrylate (MMA) using benzoyl peroxide (BPO) as an initiator.[11] The content of MSMA in the copolymer was 20 mol%. The MMA and MSMA were mixed for 1 h using dry toluene as a solvent. The BPO (0.01 mol%) was added to the solution and, subsequently, free radical polymerization was performed at 70°C. After mixing for 24 h, the copolymer was purified via repeated precipitation in dry hexane. Hereafter, the poly(methylmethacrylate-co-3-(trimethoxysilyl)propyl methacrylate) will be referred to as PMCM.

The PMCM was hydrolyzed and co-condensed with tetraethyl orthosilicate (TEOS) with HCl as a catalyst to yield hybrid sol–gel material. The TEOS solution was prepared by mixing tetrahydrofuran (THF), water, and calcium nitrate tetrahydrate (CNT) for 1 h. The molar ratio of TEOS:water:HCl:CNT was 1:3:0.01:0.15. Hereafter, this solution will be referred to as solution T. The PMCM powder was dissolved in the THF with a concentration of 20 wt%. Hereafter, this solution will be referred to as solution P. Solutions T and P were mixed for 1 h at room temperature and then poured into a Teflon mold. The gel was slowly dried for 1 week and then dried again under vacuum at 30°C for 48 h. The pure PMMA was also made for comparison through the free radical polymerization with the same method described. Hereafter, the pure PMMA and the PMMA/silica nanocomposite will be referred to as specimens P and S, respectively.

The test of the bioactivity was performed in the SBF[12] that has almost the same ion concentrations as human blood plasma.[13] Disk-shaped specimens (10 mm in diameter × 1 mm thick) were soaked in 30 mL of the SBF at 36.5°C for 1 week. After soaking, the specimens were removed from the fluid and gently rinsed with ion-exchanged distilled water and then dried at room temperature.

S. Sakka—contributing editor

Manuscript No. 187606. Received August 20, 2001; approved December 27, 2001.
This work was supported by the Intellectual Bio-interface Engineering Center (IBEC) of the Korea Science and Engineering Foundation (KOSEF) of the Korean government.

*Member, American Ceramic Society.
†Author to whom correspondence should be addressed.

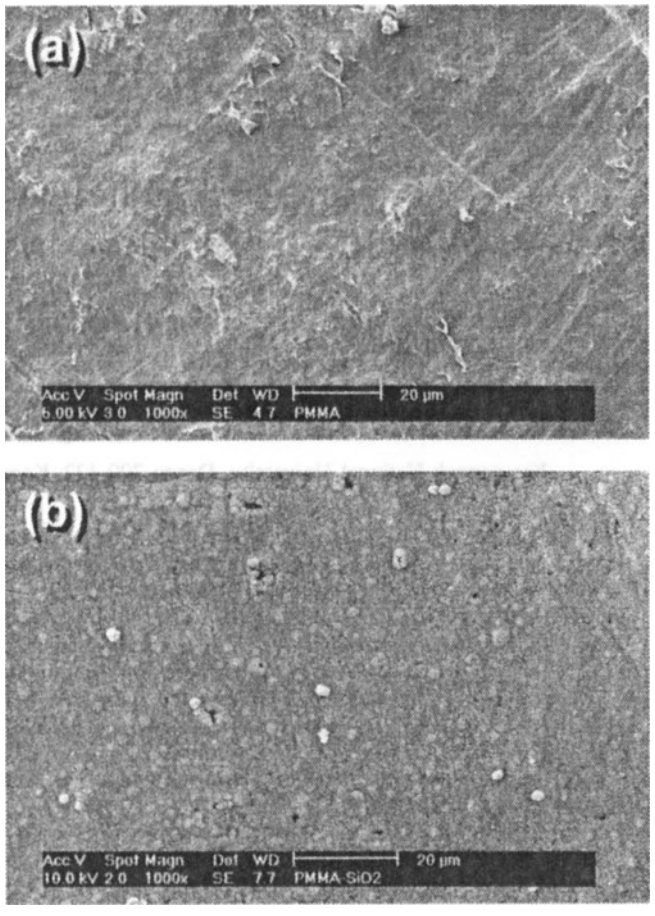

Fig. 1. Microstructures of specimens (a) P and (b) S after soaking in simulated body fluids at 36.5°C for one week.

The surface microstructures and crystal phase formed on the specimens were analyzed by field emission scanning electron microscopy (FE-SEM; XL30S, Philips Electron Optics, Eindhoven, The Netherlands) and thin film X-ray diffractometry (TF-XRD), respectively, with an angle of 1° to the direction of the incident X-ray beam. For infrared spectroscopy measurements, the pulverized specimens were diluted with 100-fold KBr powder (Spectra Tech, Shelton, CT) and the background noise was corrected with pure KBr data. The ionic concentrations of calcium, phosphorous, and silicon in the SBF were measured with inductively coupled plasma atomic emission spectroscopy (Ultima-C, Jovin-Yvon, Yvon, France) after soaking specimen S for 1 week.

III. Results and Discussions

Figure 1 shows the microstructures of specimens P and S after soaking in the SBF at 36.5°C for 1 week. A relatively rough surface with some cracks, which is believed to have resulted from the swelling of the PMMA, was observed in specimen P. However, a low crystalline HCA layer as described later was observed to form on the surface of specimen S.

Figure 2 shows the TF-XRD profiles measured for specimens P and S after soaking in the SBF at 36.5°C for 1 week. No specific peaks assigned to apatite were observed in specimen P, while two apatite peaks, denoted by "H," were observed in specimen S. Because the apatite peaks were comparatively broader than a normal apatite, it was inferred that the grown apatite crystals had low crystallinity.

Figure 3 shows the FT-IR spectra measured for specimen S before and after soaking in the SBF. The Si–O–Si band was observed at 1075, 791, 434 cm^{-1}, and the Si–OH band was observed at 960 and 845 cm^{-1} before soaking in the SBF.[14] The asymmetrical stretching (ν_3) and bending (ν_4) modes of the PO_4 ion were detected at ~1039, 602, and 564 cm^{-1}, respectively, after soaking in the SBF for 1 week. The symmetric stretching modes (ν_1 and ν_2) of the PO_4 ion were also found at ~960 and 462 cm^{-1}, respectively. Further, two stretching modes and an out-of-plane mode of CO_3 ion were also observed at ~1456, 1419, and 876 cm^{-1}, respectively. This means that the PO_4 sites of the apatite structure, i.e., B-site, were partly substituted by carbonate ions.

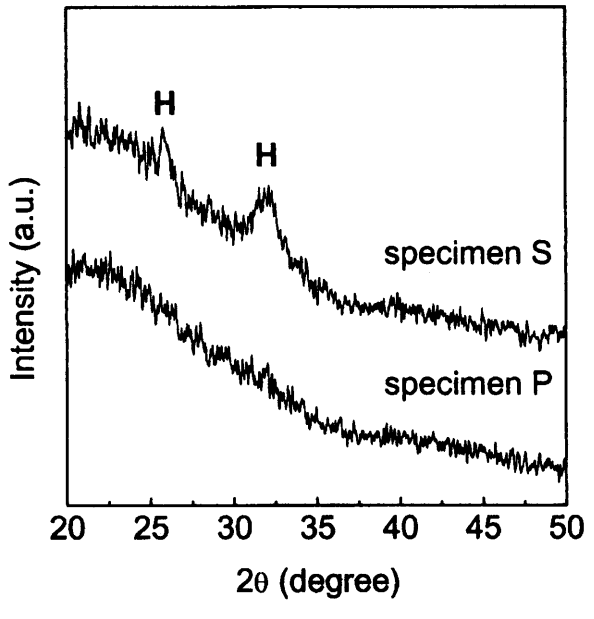

Fig. 2. Thin-film XRD results for specimens P and S after soaking in the simulated body fluids at 36.5°C for one week.

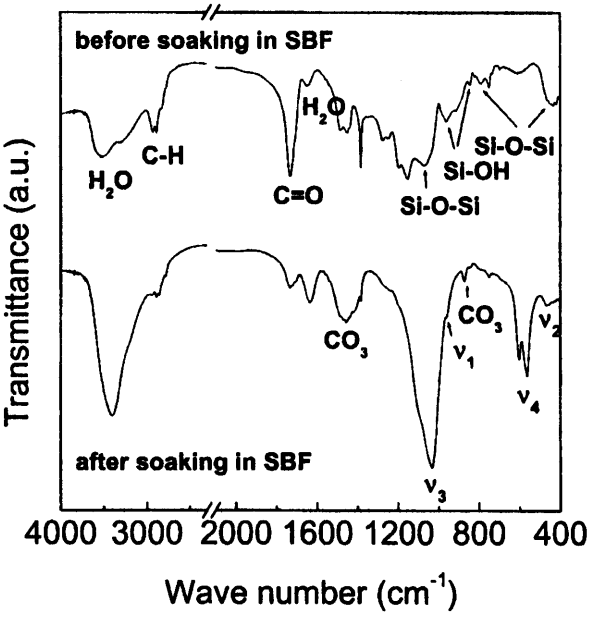

Fig. 3. FT-IR transmission spectra for specimen S before and after soaking in simulated body fluids at 36.5°C for one week.

The initial ionic concentrations of calcium, phosphorus, and silicon in the SBF were 100.20, 30.94, and 0.00 ppm, respectively. However, these concentrations became 123.33 ± 2.31, 4.31 ± 0.07, and 15.27 ± 0.06 ppm, respectively, after soaking for 1 week. The increase of ionic concentrations of calcium and silicon after soaking originated from their release from specimen S, while the decrease of ionic concentration of phosphorous might be the result of the formation of the HCA layer (Figs. 1(b) and 2).

From the above results, it can be presumed that the formation of the HCA layer is critically dependent on the silanol group and the release of calcium ion from the nanocomposite, because the HCA was not formed in the pure PMMA (Figs. 1(a) and 2). For an explanation of the nucleation and growth of the HCA layer observed in this work, the nucleation model of bioglass[2] or bioglass ceramics[15] is quite appropriate.

When the PMMA/silica nanocomposite containing calcium salt is soaked into the SBF, calcium ion is dissolved into the SBF and it produces the silanol group on the surface by exchange of the Ca^{2+} ion combined with the $Si–O^-$ group in the sample with H_3O^+ ion in the SBF. In addition, the release of Ca^{2+} ions increases ionic activity product of apatite in the SBF, so it promotes the nucleation of HCA on the silanol group.[16] Once the apatite nuclei are formed, they grow spontaneously because the SBF itself has already been supersaturated with respect to apatite.[17] The mechanical and biological assays of this nanocomposite are under investigation and will be published in the near future.

IV. Conclusions

The nanocomposite of poly(methyl methacrylate)/silica was synthesized via the sol–gel method. Its bioactivity was assessed using the SBF and low crystalline HCA was successfully formed on its surface after soaking for 1 week at 36.5°C. The formation mechanism of the low crystalline HCA was similar to that on the bioglass. This nanocomposite is likely to be useful for a bone substitute or filler for PMMA bone cement because of its bioactivity.

References

[1]G. Lewis, "Properties of Acrylic Bone Cement: State of the Art Review," *J. Biomed. Mater. Res., Appl. Biomater.*, **38**, 155–82 (1997).

[2]L. L. Hench, "Bioceramics," *J. Am. Ceram. Soc.*, **81** [7] 1705–28 (1998).

[3]W. F. Mousa, M. Kobayashi, S. Shinzato, M. Kamimura, S. Yoshihara, I. A. Zeineldin, and T. Nakamura, "Biological and Mechanical Properties of Commercial PMMA Bone Cements Containing AW-GC Filler"; pp. 545–48 in *Bioceramics*, Vol. 12. Edited by H. Ohgushi, G. W. Hastings, and T. Yoshikawa. World Scientific Publishing Co. Pte., Ltd., Nara, Japan, 1999.

[4]W. Hennig, B. A. Blencke, H. Brömer, K. K. Deutscher, A. Gross, and W. Ege, "Investigations with Bioactivated Polymethylmethacrylate," *J. Biomed. Mater. Res.*, **13**, 89–99 (1979).

[5]J. T. Heikkilä, A. J. Aho, I. Kangasniemi, and A. Yli-Upro, "Polymethylmethacrylate Composites: Disturbed Bone Formation at the Surface of Bioactive Glass and Hydroxyapatite," *Biomaterials*, **17**, 1755–60 (1996).

[6]W. F. Mousa, M. Kobayashi, S. Shinzato, M. Kamimura, M. Neo, S. Yoshihara, and T. Nakamura, "Biological and Mechanical Properties of PMMA-based Bioactive Bone Cement," *Biomaterials*, **21**, 2137–46 (2000).

[7]J. C. Behiri, M. Braden, S. Khorasani, D. Wiwattanadate, and W. Bonfiled, "Advanced Bone Cement for Long-Term Orthopedic Implantations"; pp. 301–307 in *Bioceramics*, Vol. 4. Edited by W. Bonfield, G. W. Hastings, and K. E. Tanner. Elsevier Science, London, U.K., 1991.

[8]J.-M. Yang, C.-S. Lu, Y.-G. Hsu, and C.-H. Shih, "Mechanical Properties of Acrylic Bone Cement Containing PMMA–SiO_2 Hybrid Sol–Gel Material," *J. Biomed. Mater. Res., Appl. Biomater.*, **38**, 143–54 (1997).

[9]Y. Wei and D. Jin, "A New Class of Organic-Inorganic Hybrid Dental Materials," *Polym. Prepr.*, **38** [2] 122–23 (1997).

[10]P. P. Paul, S. F. Timmons, and W. J. Machowski, "Organic-Inorganic Hybrid Dental Restorative Composites," *Polym. Prepr.*, **38**[2] 124, (1997).

[11]Y. Wei, D. Yang, and R. Bakthavatchalam, "Thermal Stability and Hardness of New Polyacrylate–SiO_2 Hybrid Sol–Gel Materials," *Mater. Lett.*, **13**, 261–66 (1992).

[12]T. Kokubo, H. Kushitani, S. Sakka, T. Kitusgi, and T. Yamamuro, "Solutions Able to Reproduce in Vivo Surface-Structure Changes in Bioactive Glass-Ceramic A-W," *J. Biomed. Mater. Res.*, **24**, 721–34 (1990).

[13]J. Gamble, *Chemical Anatomy, Physiology and Pathology of Extracellular Fluid*, 6th Ed.; pp.1–15. Harvard University Press, Cambridge, MA, 1967.

[14]X. Li and T. A. King, "Spectroscopic Studies of Sol–Gel-Derived Organically Modified Silicates," *J. Non-Cryst. Solids*, **204**, 235–42 (1996).

[15]T. Kokubo, H. Kushitani, C. Ohtsuki, S. Sakka, and T. Yamamuro, "Chemical Reaction of Bioactive Glass and Glass-Ceramics with a Simulated Body Fluid," *J. Mater. Sci. Mater. Med.*, **3**, 79–83 (1992).

[16]T. Kokubo, "Surface Chemistry of Bioactive Glass-Ceramics," *J. Non-Cryst. Solids*, **120**, 138–51 (1990).

[17]W. F. Neuman and M. W. Neuman, *The Chemical Dynamics of Bone Mineral*; p. 34. University of Chicago, Chicago, IL, 1958. □

This page intentionally left blank

journal

J. Am. Ceram. Soc., 85 [5] 1321–23 (2002)

Synthesis of Platinum/Silica Nanocomposite Particles by Reverse Micelle and Sol–Gel Processing

Dong-Sik Bae and Kyong-Sop Han

Division of Ceramics, Korea Institute of Science and Technology, Seoul 136–791, Korea

James H. Adair**

Material Research Laboratory, The Pennsylvania State University, University Park, Pennsylvania 16802

Pt/SiO_2 nanosized particles have been synthesized using a reverse micelle technique combined with metal alkoxide hydrolysis and condensation. The size of the particles and the thickness of the coating can be controlled by manipulating the relative rates of the hydrolysis and condensation reactions of tetraethoxysilane (TEOS) within the microemulsion. The average size of synthesized particles was in the size range of 21–42 nm. The effects of synthesis parameters, such as the molar ratio of water to TEOS and the molar ratio of water to surfactant, are discussed.

I. Introduction

RECENTLY, the synthesis of nanometer-sized particles of metals and semiconductors has been investigated extensively because of their novel electrical, optical, magnetic, and chemical properties.[1] The effect of particle size on the electronic and optical properties of these nanosized particles during the growth of the crystallite from the molecular level to the bulk material is an area of fundamental interest.[2] Numerous approaches have been explored for the preparation of ultrafine spherical particles, including the use of colloids, polymers, glasses, and micelles to successfully control aggregation.[3,4] Many new and unusual physical and chemical properties arise as particles attain nanosize dimensions.[5] Compared with conventional solid-state reaction methods, solution-based synthesis results in higher levels of chemical homogeneity. Also, mixing of the starting materials at the molecular level is achieved in solution-based systems; this is especially important when multicomponent oxides are being prepared. In addition, surface coating or surface modification of nanometer semiconductor and metal particles offers a new challenge to synthesis. Not only metal/silica nanocomposites, but also semiconductor/oxide and even semiconductor/insulator/metal multiple-layer heterostructures can be prepared using this method.[6]

The object of this study was to prepare silica (SiO_2) particles containing nanometer-size platinum particles by a combined reverse micelle and sol–gel technique.

II. Experimental Procedure

The experimental procedure used to prepare Pt/SiO_2 nanosized composites is illustrated in Fig. 1. Typically, microemulsions with a total volume of 20 mL were prepared at ambient temperature in a 30 mL vial with rapid stirring: these consisted of 4 mL of surfactant (Igepal CO-520, Aldrich Chemical Co., Milwaukee, WI), 10 mL of cyclohexane, 0.65–1.32 mL of $2 \times 10^{-2}M$

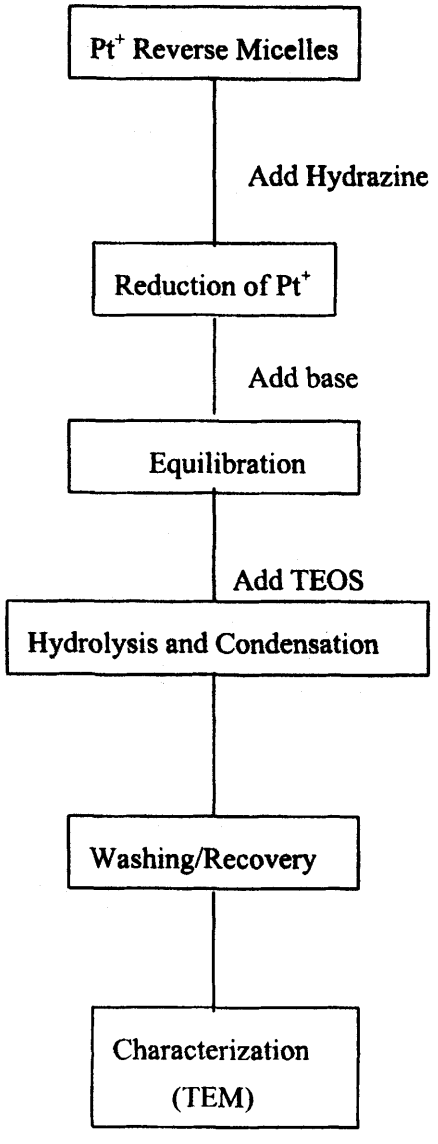

Fig. 1. Flow chart for the synthesis of Pt/SiO_2 nanocomposite particles by a reverse micelle and sol–gel process.

C. J. Brinker—contributing editor

Manuscript No. 187805. Received April 2, 2001; approved January 9, 2002.
**Fellow, American Ceramic Society.

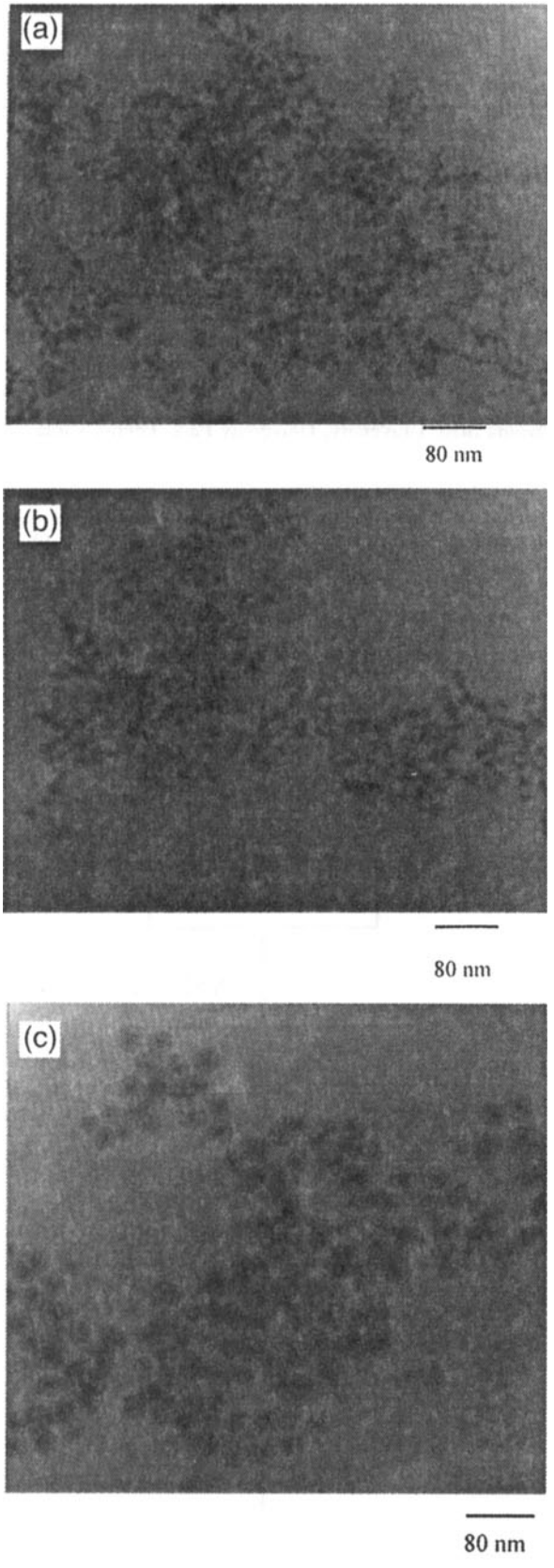

Fig. 2. TEM micrographs of Pt/SiO_2 nanocomposite particles synthesized at $H = 200$, $x = 1$ and as a function of R((a) $R = 4$, (b) $R = 6$, and (c) $R = 8$)

$H_2PtCl_6 \cdot xH_2O$ solution (Aldrich Chemical Co.), and deionized water. The size of the resulting particles was controlled by varying the ratio R = [water]/[surfactant]. The microemulsion was mixed rapidly and, after 5 min of equilibration, one drop (~0.05 mL) of hydrazine hydrate(9*M* $N_2H_4 \cdot xH_2O$, Aldrich Chemical Co.) was added as a reducing agent. TEOS was added to the microemulsion with stirring, after nanosized platinum aqueous droplets formed. The amount of TEOS was varied according to the different molar ratios of water to TEOS, H = [water]/[TEOS]. This is the most important factor that dictates the size of the nanosized particles. NH_4OH was injected into the microemulsion to accelerate the condensation reaction of metal alkoxide precursors. New reverse micelles were prepared from the nonionic surfactant–poly(oxyethylene) nonylphenyl ether (Igepal CO-520, Aldrich Chemical Co.). The surfactant was used without further purification. Other chemicals, such as tetraethoxysilane (TEOS), cyclohexane, and NH_4OH (29%) (all from Aldrich Chemical Co.), were used as-received. The structure, size, and morphology of the resulting composites were examined by transmission electron microscopy (TEM).

III. Results and Discussion

The spherical Pt/SiO_2 nanometer-sized composite particles were obtained in reverse micelles followed by *in situ* hydrolysis and condensation in the microemulsion. The average size of the cluster was found to depend on the micelle size, the nature of the solvent, and the concentration of reagent. Figure 2 shows that water/surfactants molar ratio (R) influenced the particle sizes and distribution of the synthesized Pt/SiO_2. The size of the synthesized Pt/SiO_2 particles increased with increasing water/surfactant molar ratio. The core particles are formed by a homogeneous nucleation and growth process; the shells are most likely formed through heterogeneous nucleation and growth. The nucleation and growth of platinum particles is likely to be a diffusion-controlled process through interaction between micelles, but it can be influenced by many other factors such as phase behavior and solubility, average occupancy of reacting species in the aqueous pool, and the dynamic behavior of the microemulsion.[7,8]

Figure 3 shows that the size of the composite particles decreases monotonically with H (water/TEOS mol ratio). The median particle size was determined by counting the number of particles of a given grain size in a given area. The median diameter of the Pt/SiO_2 nanocomposite particles was determined to vary from 20 to 42 nm as H varied from 50 to 200, at $R = 6$, with a standard deviation of 7 nm.

IV. Conclusion

Spherical Pt/SiO_2 nanometer-sized particles with uniform size distribution can be produced by a reverse micelle technique in conjunction with a sol–gel process, involving the hydrolysis and

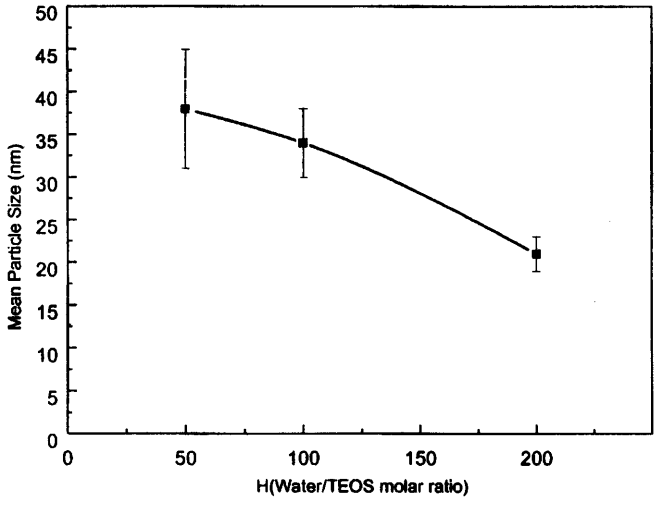

Fig. 3. Size of the synthesized Pt/SiO_2 particles, relative to the changing H ratio.

condensation of organometallic precursors. The size of the synthesized Pt/SiO_2 particle increased with increasing water/surfactants molar ratio. The average size of the synthesized Pt/SiO_2 particles decreased linearly with increasing water/TEOS molar ratio. TEM studies of particle formation indicate that the reaction process in the complex system containing reverse micelles and TEOS is governed by a diffusion-controlled process. By controlling the ratio of water to surfactant and the ratio of water to TEOS, the particle size can be adjusted.

References

[1]R. Pool, "Clusters: Strange Morsels of Matter," *Science*, **248**, 1186–88 (1990).

[2]Y. Wang and N. Herron, "Nanometer-Sized Semiconductor Clusters: Materials Synthesis, Quantum Size Effects, and Photophysical Properties," *J. Phys. Chem.*, **95**, 525–32 (1991).

[3]Y. M. Tricot and J. H. Fendler, "*In Situ* Generated Colloidal Semiconductor CdS Particles in Dihexadecyl Phosphate Vesicles: Quantum Size and Asymmetry Effects," *J. Phys. Chem.*, **90**, 3369–74 (1986).

[4]N. F. Borelli, D. W. Hall, J. H. Holland, and W. D. Smith, "Photoluminescence and Relaxation Dynamics of CdS Superclusters in Zeolites," *J. Phys. Chem.*, **92**, 4988–94 (1988).

[5]N. Ichinose, Y. Ozaki, and S. Kashu, *Superfine Particle Technology*; pp. 27–38. Springer-Verlag, New York, 1988.

[6]J. H. Adair, T. Li, T. Kido, K. Havey, J. Moon, J. Mecholsky, A. Morrone, D. R. Talham, M. H. Ludwig, and L. Wang, "Recent Developments in the Preparation and Properties of Nanometer-Size Spherical and Platelet-Shaped Particles and Composite Particles," *Mater. Sci. Eng. Rep.*, **R23** {4–5} 139–242 (1998).

[7]T. Li, J. Moon, A. A. Morrone, J. J. Mecholsky, D. R. Talham, and J. H. Adair, "Preparation of Ag/SiO_2 Nanosize Composites by a Reverse Micelle and Sol–Gel Technique," *Langmuir*, **15**, 4328–34 (1999).

[8]K. Osseo-Asare, "Microemulsion-Mediated Synthesis of Nanosize Oxide Materials"; pp. 549–603 in *Handbook of Microemulsion Science and Technology*. Edited by P. Kumar and K. L. Mittal. Basel, New York, 1999. □

This page intentionally left blank

journal

J. Am. Ceram. Soc., 84 [2] 459–61 (2001)

Synthesis of a Hydroxyapatite/Collagen/Chondroitin Sulfate Nanocomposite by a Novel Precipitation Method

Sang-Hoon Rhee*

Korea Research Institute of Chemical Technology, Daejeon 305–600, Korea

Junzo Tanaka*

National Institute for Research in Inorganic Materials, Tsukuba, Ibaraki 305–0044, Japan

A hydroxyapatite/collagen/chondroitin sulfate nanocomposite that partly mimicked the composition of cartilage was synthesized through a novel precipitation method, using a calcium hydroxide suspension and phosphoric acid solutions that contained several mixing ratios of type II collagen (Col) and chondroitin sulfate (ChS). The precipitates were shaped and consolidated via filter pressing and subsequent cold isostatic pressing, respectively. A preferential alignment of the crystallographic *c*-axis of the hydroxyapatite nanocrystals along the longitudinal direction of the Col and ChS mixture was observed. The fracture strength and Vickers hardness of the nanocomposites were in the ranges of 35–50 and 119–219 MPa, respectively. This nanocomposite may be applicable for use as a bone substitute, because of its potential capability of bone remodeling through endochondral ossification.

I. Introduction

Bone and cartilage are specialized forms of connective tissue that, similar to the other connective tissues, consists of cells and extracellular matrix. The feature that distinguishes bone from most other connective tissue is the mineralization of the matrix. This process produces an extremely hard tissue that is capable of providing support and protection. Cartilage is a key tissue in most growing bones, because bone formation is initiated from the calcification of cartilage and, given sufficient time, it will be replaced by bone via endochondral ossification. In addition, when fracture occurs and the mechanical conditions at the fracture site are unstable, a callus (which contains cartilage) forms first, followed by a gradual change to bone via endochondral ossification.[1,2] Therefore, cartilage is regarded as a precursor of bone.[3] Thus, a bone substitute that mimics the composition of cartilage may be useful for the healing of bone defects via endochondral ossification. Indeed, Hemmerle *et al.*[4] showed that hydroxyapatite powder (ranging in size from tens of micrometers to several hundred micrometers) that was blended or coated with a mixture of collagen and glycosaminoglycan had good osteoconductivity. However, the collagen used was primarily type I, whereas the collagen in cartilage is primarily type II. In addition, the powder was a fragile aggregate, so it could not be applied to the defect site where heavily loaded.

In this experiment, a hydroxyapatite/type II collagen/chondroitin sulfate nanocomposite (HAp/type II Col/ChS) that partly mimicked the composition of cartilage was synthesized using a novel precipitation method. Type II Col has been known to provide specific binding sites to chondrocyte via integrin and ligand interactions.[5,6] In addition, ChS proteoglycan has been known to promote the binding of chondronectin, which is the chondrocyte attachment factor, to type II Col, which thereby stimulates chondrocyte adhesion.[7] Therefore, when a HAp/type II Col/ChS nanocomposite will be used as a bone substitute, it is expected to provide specific binding sites to chondrocyte. After adhesion to the nanocomposite, chondrocyte will secrete new extracellular matrix material and the nanocomposite ultimately will be replaced by bone via endochondral ossification (i.e., fracture healing will be accomplished). In the nanocomposite, on the other hand, HAp will act as a source of strength and bioactivity during the remodeling of bone.

II. Experimental Procedures

The nanocomposites, which were composed of 80 wt% HAp and 20 wt% bio-organics (Col and ChS), were synthesized via precipitation with a calcium hydroxide ($Ca(OH)_2$) suspension and phosphoric acid (H_3PO_4) solutions that contained type II Col and ChS of several mixing ratios, as shown in Table I. Hereafter, the specimens as shown in Table I are referenced as ChS20, Col8ChS12, Col14ChS6, and Col20, where the numerical values that follow each abbreviation correspond to the concentrations of the respective component. The $Ca(OH)_2$ powder was made via the slaking of calcia (CaO), which was made through the calcination of calcium carbonate ($CaCO_3$, Wako Pure Chemicals Industries, Osaka, Japan) at a temperature of 1050°C for 3 h. The H_3PO_4 solutions, which contained Col and ChS, were prepared by dissolving two bio-organics to form a 0.7*M* H_3PO_4 compound (Wako Pure Chemicals Industries). The type II Col (Product TT-2, Nitta Gelatin, Inc., Osaka, Japan) was made from bovine nasal cartilage and had a molecular weight of ~300 000. The ChS (Product BN-3229, Seikagaku Kogyo Co., Tokyo, Japan) was made from bovine trachea cartilage and had a molecular weight of ~13 000. The synthesized precipitates were subjected to filtration via filter pressing at a pressure of 2 MPa and consolidated via subsequent cold isostatic pressing at a pressure of 200 MPa.

Table I. Mixing Ratios of Collagen and Chondroitin Sulfate

Component	Amount (wt%)			
	ChS20	Col8ChS12	Col14ChS6	Col20
Collagen	0	8	14	20
Chondroitin sulfate	20	12	6	0

P. W. Brown—contributing editor

Manuscript No. 189011. Received June 26, 2000; approved October 19, 2000.
This work was supported by Intellectual Biointerface Engineering Center (IBEC) of Korea Science and Engineering Foundation (KOSEF) of the Korean government.
*Member, American Ceramic Society.

The crystal phases of the specimens were identified using X-ray diffractometry (XRD). The functional groups of the HAp crystal and the two bio-organics were analyzed via diffuse reflectance Fourier-transform infrared (FT-IR) transmission spectroscopy. For the infrared spectroscopy measurements, the pulverized specimens were diluted by a factor of 10, using potassium bromide (KBr) powder, and background noise was corrected using data for pure KBr. The microstructures were observed via transmission electron microscopy (TEM) (Model JEM-2000EX II, JEOL, Tokyo, Japan), using an accelerating voltage of 200 kV. The self-assembly phenomena of the HAp crystals that formed on the bio-organic templates were assessed using electron diffraction patterns. The fracture strength was measured via the three-point bending method, using a specimen size of 3 mm × 5 mm × 20 mm.[8] The crosshead speed was 0.5 mm/min, and the span length was 15 mm. Hardness was measured using a Vickers hardness tester with a load of 29.4 N.

III. Results and Discussion

Figure 1 shows the results of XRD measurements on the as-prepared specimens. Several HAp peaks (denoted by the symbol "H") were observed in all the specimens. The HAp peaks were comparatively broader than those of a normal HAp specimen; thus, the HAp crystals that were grown were considered to have low crystallinity or small crystallite size.

Figure 2 shows the FT-IR spectra measurements of the as-prepared specimens, in addition to ChS and Col. For the ChS and ChS20 specimens, the asymmetrical stretching mode of the $(COO)^-$ and $(—SO_3)^-$ species and the $C_4—O—S$ peak shoulder were detected at ~1613, 1228, and 851 cm^{-1}, respectively. For the Col, Col8ChS12, and Col20 specimens, the C=O stretching mode and the N—H bending mode that resulted from the peptide bond of the Col were detected at ~1670 and 1560 cm^{-1}, respectively. The asymmetrical (ν_3) and symmetric (ν_1) stretching modes of the $(PO_4)^{3-}$ ion were detected at ~1038 and 963 cm^{-1}, respectively. The bending mode (ν_4) of this species also was detected at ~601 and 564 cm^{-1} in all the prepared specimens.[9] Furthermore, two stretching modes and an out-of-plane mode of the $(CO_3)^{2-}$ ion were also observed, at ~1454, 1419, and 875 cm^{-1}, respectively. This observation means that the PO_4 sites of the HAp structure (i.e., the B-site) were partially substituted by $(CO_3)^{2-}$ ions.[10] Therefore, the HAp crystals that formed on the ChS, Col, and their mixtures were identified as carbonate-containing hydroxyapatites. The FT-IR spectra that have been observed for the Col8ChS12 and Col20 specimens are almost the same as that of bone.[11]

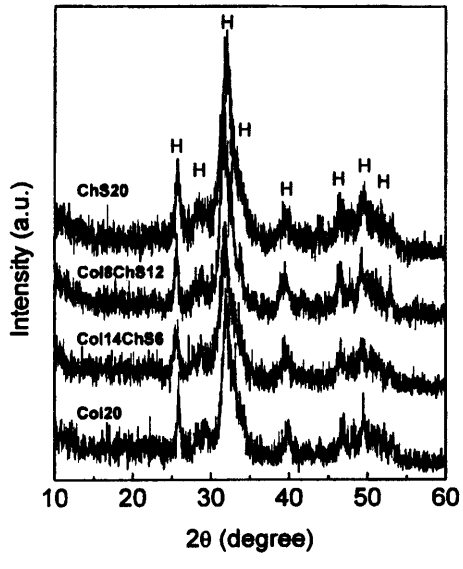

Fig. 1. XRD profiles for the ChS20, Col8ChS12, Col14ChS6, and Col20 specimens.

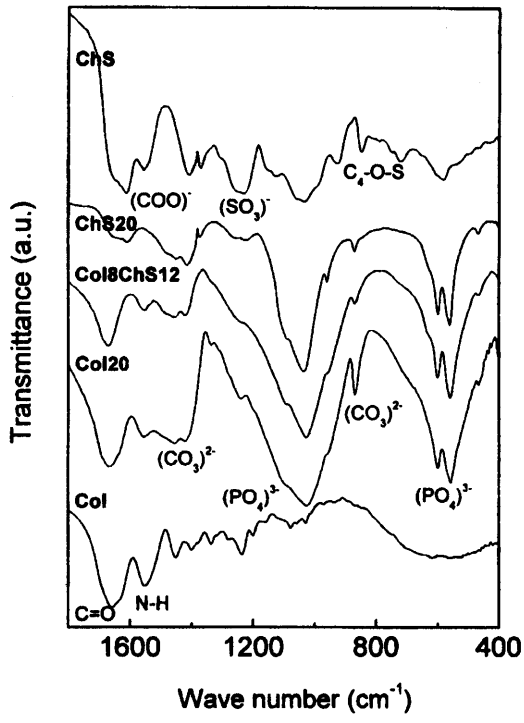

Fig. 2. FT-IR transmission spectra for the ChS20, Col8ChS12, Col14ChS6, Col20 specimens, as well as for collagen and chondroitin sulfate.

Figure 3 shows microstructures and electron diffraction patterns of the ChS20, Col20, and Col8ChS12 specimens. For the ChS20 specimen, many HAp/ChS aggregates (~200 nm × 50 nm in size), which consisted of numerous HAp nanocrystals (~30 nm × 8 nm in size) on each ChS template, were observed, as shown in Fig. 3(a). Some large HAp crystals (~100 nm × 15 nm in size), which were not formed on the ChS template, also were observed (noted by black arrows in Fig. 3(a)). This observation means that the ChS template has an inhibiting effect on the crystal growth of HAp.[12] The (002) and (004) diffractions of the HAp crystals that formed on the ChS templates exhibited an arching angle of ~10°, which means that the HAp crystals are precisely and preferentially oriented to the longitudinal direction of the ChS templates.

For the Col20 specimens, HAp nanocrystals also formed on the long Col fibers, as shown in Fig. 3(b). The size of the HAp crystals was ~50 nm × 20 nm, and the (002) diffraction exhibited an arching angle of ~60°. This result means that the HAp crystals that formed on the Col templates have more-scattered alignments than those on the ChS templates.

For the Col8ChS12 specimen, the microstructure was almost the same as that of the Col20 specimen, as shown in Fig. 3(c). No HAp/ChS aggregates, which were observed in abundance in the ChS20 specimen, were observed in the Col8ChS12 specimen. Therefore, the ChS can be considered to be bound to the Col when mixed in the H_3PO_4 solution, in a manner similar to that in hyaline and elastic cartilages.[13] The (002) and (004) diffractions of the HAp crystals also showed the preferred orientation of the HAp crystals to the longitudinal direction of the Col and ChS mixture, with an arching angle of ~60°. The electron diffraction patterns observed in the Col20 and Col8ChS12 specimens are very similar to that observed in bone.[14,15]

Table II shows the fracture strength and hardness of the specimens. The fracture strength was 35–61 MPa, and the hardness was 119–228 MPa. The value of each property increased as the content of Col in the bio-organics increased. These increases can be explained using the molecular weights of the Col and ChS. The molecular weights of the Col and ChS, which are related directly to their length, were 300 000 and 13 000, respectively. The long Col fibers (see Figs. 3(b) and (c)) might be randomly entangled in each other during the consolidation, which may result

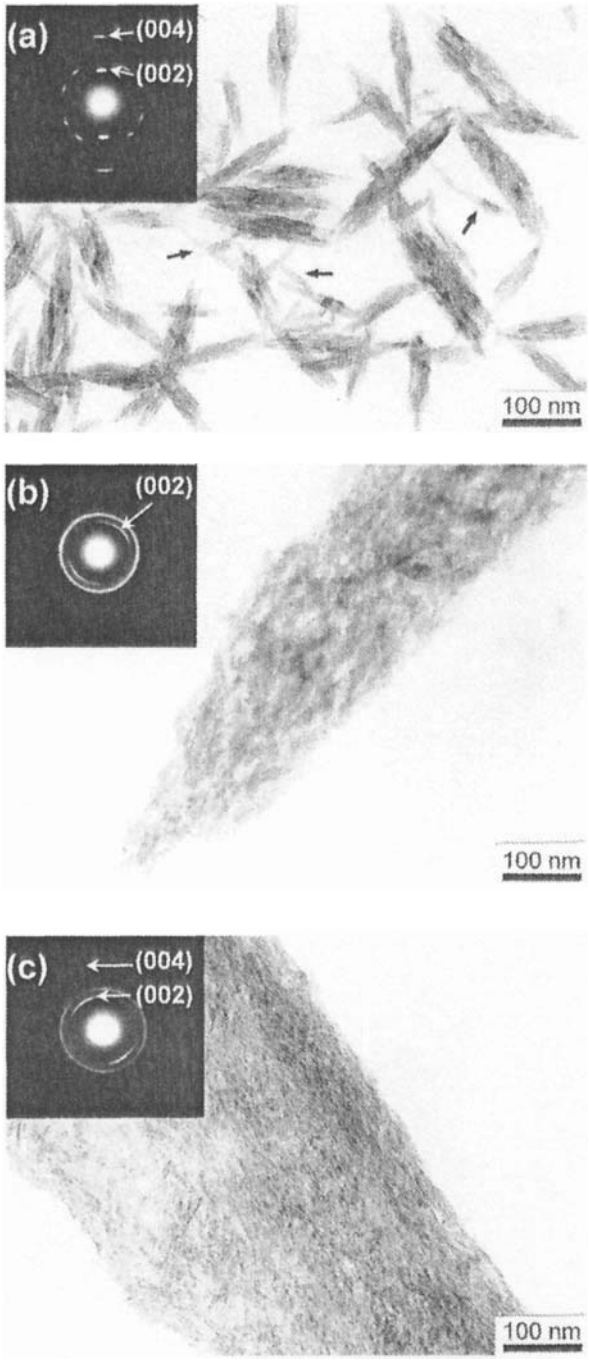

Fig. 3. TEM micrographs and electron diffraction patterns of the hydroxyapatite crystals formed on the (a) ChS20, (b) Col20, and (c) Col8ChS12 specimens.

Table II. Fracture Strength and Vickers Hardness of As-Prepared Specimens

Composite	Strength (MPa)	Hardness (MPa)
Col8ChS12	35 ± 5	119 ± 2
Col14ChS6	50 ± 1	219 ± 3
Col20	61 ± 3	228 ± 5

in the high strength. In contrast, the ChS fibers are very short (see Fig. 3(a)) and the possibility of entanglement with each other during the consolidation is unlikely. Therefore, the strength and hardness might decrease as the content of ChS in the specimens increases. In fact, the fracture strength of the ChS20 specimen could not be measured because the consolidated specimen had many cracks, which might be a result of drying; the length of the ChS fibers might be too short to hold the propagating drying cracks together.

The above-mentioned results indicate that a HAp/type II Col/ChS nanocomposite that seems to have sufficient strength and hardness to be used as a bone substitute can be made through a novel precipitation method and subsequent consolidation via filter pressing and subsequent cold isostatic pressing. It is expected that chondrocyte will preferentially adhere to the surface of the nanocomposite and bone remodeling via endochondral ossification may be accelerated. *In vivo* testing is under investigation, and the results will be published soon.

IV. Conclusion

The synthesis of a hydroxyapatite/type II collagen/chondroitin sulfate (HAp/type II Col/ChS) nanocomposite that partially mimicked the composition of cartilage was investigated. The nanocomposites were made through a novel precipitation method, using a calcium hydroxide suspension and phosphoric acid solutions that contained several mixing ratios of Col and ChS. Shaping and consolidation were possible, using filter pressing and subsequent cold isostatic pressing, respectively. The synthesized HAp nanocrystals were composed of carbonate-containing HAp, and their distribution on the Col and ChS was very similar to that of natural bone. This nanocomposite had a strength of 35–50 MPa, and its hardness was 119–219 MPa.

Acknowledgments

The authors thank Nitta Gelatin, Inc., and Seikagaku Kogyo Co. for donating the collagen and chondroitin sulfate, respectively.

References

[1]T. Yokobori, A. Oohira, and H. Nogami, "Proteoglycans Synthesized in Calluses at Various Stages of Fracture Healing in Rats," *Biochim. Biophys. Acta*, **68** [2] 174–81 (1980).

[2]M. Page, J. Hogg, and D. E. Ashhurst, "The Effects of Mechanical Stability on the Macomolecules of the Connective Tissue Matrixes Produced during Fracture Healing. I. Collagens," *Histochem. J.*, **18** [5] 251–65 (1986).

[3]M. H. Loss, L. J. Romrell, and G. I. Kaye, "Cartilage"; pp. 132–38 in *Histology*, 3rd Ed. Edited by P. A. Coryell. William and Wilkins, Baltimore, MD, 1995.

[4]J. Hemmerle, M. Leize, and J.-C. Voegel, "Long-Term Behaviour of a Hydroxyapatite/Collagen-Glycosaminoglycan Biomaterial Used for Oral Surgery: A Case Report," *J. Mater. Sci.: Mater. Med.*, **6**, 360–66 (1995).

[5]J. Mollenhauer, J. A. Bee, M. A. Lizarbe, and K. Von der Mark, "Role of Anchorin CII, a 31,000-mol-wt Membrane Protein, in the Interaction of Chondrocytes with Type II Collagen," *J. Cell Biol.*, **98** [4] 1572–79 (1984).

[6]M. Shakibaei, P. De Souza, and H.-J. Merker, "Integrin Expression and Collagen Type II Implicated in Maintenance of Chondrocyte Shape in Monolayer Culture: An Immunomorphological Study," *Cell Biol. Int.*, **21** [2] 115–25 (1997).

[7]H. H. Varner, V. J. Horn, G. R. Martin, and A. T. Hewitt, "Chondronectin Interactions with Proteoglycans," *Arch. Biochem. Biophys.*, **244** [2] 824–30 (1986).

[8]M. Kikuchi, Y. Suetsugu, J. Tanaka, and M. Akao, "Preparation and Mechanical Properties of Calcium Phosphate/Copoly-L-Lactide Composites," *J. Mater. Sci.: Mater. Med.*, **8**, 361–64 (1997).

[9]B. O. Fowler, "Infrared Studies of Apatites. I. Vibrational Assignments for Calcium, Strontium, and Barium Hydroxyapatite Utilizing Isotopic Substitution," *Inorg. Chem.*, **13**, 194–207 (1974).

[10]Y. Suetsugu, I. Shimoya, and J. Tanaka, "Configuration of Carbonate Ions in Apatite Structure Determined by Polarized Infrared Spectroscopy," *J. Am. Ceram. Soc.*, **81** [3] 746–48 (1998).

[11]R. Z. LeGros, G. Daculsi, I. Orly, M. Gregoire, M. Heughebaert, M. Gineste, and R. Kijkowska, "Formation of Carbonate Apatite on Calcium Phosphate Materials: Dissolution/Precipitation Processes"; pp. 201–12 in *Bone-Bonding Biomaterials*. Edited by P. Ducheyne, T. Kokubo, and C. A. van Blitterswijk. Reed Healthcare Communications, Reaal 2f, Leiderdorp, The Netherlands, 1993.

[12]S.-H. Rhee and J. Tanaka, "Effect of Chondroitin Sulfate on the Crystal Growth of Hydroxyapatite," *J. Am. Ceram. Soc.*, **83** [8] 2100–102 (2000).

[13]L. C. U. Junqueira, O. M. S. Toledo, and G. S. Montes, "Correlation of Specific Sulfated Glycosaminoglycans with Collagen Type I, II, III," *Cell Tissue Res.*, **217**, 171–75 (1981).

[14]D. D. Lee and M. J. Glimcher, "Three-Dimensional Spatial Relationship between the Collagen Fibrils and the Inorganic Calcium Phosphate Crystals of Pickerel (*Americanus Americanus*) and Herring (*Clupea Harengus*) Bone," *J. Mol. Biol.*, **217**, 487–501 (1991).

[15]A. L. Arsenault, "Crystal-Collagen Relationships in Calcified Turkey Leg Tendons Visualized by Selected-Area Dark Field Electron Microscopy," *Calcif. Tissue Int.*, **43**, 202–12 (1988). □

This page intentionally left blank

journal

J. Am. Ceram. Soc., 85 [8] 2033–38 (2002)

Evidence for Bulk Residual Stress Strengthening in Al_2O_3/SiC Nanocomposites

Luca Paolo Ferroni and Giuseppe Pezzotti*

Department of Materials, Kyoto Institute of Technology, Sakyo-ku, Matsugasaki 606-8585, Kyoto, Japan

The fracture behavior of Al_2O_3/SiC nanocomposites has been studied as a function of the SiC volume fraction and compared to that of the pure Al_2O_3 matrix. A pronounced strengthening effect was only observed for materials with low SiC content (i.e., ≤10 vol%) although no evidence of concurrent toughening was found. Assessment of near-tip crack opening displacement (COD) could not experimentally substantiate significant occurrence of an elastic crack-bridging mechanism, in contrast with a recently proposed literature model. Quantitative fractography analysis indicated that transgranular crack propagation in Al_2O_3/SiC nanocomposites depends on the location of the SiC dispersoids within the matrix texture; the higher the fraction of transgranularly located dispersoids, the more transgranular the fracture mode. Experimental evidence of remarkably high residual stresses arising from thermal dilatation mismatch (upon cooling) between Al_2O_3 and SiC phases were obtained by fluorescence and Raman spectroscopy. A strengthening mechanism is invoked which merely arises from residual stress through strengthening of Al_2O_3 grain boundaries.

I. Introduction

In A recent review, Sternitzke[1] has surveyed the current literature on nanocomposite materials with particular emphasis placed on structural ceramics, the work by Niihara and co-workers[2–5] being cited as the original source for the nanocomposite approach to the structural ceramic field. Experimental evidence reported by several investigators was revisited and compared, and it was pointed out that some of the mechanical properties reported by Niihara *et al.*[6] have hardly been reproduced by other researchers.[7–10]

Although a well-detectable strengthening effect has been noticed in Al_2O_3/SiC composites by several investigators, no general consensus has yet been reached about the actual microscopic mechanism behind it. Strengthening and toughening mechanisms in nanocomposite materials are still to be fully understood and a rather generalized skepticism about the original expectations for these materials is now evident in the literature.[11,12]

A consistent body of phenomenological evidence shows that strengthening in Al_2O_3/SiC nanocomposites does not actually arise from an intrinsic toughening effect. For instance, the fracture toughness of an Al_2O_3/5 vol% SiC has been measured by Zhao and co-workers[7] and found to be considerably higher than that of pure alumina only when the indentation crack-length measurement method is used. On the other hand, only a rather modest toughness increase could be observed when bend testing was carried out on precracked bars, a testing technique less sensitive to surface residual stresses. Zhao *et al.* concluded that in Al_2O_3/SiC nanocomposites the reported toughening[2–6] is biased by the indentation testing method and related to machining-induced compressive stress. More recently, Chou *et al.*[13] found that machining induces a similar magnitude of compressive residual line forces in nanocomposite and alumina. These researchers concluded that any strengthening of the nanocomposites over the alumina cannot be attributed solely to the development of compressive machining residual stresses.

Perez-Rigueiro *et al.*[12] tested several composites in which the SiC particle sizes and the volume fractions varied from 200 to 800 nm and from 5% to 20%, respectively. The dispersion of SiC nanoparticles, apart from leading to a reduction in the matrix grain size, did not actually affect the fracture toughness of the matrix. Sternitzke *et al.*[14] found very little change in fracture toughness in nanocomposites with different particle-size distributions, produced according to various processing routes. Hoffman *et al.*[15] have used a compact tension test to evaluate the fracture toughness of Al_2O_3/5 vol% SiC nanocomposite. These researchers found no rising R-curve effect and a rather low fracture toughness (i.e., K_{IC} = 2.1 MPa·m$^{1/2}$) for a crack extension of several millimeters, basically in agreement with the results by Zhao and co-workers.[7]

Pezzotti *et al.*[16] used fluorescence and Raman spectroscopy for measuring the residual microstresses stored in an Al_2O_3/5 vol% SiC nanocomposite as hot-pressed, after grinding and after polishing. Remarkably high residual stresses were systematically found which affected the strength data, thus supporting the thesis that the strengthening effect observed in this material may not arise from an actual toughness improvement but from the presence of residual stresses.

Despite the above experimental evidence, Ohji *et al.*[17] have recently proposed a "nanotoughening" effect for explaining the strengthening of the Al_2O_3/SiC system. A mechanism based on near-tip crack bridging by the nanosized SiC inclusions was considered to produce such a steep rising R-curve effect (i.e., exploited over a submicrometer crack length) to make the toughening phenomenon difficult to detect by any conventional R-curve measurement. This hypothetical "nanotoughening" mechanism was considered to directly give rise to the high fracture strength observed in the nanocomposite.

Leaving aside for the moment whether or not this argument is physically correct, it should be noted that the majority of fracture mechanics techniques allow the measurement of a rising R-curve only over relatively large crack extensions. Thus, if the near-tip crack bridging mechanism proposed by Ohji and co-workers is correct, a rising R-curve should be found only by monitoring very short crack extensions. Near-tip R-curve and crack opening displacement (COD) experiments should thus provide new physical insight to clarify the actual origin of the strengthening effect in Al_2O_3/SiC nanocomposites.

In this paper, we attempt to experimentally characterize the very-near-tip R-curve behavior and COD profile of a high-strength Al_2O_3/SiC nanocomposite. The physical origin of the strengthening effect will be discussed in light of these improved fracture

D. J. Green—contributing editor

Manuscript No. 188979. Received November 1, 1999; approved May 28, 2002.
The work of L. P. Ferroni was supported by the European Commission in the framework of the EU–Science and Technology Fellowship Program in Japan.
*Member, American Ceramic Society.

mechanics characterizations. In addition, a complete set of experimental residual stress data is collected as a function of the added SiC volume fraction by both fluorescence and Raman spectroscopy (on Al_2O_3 matrix and SiC dispersoid, respectively). According to these data, a mechanism of grain-boundary strengthening by residual stress is invoked for explaining the measured strength data.

II. Experimental Procedure

(1) *Materials and Mechanical Testing*

For brevity's sake, only a general description of the material preparation and characterization procedures is given here. More details for the respective processing procedures can be found in the cited references. Al_2O_3 (Sumitomo Chemical Ltd., AKP-53, Tokyo, Japan) and β-SiC (Ibiden Co., Ltd., Gifu, Japan) powders were mixed following the optimized procedure given by Jeong *et al.*[18] Al_2O_3/SiC nanocomposite mixtures which contained 5, 10, 20, and 30 vol% of β-SiC particles (average size ≈0.3 μm) were hot-pressed at 1600°, 1700°, 1750°, and 1800°C, respectively, for 2 h, under 30 MPa uniaxial pressure. For comparison, also monolithic Al_2O_3 was hot-pressed according to a similar cycle (1500°C, for 2 h, under 30 MPa). All of the investigated materials were nearly fully dense (>99%). The average grain size of the Al_2O_3 grains was about 1.5 μm in all of the nanocomposites and in the monolithic Al_2O_3.

Bend bars for *R*-curve determination were 3 μm × 4 μm × 20 μm in dimensions, centrally notched by a diamond cutter with a blade thickness of 0.2 mm. The relative notch length, a_0/W, was 0.5. In order to reduce the influence of the finite notch-root radius on the initial crack propagation, the bottom portion of the saw notch was sharpened by a razor blade to <10 μm. To achieve stable fracture propagation in bending geometry, the crack stabilizer designed by Nojima *et al.*[19] for a three-point bending geometry was used (span = 16 mm). The load–displacement relation was directly measured with semiconductor strain gauges placed both on the loading bar and on the tensile surface of the specimen. Further details of the notching procedure and of the bending stabilizer have been reported elsewhere.[20,21] *R*-curve data were collected from the load–displacement curves obtained with a relatively fast crosshead speed (0.1 mm/min). This crosshead speed was selected in an attempt to minimize the effect of humidity on crack growth, which may occur in Al_2O_3-based materials. The crack length was concurrently measured by scanning electron microscopy (SEM) after arresting the crack propagation. The crack resistance value, K_R, as a function of crack extension was calculated from standard fracture mechanics equations. The four-point bending flexural strength of unnotched specimens was measured on bars 3 mm × 4 mm × 35 mm, using an upper and a lower span of 15 and 30 mm, respectively. The tensile surface of the bars was ground with an 800-grit diamond wheel and successively polished with fine diamond paste (final polishing with 0.3 μm grit diamond grains for 10 h). The edges of the bars were also smoothed and polished as above. The strength values were calculated from an average of five tests on each sample.

In order to analyze the flaw tolerance of nanocomposite bodies when external damage occurs during operation, the same tests were carried out on bending bars precracked by a relatively large (≈80 μm) Vickers flaw. The influence of residual stresses associated with the indentation mark were minimized by removing a layer of ≈40–60 μm from the tensile surface (after indenting), and by successively polishing with diamond paste. Three specimens were tested for each material.

(2) *Crack Opening Displacement Profile Determination*

The experimental approach adopted for the measurement of near-tip COD into the scanning electron microscope was similar to that described by Rödel *et al.*[22,23] However, in the present investigation, equilibrium cracks were introduced with a Vickers indenter using a 300 N load. Near-tip COD profiles were observed with a field emission scanning electron microscope (FE-SEM, Model S-800, Hitachi, Tokyo, Japan) operating at 20 kV, up to its maximum magnification limit (≈60 K). In order to minimize errors involved in the COD profile measurements, all images were digitized and computer analyzed by means of commercially available image processing programs (Adobe PhotoShop). Similar to the experiments by Rödel *et al.*,[22] the edge-charging effect along the crack edges was the critical factor deciding the ultimate resolution of the COD measurement. However, lightly coating the SEM specimen by carbon before introducing the indentation mark helped to minimize the edge-charging effect. As a result, the COD analysis could be carried out up to a maximum resolution of ≈5 nm.

(3) *Fluorescence and Raman Spectroscopy*

The determination of residual stresses by fluorescence and Raman spectroscopy (in the Al_2O_3 and SiC phase, respectively) was based on the piezospectroscopy effect discussed by Ma and Clarke.[24,25] A Raman spectroscopic apparatus (ISA, T 6400 Jovin-Yvon) was used, which was equipped with an Ar-ion laser (frequency and power were 488 nm and 300 mW, respectively) as the excitation source. An optical microscope was used both to focus the laser on the sample and to collect the scattered light. Light frequencies were analyzed using a triple monochromator equipped with a charge-coupled device (CCD) camera. A neon discharge lamp was used for frequency calibration. Further details of the technique and its accuracy have been described elsewhere.[26–28] The collected data were analyzed with the curve-fitting algorithms included in the SpectraCalc software package (Galactic Industries Corp.). Residual stresses were determined by monitoring the shift of the ruby-fluorescence doublet (14 400 and 14 430 cm^{-1}) in the case of Al_2O_3 and the shift of the Raman peaks (794.1 and 970.8 cm^{-1}) in the case of SiC; the stress values were calculated from the respective frequency shifts according to the piezospectroscopic coefficients given in the literature (for Al_2O_3[29] and SiC[30]). Average stress values from about 20 measurements per specimen were calculated from data collected with a laser spot of ≈10 μm. Residual stresses were determined as a function of the volume fraction of SiC dispersoid.

III. Results and Discussion

(1) *Mechanical Properties and Fractography Results*

In Table I are summarized the results obtained by fractography analysis of crack profiles in nanocomposites containing SiC volumetric fractions ranging between 5 and 30 vol%. It can be noted that the presence of SiC particles within the ceramic matrix causes a dramatic change in fracture mode from predominantly

Table I. Fracture Mode and Particle Location in Al_2O_3/SiC Nanocomposites

	Fracture mode (%)		Particle location (%)	
	Intergranular	Transgranular	Intergranular	Transgranular
Al_2O_3	89	11	–	–
Al_2O_3/5 vol% SiC	15	85	11	89
Al_2O_3/10 vol% SiC	18	82	28	72
Al_2O_3/20 vol% SiC	43	57	63	37
Al_2O_3/30 vol% SiC	46	54	60	40

intergranular, as typically observed in alumina, to predominantly transgranular. This phenomenon has been observed by several other researchers.[2,7,8,31,32] According to our observation, with dispersion of up to 5–10 vol% SiC the fracture pattern was almost completely transgranular, while further increasing the SiC fraction partly restored the intergranular fracture mode of the mere matrix. As a result, for SiC volume fractions ≥20%, the fraction of intergranular fracture was ≈50%. Phenomenologically, the change in fracture mode is related to the location of SiC particles, namely intergranular vs transgranular (cf. Table I). For SiC volume fractions ≤20%, the percent of dispersoid located at grain boundaries is a maximum. In other words, a relative fraction of SiC ≥10 vol% is hardly introduced into the Al_2O_3 grains, whatever the nominal added fraction. Our present results agree well with a systematic study by Stearns and Harmer[33] on particle-inhibited grain growth in hot-pressed (and successively annealed) Al_2O_3–SiC nanocomposites. These researchers found that, upon annealing, the fraction of SiC particles on Al_2O_3 grain boundaries decreases to a relatively greater extent for smaller volume fractions of particles. In the present context, particle location is considered to be essential for justifying the strengthening effect, as confirmed by the strength values shown in Fig. 1. A well-detectable increase in bending strength of the composite over that of monolithic alumina was observed at low volume fractions of SiC dispersoids (≤10%). A remarkably high strength value of ≈1 GPa, which corresponds to approximately twice the value measured in pure Al_2O_3, was achieved in the material containing 5 vol% of SiC dispersoids. However, a progressive strength decrease was observed at higher SiC contents, so that the strength increase over monolithic Al_2O_3 was almost negligible when 30 vol% SiC was added. Bending strength was also measured after precracking the bend bars with an artificial flaw of size ≈80 μm. In this case, the strength values for all materials were almost the same as that found for monolithic Al_2O_3. Considering that the strength of a brittle material depends only on the square root of the critical flaw size and toughness, the reproducibility of strength data in different composites with the same flaw size suggests that no tangible toughening effect is achieved upon adding nanosized SiC particles, independent of their volume fraction.

The near-tip *R*-curve behavior was studied for the material that exhibited the highest strength value, namely the Al_2O_3/5 vol% SiC, and compared with the behavior of monolithic Al_2O_3. The results of this experiment are shown in Fig. 2. The nanocomposite showed no significant near-tip rising *R*-curve behavior, and its plateau fracture toughness was even slightly lower than that of monolithic Al_2O_3.† The crack resistance at zero crack extension, $K_R = K_{IO}$, was calculated at the onset load for nonlinear behavior in the load–displacement curve. The bending crack stabilizer allowed crack arrest after propagation of a few tens of micrometers. Upon short crack extensions, the very-near-tip bridging mechanism proposed by Ohji *et al.*[17] could not be substantiated.

(2) COD Profile Results

Ohji *et al.*[17] claimed that a few hundred nanometers is a crack extension sufficient for producing a steep rising *R*-curve behavior in an Al_2O_3/SiC nanocomposite. This speculation was based on a transmission electron micrograph showing the existence of SiC bridging sites located within a short crack extension. However, if such bridging sites provide a remarkable *R*-curve effect, the reason why such an effect is not observable upon crack extensions of ≈10 μm is not clear. In order to learn about near-tip toughening

†A lower fracture toughness of the nanocomposite as compared to monolithic Al_2O_3 should lead to a lower strength value when a controlled flaw is introduced in the material. However, in Fig. 1, our experimental data show no difference in strength between monolithic Al_2O_3 and nanocomposites when the bending bars are precracked. This discrepancy may be due to easier matrix grain cleavage when the double-notch is introduced by a razor blade[20] in the nanocomposite (e.g., the actual crack length may be longer than that nominally observed by microscopy). On the other hand, grain cleavage can also severely affect the morphology of the indentation precrack strength, thus leading to apparently higher strength data. Despite this discrepancy, which certainly testifies to the difficulty of reliably testing the flaw tolerance of nanocomposites, the modest toughness level measured here, whatever the procedure adopted, cannot justify (i.e., according to the Griffith law) the strengthening effect found in the nanocomposite.

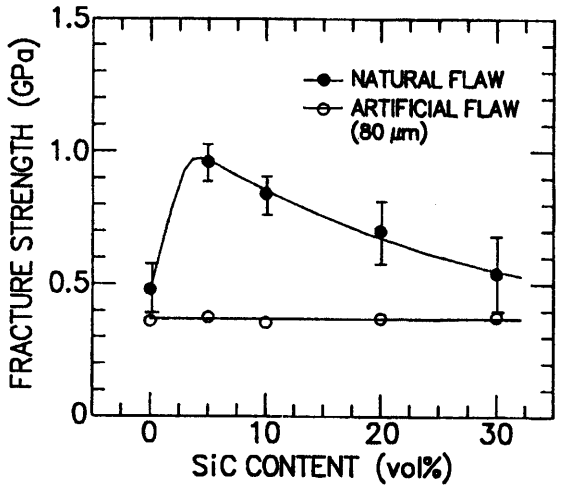

Fig. 1. Strength of Al_2O_3/SiC nanocomposites as a function of the SiC volume fraction: as hot-pressed samples (●), and samples precracked by a 80 μm Vickers indentation (○).

mechanisms, the near-tip crack opening displacement profile, $u(x)$, of both monolithic Al_2O_3 and Al_2O_3/5 vol% SiC nanocomposite was quantitatively measured by means of FE-SEM and image analysis tools. A plot of the obtained crack profiles is given in Fig. 3. In both cases, a pronounced deviation from a parabolic profile was found for $x > 100$ μm, as also observed by Seidel *et al.*[34] This phenomenon will be henceforth neglected because it is not related to the toughening behavior of the material, but it just arises from the residual stress field in the indentation contact zone. On the other hand, the COD profile in the very-near-tip zone (i.e., <10 μm) can be actually fitted with a curve which is a convolution of parabolic profiles.[34] The plotted parabolas were calculated according to the equation given by Irwin:[35]

$$u(x) = (8x/\pi)^{1/2} K_{IC}/E(1 - \nu^2) \quad (1)$$

in which the COD, $2u(x)$, is expressed as a function of the distance from the crack tip, x. K_{Ic} is the crack-tip toughness, and E and ν are Young's modulus and the Poisson ratio, respectively. Inferring the parameter E = 420 GPa and ν = 0.25, the K_{Ic} values 2.6 and 2.2 MPa·m$^{1/2}$, obtained from the fracture mechanics analysis (cf. Section III(1)) generate parabolic curves which reasonably bound the COD experimental profiles for both Al_2O_3 matrix and nanocomposite. Based on the COD data, it is argued that if a bridging

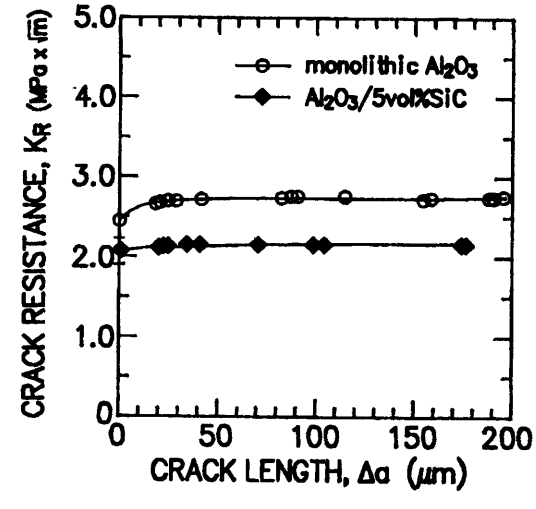

Fig. 2. Fracture toughness of monolithic Al_2O_3 (○) and Al_2O_3/5 vol% SiC (◆) as a function of the length, Δa, of stably propagated cracks.

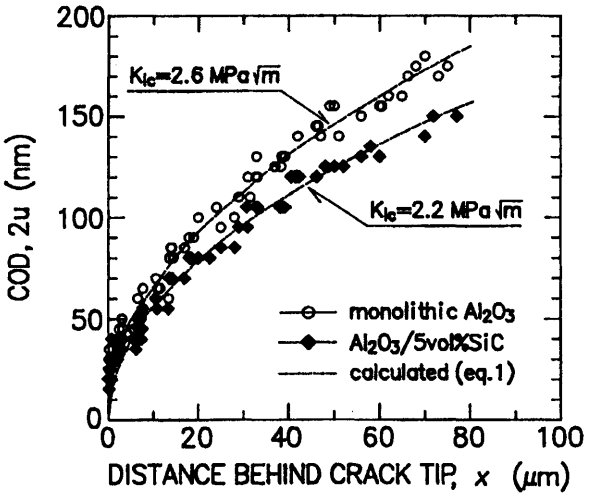

Fig. 3. COD profiles as measured in monolithic Al_2O_3 (○) and Al_2O_3/5 vol% SiC (◆). Broken lines represent the theoretical profiles calculated by Eq. (1) using the K_{IC} values given in Fig. 2.

effect is operative in the nanocomposite materials at short crack distances, its effect on toughening should be rather small. This argument is also supported by high-magnification SEM images of the crack path. In all of our observations, clear evidence of an elastic bridging mechanism by SiC particles was not found. Typical examples of interaction between cracks and SiC particles are shown in Fig. 4 for a SiC particle transgranularly located (Fig. 4(a) and a particle trapped at a triple point (Fig. 4(b)). The Al_2O_3/SiC phase boundaries were always found fractured, however close the SiC particle was to the crack tip.

Given the above evidence, we shall rule out a significant crack bridging effect and focus hereafter on the characterization of bulk residual stresses stored in the nanocomposite material. A spectroscopic analysis of residual stresses both in the matrix and in the dispersoid phase is given in the following section, which represents the experimental base to explain a strengthening effect in the absence of toughening.

(3) Residual Stress Analysis

Residual stresses were measured by piezospectroscopic techniques (on the tensile surface of bending bars) in both an Al_2O_3 matrix and a SiC dispersoid (Fig. 5). A hydrostatic tensile stress field linearly increasing with SiC volume fraction was found. The maximum tensile stress value in the Al_2O_3 matrix was 0.5 GPa, which was measured in the Al_2O_3/30 vol% SiC sample.

Residual stresses, as theoretically predicted by a stochastic model given by Kreher and Pompe,[36] are plotted for comparison in Fig. 5. They were calculated according to the following equations:

$$\langle\sigma_{ik}^{i}\rangle = \delta_{ik}[3K_mK_d/V_{fm}(K_m - K_d)] \times \{V_{fd} - [K_d(K_m - K^*)/K^*(K_m - K_d)]\}(\alpha_m - \alpha_d)\Delta T \quad (2)$$

$$K^* = V_{fm}K_m + V_{fd}K_d \quad (3)$$

where $\langle\sigma_{ik}^{i}\rangle_m$ is the average isotropic part of residual stresses in the alumina matrix, V_f the volume fraction, K the bulk modulus (260 and 330 GPa for Al_2O_3 and SiC, respectively), and α the average coefficient of thermal expansion. The subscripts m and d refer to the matrix and the dispersoid phases, respectively. δ_{ik} is the Kroenecker symbol. ΔT is the elastic stress-free temperature on cooling, which was taken as 1180°C, according to Sergo *et al.*[37] The validity of this model for ceramic composites has been discussed by other authors.[38,16] As seen from Fig. 5, good agreement is found, at low SiC fractions, between experimental results and theoretical predictions based on Eqs. (2) and (3). However, the model underestimates the residual stress values at high SiC fractions; the higher the fraction, the higher the discrepancy. In the bulk, average residual stresses in both matrix and dispersoid should obey the following equilibrium condition:

$$\langle\sigma_{eq}\rangle = V_{fm}\langle\sigma_{ik}^{i}\rangle_m + V_{fd}\langle\sigma_{ik}^{i}\rangle_d = 0 \quad (4)$$

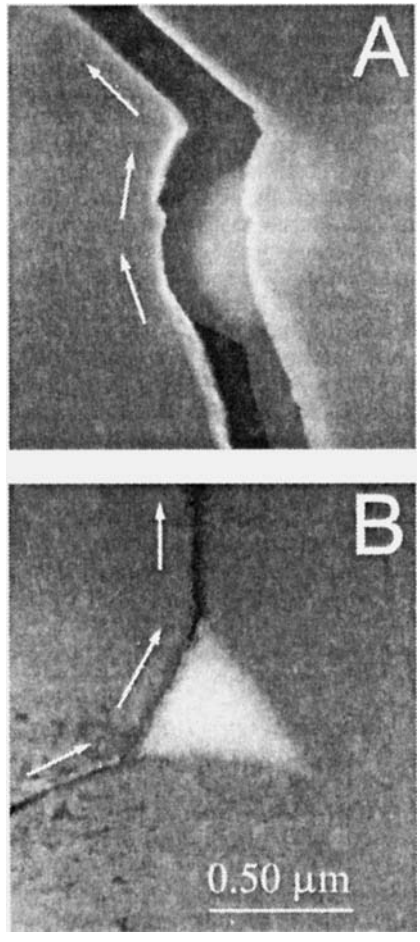

Fig. 4. SEM micrographs of typical interactions between crack and SiC inclusions: (A) transgranular particle location; and (B) intergranular particle location. Arrows indicate the direction of crack propagation.

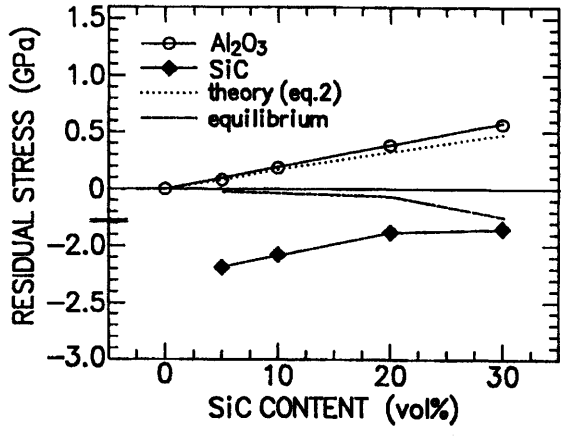

Fig. 5. Residual stresses measured by piezospectroscopic techniques in the Al_2O_3 matrix (○) and in the SiC dispersoid (◆). Experimental data for Al_2O_3 are compared to theoretical predictions (broken line) calculated from Eq. (2). The stress equilibrium condition in Eq. (3) is also shown, which gives an estimate of the experimental error involved in the present residual stress assessment.

were $\langle\sigma_{eq}\rangle$ represents an "equilibrium stress." However, if residual stress due to machining is stored nearby the surface of the specimen, the equilibrium condition may not be satisfied for an insufficient penetration of the laser beam in the material. The $\langle\sigma_{eq}\rangle$ values, as calculated in various composites, are plotted in Fig. 5. As seen, the equilibrium condition dictated by Eq. (4) is reasonably satisfied only for low added fractions of SiC, while a nonnegligible divergency (toward compressive stresses) is found at high SiC fractions. By directly measuring the extent of elastic bending in thin disk specimens, Chou *et al.*[13] estimated a maximum thickness of the residual stress layer of $\approx$10 μm in both monolithic Al_2O_3 and Al_2O_3/SiC nanocomposite. This thickness is about 2 times smaller than the depth probed by the laser beam during the present piezospectroscopic measurements. Therefore, if the discrepancy from the equilibrium state is due to the surface (compressive) residual stress arising from machining, measurements with the same laser-beam diameter, but in the confocal configuration, should enhance the magnitude of the observed $\langle\sigma_{eq}\rangle$. This is because the confocal configuration allows one to probe the stress state in the very surface of the specimens (a few micrometers in depth). A negligible difference (<5%) in the $\langle\sigma_{eq}\rangle$ values was found between surface-focused and confocal measurements for SiC contents $\leq$10 vol%. However, compressive stress values higher by $\approx$40% were found for $\langle\sigma_{eq}\rangle$ at SiC fractions >10 vol%. These results suggest that residual compressive stresses were actually introduced on the surface of the nanocomposite bending bars by grinding with an 800-grit diamond wheel. Successive polishing steps with fine diamond paste were effective in releasing the (compressive) surface residual stresses, but only for SiC fractions $\leq$10 vol%. Zhao *et al.*[7] reported that annealing was more effective in diminishing surface compressive stresses (induced by machining) in monolithic Al_2O_3 than in Al_2O_3/SiC nanocomposites. Our results are consistent with this finding, showing that the larger the SiC fraction, the more difficult the release of the machining-induced surface stresses by a standard polishing procedure. In conclusion, the piezospectroscopic assessment of residual stresses suggests that the strengthening effect observed at SiC fractions $\leq$10 vol% is rather related to bulk residual stresses from thermal expansion mismatch than to machining-induced residual stresses.

(4) Strengthening by Bulk Residual Stresses

From a phenomenological point of view, it is understood that (i) the strengthening mechanism is not arising from an actual toughening effect, and (ii) the inherently higher strength shown by Al_2O_3/SiC nanocomposites with $V_{fd} \leq 10\%$ is related to the intragranular location of SiC particles within the Al_2O_3 grains, which in turn results in a predominantly transgranular fracture mode. The change in fracture mode from intergranular to transgranular can be correlated to the bulk residual stress field developed in the material upon cooling, which arises from the higher thermal expansion coefficient of Al_2O_3 as compared to SiC. When the SiC dispersoids are transgranularly located, the tensile stresses developed in Al_2O_3 can trigger cleavage fracture in the matrix grains.[38,39] Local stresses around the SiC inclusion can be much higher than the average hydrostatic stress measured by piezospectroscopy techniques. On the other hand, an intergranular location of the SiC particles may enhance tensile stresses on grain boundaries and promote intergranular fracture propagation. The higher the fraction of SiC added (and the larger their size), the higher the probability of their intergranular location. This would explain why weaker grain boundaries are developed and a very limited strengthening is achieved for relatively high fractions of SiC (i.e., despite a higher compressive residual stress induced by machining on the surface of bending bars).

Thermal expansion anisotropy is a potential source of grain-boundary microfracture in polycrystalline Al_2O_3.[40,41] In particular, triple points are inherently weak zones due to high residual stress fields generated during cooling. Figure 6(A) shows a schematic of a grain-boundary microcrack loaded by a local residual tensile stress arising from thermal expansion anisotropy. However, if intragranular dispersoids with a lower thermal expansion are embedded in the matrix grains, a hydrostatic compressive stress field can be generated on grain boundaries upon cooling (Fig. 7(B)). Because of the overlap of such a stress field, apparently "stronger" grain boundaries and inherent grain-boundary defects, shielded by residual stresses, can be envisaged, which justifies the transgranular fracture mode and the observed strengthening.

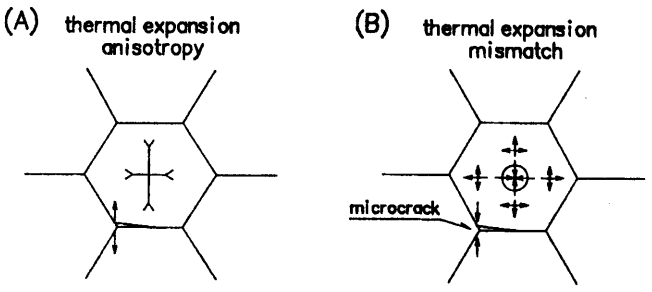

Fig. 6. Schematic illustration of the residual stress fields generated at grain boundaries and on a grain-boundary microcrack due to (A) thermal expansion anisotropy in monolithic Al_2O_3 and (B) thermal expansion mismatch in Al_2O_3/SiC nanocomposite with transgranularly located dispersoids.

According to the above-proposed mechanism, only transgranularly located SiC particles will exert a positive contribution on the inherent matrix strength. On the contrary, particles located at grain boundaries, although contributing to the development of a finer matrix grain structure, may trigger grain-boundary fracture. These two opposite effects may annihilate each other and no strength improvement be found as compared to the matrix material. In addition, it should be noted that only the finer SiC particles will be incorporated within the matrix grains, leaving the entire fraction of larger particles at grain boundaries. This factor may strongly limit the potentiality of the strengthening mechanism. Kovalev *et al.*[42] have recently proposed a quantitative model for grain-boundary strengthening in nanocomposites by misfitting intragranular inclusions. We also propose a quantitative assessment of the strengthening mechanism by bulk residual stresses in a separate publication.[43]

IV. Conclusion

The fracture properties of Al_2O_3/SiC nanocomposites have been investigated as a function of the added SiC volume fraction. Both strengthening and toughening mechanisms were discussed to explain the strength properties originally reported by Niihara *et al.*[6] Bulk residual stresses could be precisely characterized by piezospectroscopic techniques. A very-near-tip toughening mechanism based on crack-tip bridging, as proposed by other authors, has also been investigated by means of stable crack propagation techniques and by direct observation of very-near-tip COD profiles. Based on these assessments, the following conclusions were drawn:

(i) Although a detectable strengthening effect was observed at low SiC contents ($V_{fd} \leq 10\%$), no toughness increase could be measured and no toughening mechanism directly substantiated for nanocomposite materials showing high strength.

(ii) Bulk residual stresses arising from thermal expansion mismatch between Al_2O_3 and SiC were of a conspicuous magnitude. A strengthening mechanism of Al_2O_3 grain boundaries was proposed, which is operative only when SiC particles are embedded in the Al_2O_3 matrix grains. Since the probability of finding intergranularly located particles increases when increasing their volume fraction, only nanocomposites with a low SiC content show high strength.

Acknowledgments

Professor T. Nishida is sincerely acknowledged for valuable discussions on mechanical testing. We are indebted to one unknown reviewer for providing the manuscript of Ref. 43 before publication.

References

[1]M. Sternitzke, "Review: Structural Ceramic Nanocomposites," *J. Eur. Ceram. Soc.*, **17**, 1061–82 (1997).

[2]K. Niihara, "New Design Concept of Structural Ceramics—Ceramic Nanocomposites," *J. Ceram. Soc. Jpn.*, **99** [10] 974–82 (1991).

[3]K. Niihara and A. Nakahira, "Structural Ceramic Nanocomposites by Sintering Method: Roles of Nano-size Particles"; pp. 404–17 in *Ceramics: Towards the 21st Century*. Ceramic Society of Japan, Tokyo, Japan, 1991.

[4]K. Niihara and A. Nakahira, "Strengthening of Oxide Ceramics by SiC and Si_3N_4 Dispersions"; pp. 919–26 in *Proceedings of the 3rd International Symposium on Ceramic Materials and Components for Engines*. Edited by V. J. Tennery. American Ceramic Society, Westerville, OH, 1988.

[5]A. Nakahira and K. Niihara, "Sintering Behaviors and Consolidation Process for Al_2O_3/SiC Nanocomposites," *J. Ceram. Soc. Jpn.*, **100** [4] 448–53 (1992).

[6]K. Niihara and A. Nakahira, "Strengthening and Toughening Mechanisms in Nanocomposite Ceramics," *Ann. Chim. (Paris)*, **16**, 479–86 (1991).

[7]J. Zhao, L. C. Stearns, M. P. Harmer, H. M. Chan, G. A. Miller, and R. F. Cook, "Mechanical Behavior of Alumina–Silicon Carbide "Nanocomposites'," *J. Am. Ceram. Soc.*, **76** [2] 503–10 (1993).

[8]C. E. Borsa, S. Jiao, R. I. Todd, and R. J. Brook, "Processing and Properties of Al_2O_3/SiC Nanocomposites," *J. Microsc. (Oxford)*, **177**, 305–12 (1994).

[9]R. W. Davidge, R. J. Brook, F. Cambier, M. Poorteman, A. Leriche, D. O'Sullivan, S. Hampshire, and T. Kennedy, "Fabrication, Properties and Modelling of Engineering Ceramics Reinforced with Nanoparticles of Silicon Carbide," *J. Eur. Ceram. Soc.*, **16**, 799–802 (1996).

[10]B. Y. Jang, M. Enoki, T. Kishi, S. H. Lee, and H. K. Oh, "Fracture Behavior and Toughening of Alumina-Based Composites Fabricated by Microstructural Control"; pp. 371–82 in *Fracture Mechanics of Ceramics*, Vol. 12. Edited by R. C. Bradt, D. P. H. Hasselman, D. Munz, M. Sakai, and V. Ya. Shevcenko. Plenum Press, New York, 1996.

[11]L. Carrol, M. Sternitzke, and B. Derby, "Silicon Carbide Particle Size Effects in Alumina-Based Nanocomposites," *Acta Mater.*, **44** [1] 4543–52 (1996).

[12]J. Pérez-Rigueiro, J. Y. Pastor, J. Llorca. M. Elices, P. Miranzo., and J. S. Moja, "Revisiting the Mechanical Behavior of Alumina/Silicon Carbide Nanocomposites," *Acta Mater.*, **46** [15] 5399–411 (1998).

[13]I. A. Chou, H. M. Chan, and M. P. Harmer, "Machining-Induced Surface Residual Stress Behavior in Al_2O_3/SiC Nanocomposites," *J. Am. Ceram. Soc.*, **79** [9] 2403–409 (1996).

[14]M. Sternitzke, B. Derby, and R. J. Brook, "Alumina/Silicon Carbide Nanocomposites by Hybrid Polymer/Powder Processing: Microstructures and Mechanical properties," *J. Am. Ceram. Soc.*, **81** [1] 41–48 (1998).

[15]M. J. Hoffman, M. Sternitzke, J. Rödel, and R. J. Brook, "Fracture Mechanisms in a Strengthened Nano-Toughened Alumina/Silicon Carbide Composite"; pp. 179–86 in *Fracture Mechanics of Ceramics*, Vol. 12. Edited by R. C. Bradt, D. P. H. Hasselman, D. Munz, M. Sakai, and V. Ya. Shevcenko. Plenum Press, New York, 1996.

[16]G. Pezzotti, V. Sergo, K. Ota, O. Sbaizero, N. Muraki, T. Nishida, and M. Sakai, "Residual Stresses and Apparent Strengthening in Ceramic-Matrix Nanocomposites," *J. Ceram. Soc. Jpn.*, **104** [6] 497–503 (1996).

[17]T. Ohji, Y. K. Jeong, Y. H. Choa, and K. Niihara, "Strengthening and Toughening Mechanisms of Ceramic Nanocomposites," *J. Am. Ceram. Soc.*, **81** [6] 1453–60 (1998).

[18]Y. K. Jeong, A. Nakahira, P. E. D. Morgan, and K. Niihara, "Effect of Milling on the Strength of Alumina–Silicon Carbide Nanocomposites," *J. Am. Ceram. Soc.*, **80** [5] 1307–309 (1997).

[19]T. Nojima and O. Nakai, "Stable Crack Extension of an Alumina Ceramic in Three-Point Bending Test" (in Jpn.), *J. Soc. Mater. Sci. Jpn.* **42** [475] 412–18 (1993).

[20]T. Nishida, Y. Hanaki, T. Nojima, and G. Pezzotti, "Measurement of Rising *R*-Curve Behavior in Toughened Silicon Nitride by Stable Crack Propagation in Bending," *J. Am. Ceram. Soc.*, **78** [11] 3113–16 (1995).

[21]T. Nishida, Y. Hanaki, and G. Pezzotti, "Effect of Notch-Root Radius on the Fracture Toughness of a Fine-Grained Alumina," *J. Am. Ceram. Soc.*, **77** [2] 606–608 (1995).

[22]J. Rödel, J. M. Kelly, and B. R. Lawn, "*In Situ* Measurements of Bridged Interfaces in the Scanning Electron Microscope," *J. Am. Ceram. Soc.*, **73** [11] 3313–18 (1990).

[23]J. Rödel, E. R. Fuller, Jr., and B. R. Lawn, "*In Situ* Observations of Toughening Processes in Alumina Reinforced with Silicon Carbide Whiskers," *J. Am. Ceram. Soc.*, **74** [12] 3154–57 (1991).

[24]Q. Ma and D. R. Clarke, "Stress Measurement in Single-Crystal and Polycrystalline Ceramics Using Their Optical Fluorescence," *J. Am. Ceram. Soc.*, **76** [6] 1433–40 (1993).

[25]Q. Ma and D. R. Clarke, "Piezospectroscopic Determination of Residual Stresses in Polycrystalline Alumina," *J. Am. Ceram. Soc.*, **77** [2] 298–301 (1994).

[26]G. Pezzotti, H. Suenobu, T. Nishida, and O. Sbaizero, "Measurement of Microscopic Bridging Stresses in Alumina/Molybdenum Composite by *In Situ* Fluorescence Spectroscopy," *J. Am. Ceram. Soc.*, **82** [5] 1257–62 (1999).

[27]G. Pezzotti, O. Sbaizero, V. Sergo, N. Muraki, K. Maruyama, and T. Nishida, "*In Situ* Measurements of Frictional Bridging Stresses in Alumina Using Fluorescence Spectroscopy," *J. Am. Ceram. Soc.*, **81** [1] 187–92 (1998).

[28]G. Pezzotti, "Microprobe Piezo-Spectroscopy for the Micromechanical Analysis of Fracture and Deformation Phenomena in Polycrystalline Ceramics," *Compos. Sci. Technol.*, **59**, 821–31 (1999).

[29]J. He and D. R. Clarke, "Determination of the Piezospectroscopic Coefficient for Chromium-Doped Sapphire," *J. Am. Ceram. Soc.*, **78** [5] 1347–53 (1995).

[30]J. F. Di Gregorio, T. E. Furtak, and J. J. Petrovic, "A Technique for Measuring Stress in SiC Whiskers Within an Alumina Matrix Through Raman Spectroscopy," *J. Appl. Phys.*, **71** [7] 3524–31 (1992).

[31]A. M. Thompson, H. M. Chan, M. P. Harmer, and R. F. Cook, "Crack Healing and Stress Relaxation in Al_2O_3–SiC 'Nanocomposites'," *J. Am. Ceram. Soc.*, **78** [3] 567–71 (1995).

[32]T. Ohji, T. Hirano, A. Nakahira, and K. Niihara, "Particle/Matrix Interface and Its Role in Creep Inhibition of Alumina/Silicon Carbide Nanocomposites," *J. Am. Ceram. Soc.*, **79** [1] 33–45 (1996).

[33]L. C. Stearns and M. P. Harmer, "Particle-Inhibited Grain Growth in Al_2O_3–SiC: I, Experimental Results," *J. Am. ceram. Soc.*, **79** [12] 3013–19 (1996).

[34]J. Seidel and J. Rödel, "Measurement of Crack Tip Toughness in Alumina as a Function of the Grain Size," *J. Am. Ceram. Soc.*, **80** [2] 433–38 (1997).

[35]G. R. Irwin, "Fracture"; in *Handbuch der Physik*, Vol. 6. Springer-Verlag, Berlin, Germany, 1958.

[36]W. Kreher and W. Pompe, *Internal Stresses in Heterogeneous Solids*. Akademie-Verlag, Berlin, Germany, 1989.

[37]V. Sergo, X. L. Wang, D. R. Clarke, and P. F. Becher, "Residual Stresses in Alumina/Ceria-Stabilized Zirconia Composites," *J. Am. Ceram. Soc.*, **78** [8] 2213–14 (1995).

[38]Q. Ma, W. Pompe, J. D. French, and D. R. Clarke, "Residual Stresses in Al_2O_3–Zro_2 Composites: A Test of Stochastic Stress Models," *Acta Metall. Mater.*, **42** [5] 1673–81 (1994).

[39]J. Luo and R. Stevens, "The Role of Residual Stress on the Mechanical Properties of Al_2O_3–5 vol% SiC Nanocomposites," *J. Eur. Ceram. Soc.*, **17**, 1565–71 (1997).

[40]I. Levin, W. D. Kaplan, D. G. Brandon, and A. A Layyous, "Effect of SiC Submicrometer Particle Size and Content on Fracture Toughness of Alumina-SiC Nanocomposites," *J. Am. Ceram. Soc.*, **78** [1] 254–56 (1995).

[41]A. G. Evans, "Microfracture from Thermal Expansion Anisotropy—I. Single Phase Systems," *Acta Metall.*, **26**, [12] 1845–53 (1978).

[42]Y. Fu and A. G. Evans, "Microcrak Zone Formation in Single Phase Polycrystals," *Acta Metall.*, **30** [8] 1619–25 (1982).

[43]S. Kovalev, T. Ohji, Y. Yamauchi, and M. Sakai, "Grain Boundary Strength in Non-Cubic Ceramic Polycrystals with Misfitting Intragranular Inclusions (Nanocomposites)," *J. Mater. Sci.*, **35**, 1405–12 (2000).

[44]G. Pezzotti and W. Müller, "Strengthening Mechanisms in Al_2O_3/SiC Nanocomposites," *Comput. Mater. Sci.*, **22**, 155–68 (2001). □

journal

J. Am. Ceram. Soc., 84 [6] 1209–16 (2001)

Synthesis of Dense TiB_2–TiN Nanocrystalline Composites through Mechanical and Field Activation

Jae Won Lee and Zuhair A. Munir*

Facility for Advanced Combustion Synthesis (FACS), Department of Chemical Engineering and Materials Science, University of California, Davis, California 95616

Masachika Shibuya and Manshi Ohyanagi

Department of Materials Chemistry, High-Tech Research Center, Ryukoku University, Ohtsu, Japan

The synthesis of dense nanometric composites of TiN–TiB_2 by mechanical and field activation was investigated. Powder mixtures of Ti, BN, and B were mechanically activated through ball milling. Some powders were milled to reduce crystallite size but to avoid initiating a reaction. In other cases powders were milled and allowed to partially react. All these were subsequently reacted in a spark plasma synthesis (SPS) apparatus. The products were composites with equimolar nitride and boride components with relative densities ranging from 90.1% to 97.2%. Crystallite size analyses using the XRD treatments of Williamson–Hall and Halder–Wagner gave crystallite sizes for the TiN and TiB_2 components in the range 38.5–62.5 and 31.2–58.8 nm, respectively. Vickers microhardness measurements (at 2 N force) on the dense samples gave values ranging from 14.8 to 21.8 GPa and fracture toughness determinations (at 20 N) resulted in values ranging from 3.32 to 6.50 MPa·$m^{1/2}$.

I. Introduction

The unique properties of nanometric materials have generated widespread interest and research activities during the past few years.[1] Materials with phase structure modulation on a scale of less than 100 nm have properties that are not only different but in many cases superior to those with a larger grain size.[2–4] For example, results showing an increase in strength and hardness by a factor of 4–7 resulting from a decrease in crystallite size to the nanometeric range have been provided.[5–7] "Superhard" coatings (with Vickers hardness ≥0 GPa) of nanostructured materials have been made.[8]

Nanometric materials are formed either by direct deposition as thin coatings (by PVD or CVD) or as powders/clusters by a variety of methods. In a thermodynamic sense, the process of formation of nanomaterials relies on the degree of departure from equilibrium.[2,9] Methods employing this nonequilibrium approach include precipitation,[10,11] pyrolysis of organic precursors,[12,13] gas-phase condensation,[14] high-energy milling,[15–18] and others.[19,20] Except for the case of thin film formation, the preparation of dense nanomaterials requires an additional step. Consolidation of nanopowders to produce dense bodies for further property characterization has been accomplished with several techniques including sintering,[12,21] hot pressing,[12,22,23] and spark plasma (or pulsed electric current) sintering (SPS).[10,24] The major concern in all of these methods of consolidation is grain growth. In view of the nonequilibrium state of the nanomaterials and the fact that consolidation steps take place at high temperatures and require a relatively long holding time, grain growth (Oswald ripening) is anticipated. The relatively limited number of experimental data on mechanical properties on nanomaterials has been attributed to the difficulty of synthesizing dense bodies.[6]

Thus the preparation of dense nanomaterials has until recently been a two-step process involving sequential synthesis and consolidation. A few years ago, a process was developed to simultaneously synthesize and densify materials using electric field activation.[25,26] More recently this approach has been extended to the preparation of dense nanomaterials, with preliminary results on $MoSi_2$, FeAl, and $NbAl_3$.[27,28]

The process includes the use of nanometric powders, produced by ball milling, as reactants in field-activated synthesis. In this paper we present results on the simultaneous synthesis and densification of nanometric TiN–TiB_2 composites.

Because of its attractive properties, titanium diboride has been the focus of considerable attention for such potential applications as structural materials, cutting tools, armor material, and wear-resistant materials. Interest is motivated by its excellent thermomechanical properties. It has a relatively high hardness, elastic modulus, high-temperature strength, and abrasion resistance.[29,30] It is a refractory material with excellent high-temperature oxidation resistance and good thermal and electrical conductivities.[31,32] The latter property facilitates its machining by the electrical-discharge-machining (EDM) method. Its excellent chemical stability in molten metals makes it a candidate for use as a cathode material in aluminum production.[33] A variety of techniques have been used to prepare TiB_2 ceramics, including hot pressing,[34] hot isostatic pressing,[35] and high-pressure combustion synthesis.[36]

Titanium nitride possesses equally attractive properties. These include a high melting point, high hardness, and high electrical conductivity.[37] The thermochemical properties of TiN would suggest that it would be compatible with SiC, Al_2O_3, ZrO_2, Si_3N_4, and TiB_2.[38] It has a better chemical stability with iron aluminides and nickel aluminides than SiC, and thus may be used in these and other metallic phases to form metal-matrix composites.[39]

The two ceramics, TiN and TiB_2, however, are prepared in dense form by different processes. Typically, TiN is produced by chemical or physical vapor deposition (CVD or PVD) methods,[40] while TiB_2 is consolidated by hot pressing (HP) or hot isostatic pressing (HIPing). It is thus difficult to process and produce composites of these two ceramics by any of the conventionally used methods. Investigations have been made on the use of self-propagating high-temperature synthesis (SHS) to produce TiB_2 and TiN materials.[37,41–43] Composites of TiN–TiB_2 have also been made by hot-pressing TiN and TiB_2 powders, and their potential use in cutting tools and wear-resistant materials has been investigated.[44,45] More recently, such composites have been produced by reactive hot pressing using mixtures of TiH and BN,[46]

J. J. Petrovic—contributing editor

Manuscript No. 188329. Received August 28, 2000; approved February 7, 2001. This work was supported by a grant from the Army Research Office (ARO).
*Member, American Ceramic Society.

and by the SHS method using Ti, B, and BN as reactants.[47] Selected properties of these ceramic phases and their composites are shown in Table I.[40,46,48,49]

In this paper we present results on the synthesis of dense nanostructured TiB_2–TiN composites by field-activated reactions of mechanically activated powders. We use the spark plasma sintering (SPS) apparatus. In previous studies we have demonstrated the feasibility of this new method by synthesizing dense nanostructured ceramic and metallic phases.[27,28]

II. Experimental Materials and Methods

The starting materials were powders of Ti (99.7% pure), amorphous B (95%–97% pure), and BN (99.9% pure). All were purchased from the Atlantic Equipment Engineering Co. (Bergenfield, NJ). The initial particle size ranges for the three powders were 20–45, 1 (ave), and 2–3 μm, respectively. The powders were blended in a stoichiometric ratio according to the reaction

$$Ti + 0.5B + 0.5BN \rightarrow 0.5TiB_2 + 0.5TiN \quad (1)$$

They were then mixed in a Shaker-Mixer (Glenmill) for 24 h and ball-milled in a planetary mill. Milling was done using hardened bearing-steel balls and hardened steel vials with an inside diameter of 90 mm and an inside height of 100 mm. A ball-to-powder mass ratio (*B/P*) of 10:1 was used. All powder transfers to and from the vials were done in a glove box. The glove box was evacuated and back-filled three times with pure (99.99%) argon. The vial was then sealed and transferred to a Fritsch Pulverisette P7/2 planetary mill. Total milling times ranged from 0 to 25 h, but each 1 h of milling was followed by 1 h of cooling. The rotation speed of the mill speed was 250 rpm. To prevent reactions with the atmosphere, the vials were cooled in liquid nitrogen before the milled powder was removed inside the glove box. The entire procedure was repeated for different milling times; after each interval a small amount of the powder was removed for XRD analysis.

(1) X-ray Analyses

X-ray diffraction analyses were made using a Scintag XDS 2000 diffractometer with Cu$K\alpha$ radiation (λ = 1.540562 Å). The step size in 2θ was 0.01° and the time for each step scan was 10 s. The X-ray analysis included (a) phase identification and (b) crystallite size determination. For the latter, a numerical method was used which included three steps: peak fitting, Voigt analysis of peak shapes,[50,51] and Williamson–Hall (WH) and Halder–Wagner (HW) plots.[50,52] Account is also made for (1) the background using a simple polynomial (up to third order), (2) the intensity ratio of components $K\alpha_2$ and $K\alpha_1$, $R = I_{\alpha 2}/I_{\alpha 1}$, and (3) the shift parameter (δ) adjusting the angular separation of components $K\alpha_2$ and $K\alpha_1$, $\delta = 2\theta(\alpha_1) - 2\theta(\alpha_2)$. According to the analysis of Williamson and Hall,[52] the slope of the graph depends linearly on the lattice strain and the intercept varies as the reciprocal of the size of the crystallites, or

$$\beta_f^* = 1/\varepsilon + 2(\eta)d^* \quad (2)$$

where β_f^* is the integral width of a reciprocal lattice point, ε is the mean apparent volume-weighted crystallite size, η is the effective lattice deformation, and d^* (=2 sin θ/λ) is the distance of the point from the origin of the reciprocal lattice. They are calculated from the intercept and slope of the linear root-mean approximation through the experimental data points of a plot of β_f^* versus d^*.

(2) SPS Process and Apparatus

The synthesis and densification of the milled samples were conducted in a spark plasma sintering (SPS) apparatus (Model 1050, Sumitomo Coal and Mining Co.) under vacuum. The SPS apparatus is a uniaxial 100 kN press combined with a 15 V, 5000 A dc power supply to provide simultaneously pulsed current and pressure to the sample. The pulse cycle of the dc current is 12 ms on and 2 ms off.

The milled powders were placed into a graphite die, and then a 70 MPa pressure was applied. It was then heated for times ranging from 1 to 12 min at a heating rate of about 100°C·min^{-1}. The parameters of temperature, applied pressure, current, voltage, sample displacement (shrinkage), and displacement rate were measured continuously during the synthesis cycle. The displacement is the consequence of densification that results from consolidation of the powders and from the negative molar volume change associated with the synthesis reaction. The reacted samples were cooled to room temperature by turning off the power. The temperature was measured by means of an optical pyrometer focused on the graphite die surface near the center of the sample. Densified samples were ~19 mm in diameter and 5 mm thick.

III. Results and Discussion

XRD patterns were generated for all milled powders at different time intervals. The nature of the phases present and the general appearance of the peaks depended on milling time. For powders that showed no evidence of a reaction, the initially sharp diffraction lines became broadened after ball milling because of the refinement of the crystalline size and an increase in atomic-level strain. These two contributions can be separated in accordance with the WH or HW analysis, as indicated above. From the integral breadths of the diffraction lines the average crystalline size and strain could be obtained.

The XRD patterns of the Ti–B–BN powder mixture milled for different times are presented in Figs. 1 and 2. Figure 1 shows the patterns of the initial (unmilled) powder and those of powders milled up to 10 h. Since boron was amorphous, only peaks for Ti and BN appear in the pattern of the unmilled powder (pattern (a) in Fig. 1). After 0.5 h of milling the BN peaks have nearly totally disappeared and those of Ti show significant broadening and a decrease in intensity. The intensity of Ti peaks continued to decrease with increasing milling time (as seen in Fig. 1, parts (b) to (f)). Although the intensity of the Ti peaks decreased, their positions (2θ values) remained unchanged during the process of milling. This implies that the disappearance of the BN peaks is not related to any possible interaction with Ti, but is more likely the result of amorphization of the nitride phase. Literature reports indicate that such a phase transformation takes place as a result of extensive milling.[53]

Figure 2 shows the XRD patterns of reactant powders milled for 10 to 25 h as well as the pattern for the product of the self-ignited powders in air. The figure shows that with 10 h of milling, there is

Table I. Selected Properties of Sintered TiN, TiB_2, and TiN–TiB_2 Composites

Material	Crystallite size (nm)	Microhardness H_v at load (GPa)	(N)	Bend strength (MPa)	Fracture toughness K_{IC} (MPa·m$^{1/2}$)	Ref.
TiB_2		33.0 ± 0.6	0.3	450 ± 70	6.4 ± 0.4	48
TiN		19.9	0.5	260		48
TiB_2–TiN (1 wt% Ni)		20.5	196	614 ± 55	6.20 ± 0.21	46
30 wt% TiB_2–TiN		20.6	29.4		4.0	45
TiB_2–TiN (film)	3–6	18.6	0.3			49
TiB_2–TiN (bulk)	80–400	18.0 ± 1.8	0.3			49

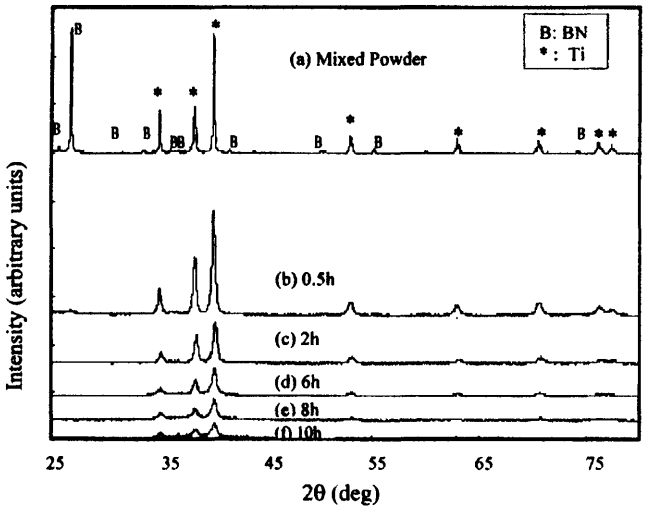

Fig. 1. XRD patterns of reactant powders milled for different times.

no evidence for product formation. The pattern shows only broadened Ti peaks. But when the milling time is increased to 12 h, new broad peaks appear which do not correspond directly to those of TiB_2 or TiN (Fig. 2, part (c)). With increased milling the intensity of the peaks shows a slight increase, and at 18 h, there is evidence of correspondence of the peaks with those of the product phases, TiN and TiB_2 (Fig. 2, part (e)). Longer milling time results in still broader peaks that are likely the result of overlapping small peaks of the two phases (Fig. 2, parts (f) and (g)).

The observed broadening of the Ti X-ray peaks with increasing milling time is the consequence of the reduction of the average crystallite size and the buildup of defects and internal strain. An interesting observation indicative of the effect of one or both of these phenomena is the self-ignition of milled powders when exposed to air. For the powder that is milled for 10 h, a spontaneous reaction occurs in air when the powders are touched while still warm from milling. The product of this spontaneous combustion contains TiN and TiB_2, as can be seen from Fig. 2, part (a).

The large surface area and increased lattice strain contribute to this enhanced reactivity. It should be noted that within the limit of X-ray detection, the product of the self-ignition contained no (crystalline) oxide phases as seen from the XRD pattern. The product contained TiN and TiB_2 only, as indicated above. The crystallite sizes of these phases were determined by the WH and HW methods to be 29.4 and 21.7 nm, and 43.5 and 25.0 nm, respectively. Although a reaction between oxygen or nitrogen and Ti or B is thermodynamically favored, the absence of detectable oxides may indicate that amorphous phases (oxides) have formed, or more likely, that O_2 and N_2 play a different role. The interaction between these gases and Ti may act only as a trigger for the reaction between the powders. It is likely that only a small amount of oxygen or nitrogen is required for this purpose. It has been reported that only 1 wt% of oxygen is needed to significantly change the eletrocatalytic properties of nanophase materials.[40] The absence of spontaneous reactions during milling is a confirmation of the presence of a relatively pure inert gas atmosphere.

Crystallite size analyses were made on milled products. Typical WH and HW plots for the Ti peaks are shown in Figs. 3(a) and (b), respectively. From such analyses we obtain the dependence of the Ti crystallite size on milling time by the two methods. The results are shown in Figs. 4 and 5. Figure 4 shows the refinement of the grain size and the increase in the strain as functions of milling time for Ti. The results in this figure are evaluated by both methods, as indicated. There is a relatively large difference between the crystallite size results and a relatively smaller difference between the strain results obtained by the two methods of analysis. The crystallite sizes obtained with the WH analysis are consistently larger. The surprisingly small grain size of the unmilled Ti powder (71–111 nm) may be related to the preparation method of this powder. The powder was made from sponge Ti. In the early stages of milling the strain value changed very little, but after about 2 h of milling, the strain increased markedly. Within the first 6 h of milling, the decrease in crystallite size for Ti was relatively linear with milling time. Figure 4 also shows that the minimum crystalline size of Ti that can be obtained before the onset of a reaction in the mill is in the range of 16.7–33.3 nm. As was pointed out above, when milling is conducted for 12 h or more, reaction between the powders occurs in the mill as shown in Fig. 2.

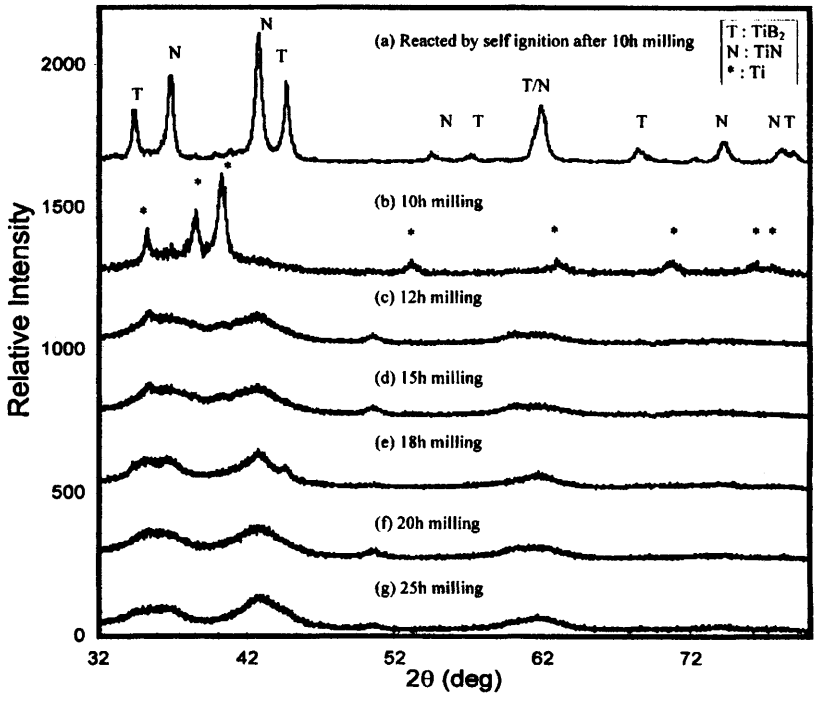

Fig. 2. XRD patterns of reactants milled for longer times and for a milled and self-ignited powder mixture.

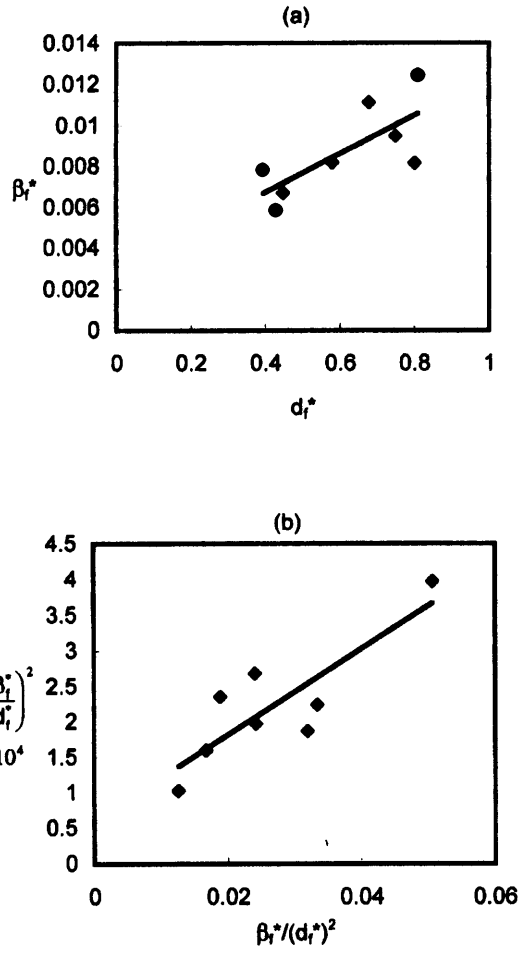

Fig. 3. Typical Williamson–Hall and Halder–Wagner plots for Ti milled for 10 h: (a) Williamson–Hall, (b) Halder–Wagner.

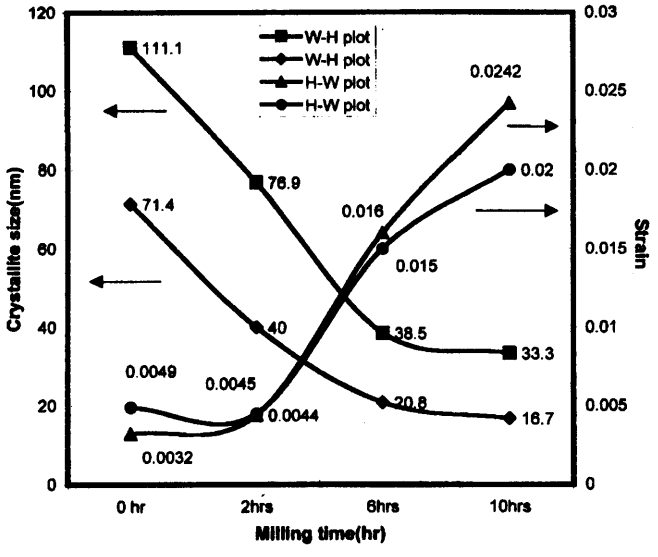

Fig. 4. Effect of milling time on crystallite size and strain for Ti.

Figure 5(a) shows the results of crystallite size analyses on milled powders (10 h) which were subsequently reacted in the SPS apparatus for 1 or 12 min, while Fig. 5(b) shows the results on powders which had reacted during a 12-h milling and subsequently reacted in the SPS for 5 or 12 min. After a 10-h milling time, the Ti crystallite size ranged from 16.7 to 33.3 nm, depending on the method of analysis. When powders milled for this time were subsequently reacted in the SPS for 1 min, the crystallite sizes of

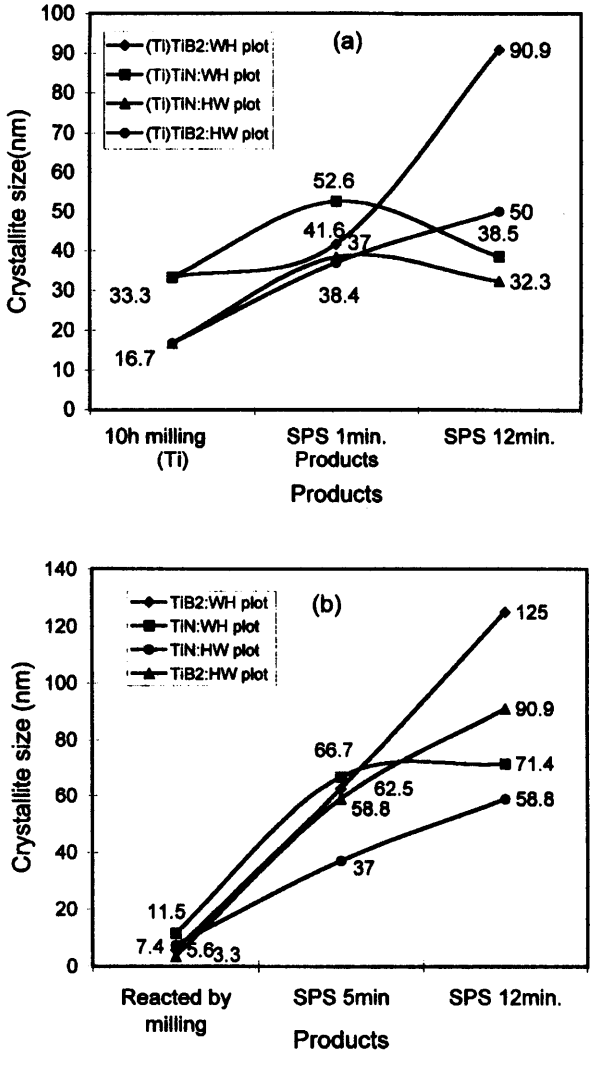

Fig. 5. Crystallite size of TiN and TiB_2 formed in the SPS: (a) reactant powders milled for 10 h (no product formation), (b) reactant powders milled for 12 h (with product formation).

the product phases, TiN and TiB_2, were 38.5–52.6 and 40.0–45.5 nm, respectively. When the reaction time in the SPS apparatus was increased to 12 min, the crystallite size of the product phases showed generally a corresponding increase, Fig. 5(a). The size ranges for TiN and TiB_2 are 47.6–62.5 and 31.2–58.8 nm, respectively. With a reaction time of 12 min, the crystallite size of TiB_2 expectedly increased but that of TiN decreased. This latter observation is not clearly understood, but may be the consequence of a partial decomposition of TiN. Generally, the crystallite sizes of the two ceramics in the product are equivalent. It should be noted that the reported crystallite sizes are subject to uncertainties associated with the analysis of the XRD results. The values are subject to estimated uncertainties of 10% to 20%.

In addition to the 10-h-milled powders, those milled for 12 h were also investigated in the SPS system. It should be recalled that after 12 h of milling a reaction takes place in the mill. Thus including this sample would provide the opportunity to investigate the effect of phase formation during milling on the subsequent reaction and densification in the SPS apparatus. The results are shown in Fig. 5(b) for samples held in the SPS apparatus for 5 and 12 min. Since the XRD patterns of the powders milled for 12 h did not directly correspond to the product phases, the results of those milled for 18 h are included in Fig. 5(b) for comparison. After a 5-min treatment in the SPS apparatus, the crystallite sizes of TiN and TiB_2 were 37.0–66.7 and 58.8–62.5 nm, respectively. Longer treatment (12 min) in the SPS of the powders milled for 12 h resulted in larger crystallite size with values for TiN and TiB_2 in

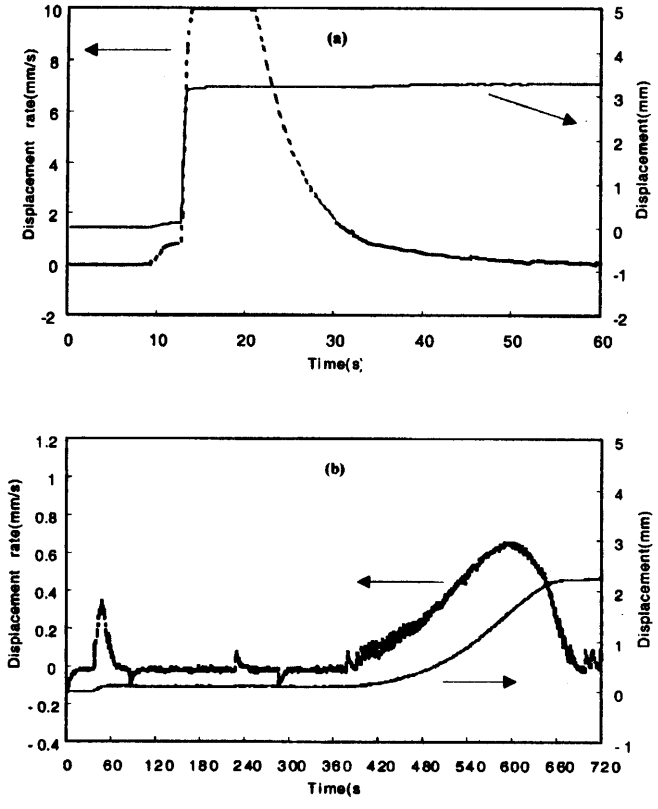

Fig. 6. Sample displacement and displacement rate during synthesis: (a) 10-h-milled reactant powders, (b) 12-h-milled reactant powders.

the ranges of 58.8–71.4 and 90.9–125.0 nm, respectively. It is interesting to note that the crystallite size of the product phases after 1 min of SPS treatment is roughly the same whether they are formed in the SPS or during milling before. However, when the treatment is longer (12 min), the size of those formed in the SPS is about one-half that of the size of those formed during milling.

Another indication of the difference between the milled-unreacted and milled-reacted samples is seen from the displacement (shrinkage) output during SPS treatment. As indicated in the Experimental Materials and Methods section, displacement occurs during the SPS process due to powder densification and due to molar volume changes resulting from the reaction. Figure 6 shows traces of the displacement (mm) and displacement rate ($mm \cdot s^{-1}$) during the SPS reaction of the 10-h- and 12-h-milled samples. All other conditions are the same. Previous experience showed that the onset of reactions in the SPS is accompanied by a sudden change (shrinkage) in the volume of the sample. The results of Fig. 6 show

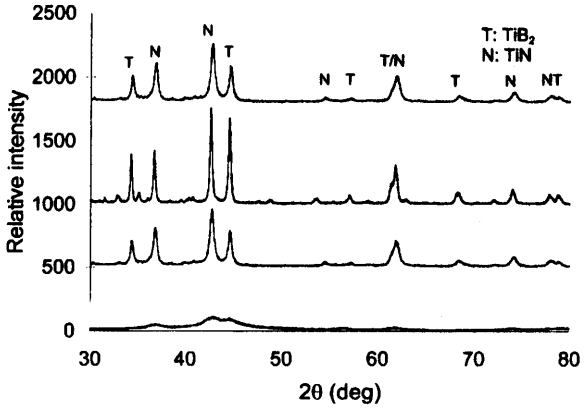

Fig. 7. XRD patterns for milled and self-ignited powders and SPS-reacted powders milled for different times.

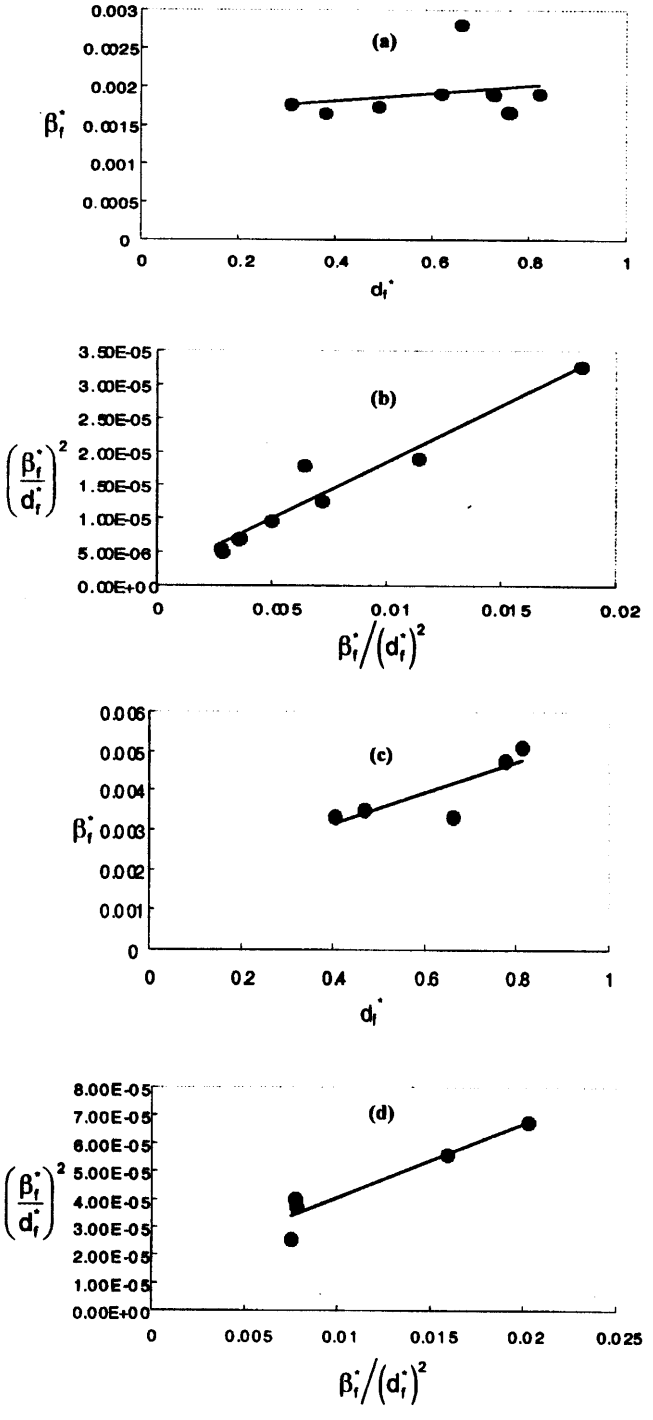

Fig. 8. Typical Williamson–Hall (WH) and Halder–Wagner (HW) plots of TiN–TiB_2 composites reacted for 5 min from powders milled for 12 h: (a) WH plot for TiB_2, (b) HW plot for TiB_2, (c) WH plot for TiN, and (d) HW plot for TiN.

that the unreacted (10-h-milled) sample experiences a sharp displacement after about 13 s of time in the SPS. In contrast, the reacted (12-h-milled) sample does not exhibit any sign of displacement until about 50 s. The displacement at this time is very small but a more significant, albeit gradual, displacement takes place at still a later time, starting at about 420 s and ending at about 660 s. The abrupt displacement for the 10-h-milled sample represents the formation reaction of the product phases, as had been confirmed by XRD in auxiliary experiments. Based on reaction (1), a molar volume change of 25.9% is anticipated, even if the starting powders are completely dense.

A comparison of the XRD patterns of samples which had self-ignited, SPS-reacted after 10- and 12-h milling, and reacted

during an 18-h milling are shown in Fig. 7. Peaks of TiB_2 and TiN are evident in the pattern of the self-ignited powder and in the SPS-reacted samples. The patterns for TiB_2 and TiN for the 10- and 12-h samples are consistent with the crystallite size evaluation. The latter show narrower peaks indicative of larger crystallite size. Typical WH and HW plots for the TiB_2 and TiN phases which were produced by reacting the 10-h-milled powders in the SPS for 1 min are shown in Figs. 8(a) through (d).

Electron microprobe (EPMA) images of SPS-synthesized samples are shown in Figs. 9(a) through (d). For the 10-h-milled sample, the backscattered electron image, Fig. 9(a), indicates a relatively uniform distribution of phases, while the corresponding image of the 12-h-milled sample, Fig. 9(c), suggests nonuniformity in phase distribution. It should be recalled that in the first case, the products were formed during the SPS treatment while in the second case they were formed (at least partially) during milling. From the X-ray dot maps for nitrogen for the 10- and 12-h-milled samples, Figs. 9(b) and (d), respectively, it can bee seen that the darker regions in the backscattered image of Fig. 9(c) are low in nitrogen and thus are likely to be the TiB_2 phase. X-ray dot maps of titanium were fairly similar for the 10- and 12-h samples.

Electron backscatter diffraction (EBSD) examinations were made on samples synthesized in this work. While this method can provide grain size information, it has a physical limitation of 200 nm and a more realistic lower limit of 500 nm.[54] It does, however, provide information on the distribution and orientation of the phases in the product. Figure 10 shows a distribution map for the two phases in a sample which was synthesized in the SPS (12 min) from powders milled for 10 h. The distribution of the TiN and TiB_2 phases appears to be relatively uniform in the product. However, there is an indication from normal and transverse maps that TiB_2 shows a tendency for preferred orientation, with the (0001) planes lying parallel to the sample surface. The TiN phase, on the other hand, shows a random orientation. The occurrence of preferred orientation is not well understood and its relation to the existence of the applied current is a matter of speculation at this point. Further work is needed to establish such a connection.

The relative density, the Vickers microhardness (at a force of ≈2 N), and the fracture toughness of selected TiN–TiB_2 nanocomposites are listed in Table II. The product of a 1-min SPS of the 10-h-milled but unreacted powders had a density of 90.1%. When the SPS treatment was extended for 12 min, the density of such a sample was 96.1%. The hardness and the fracture toughness show a corresponding increase from 14.8 to 20.6 GPa and from 3.32 to 6.50 $MPa{\cdot}m^{1/2}$, respectively. For samples which had been milled for 12 h (i.e., had reacted in the mill), the density values were 94.6% and 97.2% for SPS treatments of 5 and 12 min, respectively. The hardness and fracture toughness values for these are more consistent with those of the higher-density samples of the 10-h-milled samples. The literature hardness values listed in Table I were obtained at loads that are significantly different from the one used in this work (≈2 N). The hardness obtained on bulk TiB_2–TiN samples at a low force value (0.3 N) for composites with crystallite sizes in the range 80–400 nm is 18.0 GPa. The value obtained in this work for the highest-density samples (Table II) is about 20% higher than the corresponding literature value. It is interesting to note from Table I that the crystallite size seems to have no effect on the hardness value (last two rows). However, it is difficult to reach such a conclusion without making a systematic study in view of the possibility of an inverse Petch–Hall effect at very small crystallite sizes. No fracture toughness values were reported for samples with known crystallite size and thus a direct comparison with the present results is not possible. The values obtained in this work, for the densest samples, are comparable to those listed in Table I.

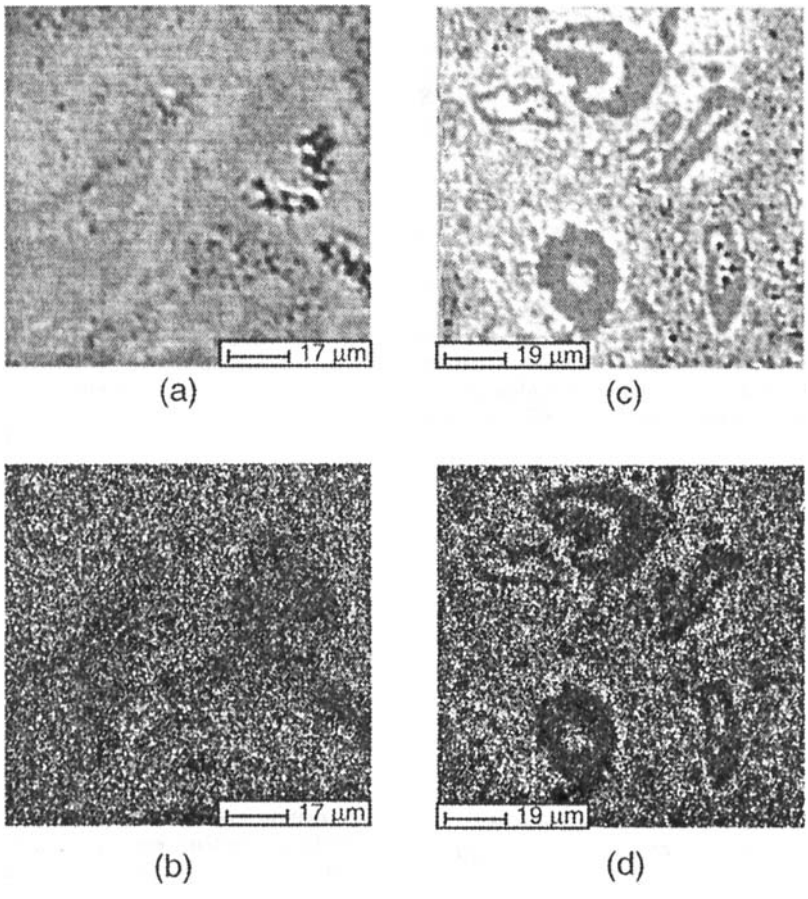

Fig. 9. Electron probe microanalysis (EPMA) images for synthesized TiN–TiB_2 composites: (a) backscattered electron (BSE) image of sample made from 10-h-milled powders, (b) X-ray dot map for N in sample of (a), (c) BSE image of sample made from 12-h-milled powders, and (d) X-ray dot map for N in sample (c).

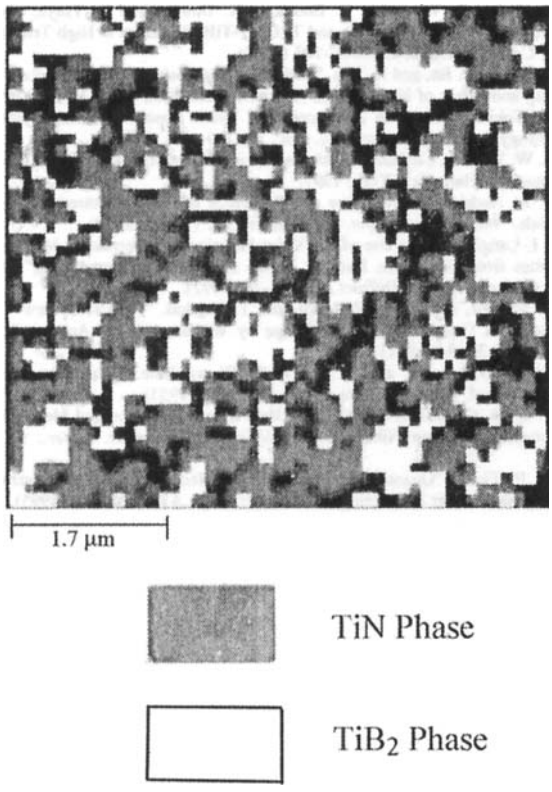

Fig. 10. Electron backscatter diffraction (EBSD) image of TiN–TiB_2 nanocomposite showing the distribution of the two phases.

Table II. Vickers Microhardness and Fracture Toughness Results on TiN–TiB_2 Nanocomposites

Milling time (h)	SPS time (min)	Relative density (%)	Microhardness (GPa)	Fracture toughness ($MPa \cdot m^{1/2}$)
10	1	90.1	14.8	3.32
10	12	96.1	20.6	6.50
12	5	94.6	18.9	3.48
12	12	97.2	21.8	5.13

IV. Conclusions

The synthesis of dense nanometric TiN–TiB_2 composites through mechanical and field activation was investigated. Powders of BN, B, and Ti were milled in a planetary ball-mill to produce nanocrystallites and then reacted under the influence of a pulsating high dc current. The reactants were simultaneously subjected to a uniaxial pressure that resulted in the formation of dense nanometric TiN–TiB_2 composites. XRD pattern analyses showed that dense composites (relative densities of 90% to 96%) can be made with crystallite sizes in the range 37–71 nm for TiN and 59–125 nm for TiB_2. The range of values depended on the method of analysis (Williamson–Hall or Halder–Wagner) and on the reaction conditions in the spark plasma sintering (SPS) apparatus used in this study. The hardness of the composites ranged from 14.8 to 21.8 GPa and the fracture toughness ranged from 3.32 to 6.50 $MPa \cdot m^{1/2}$.

Acknowledgment

We thank Ellen Carrillo-Heian for her help with the figures.

References

[1]R. Birringer, "Nanocrystalline Materials," *Mater. Sci. Eng.*, **A117**, 33–43 (1989).
[2]H. Gleiter, "Nanostructured Materials: Basic Concepts and Microstructure," *Acta Mater.*, **48**, 1–29 (2000).
[3]R. W. Siegel, "Nanostructured Materials—Mind over Matter," *Nanostruct. Mater.*, **4**, 121–38 (1994).
[4]C. C. Koch, "The Synthesis and Structure of Nanocrystalline Materials Produced by Mechanical Attrition: A Review," *Nanostruct. Mater.*, **2**, 109–29 (1993).
[5]A. Inoue, H. M. Kimura, K. Sasamori, and T. Matsumoto, "Ultrahigh Strength of Rapidly Solidified $Al_{95-x}Cr_3Ce_1Co_x$ (x = 1, 1.5, and 2%) Alloys Containing Icosahedral Phase as a Main Component," *Mater. Trans. Jpn. Inst. Met.*, **35**, 85–94 (1994).
[6]H. Hahn and K. A. Padmanabhan, "A Model for the Deformation of Nanocrystalline Materials," *Philos. Mag. B*, **76**, 559–71 (1997).
[7]R. W. Siegel and G. E. Fougere, "Mechanical Properties of Nanophase Materials," *Nanostruct. Mater.*, **6**, 205–16 (1995).
[8]S. Veprek, "Nanostructured Superhard Materials"; pp. 104–39 in *Handbook of Ceramic Hard Materials*. Edited by R. Riedel. Wiley-VCH, Weinheim, Germany, 2000.
[9]F. H. Froes, C. Suryanarayana, K. C. Russell, and C. M. Ward-Close, "Far from Equilibrium Processing of Light Metals"; pp. 1–21 in *Novel Techniques in Synthesis and Processing of Advanced Materials*. Edited by J. Singh and S. M. Copley. TMS, Warrendale, PA, 1994.
[10]L. Gao, H. Z. Wang, J. S. Hong, H. Miyamoto, K. Miyamoto, Y. Nishikawa, and S. D. Torre, "Mechanical Properties and Microstructure of Nano-SiC–Al_2O_3 Composites Densified by Spark Plasma Sintering," *J. Eur. Ceram. Soc.*, **19**, 609–13 (1999).
[11]B. Djuricic, S. Pickering, and D. McGarry, "Preparation and Properties of Alumina–Baria Nano-Composites," *J. Mater. Sci.*, **34**, 2685–94 (1999).
[12]P. Sajgalik, M. Hnatko, F. Lofaj, P. Hvizdos, J. Dusza, P. Warbichler, F. Hofer, R. Riedel, E. Lecomte, and M. J. Hoffmann, "SiC/Si_3N_4 Nano/Micro-Composites-Processing, RT and HT Mechanical Properties," *J. Eur. Ceram. Soc.*, **20**, 453–62 (2000).
[13]M. Cauchetier, X. Armand, N. Herlin, M. Mayne, S. Fusil, and E. Lefevre, "Si/C/N Nanocomposite Powders with Al (and Y) Additives Obtained by Laser Spray Pyrolysis of Organometallic Compounds," *J. Mater. Sci.*, **34**, 5257–64 (1999).
[14]R. W. Siegel, "Nanophase Materials Assembled from Atom Clusters," *Mater. Sci. Eng.*, **B19**, 37–43 (1993).
[15]J. Kano, H. Mio, and F. Saito, "Correlation of Size Reduction Rate of Inorganic Materials with Impact Energy of Balls in Planetary Ball Milling," *J. Chem. Eng. Jpn.*, **32**, 445–48 (1999).
[16]M. P. Dallimore and P. G. McCormick, "Dynamics of Planetary Ball Milling—A Comparison of Computer Simulated Processing Parameters with CuO/Ni Displacement Reaction Milling Kinetics," *Mater. Trans. Jpn. Inst. Met.*, **37**, 1091–98 (1996).
[17]E. Gaffet, "Planetary Ball-Milling—An Experimental Parameter Phase Diagram," *Mater. Sci. Eng. A*, **132**, 181–93 (1991).
[18]T. R. Malow and C. C. Koch, "Mechanical Properties, Ductility, and Grain Size of Nanocrystalline Iron Produced by Mechanical Attrition," *Metall. Mater. Trans. A*, **29A**, 2285–95 (1998).
[19]K. Takatori, T. Tani, N. Watanabe, and N. Kamiya, "Preparation and Characterization of Nano-Structured Ceramic Powders Synthesized by Emulsion Combustion Methods," *J. Nanoparticle Res.*, **1**, 197–204 (1999).
[20]V. P. Godbole, K. Dovidenko, A. K. Sharma, and J. Narayan, "Thermal Reactions and Microstructure of TiN–AlN Layered Nano-Composites," *Mater. Sci. Eng.*, **B68**, 85–90 (1999).
[21]C. E. Borsa, H. S. Ferreira, and R. H. Kiminami, "Liquid Phase Sintering of Al_2O_3/SiC Nanocomposites," *J. Eur. Ceram. Soc.*, **19**, 615–21 (1999).
[22]D. S. Cheong, K. T. Hwang, and C. S. Kim, "Fabrication, Mechanical Properties and Microstructure Analysis of Si_3N_4/SiC Nanocomposites," *Composites (Part A)*, **30**, 425–27 (1999).
[23]J. M. Wu and Z. Z. Li, "Nanostructured Composite Obtained by Mechanically Driven Reduction Reaction of CuO and Al Powder Mixture," *J. Alloy Compd.*, **299**, 9–16 (2000).
[24]L. Gao, H. Z. Wang, J. S. Hong, H. Miyamoto, K. Miyamoto, Y. Nishikawa, and S. D. Torre, "SiC–ZrO_2(3Y)–Al_2O_3 Nanocomposites Superfast Densified by Spark Plasma Sintering," *Nanostruct. Mater.*, **11**, 43–49 (1999).
[25]Z. A. Munir, I. J. Shon, and K. Yamazaki, "Simultaneous Synthesis and Densification by Field-Activated Combustion," U.S. Pat. No. 5 794 113, August 11, 1998. .
[26]I. J. Shon, Z. A. Munir, K. Yamazaki, and K. Shoda, "Simultaneous Synthesis and Densification of $MoSi_2$ by Field Activated Combustion," *J. Am. Ceram. Soc.*, **79**, 1875–80 (1996).
[27]Z. A. Munir, F. Charlot, F. Bernard, and E. Gaffet, "One-Step Synthesis and Consolidation of Nanophase Materials," U.S. Patent Application Serial No. 09/374,049; August 13, 1999.
[28]V. Gauthier, J. P. Larpin, and Z. A., Munir; unpublished results.
[29]C. Mroz, "Titanium Diboride," *Am. Ceram. Soc. Bull.*, **74**, 158–59 (1995).
[30]V. J. Tennery, C. B. Finch, C. S. Yust, and G. W. Clark, "Structure–Property Correlations for TiB_2-Based Ceramics Densified Using Active Liquid Metals"; pp. 891–909 in *Science of Hard Materials*. Edited by R. K. Viswanadham. Plenum Press, New York, 1983.
[31]M. K. Ferber, P. F. Becher, and C. B. Finch, "Effect of Microstructure of TiB_2 Ceramics," *J. Am. Ceram. Soc.*, **66**, C-2–C-3 (1983).
[32]C. Martin, B. Cales, P. Viver, and P. Mathieu, "Electrical Discharge Machinable Ceramics Composites," *Mater. Sci. Eng.*, **A109**, 351–56 (1989).
[33]C. E. Ransley, "An Instrument for Measuring the Gas Content of Aluminum Alloys during Melting and Casting," *J. Inst. Met.*, **86**, 212–19 (1957–1958).
[34]C. B. Finch, P. F. Becher, P. Angelini, S. Baik, C. E. Bamberger, and J. Brynestad, "Effect of Impurities on the Densification of Submicronmeter Titanium Diboride Powder," *Adv. Ceram. Mater.*, **1**, 50–54 (1986).

[35]S. Torizuka, J. Harada, H. Yamamoto, H. Nishiro, A. Chino, and Y. Ishibashi, "Effects of SiC Addition on the Mechanical Properties and Sinterability of TiB_2–(2 mol% Y_2O_3–ZrO_2) Composite," *J. Ceram. Soc. Jpn.*, **100**, 691–96 (1992).

[36]Y. Miyamoto, M. Koizumi, and O. Yamada, "High-Pressure Self-Combustion Sintering for Ceramics," *J. Am. Ceram. Soc.*, **67**, C-224–C-225 (1984).

[37]D. A. Hoke, M. A. Meyers, and G. T. Gray, "Reaction Synthesis/Dynamic Compaction of Titanium Diboride," *Metall. Trans. A*, **23A**, 77–86 (1992).

[38]C. K. Narula, *Ceramic Precursor Technology and Its Applications*; Ch. 5, pp. 119–49. Marcel Dekker, New York, 1995.

[39]J. K. Park and S. T. Park, "Densification of TiN–Ni Cermets by Improving Wettability of Liquid Nickel on TiN Grain Surface with Addition of Mo_2C," *Int. J. Refract. Met. Hard Mater.*, **17**, 295–98 (1999).

[40]G. M. Chow and N. I. Noskova (Eds.), *Nanostructured Materials*; pp. 47–70. Kluwer Academic Publishers, Dordrecht, Netherlands, 1998.

[41]D. A. Hoke, D. K. Kim, J. C. Lasalvia, and M. A. Meyer, "Combustion Synthesis/Dynamic Densification of TiB_2–TiC Composites," *J. Am. Ceram. Soc.*, **79**, 177–82 (1996).

[42]M. Eslamoo-Grami and Z. A. Munir, "Effect of Nitrogen Pressure and Diluent Content on the Combustion Synthesis of Titanium Nitride," *J. Am. Ceram. Soc.*, **73**, 2222–27 (1990).

[43]M. Eslamoo-Grami and Z. A. Munir, "Effect of Porosity on the Combustion Synthesis of Titanium Nitride," *J. Am. Ceram. Soc.*, **73**, 1235–39 (1990).

[44]K. Shobu and T. Watanabe, "Hot Pressing of TiN–TiB_2 System," *J. Powder Metall. Soc. Jpn.*, **32**, 215–18 (1985).

[45]K. Shobu, T. Watanabe, Y. Enomoto, K. Umeda, and Y. Tsuya, "Frictional Properties of Sintered TiN–TiB_2 and Ti(C,N)–TiB_2 Ceramics at High Temperature," *J. Am. Ceram. Soc.*, **70**, C-103–C-104 (1987).

[46]G. Zhang, Z. Jin, and X. Yue, "TiN–TiB_2 Composites Prepared by Reactive Hot Pressing and Effect of Ni Addition," *J. Am. Ceram. Soc.*, **78**, 2831–33 (1995).

[47]M. Tokita, "Trends in Advanced SPS Spark Plasma Sintering Systems and Technology," *J. Soc. Powder Tech. Jpn.*, **39**, 790–804 (1993).

[48]A. W. Weimer, *Carbide, Nitride and Boride Materials Synthesis and Processing*. Chapman and Hall, New York, 1997.

[49]R. A. Andrievski, "Structure and Properties of Nanostructured Boride/Nitride Materials," *Int. J. Refract. Met. Hard Mater.*, **17**, 153–55 (1999).

[50]J. I. Langford, "The Use of the Voigt Function in Determining Microstructural Properties from Diffraction Data by Means of Pattern Decomposition," *Proc. Int. Conf. Accuracy Powder Diffract.*, **2**, 110–26 (1992).

[51]H. Mändar, J. Felsche, V. Mikli, and T. Vajakas, "AXES1.9: New Tools for Estimation of Crystallite Size and Shape by Williamson–Hall Analysis," *J. Appl. Crystallogr.*, **32**, 345–50 (1999).

[52]G. K. Williamson and W. H. Hall, "X-ray Line Broadening from Filed Aluminium and Wolfram," *Acta Metall.*, **1**, 22–31 (1953).

[53]Y. J. Du, F. Q. Guo, and K. Lu, "Grain Size Distribution and Morphologies of Nanocrystalline Boron Nitride During Milling," *Nanostruct. Mater.*, **5**, 579–89 (1996).

[54]D. P. Field, "Quantification of Partially Recrystallized Polycrystals Using Electron Backscatter Diffraction," *Mater. Sci. Eng.*, **A190**, 241–46 (1995). □

journal

J. Am. Ceram. Soc., 84 [8] 1683–88 (2001)

Nanofiber Formation in the Fabrication of Carbon/Silicon Carbide Ceramic Matrix Nanocomposites by Slurry Impregnation and Pulse Chemical Vapor Infiltration

Nyan-Hwa Tai and Che-Fu Chen

Department of Materials Science and Engineering, National Tsing-Hua University, Hsin-Chu, Taiwan, 30013

The objectives of this work were to investigate the fabrication of carbon-fiber-reinforced SiC ceramic nanocomposites using the slurry impregnation process and the pulse chemical vapor infiltration (PCVI) process and to study the influences of processing parameters of the PCVI process on the microstructure variation of the nanocomposites. In this work, SiC nanosized powder was added to the matrix precursor (silicon powder mixed with phenolic resin), followed by the impregnation of the slurry into the preform. In the PCVI process, to densify the nanocomposites, tetramethylsilane (TMS) vapor mixed with hydrogen was used as the vapor precursor for matrix deposition. Fabrication parameters, such as reactant concentrations, pulse number, and holding time, were studied. Morphologies obtained from various processes were compared.

I. Introduction

FIBER-REINFORCED ceramic-matrix composites (CMCs) are becoming technologically important because of the introduction of reinforcing fibers to the matrix. Depending on the reinforcement, the fabrication method, the form of reinforcement, and the interfacial strength, various failure modes have been observed and several reinforcing mechanisms have been proposed.[1–5] These mechanisms can occur individually or in combination.

The processing of CMCs can be classified in two categories: conventional powder routes and novel techniques. In the powder routes, the processing of monolithic ceramics has been adopted by adding the reinforcements into the ceramic powder, followed by hot pressing and sintering, which are similar to the traditional ceramic processing.[6,7] In the novel techniques, chemical vapor infiltration, reaction bonding, sol–gel processing, polymer pyrolysis, Lanxide™ processing, and self-propagating high-temperature synthesis have been used.[8–12] Most of the processes of the novel techniques can be performed at relatively low temperatures; thus, fiber damage is alleviated and interfacial properties can be well controlled.

In the isothermal chemical vapor infiltration (ICVI) process for ceramic composites, the vapors penetrate into a low-density fibrous preform, deposit the solid product on the surface of the fibers, and thereby form the matrix of the composites.[13–15] Shrinkage is very limited in this case; therefore, a near-net-shape product can be obtained. The advantages of the ICVI process are that a preform with large dimensions and arbitrary shape can be fabricated, and multiple specimens can be treated in one process. The disadvantages of the ICVI process involve thickness limitations and long processing periods. To decrease processing periods, forced-flow temperature-gradient chemical vapor infiltration (FCVI) has been proposed.[16,17] The primary advantage of the FCVI process is that the processing period can be decreased from about one month to one day. However, only one specimen can be fabricated in a process.

To address the disadvantages of the ICVI and the FCVI processes, pulse chemical vapor infiltration (PCVI) has been developed. In the PCVI process, the reactant vapors are channeled into the chamber; after a short reaction period, the reacted vapor and remaining reactant are evacuated. Because of periodic filling and evacuation, the reactants within the preform are refreshed. As a result, the gradient of vapor concentration within the preform can be decreased, which produces ceramic composites with a low matrix gradient distribution.[18–20]

By introducing nanopowders into the ceramic material, plastic deformation of the ceramic system is observed at elevated temperature.[21–23] The deformation can extend up to 10 times its original length. The role of nanopowders in the system remains vague. In general, it is believed that grain-boundary sliding dominates the plastic deformation. Although many papers discussing the effects of nanopowders on ceramic behavior have been published, the information concerning the influences of nanopowders on property variations of continuous-fiber-reinforced ceramic composites remains very limited. A two-step process has been used to fabricate ceramic nanocomposites in this study. In the first step, a slurry combining SiC nanopowder and phenolic resin is impregnated into the fibrous perform, then a heat treatment at elevated temperature is performed. In the second step, the PCVI process is used to further densify the composites. In this paper, the pyrolysis reactions at various precursor concentrations, pulsed cycles, and holding periods are studied. Furthermore, the physical properties and the microstructure of the nanocomposites fabricated under various processing conditions are investigated.

II. Experimental Procedure

Silicon powder (99.0%, Aldrich Chemical Co., Milwaukee, WI) and SiC nanopowder (20 nm, MTI Corp., Richmond, CA) were added to a mixture of polythyleneimine (PEI; 99%, Alfa Aesar Johnson Matthey, Ward Hill, MA) and isopropyl alcohol (IPA; 99%, Tedia, Fairfield, OH), which was used as a dispersant. Eight layers of carbon-fiber cloths (W3121, 8 harness satin, Toho Rayon Co., Ltd, Mishima, Japan) impregnated with slurry were stacked in a mold. Warn pressing and stabilization were performed at 170° and 230°C, respectively, both under a pressure of 13.78 MPa. Carbonization at 1100°C in a tube furnace (Model 55342–4, Linberg, Watertown, WI) was used to evolve the non-carbon species. A SiC matrix was formed during the heat treatment at 1450°C in a graphitization furnace (Model Astro, Thermal Technology, Inc., Santa Rosa, CA) for 3 h.

R. W. Rice—contributing editor

Manuscript No. 188245. Received September 22, 2000; approved April 13, 2001.

Supported by the National Science Council, Taiwan, under Grant No. NSC-89-2216-E-007-031.

To increase the density of the composites, the specimens were subjected to slurry impregnation and heat treatment at 1450°C three times; further densification using the PCVI process was performed. In the PCVI process, the vapor-phase precursor (tetramethylsilane, TMS; 99.9%, Acros Organics, Pittsburgh, PA) was mixed with a carrier gas (hydrogen) before it was used. Forced flow instead of diffusion dominated the supply of the reactant during the deposition process. The matrix deposition in the PCVI process was affected primarily by the reactor temperature, reactor pressure, precursor concentration, pulse number, and holding time. In this work, a reaction temperature of 1100°C and a working pressure of 2.5 torr (330 Pa) (holding pressure) were selected. Figure 1 schematically depicts the setup of this study.

Density and porosity measurements according to ASTM D792 and ASTM C20 standards,† respectively, were performed. Field emission gun scanning electron microscopy (FEGSEM; Model JSM-6330F, JEOL, Tokyo, Japan) was used for the examination of microstructure on the surface and interior of the composites. Energy-dispersive X-ray spectrometry (EDS) was used for element analysis. X-ray diffractometry (XRD; Model D-Max IIB, Rigaku, Tokyo, Japan) was used for phase identification. Carbon and silicon contents in the fabricated nanometer or submicrometer fibers were calculated using the following equation:

$$\frac{C_c}{C_{Si}} = K_c \frac{I_C}{I_{Si}} \quad (1)$$

where C and I are the content of the element and integrated intensity of the EDS peak, respectively, and the subscripts C and Si represent carbon and silicon, respectively. K_c is the proportional constant.

III. Results and Discussion

(1) SiC Formation after Pyrolysis

Figure 2 shows XRD patterns of the SiC nanopowder, SiC standard powder, and as-fabricated specimens treated under various conditions. After the specimens were carbonized at 1100°C, the primary peak of the XRD pattern was the Si (111) phase, as shown in the curve of Fig. 2(a); the weak peak at 35.6° indicates the SiC (111) phase that results from the SiC nanopowder additive. When the fabricated composite was treated at 1450°C for 1 h, a stronger peak of SiC (111), as shown by the curve in Fig. 2(b), can be detected; however, Si (111) is also observed. Coexistance of SiC and silicon implies formation of SiC and residue silicon. When the reaction period was extended to 3 h, the silicon peak disappeared, which indicated that virtually all of the silicon was converted to SiC.

(2) Effects of Multiple Impregnations

Figure 3 shows the variations of density and open porosity after carbonization at 1100°C and reaction sintering at 1450°C. As expected, porosity increases when reaction sintering is applied; the porosity increase is due to the removal of non-carbon elements and the rearrangement of graphene layers within the carbonized matrix. However, the open porosity is decreased after subsequent resin impregnations.

Composition and microstructure of the fabricated composite at various depths were examined. Figure 4 shows XRD patterns of the composites at various depths. Silicon can be detected in the interlaminar region between layers 1 and 2 (named sublayer 1); however, no peak can be detected in the next interlaminar region (named sublayer 2). The nonreacted silicon has a volume change from liquid phase to solid phase during the cooling process; thus, internal thermal stresses are generated, which result in the degradation of the composite after multiple impregnations.

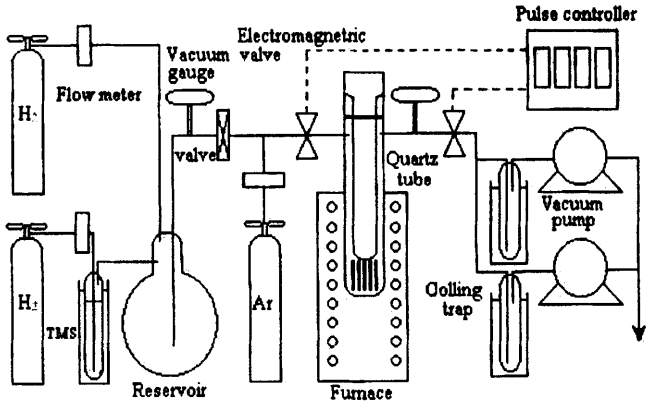

Fig. 1. Schematic of setup for the PCVI process.

(3) Formation of Submicrometer Fibers and Nanofibers

In this study, effects of three primary processing parameters i.e., holding time, reactant concentration, and pulse number, on the formation of nanofibers were investigated. Holding periods of 2, 3, and 4 s; reactant concentrations of 3, 5, and 7 vol%; and pulse number of 1000, 3000, and 5000 cycles were adopted. The denomination of mSnC/K denotes the specimen was fabricated for **m** Seconds at the condition of **n**% reactant Concentration under pulse number of $I \times 1000$ (**K**) cycles.

When examining the surface of fabricated specimens (specimen 3S5C5K), submicrometer fiber growths, as depicted in Fig. 5, across the concave surface to form a three-dimensional network structure, were detected. The diameter of submicrometer fiber is equivalent to that of the spherical juts on the concave surface, (as shown in points a and b in Fig. 5). The spherical juts are the aggregation of SiC nanopowders covered with deposited SiC. This can be verified by inspecting the surface of the specimen without PCVI deposition.

Submicrometer fibers are detected on the surface and within the specimen. On the delamination surface of the second layer of the 4S5C5K specimen, many nanofibers are observed; the diameter of the fibers decreases to <100 nm, as shown in Fig. 6. In general, the diameter of a nanofiber decreases with depth. This is reasonable, because the growth of nanofibers depends on the concentration of the reactant; the higher the concentration,

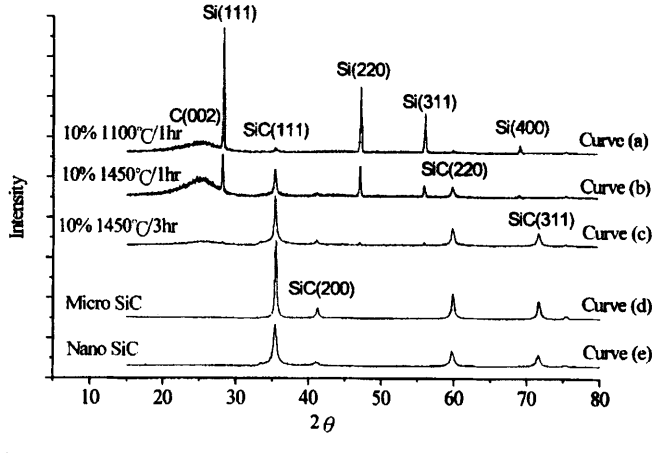

Fig. 2. XRD pattern of SiC nanopowder, SiC standard micropowder, and as-fabricated specimens treated under various conditions.

†"Standard Test Methods for Density and Specific Gravity (Relative Density) of Plastics by Displacement," ASTM Designation D792-00, and "Standard Test Methods for Apparent Porosity, Water Absorption, Apparent Specific Gravity, and Bulk Density of Burned Refractory Brick and Shapes by Boiling Water," ASTM Designation C20-00. American Society For Testing And Materials, West Conshohocken, PA.

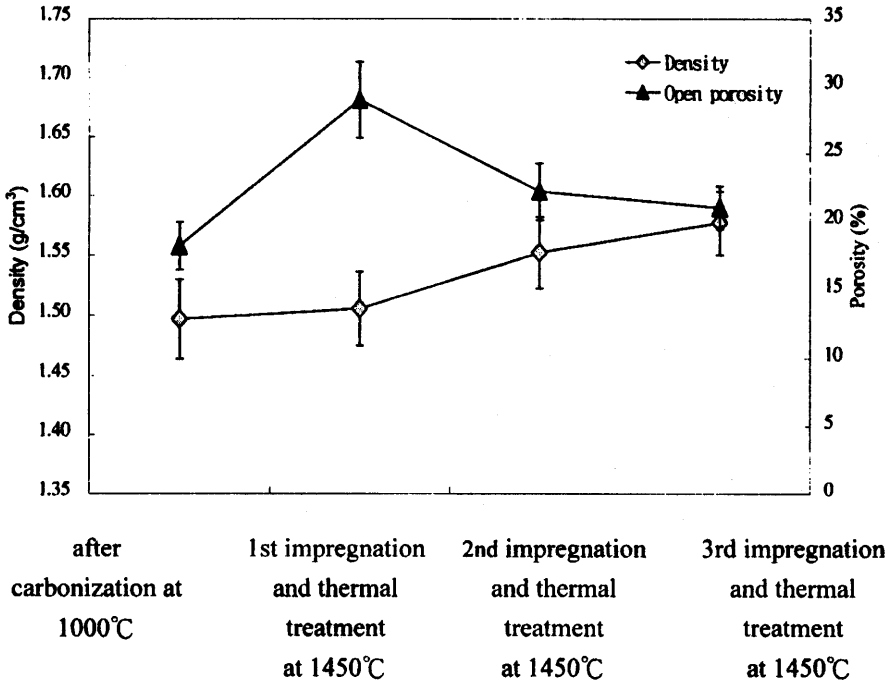

Fig. 3. Density and open porosity variations after multiple impregnation.

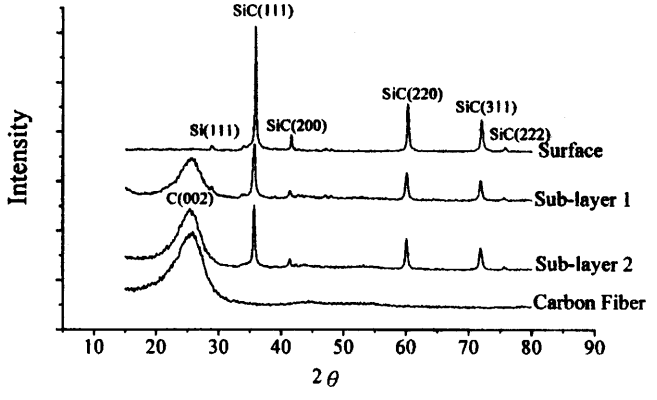

Fig. 4. XRD pattern of the carbon fiber and as-fabricated specimens at various depths.

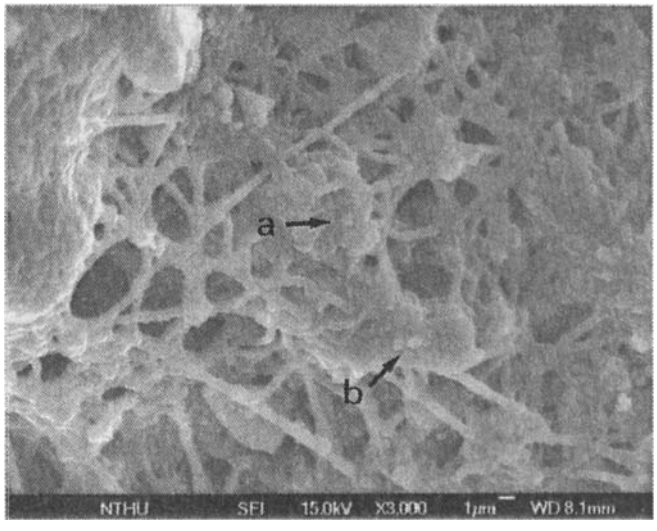

Fig. 5. Submicrometer fiber growth on the surface of the 3S5C5K specimen.

the higher the growth rate. This result is reasonable according to the Arrhenius equation, which states the deposition rate is proportional to the reactant concentration. Although decreasing the reactant concentration within the preform for obtaining a uniformly deposited matrix is one of the primary objectives of the PCVI process, the variation of nanofiber diameter at the various depths within specimen indicates that a concentration gradient remains inevitable in this study. Moreover, nodes are found in the fiber, where a sharp change in growth direction occurs.

Regarding the effect of pulse number on the formation of fibers, it seems reasonable to conclude that the number of formed fibers is proportional to pulse number; however, the answer is not so straightforward. Figures 7(a) and (b) show the fibers (or threads) on the surface of specimens 2S3C1K and 2S3C3K, respectively. The pulse numbers of the PCVI process for forming the 2S3C3K specimen is 3 times that of the 2S3C1K specimen. However, in some local area, the number of fibers (or threads) in the 2S3C1K specimen is much greater than that in the 2S3C3K specimen. This difference indicates that pulse number may not be a primary factor in the formation and growth of nanofibers. This observation seems contradictory to our knowledge; thus, it must be the case that some processing factors (such as reactant flow pattern and local surface condition) that may affect the fiber formation and growth have not been considered in this study. Moreover, it is obvious that the growth of nanofibers is heterogeneous and anisotropic; the growth rate in the axial direction is much higher than in the radial directions. This is the reason why fibers rather than rods appear in the specimen.

The nanofibers are most frequently observed in the concave surface, where high curvatures are presented. It is inferred from these observations that nucleation sites must exist in that region for nanofiber growth. Moreover, no significant deposition layer can be detected on the surface, whereas the growth of nanofibers can extend to >10 μm. The heterogeneous growth of the nanofiber makes it feasible that a catalyst reaction may occur at the tip of the fiber, which results in a rapid growth rate.

The effects of holding time on nanofiber growth were also investigated. It seems that holding time is not a critical parameter for nanofiber formation and growth. Figures 8(a) and

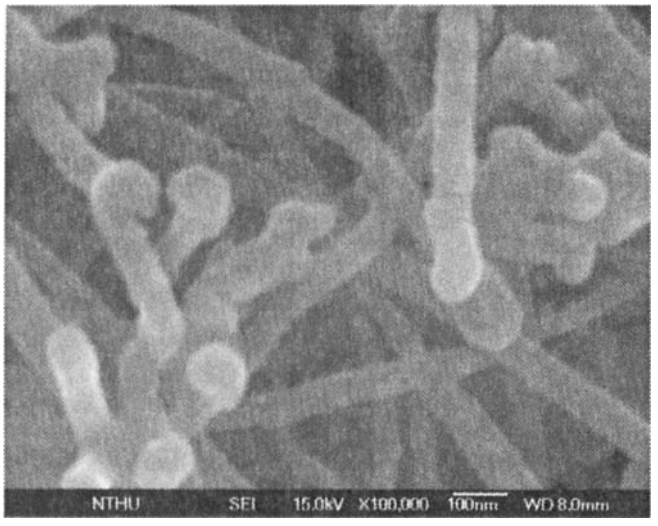

Fig. 6. Morphology on the interlaminar fracture surface of specimen 4S5C5K, diameter of the fibers are <100 nm.

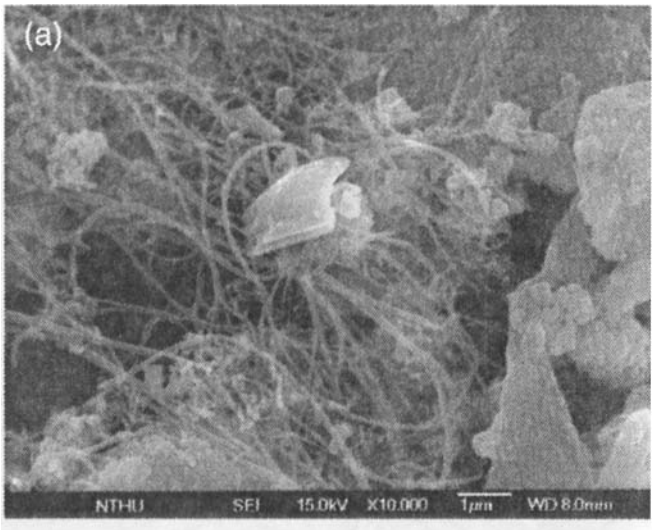

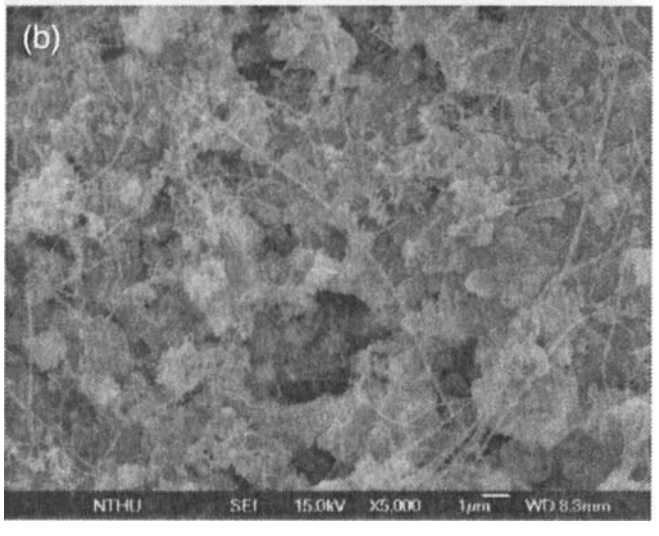

Fig. 7. Effect of pulse number on nanofiber growth on the surface of the composites: (a) specimen 2S3C1K and (b) specimen 2S3C3K,

(b) present the surface morphologies of the specimens 2S7C5K and 4S7C5K, respectively. The diameter of the fiber in specimen 4S7C5K is larger than that of the specimen 2S7C5K,

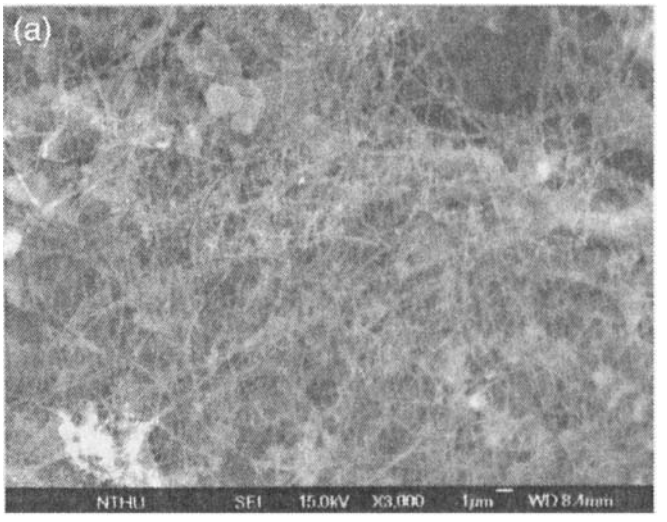

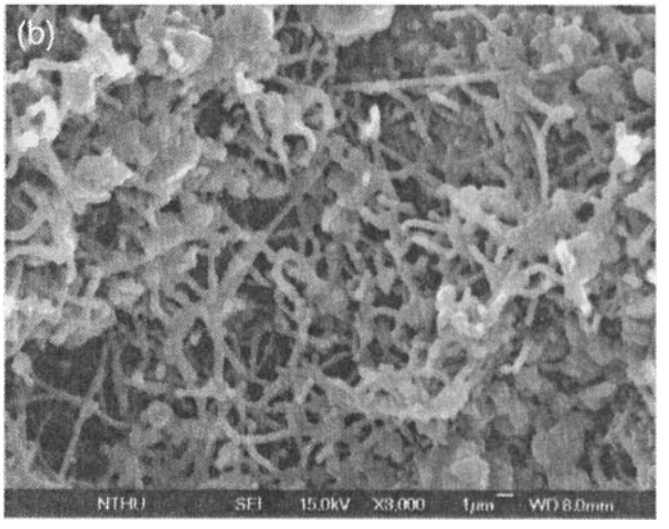

Fig. 8. Effect of holding time on nanofiber growth on the surface of the composites: (a) specimen 2S7C5K and (b) specimen 4S7C5K.

whereas there are more fibers in specimen 2S7C5K than in specimen 4S7C5K. These observations imply that, at relatively high reactant concentration, a longer holding period increases the growth of the fiber in the radial direction; however, there is no contribution to the formation of nanofibers under this condition. Moreover, it is feasible that the number of fibers is determined by other parameters, for example, nucleation sites, which are not investigated in this study. On the other hand, at relatively low reactant concentration, the difference in diameter of the nanofiber in the interior of the composites fabricated under such low concentration is not obvious. During the vacuum period, vapor is not completely evacuated, and some residual reactant remains within the composite. As a result, the exchange efficiency of the reactant vapor and the product gas is relatively low, which induces similar diameter growth in these two composites. Thus, pore network and structure skeleton affect the permeability of the specimen and influence the nanofiber growth within the composites.

PCVI is not the only process for growing nanofiber structure. When the ICVI process was adopted to densify the carbon/SiC nanocomposites for 12 h under the concentration of 7 vol%, submicrometer thread and short fiber, as shown in Fig. 9, were detected on the surface; however, less-straight fibers were observed. The fabrication parameters in the ICVI process were similar to that adopted for 4S7C5K specimen. The major difference between these two processes is that the reactants

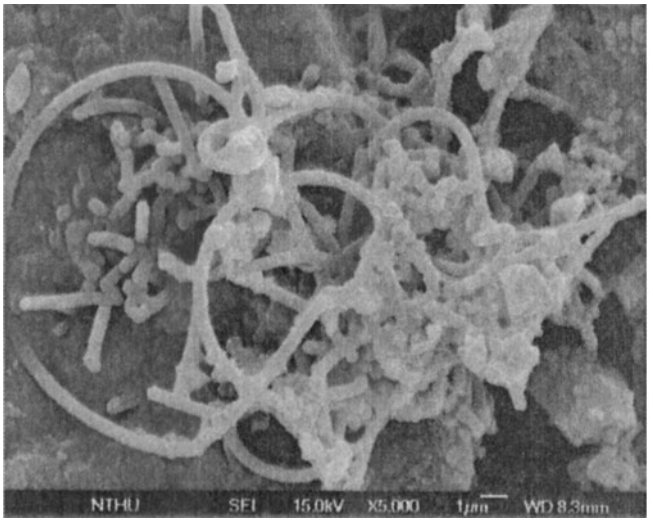

Fig. 9. Submicrometer thread and short fiber on the surface of the specimen fabricated during the ICVI process.

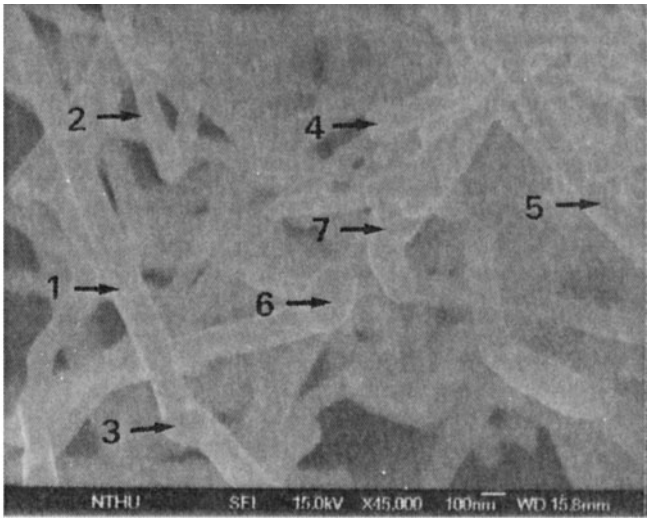

Fig. 10. Positions correspond to the element composition listed in Table I (interlaminar layer of specimen 4S5C5K).

reach the substrate through diffusion in the ICVI process, whereas it is by the assistance of forced convection in the PCVI process. Vacuum and refill steps during the PCVI process refreshes the reactant and stirs the reactants, which may be one of the significant parameters to promote the growth of nanofibers.

(4) Composition Analysis of Nanofibers

The composition of nanofibers was examined using EDX. The amount of contents were correlated using Eq. (1). The contents of the SiC standard, as-received SiC nanopowder, semifabricated specimen (heat treatment at <1450°C), and final-fabricated specimen (after PCVI densification) are listed in Table I. The compositions of the SiC nanopowder and the semifabricated specimen are near stoichiometric SiC; however, on the nanofiber, compositions of the growth deviate from the SiC stoichiometry. Furthermore, the composition is also dependent on the position of the nanofiber. At the tip, in the node, and on the base of the nanofiber, the deviation of the composition from stoichiometry is more significant than that in the straight middle region. The positions corresponding to the composition listed in Table I are shown in Fig. 10. Carbon-rich composition is detected at the tip, in the node, and on the base of the nanofiber. This is attributed to the deposited solid products containing extra carbon, and the carbon-rich composition may be helpful to the formation of the nanofiber.

Table I. Composition of As-Received SiC, Semifabricated Specimen, and Final Fabricated Specimen

Specimen	EDS integrated intensity (%)		Calculated contents (%)	
	Carbon	Silicon	Carbon	Silicon
MAC-3215 SiC standard	3.14†	96.86†	50.0	50.0
SiC nanopowder	3.18	96.82	50.30	49.70
Reaction-sintered Figure 10	3.12	96.88	49.80	50.20
Mark 1	10.00	90.00	77.40	22.60
Mark 2	16.80	83.20	86.20	13.80
Mark 3	23.50	76.50	90.40	9.60
Mark 4	22.20	31.20	90.60	9.40
Mark 5	18.50	81.50	89.70	10.30
Mark 6	38.10	61.90	95.00	5.00
Mark 7	26.20	73.80	91.60	8.40

†±0.53%.

IV. Conclusions

This work demonstrates the fabrication of ceramic nanocomposite using the slurry impregnation and the pulse chemical vapor infiltration (PCVI) methods. Generally, the product of pulse number and holding time can be used as a reference for density and porosity variation; the higher the product, the greater decrease of porosity and increase of density.

Nanometer and submicrometer fibers are detected on the specimen surface and within the nanocomposite. The diameters of the fibers depend on how deep they are located; the greater the depth from the surface, the finer the diameter of the fiber. Reactant concentration is the most important factor for nanofiber growth, whereas pulse number and holding period are less significant. Nucleation sites generated by the addition of SiC nanopowder may be the most critical factor for the formation of nanometer and submicrometer fibers. The structure skeleton may be one of the parameters to affect nanofiber growth. Composition of the nanofiber deviates from stoichiometric SiC depending on its location. Furthermore, carbon-rich composition is detected at the tip, in the node, and on the base of the nanofiber.

Acknowledgments

The authors thank Professor C. Y. Lee for valuable comments on this work and Miss W. H. Wong for assistance in the preparation of this article.

References

[1]K. K. Chawla, *Ceramic Matrix Composites*; Ch. 9. Chapman and Hall, London, U.K., 1993.
[2]R. W. Rice, "Ceramic-Matrix Composites Toughening Mechanisms: An Update," *Ceram. Eng. Sci. Proc.*, **6**, 589 (1985).
[3]D. B. Mardhall, B. N. Cox, and A. G. Evans, "The Mechanisms of Matrix Cracking in Brittle-Matrix Fiber Composites," *Acta Met.*, **33** [11] 2013 (1985).
[4]D. B. Marshall and J. E. Ritter, "Reliability of Advanced Structural Ceramics and Ceramic-Matrix Composites—A Review," *Am. Ceram. Soc. Bull.*, **66** [2] 309 (1987).
[5]G. Wei and P. F. Becher, "Development of SiC-Whisker-Reinforced Ceramics," *Am. Ceram. Soc. Bull.*, **64** [2] 298 (1985).
[6]D. W. Richerson, *Modern Ceramic Engineering: Properties, Processing, and Use in Design*. Marcel Dekker, New York, 1982.
[7]F. F. Y. Wang, *Ceramic Fabrication Processes*. Academic Press, New York, 1976.
[8]J. Minet, F. Langlais, and R. Naslain, "Chemical Vapor Infiltration of Zirconia within the Pore Network of Fibrous Ceramic Materials from $ZrCl_4$–H_2–CO_2 Gas Mixtures," *Compos. Sci. Technol.*, **37**, 79 (1990).
[9]D. P. Stinton, T. M. Besmann, and R. A. Lowden, "Advanced Ceramics by Chemical Vapor Deposition Techniques," *Am. Ceram. Soc. Bull.*, **67** [2] 350 (1988).
[10]J. N. Mangels and G. J. Tennenhouse, "Densification of Reaction-Bonded Silicon Nitride," *Am. Ceram. Soc. Bull.*, **59** [12] 1216 (1980).
[11]D. R. Ulrich, "Prospects of Sol–Gel Processes," *J. Non-Cryst. Solids*, **100**, 174 (1988).

[12]M. S. Newkirk, A. W. Urquhart, H. R. Zwicker, and E. Breval, "Formation of Lanxide Ceramic Composite Materials," *J. Mater. Res.*, **1** [1] 81 (1986).

[13]R. Colmet, I. L. Sebire, and R. Naslain, "Fibrous Alumina–Alumina Composite Materials Obtained According to a CVI Technique," *Adv. Ceram. Mater.*, **1** [2] 185 (1986).

[14]R. Naslain, H. Hannache, L. Beraud, J. Y. Rossignol, F. Christin, and C. Bernard, "Chemical Vapor Infiltration Technique"; pp. 293–304 in *Chemical Vapour Deposition*, Proceedings of Euro-CVD-IV. Edited by J. Bloem *et al.* Philips, Eindhoven, The Netherlands, 1983.

[15]N. H. Tai and T. W. Chou, "Analytical Modeling of Chemical Vapor Infiltration in Fabrication of Ceramic Composites," *J. Am. Ceram. Soc.*, **72**, 414 (1989).

[16]D. P. Stinton, A. J. Caputo, and R. A. Lowden, "Synthesis of Fiber-Reinforced SiC Composites by Chemical Vapor Infiltration," *Am. Ceram. Soc. Bull.*, **65**, 347 (1986).

[17]T. M. Besmann, B. W. Sheldon, R. A. Lowden, and D. P. Stinton, "Vapor-Phase Fabrication and Properties of Continuous-Filament Ceramic Composites," *Science (Washington DC)*, **253**, 1104 (1991).

[18]K. Sugiyama and K. Yoshida, "Pressure-Pulsed Chemical Vapour Infiltration of SiC to Two-Dimensional Tyranno/SiC–C Preforms," *J. Mater. Sci.*, **30**, 5125 (1995).

[19]K. Sugiyama and T. Kishida, "Pressure-Pulsed Chemical Vapour Infiltration of SiC to Porous Carbon Form a Gas System $SiCl_4$–CH_4–H_2," *J. Mater. Sci.*, **31**, 3661 (1996).

[20]A. Sakai, J. Gotoh, and S. Motojima, "Preparation and Characterization of SiC/C and C/SiC/C Composites Using Pulse Chemical Vapor Infiltration Process," *Mater. Sci. Eng. B.*, **38**, 29 (1996).

[21]F. Wakai, Y. Kodama, S. Sakaguchi, N. Murayama, K. Izaki, and K. Niihara, "A Superplastic Covalent Crystal Composite," *Nature (London)*, **344** [29] 421 (1990).

[22]T. Ohji, A. Nakahira, T. Hirano, and K. Niihara, "Tensile Creep Behavior of Alumina/Silicon Carbide Nanocomposite," *J. Am. Ceram. Soc.*, **77** [12] 3259 (1994).

[23]S. Komarneni, "Nanocomposites," *J. Mater. Chem.*, **2** [12] 1219 (1992). □

journal

J. Am. Ceram. Soc., 84 [9] 1921–28 (2001)

Single-Source Sol–Gel Synthesis of Nanocrystalline $ZnAl_2O_4$: Structural and Optical Properties

Sanjay Mathur,*,† Michael Veith, Michel Haas, Hao Shen, Nicolas Lecerf, and Volker Huch

Institute of Inorganic Chemistry, University of Saarland, D-66123 Saarbruecken, Germany

Stefan Hüfner

Institute of Experimental Physics, University of Saarland, D-66123 Saarbruecken, Germany

Robert Haberkorn and Horst P. Beck

Institute of Inorganic and Analytical and Radiochemistry, University of Saarland, D-66123 Saarbruecken, Germany

Mohammad Jilavi

Institute of New Materials, University of Saarland, D-66123 Saarbruecken, Germany

Nanometer-sized zinc aluminate ($ZnAl_2O_4$) particles were synthesized from heterometal alkoxides, $[ZnAl_2(OR)_8]$, possessing an ideal cation stoichiometry for the $ZnAl_2O_4$ spinel. $ZnAl_2O_4$ is formed at 400°C, which is the lowest temperature reported for the formation of monophasic $ZnAl_2O_4$. ^{27}Al magic-angle spinning nuclear magnetic resonance spectroscopy revealed that $ZnAl_2O_4$ possesses an inverse structure at <900°C, while the normal spinel phase is observed at higher temperatures. The homogeneity of the in-depth composition and Zn:Al stoichiometry (1:2) was confirmed by electron spectroscopy for chemical analysis. Evaluation of the valence-band spectra of $ZnAl_2O_4$ and ZnS suggested that the hybridization of O 2*p* and Zn 3*d* orbitals is responsible for lowering the bandgap in the latter. The average crystallite size showed an exponential relationship to the calcination temperature (X-ray diffractometry and transmission electron microscopy data). The optical spectra of different spinel powders (average particle sizes, 20–250 nm) showed that the absorption edge exhibits a blue shift as particle size decreases.

I. Introduction

NANOPHASE materials[1,2] composed of discrete grains (crystallites) and the space between the adjacent grains (grain boundary) are microstructurally heterogeneous. This heterogeneity, the ratio of the number of atoms present on the surface and inside the nanoparticle, is triggered by decrease in grain size, leading to many interesting and unusual mechanical, electrical, optical, and magnetic properties unknown in the bulk material.[2] This intrinsic property enhances the importance of nanometer-sized mixed-oxide systems used as ferroelectric, semiconducting, and catalytic materials. In the case of semiconductors such as zinc aluminate ($ZnAl_2O_4$) or gallate, the nanoparticles do not possess a conduction band consisting of a plethora of energy levels but have specific and explicit energy levels. Because of this quantization, the bandgap in semiconductor nanoclusters (quantum dots) increases by an amount inversely related to the crystallite size. This phenomenon is experimentally manifested as a blue shift in the absorption edge as the particle size decreases. $ZnAl_2O_4$ is a well-known wide-bandgap semiconductor with a spinel structure.[3] Recent investigations on ZnM_2O_4 (M = Al, Ga) compounds have shown these systems to be new transparent and electroconductive materials.[4,5] The optical bandgap of polycrystalline $ZnAl_2O_4$ (3.8 eV) indicates that the material is transparent for light possessing wavelengths >320 nm. Thus, $ZnAl_2O_4$ can be used for ultraviolet (UV) photoelectronic devices. Moreover, $ZnAl_2O_4$ spinel is useful in many catalytic reactions, such as cracking, dehydration, hydrogenation, and dehydrogenation reactions.[6] The optical and catalytic properties depend crucially on the crystallite size of the material, which has led to a spurt of activity in the preparation of fine $ZnAl_2O_4$ powders.[7–10] To the best of our knowledge, the effect of crystallite size on the optical properties of nanometer-sized $ZnAl_2O_4$ has not been investigated.

The preparation of nanocrystalline materials[7,8] from solution-based chemical approaches is expected to achieve (i) chemically homogeneous and phase-pure specimens, (ii) a narrow size distribution of particles, and (iii) low crystallization and sintering temperatures of the materials. In the context of mixed-oxide ceramics, the conventional wet-chemical techniques generally use a mixture of individual constituents to meet the synthesis of the targeted system. Because no positional control is offered, the different compounds present in the reaction mixture randomly collide to form various intermediate species with metal ratios unfavorable for obtaining a single-phase material. This limitation can be circumvented by the *single-source precursor* strategy,[11–14] which offers a positional control of atoms, because the different elements required for the final ceramic material are incorporated and chemically linked in a single molecule. This strategy of maneuvering materials from molecules is significant for obtaining mixed-metal ceramics and composites. We report here the synthesis and structural and optical properties of nanometer-sized $ZnAl_2O_4$.

II. Experimental Procedure

(1) Starting Materials and X-ray Crystallography of $[Zn\{Al(OBu^t)_4\}_2]$

The synthesis of the alkoxide precursors, $[Zn\{Al(OR)_4\}_2]$ (R = Pr^i,Bu^t), was performed taking stringent precautions against atmospheric moisture. Isopropyl and tert-butyl alcohols were dried by distillation from magnesium turnings and sodium

P. Davies—contributing editor

Manuscript No. 188242. Received September 22, 2000; approved April 4, 2001.
*Member, American Ceramic Society.
†Author to whom correspondence should be addressed: Dr. Sanjay Mathur, Institute of Inorganic Chemistry (Geb. 23.1), University of Saarland, D-66123 Saarbruecken, Germany.

metal, respectively. $[Al(OPr^i)_3]_4$, $[Al(OBu^t)_3]_2$, and $[Zn\{N(SiMe_3)_2\}_2]$ were synthesized following the published procedures.[15,16] At room temperature, freshly distilled zinc aluminum isopropoxide is a viscous liquid, which crystallizes slowly on standing for a few days. The crystallized specimens of the isopropoxide derivative, $[Zn\{Al(OPr^i)_4\}_2]$, were unsuitable for X-ray crystallography. The various crystallization attempts to obtain single crystals were not fruitful. However, the analogous tert-butoxide derivative yielded well-formed crystals, which could be used for single-crystal X-ray diffractometry (XRD) analysis. A suitable specimen of $[Zn\{Al(OBu^t)_4\}_2]$ was flame-sealed in a Lindemann capillary, under an inert atmosphere. Crystal data and structure-refinement parameters are given in Table I. Diffraction data were collected on a Stoe imaging-plate diffractometer system operating with graphite monochromated Mo$K\alpha$ radiation (λ = 0.71073 Å). Unit cell dimensions were determined from the least-squares refinement of 2θ values (>20°, <25°) for 25 accurately centered reflections. The intensities were corrected for Lorentzian and polarization factors. The structure was solved (SHELXS-86) and refined (SHELXL-97), using the SHELX package for the determination of crystal structure.[17] The oxygen atoms O(5), O(6), and O(7) of the terminal tert-butoxy ligands were found to be disordered.

$$[Zn\{N(SiMe_3)_2\}_2] + \tfrac{1}{2}[\{Al(OR)_3\}_4] \xrightarrow{ROH}$$

$$[Zn\{Al(OR)_4\}_2] + 2HN(SiMe_3)_2\uparrow \qquad (R = Pr^i, Bu^t) \quad (1)$$

$$ZnCl_2 + \tfrac{2}{n}[K\{Al(OR)_4\}]n \longrightarrow$$

$$[Zn\{Al(OPr^i)_4\}_2] + 2KCl\downarrow \quad (2)$$

(2) Instrumentation

The raw powders were sintered in a preheated laboratory tube furnace coupled with a temperature controller. The infrared (IR) spectra of the gel and calcined powders were recorded as KBr pellets by Fourier transform infrared spectrometry (FT-IR; Model 165, Bio-Rad Laboratories, Krefeld, Germany). Carbon and hydrogen contents in the gel and calcined powders were obtained using an elemental analyzer (Model CHN900, LECO Co., St. Joseph, MI). Solid-state ^{27}Al nuclear magnetic resonance (NMR) spectra of polycrystalline samples (~200–250 mg) were obtained by spectrometry (Model MSL 200S, Bruker Instruments, Inc., Billerica, MA). Powder XRD measurements were performed at room temperature, on a diffractometer (Model D 5000, Siemens Aktiengesellschaft, Karlsruhe, Germany) operating with Cu$K\alpha_1$ radiation. The average particle size was determined, using the FormFit program,[18] from the line broadening of XRD peak profiles by small crystallites. The powder morphology of the gels before and after heat treatment was investigated by scanning electron microscopy (SEM). SEM micrographs and energy-dispersive X-ray (EDX) analysis were performed in the specimen chamber of an EDX-coupled scanning electron microscope (Model CAM SCAN S4, Cambridge Instruments, Cambridge, U.K.). Transmission electron microscopy (TEM; Model JEM 200 CX, JEOL, Tokyo, Japan) images were recorded by drawing a carbon-coated copper grid through the suspensions of various ceramics in alcohol.

X-ray photoemission spectroscopy (XPS) experiments were performed (Model SSI M-Probe, Surface Science Laboratories, Mountain View, CA) using Al$K\alpha$ radiation, with an energy resolution of 0.8 eV. The binding energies could be determined within an accuracy of ±0.05 eV. The nanocrystalline samples of $ZnAl_2O_4$ and reference materials were pelletized with thin indium foils to reduce the charging phenomenon. A flood gun was used to correct the charge effect. The binding energy of the C1*s* spectra was calibrated at 284 eV. The standard samples (zinc and ZnO), measured for comparing the Zn 3*d* binding energies, were scraped *in situ* with a diamond file at a base pressure of $\geq 1 \times 10^{-10}$ mbar (1 bar = 10^{-5} Pa). For optical spectra, the light from a 30 W deuterium-lamp UV source was transmitted through a double monochromator (Model TM300, Bentham Instruments, Ltd., Berkshire, U.K.), and the monochromatic ray was focused with the help of an integrating sphere, which comprised the sample or reference material (MgO). Slits were fixed at 1 mm wide. The total hemispherical reflectance (diffused and specular) was measured in the wavelength range 230–700 nm, using an 8° angle of incidence on the pelletized samples. The spectra of the reference material were used as the spectral function of the instrument, because MgO shows no optical absorption in the measured wavelength region.

Table I. Crystal Data and Structure Refinement for $[Zn\{Al(OBu^t)_4\}_2]$

Parameter	Data/values
Empirical formula	$C_{32}H_{72}Al_2O_8Zn$
Formula weight	704.23
Temperature	293(2) K
Wavelength	0.71073 Å
Crystal system	Orthorhombic
Space group	$P2_12_12_1$
Unit cell dimensions	a = 9.353(2) Å α = 90°
	b = 16.951(3) Å β = 90°
	c = 27.180(5) Å γ = 90°
Volume	4309.2(14) Å^3
Z	4
Density (calculated)	0.913 Mg/m^3
Absorption coefficient	0.639 mm^{-1}
F(000)	1536
Crystal size	0.30 mm × 0.10 mm × 0.15 mm
Theta range for data collection	2.55°–23.86°
Index ranges	$-10 \leq h \leq 10$, $-19 \leq k \leq 19$, $-30 \leq l \leq 30$
Reflections collected	6324
Independent reflections	5606 [R(int) = 0.0736]
Absorption correction	Semiempirical (ψ-scans)
Refinement method	Full-matrix least-squares on F^2
Data/restraints/parameters	6324/0/265
Goodness-of-fit on F^2	1.038
Final R indices [$I > 2$sigma(I)]	$R1$ = 0.0820, $wR2$ = 0.2169
R indices (all data)	$R1$ = 0.0902, $wR2$ = 0.2270
Absolute structure parameter	0.003(4)
Largest diffraction peak and hole	0.721 and −0.526eÅ^{-3}

III. Results and Discussion

(1) Synthesis and Characterization of Heterometal Precursors

The heterometal Zn-Al alkoxides, $[Zn\{Al(OR)_4\}_2]$, were prepared either by the alcoholysis of zinc bis(hexamethyl disilazane), in the presence of the constituent aluminum alkoxides, in parent alcohols (Eq. (1)),[13] or by a salt elimination reaction of anhydrous zinc chloride with two equivalents of potassium tetra-isopropoxy aluminate, as described by Mehrotra *et al.* (Eq. (2)).[19]

The single-crystal XRD analysis unambiguously established the heterometal nature of the precursors and the compatibility of the cation ratio (Zn:Al = 1:2) in the molecule, with respect to the $ZnAl_2O_4$ ceramic. The molecular structure of $[Zn\{Al(OBu^t)_4\}_2]$ (Fig. 1) is based on a spirocyclic metal-oxygen framework formed by the bidentate chelation of two monoanionic $\{Al(OBu^t)_4\}^-$ moieties to an electrophilic Zn^{2+} center. The molecule crystallizes in the monoclinic space group $P2_12_12_1$, and the overall structure is essentially similar to that observed for other transition-metal tert-butoxy aluminates of the general formula $[M\{Al(OBu^t)_4\}_2]$ (M(II) = Co, Ni, Cu, Fe).[13,20] The salient crystallographic data are given in Table I. The four Zn–O distances (see caption, Fig. 1) are similar and indicate a strong chelation of the $\{Al(OBu^t)_4\}^-$ units to the zinc center. The metal–oxygen distances are within the expected range for heterometal alkoxyaluminates.[13,20] Our contention is that the mixed-metal framework does not break down into the individual alkoxides, at least during the initial stages of hydrolysis reactions.

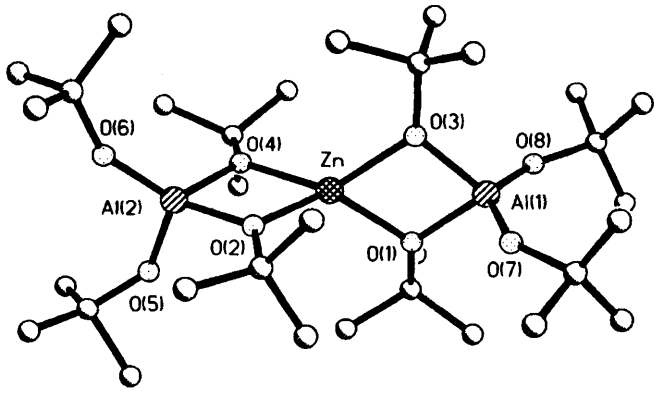

Fig. 1. Molecular structure of $[ZnAl_2(OBu^t)_8]$. Selected bond lengths (Å): Zn–O(1), 1.991(5); Zn–O(2), 1.969(5); Zn–O(3), 1.984(6); Zn–O(4), 2.003(6); Al(1)–O(1), 1.846(5); Al(1)–O(3), 1.838(6); Al(1)–O(8), 1.682(7); Al(1)–O(7), 1.658(12); Al(2)–O(2), 1.809(5); Al(2)–O(4), 1.851(6); Al(2)–O(5), 1.656(13); and Al(2)–O(6), 1.698(12).

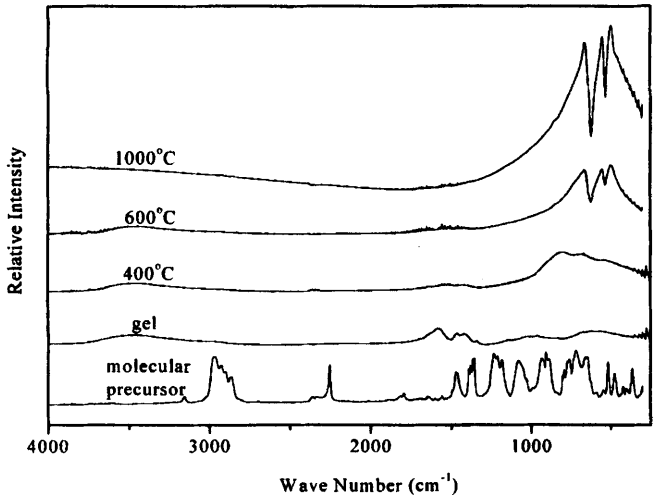

Fig. 2. FT-IR spectra of the molecular precursor, gel, and $ZnAl_2O_4$ ceramic at different calcination temperatures.

(2) Synthesis and Characterization of Gel

An isopropanol solution of $[Zn\{Al(OPr^i)_4\}_2]$ was partially hydrolyzed by adding, dropwise, a 3.0*M* solution of water in isopropyl alcohol. The resulting solution was stirred at 50°C for 12 h to obtain a stable, homogeneous suspension (sol), which transformed into a gel when allowed to stand for a few days. The removal of solvent under vacuum yielded a foamy white powder, which was dried under vacuum at 70°C (4 h). The so-obtained green precursor was heated in a laboratory furnace at 300°C, to burn out the organic residues, and calcined at higher temperatures (400°–1400°C), to obtain monophasic spinel.

In an alternative synthesis, the tert-butoxide complex, $[Zn\{Al(OBu^t)_4\}_2]$, was dissolved in isopropyl alcohol to generate *in situ* $[Zn\{Al(OPr^i)_4\}_2]$, and the mixture was hydrolyzed under similar conditions. The raw powder obtained from this mixture gave results identical to those obtained on using the isopropoxide derivative, which suggests that the metal ratio and metal-oxygen framework observed for the tert-butoxide derivative was maintained in the isopropanol solution.

(3) Characterization of the Spinel Precursor and Calcined Powders

(A) Chemical and EDX Analysis: The elemental analysis data of the gel (found (calculated) = Zn 19.17 (19.23), Al 15.70 (15.88); Zn/Al = 1.99) and the calcined samples are in good agreement with the starting composition (Zn 10.98 (11.04), Al 9.02 (9.11); Zn/Al = 2.01). An additional advantage of using alkoxide precursors is that the residual alkoxy groups in the gel rapidly decompose at temperatures lower than those required for other metallo-organic precursors, such as acetate, glycolate, and β-diketonate derivatives.[11] The product calcined at 300°C shows remarkably low organic contents (0.43% C, 0.63% H). The hydrogen contents may be the result of the adsorbed moisture. At 800°C, the ceramic is almost free from organic and hydroxide impurities (0.058% C, 0.013% H). The threshold values of the analyzer are in the same range. The average metal stoichiometry, determined by EDX analysis in the raw precursor and the heat-treated samples, corresponds (±1.0%) to the intended metal stoichiometry (Zn:Al = 1:2). The EDX measurements performed randomly at several spots across the samples show no microphase separation or compositional inhomogeneities at a submicrometer level.

(B) IR and NMR Spectroscopy: The FT-IR spectrum (Fig. 2) of the oven-dried gel (130°C) reveals the characteristic vibrations of metal-attached hydroxy (3472 cm^{-1}) and isopropoxy groups (1565, 1457, 1421, 1315, 1140, and 950 cm^{-1}).[16] The bands observed in the range 730–500 cm^{-1} can be assigned to the metal-oxygen stretching frequencies. The bands observed at ~2360 cm^{-1} can be assigned to the vibrational modes of carboxylate ions, probably formed by the reaction of CO_2, liberated during the burnout of organic contents, with the xerogel. The bands resulting from the carboxylate or hydroxy groups disappear at higher calcination temperatures (600°–1000°C), with the spectrum containing three well-defined peaks (666, 553, and 495 cm^{-1}) characteristic of the regular spinel structure, with only octahedrally coordinated aluminum centers.[8]

In the context of sol–gel chemistry of the metal aluminates, the ^{27}Al magnetic-angle spinning NMR (MAS NMR) provides an excellent means to investigate the atomic rearrangements (site exchanges) of Al^{3+} cations in the amorphous gel network to give the solid phase.[21–23] Despite the limitation of quadrupolar broadening, the ^{27}Al chemical shifts can unequivocally distinguish among four-, five-, and six-coordinate Al(III) centers. The NMR spectrum of the dried gel (Fig. 3(a)) shows three signals, at 1.17, 33.96, and 67.93 ppm. The peaks at 1.17 and 67.93 ppm are typical for six- and four-coordinate Al(III) species, whereas the chemical

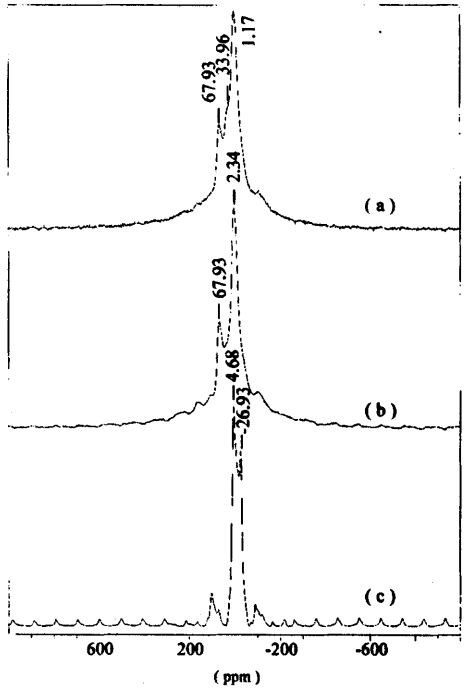

Fig. 3. ^{27}Al solid-state MAS NMR spectra of (a) Zn-Al-O xerogel and (b) $ZnAl_2O_4$ ceramic calcined at 600° and (c) 1000°C.

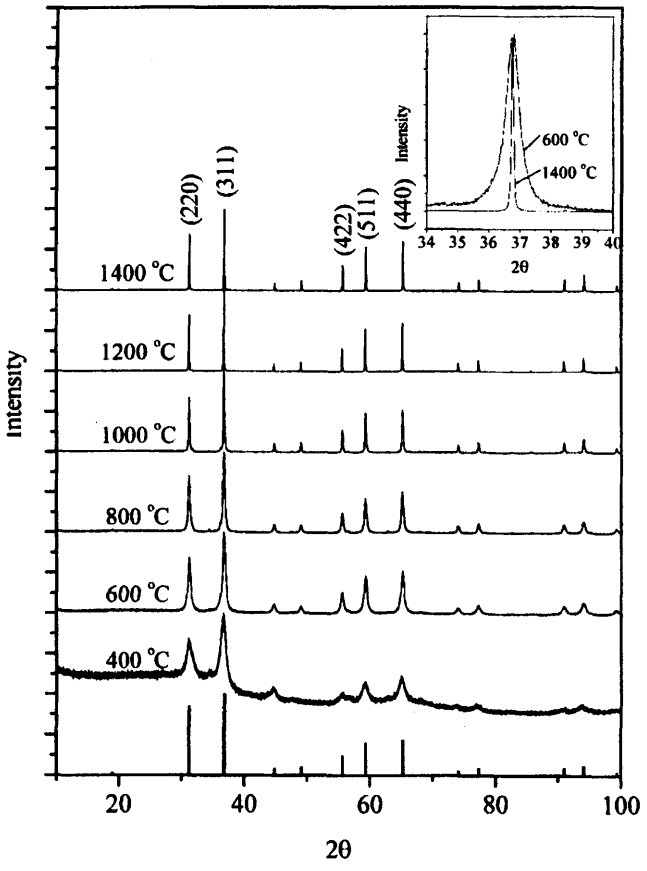

Fig. 4. Room-temperature XRD traces of the $ZnAl_2O_4$ ceramic calcined at different temperatures.

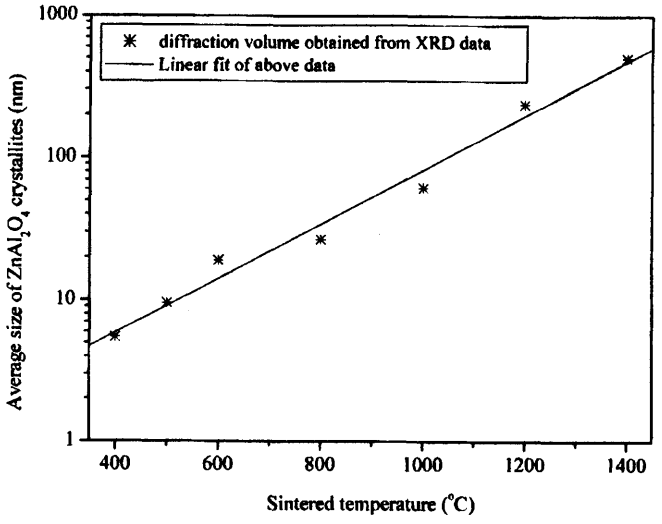

Fig. 5. Exponential relationship between the crystallite size in $ZnAl_2O_4$ ceramic and calcination temperature.

shift at 33.96 ppm can be assigned to five-coordinate Al^{3+} cations. The NMR spectrum of crystalline $ZnAl_2O_4$ heat-treated at 600°C (Fig. 3(b)) shows two distinct signals at 2.34 ppm and a low-field peak at ~61.9 ppm, corresponding to octahedral AlO_6 and tetrahedral AlO_4 sites present in the closed cubic packing of oxygen atoms. This result shows that the $ZnAl_2O_4$ spinel is partially inverse, with an occupancy ratio of Al_{Td}:Al_{Oh} = ⅓:⅔ (degree of inversion, γ, is ⅓). The absence of a signal corresponding to five-coordinate Al(III) species suggests a structural change in the gel structure (via condensation, oxolation, and alcoholation reactions), to form the cubic spinel phase containing only octahedral and tetrahedral vacancies. The intensity of the peak caused by four-coordinate aluminum centers decreases at higher calcination temperature, which illustrates the temperature dependence of the degree of structural inversion in $ZnAl_2O_4$ spinel. The NMR spectrum of the $ZnAl_2O_4$ sample heat-treated at 1000°C shows only the presence of octahedrally coordinated aluminum ions (Fig. 3(c)). The observed doublet is a result of the second-order splitting of the central transition band by nuclear-quadrupole interaction, which, along with the well-defined side bands, indicate the highly crystalline nature of the sample.

(C) Powder XRD Studies: The phase composition in the raw and calcined products was established by powder XRD (Fig. 4). The precursor powder was amorphous, whereas the sample calcined at 400°C showed $ZnAl_2O_4$ (gahnite) to be the only crystalline phase (ICCD Card File No. 5-669).[24] This is the lowest reported temperature for the formation of single-phase crystalline $ZnAl_2O_4$. The diffraction peaks in samples calcined at higher temperatures (600°–1400°C) show sharper profiles, resulting from the continuation of crystallization/ordering processes and grain growth. The calculated (FormFit) lattice parameters (a_0 = 8.0855 Å) for cubic spinel phase, in a sample calcined at 1000°C, are in good agreement with the reported value (a_0 = 8.0848 Å, ICCD Card File No. 5-669). The determination of the crystallite size from the line-shape analysis of the diffraction peaks (Fig. 5) shows a log-normal crystallite size distribution, with crystallinity growing in an exponential relationship to calcination temperature, which could also be demonstrated by recording TEM images of the same samples (see later). The effect of peak broadening by nanocrystallites is evident on comparing the (311) reflection of two samples fired at 600° and 1400°C (inset, Fig. 4).

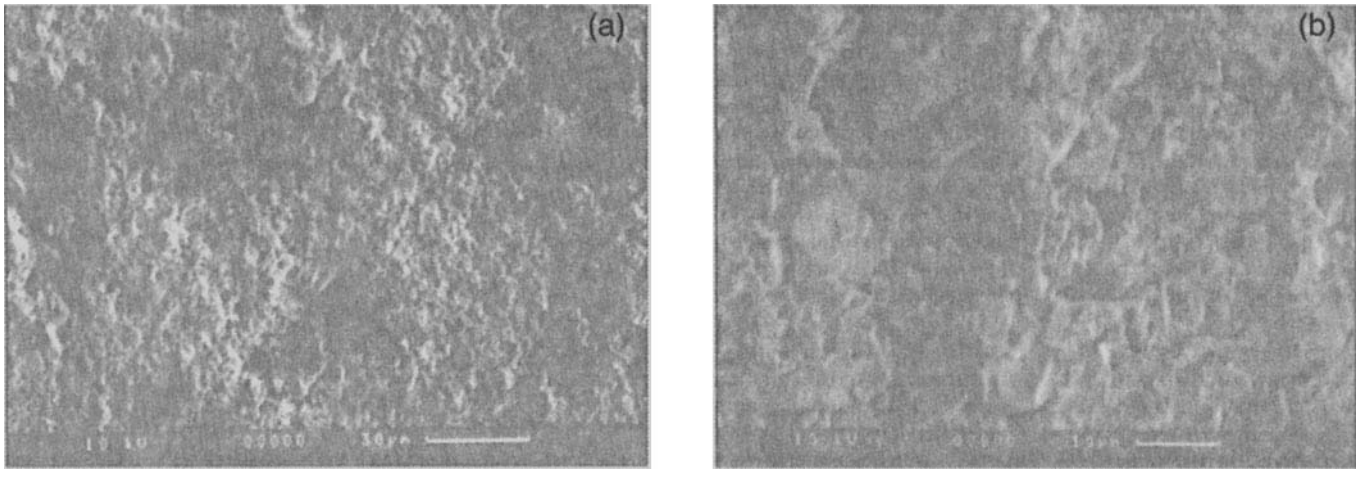

Fig. 6. SEM micrographs of (a) Zn-Al-O gel and (b) $ZnAl_2O_4$ ceramic calcined at 600°C.

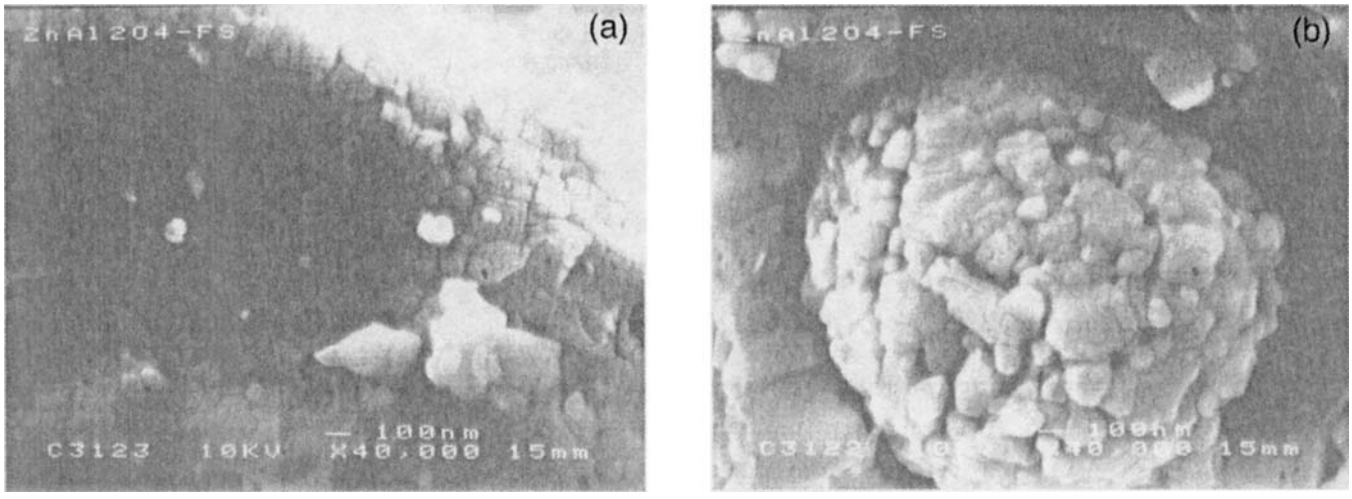

Fig. 7. SEM images of a $ZnAl_2O_4$ pellet (sintered at 1000°C): (a) surface morphology and (b) fracture surface.

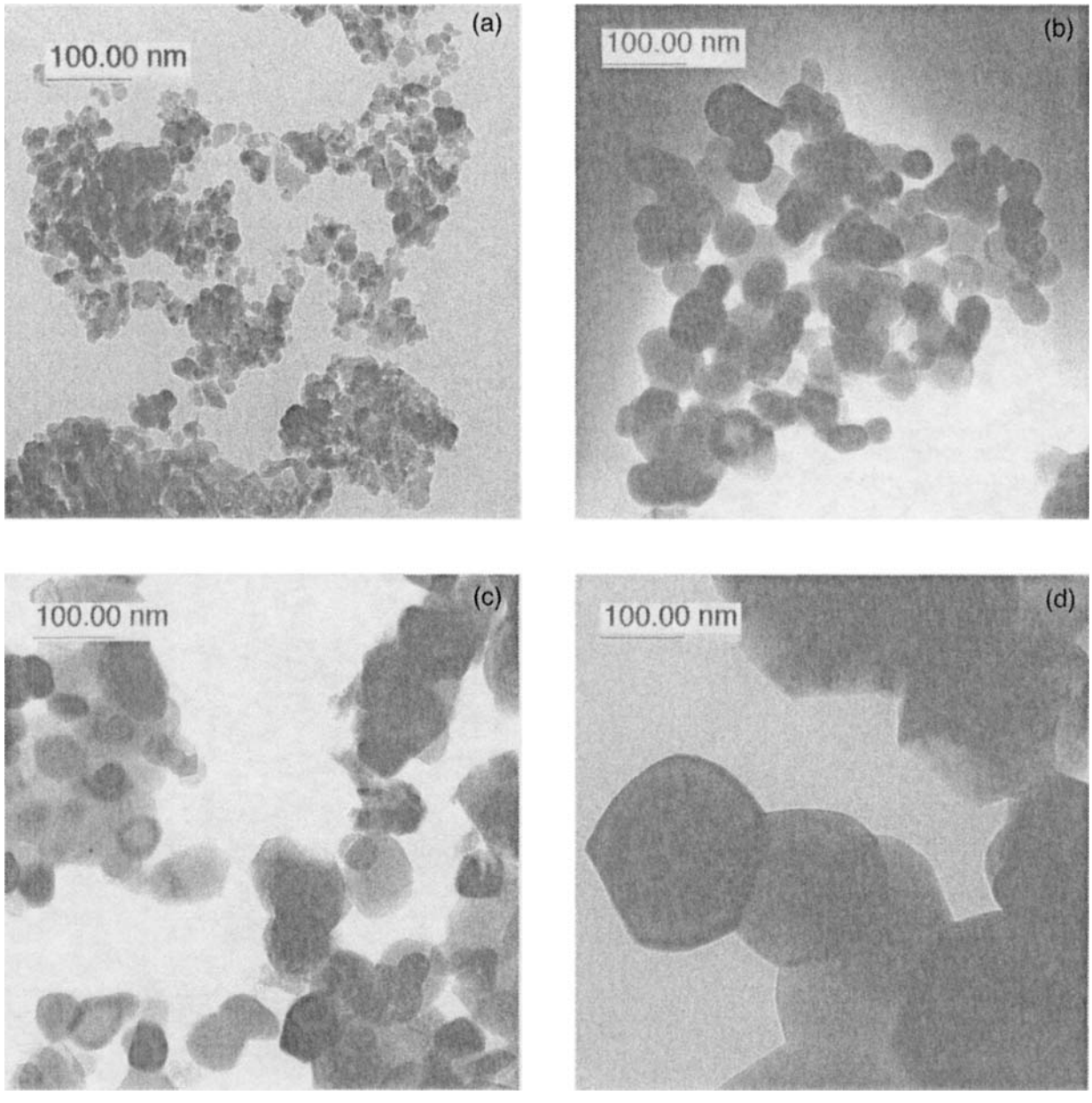

Fig. 8. TEM micrographs of $ZnAl_2O_4$ ceramic calcined at (a) 600°, (b) 800°, (c) 1000°, and (d) 1200°C.

(D) Scanning and Transmission Electron Microscopy: The typical SEM images of the Zn-O-Al gel exhibit micrometer-sized agglomeric particles with a porous structure (Fig. 6(a)), while the product calcined at 600°C consists of grains with a faceted morphology (Fig. 6(b)). The examination of the surface of a pellet sintered at 1000°C by SEM (Fig. 7(a)) shows a compact structure, and no unusual pore formation is observed among the grain boundaries. The fractograph of the pellet (Fig. 7(b)) reveals dense spherical particles comprised of tiny nanocrystallites. The TEM image of a $ZnAl_2O_4$ sample calcined at 600°C shows crystallites of nearly uniform size (15–20 nm), which grew on further heat treatment (to ~35 nm at 800°C, Fig. 8(b)). The average particle size at 1000°C was ~60 nm (Fig. 8(c)). Rapid growth was observed thereafter, and the TEM image of a powder calcined at 1200°C (Fig. 8(d)) shows dumbbell-shaped particles (~260 nm) formed by the fusion of individual crystallites.

The exponential evolution of crystallite size with increasing calcination temperature is also confirmed by the crystallite sizes calculated from the XRD data (Fig. 5). The above observation shows a direct correlation between the *volume-averaged* crystallite size distribution, calculated from the microstructural parameters of the line-shape analysis of XRD, and the *number-weighted* size distribution of particles observed in the TEM images. The high-resolution electron microscopy (HR-EM) image (Fig. 9) shows a sinterneck of two nanometer-sized $ZnAl_2O_4$ crystallites having different mutual crystallographic orientations. This image shows clear lattice fringes in the grain boundary, which suggests that the sample is free from other glassy or crystalline second phases. The grain-boundary region shows no other phase or composition present. The excessive crystallite growth at higher temperatures also indicates the absence of second-phase particles (impurities) at intergranular sites, which would otherwise prevent the grain growth by grain-boundary pinning. The observed rapid grain-boundary diffusion in the $ZnAl_2O_4$ specimen may result from a sink function of the grain boundary for defects, because the vacancy concentration in the grain boundaries is large enough when compared with the lattice. Consequently, a more rapid grain-boundary diffusion is favored in stoichiometrically pure compounds. The interatomic spacings, calculated from the high-resolution images, correspond to the cubic $ZnAl_2O_4$ phase (ICCD Card File No. 5-669).[24]

(E) X-ray Photoelectron Spectroscopy: The stoichiometric ratio of zinc to aluminum was carefully checked by XPS at different locations on the surface and in the bulk sample (after argon sputtering) and was always Zn:Al = 1:2. A further aim of the XPS studies was to eliminate the possibility of small amounts of Zn(0) in the samples, which could result from the reduction of Zn^{2+} by organic byproducts liberated in the firing steps. The Zn 2*p* XPS spectra of $ZnAl_2O_4$ and those of pure and partially oxidized zinc metal are shown in Fig. 10, together with the $L_3M_{45}M_{45}$ auger spectra of the same materials. In addition, we measured the XPS valence-band spectra for $ZnAl_2O_4$ and ZnS, to evaluate the effect of the hybridization of Zn 3*d* and O 2*p* orbitals (Fig. 11).

The difference in the Zn 2*p* core-level binding energies of zinc metal and ZnO is too small to be distinguished within the resolution limit (0.8 eV) of the electron spectroscopy for chemical analysis (ESCA) spectrometer used. However, the difference in chemical shift between zinc metal and ZnO (~4.2 eV, Fig. 10(b)) of the Zn $L_3M_{45}M_{45}$ auger line is large enough for an unambiguous analysis of the different chemical states of zinc. The auger line, in Fig. 10(b), is composed of two peaks (multiplet interactions), where the peak with larger intensity is located at the higher binding energy. In comparing the nanocrystalline $ZnAl_2O_4$ with the standards, the line at −491eV, a characteristic feature of zinc metal, was not observed in $ZnAl_2O_4$, which confirmed the presence of only bivalent zinc species in nanocrystalline $ZnAl_2O_4$.

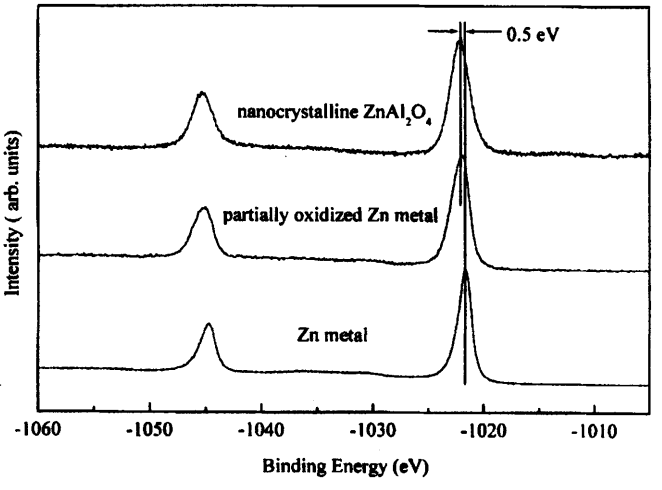

(a)

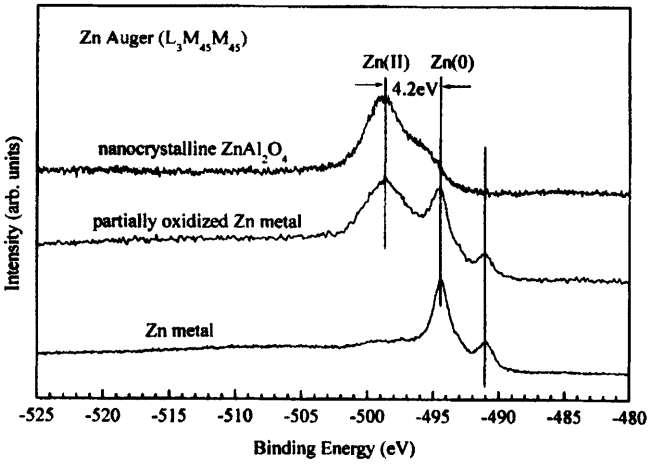

(b)

Fig. 10. Zn 2*p* XPS spectra of (a) zinc metal, partially oxidized zinc metal, and $ZnAl_2O_4$ and (b) Zn $L_3M_{45}M_{45}$ auger line in zinc metal, partially oxidized zinc metal, and $ZnAl_2O_4$.

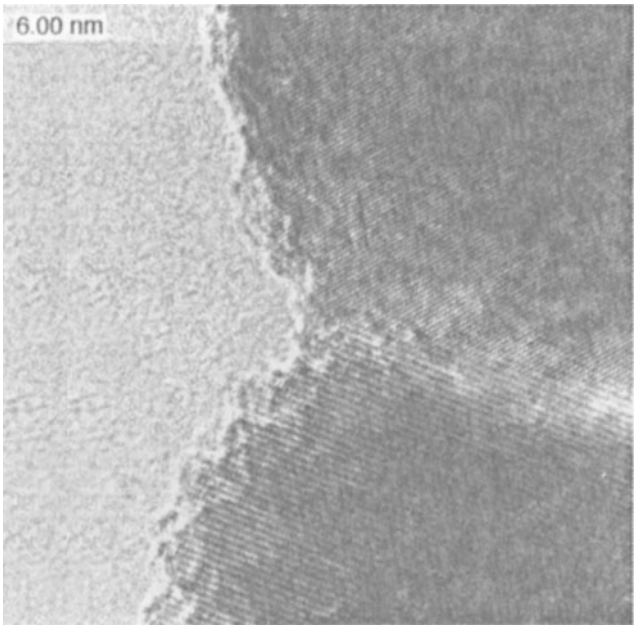

Fig. 9. HR-EM image of two sintered $ZnAl_2O_4$ nanograins (1000°C).

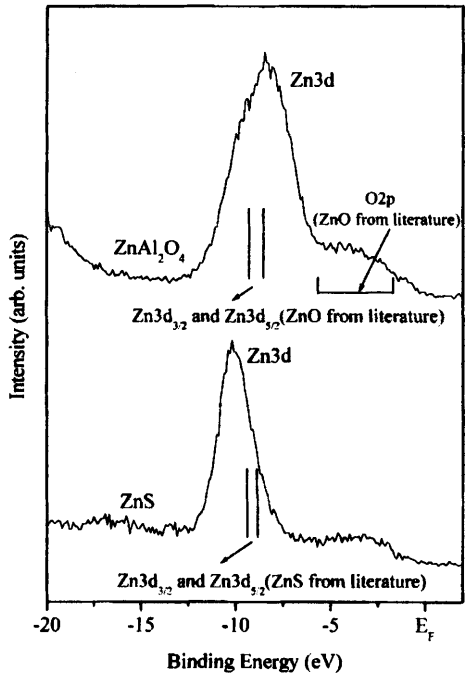

Fig. 11. XPS valence spectra of nanocrystalline $ZnAl_2O_4$ and ZnS.

In the valence-band spectra of $ZnAl_2O_4$ and ZnS (Fig. 11), the position of the Zn 3*d* lines, as obtained from the literature, is indicated and also that of the O 2*p* band in ZnO.[25] The small difference in the position of the 3*d* lines in our experiments, compared with those from the literature, may result from different normalization procedures (C 1*s*, 284 eV normalization in the present case) used in the different experiments. The large width in the Zn 3*d* level in the $ZnAl_2O_4$ spectrum is probably a result of the high Zn 3*d*–O 2*p* hybridization; however, differential charging cannot be ruled out as the broadening cause in these materials. The relatively narrow Zn 2*p* lines (Fig. 10(a)) argue against differential charging, whereas the relatively broad auger line (Fig. 10(b)) argues for differential charging.

(F) Optical Properties: The calcined (400°C) $ZnAl_2O_4$ samples were heat-treated (6 h) at 700°, 800°, 1000°, 1200°, and 1400°C, and the corresponding absorbance spectra were recorded (Fig. 12). The optical absorbencies of the samples were obtained from the calculation of total reflection, R ($\log_{10}(1/R)$). The absorbance spectra of the ZnO and Al_2O_3 standards are also shown in Fig. 12. The broad absorbance peaks observed in the UV region (220–280 nm) result from the fundamental band-to-band electron excitations and are related to the energy bandgap in the investigated samples. The bandgap can be obtained from a linear extrapolation of the absorbance edge to the wavelength axis. The bandgap (E_g) values of the $ZnAl_2O_4$ samples are in the range 4.0–4.5 eV and quite different from those of Al_2O_3 (E_g = ~3.6 eV) and ZnO (E_g = ~3.1 eV), despite the existence of the Al^{3+} and Zn^{2+} cations in $ZnAl_2O_4$. This finding corroborates the phase purity of the $ZnAl_2O_4$ samples and the absence of any microphase separation.

The effect of crystallite growth on the optical properties was investigated by comparing the spectra of $ZnAl_2O_4$ samples calcined at different temperatures. The broad shoulder observed in the 290–375 nm wavelength region for the sample calcined at 700°C probably results from some defect structure.[4] The intensity of this shoulder decreased when the sample was sintered for longer duration (Fig. 13), suggesting crystallite growth and minimization of structural defects by the thermal annealing. The absorbance edge became steeper when the calcination temperature was increased, and a "red shift" (from 4.5 to 4.0 eV) was observed (Fig. 12). It is known that the E_g value of a nanocrystalline specimen scales with its diameter (d) as $E_g \approx 1/d$, which is the case for our samples (inset, Fig. 12). A similar blue shift has been observed for the bandgap for various semiconductor particles.[2] Because the

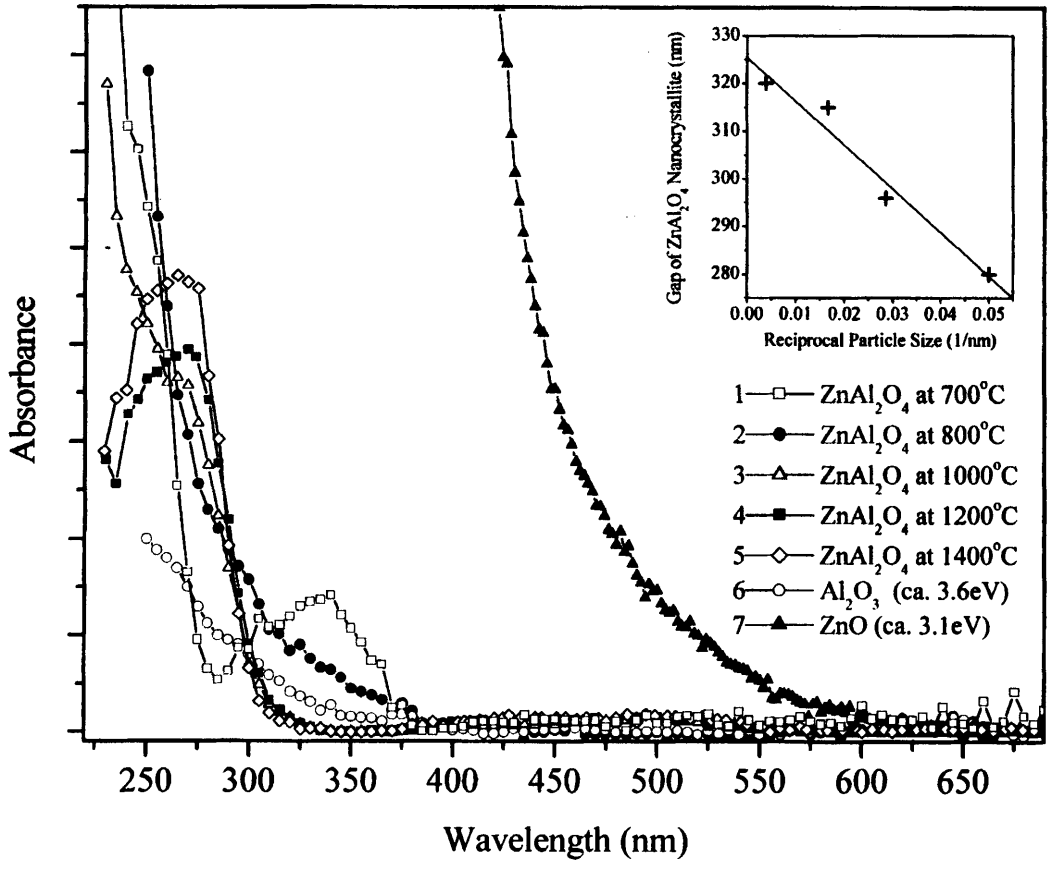

Fig. 12. Absorbance spectra (relative to MgO) of $ZnAl_2O_4$ (1–5) calcined at 700°, 800°, 1000°, 1200°, and 1400°C, respectively; Al_2O_3 (6); and ZnO (7).

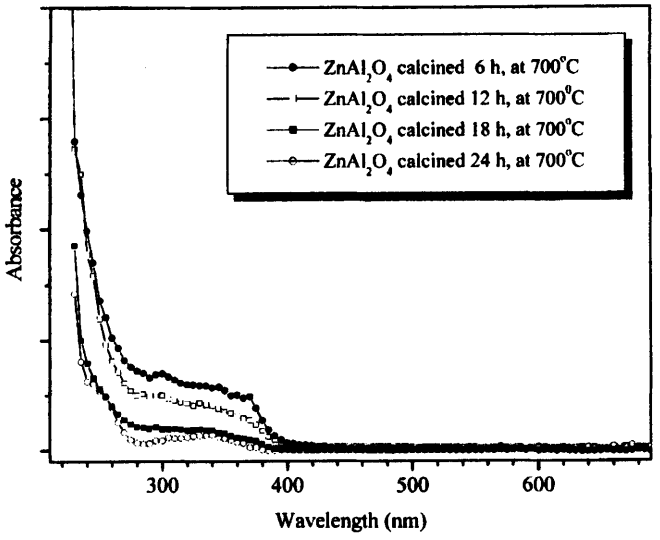

Fig. 13. Absorbance spectra (relative to MgO) of $ZnAl_2O_4$ calcined at 700°C for 6, 12, 18, and 24 h.

optical properties depend strongly on the particle size, a particle-size distribution is expected to cause inhomogeneous broadening of the optical spectra. Although the TEM images of the $ZnAl_2O_4$ samples (Fig. 8) show nearly a homogeneous dispersion of crystallites, the bandgap values derived from the diffuse reflection spectra may require a correction with respect to the particle-size dependence of light scattering, which was not applied.

IV. Conclusions

Low-temperature synthesis of nanocrystalline zinc aluminate spinel ($ZnAl_2O_4$) from single alkoxide molecules, $[ZnAl_2(OR)_8]$, is described. The ideal Zn:Al stoichiometry, with respect to the 2–4 spinel phase in the molecular precursor, results in the formation of monophasic $ZnAl_2O_4$ at 400°C, which is significantly lower than the temperatures reported for the synthesis of crystalline $ZnAl_2O_4$. The correlation of crystallite size and the optical properties of the prepared $ZnAl_2O_4$ nanoparticles shows an inverse relationship between the bandgap values and particle size. The optical properties show that $ZnAl_2O_4$ is a better candidate than ZnO for UV reflective coatings. The structural investigations using solid-state[27] Al NMR indicate that $ZnAl_2O_4$ is partially inverse at lower temperatures (<900°C, degree of inversion ~0.3); however, the regular spinel structure is obtained at ≥1000°C. A comparison of the average crystallite size obtained from the electron microscopy and powder diffraction data shows that the number-weighted (TEM) and volume-averaged (XRD) particle sizes are comparable, which corroborates the narrow size distribution found in the spinel particles in our experiments. A comparison of the valence-band spectra of $ZnAl_2O_4$ and ZnS suggests that O 2*p*–Zn 3*d* hybridization may be responsible for the lowering of the bandgap in $ZnAl_2O_4$.

Acknowledgments

The authors gratefully acknowledge the Deutsche Forschungsgemeinschaft for providing financial support to the research program *Sonderforschungsbereich 277* at the Saarland University, Saarbruecken, Germany. S. M. is thankful to the AvH Foundation, Germany, for a fellowship. We thank Dr. Michael Zimmer for recording the solid-state NMR spectra.

References

[1]A. Edelstein and R. C. Cammarata (Eds.), *Nanomaterials: Synthesis, Properties and Applications*. Institute of Physics Publishing, Bristol, U.K., and Philadelphia, PA, 1996.
[2]J. H. Fendler (Ed.), *Nanoparticles and Nanostructured Films*. Wiley-VCH, Weinheim, Germany, 1998.
[3]K. E. Sickfaus and J. M. Wills, "Spinel Compounds: Structure and Property Relations," *J. Am. Ceram. Soc.*, **82**, 3279–92 (1998).
[4]S. K. Sampath and J. F. Cordaro, "Optical Properties of Zinc Aluminate, Zinc Gallate, and Zinc Aluminogallate Spinels," *J. Am. Ceram. Soc.*, **81**, 649–54 (1998).
[5]T. Omata, N. Ueda, K. Ueda, and H. Kawazoe, "New Ultra-violet-Transport Electroconductive Oxide, $ZnGa_2O_4$ Spinel," *Appl. Phys. Lett.*, **64** [9] 1077–78 (1994).
[6]T. El-Nabarawy, A. A. Attia, and M. N. Alaya, "Effect of Thermal Treatment on the Structural, Textural, and Catalytic Properties of the $ZnO–Al_2O_3$ System," *Mater. Lett.*, **24**, 319–25 (1995).
[7]M. A. Valenzuela, P. Bosch, G. Aguilar-Rios, A. Montoya, and I. Schifter, "Comparison between Sol–Gel, Coprecipitation, and Wet Mixing Synthesis of $ZnAl_2O_4$," *J. Sol–Gel Sci. Technol.*, **8**, 107–10 (1997).
[8]A. K. Adak, A. Pathak, and P. Pramanik, "Characterisation of $ZnAl_2O_4$ Nanocrystals Prepared by the Polyvinyl Alcohol Evaporation Route," *J. Mater. Sci. Lett.*, **17**, 559–61 (1999).
[9]T. Tsuchida and S. Kitajima, "Preparation of Monodispersed, Uniform Particles of ZnO and Al_2O_3 and Application for $ZnAl_2O_4$ Formation," *J. Mater. Sci.*, **27**, 2713–18 (1992).
[10]W-S. Hong, L. C. De Jonghe, X. Yang, and M. N. Rahaman, "Reaction Sintering of $ZnO–Al_2O_3$," *J. Am. Ceram. Soc.*, **78**, 3217–24 (1995).
[11]M. Veith, S. Mathur, A. Kareiva, M. Jilavi, M. Zimmer, and V. Huch, "Low-Temperature Synthesis of Nanocrystalline $Y_3Al_5O_{12}$ (YAG) and Ce-Doped $Y_3Al_5O_{12}$ via Different Sol–Gel Methods," *J. Mater. Chem.*, **9**, 3069–79 (1999).
[12]M. Veith, S. Mathur, N. Lecerf, K. Bartz, M. Heintz, and V. Huch, "Synthesis of a $NdAlO_3/Al_2O_3$ Ceramic-Ceramic Composite by Single Source Precursor CVD," *Chem. Mater.*, **12**, 271–74 (2000).
[13](a) F. Meyer, R. Hempelmann, S. Mathur, and M. Veith, "Microemulsion Mediated Sol–Gel Synthesis of Nano-scaled MAl_2O_4 (M = Co,Ni,Cu) Spinels from Single-Source Heterobimetallic Alkoxide Precursors," *J. Mater. Chem.*, **9**, 1755–63 (1999). (b) M. Veith, A. Altherr, and H. Wolfanger, "A Single-Source CVD Precursor to $MgAl_2O_4$:$Mg\{H_2Al(OR)_2\}_2$," *Adv. Mater., CVD*, **5**, 87 (1999).
[14]M. Veith, S. Mathur, N. Lecerf, V. Huch, T. Decker, H. P. Beck, W. Eiser, and R. Haberkorn, "Sol–Gel Synthesis of Nano-scaled $BaTiO_3$, $BaZrO_3$, and $BaTi_{0.5}Zr_{0.5}O_3$ Oxides via Single-Source Alkoxide Precursors and Semi-alkoxide Routes," *J. Sol–Gel Sci. Technol.*, **17** [2] 145–58 (2000).
[15]M. F. Lappert, P. P. Power, A. R. Sanger, and R. Srivastava, *Metal and Metalloid Amides*. Wiley, New York, 1980.
[16]D. C. Bradley, R. C. Mehrotra, and D. P. Gaur, *Metal Alkoxides*. Academic Press, London, U.K., 1978.
[17](a) G. M. Sheldrick, SHELXS-86, *Program for Crystal Structure Determination*. University of Göttingen, Göttingen, Germany, 1986. (b) G. M. Sheldrick, SHELXL-97, *Program for Crystal Structure Determination*. University of Göttingen, 1997.
[18]R. Haberkorn, *FormFit—Programme for Particle Size Distribution from XRD Scans*. University of Saarland, Saarbruecken, Germany, 1997.
[19]R. C. Mehrotra, A. Singh, and S. Sogani, "Homo- and Hetero-metallic Alkoxides of Group 1, 2, and 12 Metals," *Chem. Soc. Rev.*, 215–25 (1994).
[20]M. Veith, S. Mathur, and C. Mathur, "New Perspectives in the Tailoring of Hetero(bi- and tri-)metal Alkoxide Derivatives," *Polyhedron*, **17**, 1005–34 (1998).
[21]N. Kashii, H. Maekawa, and Y. Hinatsu, "Dynamics of the Cation Mixing of $MgAl_2O_4$ and $ZnAl_2O_4$," *J. Am. Ceram. Soc.*, **82**, 1844–48 (1999).
[22]C. Gerardin, S. Sundaresan, J. Benziger, and A. Navrotsky, "Structural Investigations and Energetics of Mullite Formation from Sol–Gel Precursors," *Chem. Mater.*, **6**, 160–70 (1994).
[23]J. Sanz, A. Madani, J. M. Serratosa, J. S. Moya, and S. Aza, "Aluminum-27 and Silicon-29 Magic-Angle Spinning Resonance Study of the Kaolinite–Mullite Transformation," *J. Am. Ceram. Soc.*, **71**, C-418–C-421 (1988).
[24]Powder Diffraction File Card No. 5-669, International Centre for Diffraction Data, Newtown Square, PA, 1990.
[25]A. Goldmann and E. E. Koch, *Landolt-Bornstein. Electronic Structure of Solids: Photoemission Spectra and Related Data*, Vol. 23. Springer-Verlag, Berlin, Germany, 1989. □

J. Am. Ceram. Soc., 83 [5] 1314–16 (2000)

journal

Strengthening of Porous Alumina by Pulse Electric Current Sintering and Nanocomposite Processing

Sung-Tag Oh,*,† Ken-ichi Tajima,‡ and Motohide Ando

Synergy Ceramics Laboratory, Fine Ceramics Research Association, Nagoya 463–8687, Japan

Tatsuki Ohji*,§

National Industrial Research Institute of Nagoya, Nagoya 463–8687, Japan

Porous Al_2O_3 and SiC-dispersed-Al_2O_3 (Al_2O_3/SiC) nanocomposites with improved mechanical properties were fabricated using pulse electric current sintering (PECS). Microstructures with fine grains and enhanced neck growth, as well as high fracture strength, could be achieved via PECS of Al_2O_3. The incorporation of fine SiC particles into an Al_2O_3 matrix significantly increased the fracture strength of porous Al_2O_3. Based on microstructural observations, it was revealed that the refinement of Al_2O_3 grains and neck growth occurred by PECS and nanocomposite processing.

I. Introduction

Many technological applications exist in which porous ceramic materials are used.[1] For structural components, the presence of porosity is useful in reducing the weight of the component and increasing the strain to failure,[2] whereas for nonstructural components, porosity is essential for other functions, such as permeability or uses such as high-surface-area substrates. For both structural and nonstructural applications, however, improvements in the mechanical properties and control of strength variability are expected to increase the overall reliability of the material.

The mechanical properties of porous ceramics are determined by the volume fraction and geometry of the pores, as well as the microstructure of the solid phase, which links the properties to neck growth, solid-phase contiguity, characteristics of the grain boundary, etc.[3,4] Based on the microstructural features in porous ceramics, Green and co-workers[5,6] reported a marked increase in the strength and elastic moduli of Al_2O_3 with very little change in the pore volume. This increase in stiffness with a minimal increase in density was attributed to neck growth via surface diffusion during the sintering of Al_2O_3 at temperatures of <1000°C. Also, it has been shown that porous ceramics that attain both high porosity and high strength can be realized via the control of microstructures such as an incorporation of columnar β-Si_3N_4 in silicon nitride ceramics[7] and a dispersion of nanometer-sized Al_2O_3 into an alumina matrix.[8]

In this study, control of the solid-phase microstructure is emphasized to fabricate porous Al_2O_3 with enhanced mechanical properties. One approach to microstructural control is the use of the pulse electric current sintering (PECS) method;[9] using this process, the preferential neck growth of powders can be induced by selective local heating between the particles, because of high electric resistance.[10] The other approach is to incorporate fine second-phase particles into the matrix;[11] using this nanocomposite processing technique, a homogenous microstructure and an improvement of the mechanical properties in porous ceramics can be realized.

II. Experimental Procedure

A porous Al_2O_3 monolith and an Al_2O_3/5-vol%-SiC nanocomposite were prepared via hot pressing and the PECS method. High-purity α-Al_2O_3 powder with a mean particle size of 0.2 μm (AKP-53, Sumitomo Chemical Co., Tokyo, Japan) and β-SiC with a particle size of <0.3 μm (Ibiden Co., Ogaki, Japan) were used as starting powders. The combined Al_2O_3 and SiC powders was ball-milled in ethanol for 24 h using high-purity Al_2O_3 balls (5 mm in diameter) in a polyethylene pot. Then, soft agglomerates of the dried powders were crushed by dry ball-milling for 24 h.

The Al_2O_3 and composite powders were placed into a graphite die that had an inner diameter of 30 mm. Sintering was accomplished via PECS, using a spark plasma sintering system (Model SPS-2080, Sumitomo Coal Mining Co., Ltd., Tokyo, Japan) at a temperature of 800°–1500°C for various times under a vacuum of 6 Pa and an applied pressure of 5.5 MPa. A heating rate of 30°C/min was used from room temperature to the sintering temperature. For comparison, the same powders were compacted using a hot-pressing procedure under the same conditions. Rectangular bars with dimensions of 3 mm × 2 mm × 23 mm were obtained from as-fired disks by cutting and grinding.

Density measurements were made using the Archimedes method; water was used as the immersion medium. The fracture strength was determined using three-point bending tests with a span of 16 mm at room temperature. A load was applied parallel to the pressing axis, with a crosshead speed of 0.5 mm/min. The microstructure was observed via scanning electron microscopy (SEM).

III. Results and Discussion

The changes in the relative density of the sintered specimens for 30 min with sintering temperature are shown in Fig. 1. In comparison with hot pressing, the ceramics that were fabricated via PECS exhibited an enhanced densification. This rapid densification has been reported in the literature,[9,12] which is probably due to factors such as self-heat generation by microscopic electric

J. E. Blendell—contributing editor

Manuscript No. 188989. Received October 27, 1999; approved January 31, 2000.
Supported by AIST, MITI, Japan, as part of the Synergy Ceramics Project. A portion of the work was supported by NEDO (New Energy Development Organization). The authors are members of the Joint Research Consortium of Synergy Ceramics.

*Member, American Ceramic Society.
†Now with Dept. of Metallurgy and Materials Science, Hanyang University, Ansan 425–791, Korea.
‡Now with R&D Center Kagoshima, Kyocera Corp., Kokubu 899–4312, Japan.
§Author to whom correspondence should be addressed.

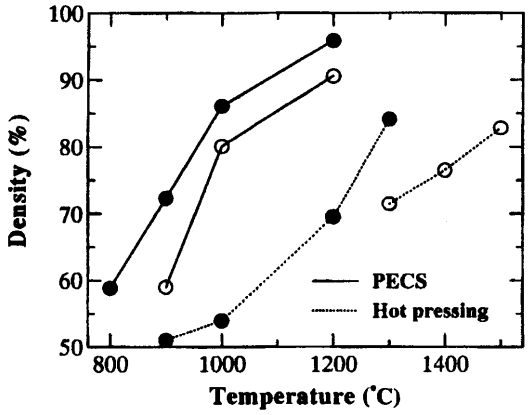

Fig. 1. Effect of sintering temperature of hot pressing (dotted line) and PECS (solid line) on the relative density for (●) the monolith and (○) the composite. Sintering time was 30 min.

discharge between particles, activation of the particle surface, and high-speed mass transfer by volume and grain-boundary diffusion, effectively exerting an influence on sintering. Figure 1 also shows that the relative density of the composites is smaller than that of the monolithic Al_2O_3 that was sintered under the same conditions. This retardation of densification, which is caused by the presence of fine SiC inclusions, can be explained by the resistance of the Al_2O_3/SiC interface to the diffusion process, as suggested by Stearns *et al.*[13]

Typical fracture surfaces of the Al_2O_3 (with a relative density of 81%), prepared via hot pressing and PECS for sintering time of 15 min, are shown in Figs. 2(a) and (b), respectively. The noted microstructural characteristics include the matrix grain size and the neck size between particles. The Al_2O_3 that was prepared via

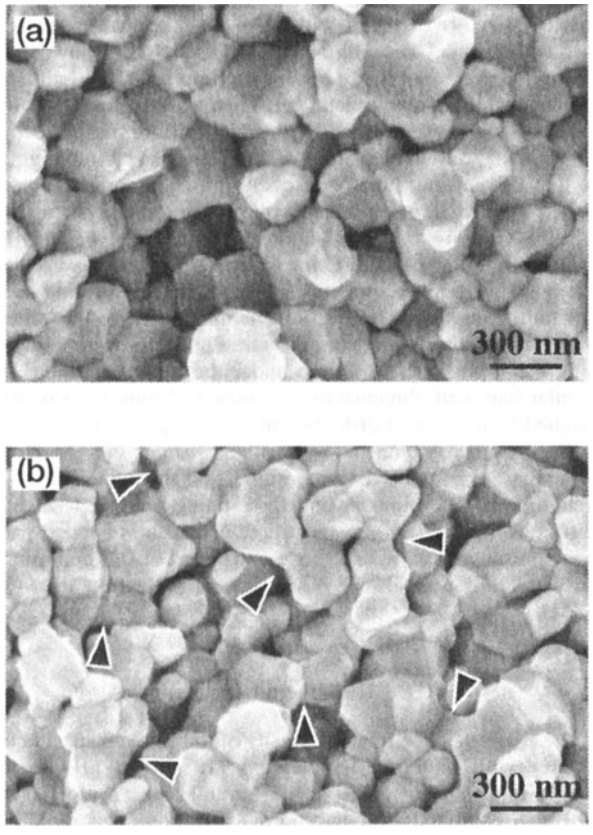

Fig. 2. SEM micrographs of typical fracture surfaces of monolithic Al_2O_3 with a relative density of 81% (fabricated via (a) hot pressing at 1300°C for 15 min and (b) PECS at 950°C for 15 min). Regions showing neck growth are indicated by arrows.

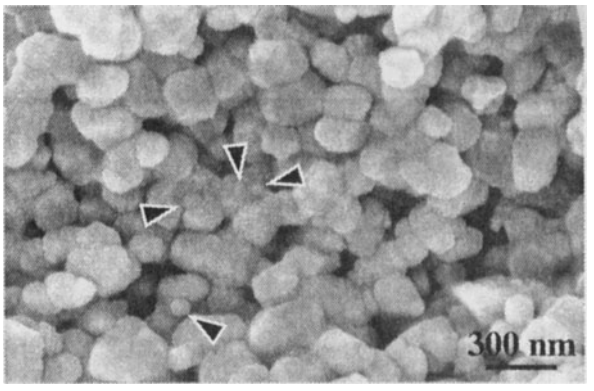

Fig. 3. SEM micrograph of a fracture surface of the Al_2O_3/5-vol%-SiC nanocomposite produced via PECS at 1000°C for 15 min. SiC particles are indicated by arrows.

PECS (Fig. 2(b)) exhibited relatively fine grains, in comparison with the hot-pressed Al_2O_3 (Fig. 2(a)). Considering the sintering temperatures of 1300°C in hot pressing and 950°C in PECS, the fine grain size can be explained reasonably as being attributable primarily to the low sintering temperature of PECS, where significant grain growth was not operative. Also, marked neck growth was realized using the PECS method, as shown in Fig. 2(b).

Generally, in PECS, a discharge between the particles is known to occur during the initial portion of the densification of nonconducting materials.[9] Also, a plasma has been reported to form during the initial stage of each current–voltage pulse.[12] Thus, these processes increase the temperature at and around the necks between particles. In addition, the selective local heating between particles that is due to high electric resistance can contribute to promotion of preferential neck growth.[10] Another factor that affects the increase in neck size is mass transfer by evaporation–condensation and surface diffusion. At the sintering temperature of 950°C in the Al_2O_3 system, evaporation–condensation and surface diffusion are more dominant than grain-boundary and volume diffusions; thus, neck growth with a minimal increase in density can be expected.[14]

Figure 3 shows an SEM micrograph of the Al_2O_3/5-vol%-SiC composite with a relative density of 82% that has been fabricated via PECS at a temperature of 1000°C for 15 min. Nanometer-sized SiC particles (indicated by arrows in the figure) are located mainly at the matrix grain boundaries and triple points. Hence, in this investigation, the composite is defined as an intergranular-type nanocomposite.[11] Also, comparison of this nanocomposite with the Al_2O_3 (Fig. 2) shows that the matrix grain was refined by the addition of 5 vol% of SiC, because of the growth restriction that is caused by the dispersion of fine SiC particles.[15]

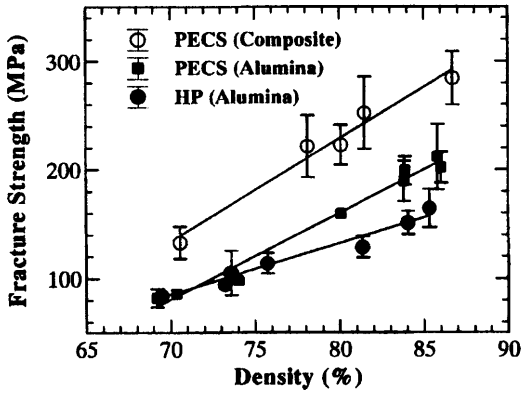

Fig. 4. Fracture strength for porous specimens after sintering to various temperatures, as a function of the percentage of the theoretical density.

Figure 4 shows fracture strengths for porous specimens that have been sintered at various temperatures, as a function of the relative density. The fracture strength of monolithic Al_2O_3 that was prepared using PECS were higher than that prepared via hot pressing. Considering the microstructure shown in Fig. 2, it is reasonable to expect the fracture strength to increase with decreasing grain size and increasing neck size, as reported by Green and co-workers.[5] Therefore, the strengthening of the Al_2O_3 that was prepared via PECS is thought to be due to grain refinement and neck growth. In comparison with the Al_2O_3, the fracture strength of the nanocomposite was enhanced significantly over the entire density range (Fig. 4). The strengthening of the composite is explained as being due to the further refinement of the Al_2O_3 matrix. In addition, grain-boundary strengthening by the intergranular SiC particles and crack-tip bridging by the SiC particles are believed to be responsible for the increase in fracture strength.[16–18]

IV. Summary

The present work emphasized control of the solid-phase microstructure to fabricate porous, Al_2O_3-based nanocomposites with a high fracture strength. The porous ceramics were prepared via the pulse electric current sintering (PECS) method. The microstructure for the porous Al_2O_3 that was prepared using PECS exhibited refinement of the Al_2O_3 grains and neck growth. As expected, the fracture strength of the Al_2O_3 prepared via PECS was higher than that for Al_2O_3 prepared via hot pressing. The incorporation of fine SiC particles into an Al_2O_3 matrix significantly increased the fracture strength of the porous Al_2O_3. The strengthening in the composite mainly was caused by refinement of the microstructure. These results indicated that powder processing and fabrication method strongly influenced the microstructure and fracture strength of Al_2O_3; thus, porous ceramics with enhanced mechanical properties can be prepared using PECS and nanocomposite processing more effectively.

References

[1]J. Saggio-Woyansky, C. E. Scott, and W. P. Minnear, "Processing of Porous Ceramics," *Am. Ceram. Soc. Bull.*, **71** [11] 1674–82 (1992).

[2]Y. Shigegaki, M. E. Brito, K. Hirao, M. Toriyama, and S. Kanzaki, "Strain Tolerant Porous Silicon Nitride," *J. Am. Ceram. Soc.*, **80** [2] 495–98 (1997).

[3]R. L. Coble and W. D. Kingery, "Effect of Porosity on Physical Properties of Sintered Alumina," *J. Am. Ceram. Soc.*, **39** [11] 377–85 (1956).

[4]D. C. C. Lam, F. F. Lange, and A. G. Evans, "Mechanical Properties of Partially Dense Alumina Produced from Powder Compact," *J. Am. Ceram. Soc.*, **77** [8] 2113–17 (1994).

[5]D. Hardy and D. J. Green, "Mechanical Properties of a Partially Sintered Alumina," *J. Eur. Ceram. Soc.*, **15** [8] 769–75 (1995).

[6]S. C. Nanjangud, R. Brezny, and D. J. Green, "Strength and Young's Modulus Behavior of a Partially Sintered Porous Alumina," *J. Am. Ceram. Soc.*, **78** [1] 266–68 (1995).

[7]C. Kawai and A. Yamakawa, "Effect of Porosity and Microstructure on the Strength of Si_3N_4: Designed Microstructure for High Strength, High Thermal Shock Resistance, and Facile Machining," *J. Am. Ceram. Soc.*, **80** [10] 2705–708 (1997).

[8]G. Li, Z. Jiang, A. Jiang, and L. Zhang, "Strengthening of Porous Al_2O_3 Ceramics through Nanoparticle Addition," *Nanostruct. Mater.*, **8** [6] 749–54 (1997).

[9]N. Tamari, T. Tanaka, K. Tanaka, I. Kondoh, M. Kawahara, and M. Tokita, "Effect of Spark Plasma Sintering on Densification and Mechanical Properties of Silicon Carbide," *J. Ceram. Soc. Jpn.*, **103** [7] 740–42 (1995).

[10]N. Murayama, "What We Can Do by Pulse Electric Current Sintering?" (in Jpn.), *Seramikkusu*, **32** [6] 445–49 (1997).

[11]K. Niihara, "New Design Concept of Structural Ceramics—Nanocomposites," *J. Ceram. Soc. Jpn.*, **99** [10] 974–82 (1991).

[12]L. Gao, Z. Shen, H. Miyamoto, and M. Nygren, "Superfast Densification of Oxide/Oxide Ceramic Composites," *J. Am. Ceram. Soc.*, **82** [4] 1061–63 (1999).

[13]L. C. Stearns, J. Zhao, and M. P. Harmer, "Processing and Microstructure Develoment in Al_2O_3–SiC Nanocomposites," *J. Eur. Ceram. Soc.*, **10** [6] 473–77 (1992).

[14]W. D. Kingery, H. K. Bowen, and D. R. Uhlmann, "Grain Growth, Sintering, and Vitrification"; pp. 448–515 in *Introduction to Ceramics*, 2nd Ed. Wiley, New York, 1976.

[15]C. S. Smith, "Grains, Phase and Interphases: An Interpretation of the Microstructure," *Trans. Metall. Soc. AIME*, **175**, 15–51 (1948).

[16]S. Jiao, M. L. Jenkins, and R. W. Davidge, "Interfacial Fracture Energy–Mechanical Behaviour Relationship in Al_2O_3/SiC and Al_2O_3/TiN Nanocomposites," *Acta Mater.*, **45** [1] 149–56 (1997).

[17]T. Ohji, T. Hirano, A. Nakahira, and K. Niihara, "Particle/Matrix Interface and Its Role in Creep Inhibition in Alumina/Silicon Carbide Nanocomposites," *J. Am. Ceram. Soc.*, **79** [1] 33–45 (1996).

[18]T. Ohji, Y.-K. Jeong, Y.-H. Choa, and K. Niihara, "Strengthening and Toughening Mechanisms of Ceramic Nanocomposites," *J. Am. Ceram. Soc.*, **81** [6] 1453–60 (1998). □

This page intentionally left blank

journal

J. Am. Ceram. Soc., 83 [7] 1816–18 (2000)

Reaction-Bonded and Superplastically Sinter-Forged Silicon Nitride–Silicon Carbide Nanocomposites

Naoki Kondo, Yoshikazu Suzuki,* and Tatsuki Ohji*

National Industrial Research Institute of Nagoya, Nagoya, Aichi 462-8510, Japan

Silicon nitride–silicon carbide (Si_3N_4–SiC) nanocomposites were fabricated by a process involving reaction bonding followed by superplastic sinter-forging. The nanocomposites exhibited an anisotropic microstructure, in which rod-shaped, micrometer-sized Si_3N_4 grains tended to align with their long axes along the material-flow direction. SiC particles, typically measuring several hundred nanometers, were located at the Si_3N_4 grain boundaries, and nanosized particles were dispersed inside the Si_3N_4 grains. A high bending strength of 1246 ± 119 MPa, as well as a high fracture toughness of 8.2 ± 0.9 MPa·m$^{1/2}$, was achieved when a stress was applied along the grain-alignment direction.

I. Introduction

Silicon nitride-based ceramics are among the most important engineering ceramics, because they exhibit high bending strength and high fracture toughness.[1,2] However, the high cost of raw Si_3N_4 powder and the difficulty of machining it make Si_3N_4 an expensive material. For the present study, two well-known processing techniques were combined, in sequence, to overcome these problems.

The first processing step in creating silicon nitride-based ceramic composites is reaction bonding (RB), for which low-cost silicon powder can be used. However, this process is accompanied by difficulty in controlling the nitridation reaction of the silicon powder.[3] Recently, several researchers have reported that the nitridation reaction can be controlled effectively by adding SiC or carbon powders to make Si_3N_4–SiC nanocomposites.[4,5] Tsuda *et al.*,[5] in particular, have reported the production of reaction-bonded Si_3N_4–SiC nanocomposites using a mixed powder of silicon and carbon as the starting powder. The cost of carbon powder is relatively low, so that adding it does not make a product expensive. Furthermore, nanocomposites have better bending strength and fracture toughness than do monolithic silicon nitrides.[6,7]

The second processing step is superplastic sinter-forging (SPSF).[8] SPSF makes near-net-shape forming of nanocomposites possible. In addition, SPSF can overcome one of the disadvantages of reaction bonding: the difficulty of obtaining full density.[3,8] Furthermore, high bending strength, as well as high fracture toughness, can be expected in specific directions, because SPSF forms a highly anisotropic microstructure.[8–10]

The present authors used the above-described strategies to produce Si_3N_4–SiC nanocomposites by the RB process, followed by SPSF. The bending strength and fracture toughness of the materials obtained were investigated in relation to the microstructure.

S.C. Danforth—contributing editor

Manuscript No. 189428. Received April 12, 1999; approved February 22, 2000.
*Member, American Ceramic Society.

II. Experimental Procedure

Silicon powder (99.9% purity, 1 μm), carbon powder (99.9% purity, 5 μm), Y_2O_3 powder (ultrafine grade, Shin-etsu Chemical Co., Tokyo, Japan), and Al_2O_3 powder (AKP 30, Sumitomo Chemicals, Tokyo, Japan) were first mixed. The weight ratio of Si:C:Y_2O_3:Al_2O_3 was 0.8084:0.0782:0.0709:0.0425, a mixture that would form (in wt%) 73.6Si_3N_4·18.4SiC · 5Y_2O_3·3Al_2O_3 (the weight ratio of Si_3N_4:SiC was 0.8:0.2), if the reactions Si + C → SiC and 3Si + 2N_2 → Si_3N_4 were completed perfectly.

The mixed powder was ball-milled for 50 h in methanol, using high-purity Al_2O_3 balls. The alumina concentration was corrected taking into account a worn-out amount of the alumina milling media, which was obtained by measuring the weight change of the media during the ball-milling. The ball-milled powder was dried and compacted, using a steel die, then cold isostatically pressed (CIPd), under a pressure of 490 MPa. The CIPd body measured ~38 mm × 17.5 mm × 26 mm, and the density was ~1.33 × 10^3 kg·m^{-3} (~53% of theoretical density). This CIPd body was reaction-bonded and then superplastically sinter-forged, using hot-pressing equipment with a graphite-resistance furnace. The details of the heating and pressing procedures are illustrated schematically in Fig. 1.

The treated CIPd body first was put into a graphite channel die with a base measuring 80 mm × 20 mm and treated by the RB process, followed by SPSF (these combined processes are hereafter denoted RB-SPSF). The atmosphere inside the furnace, nitrogen gas (99.99%) under 0.1 MPa pressure, was maintained throughout the RB-SPSF process. The CIPd body was heated to 1350°C at a rate of 10°C·min^{-1}. The RB process, resulting in the formation of Si_3N_4 and SiC, was conducted at 1350°C for 3 h; these conditions were chosen based on several reports.[4,5,11] The reacted body then was heated to 1750°C at a rate of 10°C·min^{-1}, and SPSF was conducted at 1750°C for 3 h, under an increasing load applied in three steps, as shown in Fig. 1. Each step was held for 1 h, to prevent cracking. After SPSF, the specimens

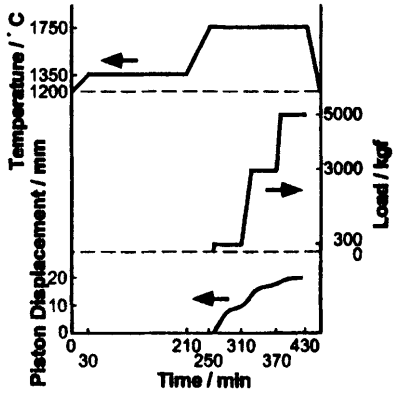

Fig. 1. Heating and pressing procedure, and piston displacement during RB-SPSF process.

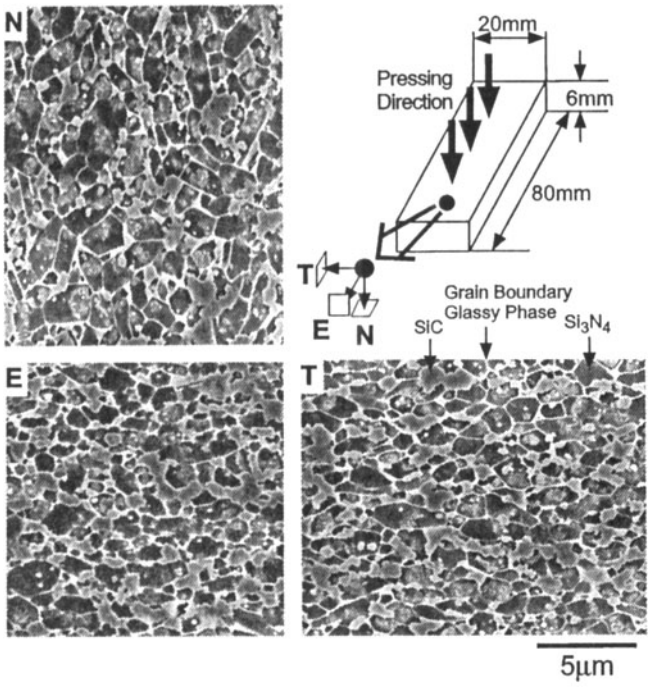

Fig. 2. Shape of the RB-SPSF specimen and SEM micrographs taken from each plane.

were cooled at a rate of $10°C \cdot min^{-1}$ to <1000°C. From that point on, the body obtained was referred to as the RB-SPSF body.

Scanning electron microscopy (SEM) and transmission electron microscopy (TEM) were used to examine the microstructure of the RB-SPSF specimens. SEM specimens were cut, ground, and polished, then plasma-etched by CF_4 and gold-coated. TEM specimens were prepared by mechanical grinding, dimpling, and ion-thinning.

Specimens measuring 3 mm × 4 mm × 40 mm, for measuring bending strength and fracture toughness, were cut from the RB-SPSF specimens, so that the stress face was perpendicular to the pressing direction. The three-point-bending strength was measured at room temperature, with a span of 30 mm and a crosshead speed of 0.5 $mm \cdot min^{-1}$. The fracture toughness, K_{Ic}, was measured by the single-edge V-notched beam (SEVNB) method, using an equation developed by Wakai *et al.*[12] The V-shaped notch, 2 mm deep, was introduced by a tapered diamond whetstone; the radius of the notch tip was ~30 μm. Loading was conducted at room temperature, with a crosshead speed of 0.5 $mm \cdot min^{-1}$.

III. Results and Discussion

The piston displacement of the hot-pressing equipment during SPSF is shown in Fig. 1. The total displacement was ~20 mm. Although the deformation rate includes shrinkage caused by sintering, the apparent deformation rate was estimated roughly as $1.85 \times 10^{-3}\ s^{-1}$. The obtained RB-SPSF body had the approximate dimensions of 80 mm × 20 mm × 6 mm, and the density was $3.26 \times 10^3\ kg \cdot m^{-3}$ (>99% of full density). This result suggests that the RB-SPSF technique has good potential for shape-forming under suitable conditions.

In Fig. 2, the directions and planes of the RB-SPSF body are designated as follows: The direction normal to the pressing direction is labeled N, the extruding direction E, and the direction transverse to the N and E directions T. Planes normal to each direction are the N, E, and T planes, respectively. X-ray diffraction analysis (XRD), which was conducted inside the RB-SPSF body, confirmed that the body consisted of β-Si_3N_4 and β-SiC. No α-Si_3N_4, silicon, or carbon peaks were detected. In addition, no other crystalline phase could be found by TEM observations.

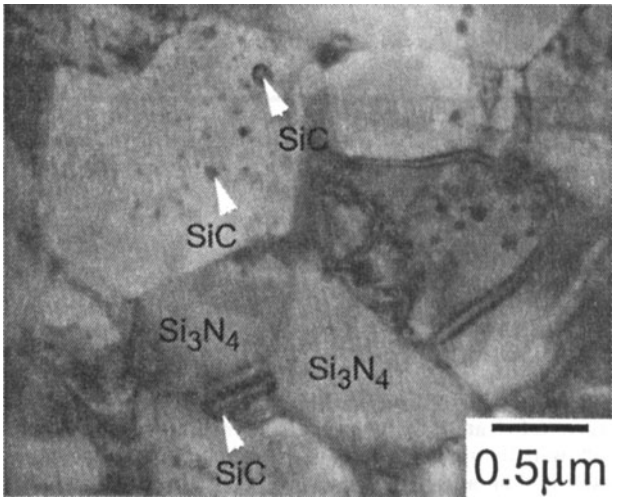

Fig. 3. TEM micrograph (T-plane) of the RB-SPSF specimen.

Figures 2 and 3 show the microstructure of the SPSF specimen. The SEM photographs in Fig. 2 are taken from the N, E, and T planes, as labeled, and the TEM photograph in Fig. 3 is taken from the T plane. The observed point was located ~20 mm in the E direction and 0 mm in the N and T directions from the center of the RB-SPSF body; this point is indicated roughly in the upper-right section of Fig. 2.

The Si_3N_4 grains shown in the SEM photographs were etched away by plasma-etching, thus enhancing the SiC grains and the grain-boundary glassy phase. Neither cavities nor microcracks (approximately >0.1 μm) were observed by SEM. Apparently, the rod-shaped, micrometer-sized Si_3N_4 grains tended to orient preferentially, with their long axes along the material-flow direction (the E direction). SiC particles, typically measuring several hundred nanometers, were located at the Si_3N_4 grain boundaries, and nanosized particles were dispersed inside the Si_3N_4 grains. Therefore, the RB-SPSF body seemed to have an anisotropic and nanocomposite-like microstructure.

The obtained RB-SPSF specimen exhibited high bending strength and high fracture toughness when a stress was applied along the grain-alignment direction (the E direction). The three-point bending strengths and fracture-toughness values for all of the five specimens were 1245 ± 119 MPa and 8.2 ± 0.9 $MPa \cdot m^{1/2}$, respectively. The loading point of these specimens was located 20 mm in the E direction from the center of the RB-SPSF body, where the microstructural observations also were conducted.

The alignment of the rod-shaped grains yielded at least two benefits to the crack-wake toughening mechanisms: (1) more rod-shaped grains were involved with the toughening; (2) the toughening worked effectively because the rod-shaped grains were aligned normal to the crack plane.

Those benefits resulted in the effective operation of the crack-wake toughening mechanism and steep *R*-curve behavior. Actually, steep *R*-curve behavior in anisotropic silicon nitrides has been reported elsewhere.[13–15] The RB-SPSF specimen which exhibited the anisotropic microstructure is also expected to show such steep *R*-curve behavior. The steep increase in fracture toughness, via a short crack extension, led to the compatible achievement of higher bending strength and higher fracture toughness.[1,8,10,13–15] In this case, as well, both high bending strength and high fracture toughness were achieved by the creation of an anisotropic microstructure.

It has been reported that dispersion of SiC particles into Si_3N_4 caused formation of uniformly elongated Si_3N_4 grains as well as refinement of these grains, resulting in high mechanical strength.[4,6,7] Similar strengthening effects can be considered in the Si_3N_4–SiC nanocomposites of this study. On the other hand, the presence of SiC particles at Si_3N_4 grain boundaries is known to suppress elongation of rod-shaped silicon nitride grains.[4,6,7] In

actuality, the aspect ratio of silicon nitride grains of the present material is small compared to that of the monolithic Si_3N_4 prepared by SPSF.[8] The low aspect ratio of the grains is presumably disadvantageous to toughening of grain bridging and pull-out.[13]

Thus, Si_3N_4–SiC nanocomposites were fabricated successfully in the present study using the RB-SPSF process. The strategies used—i.e., making Si_3N_4-based ceramics from low-cost raw powder and achieving near-net shape forming—show promise for future applications.

References

[1]M. J. Hoffmann, "Analysis of Microstructural Development and Mechanical Properties of Si_3N_4 Ceramics"; pp. 59–72 in NATO ASI Series, Series E, Applied Sciences, Vol. 276, *Tailoring of Mechanical Properties of Si_3N_4 Ceramics*. Edited by M. J. Hoffmann and G. Petzow. Kluwer Academic Publishers, Dordrecht, Netherlands, 1993.

[2]P. F. Becher, S. L. Hwang, H. T. Lin, and T. N. Tiegs, "Microstructural Contributions to the Fracture Resistance of Silicon Nitride Ceramics"; pp. 87–100 in NATO ASI Series, Series E, Applied Sciences, Vol. 276, *Tailoring of Mechanical Properties of Si_3N_4 Ceramics*. Edited by M. J. Hoffmann and G. Petzow. Kluwer Academic Publishers, Dordrecht, Netherlands, 1993.

[3]A. J. Moulson, "Review, Reaction Bonded Silicon Nitride: Its Formation and Properties," *J. Mater. Sci.*, **14**, 1017–51 (1979).

[4]S.-Y. Lee, "Fabrication of Si_3N_4/SiC Composite by Reaction-Bonding and Gas-Pressure Sintering," *J. Am. Ceram. Soc.*, **81** [5] 1262–68 (1998).

[5]H. Tsuda, T. Otsuka, H. Mabuchi, and K. Morii, "In-Situ Synthesis of Si_3N_4/SiC Composite by Reaction Hot-Pressing from Elemantal Powder," *Key Eng. Mater.*, **161–163**, 63–66 (1999).

[6]T. Hirano, T. Ohji, and K. Niihara, "Effect of Matrix Grain Size on the Mechanical Properties of Si_3N_4/SiC Nanocomposite Densified with Y_2O_3," *Mater. Lett.*, **27**, 53–58 (1996).

[7]J.-F. Yang, Y.-H. Choa, J. P. Singh, and K. Niihara, "Fabrication and Mechanical Properties of Si_3N_4/SiC Nanocomposite with Pressureless Sintering and Sinter-Post-Hipping," *J. Ceram. Soc. Jpn.*, **106** [10] 951–57 (1998).

[8]N. Kondo, Y. Suzuki, and T. Ohji, "Superplastic Sinter-Forging of Silicon Nitride with Anisotropic Microstructure Formation," *J. Am. Ceram. Soc.*, **82** [4] 1067–69 (1999).

[9]N. Kondo, T. Ohji, and F. Wakai, "Superplastic Forging of Silicon Nitride Ceramics with Anisotropic Microstructure Control," *J. Mater. Sci. Lett.*, **17**, 45–47 (1998).

[10]N. Kondo, T. Ohji, and F. Wakai, "Strengthening and Toughening of Silicon Nitride by Superplastic Deformation," *J. Am. Ceram. Soc.*, **81** [3] 713–16 (1998).

[11]N. Kondo, Y. Suzuki, and T. Ohji, "Middle Stage Heat Treatment to Control Microstructure of Reaction-Bonded Silicon Nitride-Silicon Carbide Composite," *J. Ceram. Soc. Jpn.*, **108** [5] 445–48 (2000).

[12]F. Wakai, S. Sakaguchi, and Y. Matsuno, "Calculation of Stress Intensity Factors for SENB Specimens by Boundary Collocation Procedure," *Yogyo Kyokaishi*, **93** [8] 81–82 (1985).

[13]P. F. Becher, "Microstructural Design of Toughened Ceramics," *J. Am. Ceram. Soc.*, **74** [2] 255–69 (1991).

[14]K. Hirao, M. Ohashi, M. E. Brito, and S. Kanzaki, "Processing Strategy for Producing Highly Anisotropic Silicon Nitride," *J. Am. Ceram. Soc.*, **78** [6] 1687–90 (1995).

[15]T. Ohji, K. Hirao, and S. Kanzaki, "Fracture Resistance Behavior of Highly Anisotropic Silicon Nitride," *J. Am. Ceram. Soc.*, **78** [11] 3125–28 (1995). □

This page intentionally left blank

journal

J. Am. Ceram. Soc., 83 [9] 2196–202 (2000)

Nonisothermal Synthesis of Yttria-Stabilized Zirconia Nanopowder through Oxalate Processing: I, Characteristics of Y-Zr Oxalate Synthesis and Its Decomposition

Oleg Vasylkiv* and Yoshio Sakka*

National Research Institute for Metals, Tsukuba, Ibaraki 305–0047, Japan

To obtain powder with a composition of 3 mol% Y_2O_3–97 mol% ZrO_2, a process of Y-Zr oxalate powder production has been optimized, to produce an oxalate with minimal particle size. The methodology of the nonisothermal decomposition of Y-Zr oxalate has been explained. Characteristics of the nonisothermal decomposition of different oxalates have been studied. Nanocrystalline Y_2O_3-stabilized ZrO_2 (YSZ) powder with a narrow size distribution of primary particles and aggregates was produced. The zirconia powder that was obtained from the smallest oxalate powder via nonisothermal decomposition had a particle size of 8–10 nm. The YSZ powder was weakly aggregated, with a narrow aggregate-size distribution of 70–90 nm.

I. Introduction

RECENTLY, considerable attention has been focused on the processing of advanced ceramic materials with controlled density and microstructure. Those characteristics are dependent largely on the characteristics of the green material.[1,2] As a result, they also are dependent on the particle-size distribution and particle shape, and even more so on the degree of aggregation and the aggregate-size distribution.[1]

Nanomaterials show distinct properties, because of the nature of the atomic structure in the interfacial regions. When the grain size becomes smaller than the critical scale that is associated with certain properties, such properties can change; many of these properties can be engineered through particle-size and grain-size control. The small grain size of the nanomaterials has a pronounced effect on many physical properties, such as increased strength and hardness. The dependence of such properties on the grain size means that control of the initial particle size of the starting powders is the most significant task for ceramic processing.

Nanopowders have been prepared by wet chemical methods for many years. Powders with a small particle size obtained by wet chemical processing often are heavily aggregated. Particle aggregation occurs when the precipitated precursors, or gels, are dried and milled.[3] Also, aggregation and agglomeration of the particles occurs when the precursor materials are calcined at temperatures of >600°C.[4–7] This effect reduces the sinterability of the calcined powder, which has been green-compacted via pressure filtration or slip casting.[1] As a result, it is desirable to decompose a precipitated precursor powder or gel at temperatures as low as possible, to avoid hard agglomerates in the final powder.

Zirconia ceramics, stabilized by the addition of oxides Y_2O_3, MgO, CaO, and zirconia-based composites with Al_2O_3 and TiO_2, are important materials, because of their many applications. The properties of zirconia ceramics are dependent strongly on the crystal structure and microstructure. As a result, yttria-stabilized zirconia (YSZ) is one material on which much attention has been focused, to produce ultrafine-grained ceramics for which nanosized powder is used as the starting material.

The most commonly used methods for the synthesis of mixed oxides are the various sol–gel and hydrothermal methods for the production of nanosized powder.[3–7] However, the oxalate route for obtaining small-sized zirconia powders has not been popular. It is well-known that other oxides and mixed-oxide systems, such as barium titanate, yttrium-doped ceria, neodymium-doped barium cerium oxides, and yttrium–barium systems with precise stoichiometry, have been produced successfully, using the oxalate process.[8–15]

With these objectives, we have studied the processing of zirconia and zirconia-based nanopowder preparation using the oxalate precursor method. It was expected that homogeneous mixing at the atomic level could be achieved, and that oxalate precursor-derived oxides would consist of nanosized, weakly aggregated particles with a narrow size distribution.

II. Experimental Procedure

The starting reagents were zirconium(VI) oxychloride (hydrous $ZrOCl_2 \cdot 10H_2O$ (98% pure)) and oxalic acid dehydrous $C_2H_2O_4 \cdot 2H_2O$ (>99.5% pure) (both of the latter were produced by High Purity Chemicals, Saitama, Japan). Precise amounts of the zirconium oxychloride and oxalic acid, taking into account their purity, were weighed and dissolved separately in distilled water. After obtaining homogeneous solutions, the reagents were mixed using magnetic stirring.

Eleven different concentrations of reagents in aqueous solution, and three reaction temperatures, were used to obtain different zirconium oxalates. The water content in solution was 0.5–25 L/(mol of initial reagent). The formation of zirconium oxalate is expressed by Eq. (1):

$$ZrOCl_2 \cdot 10H_2O + (COOH)_2 \cdot 2H_2O + nH_2O \rightarrow ZrO(C_2O_4) \cdot nH_2O + 2HCl + nH_2O \quad (1)$$

The reaction temperatures were 4°–20°C. Two technological routes, which are described in Fig. 1, were used to obtain the most weakly aggregated fine oxalate powder.

In the first route, the gel, or solution, of zirconium oxalate, which contained hydrochloric acid (HCl) in water, was washed and centrifuged to separate the precipitate from the HCl. In the second route, the oxalate solution was dried in an oven at a temperature of 120°C for 38 h, to evaporate the water and the HCl (the temperature of complete HCl evaporation was 110°C). The presence of Cl^- ions was tested using silver nitrate ($AgNO_3$), because, even for traces of HCl, a white precipitate will form immediately.

K. J. Bowman—contributing editor

Manuscript No. 189242. Received August 11, 1999; approved March 14, 2000.
*Member, American Ceramic Society.
Supported by the Science and Technology Agency of Japan (through a STA postdoctoral fellowship).

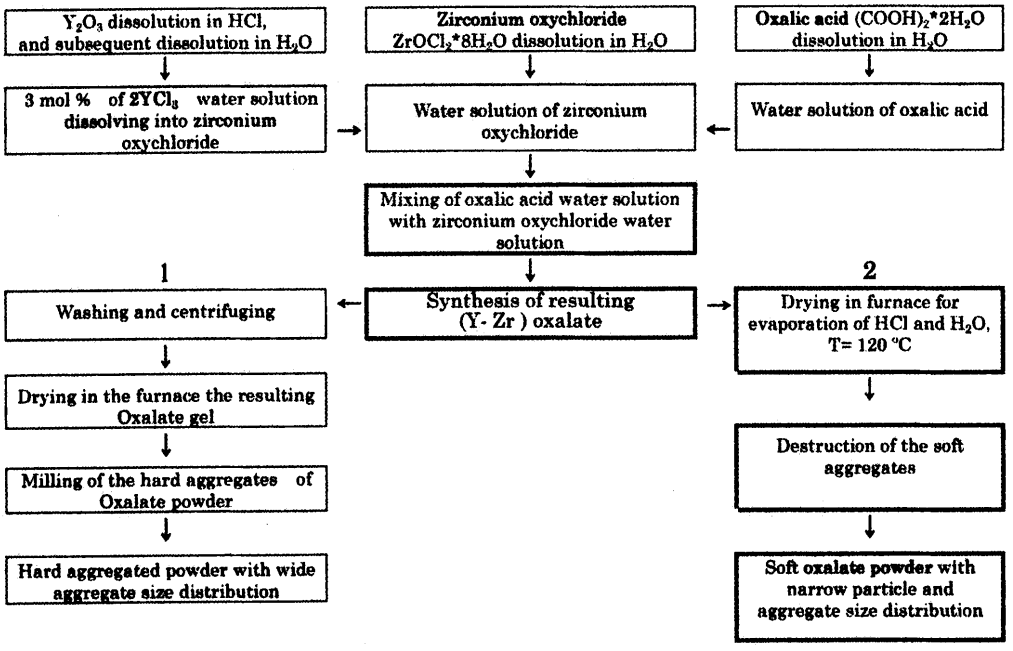

Fig. 1. Diagram of Y-Zr oxalate processing steps.

After optimization of the parameters for zirconium oxalate synthesis, Y-Zr oxalate was produced. Y_2O_3 grains (>99.5%, High Purity Chemicals) were dissolved in HCl; after the reaction temperature was decreased to <60°C, the solution was dissolved in water. A homogeneous aqueous solution of yttrium chloride (YCl_3) was obtained by mixing with a magnet stirrer for 48 h. The formation of YCl_3 is expressed by Eq. (2):

$$Y_2O_3 + 6HCl \rightarrow 2YCl_3 + 3H_2O \quad (2)$$

Y-Zr oxalate was produced using the methodology that is described in Fig. 1. Different solution concentrations were used to determine the property differences between the zirconium oxalate and Y-Zr oxalate.

Zirconium oxalates with different surface areas and Y-Zr oxalate were tested for decomposition using thermogravimetry and differential thermal analysis (TG-DTA) (Thermo Plus 2, Model TG8120, Rigaku, Tokyo, Japan). The reference used for DTA was an alumina (Al_2O_3) sample, the sample containers in the equipment were alumina, and an O_2/N_2 atmosphere was used. Linear heating rates of 60°–600°C/h and nonlinear heating programs both were used. Isothermal holdings and changes of the reaction atmosphere were not applied in this study. The TG-DTA experiments were used to determine the decomposition process, the decomposition–synthesis steps, the temperatures of final crystallization, the time duration of stages, and the weight losses at each stage, as a function of the initial oxalate surface areas. The heating-rate dependencies for the different oxalates also were obtained. DTA analysis was used to determine the thermal effects of the decomposition and crystallization stages. The TG-DTA results were used to produce nonlinear heating regimes and optimize the heating mode for controlled nonisothermal oxalate decomposition.

The nonisothermal decomposition of the final oxalate powder was optimized to obtain the finest, weakly aggregated zirconia nanopowder; a temperature–time schedule was used, to prevent hard agglomeration at high temperature. A range of heating rates of 35°–600°C/h also was used.

Phase identification of the oxide powders after decomposition of the different oxalates, and after decomposition of finest oxalate in different heating regimes, was determined via X-ray diffractometry (XRD) (Model JDX-3500, JEOL, Tokyo, Japan). Cu$K\alpha$ radiation, at 30 kV and 300 mA, was used. The patterns were recorded over a 2θ range of 20°–60° at a step size of 0.02° and interval of 0.5 s/step.

The surface area of the zirconium oxalates and evolution of the surface area during oxalate decomposition and zirconia synthesis was studied using the Brunauer–Emmett–Teller (BET) method (Model SA 3100, Coulter, Hialeah, FL). The aggregation of the zirconia powders was analyzed using a laser particle-size analyzer (Model LSPZ-100, Otsuka Electronics, Osaka, Japan). A very small amount of powder was mixed with distilled water. The pH of the water solution used for analysis was adjusted to pH 3, using HCl. Microtip ultrasonication (Model USP-600, Shimadzu, Kyoto, Japan) was used to break up powder aggregates in suspension. A range of ultrasonication times, at a frequency of 20 kHz and power of 160 W, was used to determine the effect on aggregate size. This data also are useful to obtain uniform colloids for future slip casting and pressure filtration.

Observation via transmission electron microscopy (TEM) (Model JEM-100-CX, JEOL) was used to determine the characteristics of zirconium oxalate decomposition and zirconia synthesis.

III. Results and Discussion

(1) Properties of Zirconium Oxalate Synthesis

The initial precursors of different concentration were produced by varying the water content in solution. The influence of the precursor solution concentration on the oxalate processing, and on its final surface area and particle-size distribution, was investigated. A graph of the influence of the reagent concentration is given in Fig. 2. Without considering the differences in synthesis temperature, the results show that oxalate powders with very different surface areas can be produced by changing the reagent concentration. If the water content is <5 L/(mol of reagent), the process causes the formation of a gel. As a result, the usual processing steps, such as filtration and washing for removing the HCl, are impossible. The HCl solution can be removed via centrifugation for an extended time and subsequent washing that must be repeated no less than 8–10 times. Such a procedure is very inefficient. This problem is reduced if the water content in solution is >5–6 L/mol. Figure 2 shows that, beyond the gelation zone, an intermediate zone and a zone of solution formation exist. Starting from a water content of >6 L/mol, the resulting oxalates can be precipitated, although the precipitation requires a duration of 48–120 h.

Table I shows the differences in surface areas of the oxalate powders that were obtained via washing, centrifuging, and subsequent drying and those powders that were obtained only via

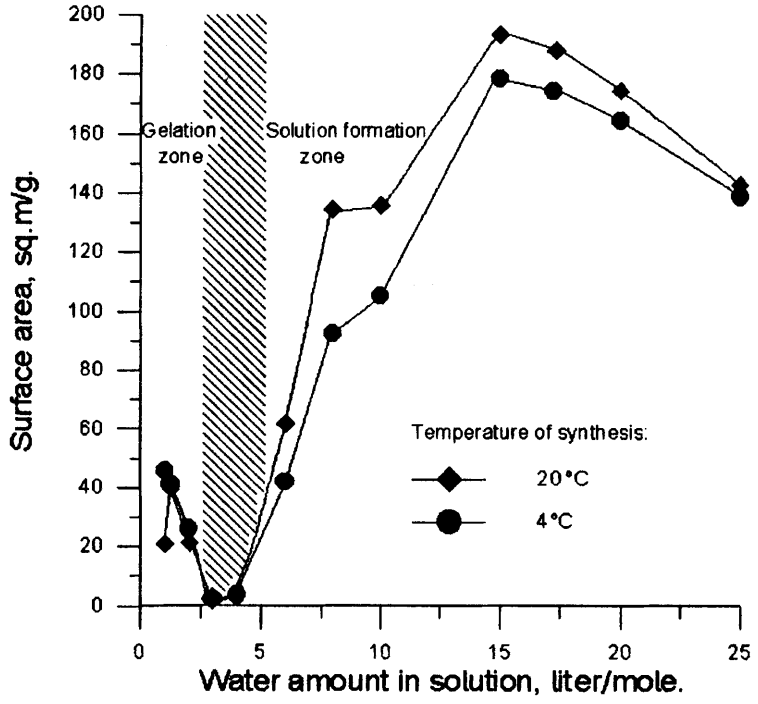

Fig. 2. Dependence of the surface area of the zirconium oxalate powder on the water content in solution during oxalate synthesis.

Table I. Surface Area of Zirconium Oxalate Powders Obtained via Routes 1 and 2, as Described in Fig. 1

Water amount in starting solution (L/mol)	Surface area of the oxalate powder (m^2/g)	
	Washed, centrifuged, and dried	Only dried
1	20.9	4.2
1.25	39.5	6.3
6	61.8	18.2
8	134.6	73.7
10	135.9	118.4

drying. The biggest difference in these two procedures was for the oxalates that were obtained from solutions with a water concentration of <10 L/mol. The standard procedure of filtration could not be used effectively, because the oxalate particle size was 5–8 nm, depending on the water content in the precursor solution, which is too fine for the filter.

There is a strong dependence of the surface area of the oxalate powder, and its particle size, on the water content of the starting solution. Figure 2 shows that a water content of 13–17 L/mol produces an oxalate powder with surface area of 170–196 m^2/g.

The dependence of the surface area of the resulting zirconium oxalate on the synthesis temperature also is shown in Fig. 2. In the gelation zone, the surface area of the resulting oxalate obtained at lower temperature was 10%–30% larger than that resulting from room-temperature synthesis. The surface area of oxalate powders that have been synthesized with 3–4 L of water/(mol of precursor) is almost the same for both temperatures. For water contents of >5 L/mol, the surface area of the oxalate that is obtained under room-temperature conditions is 10%–20% larger than that for the powder that has been processed at a temperature of 4°C. This result implies that processing at the lowest temperatures is not necessary.

(2) Synthesis of Y-Zr Oxalate

After studying the synthesis of zirconium oxalate, Y-Zr oxalate was produced. First, YCl_3 was produced by dissolving Y_2O_3 grains in HCl in concentrations that were useful for Eq. (2). This solution subsequently was dissolved in distilled water. The concentrations of the initial reagents were determined to obtain the final composition of 3 mol% Y_2O_3–97 mol% ZrO_2. Yttrium oxalate formation can be expressed by the reaction

$$2YCl_3 + 3(COOH)_2 \rightarrow Y_2(C_2O_4)_3 + 6HCl \quad (3)$$

The method used to obtain Y-Zr oxalate powder is described in Fig. 1. There were no differences in the processing method used for zirconium oxalate. The surface areas of the zirconium oxalate and Y-Zr oxalate were the same, because the content of YCl_3 in solution was very low and YCl_3 was distributed satisfactorily in the zirconium oxychloride aqueous solution.

Based on the above-described results, Y-Zr oxalate powders with five different surface areas were produced for the following analyses.

(3) TG-DTA Study of Zirconium Oxalate and Y-Zr Oxalate Decomposition

TG-DTA analysis was used to determine the characteristics of nonisothermal decomposition of oxalates with different surface areas and the decomposition with different heating rates to give the maximum surface area. Thermal decomposition of the zirconium oxalates passes through two stages. The first stage is the removal of water, and the second stage is decomposition of the dehydrated oxalate.

Differences in the initial surface area (the particle size of the initial oxalate powders) cause different weight losses during decomposition (6.2 wt% for oxalate with a surface area of 21 m^2/g, and 9.9 wt% for the finest oxalate powder (with a surface area of 196 m^2/g). These differences in the weight loss occur in the water-evaporation stage and can be explained by the fact that the oxalates with a higher surface area have a larger amount of adsorbed water than coarser powder. This observation is confirmed by the negligible differences in weight loss of the oxalates in the decomposition stage.

Figure 3 shows the DTA curves for the thermal decomposition of Y-Zr oxalates with different surface areas. Two endothermic peaks and one exothermic peak are observed. The endothermic peaks represent the water-removal and oxalate-decomposition stages, and the exothermic peak is the amorphous zirconia crystallization stage.

Table II shows the temperature intervals of oxalate decomposition and crystallization, the total weight loss, and the thermal

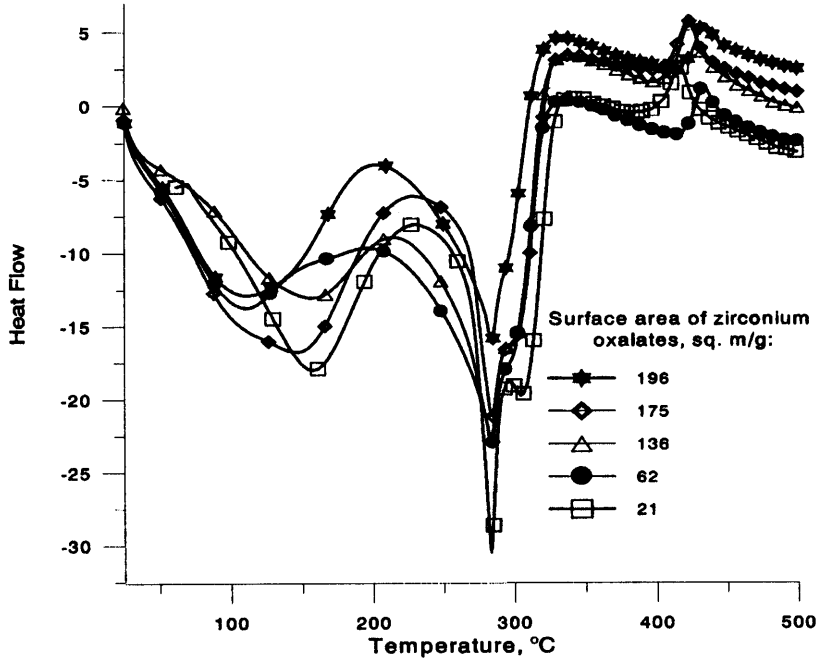

Fig. 3. DTA curves for thermal decomposition of Y-Zr oxalates obtained using various amounts of water per mole of reagents. (Heat-flow values are given in units of μV.)

Table II. Decomposition Temperatures, Weight Losses, and Temperatures of Zirconia Crystallization, for Zirconium Oxalates with Different Surface Areas

Surface area of oxalate powders (m^2/g)	Decomposition temperature interval (°C)	Total weight loss (%)	Thermal effect of decomposition (μV·s/mg)	Crystallization temperature interval (°C)
21	266–297	44.7	−451	410–442
62	258–299	44.9	−372	411–459
136	253–304	45.4	−357	413–456
175	257–308	46.8	−424	421–463
196	254–311	47.1	−395	424–466

effect of oxalates decomposition for different initial surface areas. Some small differences exist in the start and finish temperatures of the decomposition. Oxalates with the finest particles began to decompose earlier than the coarser powders and completed their decomposition at slightly higher temperatures. However, the temperature of the maximal heat flow (283° ± 0.5°C) was the same for all oxalates. The heat flow was greatest for the coarsest oxalate powder and smallest for the finest powder.

The temperature intervals of crystallization increase to higher temperatures as the initial oxalate particle size decreases. However, the thermal effect of crystallization was 71–73 μV·s/mg—almost the same for all oxalates. The temperature at which crystallization was completed for all the oxalate-derived zirconia powders was ≤470°C, if the heating rate was maintained under 60°C/h. If the finest powder decomposed earlier than the coarse powder at the oxalate-decomposition stage, such dependence was not true for the crystallization stage. The coarsest amorphous zirconia began to crystallize at lower temperatures than the finer powder. The zirconia that was obtained from the decomposition of oxalate with an initial surface area of 21 m^2/g had a crystallization temperature of 410°–442°C. The temperature range for zirconia obtained from the oxalate with the maximal surface area (196 m^2/g) was wider (424°–466°C).

The next stage of the investigation was analysis of the data on decomposition of the finest zirconia oxalate with different heating rates. The weight losses during the decomposition of Y-Zr oxalate with heating rates of 60°–600°C/h and using nonlinear heating regimes are shown in Table III. Oxalate powder with a surface area of 196 m^2/g was studied. The general scheme of decomposition was the same as that for the nonisothermal decomposition of oxalates with different initial surface areas. Weight losses in the water-removal stage were largest for the slowest heating rates. As a result, at the oxalate-decomposition and zirconia-synthesis stages, residual carbon monoxide (CO) and carbon dioxide (CO_2) must be removed. The total weight loss was almost the same. The highest temperature for the completion of decomposition was observed for the maximum heating rate, which can explain the maximum value of total weight loss.

The DTA analysis curves for the nonisothermal synthesis of stabilized zirconia powder from Y-Zr oxalate are shown in Fig. 4. Three distinct zones can be defined (as for Fig. 3): water removal, zirconia synthesis, and crystallization of the amorphous zirconia.

The temperature schedule of the oxalate decomposition in different heating regimes also is listed in Table III. The starting decomposition temperatures increased as the heating rates increased. As the heating rate increased, the heat flow also increased, in comparison with the lowest rates, and the temperature intervals of decomposition became the broadest. Decomposition at a heating rate of 60°C/h occurred over a temperature range of 73°C, whereas decomposition at a heating rate of 180°C/h occurred over a temperature range of 120°C. As a result, shifting the synthesis process to a high-temperature zone leads to coarser, aggregated powder, which will be explained in the next section. The properties of nonisothermal synthesis using the control modes (nonlinear heating regimes) will be explained in a later paper, because the control modes summarize the results of all the studies.[9–11]

The crystallization of YSZ amorphous powder (the zirconia crystallization zone in Fig. 4) is shown in Table III. Similar to that for the zirconia synthesis, the crystallization stage also was shifted to higher temperatures as the heating rate was increased. The

Table III. Synthesis of Yttria-Stabilized Zirconia from Y-Zr Oxalate with Different Heating Regimes (Surface Area of 196 m^2/g)

Heating regime	Weight loss (%)		Decomposition temperature interval (°C)	Crystallization temperature interval (°C)	Thermal effect of decomposition (μV·s/mg)
	During water removal	During oxalate decomposition			
60°C/h	8.5	38.6	252–325	446–472	35
120°C/h	6.9	40.2	253–338	455–483	37
180°C/h	6.8	40.3	255–344	453–490	46
600°C/h	6.7	40.4	262–382	459–517	48
Control mode 1	10.4	38.0	253–324	444–475	23
Control mode 2	10.5	37.7	253–319	433–465	24

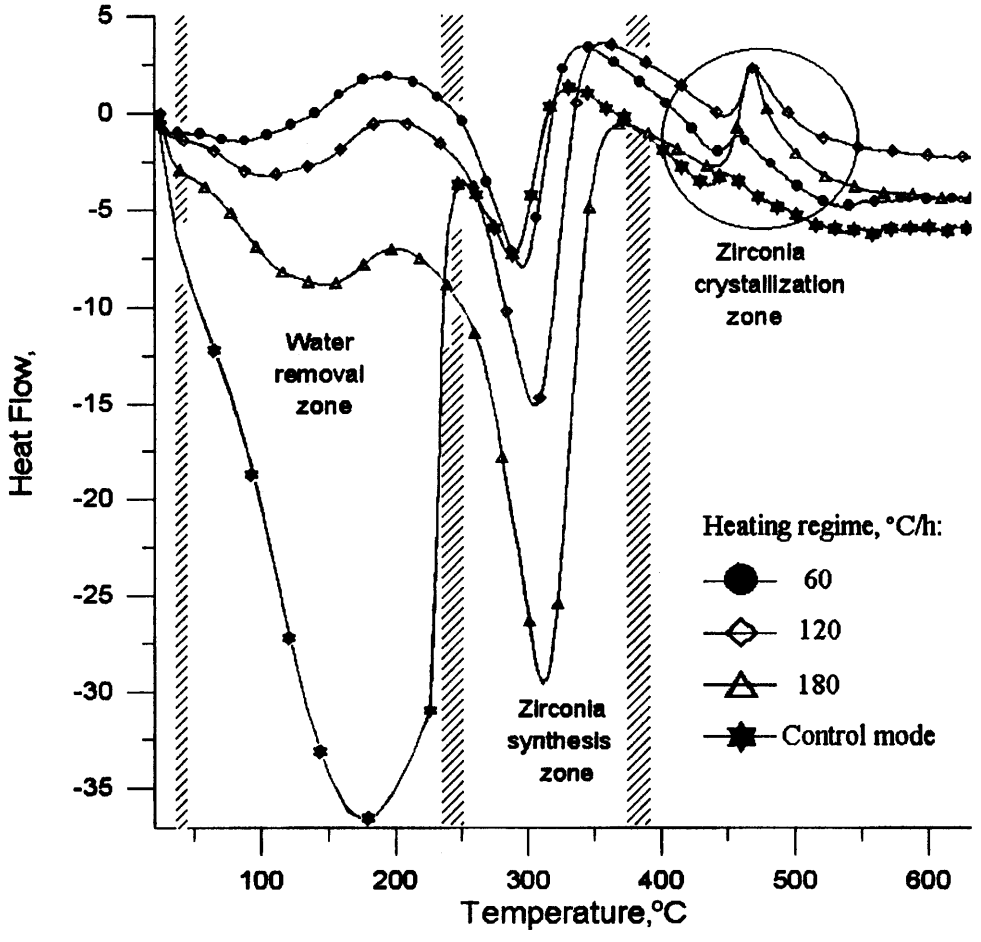

Fig. 4. DTA analysis of the nonisothermal synthesis of stabilized zirconia powder from 3Y-Zr oxalate. (Heat-flow values are given in units of μV.)

temperature intervals of crystallization also became broader. The value of the thermal effect of crystallization is smallest for the finest powder, which was prepared using the nonlinear control mode of decomposition–synthesis.

(4) Nonisothermal Synthesis of Zirconia from Zirconium Oxalate

The nonisothermal decomposition of zirconium oxalates with different surface areas was used to obtain zirconia powders with different properties. Experiments for the decomposition of oxalate powders with different surface areas at a constant heating rate determined that the best particle size, and the best degree of aggregation of the final zirconia powder, corresponded to the finest oxalate powder (synthesized under the optimal conditions). This oxalate powder had the narrowest particle-size distribution and was the most active in subsequent applications.

The evolution of the surface area of the powder during decomposition of the zirconium oxalate and zirconia synthesis under nonisothermal conditions is shown in Fig. 5. Low heating rates (35°–75°C/h) clearly produce the maximum surface area. However, after decomposition was completed under the optimal time–temperature conditions, the surface area began to decrease sharply. This decomposition route is optimal to obtain the finest weakly aggregated amorphous zirconia (nonstabilized) powders. However, amorphous powder is not useful in the further processing, and nonstabilized powders cannot be used for densification of the ceramic without microcracks. The crystallization temperature is higher than the temperature for the maximum surface area (see Tables II and III and Fig. 5). The crystallization temperatures are dependent on the surface area of the starting zirconium and Y-Zr oxalates. For slow heating of YSZ, the zone of crystallization is 440°–470°C and the maximal surface area zone is 300°–375°C. For heating rates of 180°–600°C/h, the completion temperature of zirconia synthesis is higher and the time required for oxalate decomposition is shorter. In such heating regimes, the surface area of the powder has no time to develop and the temperature becomes

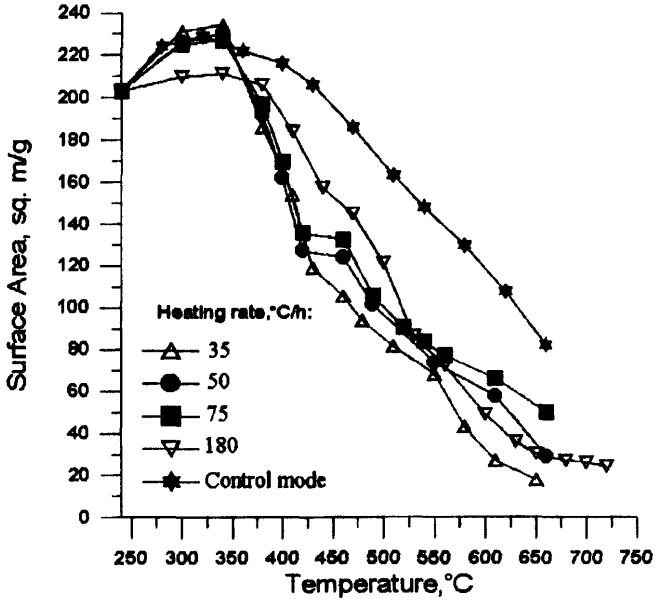

Fig. 5. Evolution of the powder surface area during zirconium oxalate decomposition and zirconia synthesis under nonisothermal conditions.

reasonable for the formation of presintered agglomerates of coarser primary particles. The temperature of crystallization in such heating regimes is 470°–530°C. This high temperature of synthesis completion can be used to obtain fine, nanosized powder; however, this powder is very aggregated and agglomerated. The particle-size distribution and powder-aggregate-size distribution for zirconia powders are shown for oxalates with different surface areas in Table IV. Naturally, powders that have been obtained from coarse, aggregated oxalate also are coarse. The degree of aggregation of such zirconia powder excludes its use in subsequent colloidal processing. The particle-size distribution and aggregate-size distribution for stabilized zirconia powders that have been obtained from the decomposition of Y-Zr oxalate in different heating regimes are shown in Table V.

Smaller crystalline zirconia powder (6–8 nm) can be obtained via decomposition of the oxalate at a heating rate of 35°C/h. However, this heating rate is very slow and the zirconia powders begin to consolidate directly after synthesis. As a result, such powder is very aggregated and further technological application is doubtful. Zirconia powders that have been obtained at heating rates of 50°–75°C/h also are very fine, such that the degree of agglomeration is low enough for further colloidal applications. Such agglomeration conditions exist only for a narrow temperature range of 430°–470°C, beyond which large aggregates develop.

Only controlled nonlinear heating (control mode) can be used to obtain zirconia powder with a narrow particle-size distribution of 8–10 nm and an aggregate size of 70–90 nm. This degree of aggregation of fine primary particles can be retained in the temperature range of 440°–640°C. Control-mode heating is a nonlinear heating regime that can be used for the synthesis of nanocrystalline stabilized zirconia. This method seems to have only advantages over linear heating, because most of its disadvantages can be avoided. Powder that is obtained using control-mode

Table IV. Size Distribution of Particles and Powder Aggregates of Zirconia Powders Obtained from the Oxalates with Different Surface Areas (Heating Rate of 50°C/h)

Surface area of oxalate powder (m^2/g)	Particle-size distribution (nm)	Powder-aggregate-size distribution (nm)
21	60–80	300–700
62	25–30	90–300
136	17–20	90–180
196	8–10	70–80

Table V. Size Distribution of Particles and Powder Aggregates of YSZ Powders Obtained via Oxalate Decomposition in Different Heating Regimes

Heating regime	Particle-size distribution (nm)	Powder-aggregate-size distribution (nm)
35°C/h	6–8	150–230
50°C/h	8–10	70–80
75°C/h	8–10	50–130
180°C/h	15–25	150–400
Control mode	8–10	70–90

Table VI. YSZ Powder-Aggregate-Size Distribution, Relative to the Microtip Treatment Time, for Finest Powder Obtained from the Oxalate, Using the Control Mode

Time of ultrasonic treatment	Powder-aggregate-size distribution (nm)
Without treatment	250–600
1 min	180–230
5 min	100–140
15 min	70–100
30 min	70–90

heating crystallizes at a high temperature (Table III), and the particle size of such powders is large, in comparison with the finest powder that is obtained using linear heating. However, the opportunity to obtain powder that is stable in the temperature range 440°–640°C makes this controlled processing very practical.

The possibility of dispersing soft aggregates using microtip ultrasonic treatment also was studied (see Table VI). Such treatment is important to obtain a uniform colloid, which is required to obtain a green compact with uniform particle distribution via slip casting. A treatment of 10–15 min is concluded to be optimal for dispersion, and longer treatment times are concluded to be ineffective.

IV. Summary

A nontraditional methodology to synthesize nanosized zirconia powder through oxalate processing has been explained. The process of zirconium oxalate synthesis has been optimized. Fine oxalate powder, with a surface area of 196 m^2/g, has been obtained and analyzed via thermogravimetry and differential thermal analysis. The methodology of nonisothermal oxalate decomposition to obtain nanopowders with narrow particle-size and aggregate-size distributions has been discussed. Data for the synthesis of zirconia powders in linear heating regimes have been included. Controlled nonlinear heating modes have been developed and optimized to obtain zirconia nanopowder with a particle size of 8–10 nm and aggregates 70–90 nm in size. Such limited aggregation can be achieved over a broad range of temperatures.

This methodology is useful to obtain nanopowders, which can be used for further colloidal processing, such as pressure filtration and slip casting. The oxalate process is useful for the synthesis of zirconia nanopowder, as well as stabilized and composite fine powders with precise stoichiometry and a low degree of aggregation.

Acknowledgment

The authors acknowledge Mr. Benjamin Hatton for his helpful suggestion in editing of this paper.

References

[1]F. F. Lange, "Powder Processing Science and Technology for Increased Reliability," *J. Am. Ceram Soc.*, **72** [1] 3–15 (1989).

[2]T. Uchikoshi, Y. Sakka, K. Ozawa, and K. Hiraga, "Pressure Filtration and Sintering of Fine Zirconia Powder," *J. Eur. Ceram Soc.*, **18** [6] 669–74 (1998).

[3]K. Lee, A. Sathyagal, P. W. Carr, and A. V. McCormick, "Synthesis of Zirconia Colloids from Aqueous Salt Solutions," *J. Am. Ceram. Soc.*, **82** [2] 338–42 (1999).

[4]P. C. Rivas, J. A. Martinez, M. C. Caracoche, A. M. Rodríguez, A. R. López García, R. S. Pavlik Jr., and L. C. Klein, "Evolution of the Phase Content of Zirconia Powder Prepared by Sol–Gel Acid Hydrolysis," *J. Am. Ceram. Soc.*, **81** [1] 200–204 (1998).

[5]C. L. Ong, J. Wang, S. C. Ng, and L. M. Gan, "Effects of Chemical Species on the Crystallization Behavior of a Sol-Derived Zirconia Precursor," *J. Am. Ceram. Soc.*, **81** [10] 2624–28 (1998).

[6]E. Tani, M. Yoshimura, and S. Sōmiya, "Formation of Ultrafine Tetragonal ZrO_2 Powder under Hydrothermal Conditions," *J. Am. Ceram. Soc.*, **66** [1] 11–14 (1983).

[7]C. L. Ong, J. Wang, L. M. Gan, and S. C. Ng, "Crystallization in Nanosized Sol-Derived Zirconia Precursors," *J. Mater. Sci. Lett.*, **15**, 1680–83 (1996).

[8]S. van der Gijp, L. Winnubst, and H. Verweij, "Peroxo-oxalate Preparation of Doped Barium Titanate," *J. Am. Ceram. Soc.*, **82** [5] 1175–80 (1999).

[9]O. Vasylkiv, "Synthesis, Morphology Evolution and, Sintering of Nano-size Barium-Titanate Powders in Nonisothermal Conditions"; Ph.D. Thesis. Kiev, Ukraine, 1997.

[10]A. Ragulya, O. Vasylkiv, and V. Skorokhod, "Synthesis and Sintering of Nanocrystalline Titanate Powder under Nonisothermal Conditions: I. Dispersity Control during Barium Titanate Synthesis from Barium-Tytanil Oxalate," *Powder Metall. Met. Ceram.*, **389** [3/4] 56–63 (1997).

[11]O. Vasylkiv, A. Ragulya, and V. Skorokhod, "Synthesis and Sintering of Nanocrystalline Titanate Powder under Nonisothermal Conditions: II. Phase Analysis of Barium-Tytanil Oxalate Decomposition Products," *Powder Metall. Met. Ceram.*, **390** [5/6] 48–55 (1997).

[12]K. Higashi, K. Sonoda, H. Ono, S. Sameshima, and Y. Hirata, "Synthesis and Sintering of Rare-Earth-Doped Ceria Powder by the Oxalate Coprecipitation Method," *J. Mater. Res.*, **14** [3] 342–48 (1999).

[13]N. Kuschevskaia, "Highly Dispersed Composite Powder Fe-Cu, Obtained by Thermo-chemical Method from Oxalates," *Powder Metall. Met. Ceram.*, **402** [7/8] 47–50 (1998).

[14]J. Van Herle, T. Horita, T. Kawada, N. Sakai, H. Yokokawa, and M. Dokiya, "Fabrication and Sintering of Fine Yttria-Doped Ceria Powder," *J. Am. Ceram. Soc.*, **80** [4] 933–40 (1997).

[15]W. Luan, L. Gao, and J. Guo, "Study on Drying of Nanoscale Powder Preparation," *Nanostruct. Mater.*, **10** [7] 1119–25 (1998). □

This page intentionally left blank

journal

J. Am. Ceram. Soc., 83 [9] 2227–30 (2000)

Calcium- and Lanthanum-Modified Lead Titanate (PCLT) Ceramic and PCLT/Vinylidene Fluoride-Trifluoroethylene 0-3 Nanocomposites

Q. Q. Zhang, H. L. W. Chan, Q. F. Zhou, and C. L. Choy

Department of Applied Physics and Materials Research Center, Hong Kong Polytechnic University, Hung Hom, Kowloon, Hong Kong

Calcium- and lanthanum-modified lead titanate (PCLT) powders with size in the nanometer range were prepared by a sol–gel process. The PCLT gel was annealed at 850°C to produce powder with an average particle diameter of 80 nm. A dense and fine-grained PCLT ceramic, with grain size of ~0.7 μm, was prepared by sintering the sol–gel-derived powder at 1150°C. The piezoelectric and pyroelectric properties of the PCLT ceramic varied linearly with the degree of poling in the ceramic. PCLT/vinylidene fluoride-trifluoroethylene (P(VDF-TrFE)) 0-3 nanocomposites with PCLT volume fractions of 0.1–0.5 were fabricated, using PCLT powders imbedded in a P(VDF-TrFE) matrix. The ceramic data were used to model the piezoelectric and pyroelectric properties of the PCLT/P(VDF-TrFE) composites, and good agreements were obtained.

I. Introduction

LEAD TITANATE (PT) is an important ferroelectric ceramic for pyroelectric and acoustic sensor applications. When PT is modified with lanthanum or calcium to form PLT or PCT, the permittivity (ε) increases and the Curie temperature (T_c) and tetragonality decrease. Moreover, the coercive field drops, and the pyroelectric coefficient exceeds that of PT.[1,2] In the conventional mixed-oxide method, the PCLT particles formed by ball milling and calcination at high temperature are too large for thin-film integrated sensor applications. Recently, the sol–gel process has attracted considerable interest, because it can be used to prepare nanocrystalline powders and large-area homogeneous thin films at a relatively low temperature.[3–6] We are interested in determining the properties of lanthanum- and calcium-modified PT (PCLT), because we have incorporated PCLT nanocrystalline powders into a vinylidene fluoride-trifluoroethylene (P(VDF-TrFE)) copolymer to form 0-3 nanocomposites for integrated pyroelectric sensor applications.[7] Data for the PCLT ceramic are required for modeling the properties of the PCLT/P(VDF-TrFE) composites.

In this study, PCLT nanocrystalline powder was prepared by a sol–gel process. The ceramic was formed by sintering the nanocrystalline powder at various temperatures. The dielectric permittivity and the piezoelectric and pyroelectric properties of the PCLT ceramic were measured and modeled. The piezoelectric coefficient, d_{33c}, and pyroelectric coefficient, p_c, of the ceramic (subscript "c" denotes the ceramic phase) were measured, as a function of the degree of poling, α_c, in the ceramic. 0-3 composites were fabricated, and the ceramic phase inside the composites was poled and the piezoelectric and pyroelectric properties of the composites measured.

II. Experimental Procedure

PCLT nanocrystalline powders ($(Pb_{0.88}Ca_{0.04}La_{0.08})Ti_{0.98}O_3$) were prepared[8] using the procedure shown in Fig. 1. Lead acetate trihydrate ($Pb(CH_3COO)_2 0.3H_2O$) and lanthanum nitrate ($La(NO_3)_3 \cdot nH_2O$) were dissolved in methanol (CH_3OH) at 70°C, and calcium acetate ($Ca(CH_3COO)_2 \cdot nH_2O$) was dissolved in deionized water, also at 70°C. After these two solutions had been mixed in a reaction flask, under stirring, CH_3COOH and $C_5H_8O_2$ were added to the solution, to prevent partial hydrolysis. The mixture was cooled to 50°C, a stoichiometric amount of tetrabutyl titanate ($Ti(OC_4H_9)_4$) was added, and the solution was refluxed at 70°C for ~3 h. The solution was then cooled to room temperature, under stirring, for 2 h, thereby forming a Pb-Ca-La-Ti complex solution. A gel was obtained by controlling the hydrolysis condition of the PCLT solution, in which the pH was adjusted to ~11 by adding water, ammonia, and alcohol. The gel was dried at 100°C for 24 h and then heated to a designated temperature, to produce PCLT powder. In our previous study[8] on the characteristics of PCLT powders produced by different annealing temperatures, we found that the (002) and (200) peaks in the X-ray diffraction pattern were well split when the gel was annealed at 850°C, indicating that tetragonal crystallites had formed. The PCLT powder used in subsequent study was annealed at 850°C

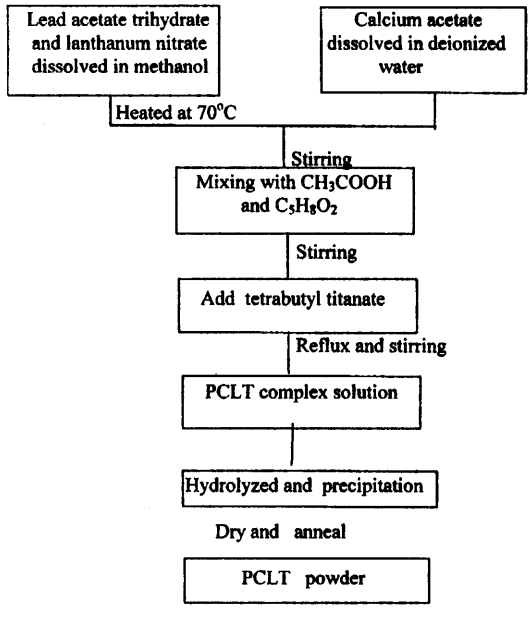

Fig. 1. Flow chart showing the procedure for preparing PCLT nanocrystalline powder by the sol–gel process.

P. P. Phule—contributing editor

Manuscript No. 189630. Received January 13, 1999; approved March 13, 2000.
Supported by the Hong Kong Polytechnic University Postdoctoral Scheme, Centre for Smart Materials, and partially by a grant from the Industry Department of the Hong Kong Special Administrative Region (ISF Project No. AF/147/98).

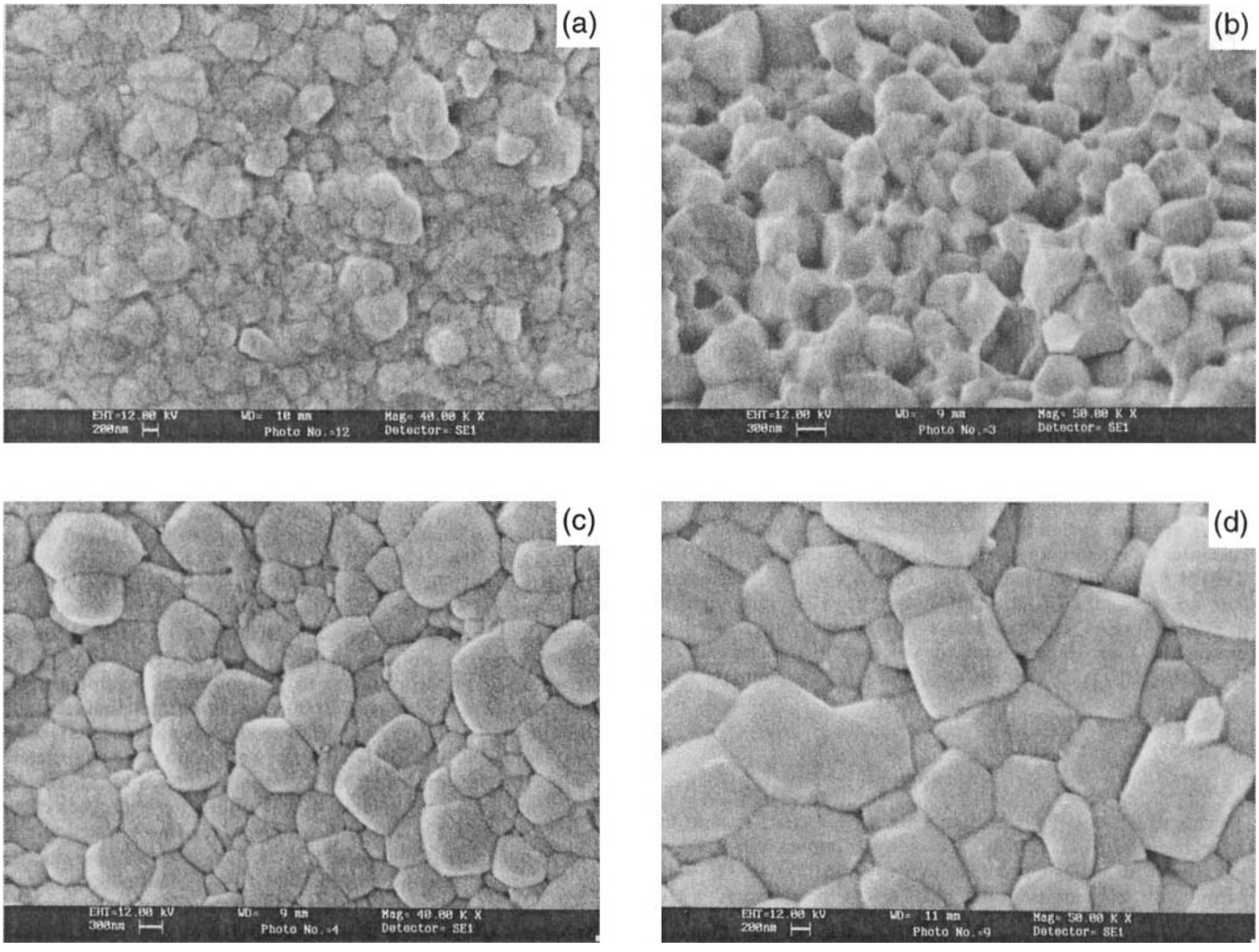

Fig. 2. SEM photographs of the fractured surface of PCLT ceramic sintered at (a) 1100°, (b) 1150°, (c) 1200°, and (d) 1250°C.

and had an average particle diameter of ~80 nm, as determined using a particle-size-distribution analyzer (Model No. Capa-700, Horiba, Ltd., Tokyo, Japan).

The PCLT powder was mixed with a binder and pressed into disk-shaped samples. Each disk was heated to ~700°C, to remove the binder, and then placed in a sealed alumina crucible with some PCLT powder in it and sintered at 1100°, 1150°, 1200°, or 1250°C for 2 h, after which the samples were polished. The resulting disks were ~0.32 mm thick and 8 mm in diameter.

To prepare 0-3 composites, P(VDF-TrFE) 70/30 mol% copolymer (T_c = 105°C, from Piezotech S.A., Saint-Louis, France) was dissolved in methyl-ethyl ketone, and a suitable amount of PCLT nanocrystalline powder then was blended into the solution. The powder in the mixture was dispersed in an ultrasonic bath before it was poured onto a petri dish. After the solvent had evaporated, the mixture was molded into a 0.2 mm thick sheet, by pressing at 200°C at a pressure of 50 kg/mm.[2] Square samples (10 mm × 10 mm) were cut from the sheet. Composites with a PCLT volume fraction, ϕ, of 0.1–0.5 were fabricated.

The fractured surfaces of the ceramic and composite samples were examined by scanning electron microscopy (SEM; Model No. Stereoscan 440, Leica Cambridge, Cambridge, U.K.). The degree of poling in the PCLT ceramic and the composite was measured by X-ray diffractometry (XRD; X'pert XRD system, Philips Analytical Products, Almelo, The Netherlands) with nickel-filtered Cu$K\alpha$ radiation. For electrical measurements, air-dried silver-paint electrodes were applied to both sides of the PCLT ceramic and the composite samples. The relative permittivity of the samples was measured at 1 kHz, using an impedance analyzer (Model No. HP4194A, Hewlett–Packard Co., Palo Alto, CA). The PCLT and composite samples were poled, by applying a dc voltage; the piezoelectric coefficient was measured, using a piezo d_{33} tester (Model No. Pennebaker 8000, American Piezo-Ceramic, Ltd., Mackeyville, PA), and the pyroelectric coefficient was measured, using a digital integration technique.[9] The measured pyroelectric coefficient contains the contributions from both the primary and the secondary pyroelectric effects, because these two effects are hard to separate.

III. Results and Discussion

(1) Microstructure and Properties of the PCLT Ceramic

Figure 2 shows SEM photographs of the fracture surfaces of the PCLT samples sintered at various temperatures. The sample sintered at 1250°C has the largest grain size; the sample sintered at 1150°C has an average grain size of ~0.7 μm, which is finer than the grain size of the ceramic prepared by the mixed-oxide technique (usually ~3–5 μm).

The PCLT samples were poled in an oil bath at 120°C, with various dc voltages, and the electric parameters were measured after the samples had been short-circuited and annealed for 17 h at 50°C. The ceramic degree of poling, α_c, was calculated from the peak height of the (200) and (002) X-ray reflections associated with the PCLT poled at 120°C under various poling fields, E, using the relation:[10]

$$\alpha_c = 1 - (I_{(002)}/I_{(200)})(I'_{(200)}/I'_{(002)}) \quad (1)$$

where $I'_{(200)}$ and $I'_{(002)}$ are the intensities of the (200) and (002) peaks after poling and $I_{(200)}$ and $I_{(002)}$ the intensities before poling.

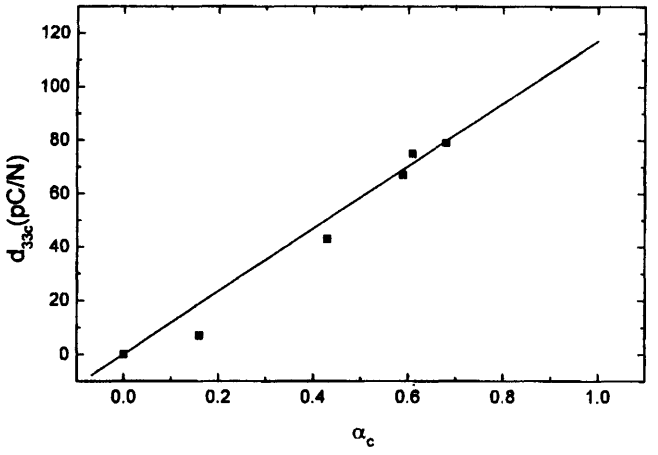

Fig. 3. Piezoelectric coefficient, d_{33c}, of PCLT ceramic sintered at 1150°C, as a function of the degree of poling, α_c ((■) experimental data; (—) best fit).

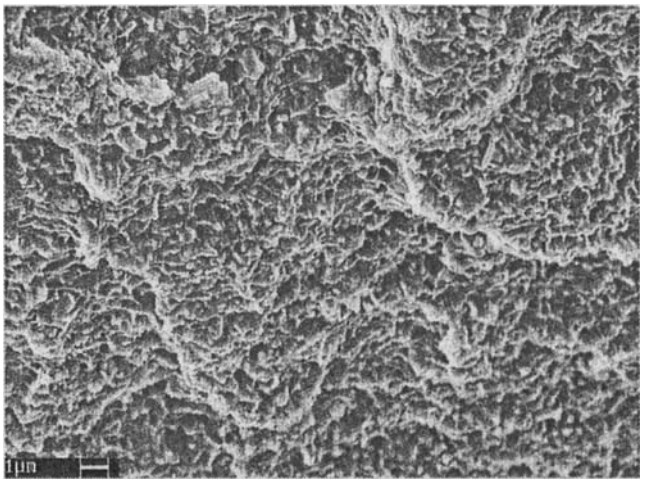

Fig. 5. SEM photograph of the fractured surface of PCLT/P(VDF-TrFE) composite with $\phi = 0.23$.

For the PCLT ceramic sintered at 1150°C and poled at 120°C, under a field of 6.8 kV/mm, $\alpha_c = 0.68$. This ceramic also has the lowest permittivity (436) and the highest piezoelectric (79 pC/N) and pyroelectric (330 μC/m^{2}K) coefficients. Variation of the room-temperature piezoelectric and pyroelectric coefficient of the PCLT sintered at 1150°C, as a function of α_c, is shown in Figs. 3 and 4, and a direct proportional relationship is observed. When fully poled, the ceramic should have $d_{33c} = 116$ pC/N and $p_c = 485$ μC/m^{2}K. These data are used in subsequent composite modeling.

(2) Microstructure and Properties of the PCLT/P(VDF-TrFE) 0-3 Composites

Figure 5 is an SEM photograph of the fracture surface of a PCLT/P(VDF-TrFE) nanocomposite with a 0.23 volume fraction of ceramic. The PCLT particles are roughly spherical and dispersed rather uniformly inside the polymer matrix, and no large agglomerations can be observed. The permittivity of the composites can be modeled by the Bruggeman equation,[11,12]

$$(\varepsilon_c - \varepsilon)/(\varepsilon)^{1/3} = (1 - \phi)(\varepsilon_c - \varepsilon_p)/(\varepsilon_p)^{1/3} \quad (2)$$

where ϕ is the volume fraction of the ceramic, and the subscripts "c" and "p" denote the ceramic and the copolymer phase, respectively. Figure 6 shows the measured ε value and the ε value calculated using Eq. (2), with $\varepsilon_p = 13.2$ (measured value) and $\varepsilon_c = 303.5$ (fitted value). The ε_c value that gives a best fit to the experimental data is different from that measured for the PCLT bulk ceramic ($\varepsilon_c = 436$ for PCLT sintered at 1150°C). This result shows that the permittivity of ceramic powder differs from that of the bulk ceramic, presumably because of the lack of large domains and grain boundaries when the ceramic is in a powder form.

The composites were next poled at 120°C in an oil bath, under various electric fields. The local field experienced by the ceramic particles inside the polymer matrix can be estimated by $L_E E$, and the local field coefficient, L_E, is given by:[13]

$$L_E = 3\varepsilon/(2\varepsilon + \varepsilon_c) \quad (3)$$

where ε_c and ε are the permittivity of the ceramic and the composite, respectively. The values of E that the composite can withstand without breakdown decrease with ϕ and are shown in Table I, together with the calculated α_c (by Eq. (1)) and L_E (by Eq. (3), using $\varepsilon_c = 303.5$). The field was maintained for 2 h at 120°C, to pole the ceramic, and then switched off before the sample was cooled to room temperature. Because the field was switched off at 120°C, which is above the T_c value of the copolymer (105°C) while it is still in a paraelectric phase, the copolymer phase should have remained unpoled and the composites should have had only the ceramic phase poled. To further confirm this phenomenon, a piece of copolymer was poled using a similar procedure, and no observable piezoelectric and pyroelectric properties were detected.

For 0-3 composites with a passive matrix, Yamazaki and Kitayama[10] and Yamada *et al.*[14] used the following equations to estimate d_{33} and p:

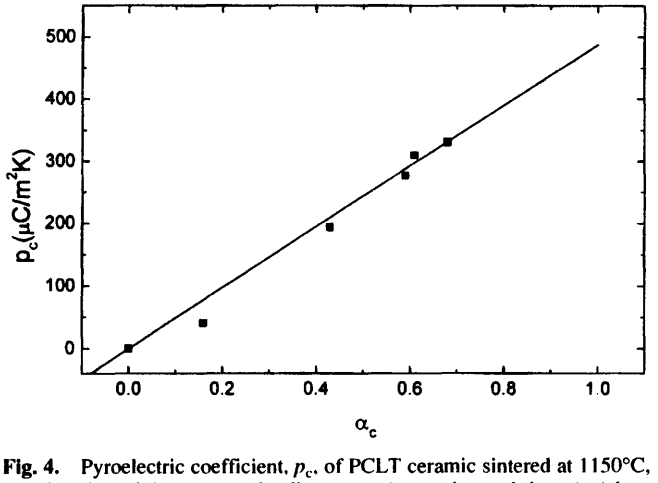

Fig. 4. Pyroelectric coefficient, p_c, of PCLT ceramic sintered at 1150°C, as a function of the degree of poling, α_c ((■) experimental data; (—) best fit).

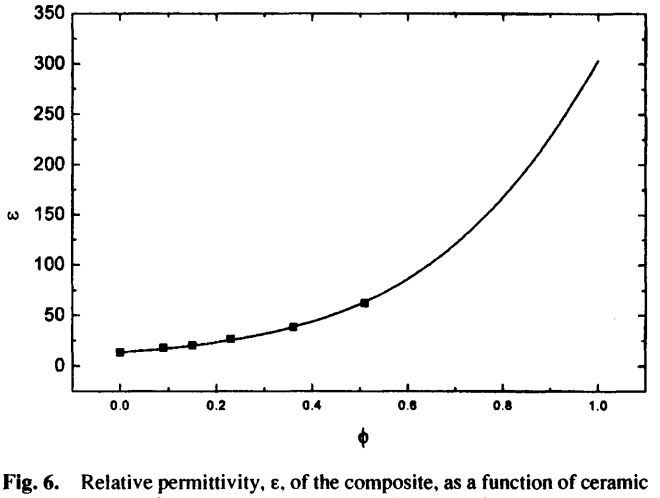

Fig. 6. Relative permittivity, ε, of the composite, as a function of ceramic volume fraction, ϕ ((■) measured data; (—) best fit, using the Bruggeman model, with $\varepsilon_c = 303.5$).

Table I. Properties of PCLT/P(VDF-TrFE) Composites with Various Volume Fractions of Ceramic (ϕ)

ϕ	E (kV/mm)	α_c	L_E
0.09	59	0.708	0.157
0.15	51	0.834	0.176
0.23	48	0.819	0.220
0.36	43	0.886	0.302
0.51	38	0.871	0.436

$$d_{33} = \phi \alpha_c L_E d_{33c} \quad (4)$$

$$p = \phi \alpha_c L_E p_c \quad (5)$$

Here, L_E is the local field coefficient, given by Eq. (3). For ϕ = 1, the values $\alpha_c d_{33c}$ = 79 pC/N and $\alpha_c p_c$ = 330 μC/m^{2}K are used. Figures 7 and 8 show that the measured data and the calculated values agree quite well.

IV. Conclusions

PCLT nanocrystalline powder was prepared using a sol–gel process. Dense PCLT ceramics with fine grain sizes were obtained by sintering the powder at various temperatures. The permittivity and piezoelectric and pyroelectric coefficients of the PCLT ceramic sintered at 1150°C were used as a reference in modeling the properties of PCLT/P(VDF-TrFE) 0-3 composites. The permittivity of the ceramic powder obtained from fitting the data to the Bruggeman equation was smaller than that measured in the bulk ceramic. The measured values of the piezoelectric and pyroelectric coefficients agreed quite well with the calculated values. Work is in progress toward developing theoretical models to predict the properties of 0-3 composites with both phases ferroelectric, and those results will be reported in the near future.

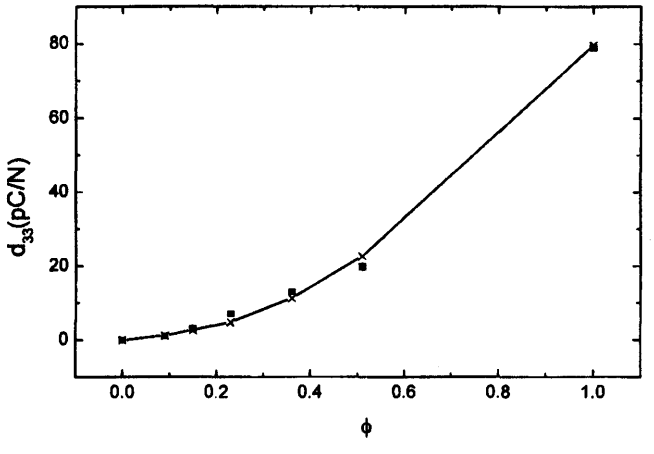

Fig. 7. Piezoelectric coefficient, d_{33}, of the composite, as a function of ceramic volume fraction, ϕ ((■) measured data; (—) curve calculated using Eq. (4)).

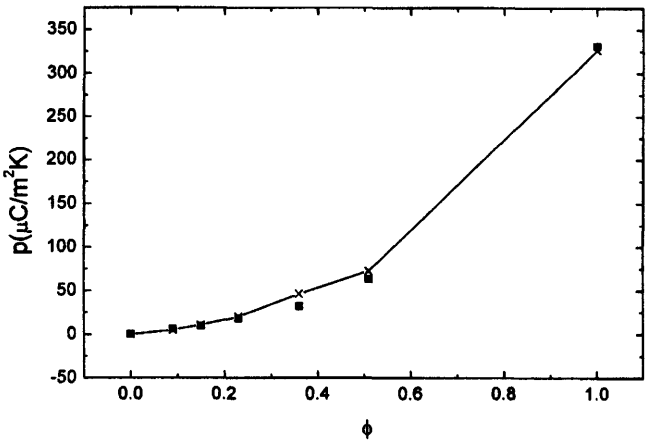

Fig. 8. Pyroelectric coefficient, p, of the composite, as a function of ceramic volume fraction, ϕ ((■) measured data; (—) curve calculated using Eq. (5)).

References

[1]J. Mendiola, C. Alemany, L. Pardo, B. Jiménez, and L. Del Olmo, "Ferropiezoelectricity of Calcium-Modified Lead Titanate Ceramics," *J. Mater. Sci.*, **22**, 4395–97 (1987).

[2]K. Kani, H. Murakami, K. Watari, A. Tsuzuki, and Y. Torii, "Sol–Gel Processing and Pyroelectric Properties of Lanthanum-Modified $PbTiO_3$ Thin Films," *J. Mater. Sci. Lett.*, **11**, 1605–607 (1992).

[3]C. D. E. Lakeman and D. A. Payne, "Processing Effects in the Sol–Gel Preparation of PZT Dried Gels, Powders, and Ferroelectric Thin Layers," *J. Am. Ceram. Soc.*, **75** [11] 3091–96 (1992).

[4]Y. Xu and J. D. Mackenzie, "Ferroelectric Thin Films Prepared by Sol–Gel Processing," *Integr. Ferroelectr.*, **1**, 17–42 (1992).

[5]S. K. Dey and R. Zuleeg, "Integrated Sol–Gel PZT Thin Films on Pt, Si, and GaAs for Nonvolatile Memory Applications," *Ferroelectrics*, **108**, 37–46 (1990).

[6]M. D. Carper and P. P. Phule, "Preparation of Oriented Thin Films Using a Spin-On Sol–Gel Process," *Appl. Phys. Lett.*, **63** [2] 153–55 (1993).

[7]Q. Q. Zhang, H. L. W. Chan, and C. L. Choy, "Dielectric and Pyroelectric Properties of P(VDF-TrFE) and PCLT/P(VDF-TrFE) 0-3 Nanocomposite Films," *Composites A (Guildford, U.K.)*, **30**, 163–67 (1999).

[8]Q. F. Zhou, X. G. Tang, L. S. Yin, J. X. Zhang, H. L. W. Chan, Q. Q. Zhang, and C. L. Choy, "Nanocrystalline Powder and Thin Films of Calcium and Lanthanum-Modified Lead Titanate by the Sol–Gel Process," *J. Korean Phys. Soc.*, **32** [2] S-1380–S-1382 (1998).

[9]Y. Xu, *Ferroelectric Materials and Their Applications*; pp. 68–71. Elsevier Science Publishers, Amsterdam, The Netherlands, 1991.

[10]H. Yamazaki and T. Kitayama, "Pyroelectric Properties of Polymer-Ferroelectric Composite," *Ferroelectrics*, **33**, 147–53 (1981).

[11]D. A. G. Bruggeman, "Berechnung Verschiedener Physikalischer Konstanten von Heterogenen Substanzen," *Ann. Phys. (Leipzig)*, **24**, 636–79 (1935).

[12]L. K. H. van Beek, "Dielectric Behavior of Heterogeneous Systems"; pp.69–14 in *Progress in Dielectrics*, Vol. 7. Heywood, London, U.K., 1967.

[13]L. D. Landau and E. M. Lifshitz, "Course of Theoretical Physics"; Ch. 2, Vol. 8 in *Electrodynamics of Continuous Media*. Pergamon Press, U.K., 1960.

[14]T. Yamada, T. Ueda, and T. Kitayama, "Piezoelectricity of a High-Content Lead Zirconate Titanate/Polymer Composite," *J. Appl. Phys.*, **53**, 4328–32 (1982). □


Ceramic
Transactions

This page intentionally left blank

PREPARATION AND CHARACTERIZATION OF IRON OXIDE-ZIRCONIA NANO POWDER FOR ITS USE AS AN ETHANOL SENSOR MATERIAL

C V Gopal Reddy* and S A Akbar
CISM, Dept. of Materials Science & Eng.
The Ohio State University
Columbus, OH 43210
USA.
*e-mail: chada@cism.ohio-state.edu

W Cao, O K Tan and, W Zhu
Sensors & Actuators Lab
School of EEE
Nanyang Technological University
Singapore-639798

ABSTRACT

Powders of composition $xZrO_2$-(1-x)Fe_2O_3 were prepared by several methods such as high-energy ball milling, co-precipitation and hydrazine methods. This paper presents the effect of the preparation methods and annealing temperatures on the ethanol gas sensitivity. Noble metals such as Pt and Pd were added in order to examine the effects on ethanol gas sensitivity. Sensors based on 1wt.% Pt + $xZrO_2$- (1-x)Fe_2O_3 demonstrated an excellent sensing performance at 230 °C for 1000 ppm of ethanol. The gas-sensing behavior of these materials to various reducing gases like CO, CH_4 and H_2 was also studied. This sensor showed good selectivity toward ethanol and thus could effectively be used as a breath sensor.

INTRODUCTION

Nano materials is a broad and interdisciplinary area of research that has seen tremendous growth in the past several years. Recent interest in nano-structured materials has been stimulated by the work of Gleiter[1] on materials produced by the gas condensation method. The method of high-energy ball milling has also received significant attention in recent years for nano particle formation. The nano-crystalline materials are usually considered to be of meta-stable nature due to high interfacial and grain boundary energies. Hence their structure and properties depend on the preparation method, as well as the time-temperature history. They show distinct properties due to different atomic structures in the interfacial region.[2] When the size of the crystals becomes smaller than a critical value, the property changes can be dramatic leading to the possibility of creating materials with unusual functionality engineered through size control.[3] Nano-crystals have been prepared for many years by chemical means such as sol-gel,

hydrothermal, and precipitation techniques.[4,5] The size of the grains in a nano-structured material has pronounced effects on many of its properties, the best known being the increase in strength and hardness. This dependence of properties on grain size is of utmost importance in the control of material synthesis and processing.

Fine particles of ferrites have been of interest due to their applications in the preparation of high-density ferrite cores, as suspension materials in ferromagnetic liquids, and as catalysts. Among these, iron oxides in particular are technologically useful as pigments and semiconductors, and also for their magnetic properties.[6] The stability and semiconducting properties of α-Fe_2O_3 allows it to be used as a photo catalyst.[7,8] Semiconducting thick films of Fe_2O_3 have been studied earlier as a sensor for CH_4, H_2 and NH_3.[9] Cantalini et al.[10,11] have also reported α-Fe_2O_3 based gas sensors. Dong et al.[12] have prepared nano-sized particles of pure γ-Fe_2O_3 by H_2-Ar arc plasma. Thick films of these sensors were shown to be sensitive to NH_3. Zeng et al. have studied high stability γ-Fe_2O_3 as a possible gas sensor for detecting several reducing gases.[13] SnO_2-Fe_2O_3 thin films have also been reported as effective humidity sensor.[14] Some researchers also reported tin doped α-Fe_2O_3 systems for sensing CH_4, CO gases.[15,16] This paper reports sensing performance of $xZrO_2$-$(1-x)Fe_2O_3$ systems.

EXPERIMENTAL

Zirconia (0.1 M) doped iron oxide (0.9 M) was prepared by high-energy ball milling from a mixture of hematite (α-Fe_2O_3) (Alfa, 99.9 %) and zirconia (m-ZrO_2) (Alfa, 99.9 %) as explained in our earlier paper.[17] In the co-precipitation method, 0.9M iron nitrate, $(Fe(NO_3)_3.\ 9H_2O$ (Merck, 99 %) and 0.1M zirconium tetra chloride, $ZrCl_4$ (Aldrich, 99 %) were taken and dissolved in deionized water (18 MΩ). Ammonia (25 %) solution was added slowly drop by drop to the above mixture solution with continuous stirring. The pH value was adjusted to around 7.5 so as to obtain a complete precipitation. The stirring was then stopped and the precipitate was allowed to settle. The products were removed from the filtration and washed with deionized water until no nitrate and chloride ions were detected by a brown ring test and silver nitrate solution. The products were dried in an oven at 120 °C for overnight.

In the hydrazine method, 0.9M ferric nitrate nano hydrate ($Fe(NO_3)_3.9H_2O$, 0.1M zirconium tetra chloride ($ZrCl_4$) and hydrazine mono hydrate ($(NH_2)_2H_2O$) (TCI, 98%) were used as the starting materials. Ferric nitrate and zirconium tetra chloride solution were prepared by dissolving above amounts in 0.1M of deionized water (18 MΩ). This aqueous solution (pH=1.86) was poured in a beaker and was stirred on a magnetic stirrer at 60 ^{0}C for 30 minutes. Hydrazine monohydrate 0.8M was added slowly to the nitrate solution through a pipette by maintaining a constant stirring until the resulting precipitate reached to pH= 8.[18]

The precipitate was separated by filtering, washed more than 15 times in deionized water to remove the adsorbed hydrazine, chloride and nitrate ions, and then dried in air. The details of the preparation procedure for these three routes are shown in Figure 1.

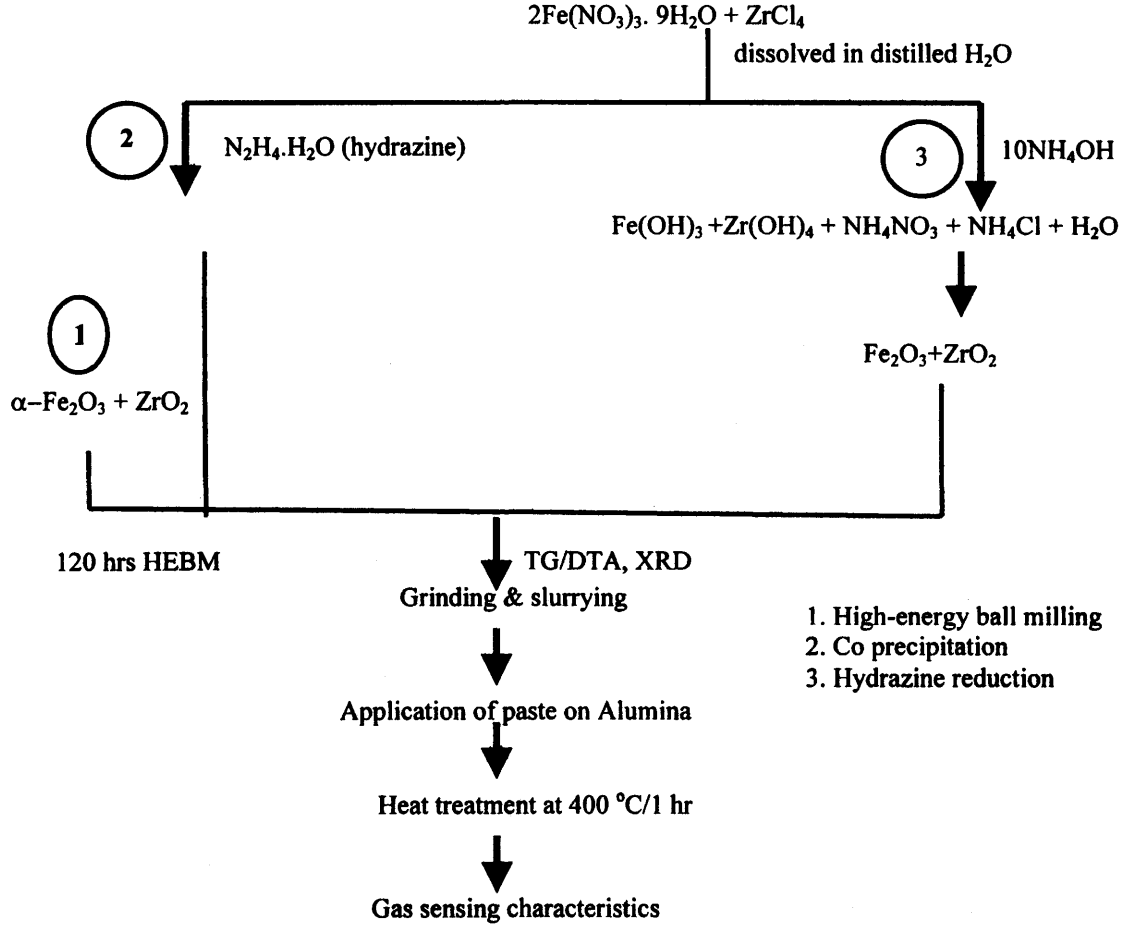

Figure 1. Flow-chart for the preparation of the sensor device: (1) high energy ball milling; (2) co-precipitation and (3) hydrazine reduction.

Thoroughly washed and dried material was then subjected to thermal gravimetric-differential thermal analysis (TGA/DTA) and X-ray diffraction (XRD). Perkin-Elemer TGA-7 and DTA-7 were used to measure the thermal properties of the materials. TG/DTA was conducted in air at a heating rate of 10 °C/min in the temperature range from the room temperature (RT) up to 1000 °C; α-Al_2O_3 was used as the reference. These materials were studied by using a Rigaku X-ray diffractometer (CuK_α radiation, λ=1.5406 Å). Pastes of these materials were prepared using a commercial organic vehicle 400 (from ESL) and

screen-printed onto Al_2O_3 substrates with inter-digital Au electrodes. The samples were then annealed at temperatures from 400 °C to 600 °C for an hour in air. The gas sensing properties were measured by using a computer-controlled gas sensing characterization system.

RESULTS AND DISCUSSION

Characterization of Material

Figure 2(a) shows the TGA-DTA curves of as-prepared $xZrO_2$-(1-x)Fe_2O_3 material by high energy ball-milling method. There is a small weight loss (loss of surface water) observed from RT up to about 850 °C. At 850 °C, a significant weight loss was observed with a total loss of about 8 %. The DTA data shows a small endothermic peak around 850 °C consistent with TGA data.

The TGA data of as prepared powder by the co-precipitation method shows a total loss of 9 % on heating (Figure 2b). The weight loss amounting to 3.5% from RT up to 100 °C is due to the loss of surface water. The rest of the weight loss up to 300 °C is due to the loss of hydroxyl groups from the powder. The DTA data shows the associated endothermic peaks at 100 °C and 255 °C, respectively. It also shows a sharp exothermic peak at 340 °C, which is attributed to a change from the amorphous to the crystalline phase.

The TG-DTA data of $xZrO_2$-(1-x)Fe_2O_3 prepared from hydrazine is shown in Figure 2(c). An endothermic peak appears at 103 °C representing the loss of surface water. An exothermic peak appears at 273 °C that corresponds to a phase change from Fe_2O_3 (Maghemite-Q) to α-Fe_2O_3. Note that the endothermic peak associated with the loss of hydroxyl group is missing because this method directly produces oxides. Another small exothermic peak observed at 725 °C without any associated change in the weight loss may be due to phase transformation in ZrO_2.

The XRD patterns for the mechanically alloyed $xZrO_2$-(1-x)Fe_2O_3 samples are shown in Figure 3a, for x = 0.1. All the peaks match with the hematite (α-Fe_2O_3) phase. With the increase of milling time, the peaks broaden due to the decrease in the grain size. For particles milled for 2 hrs, the particle size reduced down to about 25 nm. From the XRD peaks of 120 hrs milled powders, the average crystallite size calculated using Scherrer formula[19] is about 8 nm.

The XRD patterns of Fe_2O_3-ZrO_2 prepared by the co-precipitation method and calcined at 120 °C for 12 hrs, 350 °C 2 hrs. and 500 °C for 2 hrs are shown in Figure 3b. While the sample calcined at 120 °C shows an amorphous behavior, samples calcined above 350 °C exhibit a crystalline phase with peaks matching with the reported phase of hematite (JCPDS card No. 33-664). From the XRD peaks, the estimated average crystallite size is ~ 177.3Å. Figure 3 (c) shows XRD patterns of $xZrO_2$-(1-x)Fe_2O_3 that are treated at different temperatures. From RT up to 300 °C, it shows only the Maghemite-Q phase with tetragonal structure (Card No. 25-1402). Increase in the calcination temperature above 300 °C leads to

the appearance of the α-Fe_2O_3 peaks. The average crystallite size calculated using Scherrer formula is about 82 nm.

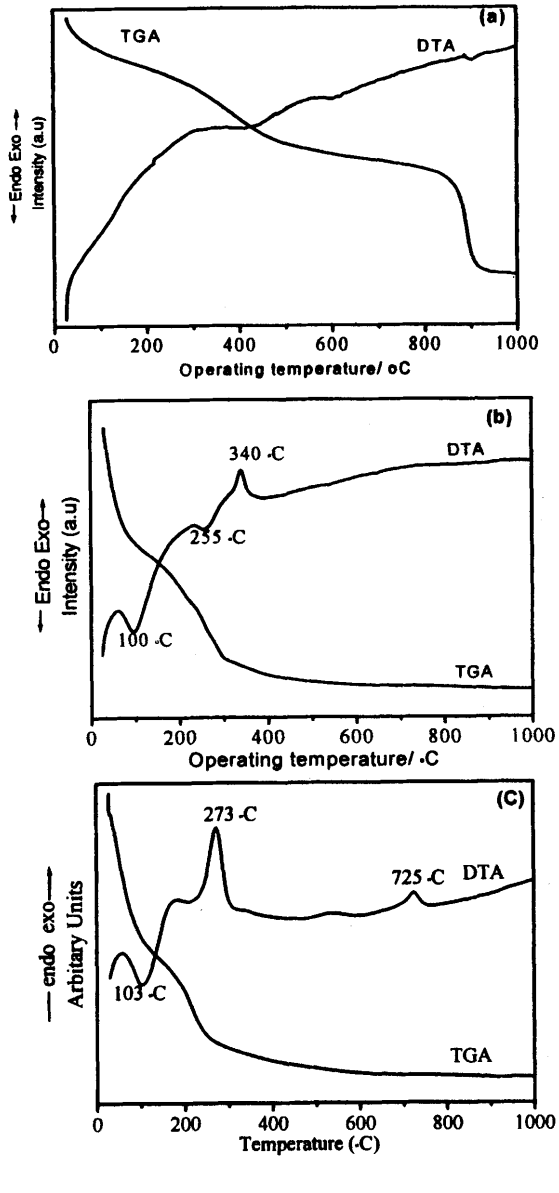

Figure 2 TGA-DTA data of $xZrO_2$-$(1-x)Fe_2O_3$ prepared by: (a) high-energy ball milling; (b) co-precipitation; and hydrazine reduction method.

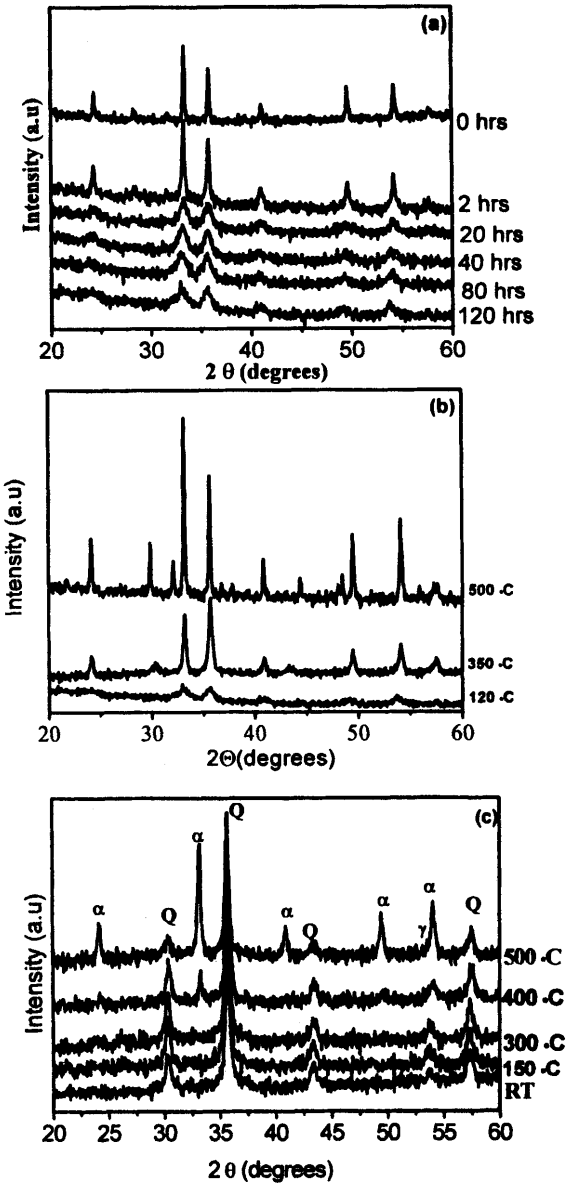

Figure 3 XRD patterns of $xZrO_2$-$(1-x)Fe_2O_3$ prepared by: (a) high-energy ball milling; (b) co-precipitation; and (c) hydrazine method. (α: α -Fe_2O_3, γ: γ-Fe_2O_3 and Q: Maghemite).

Gas Sensing Characteristics of High-Energy Ball Milling Material

The gas sensitivity (S) is defined as the ratio of the resistance of the sensor in air (R_a) to that in the test gas (R_g). We first examined the effect of different weight percentages of ZrO_2 on gas sensing properties. It was found that 10 wt.% ZrO_2 doped Fe_2O_3 sensor had a much better sensitivity to ethanol gas than a single phase Fe_2O_3 based sensor. Hence, all the sensing measurements were conducted on samples with x = 0.1.

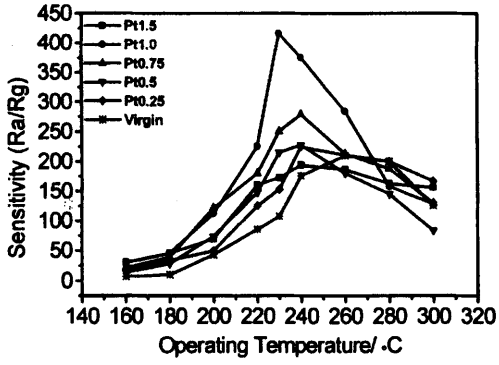

Figure 4 Sensitivity vs. the operating temperature of x ZrO_2-(1-x) Fe_2O_3 for vargin and Pt impregnated samples by high-energy ball milling.

Figure 4 shows the sensitivity of the virgin and different weight percentages of Pt impregnated material as a function of the operating temperature. Corresponding amounts of Pt chlorides were impregnated in x ZrO_2-(1-x)Fe_2O_3 followed by high-energy ball milling as described above. This device was annealed at 400 °C for 1 hr. before sensing measurements. The sample with 1 wt.% Pt showed the maximum sensitivity (~ 416) for 1000 ppm ethanol vapor at 230 °C. We also tried Pd impregnated samples, but Pt gave better response. Hence, for further studies, we selected the 1wt. % Pt sample.

Figure 5 shows the sensitivity versus the operating temperature for different milling hours from 40 to 120. The sensitivity increases with increase in milling time since longer milling produces finer particles providing higher surface area for gas sensing. For the same reason, samples calcined at lower temperatures showed better sensitivity. For these samples, the optimum operating temperature was found to be 230 °C.

Figure 6 shows the sensitivity of xZrO_2–(1-x)Fe_2O_3 to various test gases as a function of the operating temperature. It is seen that the sensor exhibits good selectivity by sensing only ethanol vapor at an operating temperature of 230 °C in the presence of other interfering gases like CH_4, CO and H_2.

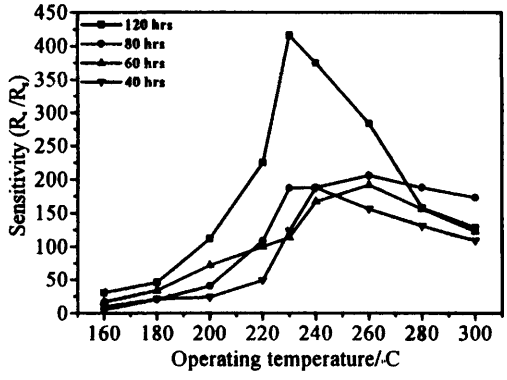

Figure 5 Sensitivity vs. operating temperature of x ZrO_2-(1-x) Fe_2O_3 + 1 wt% Pt for different milling hours.

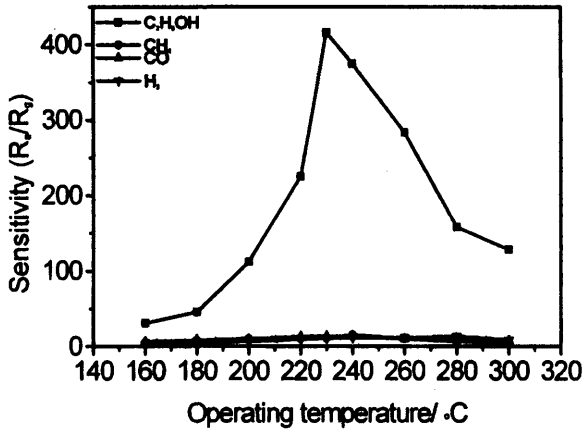

Figure 6 Sensitivity vs. operating temperature for x ZrO_2-(1-x) Fe_2O_3 + 1 wt% Pt with different reducing gases.

Gas Sensing Characteristics of $xZrO_2$–(1-x)α-Fe_2O_3 Prepared by the Co-Precipitation Method

Figure 7 shows sensitivity versus the operating temperature of virgin and 1 wt.% Pt impregnated ZrO_2–(1-x)Fe_2O_3 material prepared by the co-precipitation method. For the virgin sample the maximum sensitivity is around 170, but the Pt sample shows a maximum value of 486 at 230 °C. So we optimized the composition at 1 wt% Pt and varied the annealing temperature. Figure 8 shows the sensitivity versus the operating temperature for samples annealed at different temperatures from 400 °C to 600 °C. It is clearly seen that there is not much

difference in sensitivity with the annealing temperature, presumably because the crystallite size doesn't change.

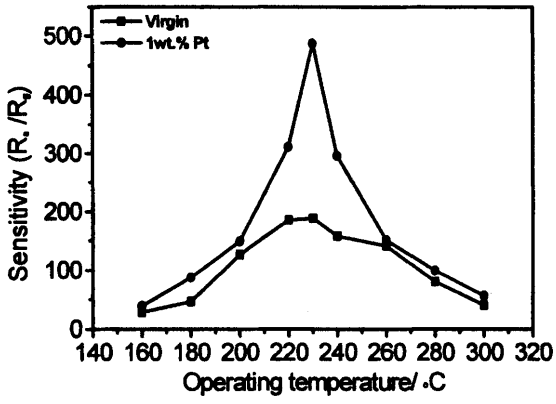

Figure 7 Sensitivity vs. operating temperature of x ZrO_2-(1-x) Fe_2O_3 + 1 wt% Pt prepared by co-precipitation for 1000 ppm ethanol.

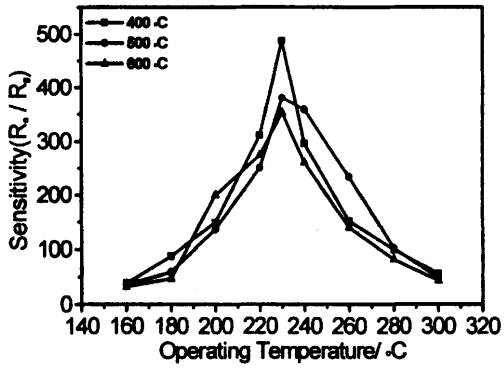

Figure 8 Sensitivity to 1000 ppm ethanol as a function of the operating temperature for xZrO_2-(1-x)Fe_2O_3 + 1wt.% Pt (co-precipitation), annealed at 400, 500 and 600 °C for 1 hour.

Gas Sensing Characteristics of xZrO_2–(1-x)Fe_2O_3 Prepared by Hydrazine Method

Figure 9 shows the sensitivity versus the operating temperature of virgin and 1 wt.% Pt impregnated ZrO_2–(1-x) Fe_2O_3 material prepared from the hydrazine method. It is clearly observed that there is not much difference in sensitivity between virgin and Pt incorporated sample. Here we observed a maximum sensitivity of 600 at 230 °C for virgin and 800 for the Pt impregnated sample.

These values are much higher compared to those of the ball milling and co-precipitation methods.

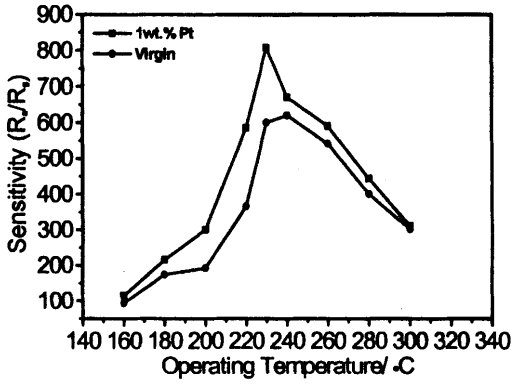

Figure 9 Sensitivity vs. operating temperature of x ZrO_2-(1-x) Fe_2O_3 + 1 wt% Pt prepared by hydrazine reduction for 1000 ppm ethanol.

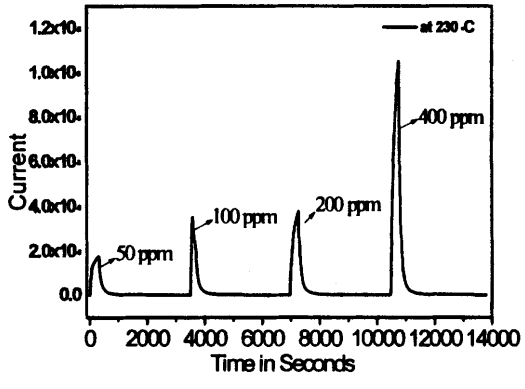

Figure 10 Current vs. time response of sensors prepared hydrazine reduction for different concentrations of ethanol at 230 °C.

Figure 10 shows the relationship between the sensitivity and the ethanol vapor concentration for the sensor operating at 230 °C. The sensitivity for 50 ppm ethanol is as high as 160. It was also observed that the sensor senses even less than 10 ppm with a substantial sensitivity. Figure 11 shows the sensitivity versus time for 1000 ppm ethanol showing a very fast response time and a sluggish

recovery. Finally, all the three methods for ethanol sensing are compared in a single graph as shown in Figure 12. From this graph we can conclude that $xZrO_2$-$(1-x)Fe_2O_3$ prepared by the hydrazine method gives the best results as an ethanol sensor compared to the other methods.

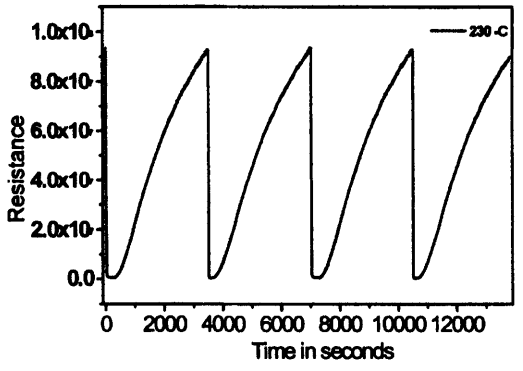

Figure 11 The response and recovery behavior of the $xZrO_2$-$(1-x)Fe_2O_3$+ 1 wt% Pt (hydrazine reduction) sensor to 1000 ppm ethanol at 230 °C.

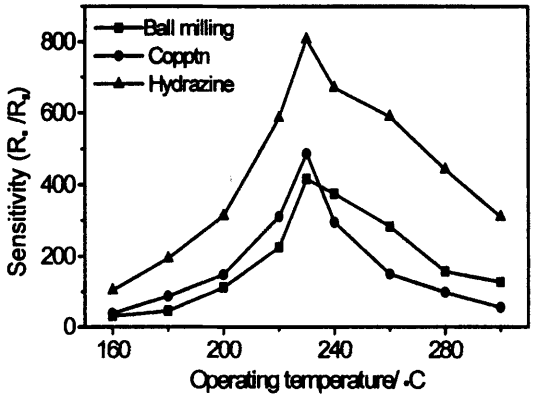

Figure 12 Comparison of the sensing behavior of x ZrO_2-$(1-x)Fe_2O_3$ + 1 wt. % Pt in 1000 ppm ethanol.

CONCLUSIONS

Nano powders of $xZrO_2$-$(1-x)Fe_2O_3$ prepared from hydrazine reduction method produces maghemite-Q (Fe_2O_3) which shows better sensitivity towards ethanol. The doping of Pt (1.0 wt%) produces a remarkable improvement in

sensitivity. It shows good sensitivity even at < 50 ppm with sufficient sensitivity. It is also highly selective compared to other interfering gases like CH_4, CO and H_2. The maximum sensitivity of $R_a/R_g \sim 800$ is observed for sensor annealed at 400 °C for 1 hr and an operating temperature of 230 °C.

REFERENCES

[1]H. Gleiter, "Nanocrystalline Materials," *Progress in Materials Science,* **33** (4) 223-315 (1989).

[2]H. Gleiter, "Nanostructured materials: State of the art and perspectives," *Nanostructured Materials,* **6** 3-14(1995).

[3]R.W. Siegel, "Creating Nanophase Materials," *Scientific American*, **275** [6] 74-79 (1996).

[4]Y. Murase and E. Kato, "Thermal Changes in Texture of Aggregates of Ultra-Fine Crystallites in Hydrolysed Zirconia Particles," *Journal of Crystal Growth* **50** (1980) 509.

[5]S. Komarneni, E. Fregeau, E. Breval and R. Roy, "Hydrothermal Preparation Of Ultrafine Ferrites and their Sintering," *Journal of The American Ceramic Society,***71** [1] C26-C28 (1988).

[6]R.M. Cornell and U. Schwertmann, "The Iron Oxides," pp. 115, VCH, New York, 1996.

[7]B.L.Yang and H.H. Kung, Oxygen on Iron-Oxide-Effect on the Selective Oxidation of Butane," Journal of Catalysis, **77** (2) 410-420 (1982).

[8]J.K. Leland and A.J. Bard, "Photochemistry of Colloidal Semiconducting Iron-Oxide Polymorphs," *Journal of Physical Chemistry*, **91** [19] 5076-5083(1987).

[9]V.V. Malyshev, A.V. Eryshkin, E.A. Koltypin, A.E. Varfolomeev and A.A. Vasiliev, "Gas sensitivity of semiconductor Fe_2O_3 based thick-film sensors to CH_4, H_2 and NH_3," *Sensors and Actuators B*, **19** 434-436 (1994).

[10]C. Cantalini, M. Faccio, G. Ferri and M. Pelino, "Microstructural and electrical properties of Si-doped- α-Fe_2O_3 sensor," *Sensors and Actuators B*, **16** 293-298 (1993).

[11]C. Cantalini, M. Faccio, G. Ferri and M. Pelino, "The influence of water vapour on carbon monoxide sensitivity of α-Fe_2O_3 microporous ceramic sensors," *Sensors and Actuators B*, **18-19** 437-442 (1994).

[12]L.F. Dong, Z. Lui and Z. Zhang, "Gas sensitivity of rare earth doped α-Fe_2O_3," *Gongneng Cailia*, **26** 416-417 (1995).

[13]H. Zeng, H. Luo, T. Zhang and R. Zhang, "Synthesis of high stability γ-Fe_2O_3 and its gas sensing characteristics," Gongneng Cailia, **26** [4] 305-308(1995).

[14]T.M. Racheva, O. Stamb, I.T. Lova and T. Donchev, "Humidity Sensitive Characteristics of SnO_2-Fe_2O_3 Thin Films Prepared by Spray Pyrolysis," Journal of Materials Science, **29** [1] 281-284 (1994).

[15]M. Takano, Y. Bando N. Nakanishi, M. Sakai and H. Okinaka, "Characterization of Fine Particles of the α-Fe_2O_3-SnO_2 System with Residual So_4^{2-} Ions on the Surface," *Journal of Solid State Chemistry,* **68** [1] 153-162 (1987).

[16]P. Bonzi, L.E. Depero, F. Parmigiani, C. Perego, G. Sberveglieri and G. Quattroni, "Formation and Structure of Tin-Iron Oxide Thin-Film CO Sensors," *Journal of Material Research,* **9** [5] 1250-1256 (1994).

[17]O.K. Tan, W. Zhu and J.Z. Jiang, "Nano structure and $xSnO_2$-$(1-x)Fe_2O_3$ material preparation for good gas sensing properties," *Proc. of 4th natl Symp. on progress of mat. Res., singapore,* pp 542- 545 (1998).

[18]C.V. Gopal Reddy, K. Kalyana Seela and S.V. Manorama, "Preparation of γ-Fe_2O_3 by the Hydrazine method: Application as an alcohol Sensor," *International Journal of Inorganic materials,* **2/4** 301-307(2000).

[19]H.P. Klug and L.E. Alexander, "X-ray diffraction procedure for polycrystalline materials," pp 125, John Wiley & Sons, New York, 1974.

INVESTIGATION OF NI-CU-ZN FERRITE WITH HIGH PERFORMANCE DERIVED FROM NANO FERRITE POWDERS

Xiaohui Wang, Weiguo Qu, Longtu Li, Zhilun Gui, Ji Zhou
State Key Lab of New Ceramic & Fine Processing
Department of Materials Science & Engineering
Tsinghua University
Beijing, 100084, P. R. China

ABSTRACT

$(Ni_{0.2}Cu_{0.2}Zn_{0.6}O)_{1.01}(Fe_2O_3)_{0.99}$ nanocrystalline powders were synthesized by a citrate precursor method. The nanocrystals with grain sizes in the range from 10nm to 60nm were obtained at various calcining temperatures. Because of excellent sintering activity, the nanocrystals can be sintered below 900℃ without the addition of sintering aids. The sintered body possesses fine-grained microstructure, showing high initial permeability up to 700 with high DC resistivity of $10^9 - 10^{10}$ ohm · cm. Influences of initial particle size as well as sintering temperature on microstructures and properties of sintered body were studied. The results show that the nanocrystalline Ni-Cu-Zn ferrite is a promising material for high frequency MLCI application.

INTRODUCTION

In the past ten years, with the development of surface mounting technology, great progresses have been made in the miniaturization of electromagnetic components. As one of the most important media materials, Ni-Cu-Zn ferrite has been commercially used to manufacture multilayer chip inductor in high frequency

region. In order to be cofired with the inner electrode (usually Ag is the most suitable internal contact material with a melting point of 961℃), Ni-Cu-Zn ferrite must be sintered below 900℃. The normal way to lower the sintering temperature is using sintering aids such as Bi_2O_3, V_2O_5 etc, which usually does great harm to the magnetic property of the ceramics acquired [1-4]. Ultrafine Ni-Cu-Zn ferrite with uniform composition, small grain size and narrow size distribution is expected to realize low-temperature sintering and attain ideal magnetic property at the same time [5].

Many methods have been developed to prepare ultrafine powder including co -precipitation, hydro-thermal method, peptization method, sol-gel method, crystal glass method, metallorganics hydrolyse method, microlatex method and so on [6-10]. In this paper, Ni-Cu-Zn ferrite nanocrystals with a composition of $(Ni_{0.2}Cu_{0.2}Zn_{0.6}O)_{1.01}(Fe_2O_3)_{0.99}$ were prepared via a citrate precursor method. The Ni-Cu-Zn ferrite nanocrystals with different grain sizes were obtained by controlling the heat-treatment conditions. The crystalline structures, sintering ability and magnetic properties of these powders were investigated.

EXPERIMENTAL PROCEDURE

Sample Preparation

The starting materials were iron nitrate, nickel acetate, copper acetate and citric acid. Firstly, iron nitrate was dissolved in distilled water before being precipitated by a ammonia solution to form $Fe(OH)_3$. Filtered, washed, the fresh $Fe(OH)_3$ precipitate was dissolved into hot citric acid solution at 60~80℃ in the ratio of 1:1 of Fe: citric acid, and a transparent solution was obtained. Then, nickel and copper acetate were added in stoichiometric quantities in the above solution to give the required composition. After that appropriate ammonia was drop into the above sol until it was neutral or slightly alkaline (pH=6-8). After heating at 125℃, dried gel were obtained. Finally, the gel was ignited or heat treated at 600℃, 700℃ and 800℃ for 4h, respectively , resulting Ni-Cu-Zn nanocrystals with different grain sizes .

The nanocrystalline powders were pre-milled and pressed into disks (10mm in diameter and 1.0mm thickness) and toroidal samples (20mm outside diameter, 10mm inside diameter and 3mm thickness) with the addition of 5wt% PVA as lubricant. The ceramic samples sintered at 870～890℃were used for magnetic property measurements.

Characterization and Property Measurements

The crystalline structures were determined by a Rigaku Powder X-Ray diffractometer using Fe K_α radiation. The morphology and grain size of the nanocrystalline powders were observed using a JEM-200CX transmission electron microscopy (TEM). The magnetic properties of the ceramics were measured using an HP 4194A Low Impedance Analyzer. The DC resistivity of the ceramic was determined using an HP 4040B Micro-amperemeter. The microstructures of the ceramics were investigated using a Zeiss CSM-950 scanning electron microscopy (SEM).

RESULTS AND DISCUSSION

Phase and Structure Analysis

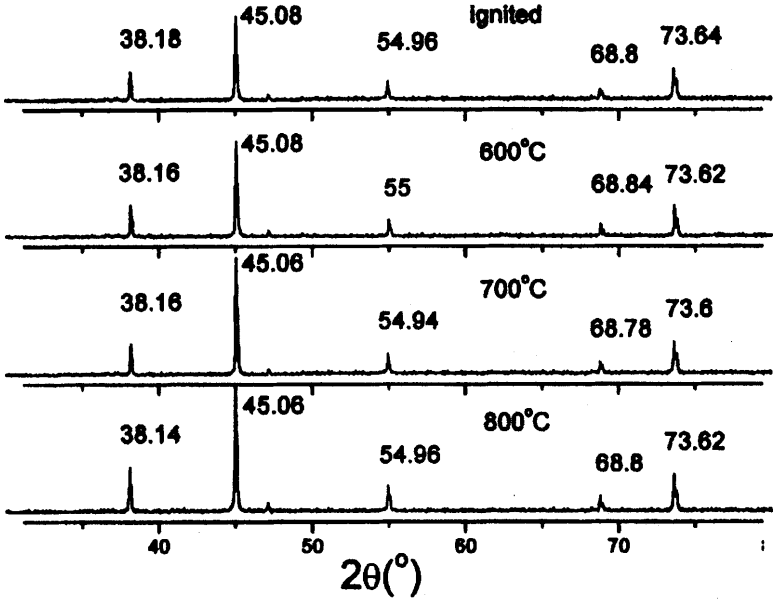

Figure 1. XRD patterns of nanocrystalline powders ignited or heat-treated at different temperatures

Figure 1 shows XRD patterns of nanocrystalline powders ignited or calcined at different temperatures. It is obvious that a single spinel phase was formed for all the powders, and the intensity of XRD peaks increased with increasing calcination temperature indicating that the crystals had been developed with the increase of heat-treatment temperature.

Grain Size and Morphology

The average grain sizes of the nonocrystalline Ni-Cu-Zn powders were calculated according to the full width at half maximum (FWHM) of the strongest peak [11]. Table I gives the average grain size data for all the powders.

Table Ⅰ. The average grain sizes of the various powders

Sample No.	1	2	3	4
Heat-treatment condition	ignited	600℃/4h	700℃/4h	800℃/4h
Average grain size (nm)	11(XRD) 8 (TEM)	18 (XRD) 20 (TEM)	26 (XRD) 30 (TEM)	60 (XRD) 80 (TEM)

Figure 2 shows the morphology of the nanocrystalline powders. The particles of all the powders were spherical in shape with uniform grain size. The grain sizes of the powders determined by TEM are also listed in table 1. With increasing heat-treatment temperature, the grains grew up.

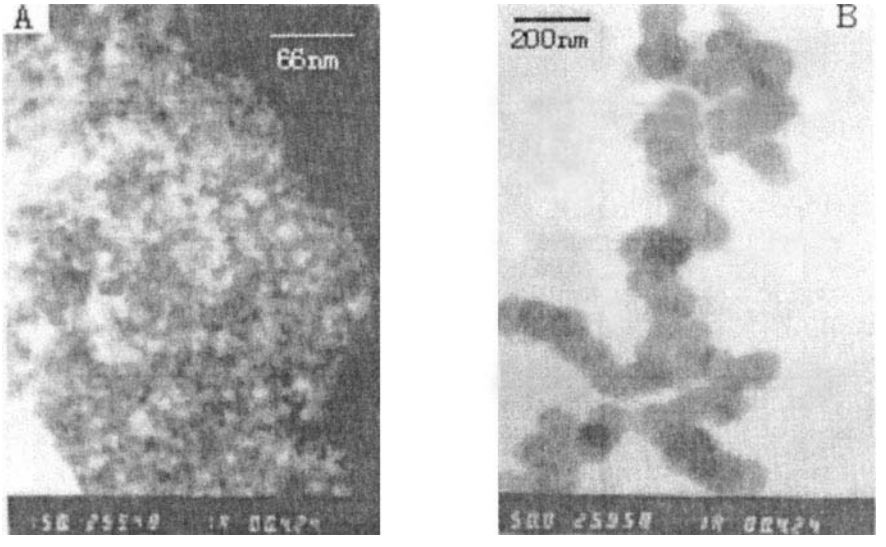

Figure 2 TEM photographs of ferrite nanocrystals
(A) Ignited powder (150 000×)
(B) Powder calcined at 800℃ (50 000×)

Magnetic and Electrical Properties

Due to the high surface area, the Ni-Cu-Zn nanocrystals prepared by this method show obviously excellent sintering activity. It could be sintered below 900 ℃ without the addition of sintering aids, avoiding the relevant deterioration of properties caused by sintering aids. The ceramics produced from nanocrystalline powders displayed better magnetic and electrical properties in comparison with those made by conventional ceramics method.

Permeability-frequency characteristics: figure 3 shows frequency-dependent

permeability curves of ceramic samples sintered at various temperatures. These ceramic samples are all derived from the powders calcined at 700℃. For comparison, a curve of ceramic prepared by conventional ceramics method is also presented in this figure. It is obvious that the initial permeability of the samples increased with the increasing sintering temperature. This could be explained by the effect of sintering temperature on the grain size. As the sintering temperature increases, the grains of the samples tend to grow and thus the domain rotation becomes much easier. The most important result is that the initial permeability of the sample sintered at 890℃ was about 700, which is really hard to be achieved using conventional ceramic method.

Figure 4 gives the permeability-frequency curves for the ceramics sintered at 890℃ derived from the powders calcined at different temperature (with various grain sizes). Obviously, the initial permeability does not change linearly with the increasing heat-treatment temperature. On the contrary, it increases first and then drops.

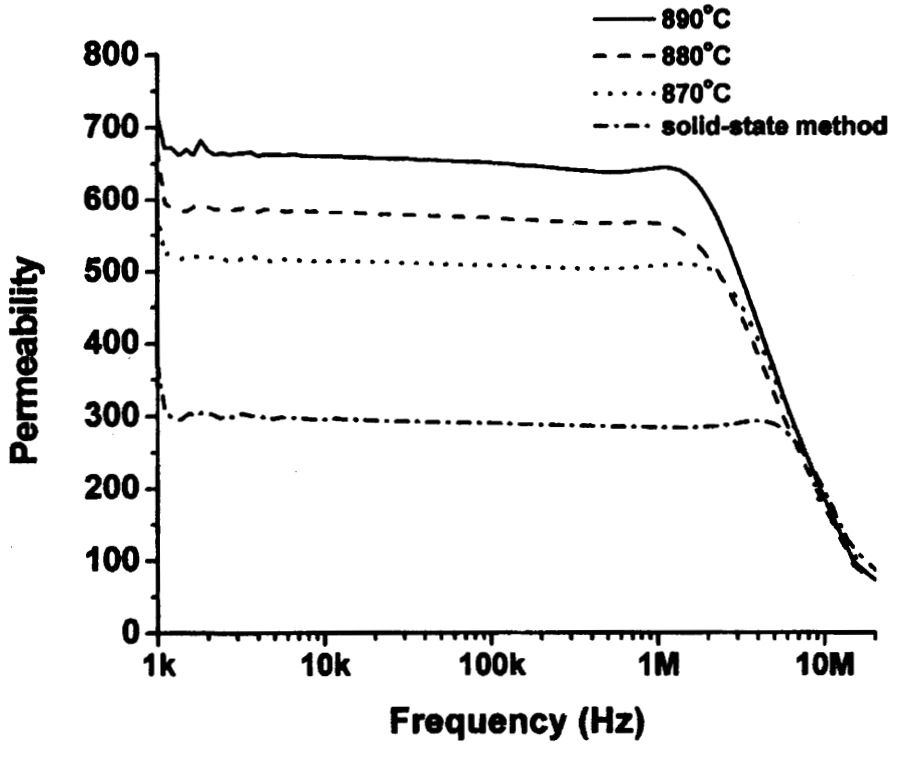

Figure 3. Frequency-dependent permeability curves of samples sintered at different temperatures

The most preferable result can be acquired by the sample derived from the powder calcined at 700℃ with average grain size of 30nm. This behavior can also be explained by the size effect of Ni-Cu-Zn nanocrystals. At the beginning, an increase in grain size of the nanocrystals can help to enlarge the ceramic grain size and reduce the resistance of domain rotation, thus increasing the initial permeability. But as the grain size of the nanocrystals increases further, the specific surface area and the surface activity decrease, which may lead to lower density of the sintered ceramic. That may be the reason for the drop of the initial permeability of the sample made from powders calcined at 800℃ with larger grain size (as shown in figure 4).

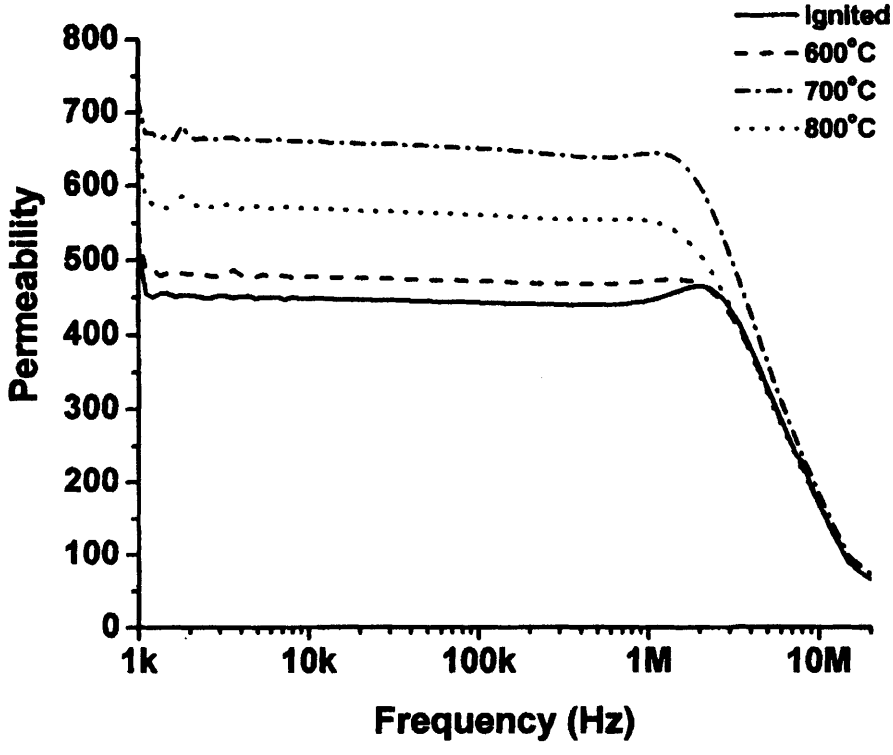

Figure 4. Frequency-dependent permeability curves of ceramics sintered at 890℃ derived from powders calcined at different temperatures

DC resistivity property: an adequate DC resistivity of the ferrite is also required in manufacturing of MLCI so as to avoid "creeping" while electroplating, which may do great harm to the quality of components. Usually, DC resistivity of $10^7 \sim 10^8$ ohm • cm can be achieved by solid-state method which can hardly fit the requirement. Whereas, ceramics sintered from the nanocrystals prepared by this method show high DC resistivity of $10^9 \sim 10^{10}$ ohm • cm, which is much more

preferable for practical production and for the reliability of the components. Figure 5 shows the SEM photos of the ceramic samples derived from the nanocrystals and that from usual powder prepared by solid-state method. It is obvious that the grains of the ceramic derived from nanocrystals are small, uniform and compacted with each other. As well known , the most important factor that affects the resistivity of ceramic is the proportion of grain boundaries in it. Obviously, this proportion is much higher for the ceramic derived from nanocrystals than that made by conventional method. That is why the ceramic sintered from the nanocrystals has much higher resistivity.

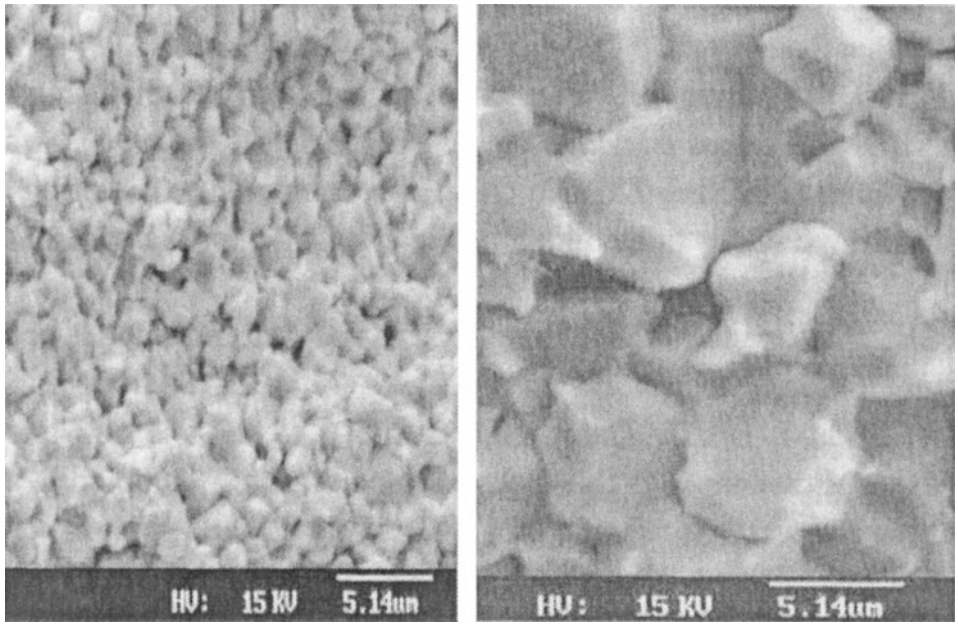

(A) (B)

Figure 5. SEM micrographs of ceramics derived from:
(A) nanocrystalline powder (5000×)
(B) powder prepared via a solid-state reaction (2000×)

CONCLUSIONS

Ni-Cu-Zn ferrite nanocrystals were successfully prepared via a citrate precursor method. Low temperature (below 900℃) sintering of Ni-Cu-Zn ferrite is realized without doping any sintering aids using the nanocrystalline powders. The magnetic and electrical properties of the ceramics derived from the nanocrystals are much better than those prepared by a conventional ceramic method. Therefore, the nanocrystalline Ni-Cu-Zn ferrite is a promising material for high frequency MLCI application.

ACKNOWLEDGEMENT

This work was supported by the National Natural Science Foundation of P. R. China under grant No.59995523.

REFERENCES

[1]Yamaguchi T, Shinagawa M, "Effect of Glass Addition and Quenching on the Relation Between Inductance and External Compressive Stress in Ni-Cu-Zn Ferrite Glass Composites", *Journal of Materials Science*, **30** [2] 504-508 (1995).

[2]Jean JH, Lee CH, "Effects of Lead(II) Oxide on Processing and Properties of Low-Temperature-Cofirable", *Journal of the American Ceramic Society*, **82** [2] 343-350 (1999).

[3]Hsu JY, KO WS, Chen CJ, "The Effect of V_2O_5 on the Sintering of NiCuZn Ferrite", *IEEE Transactions on Magnetics*, **31** [6] 3994-3996 (1995).

[4]He XH, Xiong MR, Ling ZY, Qiu QC, "Low-temperature Sintering of NiCuZn Ferrite for Multilayer-Chip Inductor", *Journal of Inorganic Materials*, **14** [1] 71-77 (1999).

[5]Date SK, Deshpande CE, "Magnetism in Materials - Processing and Microstructure", *Metals Materials and Processes*, 7 [1] 15-18 (1995).

[6]Yue ZX, Zhou J, Li LT, Zhang HG, Gui ZL, "Synthesis of Nanocrystalline NiCuZn Ferrite Powders by Sol-Gel Auto-combustion Method", *Journal of Magnetism and Magnetic Materials*, **208** [1-2] 55-60 (2000).

[7]Yue ZX, Li LT, Zhou J, Zhang HG, Gui ZL, "Preparation and Characterization of NiCuZn Ferrite Nanocrystalline Powders By Auto-combustion of Nitrate-citrate Gels", *Materials Science and Engineering B - Solid State Materials for Advanced Technology*, **64** [1] 68-72 (1999).

[8]Kim WC, Park SI, Kim SJ, Lee SW, Kim CS, "Magnetic and Structural Properties of Ultrafine Ni-Zn-Cu Ferrite Grown by a Sol-Gel Method", *Journal of Applied Physics*, **87** [9] 6241-6243, Part 3 (2000).

[9]J.F.Hochepied, "Nonstoichiometric Zinc Ferrite Nanocrystals: Syntheses and Unusual Magnetic Properties", *J.Phys.Chem.B* **104** 905~912 (2000).

[10]Hsiao-Miin Sung, Chi-Jen Chen, "Fine Powder Ferrite for Multilayer Chip Inductors", *IEEE Transactions on Magnetics*, **30** [6] 4906~4908 (1994).

[11]C. Suryanarayana and M. Grant Norton, "*X-Ray Diffraction – A Practical Approach*"; pp.207-, 1998

CRACK HEALING AND STRENGTH RECOVERY IN THERMALLY-SHOCKED SINTERED ALUMINA-SiC NANOCOMPOSITE

S. Maensiri and Steve G. Roberts
Department of Materials
University of Oxford, Parks Road
Oxford, OX1 3PH, UK.

ABSTRACT

The crack healing and strengthening of thermally-shock sintered alumina and alumina/5vol.% SiC nanocomposite were studied. Thermal shock damage was introduced by quenching in water (18 ± 2°C) from 373°C. The annealing was carried out in argon for 1-6 hours at 1300, 1500, and 1600°C. The damage and crack healing was characterised by measurements of strength in four-point bending. Annealing produced increases in strength in thermally shocked specimens of both materials towards the values for non-thermally shocked material, though this recovery was greater in the pure alumina than in the nanocomposite.

INTRODUCTION

Niihara[1] reported that annealing polished specimens at 1300°C for 2 h in Ar increased the bend strength of an alumina/ SiC nanocomposite from about 1000 MPa to 1500 MPa. This increase in strength of the nanocomposites by annealing is thought to be due to either i) the crack healing of near-surface cracks generated by machining the specimen, ii) the relaxation of local residual stress caused by the thermal expansion mismatch between matrix and SiC, and iii) subgrain boundary formation within the alumina matrix grains[1]. This annealing effect on the strength of alumina/ SiC nanocomposite has also been observed by other workers, but no other worker has yet achieved the high strength after annealing (up to 1500 MPa) reported by Niihara and his co-workers. Zhao and his co-workers[2], for example, have found an increase in the nanocomposite strength after grinding and then annealing in Ar at 1300°C for 2 h only from about 760 to 1000 MPa. Thompson *et al.*[3] and then Chou *et al.*[4] have

studied the crack healing behaviour caused by annealing, using Vickers indentations to generate precracks. It has been found[3] that when the Al_2O_3/5 vol.% SiC nanocomposites were annealed in Ar for 2 h at 1300°C, partial healing of indentation cracks occurred. This result was suggested as being a possible explanation for the post-annealing strengthening behaviour of the nanocomposites as observed by Niihara[1] and Zhao *et al.*.[2]

Wu *et al.*[5] have also investigated annealing effects on how healing in nanocomposites using Herzian indentation and line-focus accoustic microscopy (LFM). These allow them to investigate the annealing behaviour of small machining-induced flaws in nanocomposite surfaces rather than of the very large indentation flaws studied by Thompson *et al.*[3] and Chou *et al.*.[4] It was found that the strength of the nanocomposites after grinding and then annealing in Ar at 1250°C for 10 h increased from 400 to 700 MPa. Wu *et al.* proposed that a mechanism of crack healing in parallel with an oxidation reaction leads to a reduction in the surface flaw density and critical flaw size on annealing, giving rise to the high strength of the nanocomposites. Recently, Wu *et al.*[6] investigated further the mechanisms of strengthening of Al_2O_3/5 vol.% SiC nanocomposites after grinding and annealing using TEM of surface cross-sections. Their results confirmed that the annealing process led to surface crack healing.

It has been demonstrated[7-12] that the deep surface cracking introduced by thermal shocking of polycrystalline ceramics can be eliminated by heat treatment. In the present paper, we investigate the crack healing and strengthening of thermally-shocked sintered alumina and alumina/5vol.%SiC nanocomposite.

EXPERIMENTAL PROCEDURE

The materials used in this study were pressureless-sintered alumina and alumina/5vol.%SiC nanocomposite. The experimental procedures used to manufacture these materials and to prepare the rectangular bar specimens (22.0 mm x 3.0 mm x 2.5 mm) for 4-point bend tests have been described in detail elsewhere[13]. Specimen density was measured by 'Archimedes' method using distilled water. The average grain size of each material was measured using a standard line intercept technique from SEM micrographs of thermally etched polished surfaces. The basic properties of the materials investigated are summarised in Table 1.

For the damage healing study, the specimens were initially thermally shocked by quenching in water (18 ± 2°C) from 373°C. Sets of between three and five specimens were then annealed under flowing argon for various times at temperatures of 1300°C, 1500°C, or 1600°C. The heating rate and the cooling rate were 5°C/min and 15

°C/min, respectively. Tests were carried out on specimens of two surface finishes: (a) ground and (b) polished. Strength data were obtained from 4-point bend tests at room temperature. All tests were carried out on a conventional screw driven loading frame (Instron, model 8561) with a cross-head displacement speed of 0.5 mm/min using a four-point bending rig with an inner span of 6 mm and an outer span of 10 mm. The mean strength and standard deviation for each of the conditions studied was obtained using between three and six specimens. Flexural strength measurements were also obtained on specimens with no thermal shock and no heat treatment, and with thermal shock but no heat treatment.

Table 1 Properties of sintered materials investigated.

Material	Sintering condition	Density (% theoretical)	Grain size (μm)
Alumina	1600°C/2 h	99.6 ± 0.1	4.1 ± 0.9
Nanocomposite	1700°C/2 h	99.9 ± 0.6	2.8 ± 0.5

RESULTS AND DISCUSSION

Crack healing in specimens with no thermal shock

Figure 1 shows the fracture strength of as-ground and as-polished alumina and alumina/5vol.%SiC nanocomposite after annealing. For annealing at 1300°C, the strength of the as-ground alumina after annealing increased slightly when annealed, with no clear dependence on annealing time, whereas for the as-ground nanocomposite, there was a ≈ 30 % strength decrease at 120 min, and a ≈ 40 % increase at 360 min. No change in the strength after annealing was observed in the as-polished alumina, while a 10% increase in strength was found in the as-polished nanocomposite. However, no further increase in strength of the as-polished nanocomposite was seen after annealing beyond 120 min.

After annealing at 1500°C, the strength of the as-ground alumina gradually increased with increasing annealing times and reached the highest strength when annealed for 120 min; it then gradually decreased for longer annealing times. The strength of the as-ground nanocomposites after annealing slightly increased when annealed for 60 min and then decreased with increasing annealing times. The strength of the as–polished alumina and the-as polished nanocomposites after annealing shows the same behaviour pattern as the as-ground alumina although the strength of annealed as-polished nanocomposites was ≈ 15% higher than that of the alumina.

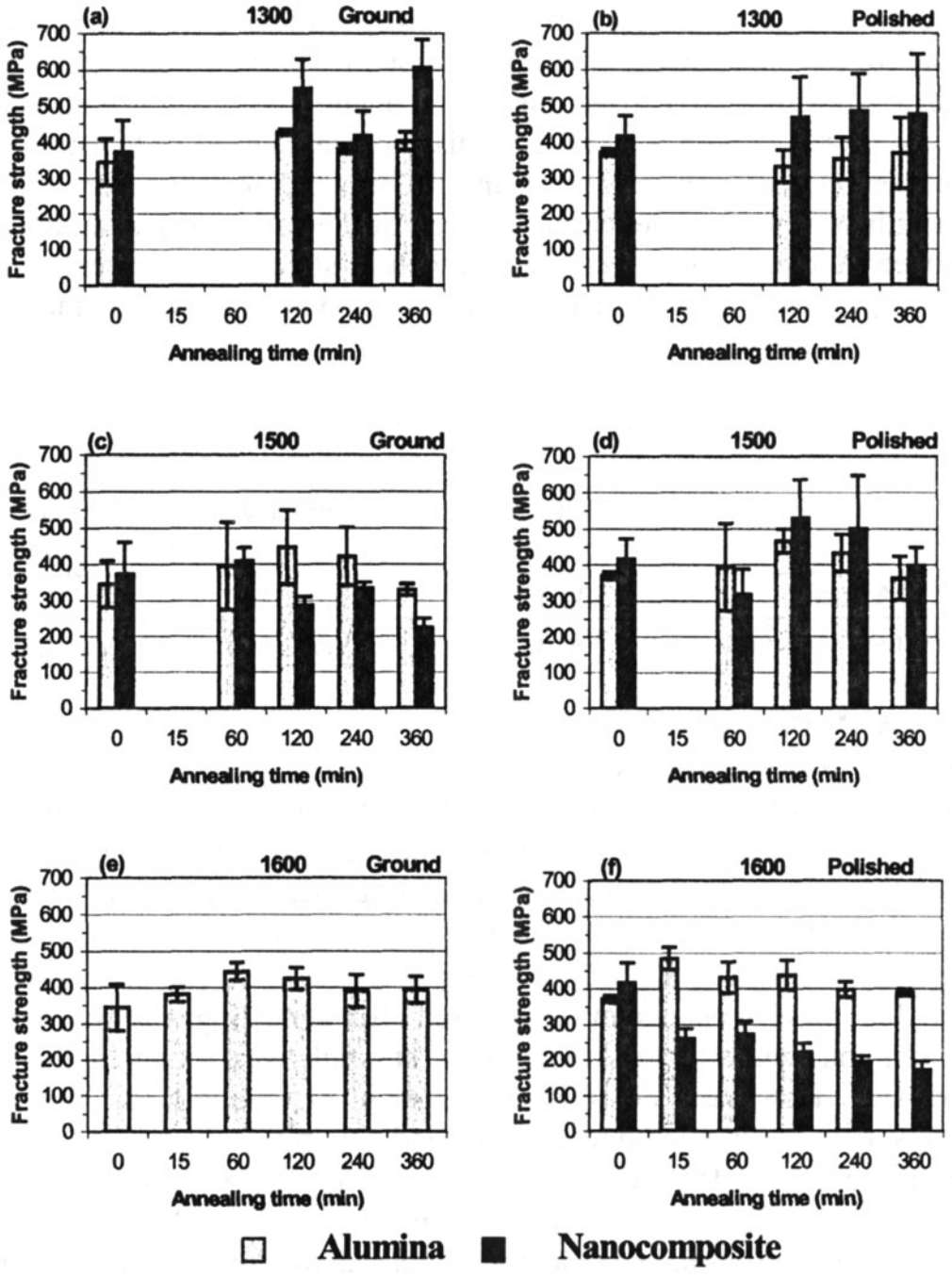

Figure 1 Fracture strength of alumina ((a), (c), and (e)) and alumina/SiC nanocomposite ((b), (d), and (f)) after annealing under flowing argon for various times at temperatures of 1300°C, 1500°C, and 1600°C.

When specimens were annealed at 1600°C (the sintering temperature for alumina), the strength of the as-ground alumina gradually increased with increasing annealing times and reached the highest strength when annealed for 120 min; it then gradually decreased for longer annealing times. However, the strength of the fully annealed ground alumina was higher than that of the original unannealed one. The strength of the as–polished alumina after annealing shows the same behaviour. On the other hand, the strength of the as-polished nanocomposites after annealing decreased with increasing annealing times; the strength was lowest (≈ 50% lost) when annealed for 360 min.

The increase in strength after annealing in both the alumina and the nanocomposite may be due to crack healing, leading to a reduction in the surface flaw density and critical flaw size. Recently, there have been numerous studies showing the importance of crack healing as a strengthening mechanism in alumina[7-12, 14-19] and alumina/SiC nanocomposites.[1-6] In the absence of chemical reactions, there are two crack healing mechanisms: (i) adhesion [8, 15-17] and (ii) diffusional bonding.[7, 9-12] Adhesion describes the process of atomic rebonding across the interface as the fracture surface mate. The rate of crack healing depends on the kinetics of atomic rebonding.[20] Diffusional bonding is driven by variations in local surface curvature and requires long-range surface rearrangement of material. The relative contribution of each mechanism to a crack-healing event is governed by their relative kinetics and consequently, by the conditions under which the crack is healing. At low or intermediate temperatures, when surface diffusion is minimal, adhesion is the dominant crack-healing mechanism. For instance, there is evidence of partial microcrack healing in alumina even at room temperature.[17] In the current study, it is still unclear which of these two mechanisms was dominant at the annealing temperatures used here.

In nanocomposites, oxidation of SiC particles has been also found to enhance such crack healing.[5] Despite the argon atmosphere used for annealing, a surface reaction product is visible, the amount of which increase with annealing time. This can be clearly seen in Figure 2, which shows oxidation of SiC particles at the surfaces of the nanocomposites. A low partial pressure of oxygen (pO_2) in the annealing furnace was thought to lead to the oxidation of SiC particles exposed on the surface:[5]

$$SiC(s) + O_2(g) \Longrightarrow SiO(g) + CO(g) \qquad (1)$$

This gaseous SiO can further react with the exposed alumina and oxygen to form mullite or a mullite composition glass:

$$2SiO(g) + 3Al_2O_3(s) + O_2(g) \Longrightarrow 3Al_2O_3.2SiO_2(s) \quad (2)$$

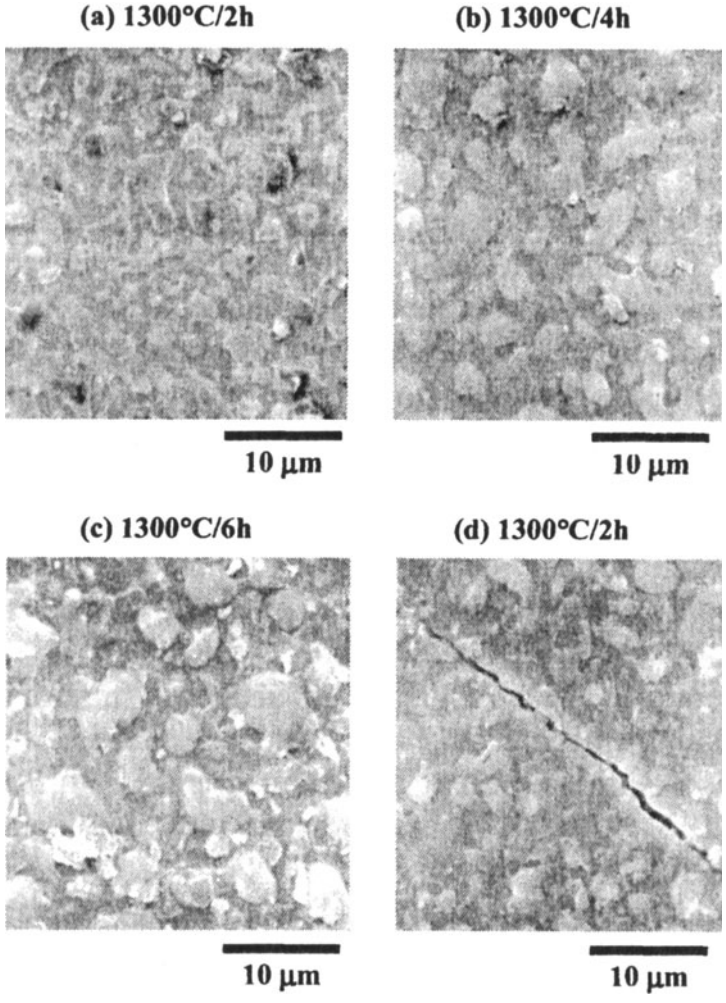

Figure 2 SEM micrographs showing surfaces of alumina/SiC nanocomposite after annealing in argon at 1300°C for (a) and (d) 2 hours, (b) 4 hours and (c) 6 hours. (d) shows partial crack healing; crack was induced by thermal shock (ΔT = 355°C). Some oxidation products can be seen on the surfaces.

If all the Si released by oxidation of SiC particles in the nanocomposite is converted to mullite there will also be a net volume expansion associated with the process, which could be responsible for crack healing.[5] Supporting evidence for this

hypothesis has been reported recently by Kim *at el.*.[21] They reported a 30% increase in strength of ground or polished alumina specimens when they were coated with a thin amorphous, mullite composition, layer produced by SiO reaction at 1400°C. Subsequent work by Wu *et al.*[6] on TEM investigations of annealed cross-sections of alumina/SiC nanocomposites also confirmed that the annealing process leads to surface crack healing.

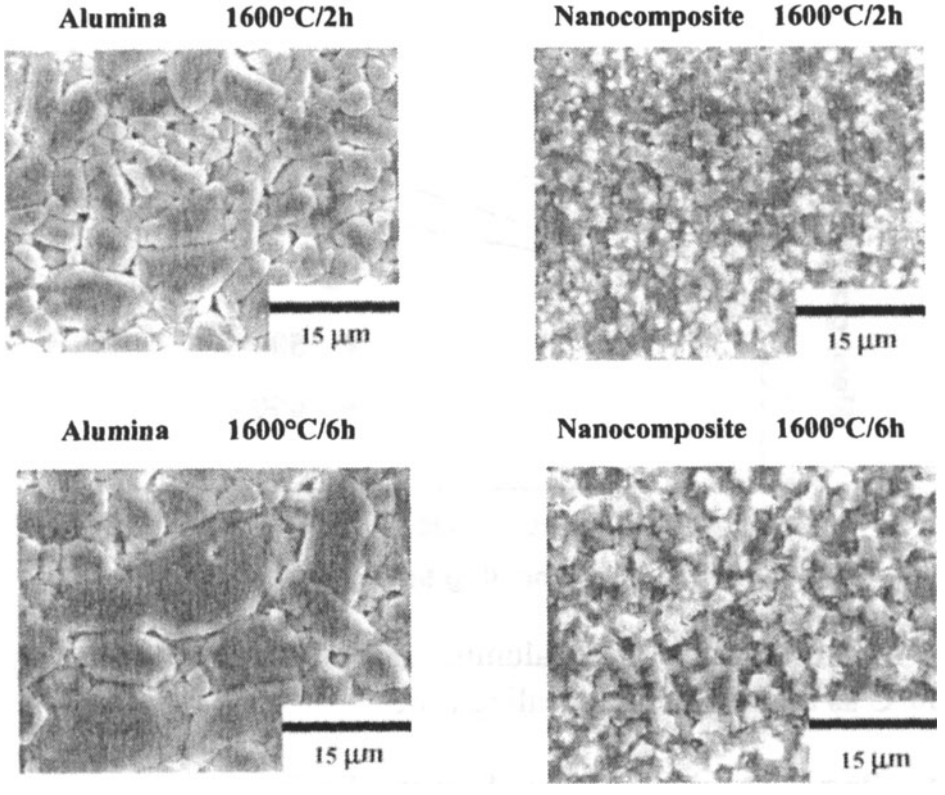

Figure 3 SEM micrographs showing surfaces of alumina (Alumina 1600) and alumina/SiC nanocomposite (C5% 1700) after annealing in argon at 1600°C for 2 h and 6 h.

The decrease in strength of alumina with prolonged annealing has been observed by other workers[7, 8, 11, 22] and has been attributed to grain growth. The grain growth depends on both annealing temperature and time. Figure 3 shows SEM micrographs of the alumina and nanocomposites after annealing at 1600°C. Figure 4 shows the grain size of the alumina after annealing at 1500°C and 1600°C. For annealing at 1500°C, the grain size increases gradually from 4 μm to 7μm with increasing annealing time up to 360 min. When annealed at 1600°C, the alumina showed a large

grain size ≈ 9 μm after annealing for 360 min. For the nanocomposite, data for grain growth were not obtainable due to the difficulties caused by surface oxidation in observation of the grain structure (See Figure 3).

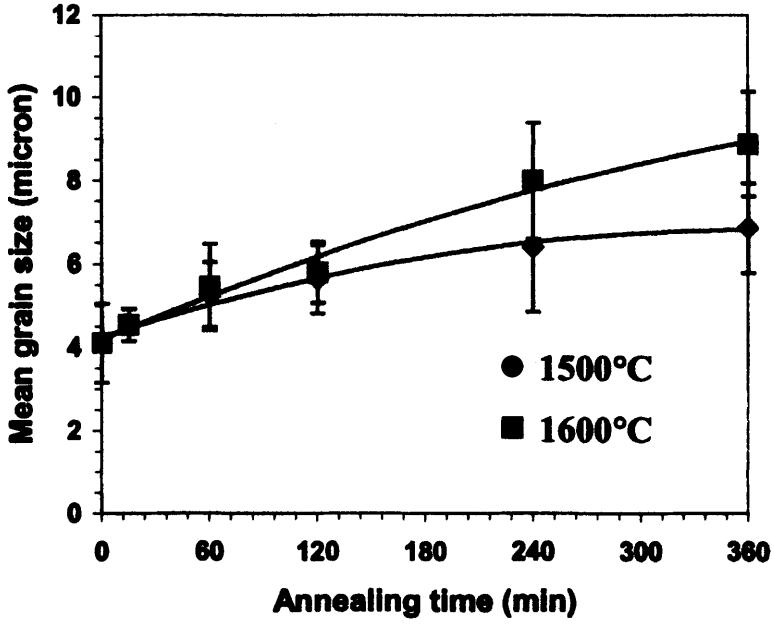

Figure 4 Mean grain size of the alumina annealed under flowing argon at 1500°C and 1600°C as a function of annealing time.

Crack healing in specimens after thermal shock

Annealing tests were performed on polished materials thermally shocked with ΔT = 373°C. This is above the temperature difference required to produce significant strength loss in all the materials used here. The room temperature strength of the as-polished specimens and those after thermal shock are shown in Table 2. Thermal shock at ΔT = 373°C causes dramatic decreases in strength. Figure 5 shows the strength of the thermally-shocked alumina and alumina/ 5vol.%SiC nanocomposite after annealing under flowing argon for various times at 1300, 1500, and 1600°C normalised to the values for non-shocked materials.

For annealing at 1300°C, strength of all the annealed thermally-shocked materials increased very slightly with annealing time, and was not completely recovered even after annealing for 360 min. In the nanocomposite, the recovery is slower than in

alumina. When annealed at 1500°C, the strength of thermally-shocked alumina both (ground and polished) increased continuously with annealing time, and was almost completely recovered within 240 min (See—Figure 5 a, b). For the ground and polished nanocomposites (See—Figure 5 c, d), the recovery is slower and strength was not completely recovered even at the longest annealing time of 360 min. In fact the strength of the ground nanocomposite slightly increased when annealed for 60 min and then decreased with increasing annealing times.

Table 2 Fracture strength of alumina and alumina/ 5vol.% SiC nanocomposite.

Material	Condition	σ_f (MPa)	
		Ground	Polished
Alumina	No quenching	345 ± 64	371 ± 10
	Quenching	**82 ± 11**	**102 ± 9**
Nanocomposite	No quenching	373 ± 88	417 ± 56
	Quenching	**49 ± 51**	**11 ± 7**

After annealing at 1600°C, the strength of thermally-shocked ground and polished alumina increased continuously with annealing time, and was completely recovered within 15 min for ground alumina and within 60 min for polished alumina (See—Figure 5 a, b). The strength of the ground alumina is first increased above that before shocking after annealing at this temperature. The strength of both ground and polished nanocomposites after annealing shows similar behaviour to that of alumina but strength was not completely recovered. The maximum strength recovery was to 25 % of the original level in the polished nanocomposite and to 40 % in the ground nanocomposite.

The current results show a strength recovery in the thermally-shocked alumina and nanocomposite. The beneficial effect of annealing on the strength of the materials studied here are attributable to crack healing, discussed in detail elsewhere.[12, 14, 16] One possible reason for the slow recovery in strength of the nanocomposite compared to that of the alumina may be attributed to the higher level of damage introduced by the thermal shock. The strength degradation caused by thermal shock was greater in the nanocomposite than in the alumina and therefore both the maximum and average crack depth in the thermally-shocked nanocomposite would be expected to be greater than in the alumina. These larger cracks will heal more slowly.

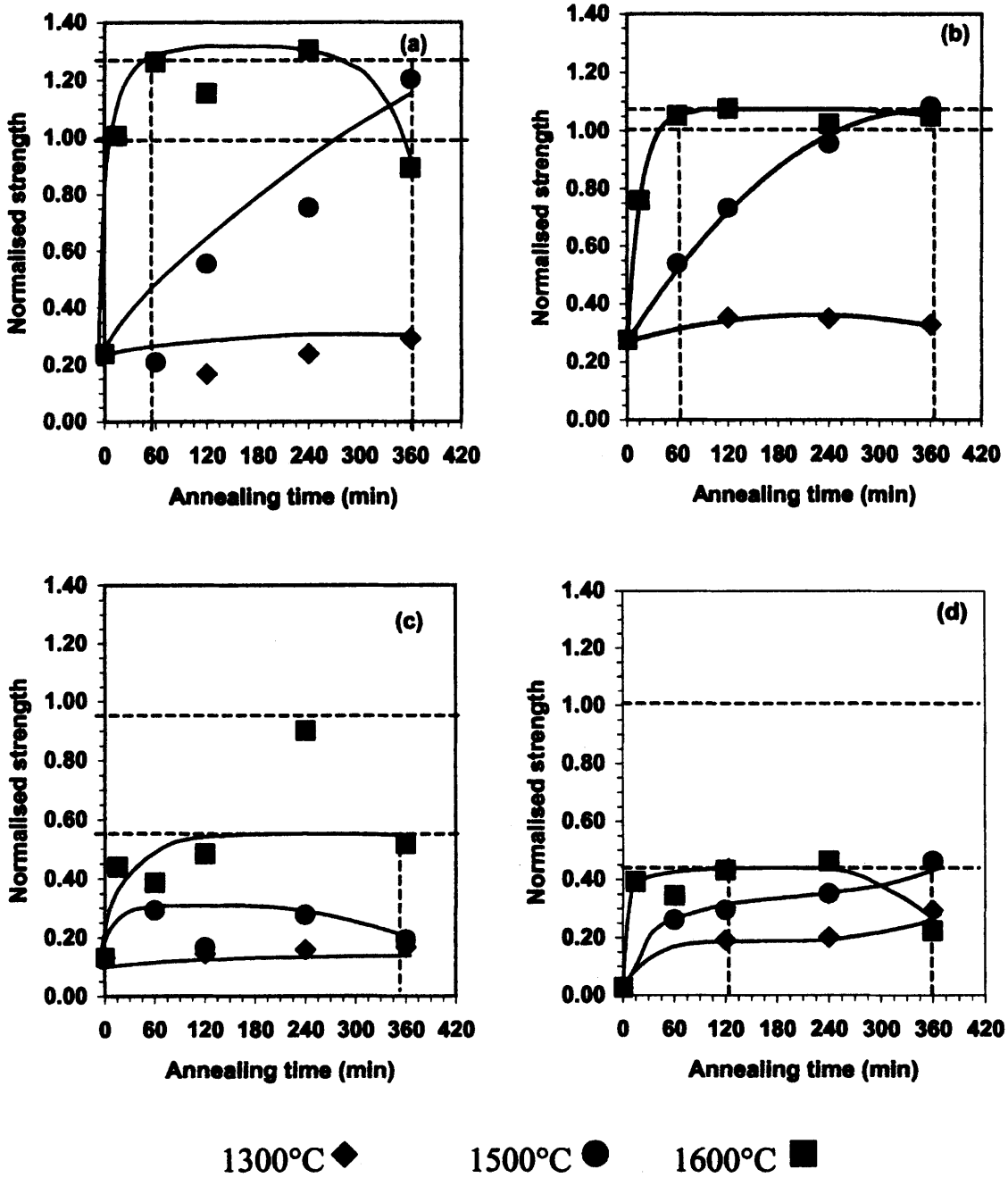

Figure 5 Fracture strength of thermally-shocked alumina (Alumina 1600) and alumina/SiC nanocomposite (C5% 1700) after annealing under flowing argon for various times at temperatures of 1300°C, 1500°C, and 1600°C. (a) and (b) are ground and polished alumina, respectively. (c) and (d) are ground and polished alumina/SiC nanocomposite, respectively.

CONCLUSION

Annealing treatments produce increases in strength in thermally shocked specimens of both alumina and nanocomposite towards the values for non-thermally shocked material. The rate of recovery was much greater in the pure alumina than in the nanocomposite. The beneficial effect of annealing on strength of the thermally-shocked alumina and the nanocomposite are attributed to crack healing. The greater thermal shock damage in the nanocomposite results in a slower recovery rate than for alumina.

Acknowledgements—S. Maensiri would like to thank the Ministry of Science, Technology, and Environment (MSTE), The Royal Thai Government, and Khon Kaen University, Thailand for financial support.

REFERENCES

[1]K. Niihara, "New Design Concept of Structural Ceramics," *J. Ceram. Soc. Jpn.*, **99** [10] 974-982 (1991).

[2]J. Zhao, L. C. Stearns, M. P. Hammer, H. M. Chan, G. A. Miller and R. F. Cook, "Mechanical Behaviour of Alumina-Silicon Carbide 'Nanocomposites'," *J. Am. Ceram. Soc.*, **76**[2], 503-510 (1993).

[3]A. M. Thompson, H. M. Chan and M. P. Harmer, "Crack Healing and Stress Relaxation in Al_2O_3-SiC "Nanocomposite"," *J. Am. Ceram. Soc.*, **78** [3], 567-571 (1995).

[4]I. A. Chou, H. M. Chan and M. P. Harmer, "Effect of Annealing Environment on the Crack Healing and Mechanical Behaviour of Silicon Carbide-Reinforced Alumina Nanocomposites," *J. Am. Ceram. Soc.*, **81** [5], 1203-1208 (1998).

[5]H. Z. Wu, C. W. Lawrence, S. G. Roberts and B. Derby, "The Strength of Al_2O_3/SiC Nanocomposites after Grinding and Annealing," *Acta mater.* **46** [11], 3839-3848 (1998).

[6]H. Z. Wu, J. M. Titchmarch, S. G. Roberts and B. Derby, "Crack Healing in an Alumina/Silicon Carbide Nanocomposite after Grinding and Annealing"; pp. 327-332 in *Nanophase and Nanocomposite Materials III, vol. 581*. Material Research Society Symposium Proceedings, 1999.

[7]F. F. Lange and T. K. Gupta, "Crack Healing by Heat Treatment. *J. Am. Ceram. Soc.*, **53** [1], 54-55 (1970).

[8]F. F. Lange and K. C. Radford, Healing of Surface Cracks in Polycrystalline Al_2O_3," *J. Am. Ceram. Soc.*, **53** [7], 420-421 (1970).

[9]T. K. Gupta, Crack Healing in Thermally Shocked MgO," *J. Am. Ceram. Soc.*, **58** [3-4], 448-449 (1975).

[10]T. K. Gupta, "Crack Healing and Strengthening of Thermally Shocked Alumina," *J. Am. Ceram. Soc.*, **59** [5-6], 259-262 (1976).

[11]T. K. Gupta, "Instability of Cylindrical Voids in Alumina," *J. Am. Ceram. Soc.*, **61** [5-6], 191-195 (1978).

[12]T. K. Gupta, "Effect of Crack Healing on Thermal Stress Fracture"; pp.365-380 in *Thermal stresses in severe environments*. Edited by D. P. H. Hasselman and R. A. Heller. Plenum Press, New York, 1980.

[13]S. Maensiri and S. G. Roberts, "Thermal Shock Resistance of Sintered Alumina/SiC Nanocomposites Evaluated by Indentation Techniques," *J. Am. Ceram. Soc.*, (Accepted)

[14]A. G. Evans and E. A. Charles, "Strength Recovery by Diffusive Crack Healing," *Acta Mater.*, **25**, 919-927 (1977).

[15]B. J. Hockey, "Crack Healing in Brittle Materials"; pp. 637-658 in *Fracture Mechanics of Ceramics, Vol. 6*. Edited by R. C. Bradt *et al.*, Plenum Press, New York, 1983.

[16]E. D. Case, J. R. Smyth and O. Hunter, Jr, "Microcrack Healing During the Temperature Cycling of Single Phase Ceramics"; pp. 507-530 in *Fracture Mechanics of Ceramics, Vol. 5*. Edited by R. C. Bradt *et al.*, Plenum Press, New York, 1983.

[17]Y. Kim, Y. and E. D. Case, "Time-Dependent Elastic Modulus Recovery Measurement on Thermally Shock SiC Fibre-Aluminosilicate Composites, Machinable Glass Ceramics and Polycrystalline Alumina," *J. Mater. Sci.* **27**, 1537-1545 (1992).

[18]S. R. Choi and V. Tikare, "Crack Healing of Alumina with a Residual Glassy Phase: Strength, Fracture Toughness and Fatigue," *Mater. Sci. Eng.*, **A171**, 77-83 (1993).

[19]J. E. Moffatt, W. J. Plumbridge and R. Herman, "High Temperature Crack Annealing Effects on Fracture Toughness of Alumina and Alumina-SiC Composite," *Brit. Ceram. Trans.*, **95** [1], 23-29 (1996).

[20]R. F. Cook, "Influence of crack velocity thresholds on stabilized nonequilibrium fracture," *J. Appl. Phys.* **65** [5], 1902-1910 (1989).

[21]H-E. Kim, A. J. Moorhead and S-H. Kim, "Strengthening of alumina by formation of a mullite/glass layer on the surface," *J. Am. Ceram. Soc.*, **80** [7], 1877-1880 (1997).

[22]J. T. B. Roberts and B. J. Wrona, "Crack Healing and Strength Recovery in UO_2," *J. Am. Ceram. Soc.*, **56** [6], 297-299 (1973).

MICROSTRUCTURE – ELECTRICAL PROPERTY RELATIONSHIP IN NANOCRYSTALLINE CeO_2 THIN FILMS

V. Petrovsky, B. P. Gorman*, H. U. Anderson and T.Petrovsky
Electronic Materials Applied Research Center, University of Missouri–Rolla, Rolla, MO 65409

ABSTRACT

Optical and electrical properties of nanocrystalline cerium oxide thin films undoped and doped by Gd and Sm were investigated. Two routes (colloidal suspensions and polymeric precursors) were used for film preparation using silica and alumina as substrates. The combination of the two preparation techniques made possible to obtain films with grain size from 5 to 100nm and wide region of the porosity (from less than 5% to 50%). The values of thickness, density and grain size were obtained from the optical measurements. Nanocrystalline films with very small grain size (less than 10nm) show small difference in the value of conductivity and activation energy for all film composition and preparation techniques investigated. For ceria films deposited on silica substrates, it was found that the conductivity decreases and activation energy increases for annealing temperatures as low as 600°C. In contrast, films that were deposited on sapphire substrates showed conductivity increases and activation energy decreases as the annealing temperature and grain size increases and approached the values obtained for dense polycrystalline specimens ($\sigma \sim 0.01$ S/cm at 600°C, E ~ 0.7 eV) at the annealing temperature of 1000°C (grain size ~ 60 nm).

INTRODUCTION

CeO_2 (ceria) based materials have been widely investigated, mainly due to high ionic conductivity. This property makes them highly desirable as electrolytes and electrodes in solid oxide fuel cells and oxygen separation membranes. Recent

* present address: Dept. of Materials Science, University of North Texas, Denton TX 76203

reviews of ceria-based materials for these applications give highly detailed properties of this system [1-3].

Ceria has a fluorite structure over a wide temperature and oxygen partial pressure range. Ce^{4+} reduces to Ce^{3+} with a decrease in oxygen partial pressure, which greatly increases the electronic portion of the conductivity. The partial pressure at which this occurs is highly dependent upon the impurity level of acceptor dopants in the raw material [4,5]. For electrolyte applications where the electronic portion of the conductivity should be kept to a minimum, CeO_2 is typically doped with acceptors such as Gd^{3+} or Sm^{3+} [6-9].

Thin film undoped and doped CeO_2 have also been extensively studied [10-12]. These studies have shown that nanocrystalline films with high ionic conductivity can be prepared, however, there may be problems associated with impurity effects related to impurities contained either in the starting materials or those resulting from interactions between the films and the substrates. Studies have also shown that increased electronic conductivity occures in the nanocrystalline region due to decreased oxygen vacancy formation energy at these grain boundaries [10,13-17]. In an effort to understand the observed effects, this investigation has focused on the study of the electrical conductivity and optical properties in porous nanocrystalline CeO_2 (99.999% purity) thin films processed using a colloidal deposition technique and dense nanocrystalline films produced by a polymer precursor process (99% purity). The grain size and porosity were varied by the sintering, and the conductivity was measured using DC 2-probe and 4-probe technique.

EXPERIMENTAL

The high purity nanocrystalline powders which were used for colloidal deposition were prepared by an aqueous precipitation processing route using 99.999% cerium (III) nitrate (Alfa Aesar, Inc.) which was dissolved in distilled water and precipitated to cerium hydroxide particles using hydrogen peroxide and ammonium hydroxide, as illustrated by Djuricic and Pickering [18]. The hydrated powder was then annealed at 150°C in order to form the full fluorite structured CeO_2 powder. Samarium doped nanocrystalline ceria was obtained from NexTech Materials, Inc. for preparation of acceptor doped porous films.

Aqueous colloidal suspensions were prepared by mixing 10 weight percent of the CeO_2 powder in pH 5 distilled water (balanced with HNO_3) along with 5 weight percent butoxyethanol to aid in drying and decrease the wetting angle. The butoxyethanol also partially polymerizes due to the acidic content of the solution,

and as a consequence aids in increasing the solution viscosity and in the formation of a continuous film. The powder was then dispersed in the solution using a high intensity ultrasonic probe for about one hour and than filtered through a 0.45μm glass fiber filter (Whatman, Inc.) in order to remove any foreign matter.

For the polymeric precursor preparation cerium and gadolinium nitrates (99% purity) were used as the cation sources and ethylene glycol was polymerizing agent. The nitrates were mixed in the desired ratio and dissolved in the water-ethylene glycol mixture. Partial polymerization was accomplished by heating the solution at 70°C for 75h. Polymerized precursors were also filtered through Whatman, Inc. glass fiber filters. Details of the polymeric solution preparation and dense film deposition are presented elsewhere [10].

Thin films were prepared by spin coating the precursor on quartz and sapphire substrates. Optical quality, both sides polished (0001) oriented sapphire substrates were used for both the optical measurements as well as the DC conductivity measurements. Single crystal quartz substrates were used only for electrical measurements to investigate possible influence of the substrate material on electrical properties of the film.

The films were deposited on the substrates by spinning at 1500rpm for 30 seconds and subsequently dried at 70°C for an hour. The films were then heat treated at 350°C for an hour and cooled back to room temperature after which subsequent coatings could be deposited. Sintering of the films was done in a small box furnace using a ramp rate of 5°C/min to the maximum temperature, with a 2 hour hold at maximum temperature. The films were characterized according to their grain size, thickness and density using X-ray diffraction, mechanical profilometry, ellipsometry, and UV-Vis spectroscopy, as shown in previous studies [11,12]. The resulting film density and thickness are shown in Fig.1 for colloidal films. It can be seen that after 400°C the initial films have density of approximately 50% and grain size of 5 nm after 400°C and densify to 85% with a grain size of 60 nm after annealing at 1000°C.

X-ray diffraction showed that the films are single-phase fluorite structured and have no reaction with the substrate visible in the XRD spectra over the investigated temperatures. Peak broadening grain size calculations (Reitfeld analyses) from the diffraction patterns correlate well with those in FESEM images (Fig.2).

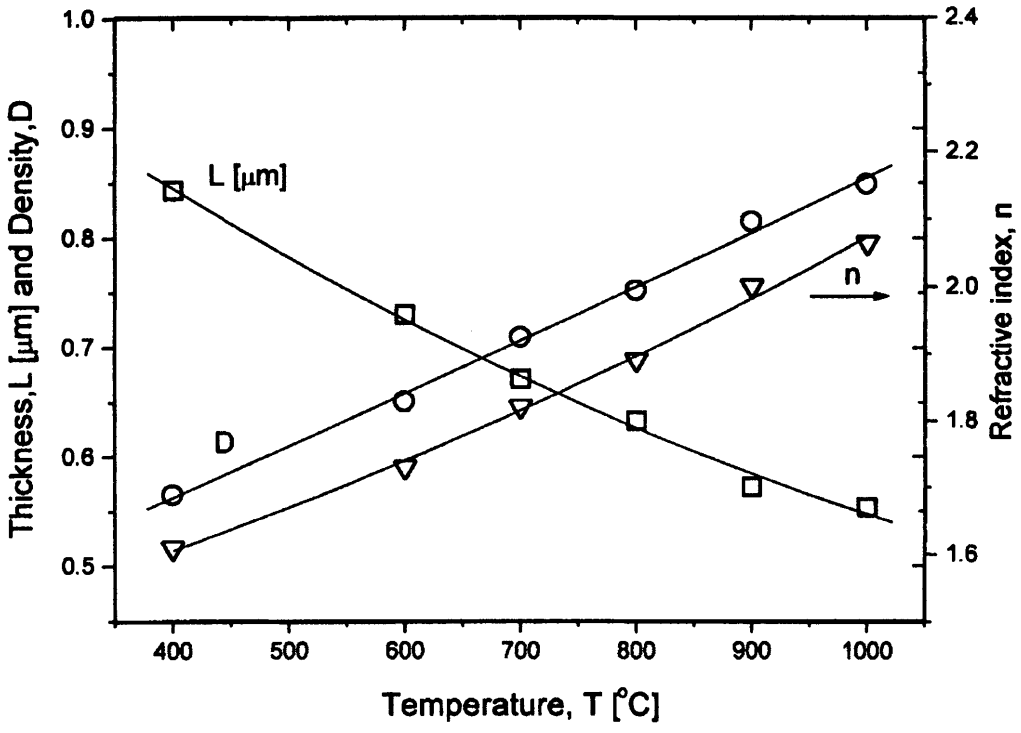

Figure 1. Change in film thickness, refractive index and density as a function of annealing temperature for colloidal processed CeO_2 thin films [11].

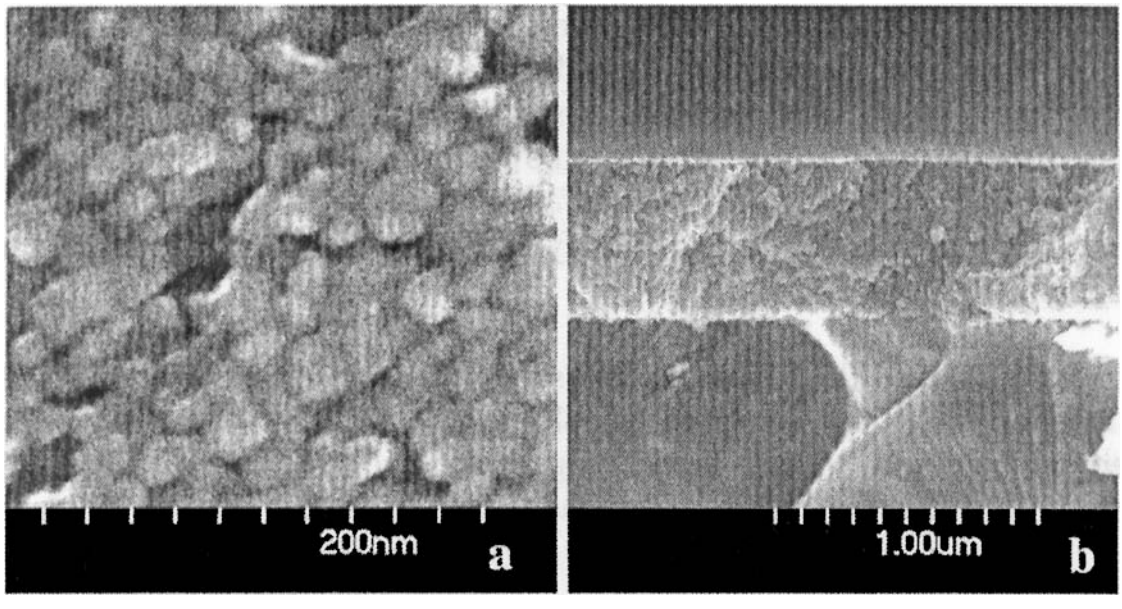

Figure 2. FESEM images of CeO_2 thin films on sapphire substrates after annealing at 700°C for 2 hours. (a) - the surface (b) - fracture cross section

DC electrical conductivity measurements were done in 4-probe and 2-probe configuration. Silver paste was used as the 4 electrode contacts for each sample. The contacts were painted on and annealed at 600°C for 1 hour (with the exception of samples sintered at 400°C, where the electrodes were annealed at the same temperature for 1 hour). After annealing, the electrodes were attached to Pt wire leads, which ultimately were contacted to the testing apparatus.

A Keithley 4915A electrometer connected to a personal computer was used as a measuring device. It was possible to make current - voltage measurements or pulsing technique in both 2-probe and 4-probe configurations. The current - voltage characteristics were used to check the ohmic character of the contacts. Delay time between each voltage application was varied in order to minimize hysteresis effects connected with the high resistance of the samples. I-V characteristics were linear, if a sufficiently long delay time was chosen. The magnitude of the delay depended on the temperature and increased up to 1s for the lower temperature region.

Pulsing techniques using direct current are particularly useful for measurements of the high resistance samples (Fig.3). With this technique it is possible to exclude the relaxation process, provide accurate measurements on the plateau and check the symmetry of the sample properties by comparing the measurements at the positive and negative bias. This technique was used for 2-probe and 4-probe measurements of the sample resistance.

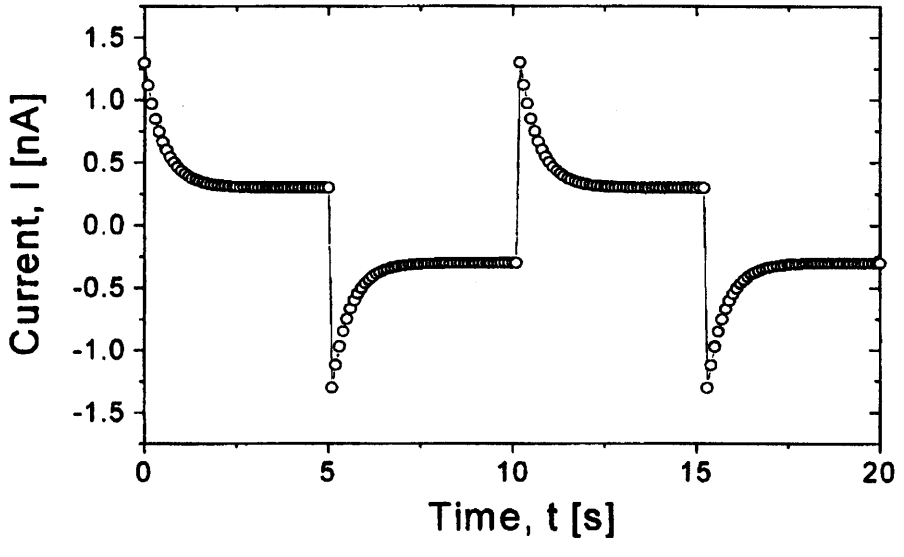

Figure 3. Pulsing technique for the measurements of ceria films.

RESULTS

Two basic features differ nanocrystalline films from microcrystalline dense specimens. First of all the starting material has extremely small grain size (almost amorphous), and it remains small (< 60 nm) over all of the temperature regions of this investigation. This high degree of disorder can effect electrical properties of the material. The question is how big this effect could be and what is the critical size of the grains to have the conductivity comparable with microcrystalline specimens of the material?

The second difference is the presence of the substrate which can effect the properties of the film by reaction with the film. The possible effect of the substrate was investigated by deposition the dense nanocrystalline films on quartz and sapphire substrates under the same conditions by the polymeric precursor process. The results of this investigation are shown in Fig.4 as an Arrhenius plot of the electrical conductivity for dense gadolinium doped ceria (CGO) films.

It can be seen from the figure that for the films annealed at 600°C or lower, the conductivity does not depend on the substrate and the activation energy is the same ~1.1eV until the film has reached temperatures exceeding about 700°C (open circles and up triangles). When the measurement and/or annealing temperature exceeds temperatures of about 700°C, the slope for the film on sapphire substrate remains the same up to 900°C while for the film on the quartz substrate shows a decrease in slope. These changes in the conductivity are nonreversible. By the time, the temperature reached 900°C, the conductivity of the film on quartz (down triangles) was about an order of magnitude lower than on sapphire (closed circles). When the films were annealed at 900°C for 3h an even larger difference was observed (open squares and diamonds). The final activation energy for the films on the quartz substrate increased to 1.2eV, whereas that on the sapphire substrate decreased to 0.9eV. There is no doubt that silica penetrates the film from the quartz substrate and suppresses the conductivity by increasing the hopping barrier for the oxygen vacancy migration. This is probably due to an increase in the grain boundary resistance.

The more difficult problem is interpretation of the data for the film on sapphire substrates. There is an increase in the conductivity and decrease in the activation energy at the sintering process, but the conductivity obtained is smaller than for dense polycrystalline specimens and the activation energy is higher (see Fig.4). Different explanations of this fact are possible. The first explanation is with the small grain size the grain boundary resistance is dominating the total resistance, the second explanation is the presence of uncontrolled contaminations in the film

and the third is diffusion of the aluminum into the film from the sapphire substrate.

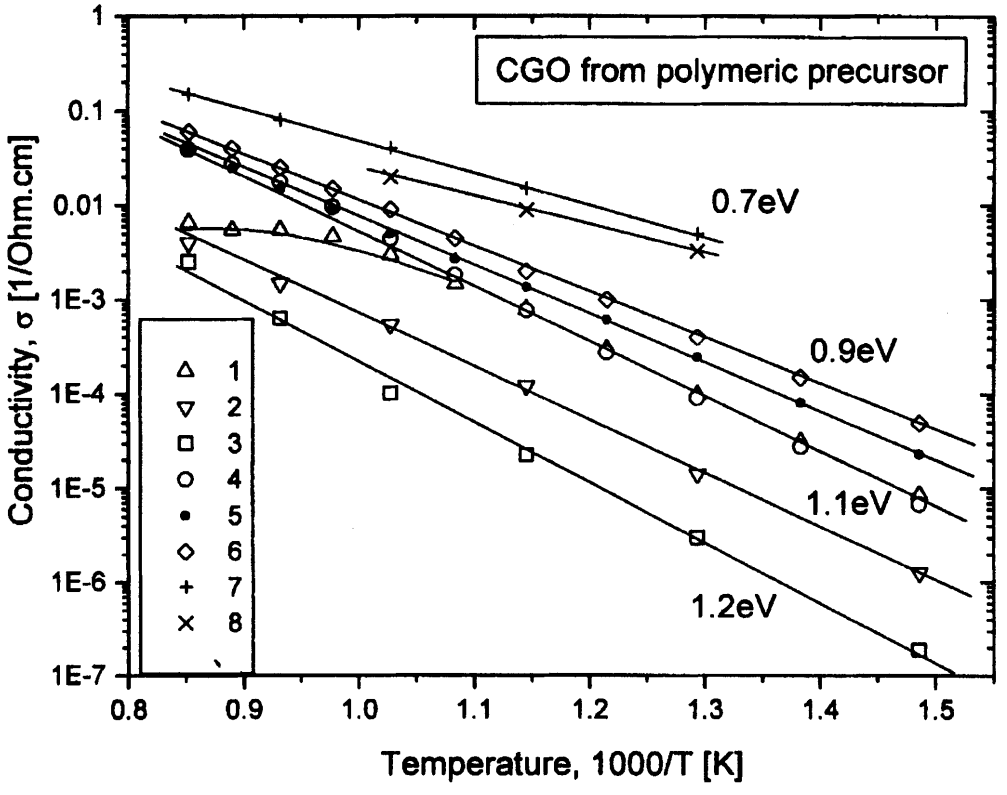

Figure 4. Temperature dependence of the conductivity for gadolinium doped ceria films deposited on quartz and sapphire substrates.
(1-3) – Film on quartz substrate, (4-6) – Film on sapphire substrate,
(7,8) – Polycrystalline specimens – literature data (7- CSO, NexTech; 8-CGO, Stele [6]]);
(1,4) – Increase temperature, (2,5) – Decrease temperature, (3,6) – Annealed at 900°C for 3 h.

The way to differentiate these effects is to use another precursors, prepared by different technology. Colloidal suspensions of samarium doped and extremely pure ceria were used for this purpose (Fig.5). It is seen from the figure that again the initial conductivity and the energy activation (E~1.1eV) are the same for the films prepared from both precursors (solid circles and diamonds). This result is quit similar to that observed for the dense films obtained from ceria-gadolinium polymeric precursor: activation energy is the same and the conductivity is only slightly smaller (which can be connected with high porosity of the colloidal films). It looks like initial conductivity is controlled by extremely small grain size and is not sensitive to the composition or precursor nature.

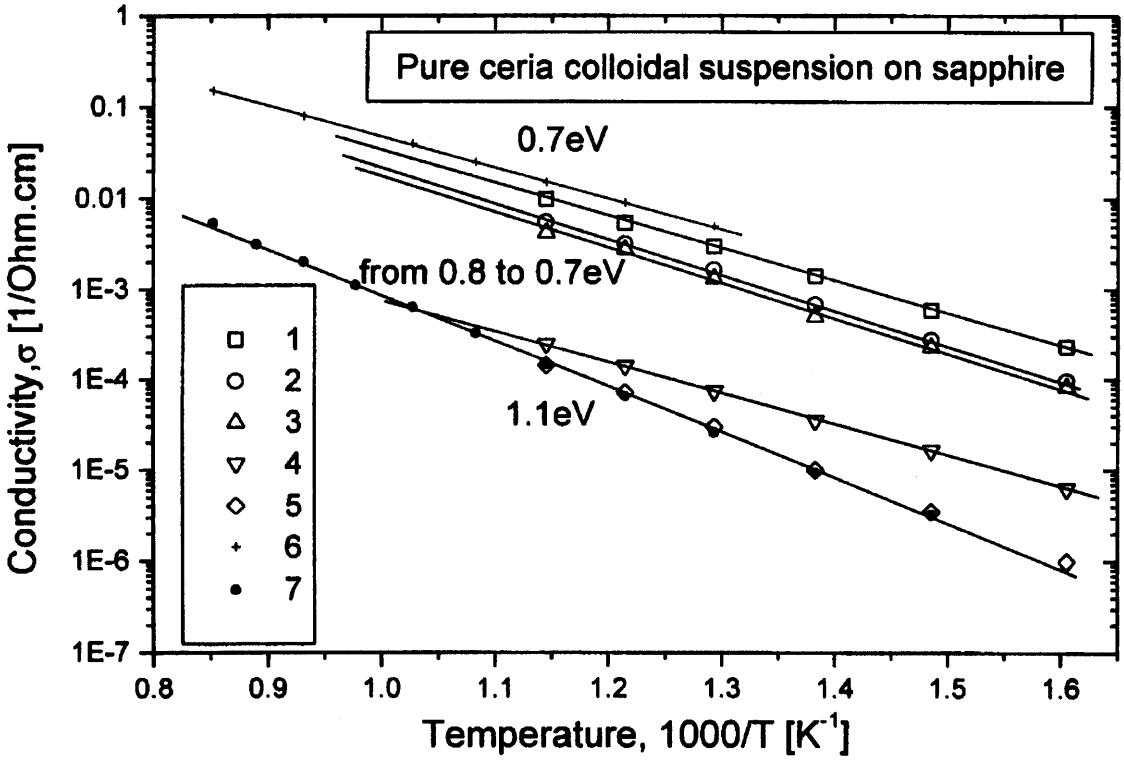

Figure 5. Temperature dependence of conductivity for pure ceria colloidal suspension. Different annealing temperatures.
(1-5) – Pure ceria film, (6) – Polycrystalline CSO, NexTech, (7) – Colloidal CSO;
Annealing temperature: 1–1000°C, 2–900°C, 3–800°C, 4–700°C, 5–600°C.

The properties of the colloidal samarium doped ceria prepared film did not change with annealing up to1000°C (temperature dependence of the conductivity remains the same), which possibly may be connected with impurities in the initial powder. (This is purely speculation, since the impurity levels have not be measured).
In the case of the films prepared with the undoped, higher purity colloidal ceria very different results were observed. As can be seen from Fig.5 the conductivity starts to increase after 700°C sintering and the activation energy decreases. The sintering at 1000°C gives the conductivity and activation energy comparable with that reported for polycrystalline specimens (see Fig.5).
The dependences of the conductivity and activation energy are presented on Fig.6 as the function of grain size. It can be seen that the activation energy decreases quickly as grain size increases from 10 to 20nm and than decreases very slowly from 0.8 to 0.7eV for further grain size increase. That suggests that the barrier for the motion of oxygen vacancies changes little after grain size reaches about 20nm and is controlled by the grains rather than grain boundaries. The question that

needs to be addressed is why the conductivity of undoped film increases to the level observed for dense polycrystalline samarium doped specimens? A possible explanation would be interdiffusion of the sapphire substrate with the film. If this were the case, the Al_2O_3 can play role of an acceptor impurity (similar to Sm_2O_3 or Gd_2O_3). Acceptor doping should be not effective for stabilized materials (Sm or Gd doped), because the addition of acceptor impurity beyond the level already there will do little to increase the conductivity. However, in the case of undoped material, such acceptor doping could result in substantial increase in the conductivity, proportionally to the acceptor concentration without changing the activation energy. This behavior is in full agreement with the experimental data presented. It is necessary to emphasize that at this time there are no data in this study to substantiate the hypothesis that such diffusion occurred, however, the acceptor behavior of alumina in the ceria-alumina-silica solid solution was shown earlier [19]. More precisely, it was shown that the ratio of Ce^{3+} / Ce^{4+} increases with the increase of alumina content.

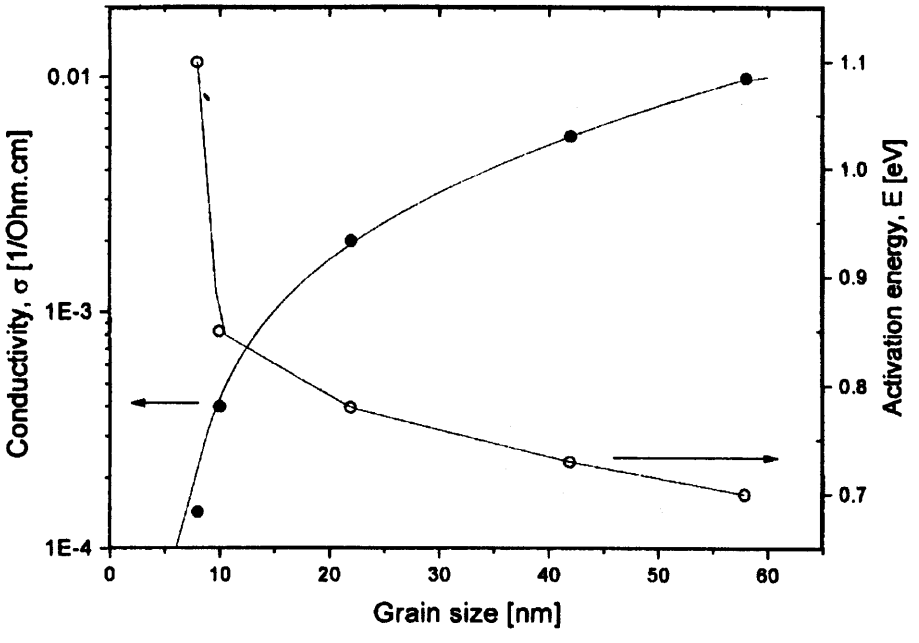

Figure 6. Electrical conductivity at 600°C and activation energy as a function of grain size. Pure ceria colloidal films.

CONCLUSIONS

- The interaction of ceria films with silica limits the use of silica as a substrate to temperatures below 600-700°C.
- Grain size limits the conductivity only in the very small grain size region (less than 10-20nm). The conductivity and activation energy is not sensitive to the composition of the film or precursor used in this grain size region.
- It is possible to achieve small activation energy (~0.7eV) and the conductivity comparable with the dense polycrystalline specimens (0.01S/cm at 600°C), if pure starting materials are used for the film preparation.

REFERENCES

1. M. Mogensen, N. M Sammes and G. A. Tompsett, Solid State Ionics **129**, 63 (2000).
2. H. Inaba and H. Tagawa, Solid State Ionics **83**, 1 (1996).
3. B. C. H. Steele, in: High Conductivity Solid Ionic Conductors, ed. T. Takahashi, (World Scientific, Singapore, 1989).
4. E. K. Chang and R. N. Blumenthal, J. Solid State Chem. **72**, 330 (1988).
5. H. L. Tuller, in: O. Toft Sorensen (Ed.), Nonstoichiometric Oxides, Academic Press, 1981, p. 271.
6. B. C. H. Steele, Solid State Ionics **129**, 95 (2000).
7. B. Zachau-Christiansen, T. Jacobsen and K. West, in: SOFC III, The Electrochemical Society, Inc., p. 104 (1991).
8. M. Godickemeier and L. J. Gauckler, J. Electrochem. Soc. **145** [2], 414 (1998).
9. H. Uchida, H. Suzuki and M. Watanabe, J. Electrochem. Soc. **145** [2], 615 (1998).
10. I. Kosacki and H. U. Anderson, Ionics **6**, 294 (2000).
11. V. Petrovsky, B. P. Gorman, H. U. Anderson and T. Petrovsky, J. Appl. Phys., submitted (2001).
12. V. Petrovsky, B. P. Gorman, H. U. Anderson and T. Petrovsky, MRS Proceedings, in print (2000).
13. H. L. Tuller, Solid State Ionics **131**, 143 (2000).
14. Y.-M. Chiang, E. B. Lavik, I. Kosacki, H. L. Tuller and J. Y. Ying, Appl. Phys. Lett. **69** [2], 185 (1996).
15. J. –H. Hwang and T. O. Mason, Z. Phys. Chem. **207**, 21 (1998).
16. T. Suzuki, I. Kosacki and H. U. Anderson, in: P. Vincenzini and V. Buscaglia (Eds.) *Mass and Charge Transport in Inorganic Materials: Fundamentals to Devices, Part A*, Techna Srl, 2000, p. 419-29.
17. A. Atkinsson and C. Monty, in: L. C. Dufour, et al. (Ed.), Surfaces and Interfaces of Ceramic Materials, Kluwer Academic, Dodrecht, The Netherlands, 1989, p. 273.
18. B. Djuricic and S. Pickering, J. Eur. Cer. Soc. **19**, 1925 (1999).
19. Sin-Lung Lin, Chii-Shyang Hvang and Jyh-Fu Lee, J.Mater.Res, **11**, 2641 (1996).

New Nanostructured Silicon and Titanium Nitride Composite Anodes for Li-Ion Batteries

Il-seok Kim[a] and Prashant N. Kumta[a]

[a]Carnegie Mellon University, Pittsburgh, Pennsylvania 15213

G. E. Blomgren[a,*]

*Blomgren consulting Services Ltd., 1554 Clarence Avenue, Lakewood, Ohio 44107

ABSTRACT

Silicon based nanocomposites containing TiN were synthesized by high-energy mechanical milling (HEMM). Mechanical milling leads to very fine amorphous silicon particles distributed homogeneously inside the TiN matrix. The Si/TiN nanocomposites synthesized using different experimental conditions were evaluated for their electrochemical properties. Results indicate that silicon in the composite alloys and de-alloys with lithium during cycling, while TiN remains inactive providing structural stability. The composite containing 33.3 mol% silicon obtained after milling for 12 h exhibited a high capacity, ≈ 300 mAh/g with good capacity retention reflective of the good phase and micro-structural stability as verified by XRD and SEM analyses. Conventional and high-resolution electron microscopy coupled with electron energy-loss spectroscopy conducted on the composites validated the existence of amorphous silicon in a nanocrystalline TiN matrix.

INTRODUCTION

Graphite has so far been the customary anode material for lithium ion batteries with a theoretical capacity of 372 mAh/g or volumetric capacity of 830 Ah/L.[1] During the last few years, however, much of the research efforts have been directed towards identifying alternative anode materials. Fuji demonstrated the potential of nanostructured materials for lithium-ion anodes in a series of patents related to tin oxide.[2] Electrochemical insertion of lithium leads to the *in situ* generation of nanosized tin clusters in a matrix comprising of an electrochemically inactive oxide glass. The system is indeed promising demonstrating an initial reversible capacity of ≈ 600 mAh/g. A major limitation of the system is however the irreversible loss of lithium consumed in the electrochemical reduction of tin oxide. Nevertheless, these initial results helped to demonstrate the possibility of minimizing or perhaps even eliminating the large volume-induced strain during cycling, characteristic of lithium containing Zintl phases by the generation of active-inactive nanostructured composites. The validity of these concepts has been further successfully demonstrated in the Sn-Fe-C, Cu-Sn and other intermetallic systems.[3-6]

In order to preserve and stabilize the original morphological state of the anode and thereby attain good electrochemical properties, various material systems have been analyzed to minimize the mechanical stress caused by the large phase transition induced volumetric changes experienced by the active phase. Most of the current studies on anode materials other than carbon have focused on creating a composite microstructure comprising an inactive host matrix containing a finely dispersed interconnected active phase.[2-6] Although these systems are promising, there are problems related to either irreversible loss, capacity and/or cyclability. These results make it very essential to focus on approaches to improve further the demonstrated concept of active-inactive composites. This would require the identification of suitable materials systems and furthermore, the use of an appropriate approach for synthesizing the nanocrystalline composite.

The technique of mechanical alloying is known for its ability to generate nanocomposite

structures of metals, ceramics, semiconductors and even polymers. In this study, we have exploited this approach to improve upon the active-inactive concept further by exploring the generation of nanocrystalline composites in the Si/TiN system for use as an anode material. The composite was synthesized by using the technique of high-energy mechanical milling (HEMM). TiN is a well-known technological material used in several applications.[7-9] Due to its good electrical conductivity, high surface area TiN is also recently attracting interest for supercapacitor applications.[10, 11] However, to the best of our knowledge, there have been no reports to date on its use as an electrode in lithium ion batteries. The basic premise of this work is therefore to demonstrate the usefulness of TiN as an electrochemically inactive matrix in the presence of an electrochemically active silicon phase. This is because of the well-known electrical and mechanical properties of TiN such as electrical conductivity, mechanical strength, combined with electrochemical inertness to lithium (potential range 0.02 → 1.2 V)[12] and chemical inertness to both lithium and silicon. However, these favorable attributes of TiN with respect to lithium and silicon can only be exploited if a suitable process for synthesizing such composites can be identified. In this context, the technique of HEMM is indeed very promising due to its proven ability to generate amorphous, metastable, and nanophase structures.[13] Initial results on this system were reported earlier by us.[14] The present paper therefore focuses on using HEMM for generating novel nanocomposites in the Si-TiN system for use as anodes in Li-ion rechargeable batteries. Experimental studies and results of the structural and electrochemical analyses are presented indicating its promising nature. In addition, electron microscopy results validating the formation of nanocomposites are also provided.

EXPERIMENTAL

Nanocomposites of silicon and TiN were prepared using a SPEX-8000 high-energy mechanical mill. Commercially obtained elemental powder of silicon (Aldrich, 99%) and TiN (Aldrich, 99%)) were used as starting materials. Stoichiometric amounts of the powder were weighed and loaded into a hardened steel vial containing hardened steel balls. All the processes prior to milling were conducted inside the glovebox (VAC Atmospheres, Hawthorn, CA) and the vial was firmly sealed to prevent and minimize any oxidation of the silicon and titanium nitride.

In order to evaluate the electrochemical characteristics, electrodes were fabricated using the as-milled powder by mixing the composition containing 87.1 wt.% active powder and 7.3 wt.% acetylene black. A solution comprising 5.6 wt.% polyvinylidene fluoride (PVDF) in 1-methyl-2-pyrrolidinone (NMP) was added to the mixture. The as-prepared solution was coated onto a Cu foil. A hockey puck cell design was used employing lithium foil as an anode and 1 M $LiPF_6$ in EC/DMC (2:1) as the electrolyte. All the batteries tested in this study were cycled for 20 cycles in the voltage range from 0.02~1.2 V employing a current density of 0.25 mA/cm^2 and a rest period of 60 s between the charge/discharge cycles using a potentiostat (Arbin electrochemical instrument). The phases present in the as-milled powders and the cycled electrode were analyzed using x-ray diffraction (Rigaku, Cu K , θ/θ diffractometer), while the microstructure and chemical composition of the electrode was examined using a scanning electron microscope (Philips XL30, equipped with EDX). The microstructure of the powder was analyzed using a transmission electron microscope (Philips EM 420). In addition, electron energy-loss spectroscopy (EELS) was used to map the elements at the nano-scale using a high-resolution transmission electron microscope (HRTEM, JEOL 4000EX).

RESULT AND DISCUSSIOIN

Preliminary experiments conducted on Si/TiN composites comprising a molar ratio of Si:TiN = 1:2 (i.e. 33.3 mol% Si) exhibited the best electrochemical properties. Hence, the rest of the work focused on this particular composition. In order to analyze the phases present after milling, x-ray diffraction was conducted on the as-milled powders obtained after milling for various time periods (see Fig 1(a)). All the peaks in the patterns correspond to TiN and the broad nature of the peaks are clearly indicative of the nanocrystalline nature of the nitride. An estimate of the crystallite sizes was made by measuring the width of the XRD peaks and using them in the Scherer equation.[15] Results indicate that

the crystallites are in the 5 ~ 7 nm range. Peak broadening due to residual internal strain was not accounted for, and hence the actual size of the crystallites can be expected to be larger. The non-observance of any silicon related peak in XRD indicates that silicon exists in an x-ray amorphous form well dispersed inside the powder even after milling for only 6 h. This suggests that the HEMM process provides enough energy to generate the nanocomposite powder of silicon and TiN, although it is not clear whether silicon reacts with TiN to form any Si-N type bonds. More extensive structural characterization using MASS-NMR may be necessary to identify the existence of these environments. Nevertheless, based on the XRD patterns, it can be convincingly argued that the composites are composed of nanosized TiN containing a uniform dispersion of silicon independent of the composition. The very small size of the silicon crystals prevents the identification of a distinct phase boundary between silicon and TiN. As a result, it is possible that there is a continuous change in volume rather than abrupt discrete transitions normally observed. Thus its influence on the neighboring inactive phase is minimized. This is in fact, an important requirement for achieving good cyclability.

The specific gravimetric and the equivalent volumetric capacity of the electrode prepared with these powders are shown in Fig. 1 (b). The gravimetric capacity was converted to the equivalent volumetric form using the calculated density of the Si/TiN composite. The overall capacity appears to decrease as the milling time is increased, indicating a reduction in the amount of the active silicon phase. The exact reason for the decrease in capacity is still not clear and further detailed characterization studies are needed. The reasons at present could be speculated. One possible reason could be that the silicon nanoparticles are embedded or enclosed by TiN during milling, thereby preventing their reaction with lithium. The composite obtained after milling for 6 h shows fade in capacity, while the samples milled for a longer time exhibit moderate to good capacity retention. H. Li, et al. have investigated Si/carbon black composite for potential use as an anode.[16] The material although exhibits an initial capacity as high as ≈ 3000 mAh/g, however shows poor retention characteristics. This could be attributed to the poor binding between the active and inactive components.

The composite obtained after milling for 12 h exhibits an initial discharge capacity of 422mAh/g but a good stable average capacity of 300 mAh/g (see Fig. 1 (b)). The overall capacity is still lower than the theoretical capacity of 776 mAh/g, calculated assuming complete reaction of silicon with 4.4 Li. Although this data corresponds to the reaction of only 1.7 Li atoms per single atom of silicon, this does not necessarily suggest the formation of Li_xSi (x=1.7) due to a large (≈ 44%) fraction of inactive silicon as mentioned above. The composite exhibits a lower gravimetric capacity in comparison to conventional carbon, however, it exhibits a ~30% higher volumetric capacity, reflecting its promising nature.

Fig. 2 shows the variation of the cell potential with time for all the twenty cycles for the composite containing 33.3 mol% silicon obtained after milling for 12 h. The plot indicates that this anode composition exhibits a smooth plateau in the low voltage range without exhibiting significant fade in capacity. The difference on the time axis between the first and subsequent cycles suggests the first irreversible capacity loss (~30%). The exact reason for the irreversible loss is still unclear at the present stage. More detailed studies would be necessary to provide further insight into this problem. Some of the more obvious reasons could be the formation of Li-containing passivation layer and/or possible oxidation of the surface of the composite. Studies to assess these reasons are currently on-going.

An SEM micrograph and the energy dispersive x-ray (EDX) map of the 12h milled powder containing 33.3 mol% silicon are shown in Fig. 3. The particles are agglomerated although they are extremely small in the range of 100~500 nm. All these particles are therefore true composites containing an intimate mixture of silicon and TiN according to the EDX analysis. Thus, there is no evidence of any crystalline Si peaks in the XRD patterns. The EDX results also show the presence of iron (≈3.3%) in the as-milled powder, arising from the vial or the balls used during milling. The relatively small amount of iron can be assumed to have no detrimental influence on the capacity.

In order to analyze any changes in the microstructure or morphology of the particles during cycling, the particles before and after cycling were observed under the SEM. Fig. 4 (a) shows the morphologies of the electrodes fabricated from the composites containing 33.3 mol% of silicon obtained after milling for 12h. The surface of the electrode after 30 cycles is devoid of any cracks, which are typically observed in other metal-based alloys that are used as anodes. Moreover, there appears to be no change in the morphology of the particles before and after cycling, which indicates

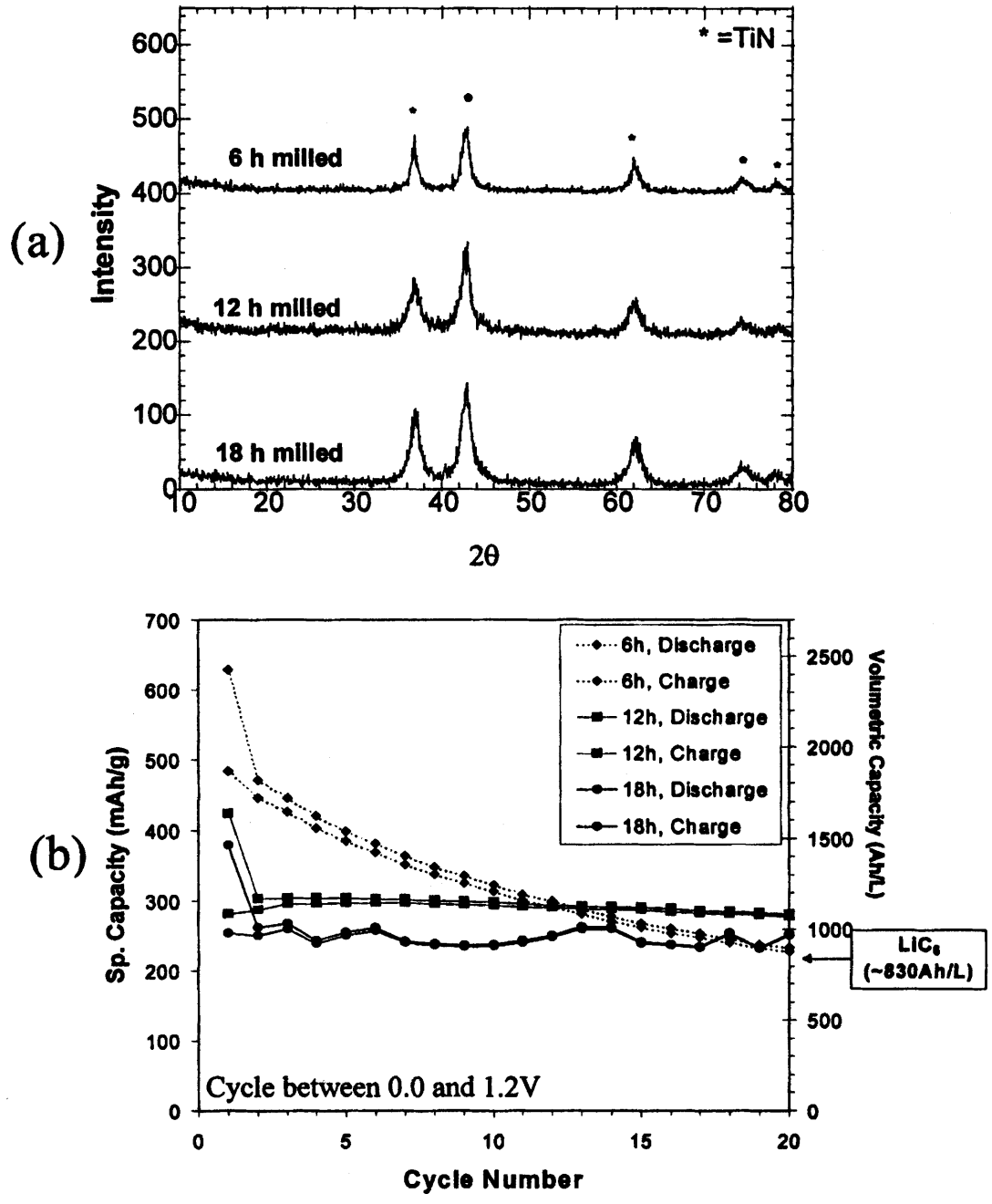

Figure 1. (a) X-ray diffraction patterns of Si:TiN = 1:2 composites milled for 6 h, 12 h and 18 h, respectively. (b) Capacity as a function of cycle number for Si/TiN nanocomposites obtained after milling for 6 h, 12 h and 18 h each.

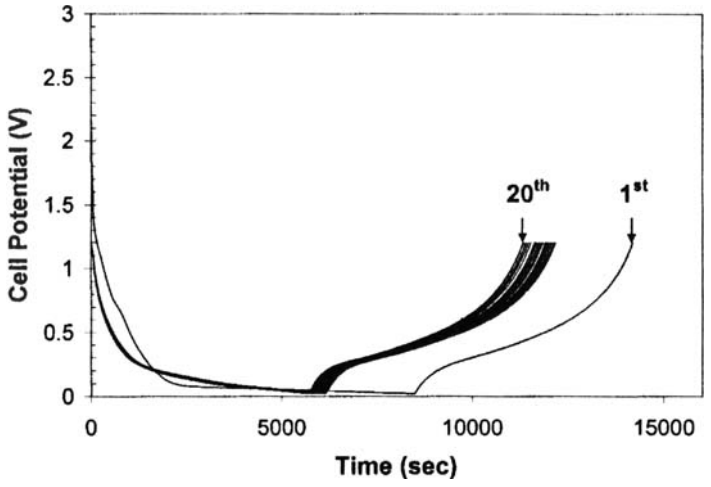

Figure 2. Cell potential profile for the first twenty cycles of the 12 h milled Si/TiN composite with Si:TiN = 1:2 molar ratio obtained after milling for 12h.

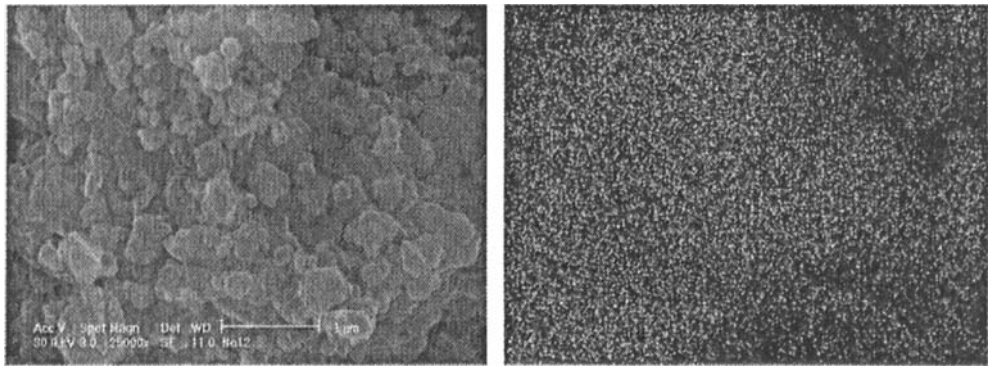

Figure 3. (a) SEM micrograph of the Si:TiN = 1:2 composite showing the nanocrystalline particles. (b) Chemical map of Si using EDX for the Si/TiN composite with Si:TiN = 1:2 molar ratio obtained after milling for 12 h. (Both images are taken at the same scale.)

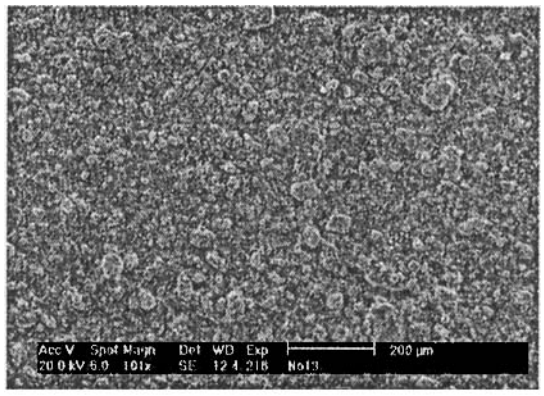

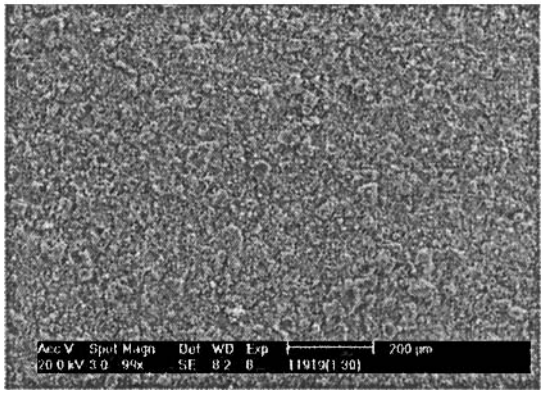

After cycling

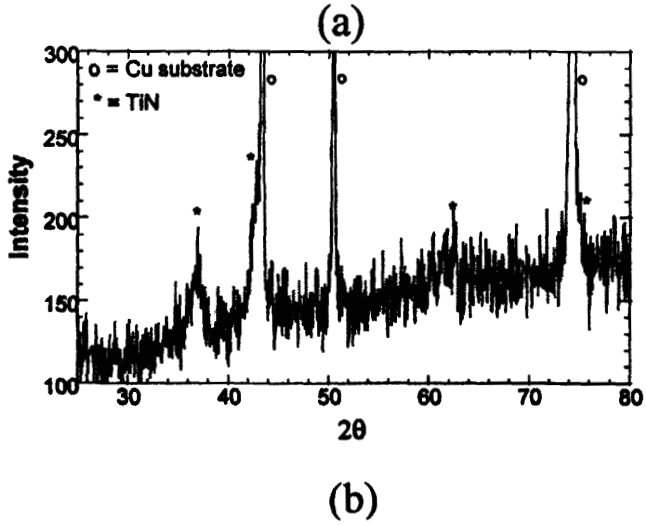

Figure 4. (a) SEM micrographs of the electrode before and after 30 cycles, (b) XRD pattern of the electrode after 30 cycles prepared with the Si/TiN composite corresponding to Si:TiN = 1:2 molar ratio obtained after milling for 12 h.

the good stability of the composite. The XRD pattern obtained on the electrode after testing for 30 cycles presented in Fig. 4 (b) is identical to Fig. 1. This suggests that silicon remains as very fine amorphous particles existing without undergoing any crystallographic phase change. The excellent stability of the electrode may be attributed to the existence of very finely dispersed amorphous silicon particles within the nanocrystalline TiN matrix. These results suggest that TiN indeed appears to be a good inactive matrix for Li-ion anodes. Furthermore, the results imply the potential of Si/TiN nanocomposites as anodes for Li-ion applications.

Transmission electron microscopy was conducted on this powder to analyze the nanocrystalline state of the composite. Figs. 5 (a) and (c) show the TEM image and selected area diffraction pattern of the 12 h milled powder containing 33.3 mol% silicon, respectively. The bright field image indicates the presence of very fine size crystallites (< 20 nm) within a single particle, indicating the true nanocomposite nature of this material. The well-defined rings in the selected area diffraction pattern correspond to the nanocrystallites of TiN with no trace of silicon being observed. This suggests that the silicon contained in the composite is amorphous as indicated by the XRD result. Fig. 5 (b) is the dark field image corresponding to the crystalline TiN phase. Comparing the region marked with an arrow in the DF and the BF images, it appears that the dark spots in the BF image correspond to TiN crystallites. Although these TEM results suggest that the composite be exactly comprised of nanosized crystallites of TiN and amorphous silicon, it is difficult to ascertain the distribution of both phases. Therefore, high-resolution transmission electron microscopy was conducted on the composite using EELS to map the distribution of the elements at the nanoscale.

Fig. 6 (a) shows the high-resolution image of the composite containing 33 mol% silicon obtained after milling for 12 h. The dark areas represent the TiN nano-crystallites while the bright regions correspond to amorphous silicon as mentioned above. Lattice fringes from the TiN particles can be observed conforming to the nanocrystalline nature of TiN. Figs. 6 (b) and (c) show the high-resolution elemental maps corresponding to silicon and Ti, respectively obtained using electron energy-loss spectroscopy (EELS). The bright regions in the map indicate the high intensity or content of each component. Elemental maps show that TiN is distributed homogeneously in the powder and silicon appears to surround the TiN particles. This suggests the influence of mechanical milling on the two materials exhibiting different hardnesses. Silicon exhibits a lower hardness in comparison to TiN and thus undergoes significant pulverization. Thus the TiN particles appear to be uniformly coated with finely milled amorphous silicon forming a nanocomposite. Generally, the samples need to be sufficiently thin for obtaining good electron energy-loss spectra.[17] However, due to the difficulties associated with sample preparation, the as-milled powder was directly used in this case. As a result, overlapping of the maps of each component can be expected and the boundaries are also possibly diffused. Nevertheless, the elemental maps do reveal two different regions separated distinctly to represent the distribution of silicon and TiN phases. These results are therefore indicative of the stability of the Si/TiN nanocomposite arising from the nanoscale distribution of the two phases achieved by mechanical milling. Results of these studies therefore reveal two aspects, the promise of Si/TiN nanocomposite as a useful electrochemical system and the potential of mechanical milling for synthesizing electrochemically active nanocomposite materials.

CONCLUSIONS

Nanostructured Si/TiN composite powders produced by HEMM are comprised of amorphous silicon and nanosized TiN. As the amount of active silicon is reduced or the milling time is increased, a reduction in the initial specific capacity was observed. The exact reason for reduction in activity is not known. The milling time appears to control the amount of active silicon exposed to lithium, and prolonged milling appears to cause an increase in the inactive portion of silicon. The electrode containing 33.3 mol% silicon, milled for 12 h shows good capacity (~300 mAh/g or ~1100 Ah/L) with little fade (~0.36% /cycle). The as-milled powder consists of agglomerates of nanosized particles, each single particle itself representing a nanocomposite of silicon and TiN as indicated by the EDX results. The electrode structure is also very stable during cycling because no cracking/crumbling and/or obvious clustering of silicon was observed after 30 cycles. The nanocomposite is composed of TiN nanocrystallites and amorphous silicon according to TEM analysis. Nanoscale elemental mapping

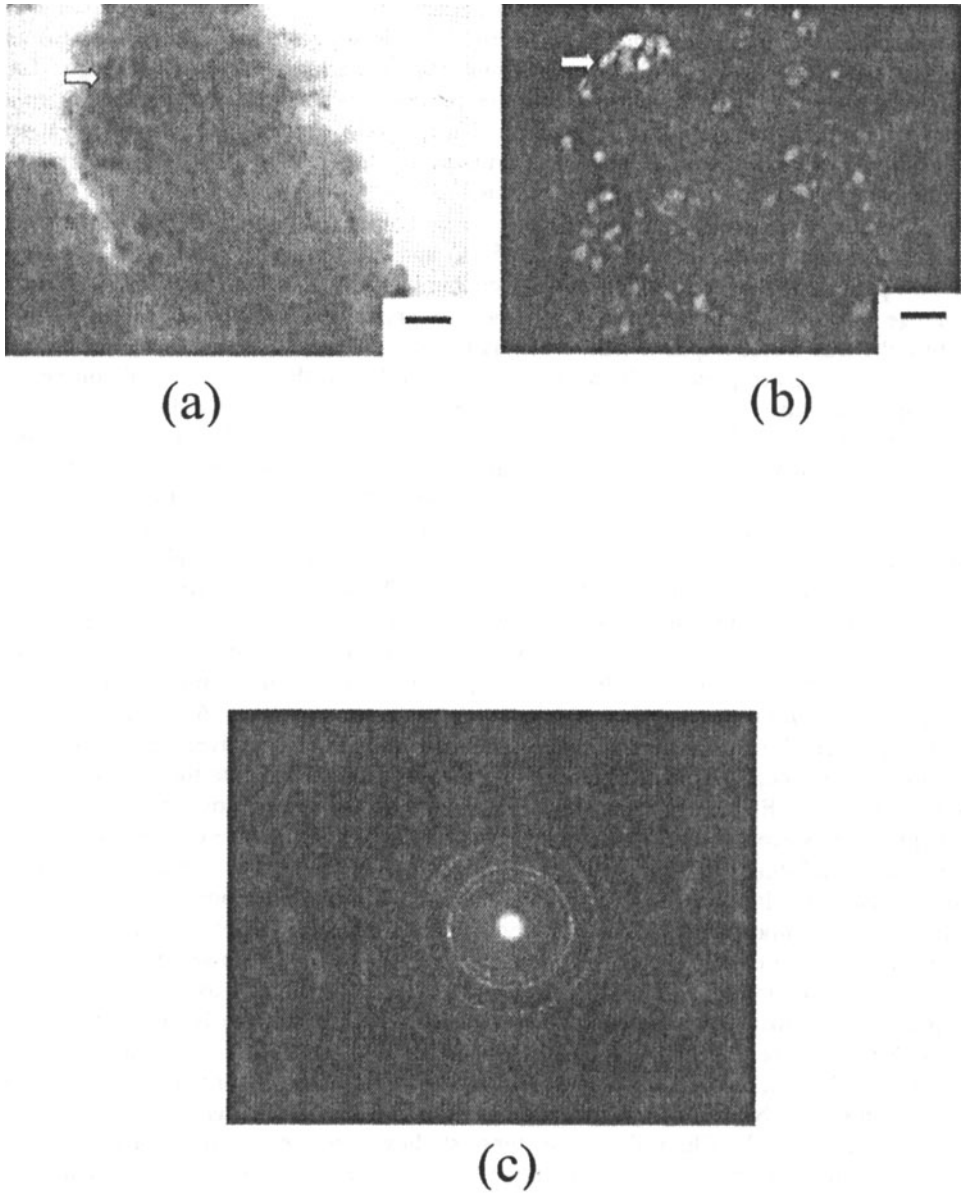

Figure 5. TEM micrographs of the Si/TiN nanocomposite containing 33 mol% Si obtained after milling for 12 h; (a) BF image, (b) DF image, and (c) SA diffraction pattern (camera length = 66cm, reduced to 30% of its original size).

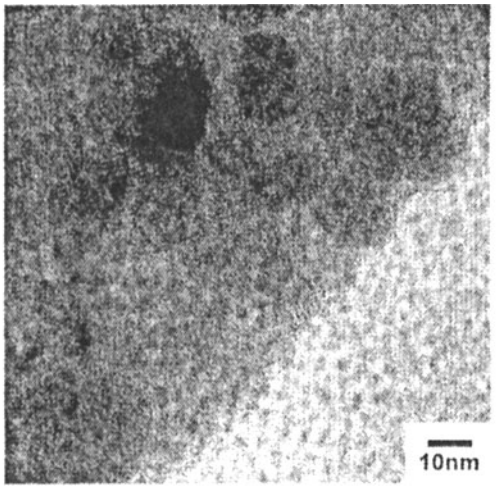

(a)

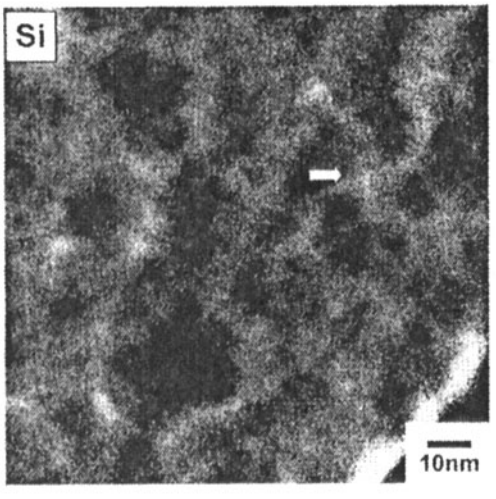

(b)

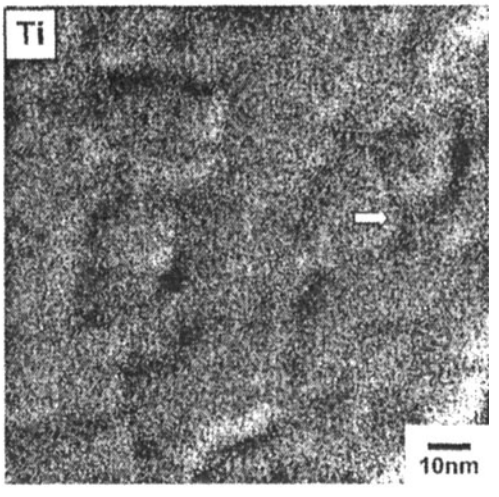

(c)

Figure 6. (a) HRTEM micrographs of the Si/TiN nanocomposite containing 33 mol% Si obtained after milling for 12 h, (b) Elemental map of Si, (c) Elemental map of Ti, which are analyzed by electron energy-loss spectroscopy (EELS). (The arrows represent the same position.)

using EELS reveals the uniform and homogeneous distribution of the two phases. These results therefore suggest that the Si/TiN nanocomposite certainly appears to be promising as an anode material although further optimization studies need to be conducted in order to demonstrate its optimum properties. Detailed structural and electrochemical studies are currently in progress and will be reported in subsequent publications.

ACKNOWLEDGEMENTS

P. N. Kumta and Il-seok Kim would like to acknowledge the support of NSF (CTS Grants 9700343, 0000563). P. N. Kumta, Il-seok Kim and G. E. Blomgren would also like to thank the financial support of ONR (Grant N00014-00-1-0516). Changs Ascending (Taiwan) and Pittsburgh Plate Glass (Pittsburgh) are also acknowledged for providing partial financial support.

REFERENCES

[1] R. A. Huggins, *Solid State Ionics*, **113-115**, 57 (1998).
[2] Y. Idota, A. Matsufuji, Y. Maekawa, and T. Miyasaki, *Science*, **276**, 1395 (1997).
[3] O. Mao and J. R. Dahn, *J. Electrochem. Soc.*, **146**, 423 (1999).
[4] K. D. Kepler, J. T. Vaughey, and M. M. Thakeray, *Electrochem. Solid-State Lett.*, **2**, 307 (1999).
[5] M. Winter and J. O. Besenhard, *Electrochim. Acta*, **45**, 31 (1999).
[6] H. Kim, J. Choi, H. J. Sohn, and T. Kang, *J. Electrochem. Soc.*, **146**, 4401 (1999).
[7] H. Zheng, K. Oka, and J. D. Mackenzie, *Mat. Res. Soc. Symp. Proc.*, **271** 893 (1992).
[8] T. Granziani and A. Bellosi, *J. Mater. Sci. Lett.*, **14**, 1078 (1995).
[9] K. Kamiya and T. Nishijima, *J. Am. Ceram. Soc.*, **73**, 2750 (1990).
[10] C. F. Windisch, Jr., J. W. Virden, S. H. Elder, J. Liu, and M. H. Engelhard, *J. Electrochem. Soc.*, **145**, 1211 (1998).
[11] M. R. Wixom, D. J. Tarnowski, J. M. Parker, J. Q. Lee, P. L. Chen, I. Song, and L. T. Thompson, *Mat. Res. Soc. Symp. Proc.*, **496**, 643 (1997).
[12] I. S. Kim and P. N. Kumta, unpublished data (1999).
[13] E. Gaffet, F. Bernard. J. C. Niepce, F. Charlot, C. Gras, G. L. Caer, J. L. Guichard, P. Delcroix, A. Mocellin, and O. Tillement, *J. Mater. Chem.*, **9**, 305 (1999).
[14] I. S. Kim and P. N. Kumta, *Electrochem. Solid-State Lett.*, **3**, 493 (2000).
[15] B. D. Cullity, *Elements of X-ray Diffraction, Second Ed.*, p. 284, Addison-Wesley, MA (1978).
[16] H. Li, X. Huang, L. Chen Z. Wu, and Y. Liang, *Electrochem. Solid-State Lett.*, **2**, 547 (1999).
[17] D. B. Williams and C. B. Carter, *Transmission Electron Microscopy*, p. 655, Plenum Press, NY (1996)

Ceramic Engineering and Science Proceedings

This page intentionally left blank

SINGLE-STEP PREPARATION OF NANOSIZED CERAMICS AND COMPOSITES FROM METAL-ORGANIC PRECURSORS

Sanjay Mathur,[a] Michael Veith,[a] Hao Shen[b] and Stefan Hüfner[b]
[a]Institute of Inorganic Chemistry and [b]Institute of Experimental Physics
Saarland University, Im Stadtwald
66123 Saarbruecken, Germany

ABSTRACT

The synthesis of nanoparticles with a precise control over composition, size, size distribution and morphology poses a fundamental scientific challenge. The chemical reactions based on a controlled interaction of atoms or molecules in vapor or liquid phase are currently the popular alternatives to obtain nanostructured films or particles. The success of *soft chemistry* methods is attributed to defined and in some cases designed molecular compounds that transform into nanocrystalline ceramics or composites via thermolysis (Chemical Vapor Deposition) and hydrolysis (Sol-Gel) reactions. The synthesis of solid materials from molecules requires much lower temperatures than those required for conventional powder syntheses or mechanical procedures. Further, the flexibility to combine different ligands or metal combinations allows the precursor designing - the so-called *single-source* approach - to meet the demands of the target material. To this end, we have examined the **single-step** conversion of various molecular sources to obtain oxides, biphasic metal/oxide composites and oxide-oxide composites. The results illustrate that a predefined reaction (decomposition) chemistry of the precursors enforces a remarkable control over morphology, composition and particle size.

INTRODUCTION

Nanocrystalline materials and nano-composites are the subject of current interest because of their unusual magnetic, optical, electronic properties resulting from the confinement of electronic and vibrational excitation, quantum size effect and large surface to volume ratio.[1] The current research trends in the field of nanocrystalline materials involve (i) preparative routes to nanoparticles or films (ii) studies on isolated nanoclusters (iii) methods of assembling (2D or 3D) nanostructures (iv) nanoclusters incorporated in suitable matrices (composite systems) (v) properties of nanoclusters in isolated, assembled and embedded forms. Although nanoclusters are receiving attention from both theoretical and experimental standpoints, the strategies to synthesise nanomaterials are not well established. The attention is being given to different methods (chemical, physical, electrochemical and mechanochemical), however reproducible and cost effective synthesis of nanomaterials with a precise control over size, size distribution, composition and morphology remains a challenge.[2] In this context, the chemical routes show a cutting edge over the physical methods because they do not need expensive instrumentation (e.g., ultra high vacuum, high energy source, etc.) and possess the inherited advantages of the unlimited potential of the chemical reactions, for instance, the possibility to synthesise almost any material, co-synthesize two or more materials simultaneously, produce extremely homogeneous alloys and composites, and tailor the composition accurately from the early stages of the process. The application of metal-organic precursors in Sol-Gel and CVD techniques has played a major role in

the development of chemical routes to materials.[3-5] Among the various metal-organic compounds – carboxylates, ß-diketonates, alkyls, alkoxides – **metal alkoxides** ($M(OR)_n$) are the most attractive precursors for the synthesis of metal oxides. What sets metal alkoxides in high-purity ceramics and composites apart from commonly used chemicals is the possibility to control and modify the structure of the molecule in such a way that it meets the need of the target material.[6-10] Other salient features include high purity, easy transformation into oxides with formation of volatile byproducts, ability to form homogeneous solution in different solvents and more importantly the facile formation of heterometal species useful for the synthesis of multicomponent materials. The present article gives a brief account of nanocrystalline ceramics and composites obtained from heterometal alkoxide precursors.

ROLE OF PRECURSOR IN THE CHEMICAL SYNTHESIS OF NANOMATERIALS

The traditional chemical synthesis involving solid-state reactions of two or more components fail to produce a narrow particle size distribution and homogeneity at the nanometer level. On the other hand, the chemical methods using metal-organic precursors appear promising for control over particle size, phase purity, chemical homogeneity, low calcination temperatures and micro-structural uniformity. Despite the proven versatility of *chimie douce* routes, their application is rather limited because not all chemical syntheses guarantee a clean and phase selective synthesis and also due to the fact that suitable precursors for the systems of interest are commercially not available. To obtain mixed-oxide ceramics, the conventional wet-chemical techniques generally use a mixture of individual constituents. Since no positional control is offered, the different compounds present in the reaction mixture randomly collide to form various intermediate species with metal ratios unfavorable for obtaining a single-phase material. The main reason being the different chemical behaviours of the individual components present in the precursor mixture that leads to component segregation, mixed phases or non-ideal stoichiometry in the final ceramic material. For a selective conversion of molecular aggregates to final oxide or composite material, we are developing **Single-Source Precursors** to bi-, tri- or multi-phasic systems in which all the phase-forming elements are assembled in a single molecular framework.

For example, in the case of sol-gel process, inhomogeneity can occur due to the differential hydrolysis tendency (an intrinsic property governed by the electropositivity of the metal) of individual components in a mixture of precursors. This has been illustrated by the synthesis of $CoAl_2O_4$ spinel from (i) a stoichiometric mixture of $[Al(OPr^i)_3]_4$ and $Co\{OC(C_6H_5)_3\}_2$ and (ii) a single molecular source, $[CoAl_2(OR)_8]$.[11] The XRD patterns (Fig. 1) of the two $CoAl_2O_4$ samples

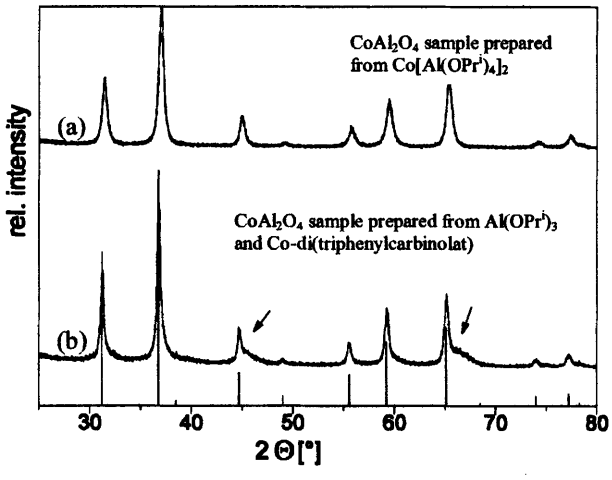

Figure 1. XRD patterns of $CoAl_2O_4$ obtained from (a) single- and (b) multi-source routes. Arrows indicate other phases.

reveal that the single-source synthesis yields, under similar experimental conditions, higher phase purity and crystallinity when compared to the spinel obtained using two separate metal sources.

Further, the isolation and characterization of preceramic aggregates is necessary to obtain pure and stoichiometric materials. The higher homogeneity promised by chemical methods is generally not achievable from a heterogeneous 'precursor cocktail' because the similar molecular building

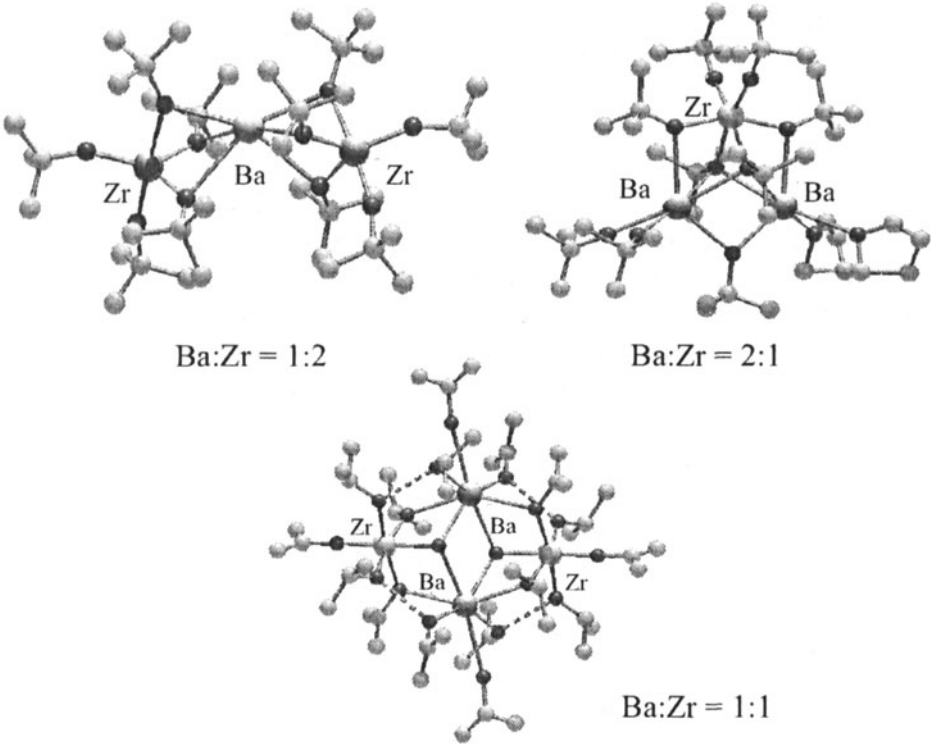

Figure 2. Molecular structures of Ba-Zr mixed-metal alkoxides with different Ba:Zr ratios.

blocks can arrange themselves in different ways to produce compounds with different metal stoichiometries. For instance, a series of molecular Ba-Zr alkoxides with different Ba:Zr stoichiometries (Ba:Zr = 1:2, 2:1 and 1:1) have been prepared using Ba and Zr alkoxides that are commonly used as in the synthesis of perovskite $BaZrO_3$. The successful isolation and characterization of different Ba-Zr alkoxides (Fig. 2) underlines the importance of characterizing the precursors system in order to be able to control the property of the resulting material. Indeed, a phase selective synthesis was possible using the single-source precursor, $[BaZr(OH)(OPr^i)_5(Pr^iOH)_3]_2$ while the other compounds produced, together with the perovskite phase, traces of Ba and Zr phases or their products in the final ceramic material.

RESULTS AND DISCUSSION

This section contains selected examples of the synthesis and characterization of nanoscaled films and particles from Single-Source alkoxide precursors.

Oxide Ceramics

(i) Nanoparticles of $ZnAl_2O_4$: The assumption that the properties of solid semiconductors are independent of their size is not valid in the nanometer regime where many of the physico-chemical characteristics of semiconductor nanoparticles are essentially different from the bulk counterparts. When the size of the nanoparticles is comparable to the Bohr radius of the excitons in semiconductors, the size effect becomes noticeable in their optical and luminescent properties. The blue shift of the excitonic absorption band in semiconductor nanocrystals with the decreasing

cluster size is a well-known manifestation of the quantum size effect. Zinc aluminate ($ZnAl_2O_4$), a wide band gap semiconductor, is a suitable candidate for reflective optical coatings. Additionally, zinc aluminate has been proposed to be a phosphor material and ultraviolet transparent electroconductive oxide. In the polycrystalline form, it is found to be highly reflective from 300 nm, which is within the ultraviolet regime of the spectrum. The optical properties of polycrystaline zinc aluminate and gallate has recently been reported,[12] however there is no report on the size-dependence of the optical properties. Using a Zn-Al heterometal alkoxide, $[ZnAl_2(OBu^t)_8]$, as a single molecular source, we have performed size-controlled synthesis of zinc aluminate spinel particles and examined the influence of average particle size on their optical properties.[13]

The molecular structure determination of $[ZnAl_2(OBu^t)_8]$ by single crystal X-ray diffraction analysis (Fig. 3a) confirmed the cation ratio (Zn:Al = 1:2) in the molecule to be appropriate for the formation of $ZnAl_2O_4$ ceramic. The precursor $[ZnAl_2(OBu^t)_8]$ was used in a sol-gel process to obtain nanoparticles of $ZnAl_2O_4$ after calcining the xerogel at 400 °C, which is the lowest temperature reported for the formation of monophasic zinc aluminate. The XRD data of the heat-treated (600-1400 °C) powders shows that no metal segregation or phase separation is observed (Fig. 3). The lattice parameters for cubic spinel phase (a_0 = 8.0855 Å), calculated from the sample calcined at 1000 °C, were found to be in good agreement with the reported value (a_0 = 8.0848 Å, JCPDS File [5-669]). The average crystallite size determined from the line shape analysis of the diffraction peaks (Fig. 3b) showed an exponential relationship to calcination temperature.

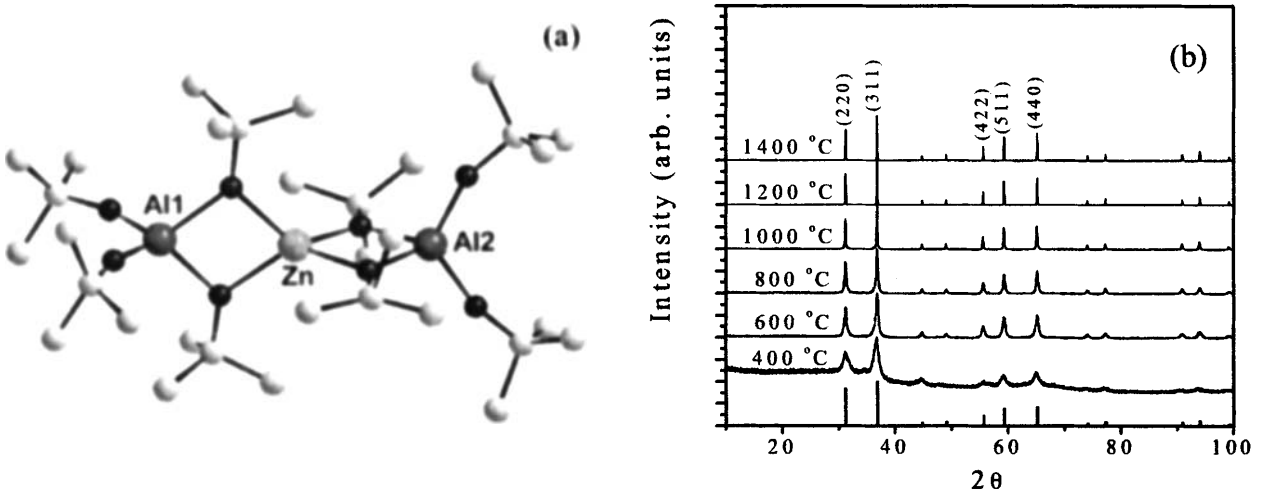

Figure 3. (a) Molecular structure of $[ZnAl_2(OBu^t)_8]$ and (b) XRD patterns of the $ZnAl_2O_4$ ceramic.

The optical absorbances (Fig. 4) of $ZnAl_2O_4$ nanocrystals with different particle sizes were obtained from the calculation of total reflection R ($\log_{10}(1/R)$). In order to detect any possible phase separation, the absorbance spectra of ZnO and Al_2O_3 standards were also recorded. The broad absorbance peaks observed in the UV region (220-280 nm) result from the fundamental band-to-band electron excitations and are related to the energy band gap in the investigated samples. The band gap values (4.0–4.5 eV), obtained from a linear extrapolation of the absorbance edge to cross the wavelength axis are quite different from those of Al_2O_3 (E_g ~ 3.6 eV) and ZnO (E_g ~ 3.1 eV) in spite of the existence of the Al^{3+} and Zn^{2+} cations in $ZnAl_2O_4$. The broad shoulder observed in the 290-375 nm wavelength region for the sample calcined at 700 °C could probably be due to some defects in the structure. The intensity of this shoulder decreased on sintering the sample for longer duration (Fig. 5a) suggesting crystallite growth and minimisation of structural defects. The structural change in the spinel structure could be discerned from the ^{27}Al solid-state NMR spectra (Fig. 5b). The absorbance edge became steeper on increasing the calcination

temperature corresponding to a 'red shift' (4.5 to 4.0 eV) on the energy scale (Fig. 4). The NMR spectrum of the xerogel showed three signals at 1.17, 33.96 and 67.93 ppm in the ranges

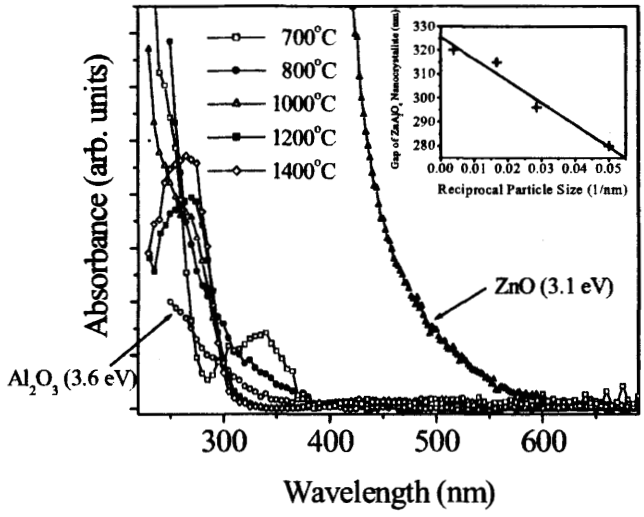

Figure 4. Absorbance spectra of the $ZnAl_2O_4$ samples.

characteristic of six-, five and four-fold coordinated Al(III) centers. The NMR spectrum of crystalline $ZnAl_2O_4$, heat treated at 600 °C, shows two distinct signals at 2.34 ppm and 61.9 ppm corresponding to Al^{3+} ions present in the octahedral (AlO_6) and tetrahedral (AlO_4) sites of the closed cubic packing of oxygen atoms. This shows the zinc aluminate spinel to be partially inverse with an occupancy ratio of Al_{Td}:Al_{Oh} = 1/3:2/3 (degree of inversion, γ = 1/3). The absence of a signal corresponding to five coordinate Al(III) species suggests a structural change in the gel structure (*via* condensation, oxolation and alcoholation reactions). The peak due to four-fold coordinated Al centers diminish in the temperature range 600-900 °C. The NMR spectrum of $ZnAl_2O_4$ sample heat treated at 1000 °C shows only the presence of octahedrally coordinated Al ions (Fig. 5), which illustrates the temperature dependence of the degree of structural inversion in zinc aluminate spinel. The observed doublet is due to the second order splitting of the central transition band by nuclear-quadrupole interaction.

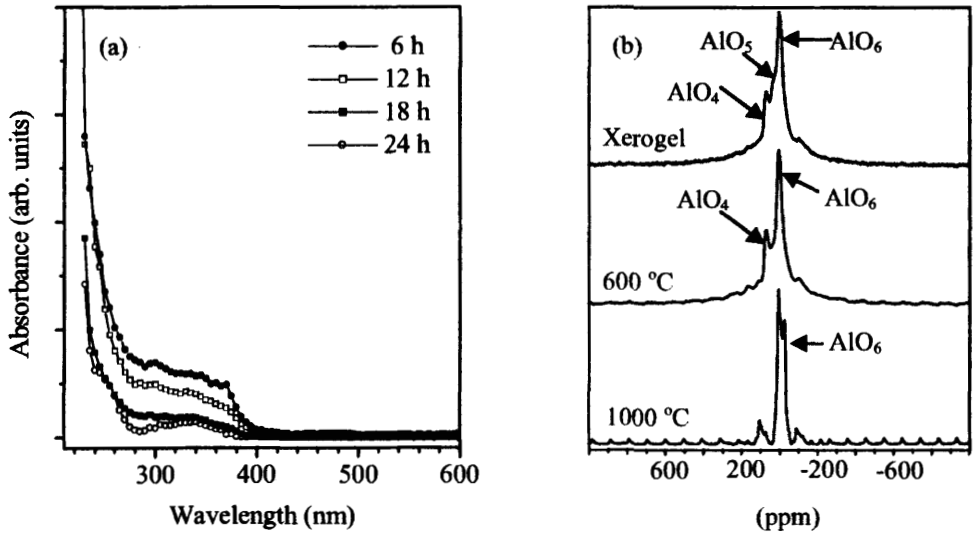

Figure 5. (a) Absorbance spectra of the $ZnAl_2O_4$ sample calcined at 700 °C for different time periods and (b) ^{27}Al solid-state MAS NMR spectra of Zn-O-Al xerogel, $ZnAl_2O_4$ ceramic calcined at 600 and 1000 °C.

(ii) Phase Selective Synthesis of $GdFeO_3$ Nanoparticles: $GdFeO_3$ belongs to the class of orthoferrites (G-type magnet), showing a strong uniaxial anisotropy and was among the first bubble domain materials discovered in the 1960's. However, due to the difficulties involved in the phase selective synthesis of $LnFeO_3$ oxides (Ln = any lanthanide element), they were abandoned in favour of the well-known magnetic garnets ($Ln_3Fe_5O_{12}$). In the chemical synthesis of lanthanide ferrates ($LnFeO_3$) at least two sources, one for Ln^{3+} and the other for Fe^{3+}, are used to obtain a precursor solution. The random mixing of the ions results in the co-existence of undesired phases (e.g., $Ln_3Fe_5O_{12}$ and Fe_3O_4) in the final product.[14] The facile formation of thermodynamically more stable garnet phase ($Ln_3Fe_5O_{12}$) with much higher magnetic moment hinders specific investigations on the weak ferrimagnetic behaviour of the orthoferrite, $LnFeO_3$. In this context, the precursors with the required cation ratio and preformed Ln–O–Fe bonds are attractive Single-Sources for the controlled synthesis of phase pure $LnFeO_3$ materials. We have synthesized a gadolinium-iron isopropoxide, $[GdFe(OPr^i)_6(Pr^iOH)]_2$, with Gd:Fe ratio 1:1 (Fig. 6).

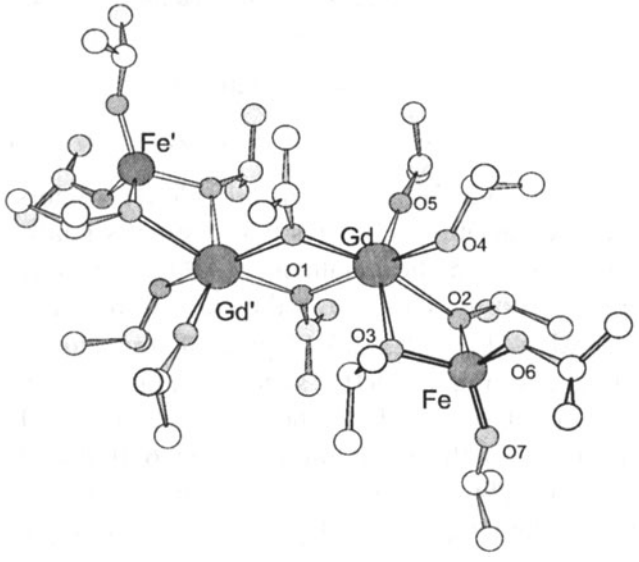

Figure 6. Molecular structure of $[\{GdFe(OPr^i)_6\}(HOPr^i)]_2$.

The sol-gel processing of alkoxides is based on inorganic polymerisation reactions in which partially hydrolysed alkoxide species condense to form multi-molecular aggregates assembled via oxo- or hydroxo groups. Further cross-linking of such building blocks favors the gelation process. The overall sol-gel reaction path is represented in equation 1.

$$\tfrac{1}{2}\,[GdFe(OPr^i)_6(Pr^iOH)]_2 \xrightarrow{\text{Hydrolysis}} 'GdFe(OH)_x(OPr^i)_{6-x}' \xrightarrow[\text{/Oxolation}]{\text{Alcoholation}} 'GdFe(OH)_x(O)_y(OPr^i)_{6-x-y/2}'$$

$$'GdFe(OH)_x(O)_y(OPr^i)_{6-x-y/2}' \xrightarrow{\text{Polycondensation}} GdFeO_3 + 'GdFe(OH)_x(O)_y(OPr^i)_z' \quad (z << x \text{ and } y) \quad \ldots\ldots (1)$$

Owing to reformed Gd–O(R)–Fe bridges in $[GdFe(OPr^i)_6(Pr^iOH)]_2$, the hydrolytic decomposition and the formation of $GdFeO_3$ occurs at a molecular level and crystalline ceramic is obtained at significantly low temperature (700 °C). Moreover, the crystalline $GdFeO_3$ is formed from an amorphous precursor without the crystallisation of any intermediate phases (Fig. 7).

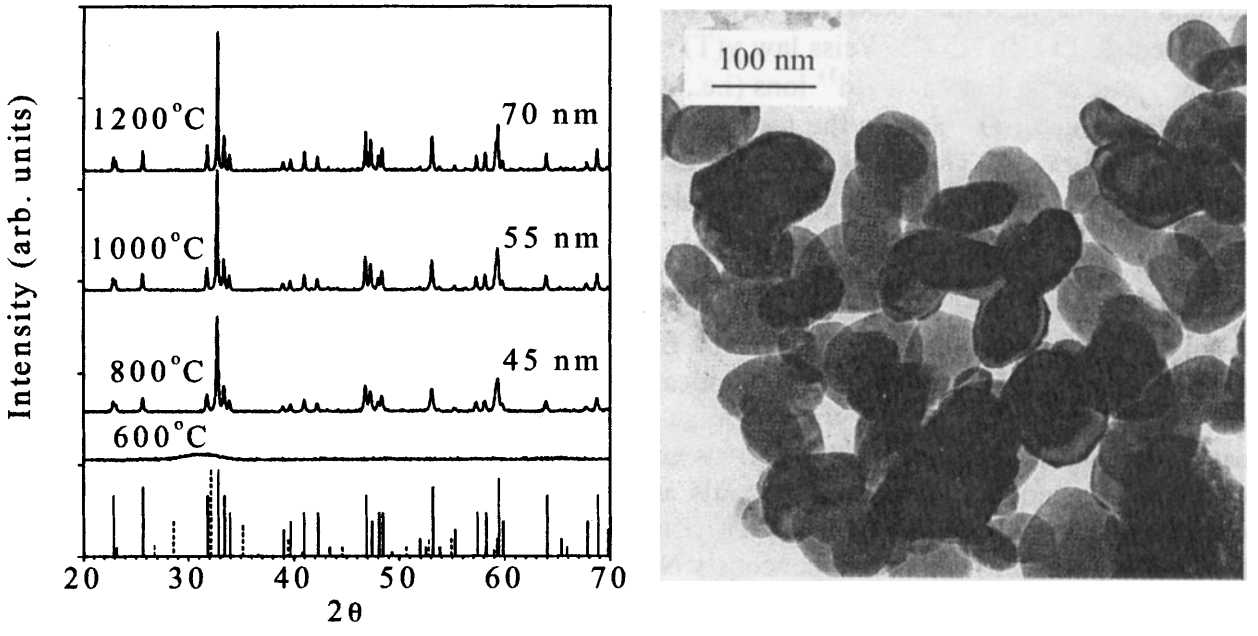

Figure 7. X-ray diffraction patterns and TEM image of $GdFeO_3$ ceramic.

The thermodynamically favored garnet composition, invariably formed in the synthesis of orthoferrites, is not observed. Further, no phase segregation or crystallisation of other stoichiometries was observed, even at higher temperatures, which confirms the compositional purity of the sample and our contention that the chemical mixing of the ions is retained during the various stages of the processing.

The TEM image (Fig. 7) of the $GdFeO_3$ ceramic calcined at 1000 °C showed faceted crystallites of nearly uniform size (~ 60 nm). According to the compositional analysis performed by TEM-EDS on individual particles, the samples are chemically homogeneous at the nanometer scale, with respect to the distribution of the metals. Orthoferrites display weak ferromagnetism arising from the low symmetry of the magnetic unit cell, which produces a spin-canted structure of the Fe sublattice. Both the temperature and field dependence of the magnetization in $GdFeO_3$ can be explained from the weak ferromagnetism of these systems,[15] and the very different ordering temperatures of Gd (~ 1 K) and Fe (~ 600 K) magnetic sublattices. The magnetic susceptibility χ_{dc}

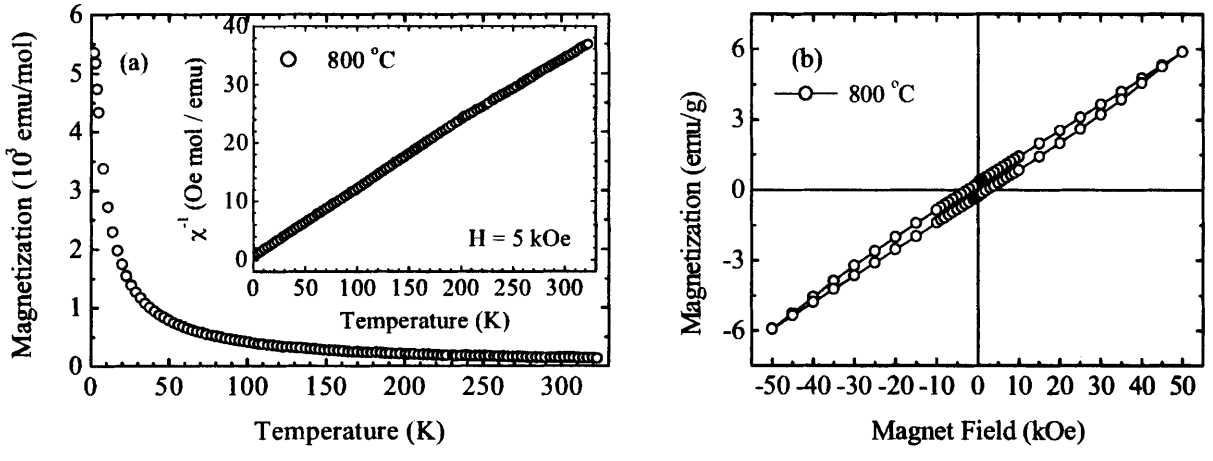

Figure 8. (a) Magnetization and inverse magnetic susceptibility (inset, a) curves and (b) M-H hysteresis (300 K) for the $GdFeO_3$ ceramic calcined at 800 °C.

shows a paramagnetic-like behaviour (Fig. 8) down to the lowest temperature available (T ~ 2 K). The calculated value (Curie-Weiss law $\chi(T) = C/(T - \Theta)$) of effective moment corresponds to the paramagnetic contribution of Gd^{3+} ions (i.e., 8.0 μ_B for an $^8S_{7/2}$ state). On the other hand, the small (negative) value of Θ supports the fact that the Gd-Gd (antiferromagnetic) exchange interactions are remarkably weak. The linear behaviour of M(H) curve with the applied magnetic field (Fig. 8), without signs of saturation up to 5 T, resembles a paramagnet.

Oxide–Oxide Composite

A New Concept for Nd-doped Oxides: Combining two phases with distinct attributes resulting in so-called nanocomposites can augment the inherent advantages of nanostructured materials. For instance, encapsulating nanocrystals of optically functional phases, in a processable matrix, forms optically active composite. The small particle size enhances the optical properties while the matrix material stabilizes the particle size and prevents random grain growth. In the context of optical materials, the neodymium-doped materials are useful as solid-state laser media, phosphors and optical amplifiers. A general problem encountered in the synthesis of Nd-doped silica glasses is the difficulty to incorporate homogeneously Nd^{3+} ions into the matrix because the dopant ions tend to cluster due to coordinative unsaturation.[16] The addition of alumina as codopant prevents the clustering of Nd^{3+} ions by forming a solvation shell of (AlO_4) and/or (AlO_6) units around the Ln^{3+} ions to keep them homogenously dispersed. The Al–O bonds preferentially surround the Ln^{3+} ions in the Ln_2O_3–SiO_2 glasses, co-doped with Al_2O_3. The role of alumina in inhibiting dopant clustering is attributed to the encapsulation of rare earth centers by alumina, which increases the minimum Ln-Ln distance in the material, presumably by forming –Ln–O–Al– linkages.[17] We have proposed a new doping concept in which $NdAlO_3$ nanocrystals, used as the optically active phase, were dispersed in an alumina matrix to obtain a novel oxide-oxide composite material. Alumina can serve as an active matrix and may interact with the surfacial Nd atoms of the $NdAlO_3$ nanocrystals to form further Nd-O-Al bonds. To verify this hypothesis, the optical properties of nanoparticles of pure $NdAlO_3$ were compared with those of the $NdAlO_3/Al_2O_3$ composite.

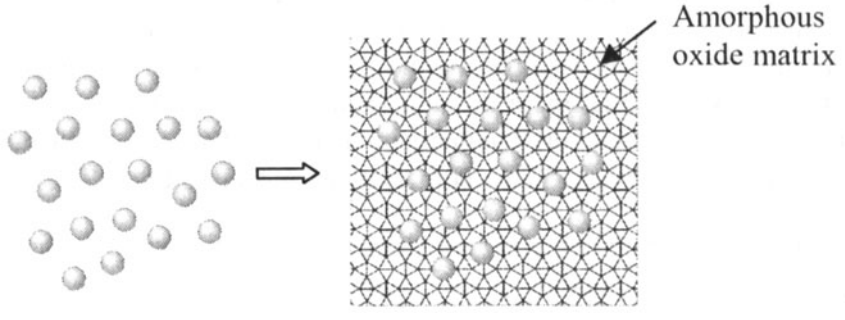

Single-phase Nanocrystals Composite Material

Scheme I

For the synthesis of monophasic $NdAlO_3$ and $NdAlO_3/Al_2O_3$ composite, the molecular precursors, $[NdAl(OPr^i)_6(Pr^iOH)]_2$ (**NA**) and $[NdAl_3(OPr^i)_{12}(Pr^iOH)]$ (**NA3**) based on Nd:Al ratios 1:1 and 1:3 (Fig. 9) were used in the sol-gel process to obtain mono- and biphasic nanomaterials according to eqs. 2 and 3.[18]

$$[NdAl(OPr^i)_6(Pr^iOH)]_2 \longrightarrow NdAlO_3 \quad \text{..... (2)}$$

$$[NdAl_3(OPr^i)_{12}(Pr^iOH)] \longrightarrow NdAlO_3/Al_2O_3 \quad \text{..... (3)}$$

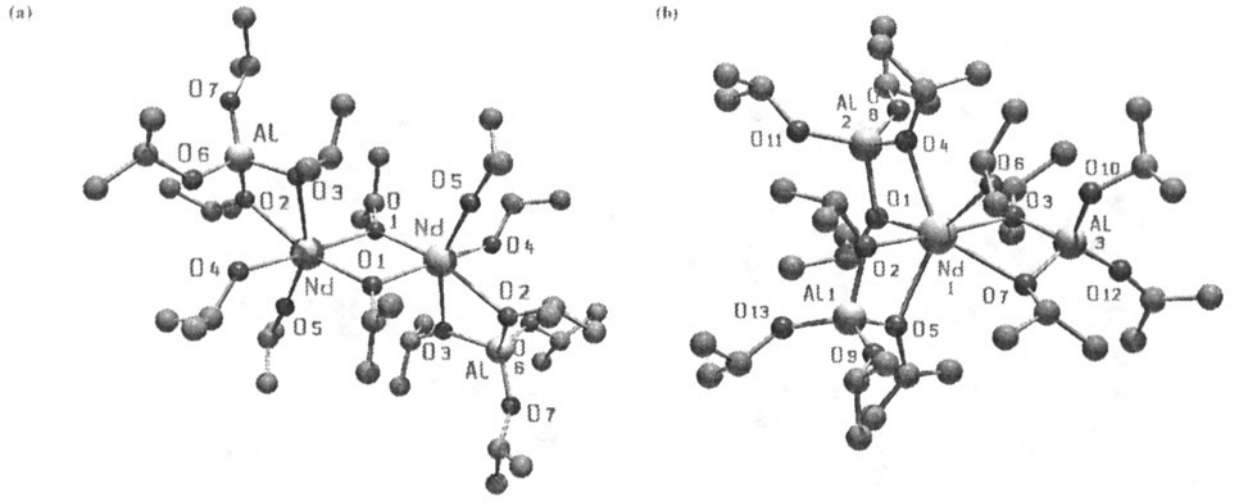

Figure 9. Molecular structures of (a) $[NdAl(OPr^i)_6(Pr^iOH)]_2$ and (b) $[NdAl_3(OPr^i)_{12}(Pr^iOH)]$.

The EDX analysis of the gels and calcined powders gave Nd:Al ratios corresponding to those present in the molecular precursors and no heterogeneity was observed on a sub-micrometer level. The TG/DTA analysis of the xerogels showed the crystallisation of $NdAlO_3$ to occur at 810 and 870 °C in the gels obtained from **NA** and **NA3**, respectively. These obervations were confirmed by the XRD measurements. The slightly higher crystallisation temperature of $NdAlO_3$ ceramic in the later system was found to be the influence of the alumina matrix (see later). The xerogel obtained from **NA** produced monophasic $NdAlO_3$ after calcination at 800 °C and no other contaminating or secondary phase was observed upto 1400 °C (Fig. 10). On the other hand, **NA3** showed $NdAlO_3$ to be the only crystalline component until 1200 °C suggesting the residual alumina content (from the stoichiometric balance and chemical analysis data) to be amorphous. Indeed, the crystallisation of aluminas (mixture of γ, κ and δ phases) was observed around 1300 °C. The TEM image of

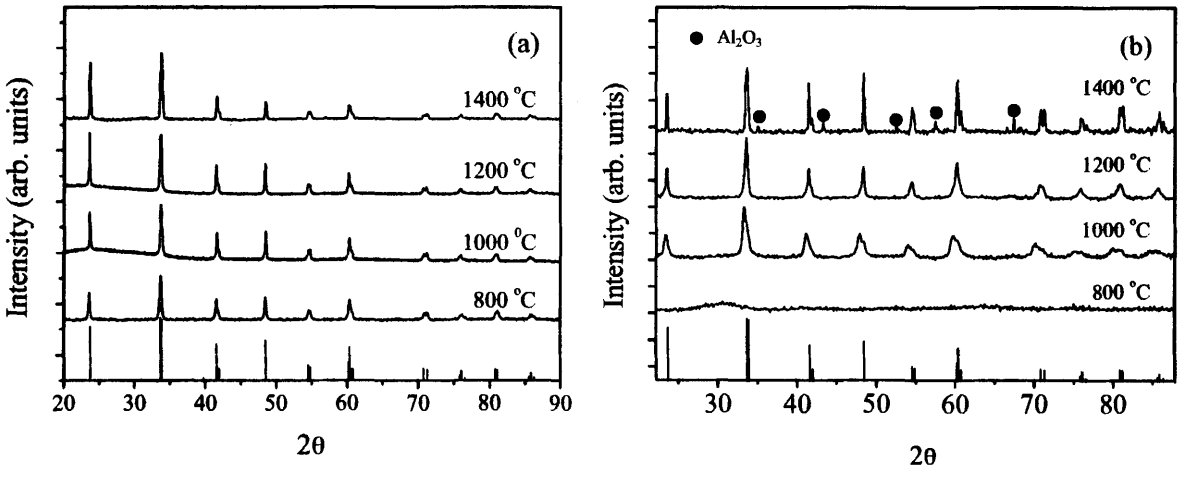

Figure 10. Temperature-dependent XRD patterns of (a) $NdAlO_3$ and (b) $NdAlO_3/Al_2O_3$.

$NdAlO_3$ sample revealed a regular dispersion of only one form of crystallites while a bimodal distribution of particles was found in the case of $NdAlO_3/Al_2O_3$ composite. The analytical electron

microscopy of the composite sample confirmed the large grains to be $NdAlO_3$ while the smaller particles forming the matrix show a composition corresponding to alumina (Fig. 11).

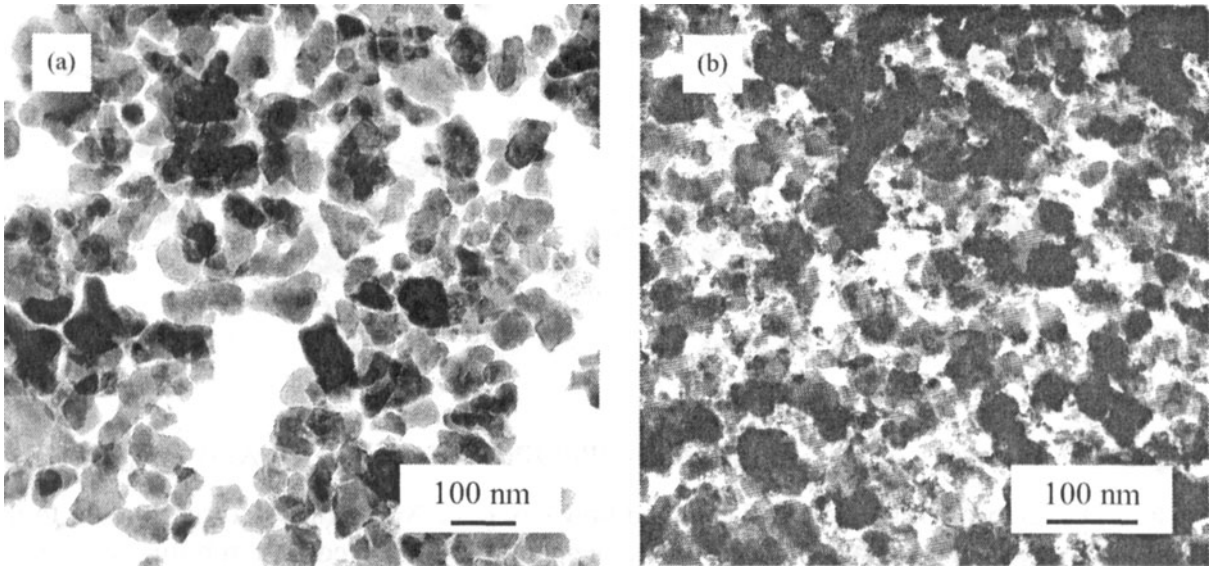

Figure 11. TEM images of (a) $NdAlO_3$ and (b) $NdAlO_3/Al_2O_3$.

Figure 12 displays the average crystallite sizes (Dm), of $NdAlO_3$ grains in two systems plotted against the calcination temperatures. The grains in pure $NdAlO_3$ powder experience an exponential growth whereas in the $NdAlO_3/Al_2O_3$ composite system the growth of $NdAlO_3$ crystallites is restricted due to the presence of a second phase. The average crystallite size of $NdAlO_3$ at

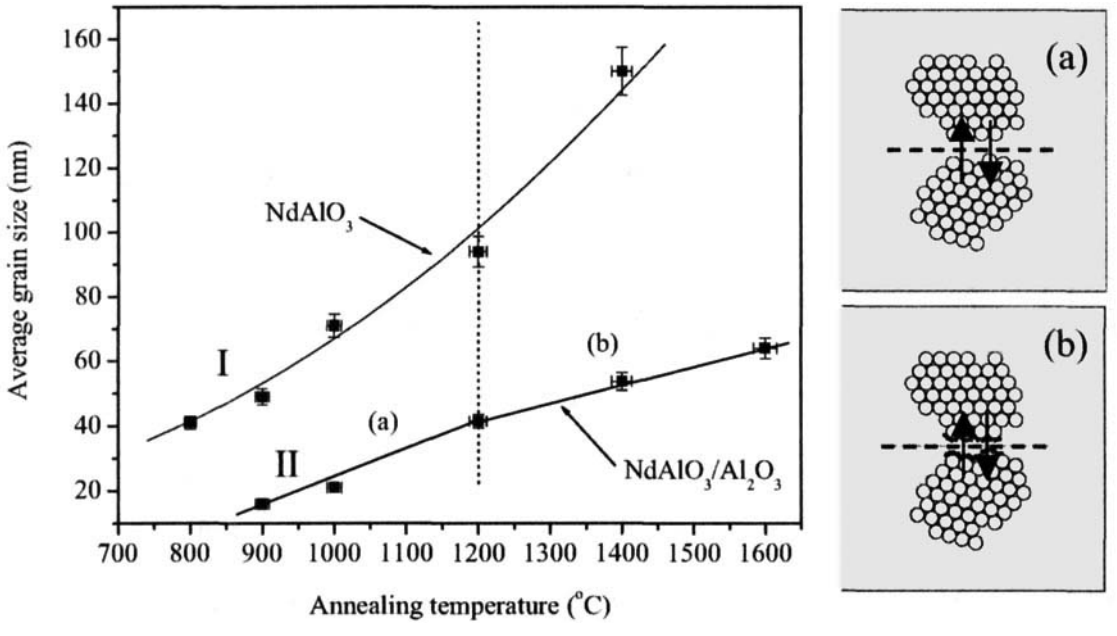

Figure 12. Dependence of the crystal growth on the calcination temperature in $NdAlO_3$ (**I**) and $NdAlO_3/Al_2O_3$ (**II**). The adjacent scheme shows the physical models of the grain growth processes in amorphous and crystalline states of the matrix in the **NA3** system and correspond to the two regimes **a** and **b** in curve II.

a particular calcination temperature is significantly larger in the single-phase system. This is due to the influence of second-phase particles (alumina), which retard the kinetics of grain growth through grain boundary pinning. The grain growth in the composite material shows two distinct regions (Fig. 12). The temperature range 800-1200 °C (part a) represents the nucleation and growth of $NdAlO_3$ crystals in an amorphous aluminium oxide medium. The growth slows down at higher temperature probably due to the different diffusion rates. Owing to its higher thermal conductivity, alumina may function as a micro-crucible and conduct heat to the embedded $NdAlO_3$ nanocrystallites thereby providing the activation energy necessary for grain growth of $NdAlO_3$. The competition between $NdAlO_3$ and alumina particles for the externally provided thermal energy results in the delayed crystallization of alumina (ca. 1200 °C, against the reported crystallization temperature ca. 750 °C for nanoscaled alumina).[19] The further restrained grain growth of $NdAlO_3$ phase in the second regime (Fig.12, Part b) is associated with the crystallization of alumina nanoparticles, adhering on the surface of the $NdAlO_3$ crystals which inhibit the percolation of ions thereby impeding the grain growth.

A comparative evaluation of the optical efficiency of Nd^{3+} ions in monophasic $NdAlO_3$ and $NdAlO_3/Al_2O_3$ composite was performed by recording the absorption and photoluminescence spetra of both the systems (Fig. 13). The high-resolution absorption spectrum ($^4I_{9/2}(1) \rightarrow {}^4F_{9/2}(1)$) of $NdAlO_3$ shows a single peak whereas the $NdAlO_3/Al_2O_3$ composite exhibits besides the main peak, a series of satellites. In the photoluminescence (PL) spectra of the two systems excited at 4 K by 351 nm radiation (Ar^+ ion laser), enhanced photoluminescence intensity (ca. 35 times) is observed for the $NdAlO_3/Al_2O_3$ sample. This observation can be attributed to the influence of the Al_2O_3 matrix on the electronic structure of Nd^{3+} ions in $NdAlO_3$ nanocrystals because the main difference between the two systems is the isolation of individual $NdAlO_3$ nanocrystallites by the Al_2O_3 matrix, in the $NdAlO_3/Al_2O_3$ composite. In view of the observed higher absorption coefficient and photoluminescence in $NdAlO_3/Al_2O_3$, it is reasonable to assume that the energy transfer from the alumina matrix to the Nd^{3+} cations is operative in the composite material. The near-surface defects in the nanoparticles are the source of nonradiative quenching sites in the luminescent materials, which decrease the luminescent intensity. It is plausible that the much smaller alumina crystallites coordinate to the $NdAlO_3$ crystallites via dangling Al-O bonds thereby amending some of these surface defects and eliminating the clustering of $NdAlO_3$ nanocrystals via a 'spacer' function.[20]

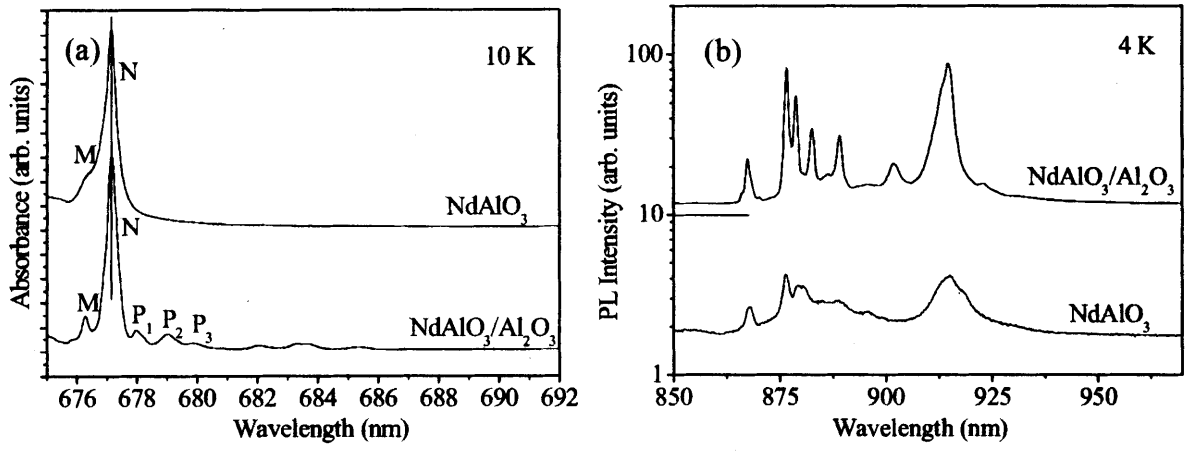

Figure 13. (a) High-resolution absorption spectra of Nd 4f ($^4I_{9/2}(1) \rightarrow {}^4F_{9/2}(1)$) and (b) photoluminescence spectra of Nd 4f $^4F_{3/2} \rightarrow {}^4I_{9/2}$ emission in $NdAlO_3$ and $NdAlO_3/Al_2O_3$ systems.

CONCLUSION

Our investigations have shown that the strategy of incorporating different elements in a molecular source to obtain the target nanocrystalline ceramic or composite from a **Single-Source** drastically simplifies the material synthesis and reduces the process parameters. The single-step transformation of molecular alkoxide derivatives for the phase selective synthesis of a large variety of ceramics and composites illustrates the potential of alkoxide precursors to '**preform**' the material on the molecular level. The positional control imposed on the phase-forming elements via chemical bonds is carried forward to the solid-state structure, which results in the evolution of crystallinity at very low temperatures and simultaneously prevents metal segregation or phase separation at the nanometer scale. In summary, metal-organic compounds with a predefined metal stoichiometry and reaction chemistry can enforce a molecular level homogeneity in the obtained materials, which is generally not achieved by the conventional chemical methods.

ACKNOWLEDGMENT

The financial support of the German Science Foundation in the framework of the priority programme *Sonderforschungsbereich-277*, at the Saarland University, is gratefully acknowledged.

REFERENCES

[1] J. H. Fendler (Editor) *Nanoparticles and Nanostructured Films* WILEY-VCH, Germany, 1998.
[2] A. Edelstein and R.C. Cammarata, (editors), *Nanomaterials: Synthesis, Properties and Applications* Institute of Physics Publishing, Bristol and Philadelphia, 1996.
[3] L.C. Klein Ed. *Sol-Gel Technology for Thin Films, Fibers, Preforms, Electronics and Speciality Forms* Noyes Pub., Park Ridge, NJ, 1988.
[4] C.J. Brinker and G.W. Scherer *Sol-Gel Science: The Physics and Chemistry of Sol-Gel Processing* Academic Press, New York, 1990.
[5] T. Kodas, M. Hampden-Smith, *The Chemistry of Metal CVD*, VCH, Weinheim, 1994.
[6] M. Veith, S. Mathur, A. Kareiva, M. Jilavi, M. Zimmer and V. Huch *J. Mater. Chem.* **9**, 3069 (1999).
[7] M. Veith, S. Mathur, N. Lecerf, K. Bartz, M. Heintz and V. Huch, *Chem. Mater.* **12**, 271 (2000).
[8] M. Veith, A. Altherr, N. Lecerf, S. Mathur, K. Valtchev and E. Fritscher, *Nanostructured Materials* **12**, 191(1999).
[9] M. Veith, S. Mathur, N. Lecerf, V. Huch, T. Decker, H.P. Beck, W. Eiser and R.Haberkorn, *J. Sol-Gel Sci. Tech.* **17**, 145 (2000).
[10] M. Veith, S. Mathur, N. Lecerf, H. Shen and S. Huefner *Chem. Mater.* **11**, 3103 (1999).
[11] F. Meyer, R. Hempelmann, S. Mathur and M. Veith *J. Mater. Chem.* **9**, 1755 (1999).
[12] S.K. Sampath and J.F. Cordaro *J. Am. Ceram. Soc.* **81**, 649 (1998).
[13] S. Mathur, M. Veith, M. Haas, H. Shen, N. Lecerf, V. Huch, S. Hüfner, R. Haberkorn, H.P. Beck, M. Jilavi *J. Am. Ceram. Soc.*, **84**, 1921 (2001).
[14] D.S. Schmool, N. Keller, M. Guyot, R. Krishnan, M. Tessier, *J. Magn Magn. Mater.* **195**, 291(1999).
[15] R.M. Bozorth, *Phys. Rev. Lett.* **1**, 362 (1958).
[16] T. Fujiama, M. Hori and M. Sasaki, *J. Non-Cryst. Solids* **121**, 273 (1990).
[17] D. Jaque, O. Enguita, J. Garcia-Sole, A.D. Jiang, Z.D. Luo, *Appl. Phys. Lett.* **76**, 2176 (2000).
[18] M. Veith, S. Mathur, H. Shen, N. Lecerf, S. Hüfner, M. Jilavi, *Chem. Mater.* **13**, 4041 (2001).
[19] G. Urretavizacya, A.L. Cavalieri, J.M.Porto Lopez, I. Sobrados, J. Sanz, *J. Mater. Synth. Process* **6**, 1 (1998).
[20] S. Mathur, M. Veith, H. Shen, S. Hüfner, M. Jilavi, *Chem. Mater.* **14**, 568 (2002).

PREPARATION AND CHARACTERIZATION OF NANOCRYSTALLINE NASICON POWDERS AND THIN FILMS

S. V. Kesapragada, S. Bhaduri,
S. B. Bhaduri, and E. G. Baburaj,
Nanomaterials and Advanced Ceramics Lab,
University of Idaho, Moscow,
ID-83844

P. A. Lessing,
Ceramics Section,
INEEL, Idaho Falls,
ID-83415

ABSTRACT

NASICON (Na superionic conductor) is a well-known family of sodium ionic ceramic conductors, with a large range of stoichiometries $Na_{1+x}Zr_2Si_xP_{3-x}O_{12}$ with $0<x<3$. This paper reports the synthesis of nanocrystalline NASICON powders and thin films by two reactive processes. Nanocrystalline NASICON powders were prepared by the auto ignition synthesis. An aqueous solution containing stoichiometric amounts of sodium nitrate, zirconyl nitrate, diammonium hydrogen phosphate, ammonium perchlorate, fumed silica and urea was used. The powders were characterized by X-Ray Diffraction (XRD) and Transmission Electron Microscopy (TEM). Phase formation was determined by XRD analysis. The heat-treated powders were nanocrystalline, with the particle size ranging from 10 to 50 nm as determined by the TEM studies. NASICON thin films were produced by a Combustion Chemical Vapor Deposition (CCVD) technique using the above combustion precursors. The as produced thin films were further characterized by XRD and Scanning Electron Microscopy (SEM).

INTRODUCTION

NASICON (Na superionic conductor) is a well-known family of sodium ionic ceramic conductors, with a large range of stoichiometries $Na_{1+x}Zr_2Si_xP_{3-x}O_{12}$ with $0<x<3$ [1,2]. These compounds are known for their applications as a solid electrolyte in solid-state electrochemical devices such as gas sensors [3,4], ion sensors [2,5], and high-energy-density batteries [6]. The conventional solid-state method [7] of preparing these materials is a tedious process involving heating the component dry oxide powders at high temperatures (>1000°C) with repeated grinding. Wet-chemical methods like the hydrothermal method and the sol-gel

processing technique have several advantages in terms of homogeneity and the fine particle nature of the products. The synthesis of phase pure NASICON is often difficult by the latter processes. Also, these processing methods require long processing times, expensive chemicals, and special equipment. Hence, as an alternative approach, a reactive process called the auto ignition synthesis is used with the aim of synthesizing NASICON powders in nano-crystalline form. This combustion technique is better suited over other synthesis routes in terms of compositional homogeneity and purity of the final product.

The combustion of redox mixtures containing metal nitrate, urea, and ammonium perchlorate in the presence of diammonium hydrogen phosphate and silica is controlled and undergoes smooth combustion reaction to yield metal phosphates of $NaZr_2P_3O_{12}$ (NZP) type. Fumed silica present in the redox mixture appears to react with the metathetically formed sodium zirconium phosphate to yield NASICON materials [8].

Thin film materials of the solid electrolyte are very promising in the fields of chemical sensors or display devices for their advantages in their performance, miniaturization, and accumulation. So far, dry process of R. F. sputtering [9], laser ablation [10] and pulsed laser deposition methods [11], as well as wet chemical processes (e.g. sol-gel) [12-16] or screen printing methods [17] have been utilized in the synthesis of NASICON thin and/or thick films. Dry processes or the sol-gel routes are promising for the preparation of thin films; however, they still have disadvantages in terms of cost and ease of handling. Combustion Chemical Vapor Deposition (CCVD) is the vapor deposition of a film near or in a flame that causes the precursors to react [18,19]. This continuous, open-air deposition process holds several advantages over more traditional processes for thin film coating. The CCVD process does not require highly specialized and expensive equipment (e.g. vacuum chambers, reaction furnaces etc.), allows for continuous production-line manufacturing, and eliminates the use of expensive, environmentally harmful (e.g. chlorine or fluorine) or toxic chemicals. The present work describes the synthesis of nanocrystalline NASICON powders and thin films using aqueous precursor solutions.

EXPERIMENTAL PROCEDURE

An aqueous solution containing stoichiometric amounts of commercially pure sodium nitrate (Alfa Aesar, 99.99%), zirconyl nitrate (Aldrich Chemical Company, 99.99%), fumed silica (Alfa Aesar, 99.5%), diammonium hydrogen phosphate (Alfa Aesar, 98.0%), ammonium perchlorate (Alfa Aesar, Reagent grade) and urea (Sigma, 99.99%) was used. Stoichiometric amounts of these reactants were dissolved by stirring them with 50 cm^3 of water in a conical flask. Initially the solution was heated on a hot plate to evaporate excess water. When the resulting slurry was heated at 450°C, the contents ignited to burn with a flame,

yielding voluminous amounts of NASICON powder. Various heat treatments were carried out on these as synthesized powders to study their effect on the NASICON phase formation.

The powders were characterized by XRD (Siemens D5000) technique, using with Cu-Kα radiation at 40kv and 30mA in the range $2\theta = 12$ to 60 degrees. Transmission Electron Microscopy (JEOL, 2010, operated at 200kV) was carried out to ascertain the powder morphology and the extent of agglomeration of the solid combustion residues. Subsequently, the as-synthesized powders were cold isostatically pressed (Iso-Spectrum CP2-60) at 25Ksi pressure for 10 minutes and the resulting green compacts were subjected to sintering in an industrial microwave furnace (Microwave Materials Technology, Knoxville, TN) operated at 1.5 KW power for 15 minutes (~1100°C). The microstructure of these sintered pellets were examined using Scanning Electron Microscopy (Leo 1530, 30kV). The samples were sputter coated with Au-Pd alloy prior to their SEM analysis.

NASICON thin films were prepared on glass, and silicon substrates via CCVD using the above mentioned precursors in ethyl alcohol. Figure 1 shows the schematic of the experimental set up. The as-synthesized NASICON thin films were characterized using XRD and SEM.

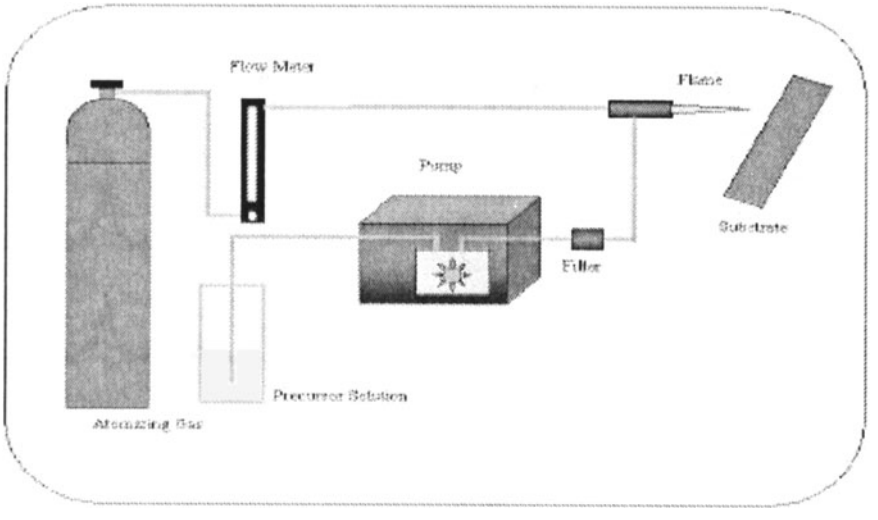

Figure 1. Schematic of the experimental set up.

RESULTS AND DISCUSSION

The XRD patterns of as-synthesized and as-heat treated powders are shown in Figure 2. The impurity phases such as ZrO_2 and $NaPO_3$ appeared in the as-synthesized XRD pattern. This is probably due to the presence of fumed silica, which reduces the flame temperature [8]. Calcination of $Na_3Zr_2PSi_2O_{12}$ between

350° to 750°C for 3hr yielded pure crystalline NASICON materials. As the calcination temperature is increased to 750°C, the impurity phases disappear. The XRD pattern of as heated powders at 750°C shows the formation of crystalline NASICON with a minimum of impurity phase. The low temperature of formation as well as the phase-pure nature of NASICON materials prepared by combustion process is notable because of the difficulty involved in preparing single-phase NASICON materials by other methods [20,21]. The TEM images of NASICON powder (Figure 3) exhibited elongated rod like crystals with size distribution in the range of 10-50nm. Agglomerates of the crystal are also visible from the micrograph. However, these are believed to be soft agglomerates as the powders are easily compacted to produce pellets.

The macro pore density of the pelletized samples is low. The density of the sample MW sintered at 1.5kW for 15min is 3.0 g/cc (92% of the theoretical density). Microwave sintering can densify NASICON pellets to high density. The SEM fractograph of the sintered sample contained faceted particles with particle size range of the order of 1.5 to 4.5 μm as shown in the Figure 4.

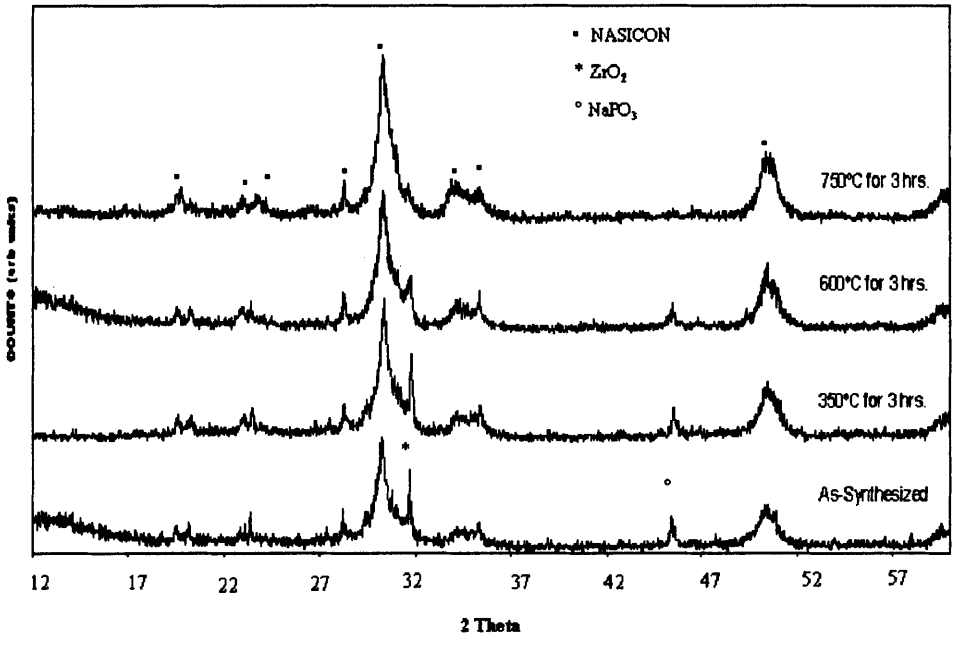

Figure 2. XRD patterns of the as-synthesized and calcined NASICON powders.

Figure 5 shows the XRD pattern of the as-produced NASICON thin film on the glass substrate. The XRD pattern confirms the presence of NASICON phase. A small amount of ZrO_2 impurity phase was observed in the as produced thin films. Figure 6 shows the SEM micrograph of the as-prepared NASICON thin film on glass substrate. The thin films were continuous with thickness in the range of 1 to 2μm.

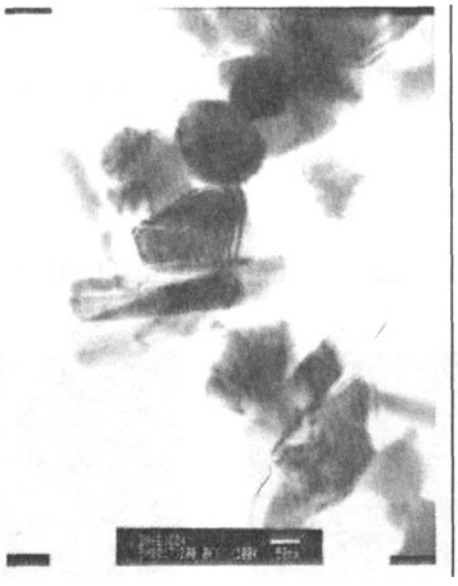

Figure 3. TEM pictures of as-synthesized NASICON powder.

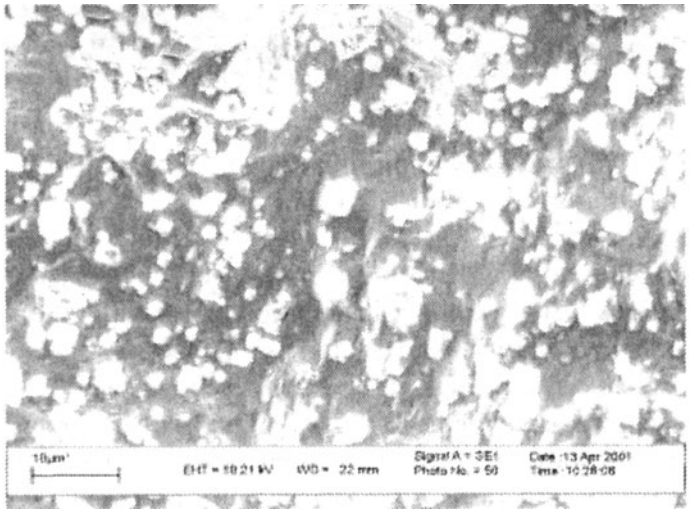

Figure 4. SEM fractograph of NASICON sample MW sintered at 1100° C for 15min.

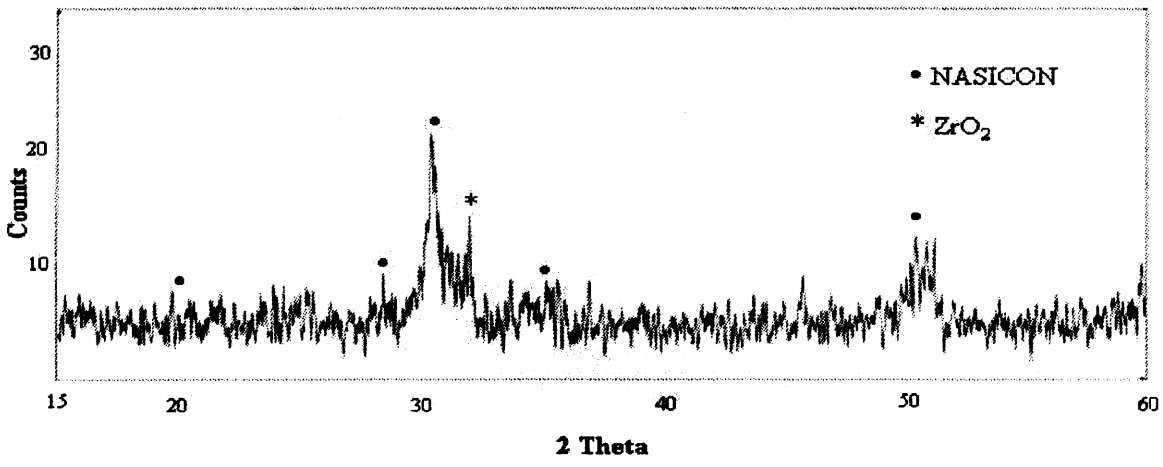

Figure 5. XRD pattern of as-produced NASICON thin film on glass substrate.

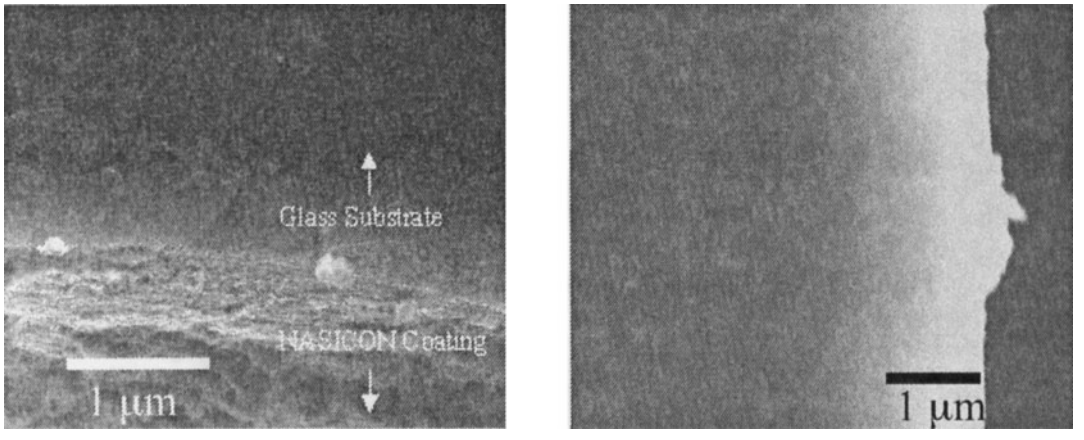

(a) (b) Figure 6. SEM images of NASICON thin film on (a) glass, and (b) Si substrates.

CONCLUSIONS

Nanocrystalline NASICON materials were prepared using combustion synthesis technique. The exothermic reaction containing the redox mixture of metal nitrates, fumed silica, urea, ammonium perchlorate and diammonium hydrogen phosphate creates high in-situ temperatures, which are utilized for the formation and crystallization of NASICON. The main advantages of the process are reduced processing time, saving in energy, and nano-crystallinity of the powders. NASICON thin films were successfully prepared by combustion CVD (CCVD) technique. The as-produced thin films were uniform and nanocrystalline.

ACKNOWLEDGEMENTS

We acknowledge the support of LDRD grant from INEEL. Further support is through DMI 9800009.

REFERENCES

[1]H. Y. P. Hong, *Mat. Res. Bull.* **11** (1976) 173.
[2]J. B. Goodenough, H. Y-P. Hong, and J. A. Kafalas, *Mat. Res. Bull.* **11** (1976) 203.
[3]Y. Saito, T. Maruyama, Y. Matsumoto and Y. Yano, *Proc. Int. Meeting Chem. Sensors,* Fukuoka (1983) 326.
[4]S. Yao, Y. Shimizu, N. Miura and N. Yamazoe, *Chem. Lett. 1990* (1990) 2033.
[5]P. Fabry, J. P. Gros, JF Million-Brodaz and M Kleitz, *Sensors and Actuators* **15** (1988) 33.
[6]B. E. Yoldas, US Patent No. 4,526,844 (1985).
[7]U. V. Alphen, M. F. Bell, and H. H. Hofer, *Solid State Ionics* **3 / 4** (1981) 215.
[8]N. A. Dhas, and K. C. Patil, *J. Mat. Chem.* **4** (1994) 491.
[9]D. Ivanov, J. Currie, H. Bouchard, A. Lecours, J. Adrain, and A. Yelon, *Extended Abstracts of the 7th International Conference on Solid-State Sensors and Actuators, Transducers '93* Yokohama, Japan (1993) 382.
[10]M. Morcrette, P. Barboux, A. Laurent, and J. Perriere, *Solid State Ionics* **93** (1997) 283
[11]R. Izquierodo, E. Quenneville, D. Trigylidas, F. Girand, M. Meunier, D. Ivanov, M. Paleologou, and A. Yelon, *J. Electrochem. Soc.* **144** (1997) L323.
[12]B. E. Yoldas, and I. K. Lloyd, *Mat. Res. Bull.* **18** (1983) 1171.
[13]Y. L. Huang, A. Caneiro, M. Attari, and P. Fabry, *Thin Solid Films* **196** (1991) 283.
[14]A. Moini, and A. Clearfield, *Adv. Ceram. Mater.* **2** (1987) 173.
[15]A. Ahmad, C. Glasgow, and T. A. Wheat, *Solid State Ionics* **76** (1995) 143.
[16]Y. Shimizu, and T. Ushijima, *Solid State Ionics* **132** (2000) 143.
[17]H. Perthuis, G. Velasco, and P. H. Colomban, *Jpn. J. Appl. Phys.* **23** (1984) 534.
[18]A. T. Hunt, W. B. Carter, and J. K. Cochran, Jr. *Appl. Phys. Lett.* **63** [2] (1993) 266
[19]W. Kern, and K. K. Schuegraf, *Handbook of Thin-Film Deposition Processes and Techniques* (1988) 1
[20]A. Ahmad, T. A. Wheat, A. K. Kuriakose, J. D. Canaday, and A. G. McDonald, *Solid State Ionics* **24** (1987) 89.
[21]H. Perthuis, and P. H. Colomban, *Mat. Res. Bull* **19** (1984) 621.

This page intentionally left blank

MANUFACTURING OF GLASS AND CERAMIC MATRIX COMPOSITES BY ELECTROPHORETIC IMPREGNATION WITH NANOSIZED POWDERS

Jan Tabellion, Christian Oetzel and Rolf Clasen
Saarland University
Department of Powder Technology
Im Stadtwald, Building 43
D-66123 Saarbrucken, Germany

ABSTRACT

Ceramic and glass components with graded structures can be produced by means of electrophoretic impregnation (EPI) of green bodies, prepared beforehand by electrophoretic deposition (EPD) or casting. In contrast to most of the common techniques components with continuously graded structures (graded pore size/density or/and graded chemical composition) are obtained. Steepness and dimension of the gradient could be adjusted reproducibly between some hundred microns and several millimeters up to centimeters. Examples are shown of silica glass green and sintered components with tailored gradient in density and pore size distribution as well as of composites of silica, alumina, ceria and zirconia with a functionally graded chemical composition. The impregnated green bodies were characterized by means of image analysis on the basis of SEM pictures and EDX analysis. The sintered components were characterized by optical spectroscopy. The influence of important process parameters of the EPI, like applied electric field strength, ζ-potential, viscosity, deposition time and pore size of the green body to particle size ratio, on the resulting graded structure is discussed.

INTRODUCTION

The strong interest in composites with functionally graded composition arises from the wish to combine the advantages of two dissimilar materials with highly incompatible properties. Joining glasses and especially silica glass to metal, e.g. for lighting applications or microelectronics, is highly complicated by the strong mismatch of the thermo-physical properties of both materials. Strong residual stresses arise during joining due to the highly different thermal expansion. To avoid or at least minimize these stresses glass-metal composites with graded junction are of great interest. The influence of a graded composition on thermal stresses is discussed in detail in [1]. Optical fibers and lenses with graded refractory index were probably the first application of functionally graded material with defined gradient that were produced on an industrial scale [2]. Other applications of ceramic-ceramic composites, where a graded interface is also advantageous, are thermal barrier coatings or tribological coatings, where hardness at high temperatures combined with a high toughness are required. Furthermore, the performance of solid oxide fuel cells can be enhanced by a functionally graded interface between cathode or anode and electrolyte. As membranes, in the field of biomaterials or as damping materials monolithic components with graded microstructure, graded density and/or pore size, are used.

Different techniques have been used for the manufacturing of graded ceramics. Coatings with graded structure have been deposited by CVD or thermal spraying. By means of dry pressing ce-

ramic composites have been shaped [3], but size and geometry of the composites are limited. Much more promising is the manufacturing of graded ceramic and glass components and composites by green forming from suspensions and sintering. In contrast to other techniques, where a gradient is formed by layer-wise deposition, continuously graded structures are achieved, e.g. by casting of suspensions. During the casting process the composition of the suspension is gradually changed [4]. Centrifugal casting of suspensions containing particles of different sizes results in coatings or monolithic components with a graded distribution of the particle size and hence with a graded density and pore structure [5]. A comprehensive overview of the different shaping techniques used as well as the basic concept of graded materials is given in [6].

A rather novel shaping technique for materials with graded structure is the electrophoretic deposition (EPD). EPD from aqueous suspensions is a low-cost, high-efficient and environmentally acceptable manufacturing technology for ceramic and glass components and composites. Furthermore, it could be shown, that green density and pore size distribution of electrophoretically deposited coatings and green bodies can be controlled and adjusted exactly and reproducibly [7]. Since the deposition rate is independent of particle size, nanosized particles can be deposited very homogeneously by EPD with high deposition rates [8] as well as powder mixtures with different particle size. Reviews about EPD as shaping technique are given in [9, 10]. In recent time several investigations were carried out to use EPD as shaping technique for graded alumina-zirconia composites [11-13]. The composition of the suspension was changed gradually during deposition and the different particles were co-deposited. A necessary demand of this process is that the different particles all are like-charged. But a difference in the ζ-potential of the particles has to be compensated by adjusting the suspension composition. Thus, the process control is rather sophisticated all the more because the particle-particle interaction can influence the motion of the particles [14]. Although a deposition of particles with different sign of surface charge is possible under certain conditions, this process is even more sophisticated to control.

In contrast, by means of electrophoretic impregnation (EPI) a continuously graded structure is achieved by deposition of nanosized or submicron particles within the pores of a green body or a fiber pre-form. The electrophoretic impregnation process is a modification of the electrophoretic deposition by the membrane method [15]. The membrane used for the EPD process is replaced either by a fiber pre-form or an open-porous green body. Thus, an impregnation of pore channels with small particles can be achieved.

EXPERIMENTAL SET-UP

Green bodies with controlled pore size and density were prepared by electrophoretic deposition (EPD) of micrometer-sized particles from aqueous suspensions or by mould casting. The powders were dispersed gradually in bidistilled water under constant torque by means of a dissolver. Vacuum was applied to avoid the incorporation of air bubbles into the suspension. To achieve an electrostatic stabilization of the particles and to adjust the ζ-potential different amounts of tetramethylammoniumhydroxide (TMAH) were added.

After drying, the green bodies were infiltrated with different nanosized particles by means of electrophoretic impregnation (EPI). Aqueous suspensions of alumina, zirconia, ceria and different fumed silica powders were prepared as described before. Stabilization and ζ-potential of the particles were adjusted by adding TMAH. The mean particle size of the Aluminum Oxide C (Degussa) with a specific surface area of 100 m^2/g (measured by nitrogen sorption) was 15 nm, whereas the zirconia (Experimental Product Zirconium Oxide, Degussa) had a mean size of 30 nm and a specific surface area of 40 m^2/g. The silica powders used were Aerosil OX50, A200 and A380 (Degussa) with a mean particle size of 40, 12 and 8 nm respectively. The figure in the product name is equal to the specific surface of the corresponding powder. The mean particle size of the ceria powder used (Nanophase Technologies) was 15 nm with a specific surface area of 57 m^2/g.

A simple experimental set-up for the electrophoretic impregnation of green bodies is shown in figure 1. For more complex shaped green bodies the set-up has to be re-adjusted with respect to electrode geometry and arrangement. The electrophoresis cell is subdivided into two chambers by the green body. One chamber was filled with a suspension, whereas bidistilled water and, where applicable, TMAH was poured into the second chamber, analogous to the membrane method. Two platinum plates were used as electrodes. The applied direct voltages were varied between 5 and 60 V. During deposition, voltage and current could be measured at up to 8 positions within the electrophoresis cell simultaneously. Furthermore, pH, electrical conductivity and temperature of the suspensions were measured.

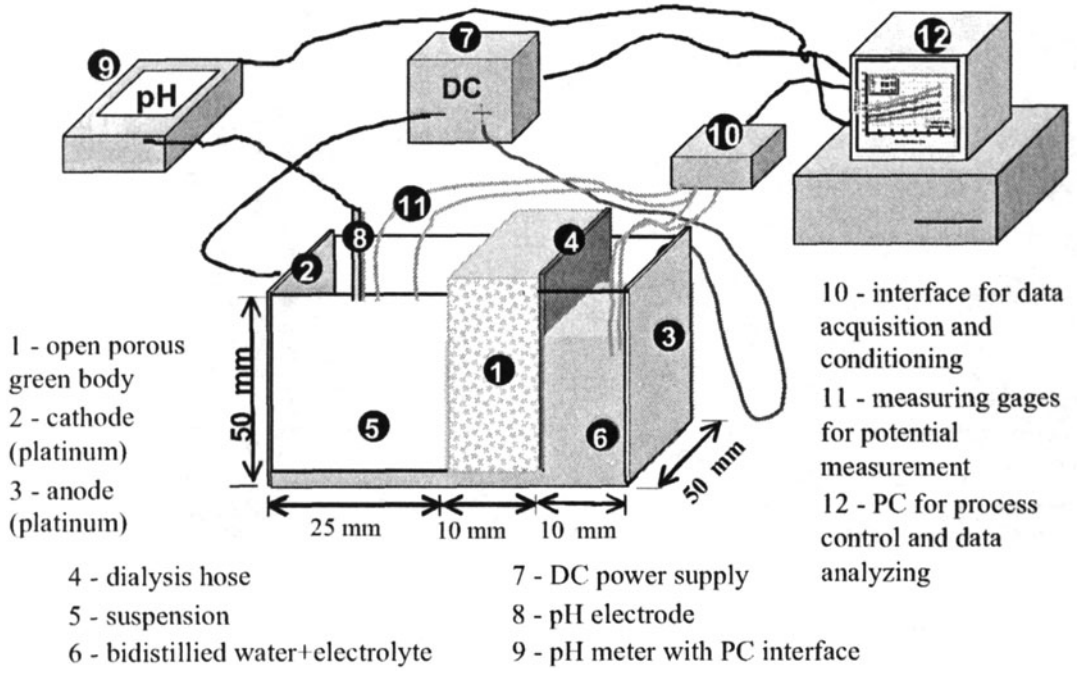

Figure 1. Experimental set-up for the electrophoretic impregnation of porous green bodies

The impregnated green bodies were characterized regarding densification, impregnated depth and gradient by means of an image analysis system (Image C) on the basis of SEM pictures and EDX analysis. Furthermore, density and pore size distribution were measured by Archimedes method and mercury porosimetry. The sintered components (vacuum, 1525 °C) were characterized by EDX analysis and Raman spectroscopy.

RESULTS AND DISCUSSION

Figure 2 shows the fracture surface (SEM image) of a silica green body with graded density and gradual change in pore size. The graded structure was achieved by electrophoretic impregnation of a silica green body with monomodal pore size distribution (mean pore size 1.8 µm) with nanosized fumed silica particles (OX50). The ratio of pore size to particle size (R/r ratio) was ≈ 90. The surface on the right-hand side was in contact with the suspension, which means that the green body was impregnated from this side. As can be seen, the visual porosity increases from the surface towards the bulk of the sample and so does the pore size. The micrograph in the upper right-hand corner shows a part of the green body at a distance of about 250 µm from surface with higher magnification. In this part of the sample all the pore channels between the coarse silica particles of

the green body are completely filled with nanosized OX50 particles. Thus, the green density was increased from 65 % of the theoretical value to 83 %TD. As a consequence thereof the mean pore size was decreased from 1.8 μm to 28 nm. With increasing distance from impregnation surface the density was found to decrease gradually whereas the pore size increased.

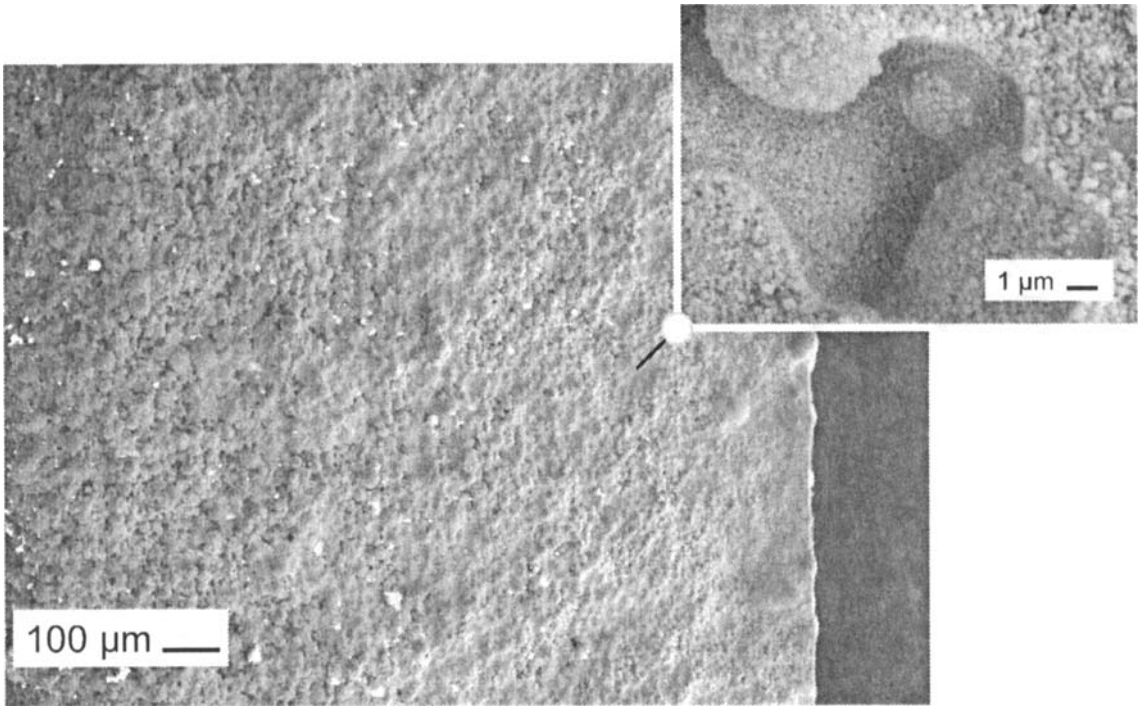

Figure 2. Silica green body with functionally graded density and pore size achieved by electrophoretic impregnation (SEM pictures, fracture surface)

The densification was determined as a function of distance from surface on the basis of SEM pictures each with equal magnification. Every 300 μm a picture was taken and the porosity determined by means of image analysis. The values were then normalized to a fully densified sample where no porosity could be observed by image analysis at the given magnification. Thus, a densification of 100 % means that all the pore channels in the green body are completely filled with nanosized particles and the only pores that still exist within the impregnated green body are those between the nano-particles.

To enable a reproducible tailoring of densification or gradient, the influence of important parameters of the EPI on densification and impregnation depth was investigated. The parameters varied were the applied electric field strength, pH, TMAH content, solids content, particle size and ζ-potential of the green body. Viscosity and electrical conductivity of the suspensions as well as ζ-potential of the particles were influenced indirectly. The investigations were carried out for fumed silica, zirconia, alumina and ceria. Some of the results for the impregnation of silica green bodies with different nanosized silica powders are shown below. Silica was chosen as a matrix material due to the fact that the sintered bodies could easily be characterized visually and by optical spectroscopy. Further results will be published in more detail.

Figure 3 shows the increase in density of silica green bodies after EPI with different nanosized fumed silica particles as a function of distance from impregnation surface. The smaller the particle size, which means the higher the R/r ratio, the bigger the increase in density near the impregnation

surface. With increasing distance from surface the difference in densification becomes smaller. The high R/r ratios of all particles result in a deep impregnation of the green bodies.

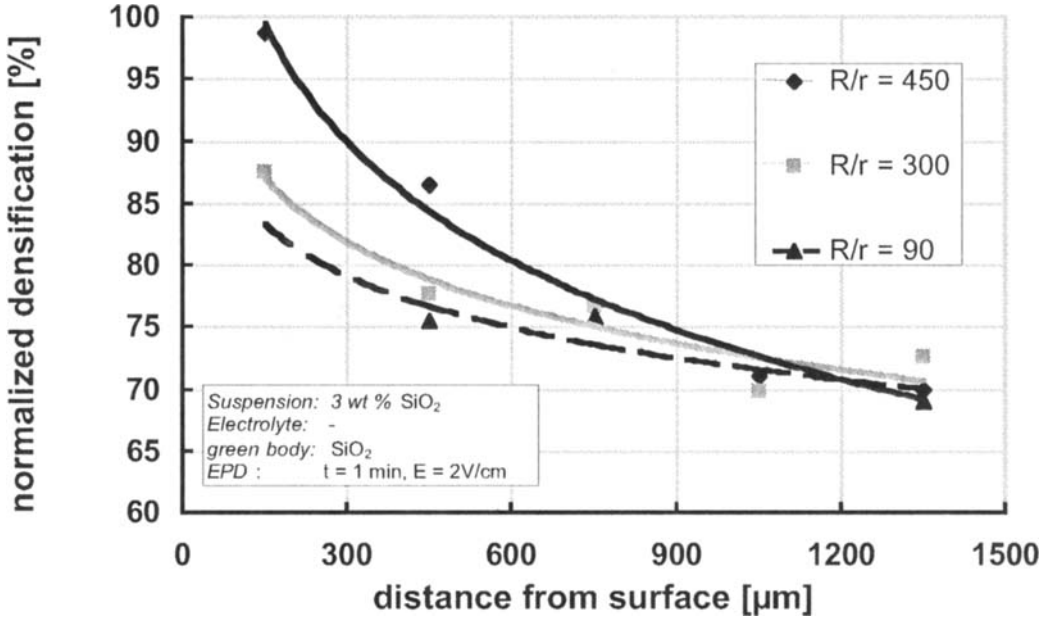

Figure 3. Influence of particle size on densification and steepness of gradient of silica green bodies impregnated with nanosized fumed silica powders of different particle size

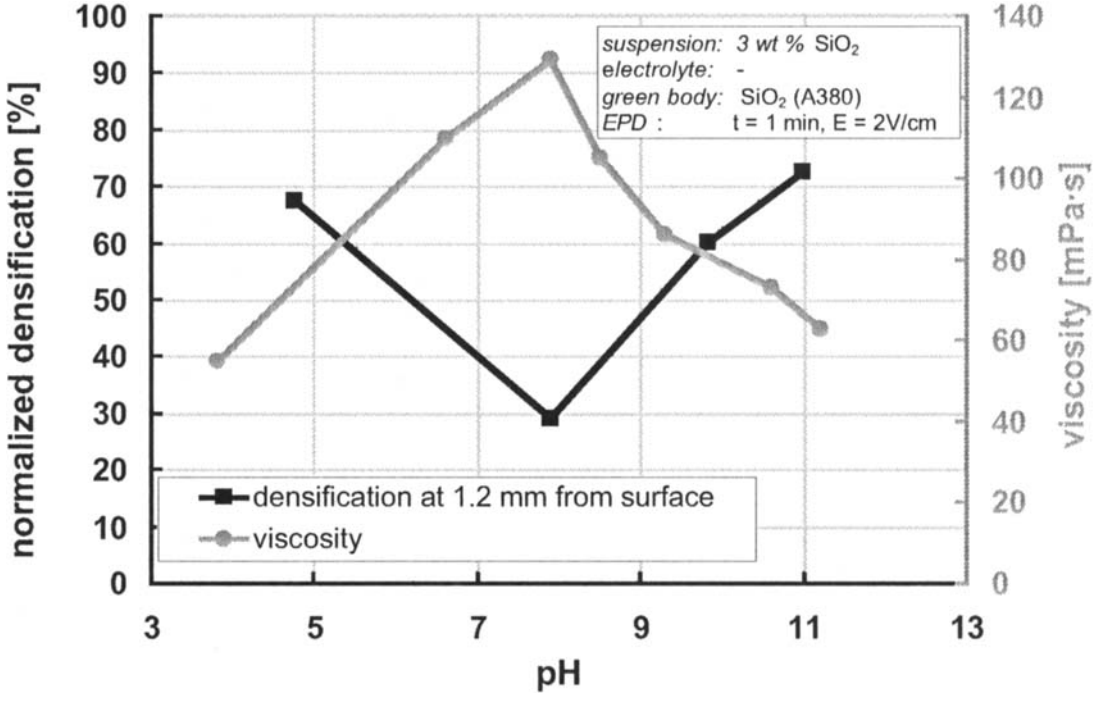

Figure 4. Influence of pH and viscosity on the densification of a silica green body by electrophoretic impregnation with nanosized fumed silica particles (A380)

Figure 4 shows the densification of a silica green body after EPI with A380 at a distance of 1.2 mm from the impregnation surface as a function of pH (titrated with TMAH). Furthermore, the viscosity of the aqueous A380 suspension used is plotted. A distinct minimum of the densification was observed for pH 8, which correlates with a maximum of the viscosity. This can be explained by a formation of a 3-dimensional network of silica agglomerates stabilized by hydrogen bonds, which aggravates the penetration of the particles into the pores of the green body.

The impregnated green bodies were sintered to investigate the influence of densification or density and pore size gradient on sintering behavior (sintering temperature) and properties of the sintered components. In figure 5 three sintered samples with different steep density gradient after EPI are shown. The samples were sintered at 1550 °C, where the not densified silica is not yet sintered to full density and is therefore not transparent. The densification with the nanosized particles enables a better sinterability and hence results in fully transparent silica glass Thus, the width of the transparent part of the samples is a measure for a certain amount of densification. It can clearly be seen in figure 5 that by EPI densified depth or density gradient can be adjusted in a wide range between a few ten microns and some millimeters or even centimeters. Furthermore, also a homogeneous densification can be achieved resulting in lower sintering temperatures.

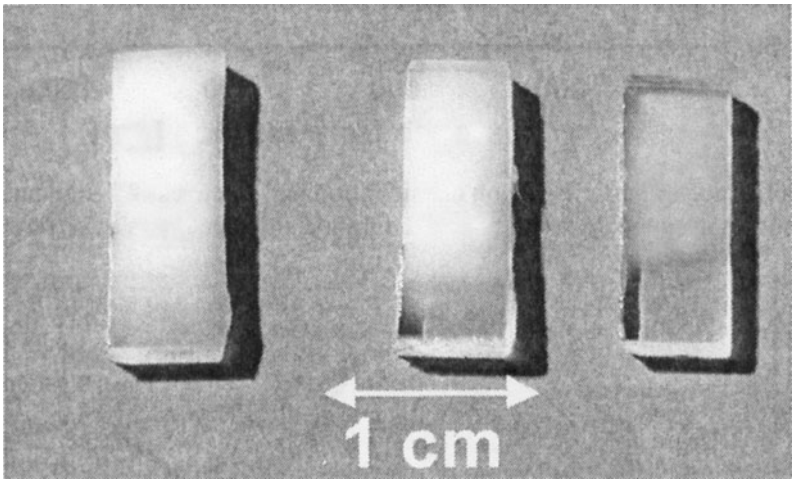

Figure 5. Silica glass samples with different steep graded density after sintering under vacuum at 1550 °C

Electrophoretic impregnation cannot only be used to produce components with graded density and pore size, but also to prepare graded composites of different materials. Figure 6 shows a SEM picture of the fracture surface of a silica green body electrophoretically impregnated with alumina. This example was chosen to investigate the parameters of the process due to the fact, that these samples could be characterized easily in green and sintered state. The alumina particles act as crystallization germs within the silica glass matrix and originate the formation of cristobalite. After sintering and polishing of such an impregnated sample the Raman intensity was measured as a function of the distance from impregnation surface. Every 200 µm a spectrum was measured. Figure 7 shows some of these Raman spectra and a part of the sintered composite. Near the surface sharp distinct peaks were observed which could be associated to cristobalite. With increasing distance from impregnation surface the intensity of the cristobalite peaks diminishes and is superimposed by the silica glass spectrum. At position 4 only the silica glass spectrum was observed. Even though this was only a semi-quantitative analysis, it can be seen, that after sintering of the electrophoretically impregnated green body a composite with graded composition was achieved.

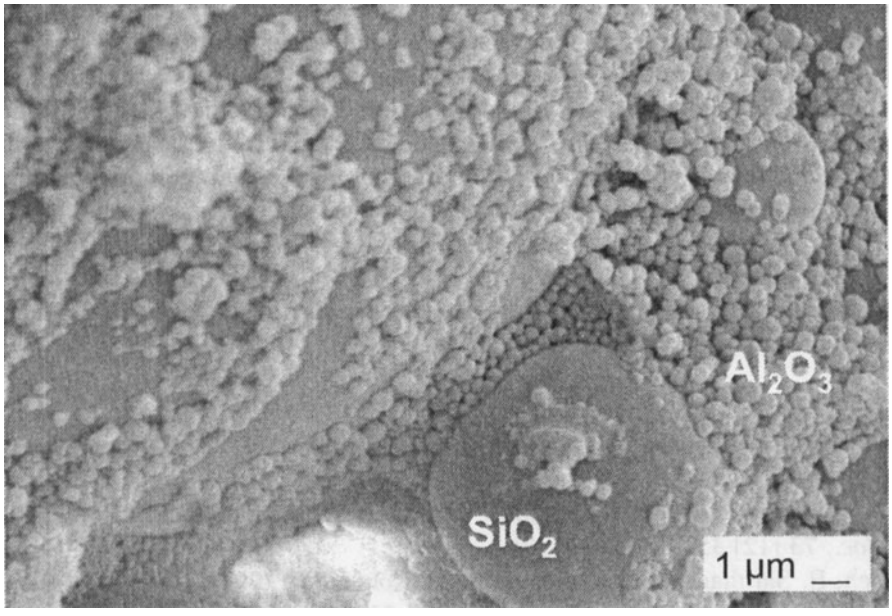

Figure 6. Silica-alumina FGM (green body) prepared by electrophoretic impregnation of a silica green body

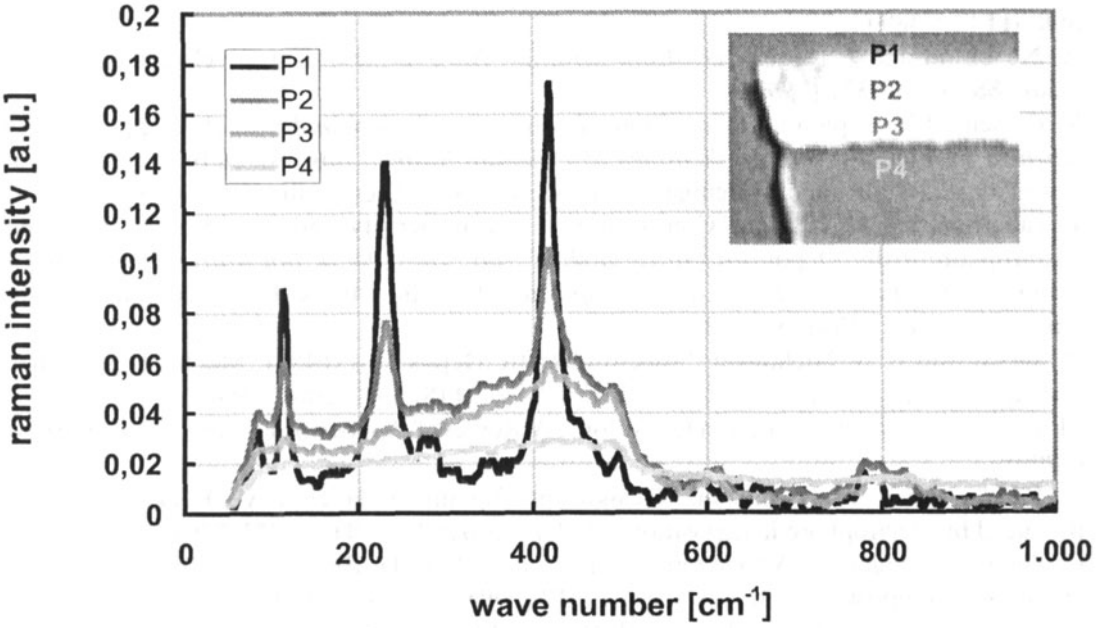

Figure 7. Position sensitive characterization of a functionally graded silica-alumina composite (after sintering under vacuum at 1550 °C) by Raman spectroscopy

CONCLUSIONS

Electrophoretic impregnation is a technique by which nanosized and submicron particles can be deposited within the pores of ceramic or glass green bodies or fiber pre-forms. Thus, nanosized secondary phases can be incorporated into a matrix to fulfil specific functions. A densification of a

green body can be achieved either homogeneously, graded or locally to improve green strength and sintering behavior. Furthermore, functionally graded components can be manufactured with graded density and/or pore size distribution as well as graded chemical composition. In contrast to most of the common techniques, a really continuous gradient is achieved. It could be shown that depth of impregnation and steepness of gradient could be tailored exactly and reproducibly by adjusting the process parameters of the EPI. Sintered composites and components with a continuous gradient from some ten microns up to several millimeters or centimeters could be produced.

ACKNOWLEDGEMENT

The authors gratefully acknowledge the financial support of the German Science Foundation (Deutsche Forschungsgemeinschaft, DFG).

LITERATURE

[1] N. Noda, "Thermal stresses in functionally graded materials.," *J. Thermal Stresses,* **22** 477-512 (1999).

[2] J. B. MacChesney and D. DiGiovanni, "Materials Development of Optical Fiber," *J. Am. Ceram. Soc.,* **73** [12] 3537-3555 (1990).

[3] M. Bartsch, B. Saruhan, M. Schmücker and H. Schneider, "FGM-oxidation protection system for nonoxide ceramics.," *Mater. Sci. Forum,* **308-311** 250-255 (1999).

[4] B. R. Marple and J. Boulanger, "Graded casting of materials with continuous gradients," *J. Am. Ceram. Soc.,* **77** [10] 2747-2750 (1994).

[5] T. Moritz, G. Werner, G. Tomandl, M. Mangler, H. Eichler, U. Lembke and W. Hauffe, "Characterization of thin ceramic layers with a graded pore structure.," *Mater. Sci. Forum,* **308-311** 884-889 (1999).

[6] A. Neubrand and J. Rödel, "Gradient material: An overview of a novel concept," *Z. Metallkd.,* **88** [5] 358-371 (1997).

[7] R. Clasen, "Electrophoretic deposition of compacts of nanosized particles"; pp. 169-184 in *Science, Technology, and Applications of Colloidal Suspensions,* Edited by J. H. Adair, J. A. Casey, C. A. Randall and S. Venigalla. Am. Ceram. Soc., Westerville (USA), 1995.

[8] J. Tabellion and R. Clasen, "Controlling of Green Density and Pore Size Distribution of Electrophoretically Deposited Green Bodies"; pp. 185-196 in *Innovative Processing and Synthesis of Ceramics, Glasses, and Composites IV.,* Edited by N. P. Bansal and J. P. Singh. Am. Ceram. Soc., Westerville, 2000.

[9] P. Sarkar and P. S. Nicholson, "Electrophoretic Deposition (EPD): Mechanisms, Kinetics, and Application to Ceramics," *J. Am. Ceram. Soc.,* **79** [8] 1987-2001 (1996).

[10] M. S. J. Gani, "Electrophoretic Deposition - A Review," *Industrial Ceramics,* **14** [4] 163-174 (1994).

[11] B. Hatton and P. S. Nicholson, "Design and fracture of layered Al_2O_3/TZ3Y composites produced by electrophoretic deposition," *J. Am. Ceram. Soc.,* **84** [3] 571-576 (2001).

[12] C. Zhao, J. Vleugels, L. Vandeperre, B. Basu and O. V. D. Biest, "Y-TZP/Ce-TZP functionally graded composite," *J. Mater. Sci. Lett.,* **17** [1998] 1453-1455 (1998).

[13] C. Zhao, J. Vleugels, L. Vandeperre, B. Basu and O. v. d. Biest, "Graded tribological materials formed by electrophoresis," *Mater. Sci. Forum,* **308-311** 95-100 (1999).

[14] A. Börner, R. Herbig, M. Mangler and G. Tomandl, "Forming of a gradient ceramic material by electrophoretic deposition," *Mater. Sci. Forum,* **308-311** 89-94 (1999).

[15] R. Clasen, "Forming of compacts of submicron silica particles by electrophoretic deposition"; pp. 633-640 in *2nd Int. Conf. on Powder Processing Science,* Edited by H. Hausner, G. L. Messing and S. Hirano. Deutsche Keramische Gesellschaft, Köln, Berchtesgaden, 12.-14. 10. 1988, 1988.

COMPARATIVE INVESTIGATION OF Al_2O_3- AND ZrO_2 NANOPOWDERS SYNTHESIZED BY DIFFERENT METHODS

Stephan Appel and Rolf Clasen
Saarland University
Department of Powder Technology
Im Stadtwald, Building 43
D-66123 Saarbrücken, Germany

Andrei Chkourankov, Harald Natter and Rolf Hempelmann
Saarland University
Physical Chemistry
Im Stadtwald, Building 9
D-66123 Saarbrücken, Germany

Sabine Schlabach, Bin Xu and Dieter Vollath
IMF III, Research Center Karlsruhe
P. O. Box 3640
D-76021 Karlsruhe
Germany

ABSTRACT

Nanosized powders offer new possibilities for the preparation of advanced materials. Therefore these powders should show certain properties like shape, density and phase composition. Different nanosized alumina and zirconia powders were prepared via gas phase synthesis and wet chemical reaction. While pure alumina showed the typical phase transition from γ, δ to α-phase at 1100 to 1200 °C, Fe_2O_3-doping seems to reduce the phase transition temperature significantly. All powders had to be calcined to achieve a crystalline structure. These first results of this comparative investigation indicate that gas-phase deposited powders are more qualified for the preparation of advanced materials.

INTRODUCTION

For the production of nanosized ceramic powders a number of synthesis techniques are currently available. Important examples are precipitation methods [1], the sol-gel technology [2], spray pyrolysis [3], flame hydrolysis and inert gas condensation [4]. The highest amount of nanosized powders are produced on an industrial scale with more than 100.000 t/a via flame hydrolysis (e.g. Aerosil®, Degussa AG, Hanau, Germany). These powders (mostly silica, titania, and alumina) are mainly used as additives and the potential as high-end starting powders for advanced ceramics is by far not exploited. For the preparation of advanced ceramics it is important that these nanopowders show suitable properties for forming high-density compacts, which can be completely sintered. Therefore is the objective of this

paper to compare nanopowders made by different methods with respect to their suitability for making advanced materials. Besides Aerosils® nanosized alumina and zirconia powders made by electrodeposition under oxidizing conditions (EDOC) [5], the microwave plasma technique [6], [7], [8] and the synthesis in a pulsation reactor [9] are used. The characteristic properties, which are important for the preparation of advanced ceramics, are measured. Particle size, pycnometric density, phase composition and agglomerating behavior have influence in the sintering behavior. Crystallization and phase transformations have been studied by temperature dependent XRD, thermogravimetry (TG) and difference scanning calorimetry (DSC).

STARTING POWDERS

Besides the alumina and zirconia powders, which are delivered by Degussa AG, Hanau (Germany), or IBUtec, Weimar (Germany), on a industrial scale (at least testing powders, available in larger quantities), the powders synthesized via EDOC methods or microwave plasma deposition were prepared for this comparative investigation. Especially the deposition rate of the applied microwave apparatus was not very high. Therefore only small quantities of some grams and a restricted number of compositions very available for these measurements.

PROPERTIES OF SYNTHESIZED NANOPOWDERS

The basic differences between the gas phase deposited powders and the powders made by wet electrochemical reactions is shown in fig. 1. While single, slightly agglomerated particles are formed in the low pressure plasma, the

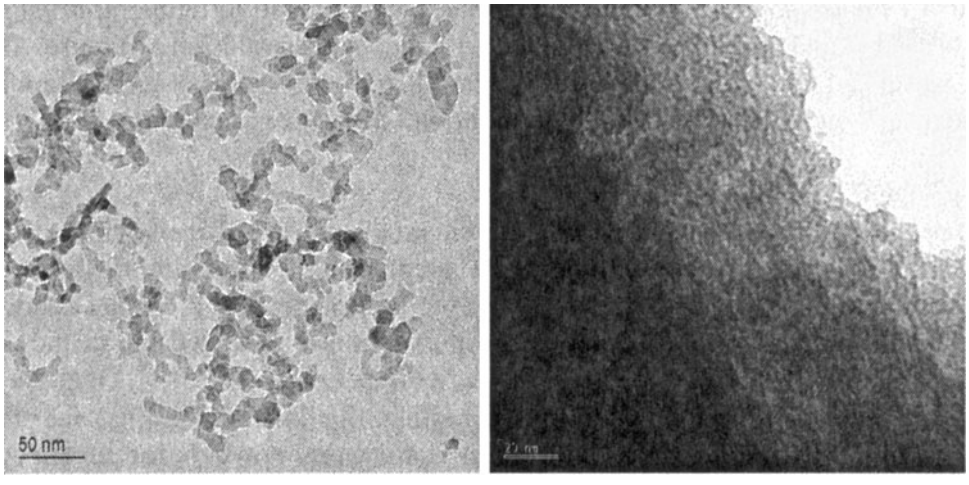

Fig. 1 TEM pictures of microwave plasma generated nanosized Al_2O_3 (left) and ZrO_2 (right) made with EDOC process

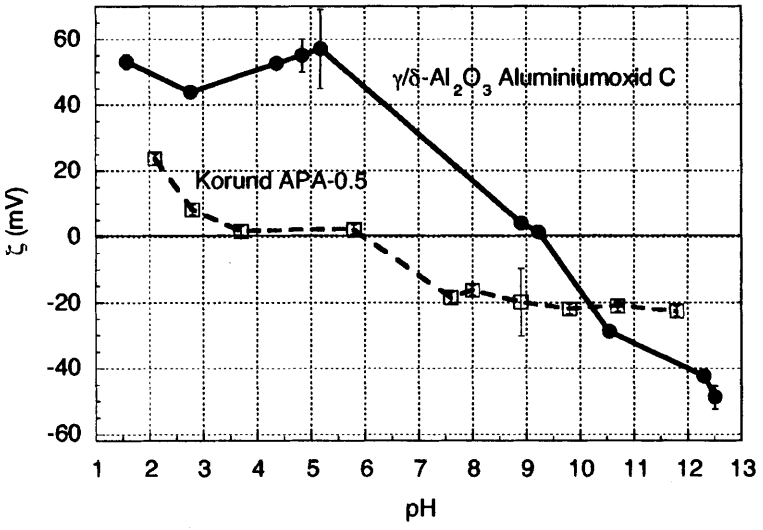

Fig. 2 Zeta potential of different alumina powders

EDOC zirconia particles still stick heavily together. Another difference is shown in fig. 2, where the zeta potential of Degussa Al_2O_3 powder (Aluminiumoxid C, commercial powder) is plotted and compared to a commercial, submicron alumina powder. Therefore these powder characterizations are necessary before further processing in the direction of material preparation is considered.

RESULTS OF TG AND DSC MEASUREMENTS

As most of the gas phase synthesized powder were amorphous after deposition, the phase transitions were measured by DSC. Additionally, the weight

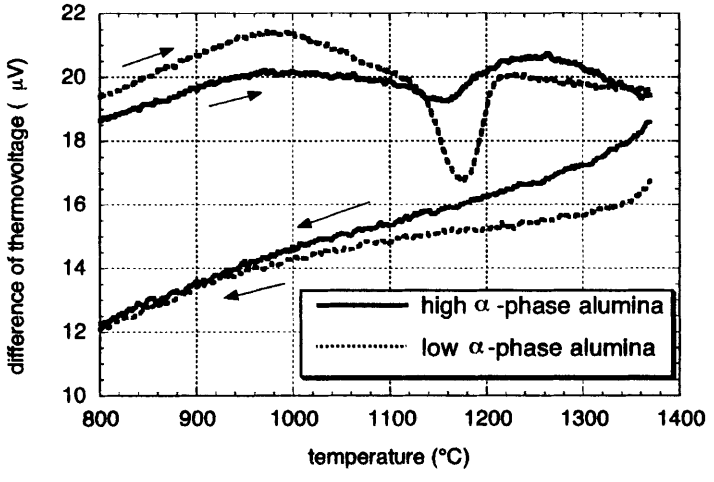

Fig. 3 Comparison of DSC measurements of different IBUtec alumina powders

changes were recorded (TG). The IBUtec alumina shows the typical phase transition at 1100 °C, see fig. 3. The transition for the pure microwave plasma alumina is slightly higher (fig. 4). For the microwave plasma zirconia powder a hysteresis

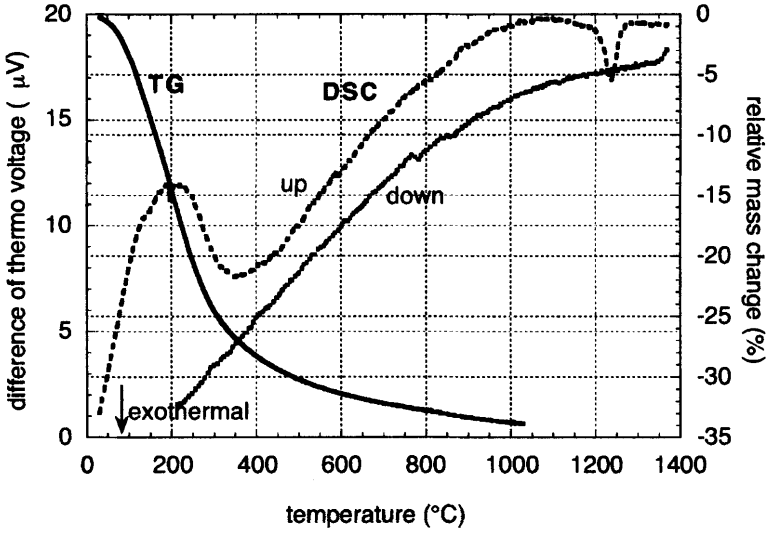

Fig. 4 DSC measurement of microwave plasma synthesized alumina powders

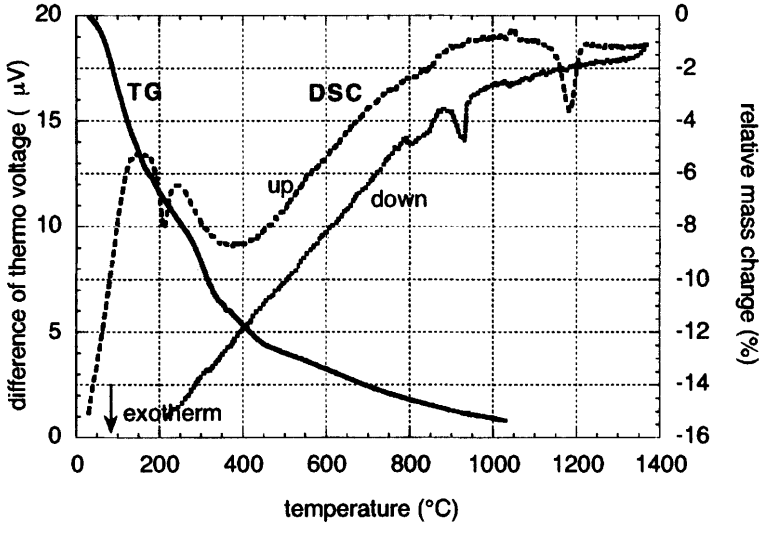

Fig. 5 DSC measurement of microwave plasma synthesized zirconia powders

for the phase transition monoclinic - tetragonal is observed. The loss of weight, which shows no specific temperature dependence, is due to loss of surface water. Compared to fig. 4, the addition of approx. 1 wt.-% Cr_2O_3 added to alumina reduces slightly the transformation temperature. In contrast to this result, the addi-

tion of 1 wt.-% Fe_2O_3 causes significant changes. The sharp peak, which seems to be attributed to the phase transition to the α-phase, shifts to 300 °C. In the second paper presented at this conference, where the sintering behavior of compacts of these powders is reported, it is proved that the α-phase was formed below 900 °C.

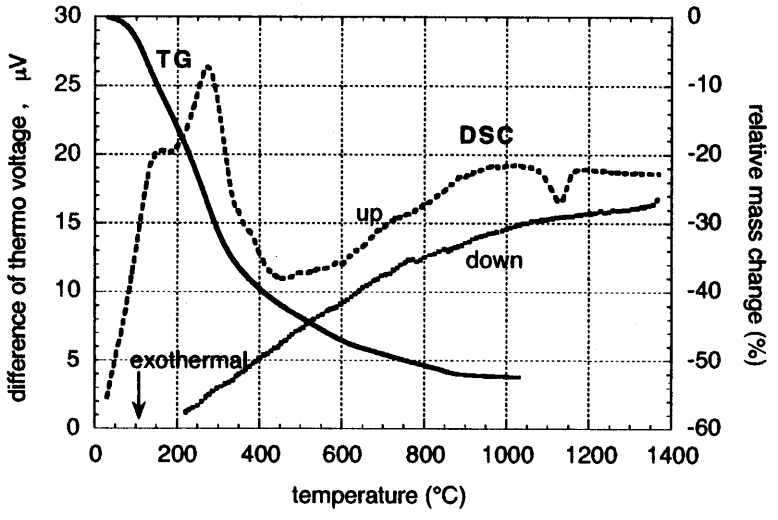

Fig. 6 DSC measurement of microwave plasma synthesized 1 Cr_2O_3-Al_2O_3-powders

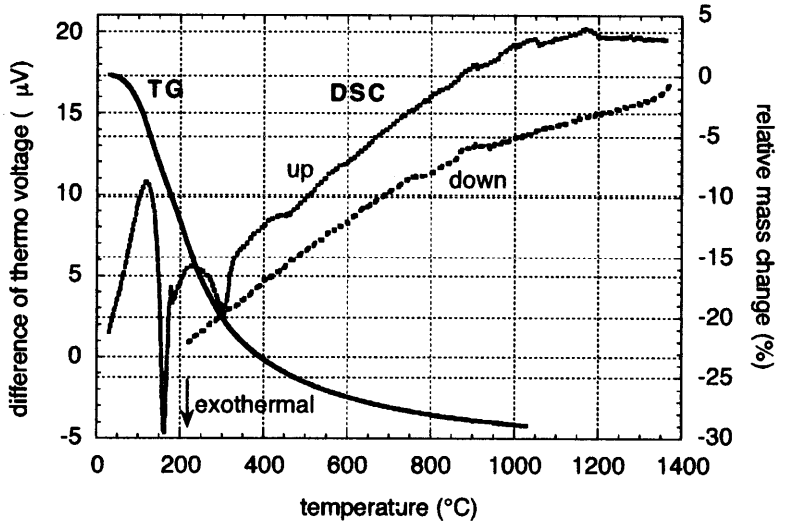

Fig. 7 TG and DSC of microwave plasma synthesized 1 Fe_2O_3-Al_2O_3

RESULTS OF XRD MEASUREMENTS

X-ray diffraction (XRD) measurements were performed to identify the crystalline phases of the generated powders. All gas phase synthesized powders were primarily amorphous. This is shown for microwave plasma alumina in fig. 8. As a second precursor can be incorporated into the microwave plasma apparatus after

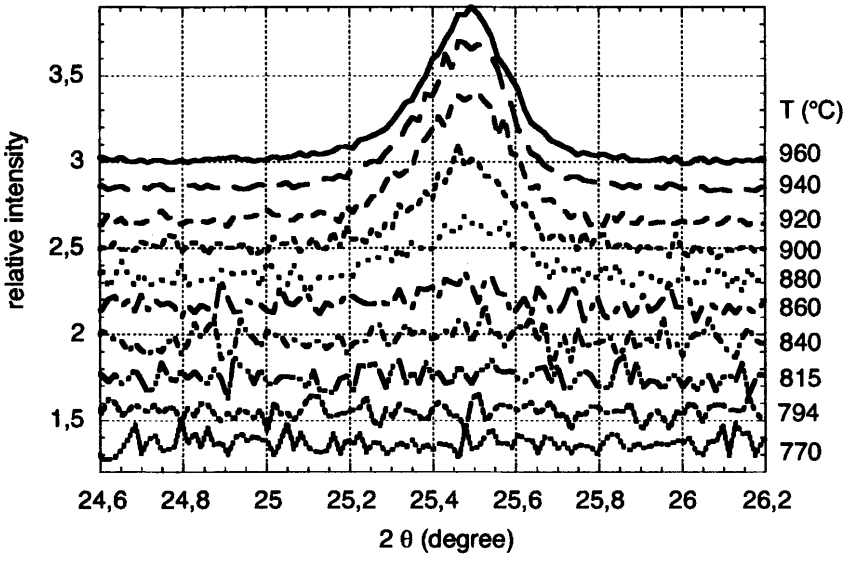

Fig. 8 XRD spectra of microwave plasma synthesized Al_2O_3 powder at increasing temperatures

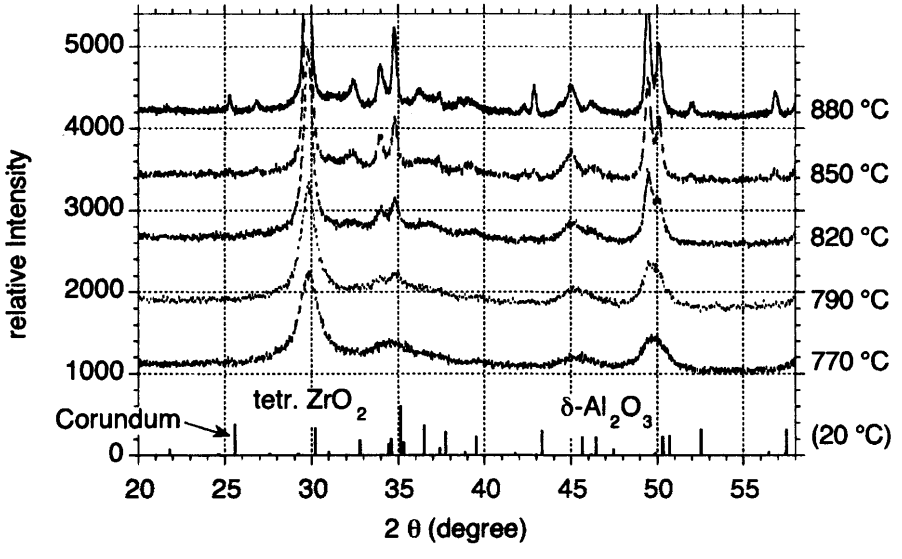

Fig.9 XRD spectra of microwave plasma synthesized zirconia-alumina core-shell powders

generation of particles, core shell structures can be perfectly achieved with this method. The formation of the crystalline alumina layer on the zirconia particles is observed at similar temperatures.

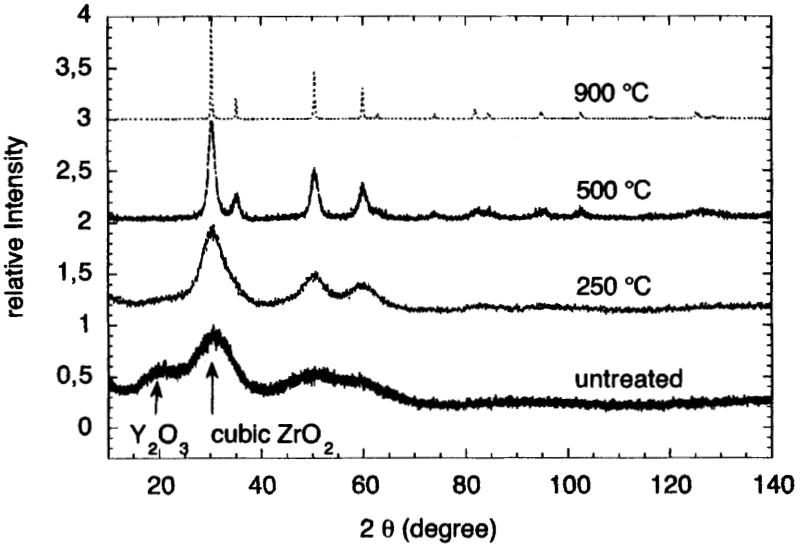

Fig. 10 XRD spectra of 10Y-ZrO_2 EDOC powders at increasing temperatures

After precipitation EDOC zirconia powder shows broad peaks which are attributed to very small crystals. As the particles are strongly agglomerated, a significant grain growth occurs during heating. This can be concluded from the sharp XRD-peaks at 900 °C. Furthermore, there is an indication from the XRD-spectrum of the untreated powder that yttria and zirconia are primarily precipitated in separated phases. During heat treatment a homogeneous phase is formed.

CONCLUSIONS

The investigations and comparison of the different nanopowders showed that a lot of properties have to be measured for evaluating the potential of preparing advanced materials from these powders. From the first results reported in this paper it can be concluded that commercially available or microwave plasma powders, deposited from the gas phase, are better suited than wet-phase precipitated powders. In addition, no organics have to be added for stabilization for the gas-phase powders, which have to be completely removed before sintering. For alumina the transition to the stable α-phase can be influenced by dopings. Most significant results were obtained for Fe_2O_3-doping.

ACKNOWLEDGEMENT

This project "Optoceramics" is part of the DFG program "From Molecules to Materials". The financial support from the Deutsche Forschungsgemeinschaft (DFG) is gratefully acknowledged.

REFERENCES

[1]T. L. Wen, V. Hebert, S. Vilminot, J. C. Bernier, "Preparation of nanosized yttria-stabilized zirconia powders and their characterization",*J. Mater. Sci.* ,**26** 3787-3791 (1991).

[2]B. Fegley, E. A. Barringer, "Synthesis, characterization, and processing of monosized ceramic powders": pp. 187-197 in *Ultrastructure processing of ceramics, glasses, and composites.* L. L. Hench, D. R. Ulrich, Eds. , J. Wiley & Sons, New York, 1984.

[3]G. L. Messing, S.-C. Zhang, G. V. Jayanthi, "Ceramic Powder Synthesis by Spray Pyrolysis",*J. Am. Ceram. Soc.* ,**76** [11] 2707-2726 (1993).

[4]H. Hahn, J. A. Eastman, R. W. Siegel, "Processing of nanophase ceramics": pp. 1115-1123 in *Ceramic Transactions, Ceramic Powder Science II, B* G. L. Messing, E. R. Fuller, H. Hausner, Eds. , 1988.

[5]R. Hempelmann, H. Natter, "Elektrochemische herstellung amorpher und kristalliner Metalloxide mit Teilchengrößen im Nanometerbereich", DE Patent No. 19840842, 07.09.1998.

[6]D. Vollath, K. E. Sickafus, "Synthesis of nanosized ceramic oxide powders by microwave plasma reactions",*NanoStructured Mater.* ,**1** 427-437 (1992).

[7]D. Vollath, K. E. Sickafus, "Synthesis of ceramic oxide powders in a microwave plasma device",*J. Mater. Res.* ,**8** [11] 2978-2984 (1993).

[8]D. Vollath, D. V. Szabó, "Nanocoated particles: a special type of ceramic powder",*Nano Structured Materials* ,**4** [8] 927-938 (1994).

[9]S. Begand, S. Ambrosius, "Herstellung nanoskaliger Pulver durch thermische Synthese im Pulsaktionsreaktor",*cfi/Ber. DKG* ,**75** [9] 12-16 (1998).

CHARACTERIZATION OF DOPED GLASSES MANUFACTURED BY SINTERING OF NANOPARTICLES

Karsten Smeets and Rolf Clasen
Saarland University
Department of Powder Technology
Im Stadtwald, Building 43
D–66123 Saarbrücken, Germany

ABSTRACT

Gold ruby glass is conventionally manufactured by melting technology. Disadvantageous is the difficulty to control size and distribution of the nanosized gold particles. In order to diminish these disadvantages, the samples of this study are manufactured by sintering of silica green bodies. Here, a homogeneous and sharp pore size distribution can be realized, because the pore size is a function of the particle size of the powder used. These green bodies are impregnated with gold salt solutions. Since the forming gold particles are incorporated within the pores, their size and distribution should be governed by the pore size of the green body. In this paper, different colored samples are investigated by means of optical spectroscopy. UV-VIS transmission spectra, FT-IR and Raman spectra of sintered gold ruby glass are shown and compared to commercially available glasses. Differences occur mainly due to the different doping concentrations and the different matrix glass compositions.

INTRODUCTION

The usage of nanosized powders enables the manufacture of advanced glasses and ceramics, either coatings or components, with enhanced or new properties [1]. Maximum processing temperatures can be decreased significantly due to the high sintering activity of such powders. Accordingly, high purity silica glasses can be manufactured at 1,500 °C starting from nanosized fumed silica powders [2]. These glasses can easily be colored by soaking green bodies with salt solutions, containing coloring admixtures. For glass, it is problematic to achieve a red coloration; despite Samarium ions, the dopants can either be metallic gold or copper particles or semiconducting particles (CdS_xSe_{1-x}-doped glass). In both systems it is important to get particles in the nanometer range (2 to 20 nm) [3,4]. Both Au-/Cu-

and CdS_xSe_{1-x}-doped glasses exhibit interesting optical characteristics and have attained great interest in recent years due to their high nonlinear refractive indices [4-6]. Although color and production technology is similar, the functionality of the coloration differs [3]. For doping with semiconductors it is the light absorption of the nanosized CdS_xSe_{1-x} particles with coincidence of quantum-size effects. For doping with nanosized metal particles the classical Mie theory was improved, especially for small clusters [4, 7].

The traditional manufacturing method for this type of glasses is the melting technology. Here, precipitating of solved metal ions, which are reduced during an additional annealing step, forms the secondary phase. The temperature – time program allows control of nucleation and grain growth rate in such a manner that a very narrow particle size distribution is available after precipitation. Unfavorably, however, are the restricted number of material compositions and the lack of possibilities to control size, shape and location of the precipitated particles. In order to improve these parameters, plenty of process variations have been examined. These improvements comprise for instance photosensitive nucleation [8], ion exchange with a subsequent reduction [9] and manufacturing of layers via sputtering or evaporation [10]. Apart from these process improvements in classical melting technology, other technologies have been applied. One of these technologies, which provided a lot of publications in recent years, is the sol-gel process [11-14]. In comparison to other technologies, the sol-gel process is more flexible and has wider variation possibilities, but only thin layers (< 1 μm) can easily be manufactured. Problematic, however, is the production of large, monolithic compacts due to the cracking danger during drying. This can only be reduced by expensive supercritical drying [15] or by adding filler particles [16].

The technology which is applied in this paper, is the sintering of colloidal or particulate gels. One advantage is the significantly reduced processing temperature (1,250 °C to 1,450 °C) in comparison with melting technology (approx. 2,300 °C). Additionally, large silica glass bodies with complex geometry and sharp edges can be fabricated in a cheap and easy manner. Furthermore, the open pore structure can be used for modification of the green bodies. This comprises purification, densification or doping, e.g. incorporation of nanosized secondary phases. Doping processes can be subdivided into different vapor deposition techniques, solution- or suspension-based techniques. By use of salt solutions it is possible to manufacture vitreous silica in many colors [17].

EXPERIMENTAL SET-UP

All suspensions were prepared in a dissolver (PC Laborsysteme Ltd., type LDV1), with maximum 5,000 r.p.m. under a constant torque of 12 N·m. Different nanosized fumed silica powders (Degussa Aerosil OX50, A200 or A380 with mean particle sizes of 40 nm, 12 nm or 8 nm respectively) were gradually poured

into pure double distilled water. All suspensions were electrostatically stabilized by tetramethylammoniumhydroxide (TMAH). Additionally, vacuum was applied in order to remove remaining air bubbles.

Two methods of green body preparation have been examined. The first is the colloidal gel technique. Here, highly filled suspensions (40 to 50 wt %) were mixed with methyl formate in order to reduce the pH value to 7 to 8. This resulted in a vigorous increase in viscosity. The suspensions were poured into tubes. There these suspensions can solidify and dry. After one day the molds could be opened. Secondly, less filled suspensions (up to 30 wt %) were used for electrophoretic deposition (EPD) to form green bodies. This and the electrophoretic impregnation process (EPI) were carried out by the membrane method [18] in a twice subdivided electrophoresis cell with a length of 23 mm per cell part. Additionally, a dialysis hose was put between the two cell parts as ion permeable membrane.

The doping was incorporated either by soaking or by electrophoretic impregnation. In the first case, the green body was immersed in aqueous or alcoholic metal salt solutions. Alcohol was used because of its lower surface tension. In case of the electrophoretic impregnation, an open-porous green body was used instead of the ion permeable membrane of the EPD. The doping suspension was poured into one deposition chamber. The other chamber was filled with water containing an appropriate electrolyte concentration. After a second drying step the samples were sintered in a vacuum furnace or in a zone-sintering furnace (velocity: 1 cm/min) at respective temperatures.

RESULTS AND DISCUSSION

If UV-VIS spectra of sintered gold ruby glass are compared to those of molten glass samples (Au-doped borosilicate glass of Schott and Au-doped lead borate glass of Nachtmann) differences can be recognized in both intensity and position of the main absorbance (see Figure 1). The low transmittance of the lead borate glass at lower wavelengths can be explained by the high doping concentration (160 ppm) compared to the other samples: the sintered sample was soaked with a 200 times diluted gold salt solution [19]. This is due to the fact that the lead borate glass is used to manufacture flashed glass. Thus, this glass is more intensively colored. The main peaks of the two molten glasses and of the sintered sample are positioned at different wavelengths. This is due to the fact that the position of the main absorbance depends both on the size of the gold particles and on the different refractive indices of the matrix glasses. Furthermore, the lower transmittance of the silica glass at higher wavelengths is due to the fact that this sample was sintered and still contains a few air bubbles that were formed in the suspension. In contrast, both multi-component glasses were molten at much lower viscosity. The formation of bubbles can be avoided by use of green bodies with better homogeneity like those manufactured by means of electrophoretic deposition.

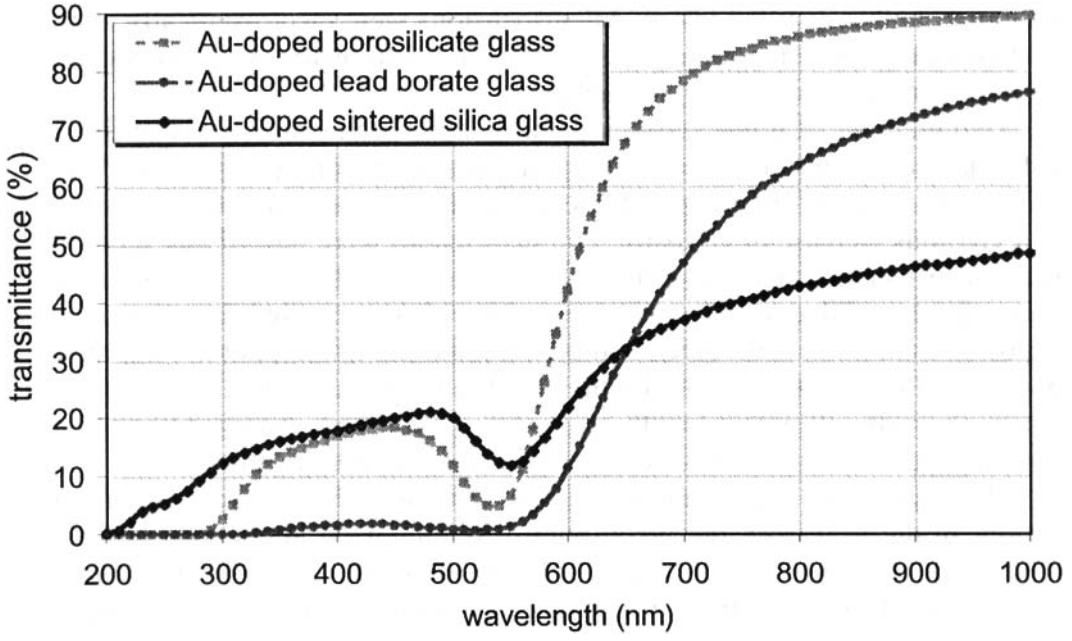

Figure 1: Transmission spectra of gold ruby glasses with different matrix glasses. The doping of the lead borate sample is 160 ppm; that is much higher than for the other samples. The peak position of the main absorption is a function of both particle size and glass composition. Due to some air bubbles, the sintered sample has a lower transmittance at higher wavelengths.

The samples were further investigated by means of FT-IR and Raman spectroscopy. In Figure 2 the IR spectra of the doped samples and of two matrix glasses are shown. Unfortunately, only lead borate glass samples with compositions different to that of the doped sample could be investigated. The undoped samples consist of more PbO and, hence, less SiO_2. The main peak is shifted towards lower wave numbers.

As can be seen for the silica samples, there are no significant differences in both peak heights and positions. All peaks and shoulders are typical for silica glass. No additional peaks occur. For the borosilicate samples, the peak position is shifted towards lower wave numbers in case of gold incorporation. Additionally, the intensity of the main peak decreases. The lead borate sample with 160 ppm gold doping does not show additional peaks compared to the IR spectrum of an undoped glass with different, but similar composition.

It has to be mentioned that peaks can be shifted in IR reflectance measurements. Thus, a Kramers-Kronig analysis is recommended. These investigations have not been finished yet and, hence, cannot be shown here.

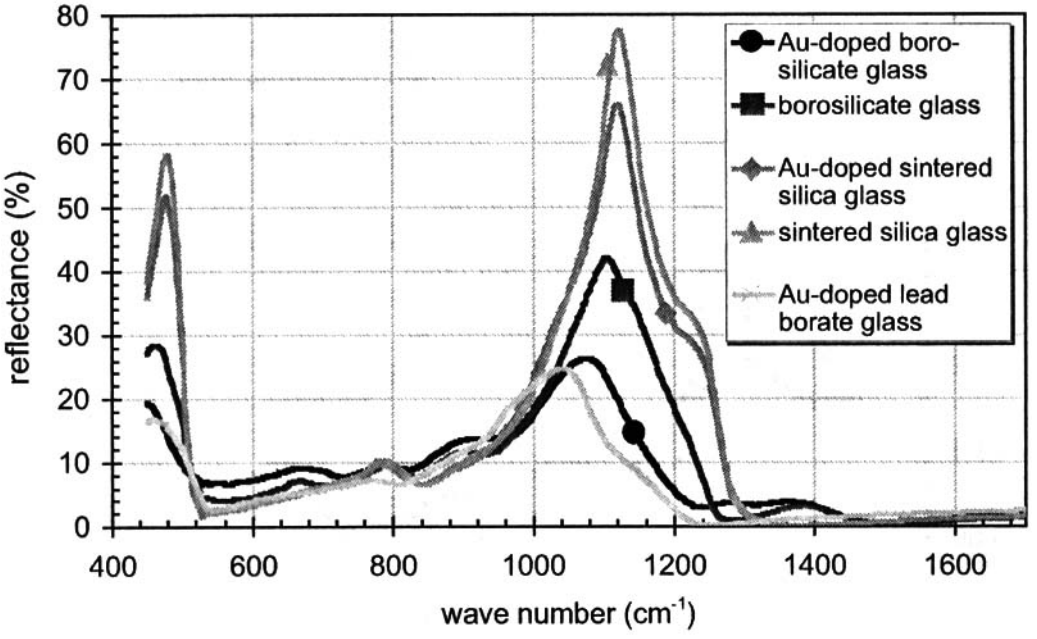

Figure 2: FT-IR spectra of the gold doped samples and two matrix glasses. There are no significant differences between the spectra of doped and undoped silica samples. For the borosilicate glass samples, the peak is shifted towards lower wave numbers by incorporation of gold particles.

Comparing the Raman spectra of the different glass samples, remarkable differences can only be seen for the silica samples. Here, two additional peaks occur at about 1450 cm^{-1} and at about 1720 cm^{-1}. The investigations so far could not attribute these two peaks doubtlessly to the incorporated nanosized gold particles. In contrast, the strong decrease at 509 cm^{-1} and the defect peak at 606 cm^{-1} are clearly recognizable. Additionally, there is another peak around 800 cm^{-1} that can also be seen in the IR spectrum at the same wave number.

For the lead borate sample, there is a strong peak detectable at around 1050 cm^{-1}, at the same wave number as in the IR spectrum. In case of the undoped lead borate glass there is a peak around 1220 cm^{-1} that does not occur in the IR spectrum.

In contrast to the IR spectra, no peaks around 1100 cm^{-1} occur for both silica and borosilicate glass. For the two borosilicate glass samples, there are two main peaks, one at 100 cm^{-1} and another one at 450 cm^{-1}.

Investigations at another series of doped samples showed similar results. In most cases, no significant shift in peak position and/or additional peaks could be determined.

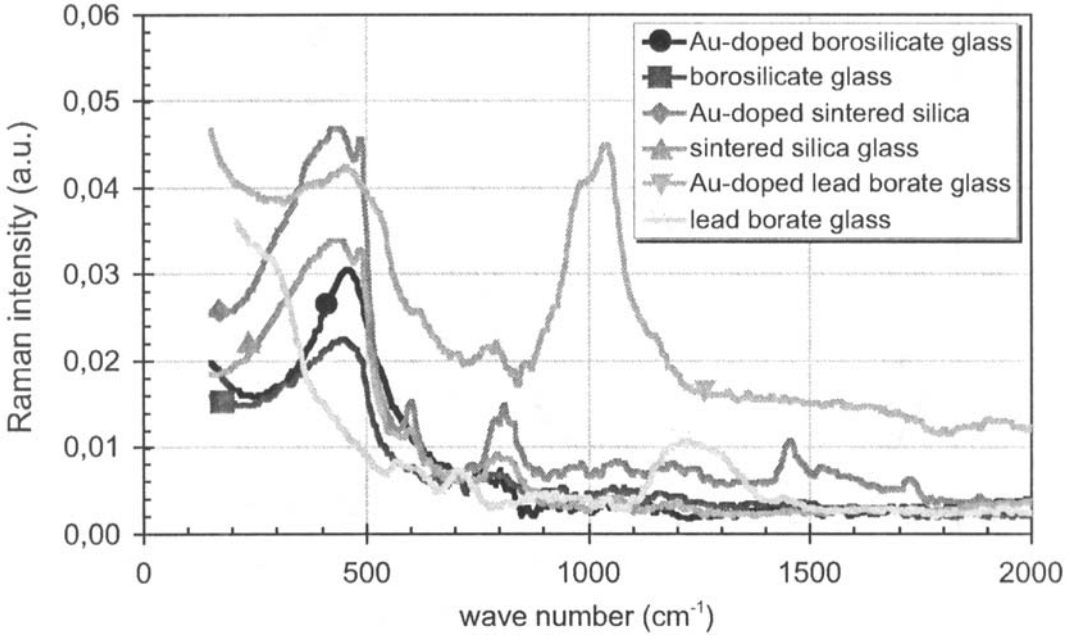

Figure 3: Raman spectra of doped and undoped glass samples. Significant differences only occur for gold ruby silica glass compared to undoped silica glass. For the borosilicate glasses, there are no additional peaks and the peak positions are at the same wave numbers.

CONCLUSIONS

Gold ruby silica glass was manufactured with gold particles of 2 to 3 nm in diameter by soaking green bodies made from nanosized fumed silica powders with methanolic gold chloride solutions, 200 times diluted. The subsequent sintering was carried out at 1,250 °C. Due to the homogeneous distribution of the precipitated gold the sintered glass is homogeneously colored and exhibits the typical red-violet coloration.

The characterization of different ruby colored glass samples by means of UV-VIS spectroscopy indicates that the main absorption of the sintered sample is at slightly higher wavelengths. This is mainly due to the different matrix glass compositions and due to the fact that absorption is a function of gold particle size. The matrix glasses used are silica, lead borate and borosilicate glass. These glasses can be distinguished by means of FT-IR and Raman spectroscopy.

The IR spectra of the doped samples are comparable to those of the undoped glasses except for the peak position of the doped borosilicate glass. In the Raman spectra additional peaks occur for the gold doped silica glass. If these peaks can be attributed to the nanosized gold particles is not fully clarified yet.

ACKNOWLEDGMENTS

The authors would like to acknowledge the financial support of the German Science Foundation (Deutsche Forschungsgemeinschaft, DFG) within the Sonderforschungsbereich (SFB) "Grenzflächenbestimmte Materialien" (interface-determined materials).

REFERENCES

[1] H. Gleiter, "Nanostructured materials: Basic concepts and microstructure," *Acta mater.*, **48** 1-29 (2000).

[2] R. Clasen, "Preparation and sintering of high-density green bodies to high purity silica glasses," *J. Non-Cryst. Solids,* **89** 335-344 (1987).

[3] W. Vogel, *Glaschemie*, 3. Auflage ed. Springer Verlag, Berlin, Heidelberg, New York, 1992.

[4] U. Kreibig and M. Vollmer, *Optical Properties of Metal Clusters*, ed. Springer Verlag, Berlin-Heidelberg, 1995.

[5] J. H. Adair, T. Li, T. Kido, K. Havey, J. Moon, J. Mecholsky, A. Morrone, D. R. Talham, M. H. Ludwig and L. Wang, "Recent developments in the preparation and properties of nanometer-size spherical and platelet-shaped particles and composite particles," *Mater. Sci. & Eng.*, **R 23** [4-5] 139-242 (1998).

6 J. Matsuoka, R. Mizutani, S. Kaneko, H. Nasu, K. Kamiya, K. Kadone, T. Sakaguchi and M. Miya, "Sol-Gel Processing and Optical Nonlinearity of Gold Colloid-Doped Silica Glass," *J. Ceram. Soc. Jpn.*, **101** 51-55 (1993).

[7] J. Lermé, B. Palpant, E. Cottancin, M. Pellarin, B. Prével, J. L. Vialle and M. Broyer, "Quantum extension of Mie's theory in the dipolar approximation," *Phys. Rev. B,* **60** [23] 16151-16156 (1999).

[8] R. J. Futato and R. H. Doremus, "Nucleation in Photosensitive Gold Ruby Glass," *J. Am. Ceram. Soc.*, **63** [3-4] 157-160 (1980).

[9] P. Sarkar, J. Kumar and D. Chakravorty, "Microstructure and optical absorption of silver granules in oxide glasses produced by ion-exchange and reduction treatments," *J. Mater. Sci.*, **18** 250-256 (1983).

[10] S. Motofumi and T. Yasunori, "Optical anisotropy and columnar structure of obliquely deposited thin films containing fine metal particles," *J. Non-Cryst. Solids,* **150** 148-152 (1992).

[11] J. Matsuoka, R. Mizutani, H. Nasu and K. Kamiya, "Preparation of Au-Doped Silica Glass by Sol-Gel Method," *J. Ceram. Soc. Jpn.*, **100** [4] 599-601 (1992).

[12] M. Nogami, A. Kato and Y. Tanaka, "Sol-gel preparation of CdS_xSe_{1-x} solid solution microcrystal-doped glasses," *J. Mater. Sci.*, **28** 4129-4133 (1993).

[13] T. Yazawa, K. Kadono, H. Tanaka, T. Sakaguchi, S. Tsubota, K. Kuraoka, M. Miya and W. De-Xian, "Preparation and optical property of monolithic silica

gel uniformaly dispersed with gold colloid from aqueous solution," *J. Non-Cryst. Solids,* **170** 105-108 (1994).

[14] S. T. Selvan, Y. Ono and M. Nogami, "Polymer-protected gold clusters in silica glass," *Mater. Lett.,* **37** 156-161 (1998).

[15] M. J. v. Bommel and A. B. d. Haan, "Drying of silica gels with supercritical carbon dioxide," *J. Mater. Sci.,* **29** 943-948 (1994).

[16] M. Toki, S. Miyashita, T. Takeuchi, S. Kanbe and A. Kochi, "A large-size silica glass produced by a new sol-gel process," *J. Non-Cryst. Solids,* **100** 479-482 (1988).

[17] R. Clasen, "Preparation of coloured silica glasses made by sintering of particulate gels," *Glastech. Ber.,* **66** [11] 299-304 (1993).

[18] R. Clasen, "Forming of compacts of submicron silica particles by electrophoretic deposition"; pp. 633-640 in *2nd Int. Conf. on Powder Processing Science,* ed. Edited by H. Hausner, G. L. Messing and S. Hirano. Deutsche Keramische Gesellschaft, Köln, Berchtesgaden, 12.-14. 10. 1988, 1988.

[19] K. Smeets, J. Freund, R. Clasen and T. Krajewski, "Optical properties of sintered red vitreous silica"; pp. 601-610 in *Innovative Processing and Synthesis of Ceramics, Glasses, and Composites IV.,* ed. Edited by N. P. Bansal and J. P. Singh. Am. Ceram. Soc., Westerville, 2000.

PREPARATION OF PLZT POWDERS FROM NANO SIZED OXIDES

Erik Bartscherer, Kathy Sahner and Rolf Clasen
Saarland University
Department of Powdertechnology
D-66123 Saarbrücken
Germany

ABSTRACT

The mixed oxide route is the most economical and simple way to prepare ceramic PLZT powders. This method was improved, so that it can compete with more sophisticated preparation routes like coprecipitation and the hydrothermal synthesis. The use of titanium and zirconium oxides with particle sizes of 20-40 nm instead of the usual several micrometer sized powders allows the preparation of a homogeneous PLZT powder. Due to the higher reactivity of the nano powders the calcination temperature could be reduced from 900°C to 700°C and the calcination time was reduced to one hour. In the case of microwave calcination the PLZT powder could be calcined at 900 °C within 30 minutes. The resulting PLZT particles had diameters of 200-400 nm.

INTRODUCTION

Lanthanum modified lead zirconate titanate (PLZT) ceramics are traditionally made from powders formulated from individual oxides [1-4] or compounds, such as carbonates, acetates or nitrates that decompose into oxides at high temperatures. This mixture forms the PLZT phase during a calcination process at 900 °C that normally takes several hours. This mixed oxide process is still used for the preparation of piezoelectric ceramics [5], because it is the most economical one [4, 6]. However, the newer electrooptic ceramics need precursor powders of a higher quality. Higher purity, more homogeneous and higher reactivity powders are required. Furthermore, a small particle size is favorable [7, 8] to obtain dense ceramics by sintering. New methods have been developed to produce powders with such properties. Chemical coprezipitation [9] from a solution of lead, lanthanum, zirconium and titanium compounds results in homogeneous powders with particle sizes of 0.1μm. Due to their smaller particle size, these powders are more reactive than that ones prepared by the mixed oxide route, so they can be

calcined at lower temperatures (550 °C / 16h) Other methods to prepare homogenous powders from solutions are drying [10], freeze drying or spray drying. Drying typically results in powders with a particle size of 10-20 µm. The other drying processes mentioned before can deliver finer powders, but they are more complicated than coprecipitation. Another possible route are sol-gel techniques, which could be used to prepare PLZT films and even powders. These deliver fine results for thin films, but the preparation of powders for PLZT bulk ceramics by sol-gel processes is too expensive for an application beyond laboratory scale. A newer method is hydrothermal synthesis [11, 12]. The ceramic powder is precipitated from an aqueous solution in an autoclave at both high temperatures and pressures. The resulting particles have a size of 0.2 to 1 µm, depending on the process parameters.

By some of these methods nano PLZT powders with particle sizes of 100-300 nm can be produced, while the mixed oxide route is limited to particles in the range of 1-3 µm. Nevertheless, the mixed oxide route is the most economical and technically simplest method.

The intent of this work was to improve the mixed oxide route, so that it can compete with other powder preparations for high quality applications. Due to the hardness and high melting temperature of the zirconium and titanium oxides the morphology of the calcined powders strongly depends on these starting materials. The particle size of the lead and lanthanum oxide was not considered to be significant, because of the high mobility and rapid diffusion of the lead and lanthanum ions at the calcinating temperature. The usage of nanosized zirconium and titanium oxides instead of powders with micrometer particles should result in finer PLZT powders. In addition, the larger surface and thus higher reactivity of the nano powders should allow lower calcination temperatures and shorter calcination times.

EXPERIMENTAL

Powder Preparation

It is well known that a high purity and a small particle size of the starting materials is important. So lead oxide (alfa-Aesar Nr. 14240) of 99,99 % purity and a mean particle size of 20 µm was used. The lanthanum oxide (Chempur Nr. 004762) had a purity of 99,99 % and a mean particle size of 6 µm. The zirconium (Degussa Zirkonoxid VP) and titanium oxide (Degussa Titanoxid P25) nano powders both had a purity of 99 %+ and mean particle sizes of 25 nm.

The oxide powders were combined according to the formula $Pb_{1-x}La_x(Zr_{0,65}Ti_{0,35})_{1-x/4}$. Depending on the intended use of the PLZT powder 3-10 % excess of lead oxide was added. The mixture of oxide powders was ball milled for 2 h. Due to the large volume of the nano powders, they were first suspended in

ethanol to fit into the mill jar. A zirconia mill jar and zirconia balls were used. The resulting slurry was dried for 24 h at room temperature. The orange powder obtained was calcined at temperatures between 400 and 1000 °C and times between 30 and 120 min. In the case of microwave calcination the samples were treated at 400 to 1000 °C for 15, 30 or 60 minutes. The samples used for the microwave treatment were cold pressed pellets with a diameter of 10 mm and a thickness of 2 to 4 mm. They were produced by uniaxial pressing at 200 MPa. The microwave treatment was carried out with 2,45 GHz single mode microwave (maximum power output 2 KW). The calcined powder was ball milled again in ethanol for 2 hours and dried 24 hours at room temperature. As before zirconia balls and jar were used for the milling process.

CHARACTERIZATION

The powders prepared were characterized by means of X-ray diffraction (Siemens D500 with a position sensitive detector, λ=CuK$_{\alpha 1}$), TGA-DTA thermal analysis (Netzsch STA 409), specific surface area measurements (Micromeretics ASAP2400) and particle size distribution measurements by photon correlation spectroskopy (Malvan Zetasizer 3000).

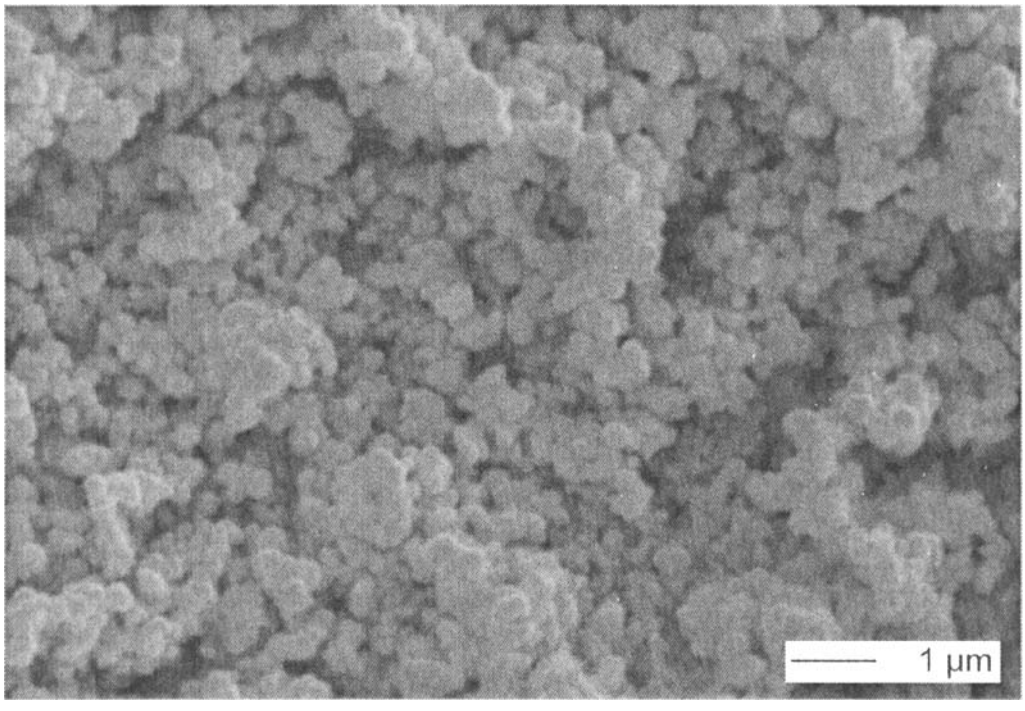

Figure 1, SEM Picture of the PLZT powder prepared by the improved mixed oxide route

RESULTS

Figure 1 shows a typical SEM picture of a calcined and ball milled PLZT powder. The spherical particles have diameters of 200 to 400 nm. The particle size distribution seems to be monomodal and relatively narrow. The results obtained from SEM analysis were verified by measurements of the particle size distribution (Figure 2).

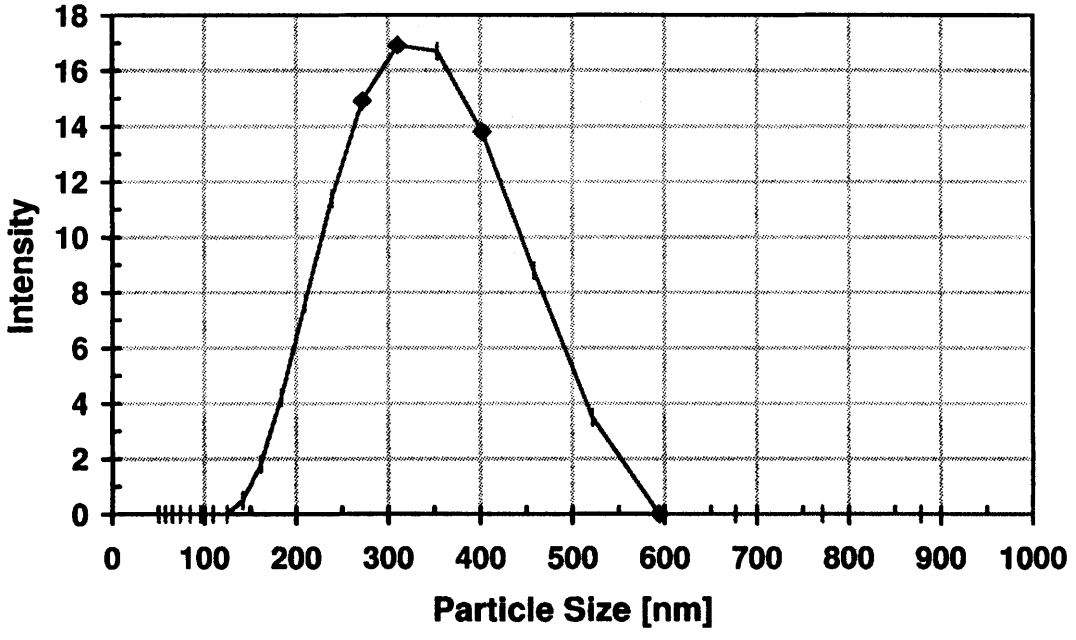

Figure 2, Particle size distribution measured by Photon Correlation Spectroscopy

The PLZT powders consist of particles with diameters from 100 to 600 nm. The average particle size is about 320 nm. The powders have a d_{50} rate of 300 nm and a d_{95} rate of 450 nm. The specific surface of the PLZT powder is 5 m^2/g. The calculated particle diameter from the data of the specific surface area measurement assuming spherical particles is 750 nm.

Figure 3 shows the X-ray diffraction spectra of PLZT powders calcined at several temperatures for one hour. The analysis of the raw powder shows the signals of the oxide powders used. After calcination at 600 °C these signals were smaller and the signals of the PLZT phase were already visible. The data of the PLZT powder calcined at 700 °C shows the pure PLZT phase with no individual oxides left. It is similar to the data taken from the powder, that was calcined at 900 °C, which shows only sharper peaks.

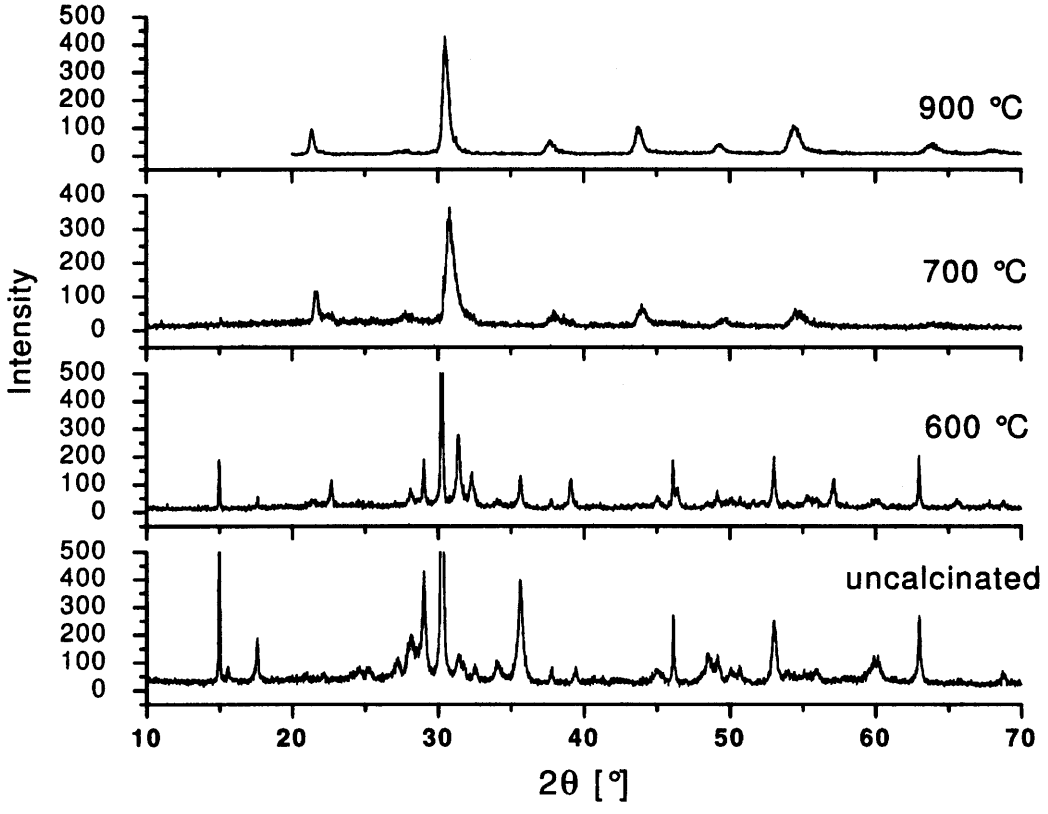

Figure 3, XRD spectra of PLZT powders, raw and calcined for 1 hour at 600, 700 and 900 °C

The powder calcined by microwave shows although a complete formation of the PLZT phase after treatment at 900 °C (Figure 4). In contrast to the furnace calcination the formation of the PLZT phase is complete after 30 minutes. Nevertheless, there still were impurities observed, which could be identified as lead oxide.

DISSCUSION

It has been shown, that the usage of nano scaled titanium and zirconium oxide powders can improve the preparation of PLZT powders by the mixed oxide route. As estimated this improves the process by an enhanced homogeneity of the raw powders. The high reactivity of these nano scaled powders due to their high specific surfaces enables a calcination process at lower temperatures and in

shorter times. So the calcination temperature necessary could be reduced from 900 °C to 700 °C and the calcination time could reduced to one hour. The calcination behavior of these powders resembles those of other PLZT powders, as be obtained by coprecipitation and sol-gel methods.

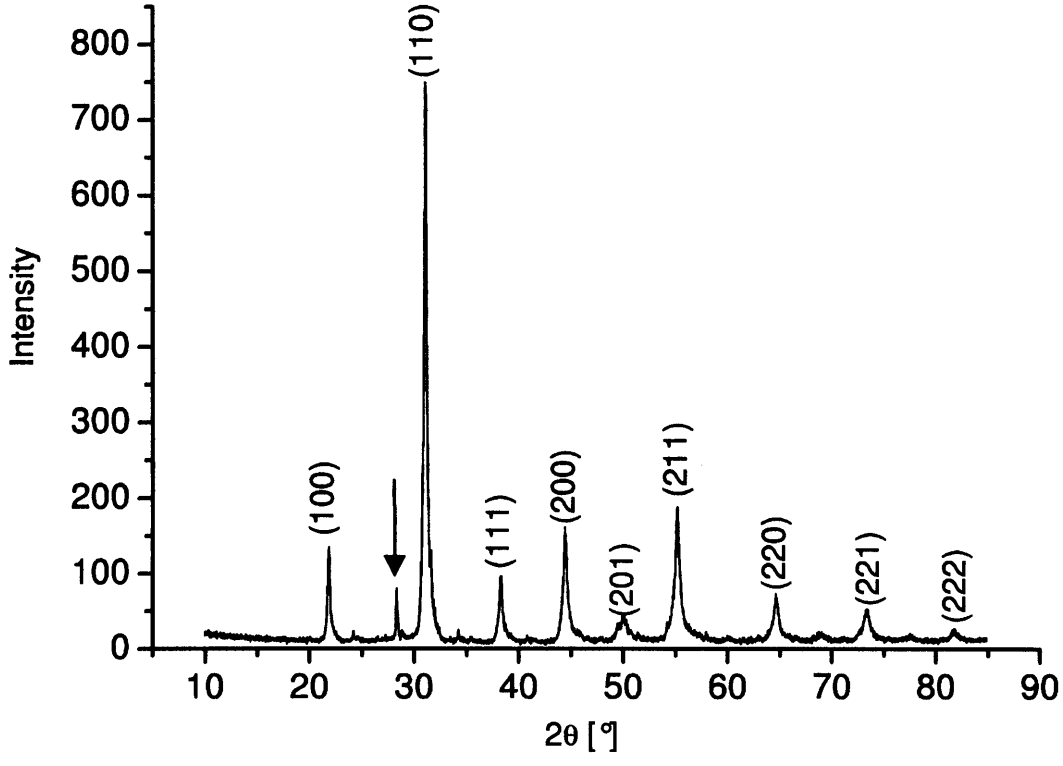

Figure 4, XRD analysis of PLZT powder calcined by microwave heating, arrow: signal of lead oxide

ACKNOWLEDGEMENTS

The authors gratefully acknowledge the financial support of the German Science Foundation (Deutsche Forschungsgemeinschaft, DFG) within the scope of the "Graduiertenkolleg: Novel advanced materials for more efficient conversion of energy".

REFERENCES

[1] G. H. Haertling, "Hot-Pressed Ferroelectric Lead Zirconate Titanate Ceramics For Electro-Optical Applications," *Ceramnic Bulletin,* **49** [6] 564-567 (1970).

[2] G. H. Haertling, "Improved Hot-Pressed Electrooptic Ceramics in the (Pb, La)(Zr, Ti)O_3 System," *J. Am. Ceram. Soc.,* **54** [6] 303-309 (1971).

[3] G. H. Haertling and C. E. Land, "Hot-Pressed (Pb, La)(Zr, Ti)O_3 Ferroelectric Ceramics for Electrooptic Applications," *J. Am. Ceram. Soc.,* **54** [1] 1-11 (1971).

[4] K. Nagata, H. Schmitt, K. Stathakis and H. E. Müser, "Vacuum Sintering of Transparent Piezo-Ceramics," *Ceramurgia International,* **3** [2] 53-56 (1977).

[5] P. Sun, C.-N. Xu, M. Akiyama and T. Watanabe, "Controlled Oxygen Partial Pressure Sintering of (Pb, La)(Zr, Ti)O_3 Ceramics," *J. Am. Ceram. Soc.,* **82** [6] 1447-1450 (1999).

[6] G. H. Haertling, "Ferroelectric Ceramics: History and Technologie," *J. Am. Ceram. Soc.,* **82** [4] 797-818 (1999).

[7] M. Awano and H. Takagi, "Synthesis of PLZT Ceramics by Coprecipitation Method and the Effect of Grinding on Synthesis and Sintering Behavior of Powders," *J. Mater. Sci. Lett.,* **101** 119-123 (1993).

[8] K. Nagata, T. Kiyota and M. Furuno, "Long-Size Electro-Optic PLZT Ceramics Fabricated by Doctor Blade Method," *Ferroelectrics,* **128** 49-54 (1992).

[9] Y. Abe, T. Tanaka, K. Kakegawa and Y. Sasaki, "Synthesis of compositionally homogeneous $Pb(Zr_xTi_{1-x})_{1-y}(Mg_{1/3}Ta_{2/3})_yO_3$ by wet-dry combination method and its dielectric properties," *Mater. Lett.,* **47** 308-313 (2001).

[10] K. L. Yadav and R. N. P. Choudhary, "Synthesis and characterization of PLZT (10/65/35)," *J. Mater. Sci.,* **28** 769-772 (1993).

[11] M. Traianidis, C. Courtois and A. Leriche, "Mechanism of PZT crystallisation under hydrothermal conditions Development of a new synthesis route," *J. Eur. Ceram. Soc.,* **20** 2713-2720 (2000).

[12] S. Nualpralaksana, S. Phanichphant, M. Hengst and R. B. Heimann, "Hydrothermal Sythesis of Lead Zirconate Titanate (PZT) and Lead Lanthanum Zirconate Titanate Naonpowders," *cfi/Ber. DKG,* **78** [5] E34-E38 (2001).

This page intentionally left blank

SINTERING BEHAVIOR AND GRAIN STRUCTURE DEVELOPMENT OF ZrO_2- AND Al_2O_3-COMPACTS FABRICATED FROM DIFFERENT NANOSIZED POWDERS

Stephan Appel and Rolf Clasen
Saarland University
Department of Powder Technology
Im Stadtwald, Building 43
D-66123 Saarbrücken, Germany

Sabine Schlabach, Bin Xu and
Dieter Vollath
IMF III, Research Center
Karlsruhe, P. O. Box 3640
D-76021 Karlsruhe, Germany

ABSTRACT

The sintering temperature of compacts from nanosized powders can be significantly reduced if a suitable starting powder is available. Therefore different nanopowders were investigated and compared. For alumina powders, problems arise due to the phase transformation to the high temperature α-phase. Doping with FeO reduces the phase transition temperature. Thus a transparent α-alumina compact could be sintered at 900 °C, which is surprisingly low. For zirconia, only yttrium-stabilized powders lead to compacts with high mechanical strength.

INTRODUCTION

Sintering is the final step in the preparation of advanced ceramics. If nanosized starting powders are used, the sintering temperature is lowered. The influence of particle size on the sintering behavior has been studied with ZrO2 powders synthesized by different methods like the Sol Gel or precipitation methods [1-4] and the Inert Gas Condensation (IGC) [5]. Effects of powder agglomeration are also known [6].

The transition alumina powders generally have a characteristic sintering behavior consisting of a region of very fast sintering rates between ≈ 1000 °C and 1200 °C, followed by a transition to much lower sintering rates at higher temperatures [7]. The exact temperature, at which the rapid densification starts, depends of the ratio of the different metastable phases in the ultrafine starting powder. Formation of α-Al_2O_3 from γ-Al_2O_3 occurs via a series of polymorphic transformations $\gamma \rightarrow \delta \rightarrow \theta \rightarrow \alpha$. The stable α-modification forms at temperatures higher

than 1200 °C [8]. Compacts of nanosized α-Al_2O_3 produced by mechanical grinding in a planetary mill exhibit enhanced sintering kinetics and yield dense material at 1200-1270 °C. During study of the sintering behavior of γ-Al_2O_3, measurable shrinkage is observed at 1000 °C followed by rapid sintering at between 1125-1175 °C. The compact reached a relative density of 0,82 after sintering at 1350 °C [7]. In Ref. 9 it was observed that the densification of high density compacts is affected detrimentally by the phase transition in the range of 1050 °C to 1150 °C. Seeding with α-Al_2O_3 into ultrafine γ-Al_2O_3 powder lowers the phase transition temperature with increase in seed population in the γ-Al_2O_3 matrix and alters significantly the microstructure and density of the sintered body.

In this study the sintering behavior of compacts fabricated from different nanopowders is investigated. The powders are synthesized by the following methods: the flame hydrolysis with the Aerosil®-Technique of Degussa AG (Hanau, Germany), microwave plasma synthesis and the synthesis in a pulsation reactor of IBUtec Company (Weimar, Germany). These methods are described in detail in another paper presented at this conference.

SAMPLE PREPARATION

Although dry pressing is not a very suitable method for forming homogeneous compacts, this methods was chosen because only small quantities of several grams were available of the microwave plasma synthesized powders. A comparison of the densification behavior of Degussa and IBUtec nanosized alumina powder during uniaxial pressing is shown in fig. 1. No significant differences can be observed for the different powders. It is obvious that pressures higher than 500 MPa are not useful.

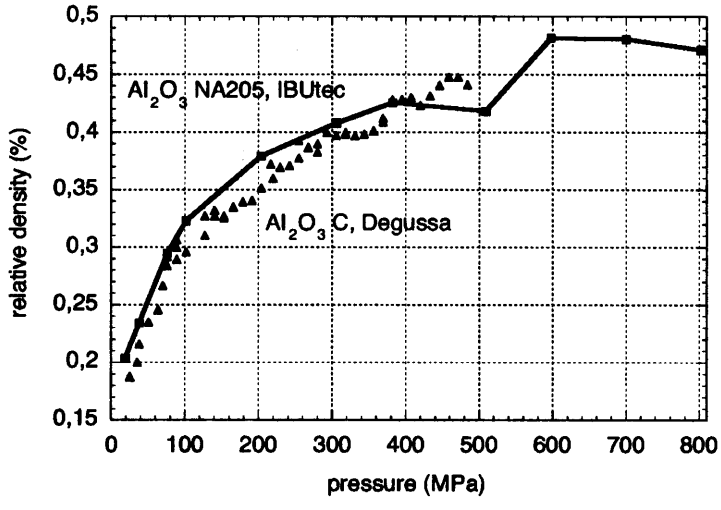

Fig. 1 Green density of uniaxially pressed compacts

SINTERING OF ALUMINA NANOPOWDERS

The dry pressed compacts were isothermally sintered under ambient conditions. For the IBUtec and the Degussa alumina powders sintering starts at approx. 1000 °C, see fig. 2 and 3. The phase transition from the γ, δ to the α-phase at 1200 °C leads to an increased sintering rate. Due to significant grain growth, no complete densification could be reached with compacts of these powders. This is shown in SEM pictures in fig. 4, where a grain diameter of more than 100 nm is observed at temperatures of 1200 °C:

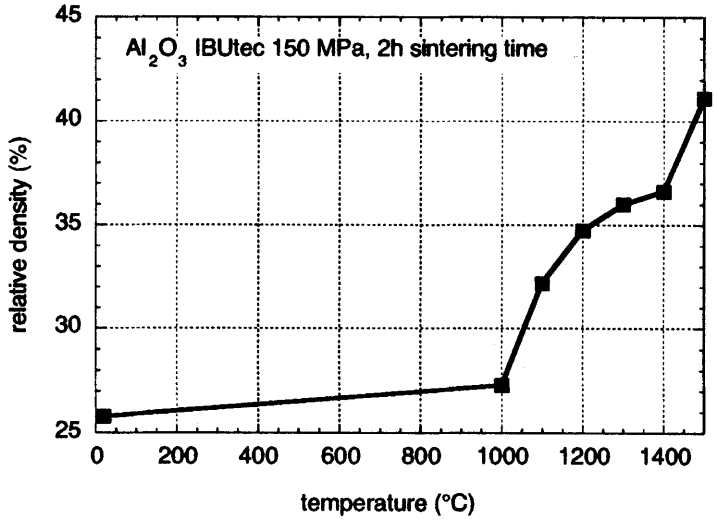

Fig. 2 Sintering density of IBUtec Al_2O_3-compact

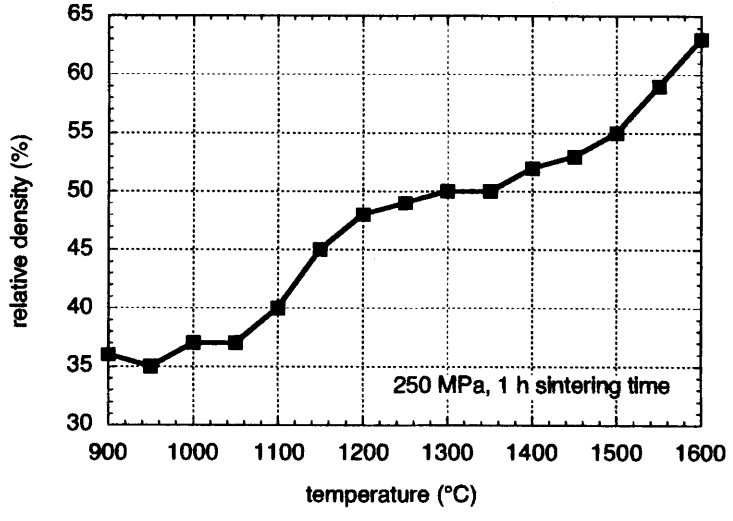

Fig. 3 Sintering density of Degussa Al_2O_3-compact

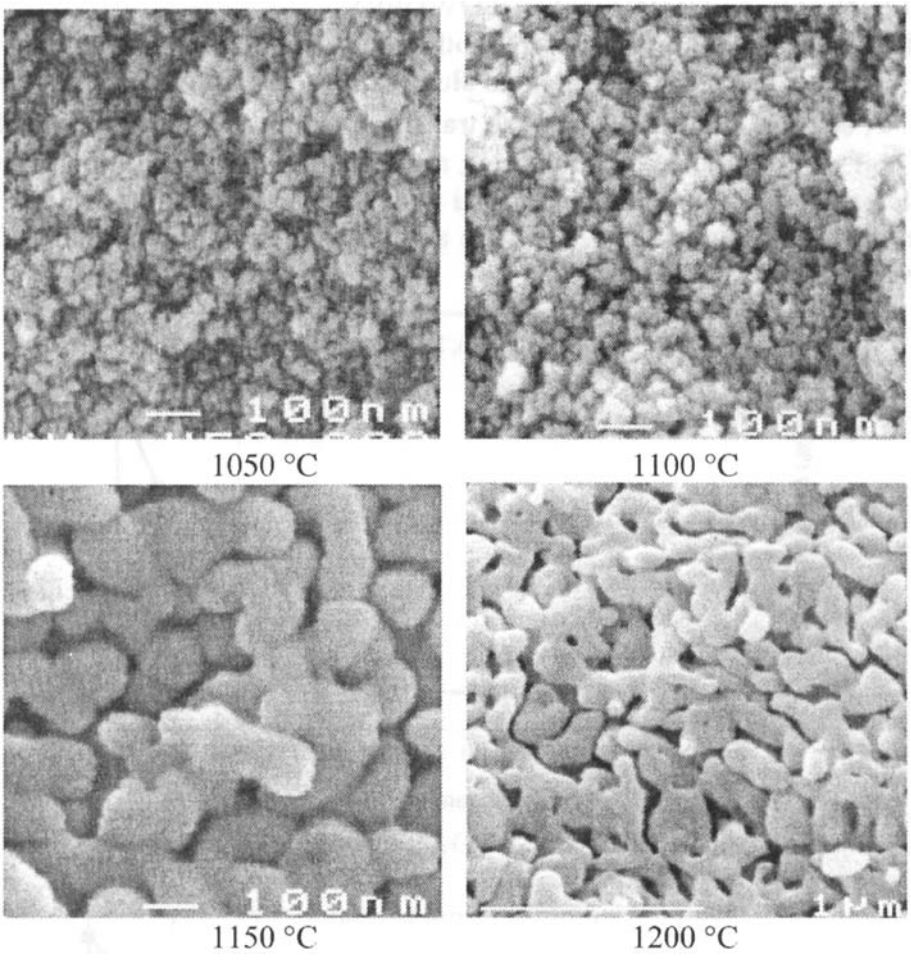

Fig. 4 Grain growth of Degussa Al_2O_3 compacts (dry pressed 250 MPa)

A significant improvement was observed for the microwave plasma Fe_2O_3-doped alumina powder. As it was suggested in the companion paper on the nanopowder characterization, the phase transition to the α–phase takes already place at 300 °C. Therefore the sintering is not disturbed by a phase transition. As shown in fig. 5, a compact, uniaxially pressed of this doped powder with 500 MPa, could be completely sintered to a nearly transparent alumina ceramic at a sintering temperature of only 900 °C.

The cracks are attributed to the dry pressing, where only a low homogeneity can be achieved. Similar cracks are observed in uniaxially pressed silica glass samples, which can be easily sintered from compacts of Degussa Aerosil OX50 powders to completely transparent glasses. The XRD-measurement of this sample showed that the stable α–phase was reached.

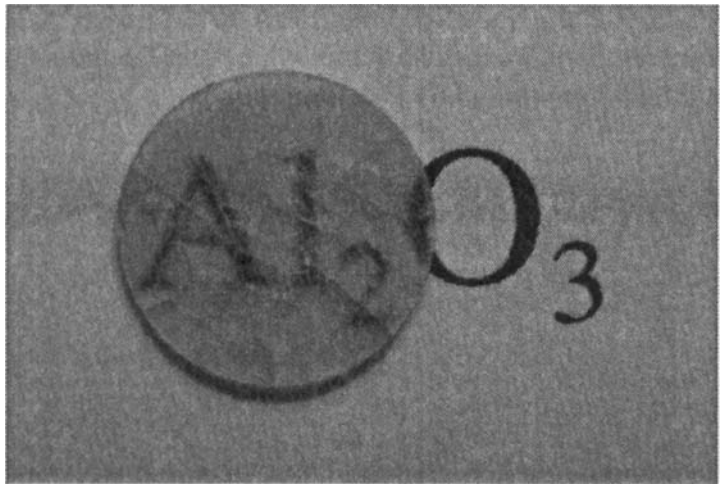

Fig. 5 Transparent compact of microwave plasma-synthesized 1 % Fe_2O_3-Al_2O_3-powder, dry pressed at 500 MPa and sintered at 900 °C

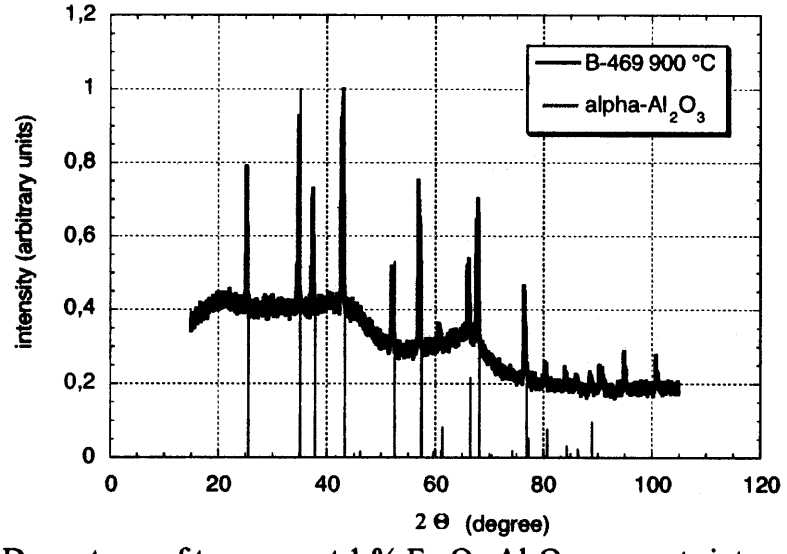

Fig. 6 XRD spectrum of transparent 1 % Fe_2O_3-Al_2O_3 compact sintered at 900 °C

SINTERING OF ZIRCONIA NANOPOWDERS

Compacts of different zirconia nanopowders were also formed by dry pressing and isothermally sintered of the compact under ambient conditions. A nearly complete densification can be achieved below 1200 °C, see fig. 7. Thus no stabili-

zation is necessary, if the operation conditions do not exceed this temperature. At higher sintering temperature the phase transition from the monoclinic to tetragonal phase and grain growth takes place (fig. 8).

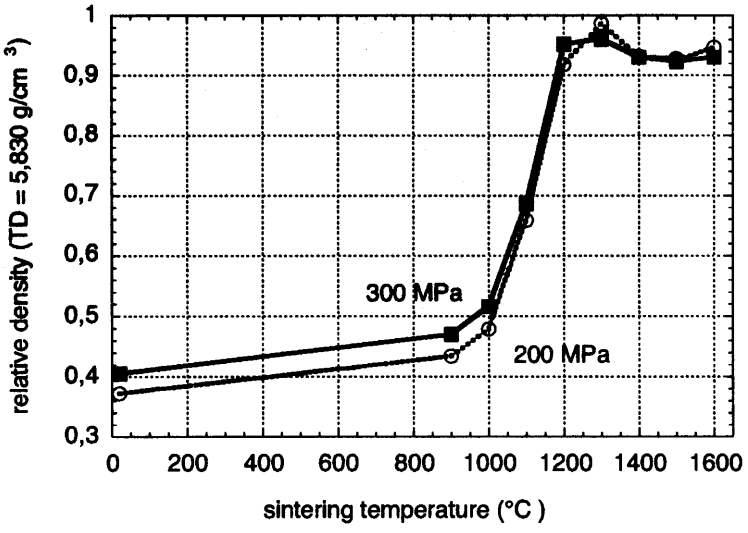

Fig. 7 Sintering density of undoped Degussa ZrO_2 -compact

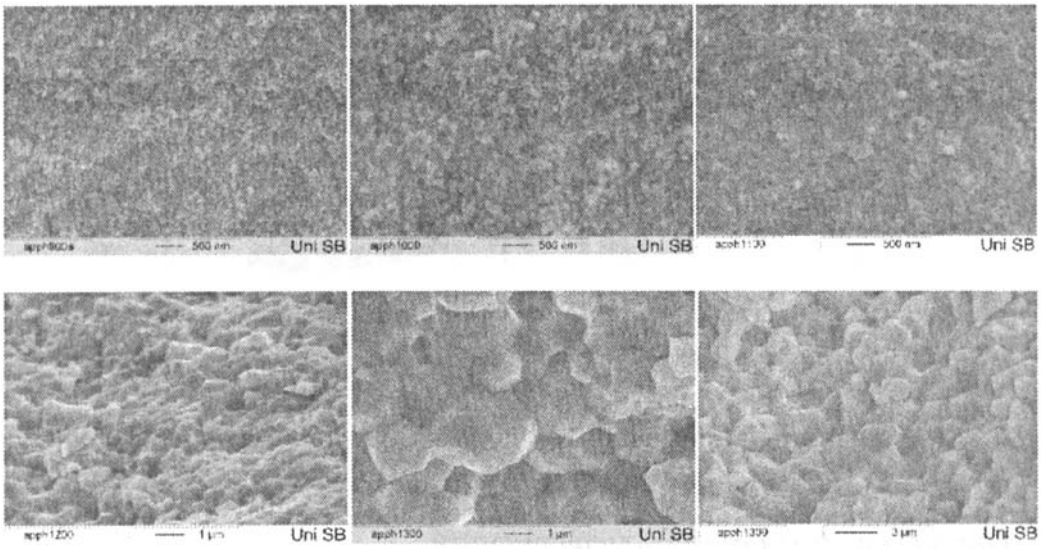

Fig. 8 SEM pictures of grain growth of undoped Degussa ZrO_2-powder sintered at (from left to right), upper row: 900 °C, Mag. ×20000, 1000 °C, Mag. ×20000, 1100 °C, Mag. ×20000; and lower row: 1200 °C, Mag. ×10000, 1300 °C, Mag. ×10000,, 1300 °C, Mag. ×5000

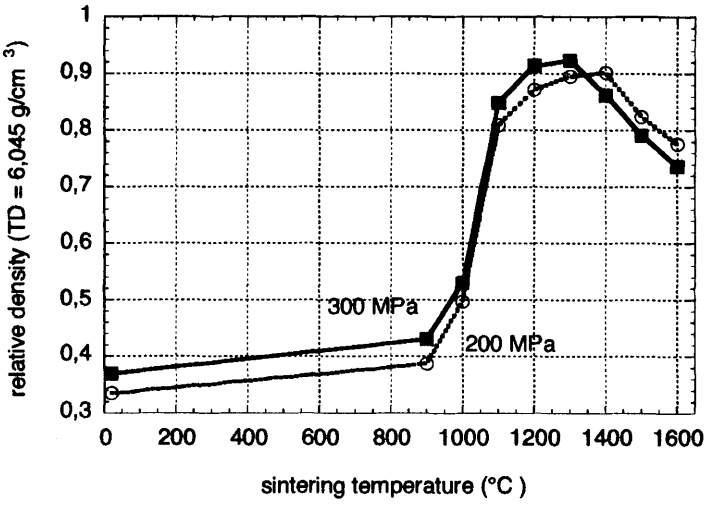

Fig. 9 Sintering density of Degussa 6 mole-% Y_2O_3- ZrO_2 -compact

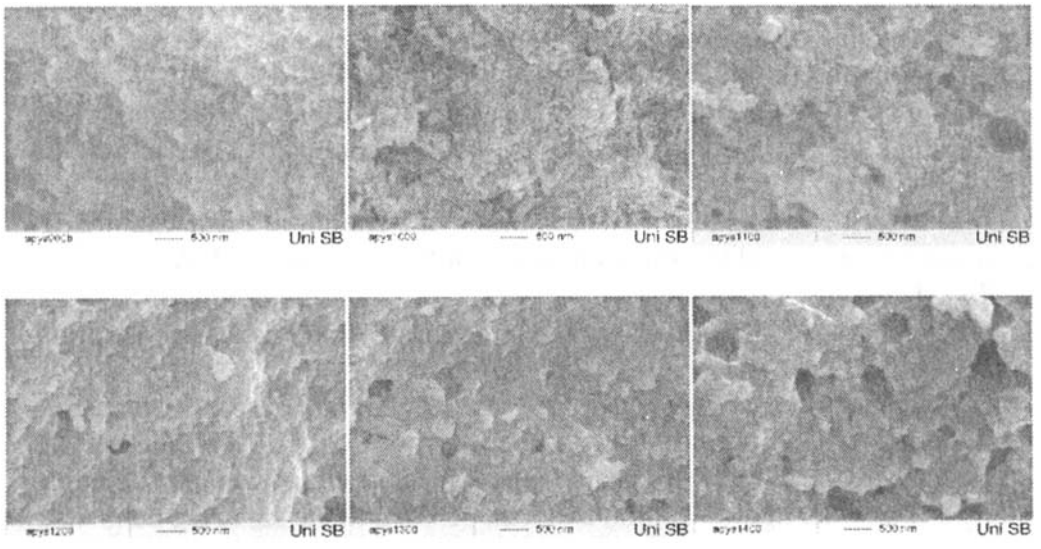

Fig. 10 SEM pictures of grain growth of Y_2O_3-doped Degussa ZrO_2-powder sintered at (from left to right), upper row: 900 °C Mag. ×20000, 1000 °C Mag. ×20000, 1100 °C Mag. ×20000; lower row: 1200 °C Mag. ×20000, 1300 °C Mag. ×2000, 1400 °C Mag. ×20000

For doped zirconia powders (6 mole-% Y_2O_3) the sintering behavior seems to be alike, but the grain growth is much smaller. Also some voids are formed, which also decrease the sintering density above 1300 °C; a mechanical bending strength of 290 MPa was obtained (sintering temperature 1500 °C).

CONCLUSIONS

As no nanosized pure α-alumina powder is available, the phase transitions associated with use of nanosized alumina of other crystal structure hinders the sintering. The application of FeO-doped alumina powder leads to a significant reduction of phase transition temperature. This enabled the sintering of a nearly transparent α-alumina ceramic at 900 °C, which is a surprisingly low temperature. Gas phase deposited nanoscaled zirconia powders can be completely sintered at 1200 °C. Y_2O_3doped zirconia shows reduced grain growth and increased mechanical strength.

ACKNOWLEDGEMENT

This project "Optoceramics" is part of the DFG program "From Molecules to Materials". The financial support from the Deutsche Forschungsgemeinschaft (DFG) is gratefully acknowledged.

REFERENCES

[1]W. H. Rhodes, "Agglomerate and Particle Size Effects on Sintering Yttria-Stabilized Zirconia", J. Am. Ceram. Soc., **64** [1] 19-22 (1981).

[2]M. A. C. G. v. d. Graaf, J. H. H. Termaat, A. J. Burggraaf, "Microstructure and sintering kinetics of highly reactive ZrO_2-Y_2O_3 ceramics", J. Mater. Sci., **20** 1407-1418 (1985).

[3]D. L. Bourell, Parimal, "Sol-Gel Synthesis of Nanophase Yttria-Stabilized Tetragonal Zirconia and Densification Behavior below 1600 K", J. Am. Ceram. Soc., **76** [3] 705-711 (1993).

[4]X.-X. Jiang, D.-S. Huang, L. Weng, "Sintering characteristics of microfine zirconia powder", J. Mater. Sci., **29** 121-124 (1994).

[5]G. Skandan, "Processing of Nanostructured Zirconia Ceramics", Nanostructured Materials, **5** 111-126 (1995).

[6]D.-M. Liu, J.-T. Lin, W. H. Tuan, "Interdependence between green compact property and powder agglomeration and their relation to the sintering behaviour of ziconia powder", Ceram. Int., **25** 551-559 (1999).

[7]S. J. Wu, L. C. D. Jonghe, "Sintering of Nanophase gamma-Al_2O_3 Powders", J. Am. Ceram. Soc., **79** [8] 2207-2211 (1996).

[8]R. Hempelmann, H. Natter, "Elektrochemische Herstellung amorpher und kristalliner Metalloxide mit Teilchengrößen im Nanometerbereich", DE Patent No. 19840842, 07.09.1998.

[9]J.-P. Ahn, J.-K. Park, H.-W. Lee, "Effect of compact structures on the phase transition, subsequent densification and microstructure evolution during sintering of ultrafine gamma alumina powder", NanoStruct. Mater., **11** [1] 133-140 (1999).

ADVANCED CERAMIC OR GLASS COMPONENTS AND COMPOSITES BY ELECTROPHORETIC DEPOSITION/IMPREGNATION USING NANOSIZED PARTICLES

Jan Tabellion and Rolf Clasen
Saarland University
Department of Powder Technology
Im Stadtwald, Building 43
D-66123 Saarbrucken, Germany

ABSTRACT

Nano-particles can be used in ceramic processing to fulfill specific functions within a glass or ceramic matrix where the functionality is governed by their size. Furthermore, they can be used for the manufacturing of bulk ceramic or glass components, coatings and composites, taking advantage of their enhanced sinterability, which results in a significantly reduced sintering temperature. By means of electrophoretic deposition ceramic and glass coatings and components can be shaped fast, cost efficient and environmentally acceptable from aqueous suspensions. Homogeneous compacts with complex geometry and uniform wall thickness can be shaped. Since the deposition rate is independent of particle size, homogeneous green bodies with high density (> 80 %TD) could be prepared by deposition of powder mixtures with non-monomodal particle size distribution. Thus components of different shapes could be manufactured near-shape due to the reduced shrinkage during sintering (< 10 % linear shrinkage). By means of electrophoretic impregnation of porous green bodies with nanosized particles, ceramic or glass components with functionally graded density or/and chemical composition could be produced.

INTRODUCTION

There are mainly three different fields of application for nanosized particles in manufacturing of glasses and ceramics. First of all nano-particles can be used to fulfill a specific function within a glass or ceramic matrix (e.g. gold-ruby glass). In this case functionality is governed by the size of this secondary phase [1, 2]. Since only small amounts of nanosized particles are required the normally high production costs for nanosized particles and the small yield of most powder synthesis processes do not preponderate too much. By doping of glasses and ceramics with nanosized phases optical, electrical and magnetic properties can be achieved that are not possible otherwise [3-5].

The second field of interest is the deposition of ceramic and glass coatings. Due to the high specific surface area and the short diffusion paths of the nanosized particles, the sintering temperatures are decreased significantly. Thus, deposition and sintering of coatings with high melting point on substrates with low thermal stability becomes possible. Thick borosilicate glass coatings from nanosized particles on soda-lime glass substrates, e.g. bottles, can enhance the strength and thus enables reduction of wall thickness [6].

For an economic production of large monolithic components "production-capable" powders have to be on-hand. This means that the powders have to be available in sufficient quantities with reproducible properties at reasonable costs. Furthermore, the particles should exist in their thermodynamically stable modification with a dense globular morphology, a particle size smaller than

50 nm and a low tendency towards agglomeration. But only few nano-powders available fulfill these requirements. Large highest-purity silica glass components for optical applications can be manufactured from nanosized fumed silica powders, available in a scale of hundreds of tons per year (e.g. Degussa Aerosil OX50, A380) at temperatures as low as 1250 °C [7-9]. For all other materials manufacturing of large ceramic and glass components from nano-powders is only reasonable, if the properties required cannot be achieved with larger particles. For the molding of very fine ceramic structures, required e.g. in micromechanics or microelectronics, the particle size has to decrease with decreasing profile dimensions [10]. Due to the small grain size of the nanosized primary particles and the low sintering temperatures the use of nano-powders for the manufacturing of translucent or transparent opto-ceramics is of high interest. If grain growth during sintering can be minimized, fully dense ceramics with a grain size smaller than 100 nm can be achieved, which show a much better optical transmission than conventional products [11-13]. The mechanical behavior of ceramics with nanosized grain structure differs from that of conventional ceramics because of the significantly higher specific grain boundary area. At elevated temperatures zirconia shows a significantly increased plasticity, which enables plastic deformation and hence, the manufacturing of complex shaped dense zirconia components [14, 15].

Most of the shaping techniques known from ceramic processing does not fulfill the requirements that arise due to the use of nano-powders. Although dry pressing is a widely used technique for compaction of nano-powders on a laboratory scale, it is not suitable for manufacturing on an industrial scale. Only very small amounts of nanosized powders can be pressed due to their very low bulk density. Furthermore, size and geometry of the samples are limited and the green bodies pressed from usually highly agglomerated nano-powders often show a poor microstructural homogeneity, which is unfavorable because sintering behavior is directly related to microstructure [16].

Therefore only suspension-based techniques are suitable for the shaping of glass or ceramic components from nanosized powders. As high a green density as possible combined with a small and homogeneous pore distribution is desirable. In the case of slip casting the deposition rate diminishes strongly with decreasing particle size. Furthermore, suspensions with high solids content have to be used, to achieve a sufficient green density. And inhomogeneity within the suspension can result in green bodies with inhomogeneous microstructure.

In contrast, the deposition rate is independent of particle size for electrophoretic deposition (EPD). Therefore EPD is a very promising shaping technique for ceramic and glass components and composites using nanosized powders. Silica glasses were manufactured with a deposition rate as high as 0.5 $g/cm^2 \cdot min$ from aqueous suspensions of nanosized fumed silica [17]. Green density and pore size distribution of such silica green bodies can be tailored by adjusting the processing parameters [18]. High green densities can by achieved by EPD from suspensions with relatively low solids content. Due to the low solids content and the high electrostatic stabilization of the particles, normally adjusted for EPD, very homogeneous green bodies with narrow and monomodal pore size distribution are obtained. From nanosized zirconia powders, synthesized by laser ablation, zirconia components with a density of 99 % of the theoretical value and a grain size of ≈ 300 nm could be prepared by EPD and pressureless sintering (1300 °C) [19]. Furthermore, powder mixtures of coarse and nanosized particles with non-monomodal size distribution can be deposited very homogeneously.

In principle, electrophoretic deposition from aqueous suspensions is a low-cost, high-efficient and environmentally acceptable manufacturing technology for ceramic and glass coatings as well as bulk components and composites. Apart from monolithic ceramic components of alumina [20], zirconia [21] or SiC [22], functional coatings for SOFCs [23] or photovoltaics [24] have been deposited by EPD. Furthermore, fiber-reinforced composites were produced by electrophoretic deposition of different matrix materials in the spacing between fiber preforms [25]. Comprehensive reviews about EPD as shaping technique for ceramics can be found in [26, 27].

EXPERIMENTAL SET-UP

Electrophoretic deposition (EPD)

The solids content of the suspensions was varied between 10 and 75 wt % for particles with very high surface area and powder mixtures of nanosized and coarse particles respectively. The particles were dispersed gradually in bidistilled water under constant torque by means of a dissolver. Vacuum was applied during all preparation steps to avoid the incorporation of air bubbles into the suspension. Different amounts of tetramethylammoniumhydroxide (TMAH), acetic acid or salt acid were added, to achieve an electrostatic stabilization of the particles and to adjust the ζ-potential. The suspensions were shaped either by casting in latex moulds or electrophoretically deposited by means of the membrane method [28]. A simple experimental set-up for the electrophoretic deposition of plates is shown in figure 1. In this case regenerated cellulose was used as ion-permeable membrane, separating suspension (deposition chamber) and water. For more complex shaped components different other membrane materials had to be used. All electrophoretic depositions were carried out under constant applied voltage.

After shaping, the green bodies were dried in air under ambient humidity, no cracking occurred. Sintering of the compacts was carried out either under vacuum, atmosphere or in a zone-sintering furnace.

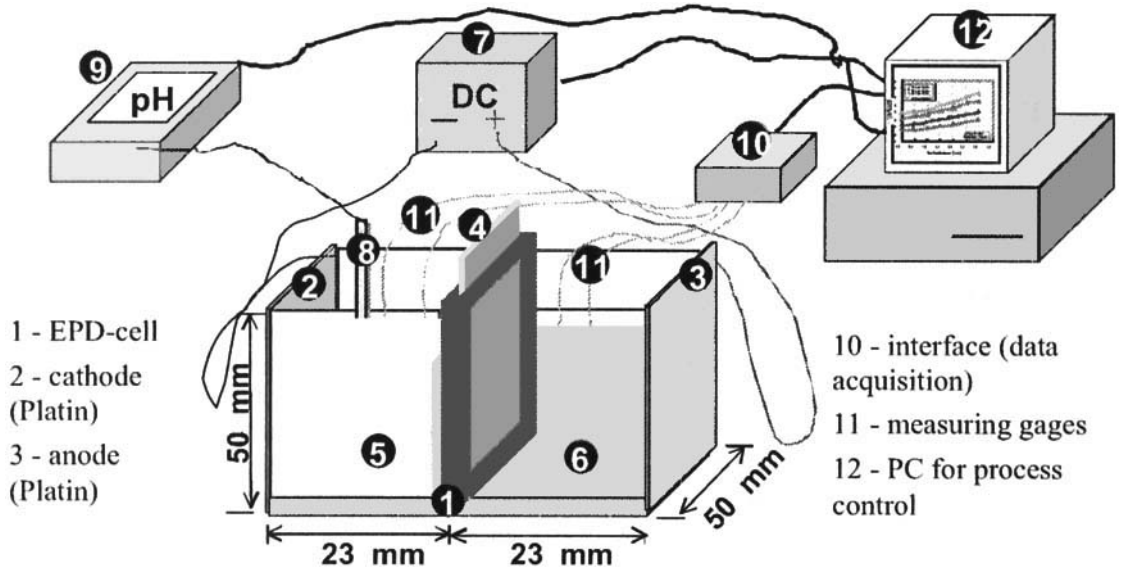

Figure 1. Schematic view of a simple experimental set-up for the electrophoretic deposition

Electrophoretic impregnation (EPI)

In case of the electrophoretic impregnation only diluted aqueous suspensions of different nanosized powders were used. The solids content varied between 3 and 20 wt %. The particles were again dispersed in bidistilled water by means of a dissolver as described before. Stabilization and ζ-potential of the particles were adjusted by adding TMAH. A schematic drawing of the EPI process is shown in figure 2. Electrophoretically deposited and cast silica green bodies were impregnated. The mean pore size of these green bodies was 2.6 to 3.0 μm.

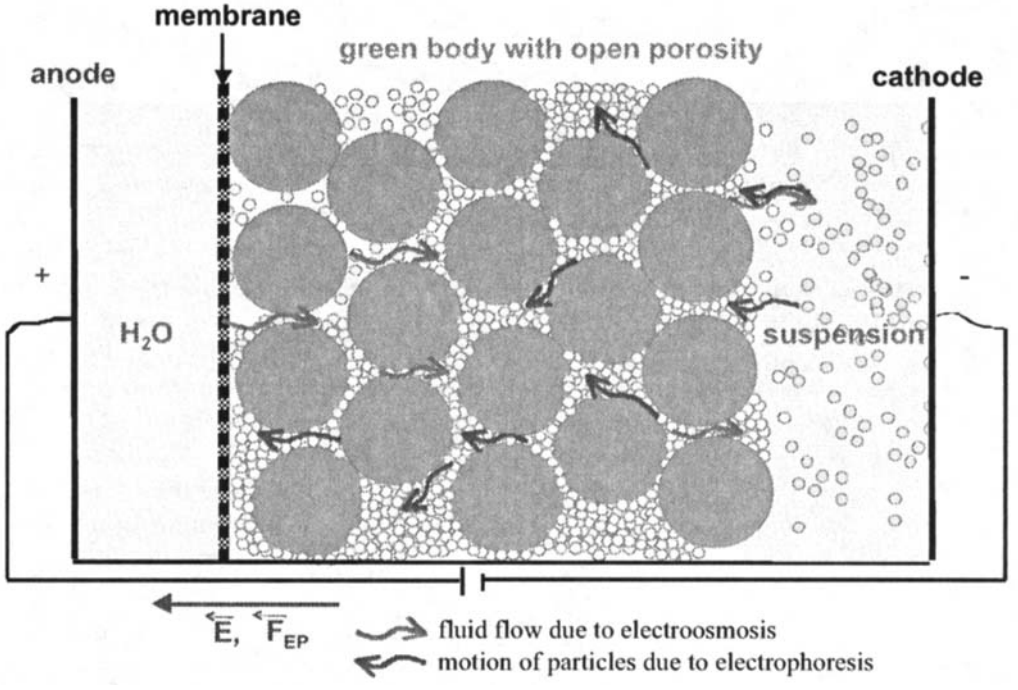

Figure 2. Schematic drawing of the electrophoretic impregnation process

RESULTS AND DISCUSSION

Manufacturing of ceramic and glass components using nanosized powders

Silica glass green bodies were shaped by means of electrophoretic deposition of nanosized fumed silica particles (OX50). Very homogeneous green bodies with narrow pore size distribution were achieved. By adjusting the processing parameters of the EPD (applied electric field, TMAH content, solid content) the mean pore size could be shifted from 40 to 15 nm. Green densities from 30 to 48 % of the theoretical value were obtained. These results will not be discussed here, but can be found elsewhere [18]. The influence of deposition time and applied electric field strength on wall thickness of the silica green bodies is shown in figure 3. A nearly linear increase of thickness with time was observed for not too long a deposition time. After a certain deposition time the deposition rate decreases strongly, because nearly all particles have been deposited. Furthermore, it can be seen that green bodies with a well-defined wall thickness can be deposited electrophoretically by adjusting both deposition time and electric field strength. Thus, a silica green body with a uniform wall thickness of 10 mm was achieved after 10 minutes for a field strength of 3 V/cm and after 7 minutes for 4 V/cm.

The influence of different shaping techniques on the properties of a green body manufactured from nano-particles was investigated. Silica green bodies were produced from an aqueous suspension with 30 wt % nanosized fumed silica (OX50) by means of particulate gel casting, pressure casting and electrophoretic deposition. As mentioned above, the deposition rate for the casting processes is lower than that of the EPD by a factor of 10 to 100. The resulting green bodies were characterized by means of mercury porosimetry. The results are shown in figure 4, where the specific (per gram) total pore volume is plotted versus pore radius. The specific total pore volume is directly correlated to the porosity of the samples, because no closed porosity was existed within the green bodies. According to this the density of the electrophoretically deposited green body is higher compared to other samples.

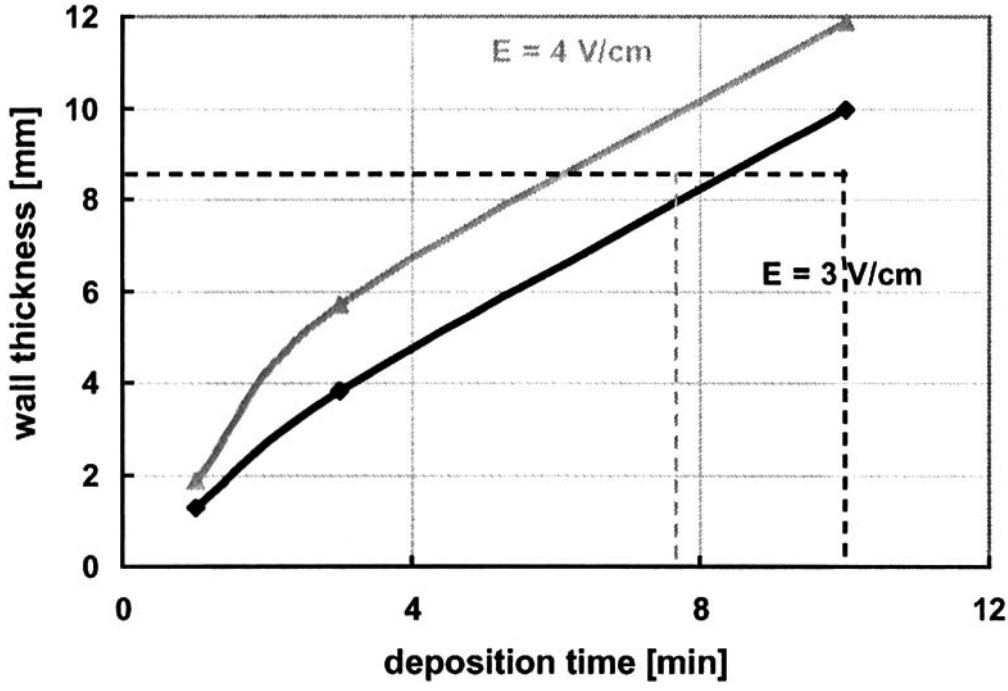

Figure 3. Wall thickness of silica green bodies electrophoretically deposited from aqueous suspensions of nanosized fumed silica powders (OX50) as function of deposition time and applied electric field strength.

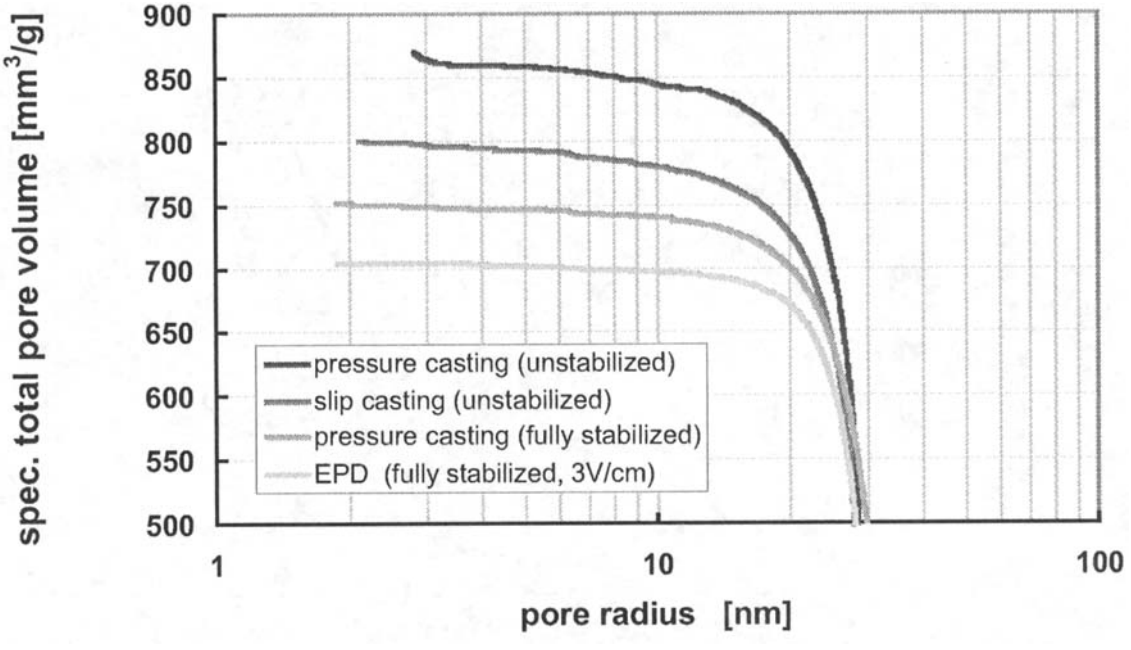

Figure 4. Comparison of porosity of silica green bodies prepared from similar aqueous suspensions of nanosized fumed silica (OX50) by different shaping techniques

Figure 5 shows an example of a ceramic green body shaped by electrophoretic deposition of nanosized particles. The inner diameter of the tube with a wall thickness of 2 mm is 24 mm.

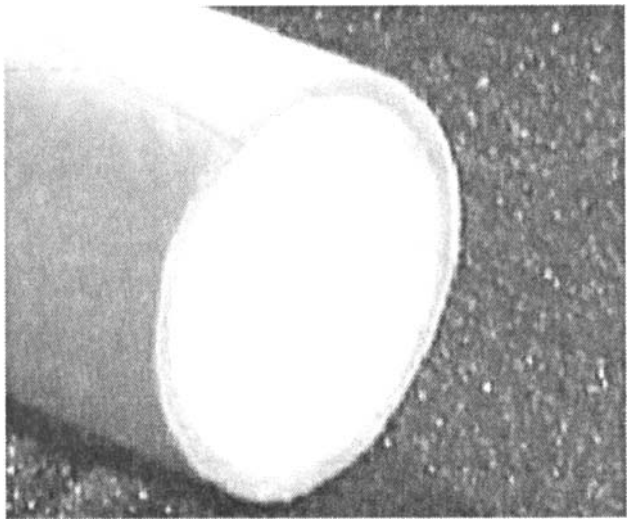

Figure 5. Ceramic tube (green body; $r_i = 12$ mm, wall thickness = 2 mm) shaped by electrophoretic deposition from an aqueous suspension of nanosized particles

The discrepancy in density between silica green bodies shaped with different techniques, that was found by mercury porosimetry, renders a different sintering behavior. The higher the porosity, the higher the sintering temperature and the more difficult a fully dense sintered body can be achieved. But even for green bodies with similar green density, different sintering behavior was found depending on the shaping technique.

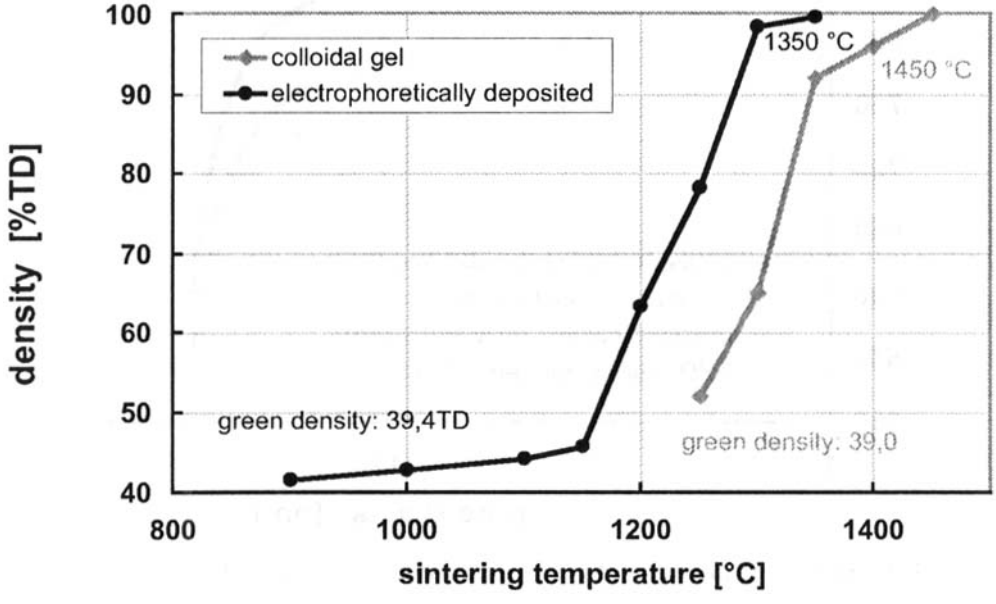

Figure 6. Comparison of the sintering behavior of silica green bodies shaped by electrophoretic deposition and particulate gel casting respectively (similar green density)

Figure 6 shows the sintering behavior of two silica green bodies with similar green density shaped by colloidal gel casting and electrophoretic deposition respectively. The silica green body shaped by EPD was sintered to a fully dense, fully transparent silica glass at 1350 °C, whereas a sintering temperature of 1450 °C was necessary to achieve a dense silica glass from the gel-casted green body. This is obviously related to the more homogeneous microstructure and the very narrow pore size distribution of the electrophoretically deposited green body.

Near-shape manufacture of ceramic and glass components with complex geometry

As mentioned before, manufacturing of large monolithic ceramic and glass components is limited to materials, where powders are available in large-scale and are inexpensive. For all other materials production on a competitive basis is impossible. Using nanosized powders, green densities that can be reached are limited down to less than ~ 60 %TD, because of the high surface area of the particles. Thus high shrinkage (up to 43 % for particles of about 8 nm size) occurs during drying and sintering of the green bodies. To avoid the formation of cracks a sophisticated drying program has to be used, especially for larger components with complex shape. Hence, near-shape production of complex-shaped large components is difficult.

Combining nanosized and micrometer sized particles the costs for raw materials can be diminished significantly. Furthermore, by optimizing the particle size distribution of the powder mixtures, green densities up to 84 % of the theoretical value can be achieved. The low porosity of such green bodies results in a decreased shrinkage during sintering. A linear shrinkage of only 7 % during sintering could be reached. Besides, the nanosized particles act as an inorganic binder between the micrometer sized particles. Thus, the strength of the green bodies is increased significantly compared to green bodies from pure micrometer sized particles. In figure 7 two examples of silica green bodies are shown together with the sintered components produced thereof. The silica glass owl on the left-hand side was manufactured by mold casting of an aqueous suspension of pure nanosized fumed silica (OX50). A linear shrinkage of ~ 27 % was observed after sintering. On the right-hand side a sintered silica glass component produced from a powder mixture of coarse and nanosized particles is shown with the corresponding green body. The linear shrinkage was about 8 %. An increase of about 100 °C in sintering temperature was necessary compared to the green body from pure OX50, to achieve a fully dense silica glass from the green body produced from the powder mixture.

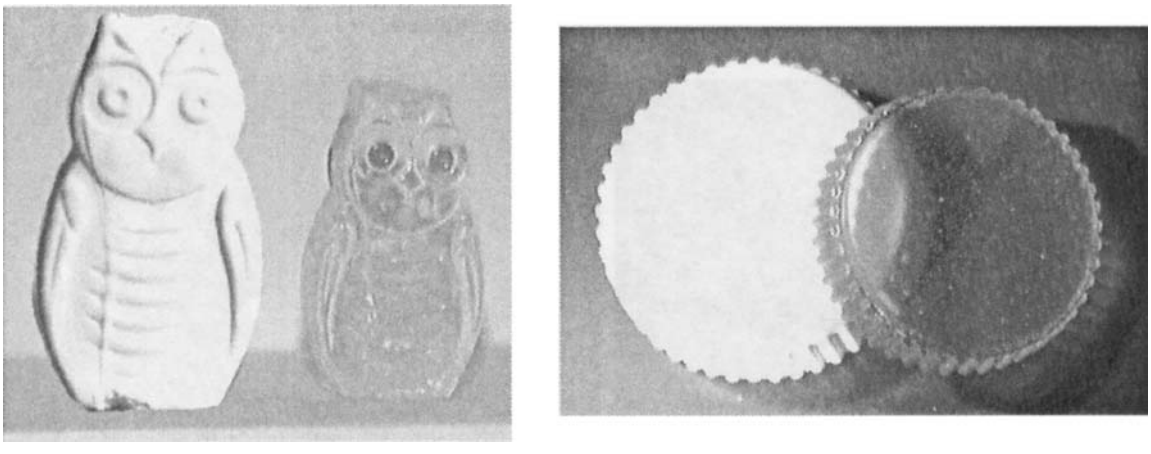

Figure 7. Near-shape manufacturing of silica glass components by casting of suspensions with optimized particle size distribution (nanosized and coarser particles) and hence minimized shrinkage (left: green and sintered silica owl from pure nanosized fumed silica; left: silica green and sintered component from powder mixture)

Figure 8 shows an example of a sintered (99 % density) zirconia tube, shaped by electrophoretic deposition of powder mixtures of coarse and nanosized particles.

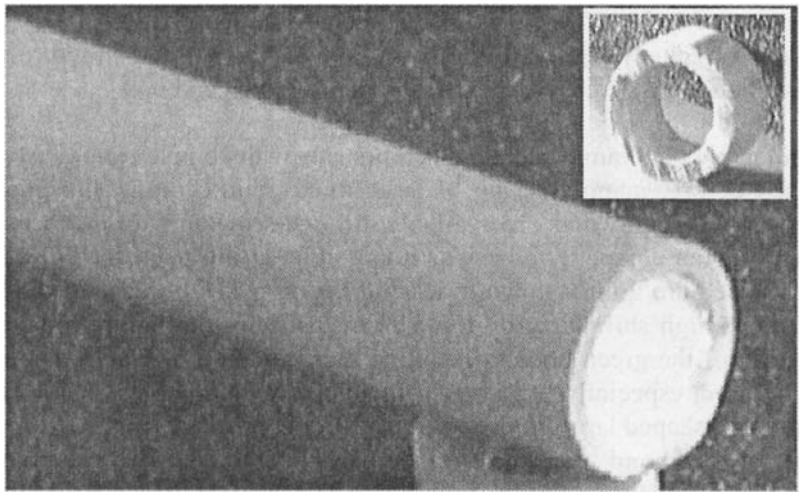

Figure 8. Sintered zirconia tube shaped by EPD of a powder mixture of nanosized and micrometer sized zirconia particles from an aqueous suspension (density = 99 %TD)

Manufacturing of composites by means of electrophoretic impregnation (EPI)

Ceramic and glass components and composites with continuously graded structure can be manufactured by means of electrophoretic impregnation (EPI). Nanosized or submicron particles are deposited within the pores of ceramic or glass green bodies. The EPI can be used for mainly three applications. First, functional nanosized secondary phases can be incorporated into a porous matrix material to realize a specific, often size-dependent, function after. This is important for all dopings, like e.g. CdS or CdSe for red coloration of glass, that show only poor or no solubility and cannot be incorporated from the liquid phase. Thus, optical or electrical properties of ceramics and glasses can be changed. The doping of the matrix can either be homogeneous, graded or local.

Furthermore, a densification of a green body can be achieved by EPI again either homogeneously, graded or locally to improve green strength and sintering behavior. Monolithic components with graded density and/or graded pore structure can be produced.

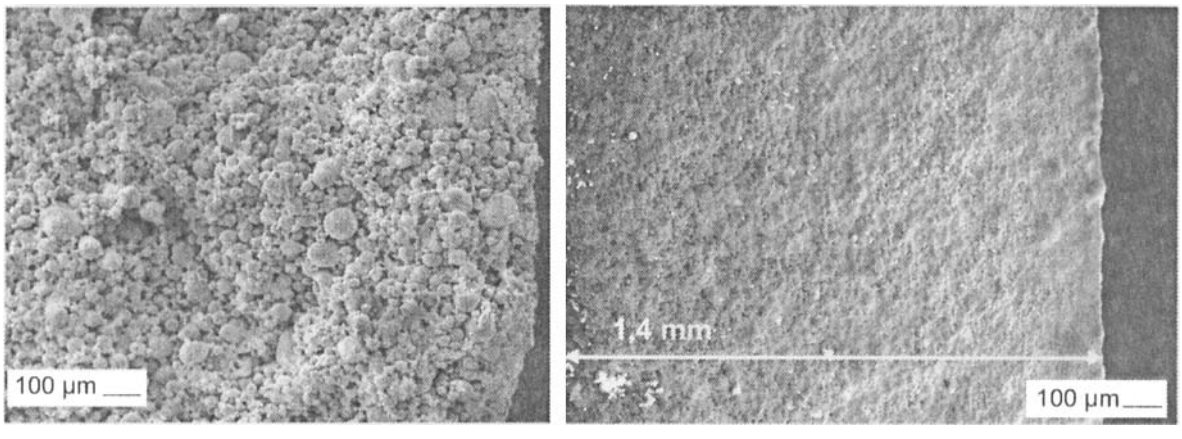

Figure 9. Silica green body with functionally graded density and pore size (right) prepared by EPI of a silica green body (left) with nanosized fumed silica particles (OX50)

In figure 9 a SEM picture of the fracture surface of a silica green body with graded pore structure and density is shown on the left-hand side. The graded structure was obtained by electrophoretic impregnation of a homogeneous silica green body with monomodal pore size distribution (mean pore size = 1.8 μm) with nanosized fumed silica particles (OX50). The density changes gradually from impregnation surface (surface in contact with suspension, right-hand side) towards bulk from 65 % to 83 %TD, whereas the pore size increases from 28 nm to 1.8 μm (measured by mercury intrusion of thin samples). It could be shown that steepness of the gradient could be adjusted reproducibly over a dimension between some hundred microns and several millimeters up to centimeters.

Composites with graded chemical composition can be manufactured by EPI. In contrast to most of the common techniques such as pressing or layer-wise deposition, a truly continuous gradient is achieved. Figure 10 shows a SEM picture of the fracture surface of a silica green body, that was electrophoretically impregnated with submicron alumina particles. A composite with graded composition was achieved. The alumina particles act as crystallization nuclei within the silica glass matrix and originate the formation of cristobalite. Thus, after sintering of the impregnated green bodies, partially transparent dense composites were achieved. The compositional gradient could be determined by Micro-Raman spectroscopy, where every 200 μm a Raman spectra was measured. A gradual decrease of the intensity of the cristobalite Raman peaks was observed with increasing distance from impregnation surface. Three sintered samples with different impregnation depths are shown in figure 11.

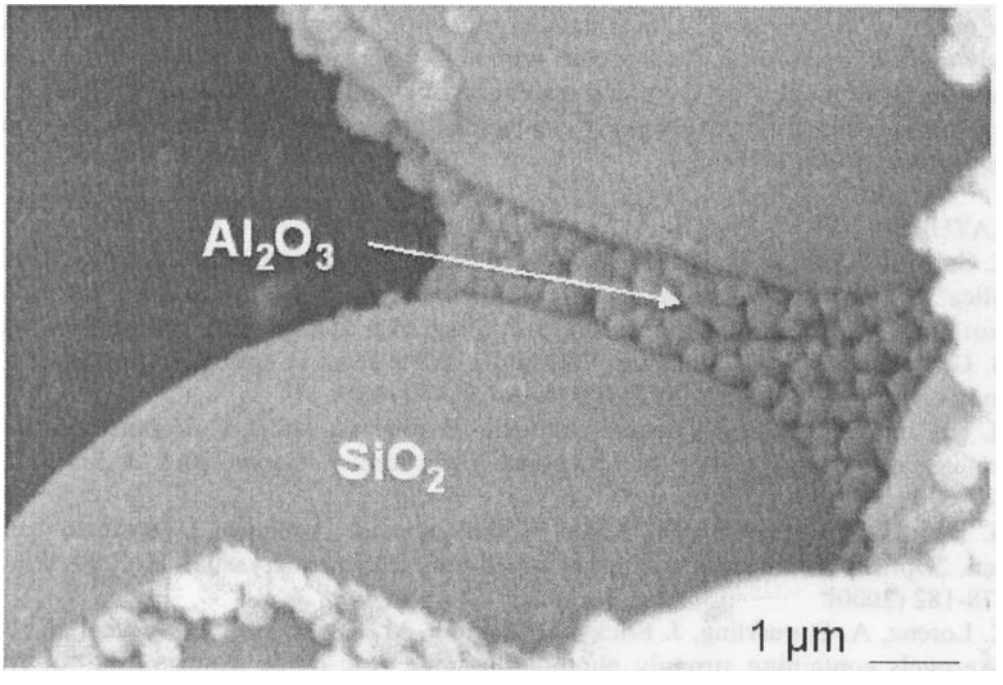

Figure 10. SEM picture of the fracture surface of the green body of a silica alumina composite with continuously graded composites manufactured by EPI

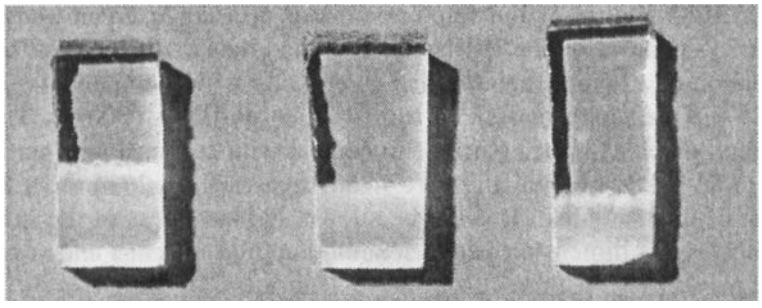

Figure 11. Functionally graded silica alumina composites after sintering at 1550 °C

CONCLUSIONS

By means of electrophoretic deposition even complex shaped glass and ceramic bulk materials can be manufactured from nano-particles on a competitive basis with high deposition rates. The properties of the green bodies deposited by EPD can be tailored reproducibly and the microstructural homogeneity is much better, compared to other shaping techniques. The sintering temperatures are decreased significantly. Since the deposition rate is independent of particle size powder mixtures of coarse and nanosized particles can be deposited homogeneously by EPD. Thus, high green densities up to more than 80 % of the theoretical value can be obtained resulting in a minimized shrinkage during sintering (linear shrinkage < 8 %). Furthermore, green density is increased significantly by an addition of nanosized particles that act as an inorganic binder phase.

By means of electrophoretic impregnation monolithic components and composites with continuously graded structure can be produced with adjustable steepness and dimension of the gradient from some 10 microns up to several millimeters or centimeters. Furthermore, functional secondary phases with insufficient solubility can be incorporated into the pores of a green body either homogeneously, graded or locally.

LITERATURE

[1] K. Smeets, J. Freund, R. Clasen and T. Krajewski, "Optical properties of sintered red vitreous silica"; pp. 601-610 in *Innovative Processing and Synthesis of Ceramics, Glasses, and Composites IV.*, Edited by N. P. Bansal and J. P. Singh. Am. Ceram. Soc., Westerville, 2000.

[2] B. G. Potter and J. H. Simmons, "Quantum size effects in optical properties of CdS-glass composites," *Phys. Rev. B.*, **37** [18] 10 838-10 845 (1988).

[3] H. Hoffmann, J. Dutta, S. Scholz-Odermatt, R. Vacassy and J.-C. Valmalette, "Potential of nanosized ceramic powder for functional applications," *Ceram. Eng. & Sci. Proc.*, **18** [4] 687-694 (1997).

[4] G. Tamulaitis, V. Gulbinas, G. Kodis, A. Dementjev, L. Valkunas, I. Motchalov and H. Raaben, "Optical nonlinearities of glass doped with PbS nanocrystals," *J. Appl. Phys.*, **88** [1] 178-182 (2000).

[5] C. Lorenz, A. Emmerling, J. Fricke, T. Schmidt, M. Hilgendorff, L. Spanhel and G. Müller, "Aerogels containing strongly photoluminescing zinc oxide nanocrystals," *J. Non-Cryst. Solids*, **238** 1-5 (1998).

[6] S. Rosenbaum and R. Clasen, "Electrospraying of glass - preparation of glass coatings on glass," *J. Aerosol Sci.*, **30** 975-976 (1999).

[7] R. Clasen, "Preparation and sintering of high-density green bodies to high purity silica glasses," *J. Non-Cryst. Solids*, **89** 335-344 (1987).

[8] R. Clasen, "Preparation of glasses and glass coatings by sintering nanoscaled glass powders"; pp. 166-173 in *Fundamentals of Glass Science and Technology 1997*, Glass Research Institute, Växjö, Sweden, 1997.

[9] J. B. MacChesney, D. W. J. Jr., S. Bhandarkar, M. P. Bohrer, J. W. Fleming, E. M. Monberg and D. J. Trevor, "Optical fibers by a hybrid process using sol-gel silica overcladding tubes," *J. Non-Cryst. Solids,* **226** 232-238 (1998).
[10] H.-J. Ritzhaupt-Kleissl, W. Bauer, E. Günther, J. Laubersheimer and J. Haußelt, "Development of ceramic microstructures," *Microsyst. Technol.,* **2** 130-134 (1996).
[11] M. R. Gallas, B. Hockey, A. Pechenik and G. J. Piermarini, "Fabrication of Transparent g-Al_2O_3 from Nanosize Particles," *J. Am. Ceram. Soc.,* **77** [8] 2107-2112 (1994).
[12] X. Yang and M. N. Rahaman, "Thin Films by Consolidation and Sintering of Nanocrystalline Powders," *J. Europ. Ceram. Soc.,* **17** 525-535 (1997).
[13] N. Saito, S.-I. Matsuda and T. Igegami, "Fabrication of Transparent Yttria Ceramics at Low Temperature Using Carbonate-Derived Powder," *J. Am. Ceram. Soc.,* **81** 2023-2028 (1998).
[14] A. J. A. Winnubst, M. M. R. Boutz, Y. J. He, A. J. Burggraaf and H. Verweij, "Plasticity of Nanocrystalline Zirconia Ceramics and Composites," *Ceram. Intern.,* **23** 215-221 (1997).
[15] I.-W. Chen and L. A. Xue, "Development of superplastic structural ceramics," *J. Am. Ceram. Soc.,* **73** [9] 2585-2609 (1990).
[16] M. J. Mayo, "Processing of Nanocrystalline Ceramics from Ultrafine Particles," *Int. Mater. Rev.,* **41** 85-115 (1996).
[17] R. Clasen, "Electrophoretic deposition of compacts of nanosized particles"; pp. 169-184 in *Science, Technology, and Applications of Colloidal Suspensions,* Edited by J. H. Adair, J. A. Casey, C. A. Randall and S. Venigalla. Am. Ceram. Soc., Westerville (USA), 1995.
[18] J. Tabellion and R. Clasen, "Controlling of Green Density and Pore Size Distribution of Electrophoretically Deposited Green Bodies"; pp. 185-196 in *Innovative Processing and Synthesis of Ceramics, Glasses, and Composites IV.,* Edited by N. P. Bansal and J. P. Singh. Am. Ceram. Soc., Westerville, 2000.
[19] K. Moritz, R. Thauer and E. Müller, "Electrophoretic deposition of nano-scaled zirconia powders prepared by laser evaporation," *cfi/Ber. DKG,* **77** [8] E8-E14 (2000).
[20] B. Ferrari and R. Moreno, "Electrophoretic Deposition of Aqueous Alumina Slips," *J. Eur. Ceram. Soc.,* **17** 5449-556 (1996).
[21] F. Harbach and H. Nienburg, "Homogeneous Functional Ceramic Components through Electrophoretic Deposition from Stable Colloidal Suspensions - I Basic Concepts and Application to Zirconia," *J. Eur. Ceram. Soc.,* **18** 675-683 (1998).
[22] L. Vandeperre, O. v. d. Biest, F. Bouyer, J. Persello and A. Foissy, "Electrophoretic Forming of Silicon Carbide Ceramics," *J. Eur. Ceram Soc.,* **17** 373-376 (1997).
[23] I. Zhitomirsky and A. Petric, "Electrophoretic deposition of ceramic materials for fuel cell applications," *J. Europ. Ceram. Soc.,* **20** [12] 2055-2061 (2000).
[24] D. Matthews, A. Kay and M. Grätzel, "Electrophoretically deposited titanium dioxide thin films for photovoltaic cells," *Aust. J. Chem.,* **47** 1869-1877 (1994).
[25] A. R. Boccaccini, C. Kaya and H.-G. Krüger, "Manufacturing of fiber-reinforced ceramic and glass matrix composites by electrophoretic deposition - A Review (German)," *Chem.-Ing. Tech.,* **73** [5] 443-452 (2001).
[26] M. S. J. Gani, "Electrophoretic Deposition - A Review," *Industrial Ceramics,* **14** [4] 163-174 (1994).
[27] P. Sarkar and P. S. Nicholson, "Electrophoretic Deposition (EPD): Mechanisms, Kinetics, and Application to Ceramics," *J. Am. Ceram. Soc.,* **79** [8] 1987-2001 (1996).
[28] R. Clasen, "Forming of compacts of submicron silica particles by electrophoretic deposition"; pp. 633-640 in *2nd Int. Conf. on Powder Processing Science,* Edited by H. Hausner, G. L. Messing and S. Hirano. DKG, Köln, Berchtesgaden, 1988.

This page intentionally left blank

PHYSICAL AND MECHANICAL PROPERTIES OF MICROWAVE SINTERED NANO-CRYSTALLINE HYDROXYAPATITE

M.G. Kutty, J. P. Olberding, S. Bhaduri, J.R. Jokisaari, and S.B. Bhaduri
Department of Materials and Metallurgical Engineering
University of Idaho
Moscow, Idaho 83844-3024.

ABSTRACT

Nanocrystalline HA powder produced via a chemical precipitation technique was sintered in a microwave furnace at various temperatures (1000–1300°C). The phase content and microstructure of the samples were examined using a Scanning Electron Microscope and via X-ray Diffraction (XRD). Hardness and fracture toughness were measured by Vickers indentation technique. The results showed that microwave sintering of nHA can produce high densities while maintaining nanocrystalline grain sizes. Grain size values as low as 280 nm were obtained in samples sintered at 1000°C for 20 minutes. Fracture toughness values were found to decrease and hardness values to increase respectively, with an increase in grain size. An optimum combination of hardness and toughness we obtained in samples sintered at 1050°C with a density of more that 95%, hardness of 5.96 GPa and fracture toughness of 1.72 MPa√m.

INTRODUCTION

Nanostructured materials have received much attention the last two decades due to their potential to achieve properties superior to conventional engineering materials. Nanostructured metals and ceramics have been shown to exhibit improved mechanical properties. Superplasticity has been ascertained for several nanocrystalline metal and ceramic systems. Some nanocrystalline ceramics exhibit plasticity at temperatures far below the plasticity onset temperatures in their conventional counterparts with larger grains [1-3]. However, more effort is needed to understand the mechanisms of plasticity and low temperature superplastic behavior [4-6]. More refined analysis is currently underway to investigate these discrepancies.

Hydroxyapatite (HA), a biocompatible ceramic, has the potential to be an excellent implant material by itself [7,8]. However, its application has been limited to non-load bearing implants due to its low strength and fracture toughness [9-10]. Nanostructured hydroxyapatite (HA) has been produced with the aim of improving its

mechanical properties. Various routes have been established to synthesis nanocrystalline HA powders [11]. However, densification/consolidation of these powders to produce nanostructured bulk ceramics has had limitations.

The key issue in sintering nanoceramics is how to achieve high density while maintaining nanocrystalline grain sizes. While the ultrafine grain size is helpful in achieving up to 90% of theoretical density, grain growth increases rapidly beyond this level. Two strategies may be useful to counter grain growth, microstructural tailoring or activated sintering [12,13]. Microstructural tailoring calls for the addition of dopants or secondary phases. In the present case, these additions are not necessarily acceptable. Hence, we have utilized an activated sintering technique.

Microwave sintering is an example of the activated sintering process. High heating rates can be generated due to direct absorbtion of microwaves within the sample, as is shown in the literature [14,15]. Microwave processing of materials has received attention due to its ability to save energy, achieve rapid sintering, and produce new microstructures as compared to conventional techniques. Sintering of HA by microwave techniques was reported by Fang et al. In their work, HA produced via hydrolysis was consolidated in a microwave furnace to produce densities up to 97 % of the theoretical value [16-18].

While the efficacy of microwave sintering of HA was proven in references 16 to 18, there is a lack of data on the capability of HA to absorb microwaves and on the mechanical properties of these materials, in particular, fracture toughness. It is also widely known that there is a strong dependence of material properties with the synthesis and processing route of the precursor material. Recently our group reported the microwave processing of nanocrystalline HA powders produced via a chemical precipitation technique [19]. Consolidation was achieved in 20 minutes in a 2.45 GHz microwave system to achieve densities up to 97% of the theoretical value. We also demonstrated, through dielectric measurements, the important role played by preheating supplied by a susceptor in microwave processing of HA.

In the current work, nanocrystalline HA powder produced via a chemical precipitation technique was sintered in a microwave furnace at various temperatures (1000 – 1300°C). The microstructure of samples sintered through these several different regimens were observed under the Scanning Electron Microscope and the phases present were evaluated via X-ray Diffraction (XRD). Hardness and fracture toughness was measured via Vickers indentation technique since these properties are influenced by the grain size.

MATERIALS AND METHODS

An aqueous precipitation technique was used to prepare the starting nanocrystalline hydroxyapatite powder. Details of this work is reported elsewhere [19-21]. The powder was sieved to <45 μm and pressed into 20 mm diameter discs by uniaxial pressing at 40 MPa followed by cold isostatic pressing at 150 MPa for 20 minutes. Sintering was performed in a microwave furnace (M.M.T., Knoxville, TN) provided with a variable power output magnetron source capable of operating from 0 to 3 kW at 2.45 GHz. The cavity is large and overmoded, thus ensuring mixing of the microwave modes and resulting in a homogeneous field distribution. The HA compacts were sandwiched between two SiC suceptors and surrounded with alumina fiber insulation before sintering over the temperature range of 1000°C to 1300°C with intervals of 50°C. The sintering time for all the samples was kept constant, at a duration of 20 minutes. The temperature of the surface of the samples was measured via a two-color optical pyrometer (Model M77, Mikron Corp.) and the microwave power input of the system adjusted accordingly to maintain the required temperature.

The phases present in the sintered samples was determined via X-ray diffraction (XRD) using a Siemens X-ray Diffractometer (D5000) with CuK_{α} radiation, and operated at 40 kV and 30 mA. The microstructure of the sintered samples was evaluated by a Leo 1430 Scanning Electron Microscope (SEM) operating at 20 kV. Prior to SEM analysis, both polished and fractured surface samples were gold-coated. The density of the sintered compacts was measured by water immersion technique and the relative density was calculated by taking the theoretical density of HA to be 3.156 gcm^{-3}. Vickers indentation tests were done on polished samples to obtain hardness and fracture toughness. A microindentor was used with a load of 500g applied for 15 seconds. In total, 10 indents were made for each sample and they were distributed all around the surface. Fracture toughness (K_{1c}) was estimated from the equation;

$$K_{1c} = A\,(E/H)^{1/2} P c^{-3/2}$$

Where A equals 0.016 [22]. E is the elastic modulus, H is the hardness, c is half the indentation crack length, and P is the applied load. In these calculations, E was taken as 115 GPa [22].

RESULTS AND DISCUSSION

The XRD pattern of the HA samples sintered at various temperatures showed no indication of any other residual phases such as tri-calcium phosphate, tetra-calcium phosphate or calcium oxide, etc. The fact that no decomposition was observed upon sintering at these temperatures could be due to the rapid sintering achieved in the microwave. Conventional sintering of HA in a furnace has been shown to result in decomposition at temperatures as low as 1100°C [23]. A temperature of decomposition as

high as 1350°C has also been reported, with the control of sintering conditions. However, this has also been shown to lead to extensive undesirable grain growth.

Table 1: Change of Physical and Mechanical Properties with Sintering Temperature

Temp. °C	Density % (relative)	Grain Size (μm)	Std.Dev. (μm)	Hv(GPa)	Std. Dev. (Gpa)	K_{1c} (MPa√m)	Std. Dev. (MPa√m)
1000	90.8	0.28	0.12	3.85	0.42	1.75	0.17
1050	95.2	0.35	0.12	5.96	0.89	1.72	0.24
1100	96.5	1.32	0.34	6.19	0.41	1.33	0.10
1150	96.7	0.77	0.52	6.38	0.3	1.16	0.10
1200	96.6	1.40	0.39	6.13	0.27	1.45	0.15
1250	97.0	2.21	0.74	5.39	0.38	1.18	0.06
1300	98.0	1.24	0.45	6.00	0.43	1.38	0.14

Table 1 shows the change of various physical and mechanical properties with sintering temperature. The relative density of the sample sintered at 1000°C is only 90.8% as compared to the highest value of 98% for samples sintered at 1300°C. The density achieved from the microwave sintering is higher than those reported for nano-HA samples sintered using conventional methods and a fast firing schedule [23]. A density of 97-98% is usually achieved when HA is sintered with a furnace holding time of 1 hour at a temperature of 1100°C. This result clearly indicates that microwave sintering is an effective method for fast consolidation of HA.

Figure 2 shows the microstructure of a fractured surface on the sintered sample at different sintering temperatures. The grain boundaries are visible and indicate equiaxed grain features. The sub-micron size grains are visible in samples sintered at 1000°C and 1050°C with grain sizes of 0.28±0.12 μm and 0.35±0.12 μm respectively (Table 1). Beyond these temperatures, there is a rapid increase in grain size. The sample sintered at 1250°C has the highest value of 2.21 μm. However, these values are far smaller than grains sizes obtained for conventional sintering techniques with values as high as 20 μm reported [23].

Figure 3(a) shows an impression of a Vickers indent on a polished sample. The brittle nature of the sample is indicated by the cracks propagating in straight lines from the edge of the indent. Under low magnification, the cracks seem to propagate in a straight line from the edge of the indent. Under higher magnification (figure 3b), however, the crack can be seen to follow a zig-zag path, indicating intergranular fracture. The hardness values are shown in Table 1. The sample sintered at 1000°C has the lowest

value while the sample sintered at 1150°C has the highest of 3.85±0.42 GPa and 6.38±0.10 GPa respectively. The fracture toughness value also varies with sintering temperature with the sample sintered at 1000°C having the highest value (1.75±0.17 MPa√m) and the sample sintered at 1150°C having the lowest value (1.16±0.10 MPa√m). The variation of the average Vickers hardness and fracture toughness (K_{1c}) of samples sintered at various temperatures is shown in Figure 4. From this, it is evident that there is an inverse relationship

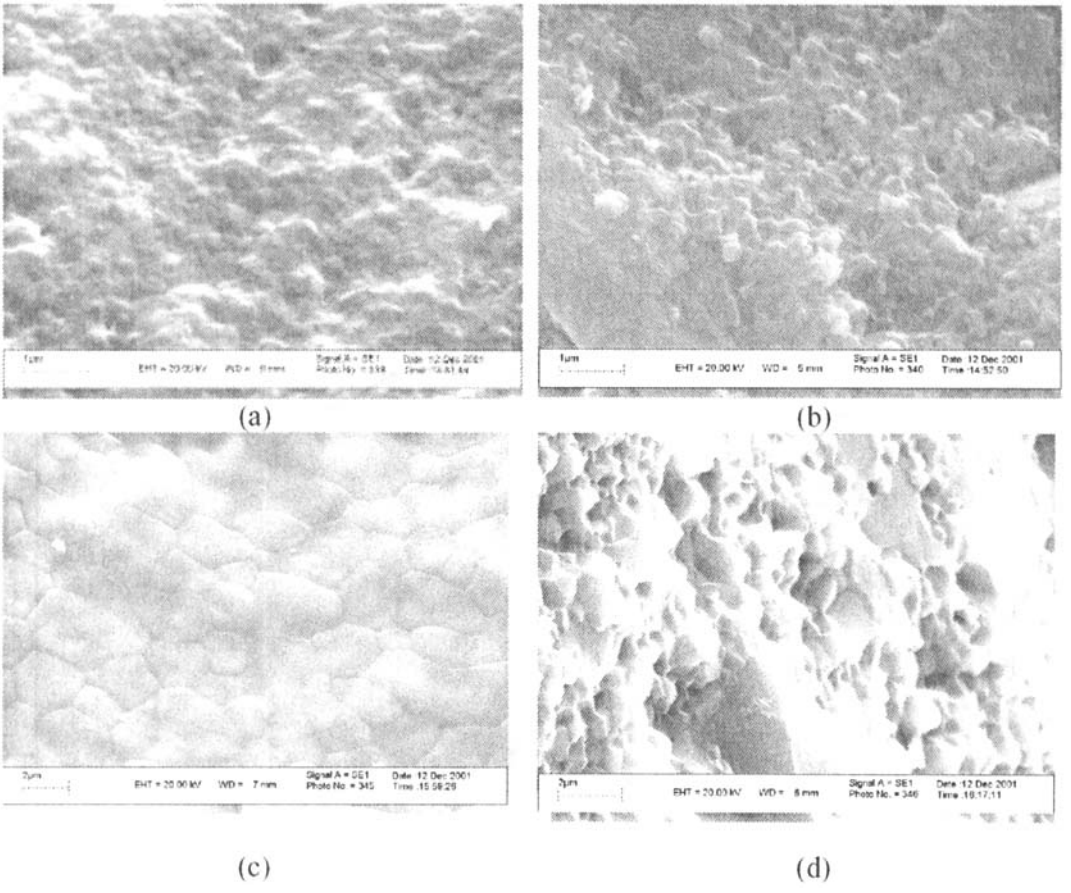

Figure 2: Microstructure of HA samples sintered at various temperatures (fractured surfaces).

Sintering temperatures are: (a) 1000 °C (b) 1100 °C (c) 1200 °C (d) 1300 °C

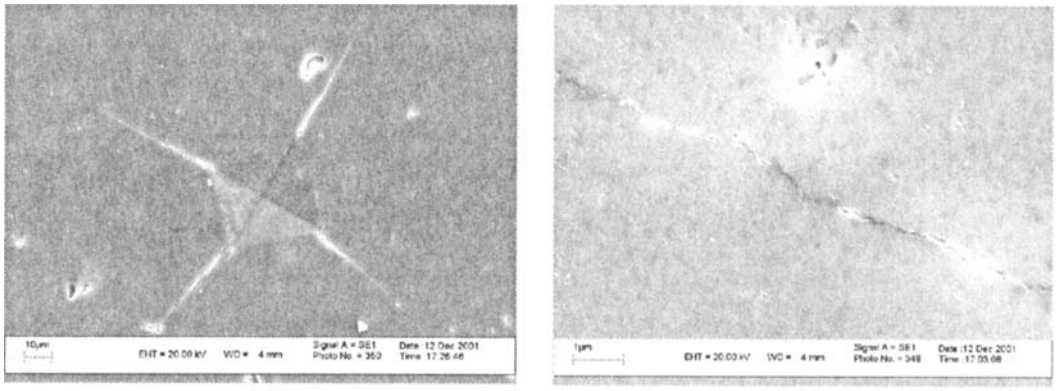

(a) (b)

Figure 3: (a) An impression of a vickers indent; (b) a crack propagating from an indent.

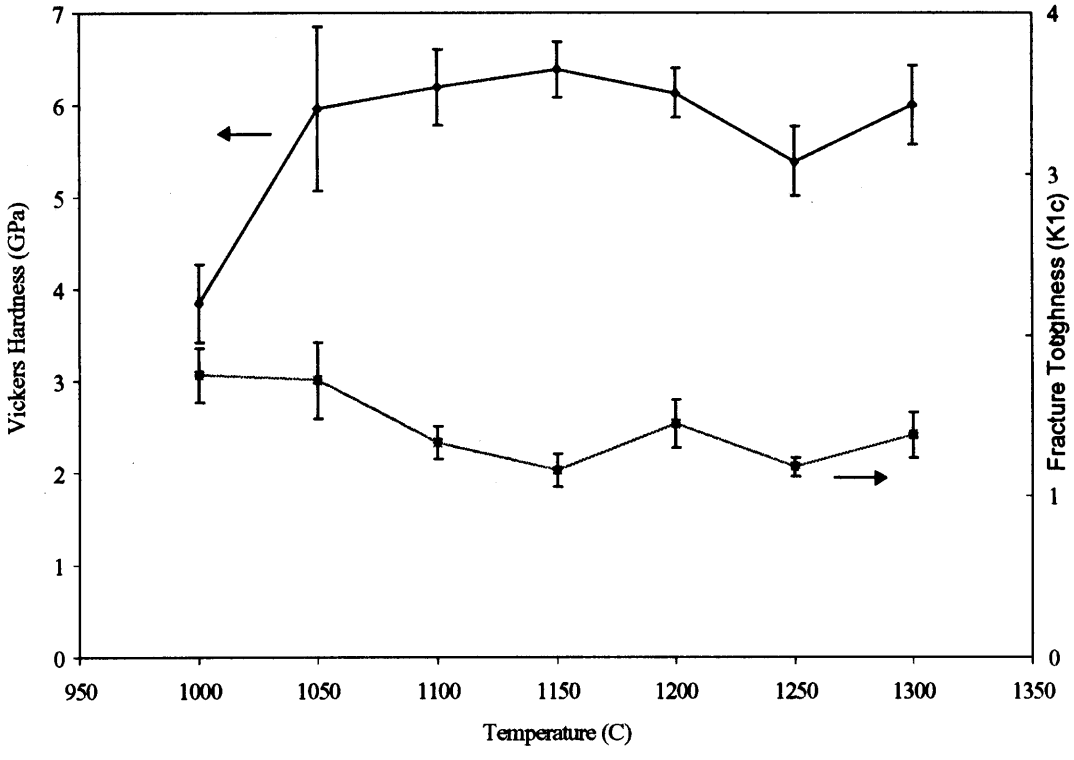

Figure 4: Change in Vickers Hardness and Fracture Toughness with temperature.

between the fracture toughness and hardness values. Yubao observed a drop in fracture toughness for HA specimens having grain size greater than 0.4 μm [24]. The decrease in fracture toughness with increasing grain size observed may be due to the effect of microcracking. Of the present study, the best properties, with both high hardness and

fracture toughness, were of those samples sintered at 1050°C, achieving a density of more than 95% with an average grain size of 0.35 μm. We believe these enhanced properties are due to the improved microstructure obtained at this sintering temperature.

CONCLUSIONS

In this present study, the result has shown that it is viable to produce nano-structured HA through microwave sintering. Grain size values as low as 0.28 μm were obtained in sample sintered at 1000°C. Fracture toughness values were found to decrease with increasing grain size, decreasing from 1.75 MPa√m to 1.38 MPa√m for a grain size change from .28 μm to 1.24 μm. Hardness values were found to increase from 3.85 GPa to 6.00 GPa over the same grain size interval. The best overall properties, with both high hardness and fracture toughness, were found in samples sintered at 1050°C, achieving a density of more than 95% with fracture toughness and hardness values of 1.72 MPa√m and 5.96 GPa, respectively.

ACKNOWLEDGMENTS

We acknowledge the support of NSF DMI-9800009

REFERENCES

1. J. Karch, R. Birringer, and H. Gleiter, Nature, 330 (1987) 556.
2. Z. Cui, and H. Hahn, Nanostructured Materials, 1 (1992), 419.
3. L. Chen, T. Rouxcel, R. Chaim, H. Vesteghem, and D. Sherman, Mater. Sci. Forum, 245 (1997), 243.
4. M.J. Mayo, Nanostructured Materials, 9 (1997) 717.
5. Y. Champion, S. Guerin-Mailly, L. Bonnentien, and P. Langlois, Scripta Mater., 44 (2001) 1609.
6. E. Arzt, Acta Mater., 46 (1998) 5611.
7. L.L. Hench, J. Am. Ceram. Soc., **74** 1487 (1991).
8. M. Akao, H. Aoki, K. Kato and A. Sato, J. Mater. Sci., **17**, 343 (1982).
9. G. Willmann, British Ceramic Transactions, **95**, 212 (1996).
10. P.E. Wang and T. K. Chaki, J. Mater. Sci. Mater in Med., **4**, 150 (1993).
11. L.L. Hench, J. Am. Ceram. Soc., **74** 1487 (1991).
12. S. Bhaduri, S.B. Bhaduri, and E. Zhou, J. Mater. Res., 13 (1998) 156.
13. S. Bhaduri and S.B. Bhaduri, JOM, 50 (1998) 44.
14. W. H. Sutton, Am. Ceram. Soc. Bull., 68 (1989) 376.
15. D.M. Mingos, Adv. Mater., 5 (1993) 857.
16. Y. Fang, D.K. Agrawal, D.M. Roy and R. Roy, J. Mater. Res., 7 (1992) 14 490.

17. Y. Fang, D.K. Agrawal, D.M. Roy and R. Roy, J. Mater. Res., Vol. 9, No. 1 (1994) 180.
18. Y. Fang, D.K. Agrawal, D.M. Roy and R. Roy, Mater. Lett., 23 147-51 (1995).
19. M.G. Kutty, J.R. Jokisaari, S. Bhaduri, S.B. Bhaduri, Ceram. Eng. And Sci. Proc., 22 (2001) 587.
20. M. Jarcho, C.H. Bolen, M.B. Thomas J. Bobick, J.F. Kay and R.H. Doremus, J. Mater. Sci. 11 (1976) 2027.
21. G. Muralithran and S. Ramesh, Ceram. Int., 26 (2000) 221.
22. T.P. Hoepfner and E.D. Case, pp53. in Bioceramics: Materials and Applications III, Eds. B George, R.P Rusin, G.S. Fishman and V. Janas (2000), Am, Ceram. Soc., Westerville, OH.
23. M. Jarcho, C.H. Bolen, M.B. Thomas, J. Bobick, J.F. Kay and R.H. Doremus, J. Maters Sci. 11 (1976) 2027.
24. L. Yubao and K. De Groot, Biomaterials, 15 (1994) 835.

PROPERTIES AND MICROSTRUCTURE OF ALUMINA-NIOBIUM AND ALUMINA-NEODYMIUM TITANATE NANOCOMPOSITES MADE BY NOVEL PROCESSING METHODS

Joshua D. Kuntz, Guo-Dong Zhan, Julin Wan, and Amiya K. Mukherjee
Department of Chemical Engineering & Materials Science
University of California, Davis, CA 95616

ABSTRACT

Alumina-niobium and alumina-neodymium titanate nanocomposites have been fabricated using high-energy ball-milling and Spark Plasma Sintering (SPS). The 10 vol% niobium nanocomposite has a fracture toughness of 7 $MPam^{1/2}$ and a hardness of 22.5 GPa. This is nearly twice as tough as a pressureless sintered composite of the same composition reported in work by Garcia et al [1]. The 9 vol% neodymium titanate nanocomposite increased toughness to 5.7 $MPam^{1/2}$ and was able to retain a hardness value of 19.2 GPa. The increase in toughness in the alumina-niobium can be attributed to ductile-phase toughening, while alumina-neodymium titanate relies on the newly proposed toughening mechanism of piezoelectric-phase strain relief.

INTRODUCTION

It has been proposed that nanocrystalline ceramics exhibit significantly different properties than conventional ceramics due to the changes in material processes when grain-size is reduced to the order of 100 nm. A great deal of research has already gone into the effort of producing nanocrystalline ceramics to investigate these properties [2-7]. Work by Mishra et al. has already shown that the Hall-Petch relationship between hardness and grain size exhibits a discontinuity in slope in the nanocrystalline regime of alumina [8]. Thus far, the research in nanocrystalline ceramics shows that they are not inherently tougher than their microcrystalline brethren. This would limit nanocrystalline ceramics to the same family of uses as conventional ceramics, thus preventing their wide spread application. In our attempt to increase the toughness of nanoceramics we have employed two types of alumina-based composites. Metallic-phase toughening has been investigated through the inclusion of the niobium and a newly proposed mechanism of piezoelectric-phase strain relief through the addition of neodymium titanate.

In ductile phase toughening the metallic phase can be distributed in two ways. When the metallic component forms a continuous phase as in figure 1(a), nano-nano layer type nanocomposite, a plastic zone at the crack tip provides a major contribution to toughness [9]. On the other hand, when the ceramic is the continuous phase as in Figure 1(b), crack bridging by ductile ligaments in the crack wake would be the principle toughening mechanism [10]. Both nanocomposite types are combined for the present study. An ideal metallic phase for alumina-based composites is niobium. The refractory properties of niobium prevent the metallic phase addition from lowering the possible service temperature of the composite. Also, the superb bonding interface between alumina and niobium combined with the low thermal expansion coefficient mismatch leads to interfacial strength and low residual stresses between the two phases [11]

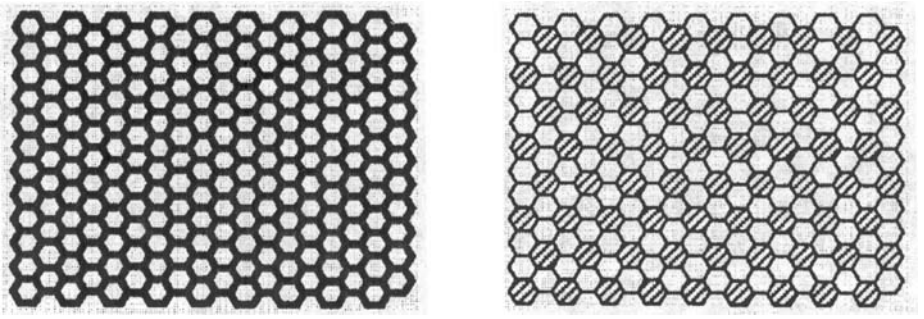

(a) nano-nano layer type (b) nano-nano type

Figure 1. Nanocomposite types for ductile phase toughening

Domain switching as a toughening mechanism has been recognized in ferroelectric-ferroelastic materials where either an applied compressive stress or electrical field led to domain switching [12]. Moreover, piezoelectric ceramics are capable of converting mechanical energy to electric energy and vice versa. Based on the domain switching and/or piezoelectric effect in ferroelectrics or piezoelectric ceramics, a new toughening mechanism was applied and proven in nanocrystalline alumina nanocomposites. In the present study, neodymium titanate ($Nd_2Ti_2O_7$) was selected as a piezoelectric second phase for high temperature application because it exhibited piezoelectric and electro-optic properties and had a Curie temperature in excess of 1500 °C [13]. The addition of a piezoelectric phase ($Nd_2Ti_2O_7$) to the alumina matrix is expected to increase toughening by converting stress-strain energy to electrical energy during localized deformation. The electrical energy is produced in the piezoelectric phase, during the application of an applied stress, by the polarization of the material, induced by strain in the crystal structure.

EXPERIMENTAL PROCEDURES

Novel Processing Routes

One of the main hurdles to the production of nanocrystalline ceramics is the ability to retain a nano-scale grain-size and still obtain full density. The advanced consolidation technique employed in the present study to overcome this hurdle is spark plasma sintering (SPS). It is a low pressure sintering method based on high temperature plasma (spark plasma) momentarily generated in the gaps between powder materials by electrical discharge at the beginning of ON-OFF DC pulsing. The ON-OFF DC pulse energizing method could generate: (1) spark plasma, (2) spark impact pressure, (3) Joule heating, and (4) an electrical field diffusion effect. In this process, powders were loaded into a graphite die and were heated by passing an electric current through the assembly. SPS rapidly consolidates powders to near theoretical density through the action of a rapid heating rate, pressure application, and proposed powder surface cleaning. While the exact phenomena that are occurring are still under debate, the results cannot be disputed. In both materials systems in this study, near full theoretical density was achieved for sintering durations as low as 3 minutes.

Alumina-Niobium Synthesis

Starting powders of nano-scale γ-alumina (29 nm from Nanophase Technologies Corporation, Darien, IL) and micron-scale niobium (74 micron from Goodfellow Cambridge Limited, Cambridge, England) and aluminum (325 mesh from Johnson Matthey Electronics, Ward Hill, MA) were mechanically milled using high-energy ball-milling (in a Spex 8000 mixer mill in a WC vial) with a polyvinyl alcohol (PVA) milling agent. The aluminum was added to act as a getter for oxygen to prevent the oxidation of niobium during ball-milling and the subsequent processing

steps. Milling was followed by a vacuum heat treatment at 350°C for 3 hrs, for the removal of the PVA. SPS consolidation was performed under 63 MPa of uniaxial pressure at 1100°C with a heating rate of 200°C/min. in a Dr. Sinter SPS-1050 equipment. The specimen had the composition of Al_2O_3/10 vol.% (Nb/10 wt.% Al).

Alumina-Neodymium Titanate Synthesis

High purity powders of Nd_2O_3 (99.9%, 325 mesh, from AEE High Purity Metals and Compounds, NJ) and TiO_2 (obtained from Nanophase Technologies Corporation, Darien, IL, ~30 nm) in the molar 1:2 were wet mixed for 24 h in ethanol with zirconia balls. The mixture was heated at 1425 °C for 6 h to synthesize $Nd_2Ti_2O_7$ by solid-state reaction. The pure α-Al_2O_3 nano-powder had an average particle size of ~50 nm (obtained from Baikowski International, Charlotte, NC) and surface area of 30 m^2/gm. The synthesized $Nd_2Ti_2O_7$ powders were mixed with the above α-Al_2O_3 nano-powder for 24 h in ethanol using zirconia ball media at 6, 9, and 14 vol.%, respectively. The composite powders were consolidated through SPS at different temperatures at a heating rate of 200 °C/min under a pressure of 63 MPa in a vacuum atmosphere (Dr. Sinter SPS-1050, Japan).

Characterization Methods

The final densities of the materials were determined by the Archimedes' method with deionized water as the immersion medium. The theoretical densities of the specimens were calculated according to the rule of mixtures. The microstructural observation and analysis were carried out using an FEI XL30-SFEG high-resolution scanning electron microscope with a resolution better than 2 nm and magnification over 600 kX. Additional evaluation was performed on a Philips CM-200 with a field emission gun operating at 200 kV. This instrument has a Link energy dispersive X-ray detector with energy resolution of 1.36 eV and a Gatan imaging filter with 1kx1k CCD camera and energy resolution of 0.9 eV with 1nm spatial resolution. The phases present were determined by X-ray diffraction (XRD) using CuKα radiation. Indentation tests were performed on a Wilson Tukon hardness tester with a diamond Vickers indenter. Bulk specimens were sectioned and mounted in epoxy, then polished though 0.25-micron diamond. The indentation parameters for fracture toughness (K_{IC}) and Vickers hardness measurements were a 1 kg load with a dwell of 15s. K_{IC} values were calculated using Niihara et al.' equation for Palmqvist cracks [14].

RESULTS AND DISCUSSION

The SPS processing conditions for the nanocomposites are given in Table I. The sintering temperature and dwell time were minimized to limit grain growth. The pure α-Al_2O_3 nanopowder could be consolidated by SPS at 1150 °C for 3 min to get full density. It is very interesting to note that the Al_2O_3/6 vol.% $Nd_2Ti_2O_7$ composite could be sintered at a significant lower temperature of only 1000 °C to obtain almost full density while the Al_2O_3/9 vol.% $Nd_2Ti_2O_7$ needed to be sintered at 1100 °C for 3 min. Additionally, the addition of second phase into pure alumina seems to lower the sintering temperature.

Table I. Processing Conditions of Al_2O_3-based Nanocomposites

Material	Temperature (°C)	Dwell time (min)	Relative Density (%TD)
Pure α-Al_2O_3	1150	3	100
Al_2O_3/10 vol.% Nb-phase	1100	3	98
Al_2O_3/6 vol.% $Nd_2Ti_2O_7$	1000	1	99
Al_2O_3/9 vol.% $Nd_2Ti_2O_7$	1100	3	98
Al_2O_3/14 vol.% $Nd_2Ti_2O_7$	1150	3	100

The microstructures of the fractured surface in these materials are shown in Figures 2 and 3. Figure 2a is the typical SEM image of pure α-Al_2O_3 consolidated at 1150 °C, indicating a mixture of transgranular and intergranular fracture mode. The microstructures in Al_2O_3/6 vol.% $Nd_2Ti_2O_7$ (Figure 2b), Al_2O_3/9 vol.% $Nd_2Ti_2O_7$ (Figure 2c), and Al_2O_3/14 vol.% $Nd_2Ti_2O_7$ (Figure 2d) nanocomposites consisted of ultra-fine equiaxed grains. Figure 3 shows the fracture surface of the Al_2O_3/10 vol.% Nb-phase nanocomposite with predominantly intergranular fracture. These results demonstrate the effectiveness of spark plasma sintering over conventional methods in obtaining alumina and alumina matrix nanocomposites at quite lower temperatures and shorter sintering duration resulting in high density and ultrafine grain size.

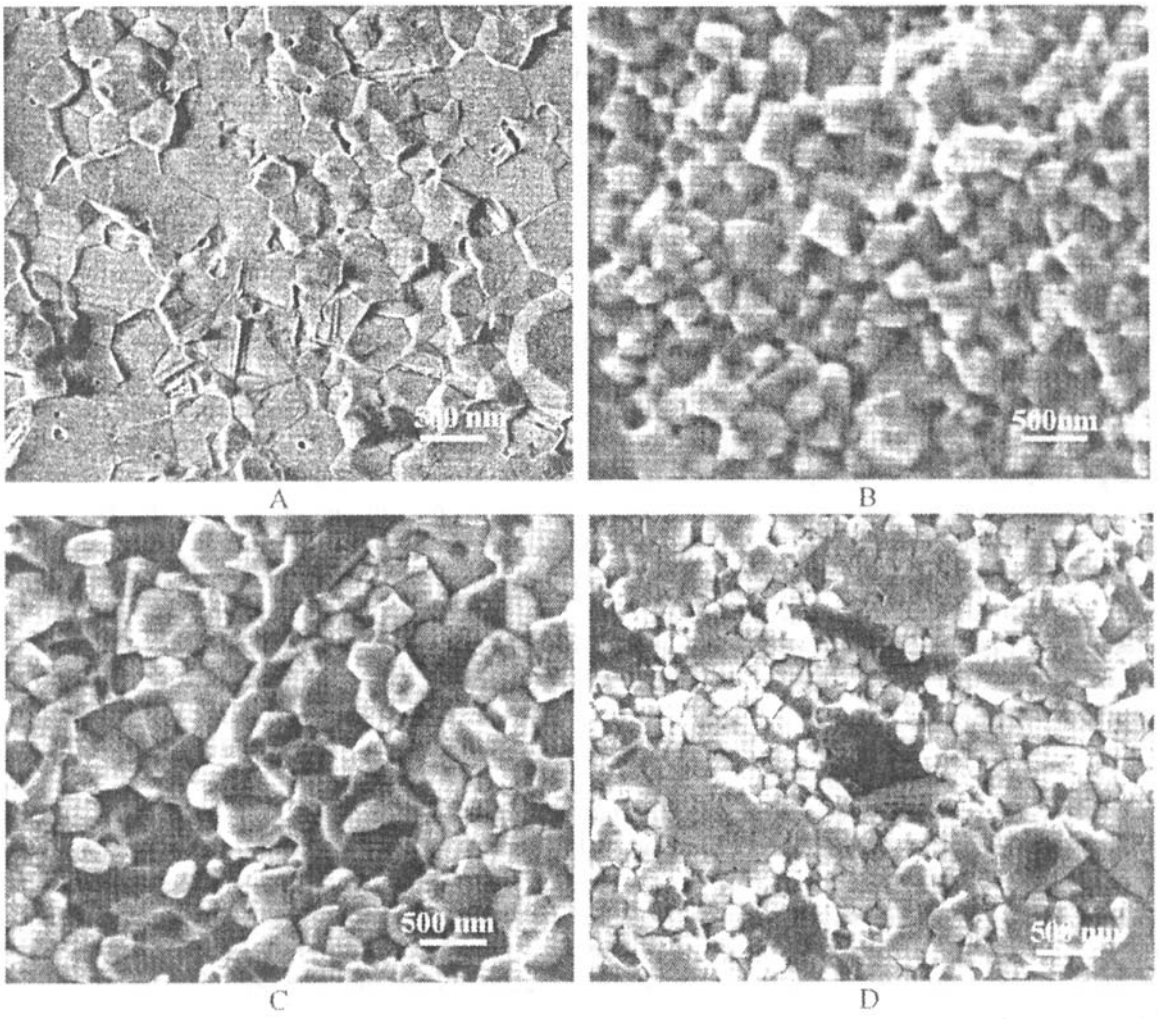

Figure 2. High-resolution scanning electron micrographs of (a) pure α-Al_2O_3, (b) Al_2O_3/6 vol% $Nd_2Ti_2O_7$, (c) Al_2O_3/9 vol% $Nd_2Ti_2O_7$, and (d) Al_2O_3/14 vol% $Nd_2Ti_2O_7$ nanocomposites consolidated by SPS

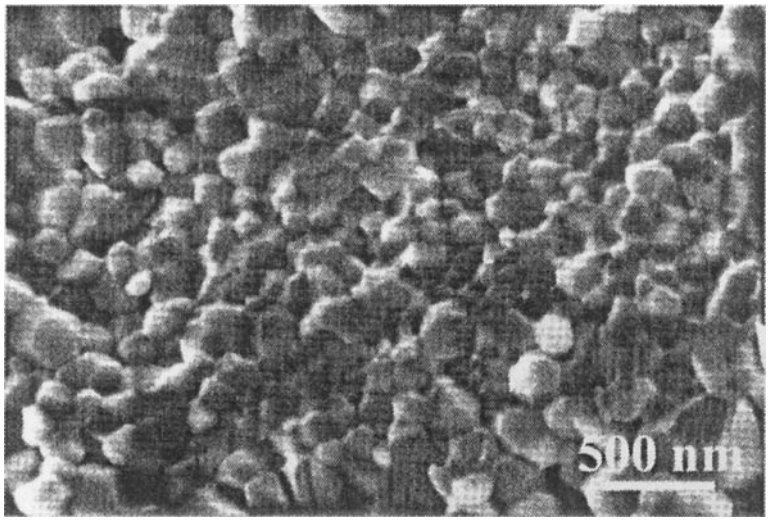

Figure 3. High-resolution scanning electron micrograph of Al_2O_3/10 vol% Nb-phase nanocomposite

In regard to piezoelectric toughening mechanism [15], it is important to prevent the piezoelectric second phase from reacting with the alumina matrix. XRD results (Figure 2) showed that the sintered Al_2O_3/6 vol.% $Nd_2Ti_2O_7$ composite consisted of α-Al_2O_3 as a major phase and the co-existence of $Nd_2Ti_2O_7$ phase. No other phase was detected, indicating that no chemical reaction between α-Al_2O_3 and $Nd_2Ti_2O_7$ phases occurred during sintering. Similar results were observed in Al_2O_3/9 vol.% $Nd_2Ti_2O_7$ composite.

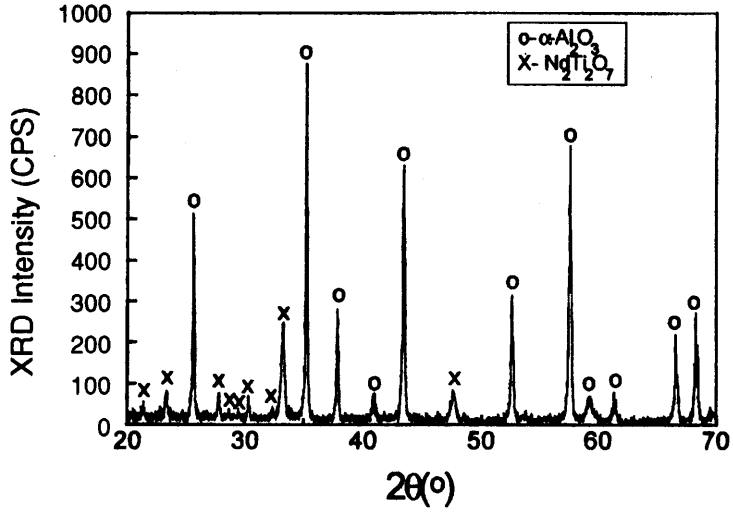

Figure 4. XRD pattern in dense Al_2O_3/6vol%$Nd_2Ti_2O_7$ composite.

In the ductile phase toughening mechanisms the Nb-phase distribution is key in the degree of toughening of the composite. In work by Garcia et al. [1] an Al_2O_3/10 vol% Nb composite was created through pressureless sintering, which differs from the present study only in the morphology of the Nb-phase. In said work, the Nb is equal in grain-size to the matrix and evenly distributed, whereas Figure 5 shows the niobium in the present study is present as ~20 nm inclusions predominantly at the grain boundaries, but also in the interior, or as a continuous wetted layer at the alumina grain boundaries.

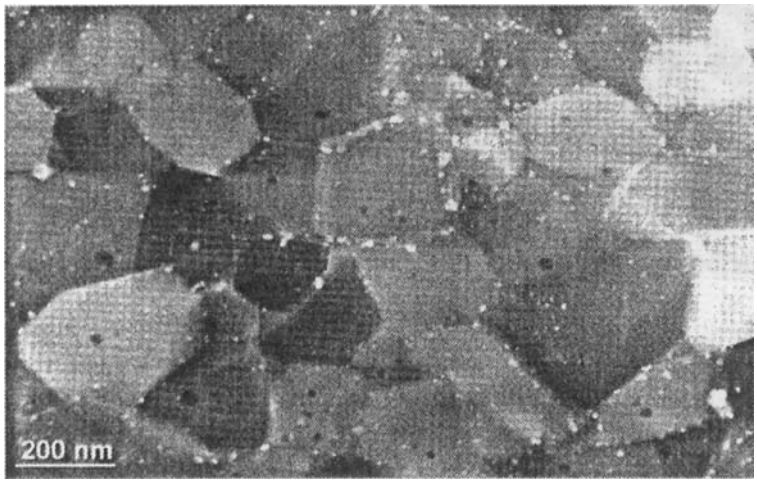

Figure 5. Dark field STEM image of the Al_2O_3/10 vol% Nb-phase nanocomposite

Table II summarizes the physical and mechanical properties for the present materials. In comparison to pure alumina, a significant improvement in fracture toughness was observed in the alumina-neodymium titanate nanocomposites, suggesting that adding piezoelectric phase into nanocrystalline alumina is very effective for toughening. The highest toughness was achieved in the Al_2O_3/9 vol.% $Nd_2Ti_2O_7$ nanocomposite, indicating that there is an optimum composition in incorporating second piezoelectric phase into nanocrystalline alumina for toughening. Moreover, it can be noted that the hardness for these nanocomposites is just slightly less than pure alumina. The lower hardness of the nanocomposites in spite of the finer grain-size may be due to the lower hardness of the piezoelectric phase. When comparing the work of Garcia et al. [1] with the present study it is interesting to note that by only changing the Nb-phase distribution one can more than double the toughness of the composite and improve upon the hardness at the same time.

Table II. Physical and Mechanical Properties of Alumina Nanocomposites

Material	Grain size (nm)	Hardness (GPa)	Toughness ($MPam^{1/2}$)	Reference
Pure α-Al_2O_3	349	20.3 ± 0.3	3.3 ± 0.1	Present study
Al_2O_3/6vol% $Nd_2Ti_2O_7$	243	19.7 ± 0.2	5.2 ± 0.4	Present study
Al_2O_3/9vol% $Nd_2Ti_2O_7$	81	19.2 ± 0.3	5.7 ± 0.4	Present study
Al_2O_3/14vol% $Nd_2Ti_2O_7$	225	19.9 ± 0.1	5.0 ± 0.2	Present study
Al_2O_3/10 vol% Nb-phase	~200	22.5 ± 0.4	7.0 ± 0.2	Present study
Al_2O_3/10 vol% Nb	~200	18.5	3.1 ± 0.4	Garcia, et al [1]

SUMMARY

Through the use of HEBM and SPS two alumina-based nanocomposites were produced that provide significant improvements in the fracture toughness of nanocrystalline alumina. Evidence of toughening due to the presence of a piezoelectric phase has been shown. The improvement in fracture toughness of the Nb-phase toughened nanocomposite in the present work over previous work by Garcia et al. [1] can be attributable only to the variation in ductile phase morphology between the two composites.

ACKNOWLEDGEMENTS

This material is based upon work supported by, or in part by, the U. S. Army Research Laboratory and the U. S. Army Research Office under contract/grant number G-DAAD19-00-1-0185.

SEM images were obtained at the Facility for Advanced Instrumentation (FAI) at UC Davis and TEM at the National Center for Electron Microscopy (NCEM) at the Lawrence Berkeley Laboratory. Special thanks to Chris Nelson at NCEM and Mike Dunlap at FAI for their assistance.

REFERENCES

[1] D.E. Garcia, S. Schicker, J. Bruhn, R. Janssen and N. Claussen, *Journal of the American Ceramic Society.* 1998;81:429.

[2] H. Gleiter, *Progress in Materials Science*, 1989: 33:223.

[3] R.S. Mishra, J.A. Schneider, J.F. Shackelford, and A.K. Mukherjee, *NanoStructural Materials*, 1995: 5:525.

[4] E.J. Gonzalez, B. Hockey, and G.J. Piermarini, *Materials and Manufacturing Processes*, 1996: 11: 951.

[5] M.J. Mayo, *NanoStructural Materials*, 1997: 9: 717.

[6] S. Bhaduri and S.B. Bhaduri, *NanoStructural Materials*, 1997: 8: 755.

[7] S.C. Liao, Y.J. Chen, B.H. Kear, and W.E. Mayo, *NanoStructural Materials*, 1998: 10: 1063.

[8] R.S. Mishra, C.E. Lesher and A.K. Mukherjee, *Journal of the American Ceramic Society.* 1996;79:2989.

[9] D.B. Marshall, W.L. Morris, B.N. Cox and M.S. Dadkhah, *Journal of the American Ceramic Society.* 1990;73:2938.

[10] H.E. Deve, A.G. Evans, G.R. Odette, R. Mehrabian, M.L. Emiliani and R.J. Hecht' *Acta Metallurgica et Materialia.* 1990;38:1491.

[11] S.M. Lane, S.B. Biner and O. Buck, *Materials Science & Engineering A (Structural Materials: Properties, Microstructure and Processing).* 1998;A246:244.

[12] K. Mehta and A.V. Virkar, *Journal of the American Ceramic Society*, 1990: 73: 567.

[13] G. Winfield, F. Azough and R. Freer, *Ferroelectrics*, 1992: 133:181.

[14] K. Niihara, R. Morena, D.P.H. and Hasselman, *Journal of Materials Science Letters*, 1982: 1:13.

[15] B. Yang and X.M. Chen, *Journal of the European Ceramic Society*, 2000: 20:1687.

This page intentionally left blank

A NOVEL HYBRID ROUTE TO CHEMICALLY-TAILORED, THREE-DIMENSIONAL OXIDE NANOSTRUCTURES: THE BASIC (BIOCLASTIC AND SHAPE-PRESERVING INORGANIC CONVERSION) PROCESS

Ken H. Sandhage, Matthew B. Dickerson, Philip M. Huseman, Frank M. Zalar, Mark C. Carroll, Department of Materials Science and Engineering, The Ohio State University, 481 Watts Hall, 2041 College Road, Columbus, OH 43210

Michelle R. Rondon, Department of Microbiology, The Ohio State University, 452 Bioscience Building, 484 W. 12th Avenue, Columbus, OH 43210

Eryn C. Sandhage, Jones Middle School, Upper Arlington, OH 43221

ABSTRACT

A novel, hybrid route to chemically-tailored oxide nanostructures with complex, three-dimensional (3D) shapes is introduced: the **Bioclastic*** and **S**hape-preserving **I**norganic **C**onversion (**BaSIC**) process. This process couples the massively-parallel and precise replication of biological organisms with rapid, shape-preserving chemical conversion via fluid/solid reactions, so that large numbers (billions) of identical 3D nanostructures can produced with desired (non-natural) compositions. The BASIC process is demonstrated by converting ornate, SiO_2-based diatom frustules (microshells) into MgO nanostructures that retain the frustule shapes and fine features. Such MgO nanostructures are attractive for biomedical and environmental applications (e.g., drug delivery, water purification). By choosing among the numerous shapes and fine features available in

*Bioclastic: *adj*; "of rock or similar material attaining its present form through the action of living organisms" [1]. "Bioclastic" is more appropriate than "biomimetic" for this process because a biological organism is actually being utilized (not just mimicked) to fabricate nanoparticle structures.

bioclastic structures (from diatoms, radiolaria, sponges, silicoflagellates, etc.), and by using other reactive gases, meso/nanostructures with a wide variety of shapes, features, and compositions may be mass produced by the BaSIC process.

INTRODUCTION

An increasing amount of international research and development activity is being devoted to the generation of miniature devices for a host of important applications in medicine (e.g., drug delivery capsules, membranes for protein separation or cell immuno-isolation), environmental protection (e.g., sensors for pollutants or pathogens, filters for waste water treatment), manufacturing (e.g., microrobots, mesoporous substrates for catalysis, microdies), telecommunications (e.g., microtransducers, positioning devices for optical fibers and lenses), and transportation (e.g., microcombustors, microengines) [2-9]. For optimal device performance in many of these applications, well-defined features (pores, channels, cavities, etc.) on the mesoscale (10^2 nm) or nanoscale (10^1 nm) are required. Much of the worldwide effort on micro/mesoscale fabrication has relied upon techniques developed for the microelectronics industry (e.g., the micromachining of silicon by lithographic methods or deep reactive ion etching) [2,3]. Unfortunately, these synthetic "top-down" approaches can not be easily adapted for the mass production of non-silicon devices with complex, three-dimensional (non-planar, curved) shapes and features on the mesoscale or nanoscale [3].

A wide variety of rigid microscopic structures with intricate, three-dimensional (3D) shapes and mesoscale-to-nanoscale features are generated by natural organisms [10]. Among the most ornate of such bioclastic structures are the frustules (microshells) of diatoms [10-13]. Diatoms (*Bacillariophyta*) are single-celled algae that are ubiquitous to marine and freshwater environments; indeed, diatoms are believed to account for up to one-fourth of the global primary production of carbon [7,11-14]. Diatoms form rigid cell walls (frustules) comprised of organic macromolecules and amorphous silica nanoparticles [14,15]. Each of the $\approx 10^5$ diatom species forms a frustule with unique shape and surface features [11,12]. Frustules may assume a variety of elongated (pennate) or radially-symmetric (centric) shapes, with maximum dimensions ranging from less than one micron to several hundreds of microns for various species [10-15]. The surfaces of diatom frustules possess fine features (pores, ridges, protuberances, etc.) arrayed in intricate patterns specific to a given species. These features possess dimensions ranging from the microscale scale to the nanometer

scale. The complex 3D structure of a given frustule can be replicated in large quantities by biological reproduction. The rate of diatom reproduction depends on a number of parameters (e.g., silicic acid concentration, nutrient concentration, temperature, light, etc.) [11-13,16]. Under proper conditions, diatom reproduction can occur several times per day, so that large numbers of frustules of identical shape may be produced in a relatively short period of time (e.g., 2^{30} = 1.07 billion similarly-shaped frustules would be generated in 10 days at a sustained reproduction rate of 3 times per day, or in 15 days at a sustained rate of 2 times per day). Such massively-parallel, precise, 3D self-assembly of silica nanoparticles under environmentally benign conditions is highly attractive for nanotechnological applications. However, the silica-based composition of diatoms severely limits the range of potential applications. Silica is not bioinert, nor is it chemically compatible with basic oxides or basic melts [14,17]. At high temperatures, amorphous silica exhibits poor creep resistance and is not structurally stable (due to crystallization).

A number of research groups have demonstrated that shaped macropreforms of silica or other oxides can be converted into new compositions, that retain the starting preform shape, through the use of displacement (oxidation-reduction) reactions with molten metals [18-24]. Breslin, et al. generated co-continuous composites of Al_2O_3 and Al-Si by immersing dense preforms of amorphous SiO_2 into molten Al at 1000-1300°C [18]. The reduction in solid volume associated with converting 3 moles of SiO_2 into 2 moles of Al_2O_3 provided additional internal volume for the molten Al-Si alloy, so that the final composite retained the shape of the starting dense SiO_2 preforms [18]. Loehman, et al. have also generated dense, near net-shaped Al_2O_3/Al-Si composites by exposing dense preforms of polycrystalline mullite, $Al_6Si_2O_{13}$, to molten Al or Al-Si [19]. Claussen, et al. have used gas pressure infiltration or squeeze casting to rapidly infiltrate porous oxide preforms (e.g., TiO_2, Nb_2O_5) with molten Al [20,21]. Reaction of the molten aluminum with the oxide generated co-continuous, near net-shaped composites of alumina with one or more aluminide compounds (e.g., $Al_2O_3/TiAl_3$, $Al_2O_3/NbAl_3/Nb_2Al$ composites). Sandhage, et al. have also used reactive melt infiltration to convert porous ceramic-bearing preforms into new ceramic/metal composites of high density and near net shape [22-24]. In the latter case, displacement reactions were chosen that yielded an increase in solid ceramic volume, so that composites (e.g., MgO/Mg-Al, $MgAl_2O_4$/Fe-Ni-Al, ZrC/W) with relatively high ceramic contents (up to 86 vol%) could be directly produced.

The objective of this paper is to introduce a revolutionary new, hybrid nano-fabrication route: the **Bioclastic and Shape-preserving Inorganic Conversion (BaSIC)** process [25]. Biologically self-assembled ceramic (bioclastic) nanostructures with complex 3D shapes are utilized as preforms in this process. Massively-parallel and precise biological reproduction may be used to generate large numbers (billions) of such preforms with identical shapes. With the BASIC process, such self-assembled nanostructures are converted into new compositions via shape-preserving reactions with fluids (gases or liquids). By coupling bioclastic self-assembly with near net-shape reaction processing, significant limitations encountered with top-down processing (difficulty in fabricating three-dimensional nanostructures with complex - nonplanar, curved - shapes) and bottom-up processing (very restricted range of self-assembled chemistries) can be avoided. The feasibility of the BaSIC process is demonstrated in this paper by converting diatom frustules (self-assembled, 3D, SiO_2 nanoparticle structures) into MgO nanostructures (e.g., for biomedical and environmental applications).

EXPERIMENTAL PROCEDURE

Diatoms were obtained in the form of diatomaceous earth (*Aulacoseira, Cyclotella*) or as algal cultures (*Cyclotella, Synedra*; Carolina Biological Supply Co., Burlington, NC). In the latter case, diatom culture growth was conducted in glass flasks sterilized in an autoclave. A 1 ml culture batch was added to 50 ml of an aqueous solution with appropriate growth media (Alga-Gro® freshwater medium for *Synedra*, Alga-Gro® seawater medium for *Cyclotella*; Carolina Biological Supply Co.) and sodium metasilicate as the silica source. Culture growth was allowed to proceed at 23°C for 21 days with a 12 hour light (fluorescent)/12 hour dark cycle. Prior to reaction with Mg(g), the diatomaceous earth and cultured diatoms were heated to 600°C for 8 hours in air to pyrolyze the organic material. The pyrolyzed frustules were then deposited onto a steel substrate. The substrate was placed inside a steel tube (internal dia. = 4.1 cm; internal length = 20.2 cm) along with 4-6 grams of magnesium, and the tube was then welded shut. The sealed tubes were then heated to 900°C and held for 4 hours in flowing argon (to minimize oxidation of the steel tube) within a tube furnace. After this heat treatment, the steel tube was cut open and the reacted frustules were removed. Secondary electron images of diatom frustules before and after reaction were obtained with a Model XL30 field emission gun scanning electron microscope (Philips Electron Instruments, Eindhoven, The Netherlands).

Cross-sections of reacted frustules were prepared with a focused ion beam instrument (Model Strata DB-235 System, FEI Company, Hillsboro, OR). Bright field images of such cross-sections were obtained with a CM-200T transmission electron microscope (Philips). The scanning and transmission electron microscopes were both equipped with a Si/Li energy-dispersive x-ray detector (Edax International, Mahwah, NJ) for microchemical analyses.

RESULTS AND DISCUSSION

Secondary electron images of the frustules of several pyrolyzed diatoms (*Synedra, Cyclotella, Aulacoseira*) are shown in Figure 1. *Synedra* frustules (Figs. 1a, 1b) possess the shape of flattened needles. The overlapping halves of the pennate *Synedra* frustule can be seen in Figure 1b*. The flat surfaces of these frustules are decorated with uniformly-spaced rows of fine pores (a few hundred nm in diameter) oriented in a direction perpendicular to the long needle axis. The diatom *Cyclotella* possesses a disk-shaped (centric) frustule (Fig. 1c) that consists of two overlapping, petri dish-shaped halves. The surface of this frustule is partially covered with narrow grooves (a few hundred nm in width) that radiate inward from the outside perimeter. The *Aulacoseira* frustule (Figs. 1d, 1e) consists of two capsule-shaped halves joined end-to-end so as to form a longer cylindrical assembly (one of these halves is shown in Fig. 2c below). One end of each capsule (half frustule) possesses a circular opening (Fig. 1e), whereas the other end (not shown) is closed and exhibits finger-like protuberances (see Fig. 2c) that interlock with those of another capsule to form the longer assembly. Regularly- spaced rows of fine pores (a few hundred nm in diameter) run along the cylindrical walls of the *Aulacoseira* frustule (Figs. 1d, e).

These diatom frustules were sealed within steel tubes, along with solid magnesium, and then heated to 900°C for 4 h. At this temperature, the magnesium melted and partially vaporized within the steel tubes (the equilibrium pressure of magnesium vapor over molten magnesium at 900°C is 0.16 atm [27]). Upon exposure to magnesium vapor, the silica within the diatoms underwent the following displacement (oxidation-reduction) reaction:

$$2Mg(g) + SiO_2(s) \Rightarrow 2MgO(s) + [Si] \quad (1)$$

*The frustule of each diatom is composed of two overlapping halves (note: the word "diatom" is derived from the Greek word "diatomos" which means "cut in half" [1]).

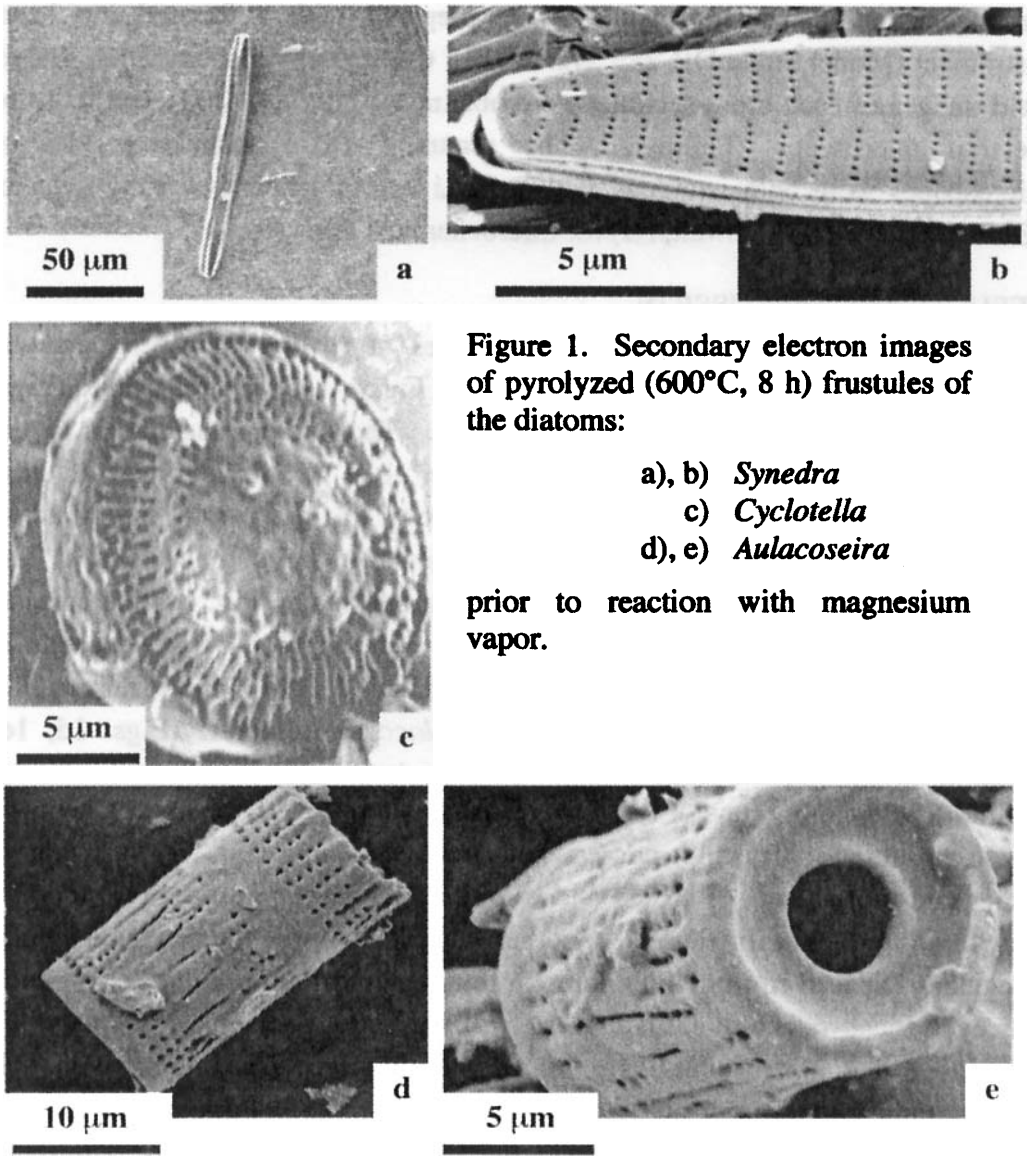

Figure 1. Secondary electron images of pyrolyzed (600°C, 8 h) frustules of the diatoms:

a), b) *Synedra*
c) *Cyclotella*
d), e) *Aulacoseira*

prior to reaction with magnesium vapor.

where [Si] refers to silicon dissolved within a Mg-Si liquid. The latter [Si] liquid formed by the continued reaction of gaseous magnesium with the elemental silicon generated upon the reduction of silica [26]. Thermodynamic calculations indicate that reaction (1) is strongly favored under these conditions [27]. Secondary electron images of reacted *Aulacoseira* and *Cyclotella* frustules are shown in Figure 2a and 2b, respectively. Although the frustule surfaces became more granular in appearance after reaction with Mg(g), the overall frustule shapes

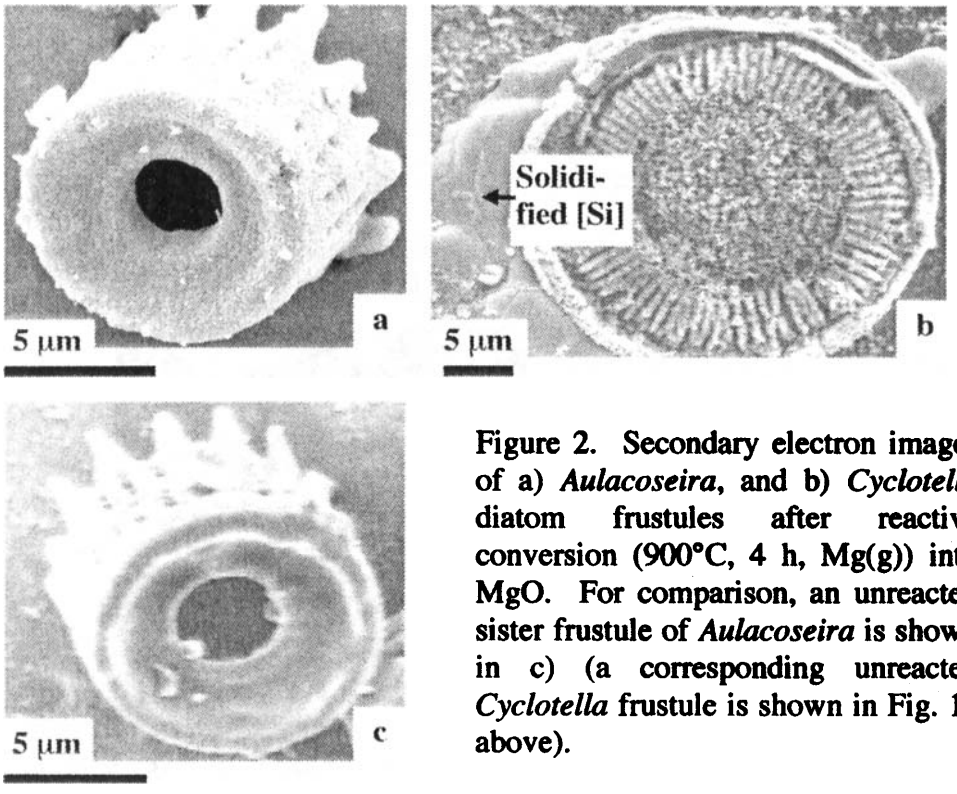

Figure 2. Secondary electron images of a) *Aulacoseira*, and b) *Cyclotella* diatom frustules after reactive conversion (900°C, 4 h, Mg(g)) into MgO. For comparison, an unreacted sister frustule of *Aulacoseira* is shown in c) (a corresponding unreacted *Cyclotella* frustule is shown in Fig. 1c above).

and fine features (mesoscale pores, grooves, protuberances) were retained. Energy-dispersive x-ray (EDX) analyses of the outside surfaces of these frustules during scanning electron microscopy revealed peaks for Mg and O, but not for Si, which was consistent with conversion of the SiO_2 into MgO. X-ray diffraction (XRD) analyses also yielded peaks for magnesia, but not for any crystalline silica polymorphs (such as quartz, cristobalite, or tridymite). The molten [Si] product of reaction (1) seeped out of the reacted frustules and solidified upon cooling. Such solidified [Si] can be seen below the reacted *Cyclotella* frustule in Fig. 2b. The reacted frustules could be easily plucked from this solidified Mg-Si (as was the case for the reacted *Aulacoseira* frustule shown in Fig. 2a).

The reacted frustules were also examined by transmission electron microscopy (TEM) in order to: i) evaluate the microstructure of the reaction product(s) and ii) determine whether unreacted silica was present below the magnesia detected on the frustule surface (note: subsurface amorphous silica can be difficult to detect by XRD or SEM/EDX analyses). Cross-sections of the wall of the reacted frustules were prepared by focused ion beam milling. Secondary electron images of a reacted *Aulacoseira* frustule at various stages of focused ion

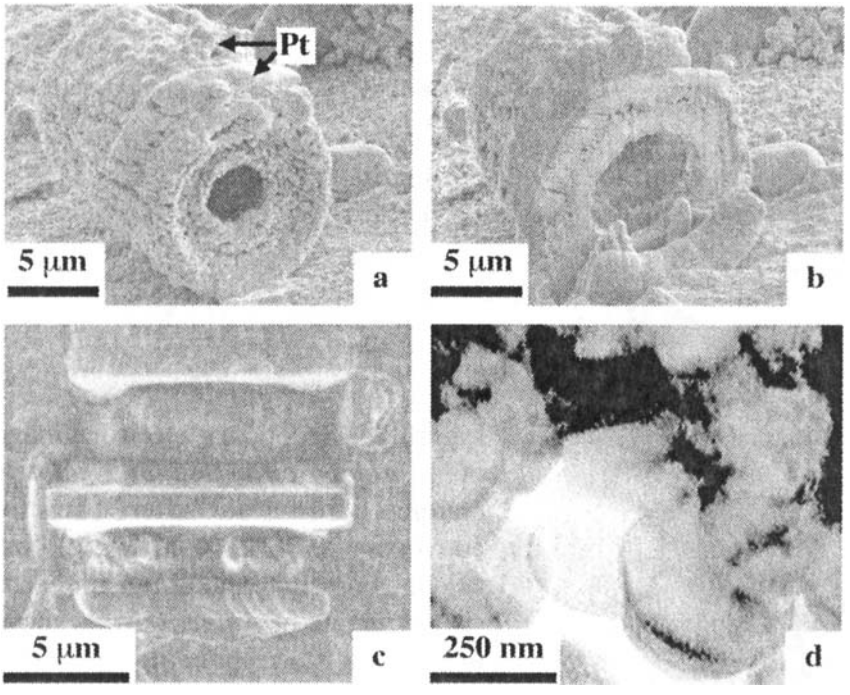

Figure 3. a), b), c) Secondary electron images of an *Aulacoseira* frustule after reaction for 4 h at 900°C with Mg(g). The image in a) reveals the frustule after deposition of a Pt coating. Side and top-down views of the wafer-shaped cross-section cut out by the focused ion beam are shown in b) and c). A bright field TEM image of this cross-section is shown in d).

beam milling are shown in Figs. 3a-c. The reacted frustule was first coated with a layer of platinum (Fig. 3a) in order to avoid fragmentation of the cross-section during milling. A focused ion beam was then used to remove material from both sides of a wafer-shaped cross-section, as shown in Figs. 3b and 3c. A bright field TEM image obtained from this cross-section is shown in Fig. 3d. Round grains with diameters of a few hundred nanometers were observed throughout the cross-section, which was consistent with the grain morphology observed on the surface of the reacted frustule by scanning electron microscopy (see Fig. 2a). TEM/EDX analyses of these rounded grains revealed peaks for Mg and O, but not for Si. The absence of silicon throughout the specimen cross-section confirmed that: i) the conversion of SiO_2 to MgO by reaction (1) was completed within 4 h at 900°C, and ii) the liquid [Si] product of this reaction had completely seeped out of the frustule during this heat treatment, apparently due to poor wetting with MgO.

Such poor wetting was also consistent with the weak adhesion of the solidified [Si] with the converted (MgO) frustules.

This work demonstrates the feasibility of the BASIC process. Biogenic oxide nanoparticle assemblies with complex three-dimensional shapes can be converted, via gas/solid reactions, into new compositions while retaining the same shapes and fine features. The mesoporous magnesia structures generated in the present work are attractive for a variety of uses, including: i) bioinert microcapsules for delivering very small doses of medication, ii) efficient filters for removing heavy metals from waste water, or for separating fine contaminant particles from basic fluids, iii) fine scale, controlled-shape (needles, tubes, disks, etc.), light weight (ρ[MgO] = 3.58 g/cm^3) filler or reinforcement phases for polymer-matrix composites, and iv) high-surface-area, chemically-compatible substrates for catalytic syntheses of certain petrochemicals [28-30].

Although the focus of this paper has been the shape-preserving conversion of certain diatom frustules into magnesia, the BASIC process is certainly not limited to these preforms or to MgO-based components. Self-assembled, three-dimensional bioclastic meso/nanostructures with a wide variety of other shapes, fine features, and chemistries could also be chemically modified (e.g., nanostructures of: silica from radiolaria, silicoflagellates, sponges; iron oxide from chiton teeth or bacteria; manganese oxides from fungi [12,31]). Other gaseous reactants than magnesium (e.g., reactive halides, organometallics, or other elemental gases) could be used in the conversion process to generate a host of oxide or oxide/metal products. Given such a large selection of possible shapes and chemical reactions, the BASIC process could be used to produce a multitude of meso/nanostructures with desired compositions for optimal electromagnetic, optical, thermal, chemical, or mechanical properties.

A wide diversity of frustule shapes, sizes, and fine surface features exists among the $\approx 10^5$ diatom species [11,12]. Given such natural variations in frustule geometry, it seems likely that many non-existing genomic modifications of diatom frustules may also be viable. If future genetic engineering yields frustules with tailored shapes and features (e.g., microneedles, micronozzles, microbearings, microchambers, etc.), then the shape-preserving gas/solid reactions of the type discussed in the present paper could be used to convert such shape-tailored preforms into preferred compositions for particular microdevice applications. Indeed, a unique coupling of genetic tailoring, biological replica-

CONCLUSIONS

Nanoparticle assemblies with complex 3D shapes and tailored chemistries have been fabricated by a novel, hybrid route: the BaSIC (Bioclastic and Shape-preserving Inorganic Conversion) process. With this process, biologically self-assembled ceramic (bioclastic) nanostructures can be converted into new compositions via the use of shape-preserving gas/solid reactions. To demonstrate this process, diatom microshells (i.e., silica nanoparticle assemblies) have been converted into magnesia. Several diatom species (*Aulacoseira*, *Cyclotella*, *Synedra*) with pennate or centric microshells (frustules) were obtained from algal cultures or as diatomaceous earth. After removal of organic material by pyrolysis, the frustules were exposed to magnesium vapor at 900°C. The Mg(g) underwent a displacement (oxidation-reduction) reaction with the amorphous SiO_2 in the frustules to yield MgO and Si dissolved in a Mg-rich liquid. The Mg-Si liquid seeped out of the frustule during the course of reaction (this liquid did not wet the MgO), so that the SiO_2 frustule was converted directly into MgO. TEM analyses indicated that the displacement reaction was completed within 4 h at 900°C. The resulting MgO nanoparticle assemblies retained the shapes and fine features (mesoscale pores, ridges, protuberances) of the starting frustules. Such MgO nanoparticle structures are attractive as mesoporous filters, mesoporous microcapsules, microfillers/reinforcements, and catalyst substrates for medical, environmental, and manufacturing applications. By choosing among numerous natural bioclastic nanostructures and reactant gases, the BASIC process could be used to produce meso/nanostructures with a wide variety of shapes, surface features, and compositions. Furthermore, if future genetic engineering of mineral-forming organisms yields bioclastic nanostructures with tailored shapes, then synergistic coupling of such genetic manipulation with the BASIC process would allow for the mass production of Genetically Engineered Microdevices (GEMs) for numerous domestic and military applications.

ACKNOWLEDGEMENTS

The authors are grateful to Dr. Monica Schoenwaelder (Alfred Wegener Institute for Polar and Marine Research, Bremerhaven, Germany) and Dr. Rex Lowe (Biology Dept., Bowling Green State University, Bowling Green, OH) for

informative discussions on diatom biology. Technical support provided by Mr. Cameron Begg (secondary electron microscopy) and Mr. Henk Colijn (x-ray diffraction, focused ion beam machining) is also acknowledged. Financial support was provided by the Air Force Office of Scientific Research (Grant No. F49620-01-1-0507; Dr. Joan Fuller, Dr. Paul Trulove).

REFERENCES

1. *Webster's Third New International Dictionary*, unabridged, Edited by P. B. Gove. Merriam-Webster, Springfield, MA, 1993.
2. M. Madou, *Fundamentals of Microfabrication*, CRC Press, New York, 1997.
3. C. S. Foong, K. L. Wood, and I. Busch-Vishniac, "Design Assessment of Micro-Electro-Mechanical Systems with Applications to a Microbiology Cell Injector"; pp. 49-63 in *Micromechanical Systems (MEMS) 1993*, Edited by A. P. Pisano, J. Jara-Almonte, and W. Trimmer. ASME, New York, 1993.
4. T.A. Desai, D. Hansford, M. Ferrari, "Characterization of Micromachined Silicon Membranes for Immunoisolation and Bioseparation Applications," *J. Membrane Sci.*, **159**, 221-231 (1999).
5. S. Britland, E. Perez-Arnaud, P. Clark, B. McGinn, P. Connolly, G. Moores, "Micropatterning Proteins and Synthetic Peptides on Solid Supports: A Novel Application for Microelectronics Fabrication Technology," *Biotechnol. Prog.*, **8**, 155 (1992).
6. C. van Rijn, M. van der Wekken, W. Nijdam, M. Elsenspoek, "Deflection and Maximum Load of Microfiltration Membrane Sieves made with Silicon Micromachining," *IEEE J. Microelectromech. Syst.*, **6** [1] 48-54 (1997).
7. M.W. Anderson, S.M. Holmes, N. Hanif, C.S. Cundy, "Hierarchical Pore Structures through Diatom Zeolitization," *Angew. Chem. Int. Ed.*, **39** [15] 2707-2710 (2000).
8. A.M. Flynn, L.S. Tavrow, S. F. Bart, R. A. Brooks, D. J. Ehrlich, K. R. Udayakumar, and L. E. Cross, "Piezoelectric Micromotors for Microrobots," *IEEE J. Microelectromech. Syst.*, **1** [1] 44-51 (1992).
9. A.H. Epstein and S.D. Senturia, "Macro Power from Micro Machinery," *Science*, **276**, 1211 (1997).
10. S. Mann and G.A. Ozin, "Synthesis of Inorganic Materials with Complex Form," *Nature*, **382**, 313-318 (1996).
11. F. E. Round, R. M. Crawford, D. G. Mann, *The Diatoms: Biology & Morphology of the Genera*, Cambridge University Press, 1990.
12. H. Tappan, *The Paleobiology of Plant Protists*, W. H. Freeman & Company, San Francisco, CA, 1980.
13. J.C. Lewin and R.R.L. Guillard, "Diatoms," *Annual Rev. Microbiol.*, **17**, 373-414 (1963).
14. J. Parkinson and R. Gordon, "Beyond Micromachining: the Potential of Diatoms," *Trends in Biotechnology*, **17** [5] 190-196 (1999).
15. S. A. Crawford, M. J. Higgins, P. Mulvaney, R. Wetherbee, "Nanostructure of the Diatom Frustule as Revealed by Atomic Force and Scanning Electron Microscopy," *J. Phycol.*, **37**, 543-554 (2001).

16. R. W. Eppley, "The Growth and Culture of Diatoms," pp. 24-64 in *The Biology of Diatoms*. Edited by D. Werner. Univ. California Press, Berkeley, CA, 1977.
17. U. Anderegg, S. Vorberg, K. Hermann, U. F. Haustein, "Silica Directly Induces Intercellular Adhesion Molecule 1 (ICAM-1) Expression in Cultured Endothelial Cells," *Eur. J. Dermatol.*, **7** [1] 27-31 (1997).
18. M.C. Breslin, J. Ringnalda, L. Xu, M. Fuller, J. Seeger, G.S. Daehn, T. Otani, and H.L. Fraser, "Processing, Microstructure and Properties of Co-Continuous Alumina/Aluminum Composites," *Mater. Sci. Eng.*, **A195**, 113-119 (1995).
19. R. E. Loehman, K. G. Ewsuk, A. P. Tomsia, "Synthesis of Al_2O_3-Al Composites by Reactive Metal Penetration," *J. Am. Ceram. Soc.*, **79** [1] 27-32 (1996).
20. F. Wagner, D. E. Garcia, A. Krupp, N. Claussen, "Interpenetrating Al_2O_3-$TiAl_3$ Alloys Produced by Reactive Infiltration," *J. Euro. Ceram. Soc.*, **19**, 2449-2453 (1999).
21. C. Scheu, G. Dehm, W. D. Kaplan, F. Wagner, N. Claussen, "Microstructure and Phase Evolution of Niobium-Aluminide-Alumina Composites Prepared by Melt-Infiltration," *Phys. Stat. Sol. (a)*, **166**, 241-255 (1998).
22. K.A. Rogers, P. Kumar, R. Citak, K.H. Sandhage, "The Fabrication of Dense, Shaped Ceramic/Metal Composites at ≤1000°C by the Displacive Compensation of Porosity," *J. Am. Ceram. Soc.*, **82** [3] 757-60 (1999).
23. P. Kumar and K.H. Sandhage, "The Displacive Compensation of Porosity (DCP) Method for Fabricating Dense, Shaped, High-Ceramic-Bearing Bodies at Modest Temperatures," *J. Mater. Sci.*, **34** [23] 5757-5769 (1999).
24. M.B. Dickerson, R.L. Snyder, and K.H. Sandhage, "Dense, Near Net-Shaped Carbide/Refractory Metal Composites at Modest Temperatures by the Displacive Compensation of Porosity Method," *J. Am. Ceram. Soc.*, in press.
25. K.H. Sandhage, "Shaped Microcomponents via Reactive Conversion of Biologically-derived Microtemplates," *U.S. Patent Application*, under review.
26. A.A. Nayeb-Hashemi and J.B. Clark, "The Mg-Si (Magnesium-Silicon) System," *Bull. Alloy Phase Diagrams*, **5** [6] 584-592 (1984).
27. I. Barin, *Thermochemical Data of Pure Substances*, VCH Verlagsgesellschaft, Weinheim, Germany, pp. 868, 1359, 1360, 1989.
28. J.S. Lindberg, M.M. Zobitz, J.R. Poindexter, C.Y.C. Pak, "Magnesium Bioavailability from Magnesium Citrate and Magnesium Oxide," *J. Am. Coll. Nutr.*, **9** [1] 48-55 (1990).
29. D.N. Tallman and J.E. Pahlman, "Magnesium Oxide Filtration Research," *Information Circular No. 9138*, U.S. Bureau of Mines, Minneapolis, MN, 1987.
30. T. Klicpera, M. Zdrazil, "High Surface Area MoO_3/MgO: Preparation by Reaction of MoO_3 and MgO in Methanol or Ethanol Slurry and Activity in Hydrodesulfurization of Benzothiophene," *Appl. Catal. A*, **216** [1] 41-50 (2001).
31. H.A. Lowenstam and S. Weiner, "Mineralization by Organisms and the Evolution of Biomineralization," pp. 191-203 in Biomineralization and Biological Metal Accumulation, Edited by P. Westbroek and E. W. de Jong, D. Reidel Publishing Company, Dordrecht, Holland, 1983.

SILICON NITRIDE/SILICON CARBIDE NANOCOMPOSITES FROM POLYMER PRECURSOR

Julin Wan, Matthew J. Gasch and Amiya K. Mukherjee
Department of Chemical Engineering and Materials Science
University of California
Davis, CA 95616

ABSTRACT

Nanocomposites of silicon nitride and silicon carbide were processed by different routes based on polymer precursor pyrolysis. Electric field assisted sintering (EFAS) can lead to either micro-nano or nano-nano composites, depending on the amount of oxide additive. In-situ pyrolysis/consolidation produced nano-nanocomposites with bi-crystal boundaries free of glassy grain boundary phases, while small amount of residual amorphous Si-C-N phase is retained at triple junctions. High pressure sintering results in a diversity of microstructures, from amorphous to nanocrystalline. The details of the microstructures were studied by high-resolution transmission electron microscopy (HRTEM).

INTRODUCTION

Over the past decade, inorganic polymer precursor related techniques have evolved from an effective means for making low-dimension materials (powders, fibers, coatings), to techniques that are capable of processing bulk ceramics.[1,2] The traditional way of producing silicon nitride/silicon carbide composites is sintering of powder mixtures of crystalline silicon nitride and silicon carbide. This kind of technique has two intrinsic problems: one is the effectiveness of mixing, the inadequacy of which might lead to inhomogeneity of the microstructure; the second problem is that, the grain size of the sintered material is limited by the crystallite size of the starting powders, this makes it difficult to manufacture nanocomposites (with mean grain size smaller than 100 nm).[3] Polymer precursor related techniques can provide a solution to these problems. The pyrolysis product of the polymer precursor is usually amorphous Si-C-N, in which the component elements are mixed homogenously to the molecular level. Through a certain crystallization process, this amorphous network can be transformed into silicon nitride and silicon carbide composites with the two phases homogenously dispersed.[4] The grain size of the composites from crystallization of the amorphous Si-C-N is determined by the nucleation and grain growth, it is irrelevant to the particle size of the powder. Furthermore, the chemical composition of the amorphous Si-C-N pyrolysis product is determined by the chemistry of the polymer precursor, and also is sensitive to the environmental atmosphere of pyrolysis, therefore can be manipulated to produce different phase compositions.[5,6] These characteristics of the polymer precursor-related techniques guarantee that it is possible to achieve some unique microstructures that cannot be produced by conventional methods, especially nanocrystalline composites.

This paper is a short review of the efforts made at University of California, Davis, in obtaining nanocrystalline composites of silicon nitride and silicon carbide. The target of this research is to evaluate the high temperature mechanical property (mainly creep resistance and

superplasticity) of covalent ceramics when the grain size falls into nanometric range. However, since the mechanical testing is still underway, only issues of processing and microstructure will be discussed in this report.

EXPERIMENTAL PROCEDURE

Raw material and polymer manipulation

Commercially available Ceraset SN polyureasilazane (Commodore Polymer Technologies, Columbus, OH.) was used as the raw material. The liquid polymer was cross-linked in nitrogen atmosphere at 260°C with 0.5wt% dicumyl peroxide as catalyst. Infusible polymer thus obtained was crushed into powder with a mean particle size of about 10 microns. Pyrolysis of the polymer powder towards 1450°C leads to amorphous Si-C-N with a nominal formula of $Si_{1.00}C_{1.55}N_{0.81}O_{0.17}$. Increase of nitrogen content in the amorphous powder can be realized by a heat-treatment at temperatures between 300~800°C, before the pyrolysis is completed. The replacement of carbon-containing functional groups (e.g., $-CH_3$) by $-NH_2$ is responsible for this increase in nitrogen.[7] This treatment was used in the EFAS and in-situ pyrolysis/consolidation.

Sintering by electric field assisted sintering (EFAS)

EFAS conducted with Dr. Sinter® 1050 spark plasma sintering system (Sumitomo Coal Mining Company, Ltd.), using 1450°C pyrolyzed Si-C-N powder with varied amount of yttria additive and varied nitrogen content. After applying the given pressure (63MPa), samples were heated to 600°C in 2 minutes and then ramped to 1600°C at a fixed rate of 100°C/min. Temperature was held at 1600°C for 10 minutes before turning off the power.

In-situ pyrolysis/consolidation

The consolidation of the materials without using additives was conducted through a route called pre-pyrolysis/binding/pyrolysis. This processing method has been described elsewhere.[8] The cross-linked powder was partially ceramized by a pre-pyrolysis heat-treatment at 400-800°C, then coated with Ceraset SN liquid polymer and pressed into shape by cold isostatic pressing. The green compacts were then pyrolyzed to about 1000°C to obtain amorphous Si-C-N ceramics. A further heat-treatment at temperatures between 1550-1650°C was necessary to crystallize the material into composites of silicon nitride and silicon carbide. Ammonia treatment was conducted before the pre-pyrolysis to alter nitrogen content.

High pressure sintering (HPS)

The polymer powder was heat-treated in nitrogen atmosphere at 1450°C/4hours for complete ceramization. The amorphous Si-C-N powder thus derived was mixed with 8wt%Y_2O_3, or 5wt% Y_2O_3 plus 5wt% $MgAl_2O_4$ by high-energy ball milling. Sintering was conducted with a Boyd-England piston-cylinder apparatus, at temperatures 1400-1600°C and under pressure of 1-2GPa. In order to prevent grain growth, the sintering duration was kept at about 10 minutes. Details about the experimental set-up for this method can be found elsewhere.[9]

RESULTS AND DISCUSSION

EFAS-processed nanocomposites

EFAS is analogous to conventional hot-pressing, except that a pulsing electric current passes the die/punch assembly during sintering. Like in hot pressing, sintering of amorphous Si-C-N with a high amount of additive (e.g., 8wt% Y_2O_3) leads to micro-nano structure of silicon nitride/silicon carbide composites (Fig. 1(a)), which is a sub-micron matrix of silicon nitride and silicon carbide, with nanometric SiC inclusions in silicon nitride grains. One unique feature of these composites made from amorphous Si-C-N is that they usually contain turbostratic graphite at the intergranular

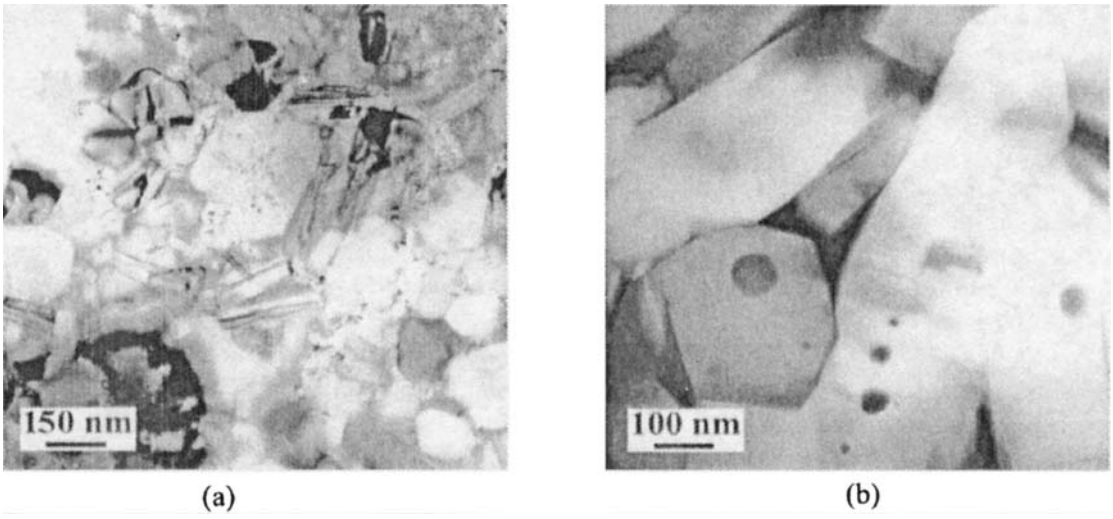

Fig. 1 Micro-nano composites processed by EFAS of amorphous Si-C-N with 8wt% Y_2O_3, starting with powders
(a) pyrolyzed in nitrogen to 1450°C
(b) subjected to 600°C/1hr ammonia treatment before pyrolyzed to1450°C in N_2

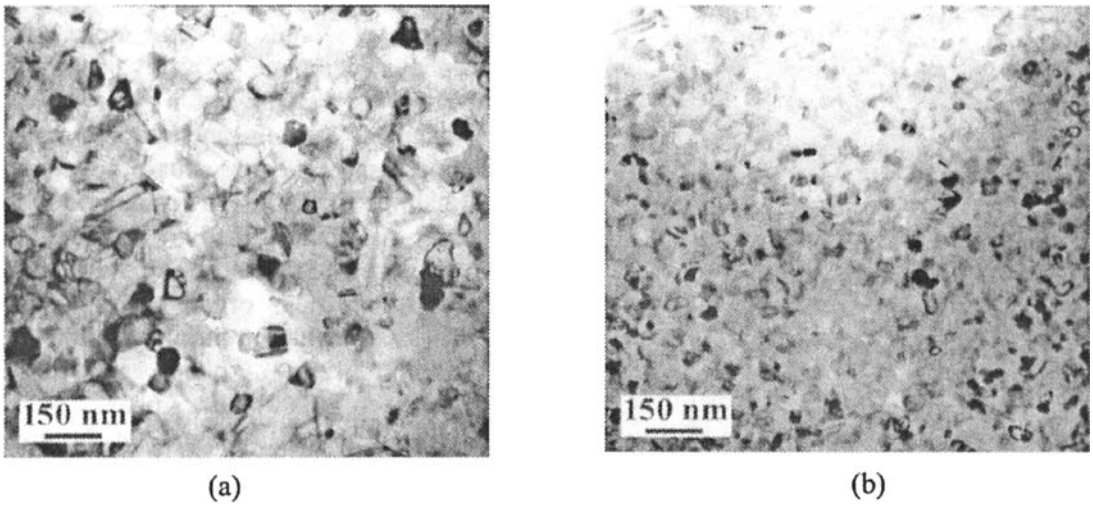

Fig. 2 Nano-nano composites processed by EFAS of amorphous Si-C-N at 1600°C/10min with
(a) 3wt% Y_2O_3 (b) 1wt% Y_2O_3

regions, as a result of the excess carbon content in the amorphous Si-C-N. Decrease of carbon content by an ammonia treatment to the polymer precursor prior to the pyrolysis can lead to decrease of the intergranular graphite phase, along with the phase ratio of SiC versus Si_3N_4.

This pre-pyrolysis ammonia treatment was found to be most effective if conducted at around 600°C, as a result of the compromise between the number of available active functional groups and the thermal activation of the group-exchange reactions. A 600°C/1hr ammonia treatment to the polymer powder can result in X-ray pure silicon nitride after EFAS. The grain size of the

sintered material, as shown in Fig. 1(b), is larger than the composite sintered from powders without ammonia-treatment, due to the lack of grain-growth restriction from silicon carbide. However, it can be seen that there still is a small amount of intragranular SiC in silicon nitride grains.

Decrease of additive amount results in decreased amount of liquid phase during sintering of the materials. Liquid phase sintering mechanisms, mainly the solution-reprecipitation process, plays a less dominant role in these cases. Solid-state processes such as diffusion become more important. Solid-state sintering mechanisms have a slower kinetics than liquid phase sintering, therefore they require a longer time to reach full density. However, in the case of EFAS, effective sintering can be achieved at 1600°C within 10 minutes, when the yttria content is as low as 1wt%.[10]

The most significant effect the amount of additive has on the microstructure of the sintered composites is shown in Fig. 2. When the weight percentage of yttria decreases from 8% to under 3%, the microstructure changes from micro-nano structure to a nano-nano structure with the grain size of both the silicon nitride and silicon carbide phases falls into the nanocrystalline regime. The mean grain size of the 1wt% Y_2O_3 sample is as small as 38 nm. This retarded grain growth is believed to be a result of the lack of a continuous liquid phase, which inhibits the process of grain growth by the mechanism of solution-reprecipitation.

Nanocomposites processed by in-situ pyrolysis/consolidation

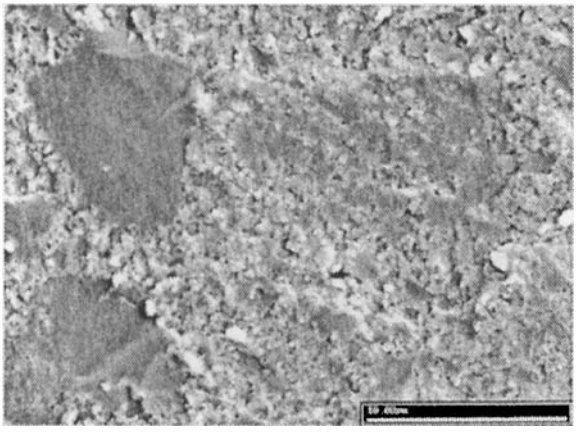

Fig. 3 Fracture surface of the consolidated amorphous Si-C-N

The crucial point of producing nanocomposites by this technique is to produce a consolidated, crack-free amorphous ceramic body by controlled pyrolysis. The conversion of polymer precursor into ceramics includes removal of oligomers and other gaseous products and the retaining of the Si-C-N backbone of the polymer molecules. Due to the fact that pre-pyrolyzed particles are already devoid of most of their organic components, weight-loss, volume shrinkage and gas evolution during pyrolysis are mostly restricted to the binder phase, which accounts of about 15~25wt% of the green body. As a result, in comparison with the warm-pressing/pyrolysis method to make bulk amorphous Si-C-N, which is based on pyrolysis of entirely polymer green compacts, the present method features higher density (~2.3g/cm^3), lower volume shrinkage, and the materials are less prone to cracking therefore larger viable size.[8] Another important feature in the amorphous Si-C-N produced by this approach is that the materials are virtually free of open porosity, as indicated by mercury porosimetry.[8] The amorphous Si-C-N contains small amount of closed pores with nanometric size, shown in Fig. 3.

The stability of the amorphous ceramic network of the pyrolysis product was found to be strongly dependent on the chemistry of the pre-pyrolyzed powder.[7, 11] Without ammonia treatment, the amorphous ceramics can resist crystallization up to 1450°C.

Heat-treatment at 1550°C leads to partially crystallization of the material. Si_3N_4, SiC as well as Si_2N_2O grains were found to develop independently within the amorphous network.

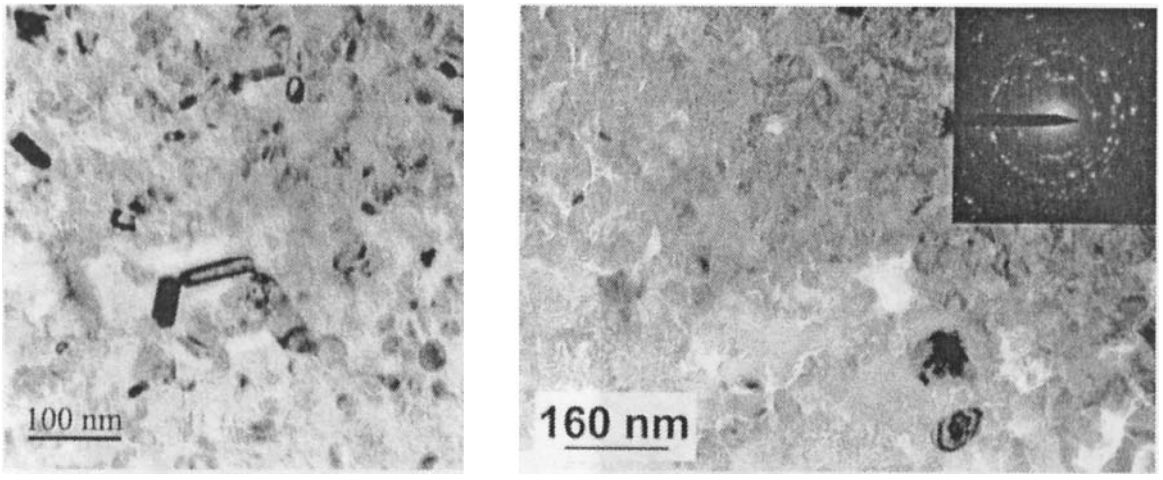

(a) (b)

Fig 4 Nanocrystalline microstructures obtained by crystallization of consolidated amorphous ceramics
(a) Without ammonia treatment, crystallized at 1650°
(b) Ammonia treated at 600°C, crystallized at 1450°C

Turbostratic graphite, which is a common feature of Si-C-(N) ceramics when there is excess amount of carbon, was also observed. Crystallization at 1650°C for 2 hours results in Si_3N_4/SiC nano-nano composite with a mean grain size of about 30nm, as can be seen in Fig. 4 (a). While if the pre-pyrolyzed powder was treated in ammonia at 600°C, at 1450°C the material is already fully crystalline, with α-Si_3N_4 as the only phase detectable by XRD or SAD (Fig. 4(b)). This enhanced crystallization is a result of the enhanced role of the interface between the pre-pyrolyzed particles and the binder phase in accelerating the crystallization process (inhomogeneous crystallization).

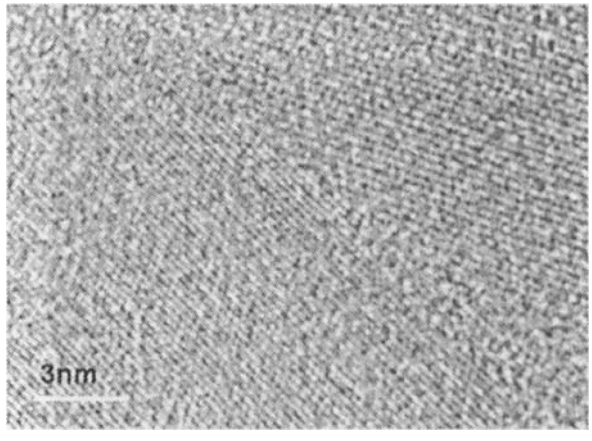

Fig. 5 Grain boundary in the nano-composites produced by crystallization of amorphous Si-C-N

Due to the lack of oxide additive, most of the dual-grain junctions (grain boundaries) were found to be free of a glassy grain boundary phase (Fig. 5), although it is apparent that a residual amorphous phase exists at multi-junctions.

Nanocomposites produced by high pressure sintering

High pressure sintering (HPS) was attempted in an effort to make superplastic nanocomposites. Since the established superplastic deformation mechanism in silicon nitride

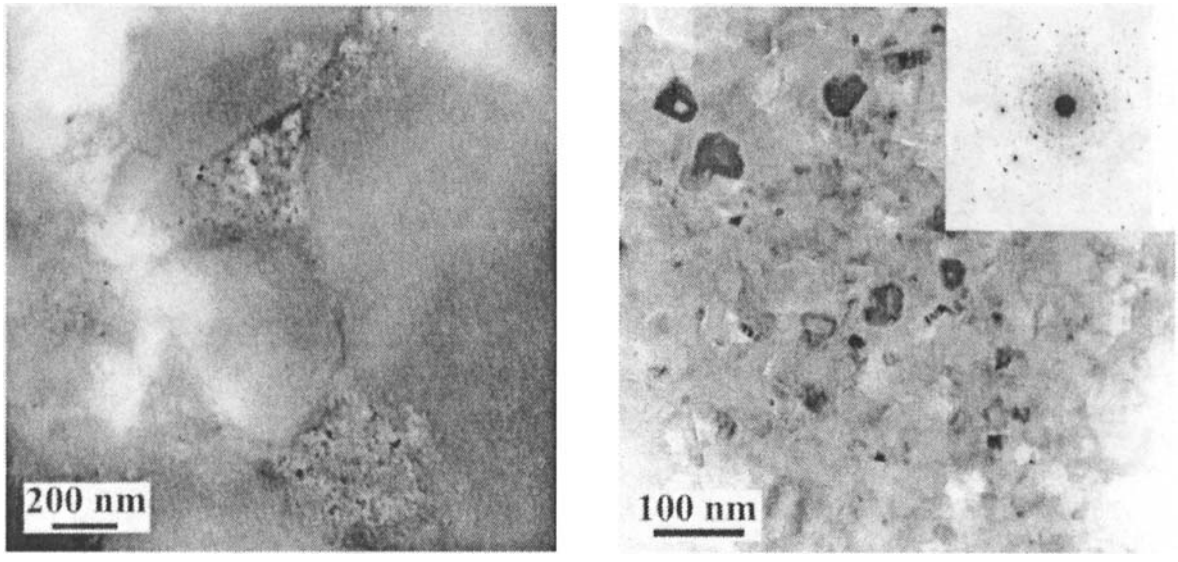

(a) (b)

Fig. 6 Microstructure of materials sintered by HPS from amorphous Si-C-N with yttria additive (a) 1400°C/10min (b) 1600°C/10min

ceramics is liquid-phase based solution-precipitation, a high level of oxide additive (equivalent to larger amount of liquid phase at high temperatures) is likely to be necessary. With the two routes introduced above, nano-nano microstructure cannot be achieved when the additive amount is too high (e.g., >5wt%Y_2O_3). The two types of sintering additives used in this study, one is 8wt% Y_2O_3 and the other is 5wt% Y_2O_3 plus 5wt% $MgAl_2O_4$, represent additive systems that are likely to produce high viscosity and low viscosity glassy phases after sintering

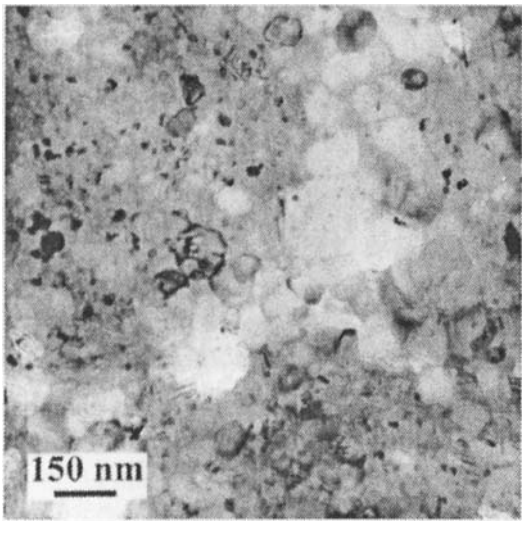

Fig. 7 Inhomogeneous microstructure in nanocomposites produced by HPS (1600°C/10min) of Si-C-N containing 5wt%Y_2O_3/ 5wt%$MgAlO_4$

Between the sintering temperatures 1400-1600°C, the materials can be sintered to densities of 2.85-2.96g/cm^3. XRD shows increasing crystallinity with increasing temperature. TEM images of the materials with 8wt% Y_2O_3 as additive are shown in Fig. 6. Although the material sintered at 1400°C is amorphous as shown by XRD, there are regions that have undergone preliminary crystallization, and have crystallites (mainly silicon nitride) of about 10nm immersed in an amorphous matrix, as shown in Fig. 6 (a). Sintering at 1500°C results in crystallization of most of the material. While only regions that was originally occupied by extremely large Si-C-N particles remain amorphous, these regions were found to be depleted of yttrium and oxygen as compared with the rest of the material. Sintering at 1600°C

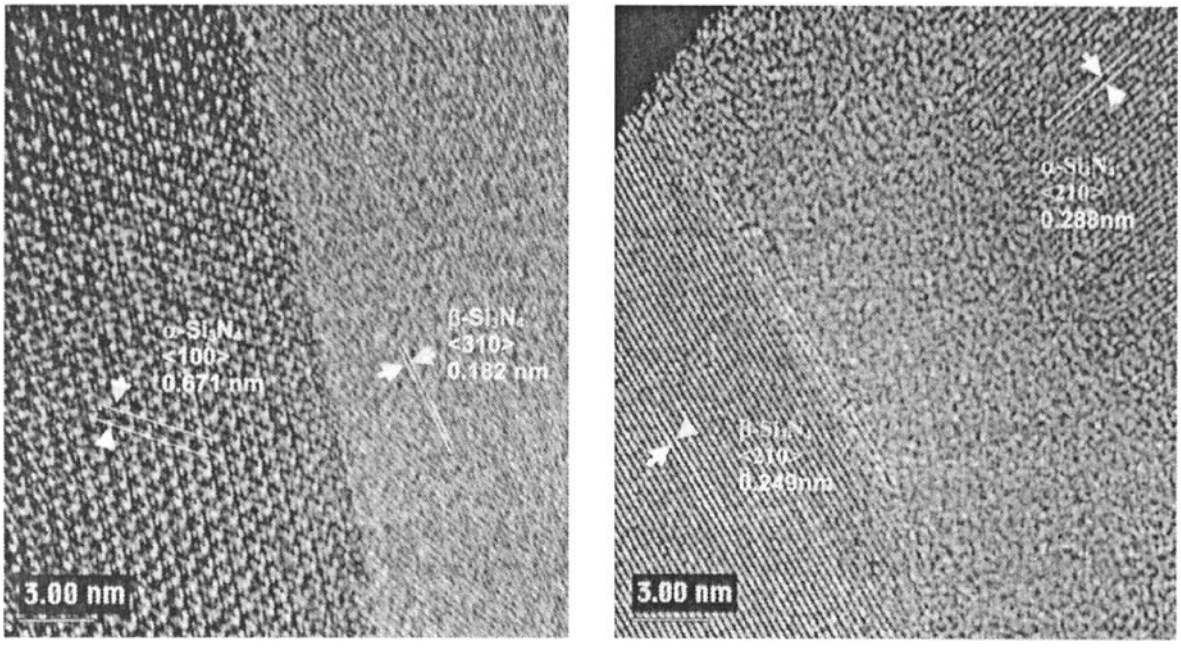

(a) (b)

Fig. 8 Examples of the grain boundary condition in HPS produced nanocomposite (with 8wt%Y_2O_3, sintered 1600°C/10min)
(a) Glass-free boundary (b) Boundary with thick glassy phase

for 10 minutes lead to full crystallization and the grain size of both silicon nitride and silicon carbide phases are about 50nm, see Fig. 6(b). Two kinds of mechanisms are involved: (1) the solution of the Si-C-N by the oxynitride liquid phase and precipitation of silicon nitride and silicon carbide grains; this mechanism proceeds from the intergranular regions into the interior of the Si-C-N particles; (2) homogeneous crystallization of the Si-C-N into crystalline phases; this is a solid state process that is enhanced by the high applied pressure during sintering

The microstructure of the material with 5wt%Y_2O_3/5wt%$MgAl_2O_4$ at 1600°C is shown in Fig.7. This microstructure indicates an inhomogeneous grain size distribution at different regions of the material. In some locations silicon nitride and silicon carbide forms a nice nano-nano structure. In other regions, silicon nitride grains can grow to as large as 200nm, and engulf nano-sized SiC to form a micro-nano structure. This inhomogeneity in grain size reflects the inhomogeneous distribution of oxide additive, and thus the abundance of liquid phase of low viscosity (due to the existence of spinel) promotes grain growth; while the interior regions undergo solid-state crystallization, which is of much slower kinetics. The grain size inhomogeneity also exists in the 8wt%Y_2O_3 material, but to a much less extent, owing to the higher viscosity of liquid phase.

The most distinct feature of the grain boundary condition of the HPSed nanocomposites is the widespread distribution of thickness of grain boundary amorphous layer. Unlike in conventional silicon nitride, in which the grain boundary thickness is relatively narrowly distributed (0.5-2.0nm),[1] the grain boundary thickness in the nanocomposites can be near to zero, or to over 10nm. Examples are shown in Fig. 8 for grain boundaries between α- and β-Si_3N_4. It is still an open question whether this unique feature of grain boundary is due to the nonequilibrium

nature of the processing technique (high pressure, low temperature sintering), or alternatively a result of the unique chemistry of the grain boundary phase which contains excess carbon.

SUMMARY

Three categories of processing routes have been attempted to make silicon nitride/silicon carbide nanocomposites with varied grain-size, phase proportion and grain boundary conditions. All of the methods are capable in producing nano-nanocomposites with grain-size far below 100nm. EFAS is suitable to produce nano-nano composites when additive amount is low, while micro-nano composites were resulted with high additive level; In-situ pyrolysis/consolidation can produce nano-nano composites without additive; HPS is the viable way to produce nano-nanocomposites with large amount of additive, while the homogeneity of the microstructure is dependent on the viscosity of the grain boundary phase. The high temperature properties of the nanocomposites are yet to be determined.

ACKNOWLEDGMENT

This research is supported by the US Office of Naval Research (Grant No. N00014-00-1-0186). Thanks to Chris Nelson of NCEM for his help in gathering TEM data.

REFERENCES

[1]J. Bill and F. Aldinger, "Precursor-Derived Covalent Ceramics"; pp. 33-51 in *Precursor-Derived Ceramics*, Edited by J. Bill, F. Wakai and F. Aldinger. Wiley-VCH, Weinheim, 1999.

[2] E. Kroke, Y.-L. Li, C. Konetschny, E. Lecomte, C. Fasel, R. Riedel, "Silazane Derived Ceramics and Related Materials", *Mater. Sci. Eng.*, **R26**, 97-199 (2000).

[3] M. Sternitzke, "Review: Structural Ceramic Nanocomposites," *J. Europ. Ceram. Soc.*, **17**, 1061-1082 (1997).

[4] H. J. Kleebe, D. Suttor, H. Müller and G. Ziegler, "Decomposition-Crystallization of Polymer-Derived Si-C-N Ceramics," *J. Am. Ceram. Soc.*, **81**, 2971-2977 (1998).

[5] G. T. Burns and G. Chandra, "Pyrolysis of Preceramic Polymers in Ammonia: Preparation of Silicon Nitride Powders," *J. Am. Ceram. Soc.*, **72**, 333-337 (1989).

[6] D. Galusek, S. Reschke, R. Riedel, W. Dressler, P. Sajgalik, Z. Lences and J. Majling, "In-Situ Carbon content Adjustment in Polysilazane Derived Amorphous SiCN Bulk Ceramics," *J. Europ. Ceram. Soc.*, **19**, 1911-1921 (1999).

[7] J. Wan, M. J Gasch,. A.K. Mukherjee, "Effect of Ammonia Treatment on the Crystallization of Amorphous Si-C-N Ceramics Derived from Polymer Precursor Pyrolysis," accepted by *J. Am. Ceram. Soc.*

[8]J. Wan, M. J. Gasch and A. K. Mukherjee, "Silicon Carbonitride Ceramics Produced by Pyrolysis of Polymer Ceramic Precursor," *J. Mater. Res.*, **15** [8] 1657-1660 (2000).

[9] M.J. Gasch, J. Wan and A.K. Mukherjee, "Preparation of a Si_3N_4/SiC Nanocomposite by High-Pressure Sintering of Polymer Precursor Derived Powders," *Scripta Mater.*, **45**, 1063-1068 (2001).

[10] J. Wan, M.J. Gasch and A. K. Mukherjee, "Nano-nano Composites of Silicon Nitride and Silicon Carbide Fabricated by Electric Field Assisted Sintering," submitted to *J. Am. Ceram. Soc.*.

[11] J. Wan, M. J. Gasch, A. K. Mukherjee, "Consolidation and Crystallization of Si_3N_4/SiC Nanocomposites from a Poly(urea-silazane) Ceramic Precursor," *J. Mater. Res.*,**16**, 3274-3286 (2001).

[12] H.-J. Kleebe, M. K. Cinibulk, R. M. Cannon and M. Rüler, "Statistical Analysis of the Intergranular Film Thickness in Silicon Nitride Ceramics," *J. Am. Ceram. Soc.*, **76**[8] 1969-77 (1993).

PROPERTIES OF Si_3N_4 - $MoSi_2$ COMPOSITES WITH A NANOSTRUCTURED MATRIX

D. Sciti, S. Guicciardi, A. Bellosi
CNR-IRTEC, Via Granarolo 64, I – 48018 Faenza, Italy

ABSTRACT

Si_3N_4 - composite materials containing different amounts of $MoSi_2$ were produced by hot pressing. $MoSi_2$ particles (mean size 0.8 μm) were homogeneously dispersed within a nanostructured Si_3N_4 matrix (mean grain size < 0.2 μm). The influence of $MoSi_2$ inclusions on microstructure and electrical and mechanical properties of the composites is discussed.

As a result of both the refined microstructure of the matrix and presence of ductile inclusions, these materials possess good mechanical properties, with a bending strength up to 1130 MPa (RT) and 880 MPa (1000°C) and a fracture toughness up to 6 MPa·m ^{½}. Electrical resistivity drops to ~10^{-3} Ω·cm.

INTRODUCTION

Silicon nitride and molybdenum disilicide have recently attained a considerable attention as matrix and/or reinforcing phase for the development of high performance structural or functional ceramic composites. [1-4]

Silicon nitride is one of the most important structural ceramic materials because of its combination of high-temperature refractoriness, high strength, low thermal expansion coefficient, low density and high-temperature oxidation resistance. Silicon nitride is difficult to densify due to the low diffusion coefficient. Conventionally fully dense materials can be obtained through liquid-phase sintering with the addition of sintering aids. The addition of $MoSi_2$ can further improve the performance of Si_3N_4, especially if a suitable control of the morphology, particle size and degree of dispersion of the second phase is performed. An important factor is the amount of $MoSi_2$: if it is higher than about 30 vol %, the resulting composite is electroconductive. This is advantageous from different points of view: on one hand the materials associate electroconductive functions to enhanced thermo-mechanical behaviour, on the other hand complex shapes can be made by electrodischarge machining starting from simple shaped pieces. These composites can be used in electrical applications such as heaters and igniters.

In this paper, composites containing different amounts of $MoSi_2$ were produced by hot pressing. Alumina and yttria are the additives selected for the densification of Si_3N_4. This system (Si_3N_4 + Al_2O_3 +Y_2O_3) has been studied previously and picked as the matrix for the present composite materials due to its high sinterability and excellent mechanical properties such as fracture toughness and flexural strength. [5]

EXPERIMENTAL

Commercial powders were used as raw materials. Their main characteristics are indicated below.

- Si_3N_4 powder (Ube-SN-E10): 95 vol % α-Si_3N_4 and 5 vol % β-Si_3N_4, specific surface area: 11.5 m^2/g, mean particle size: 0.16 μm, chemical composition: O:1.09 %, Cl: 0.01 %, Fe: 0.01 %, Ca: 0.005 %, Al: 0.005 %;

- $MoSi_2$ (Aldrich): purity 99 %, mean particle dimension 1-2 μm, d_{50} 2.7-2.8 μm, crystalline phase: tetragonal $MoSi_2$.

As sintering aids for the Si_3N_4 matrix, Al_2O_3 Ceralox HPa0.5 and Y_2O_3 HC-Starck, were selected. The following compositions were prepared:

- 64.5 vol % Si_3N_4 + 30 vol % $MoSi_2$+ 1.8 vol % Al_2O_3 + 3.7 vol % Y_2O_3, labelled SN3
- 55.3 vol % Si_3N_4 + 40 vol % $MoSi_2$+ 1.5 vol % Al_2O_3 + 3.2 vol % Y_2O_3, labelled SN4.

The powders were mixed by ball milling using Si_3N_4 balls for 24 h in ethyl alcohol. Then they were dried using a rotary evaporator and sieved. Sintering was performed by hot-pressing at 1720 - 1740°C with an applied pressure of 30 MPa and holding time of 10 min, in vacuum. The final densities were determined using Archimede method.

Dense samples were examined by X-ray diffraction (XRD) to determine crystalline phases. The specimens were cut, polished and etched in a O_2/CF_4 plasma. The microstructures were observed by SEM; micrographs of selected samples were analysed by image analysis (Image Pro-plus 4.0, Media Cybernetics, Silver Springs, USA) to determine mean grain size of $MoSi_2$ inclusions and of Si_3N_4 matrix grains.

Young modulus (E) was measured by resonant frequency on specimens of 28 × 8 × 0.8 mm^3 using an H&P gain-phase analyser.

On polished surfaces, Vickers microhardness (HV) was measured with a load of 9.81 N, using a Zwick 3212 tester.

Fracture toughness (K_{Ic}) was evaluated using the chevron-notched beam (CNB) in flexure. The bars, 25 x 2 x 2.5 mm^3 (length x width x thickness, respectively) were notched with a 0.08 mm diamond saw; α_0 and α_1 were about 0.12 and 0.80, respectively. The flexural tests were performed on a semi-articulated alumina four-pt jig with a lower span of 20 mm and an upper span of 10 mm on an Instron mod.1195 universal screw-type testing machine. The specimens, three for each composition, were deformed with a crosshead speed of 0.05 mm/min. The "slice model" equation of Munz et al. [6] was used for the calculation of K_{Ic}.

Flexural strength (σ), up to 1300°C, was measured with an Instron mod 6025, on chamfered bars of 25 × 2 × 2.5 mm^3 (length × depth × width), in 4-pt bending with 20 mm and 10 mm as outer span and inner span, respectively, using a crosshead speed of 0.5 mm/min. For high temperature tests, a soaking time of 18 min was set to reach thermal equilibrium before starting the test.

The electrical resistivity measurements were carried out using a four probe DC method at room temperature, inducing a current in bar specimens of 2 x 2.5 x 25 mm^3.

RESULTS AND DISCUSSION

Microstructure

The composites reached full density after the hot-pressing route, as confirmed by the absence of porosity ascertained through microstructural analyses. As crystalline phases, both α- and β-Si_3N_4 and tetragonal $MoSi_2$ are present. No reaction occurred between $MoSi_2$ and Si_3N_4 as already reported in literature.[2]

In Fig. 1a,b, an example of polished surface of the composites is shown. $MoSi_2$ inclusions present a brighter contrast than the silicon nitride matrix. In spite of the difference between thermal expansion coefficients ($MoSi_2$: $9 \cdot 10^{-6}$ °C^{-1}, Si_3N_4: $3 \cdot 10^{-6}$ °C^{-1}), good adhesion was found between the two phases.

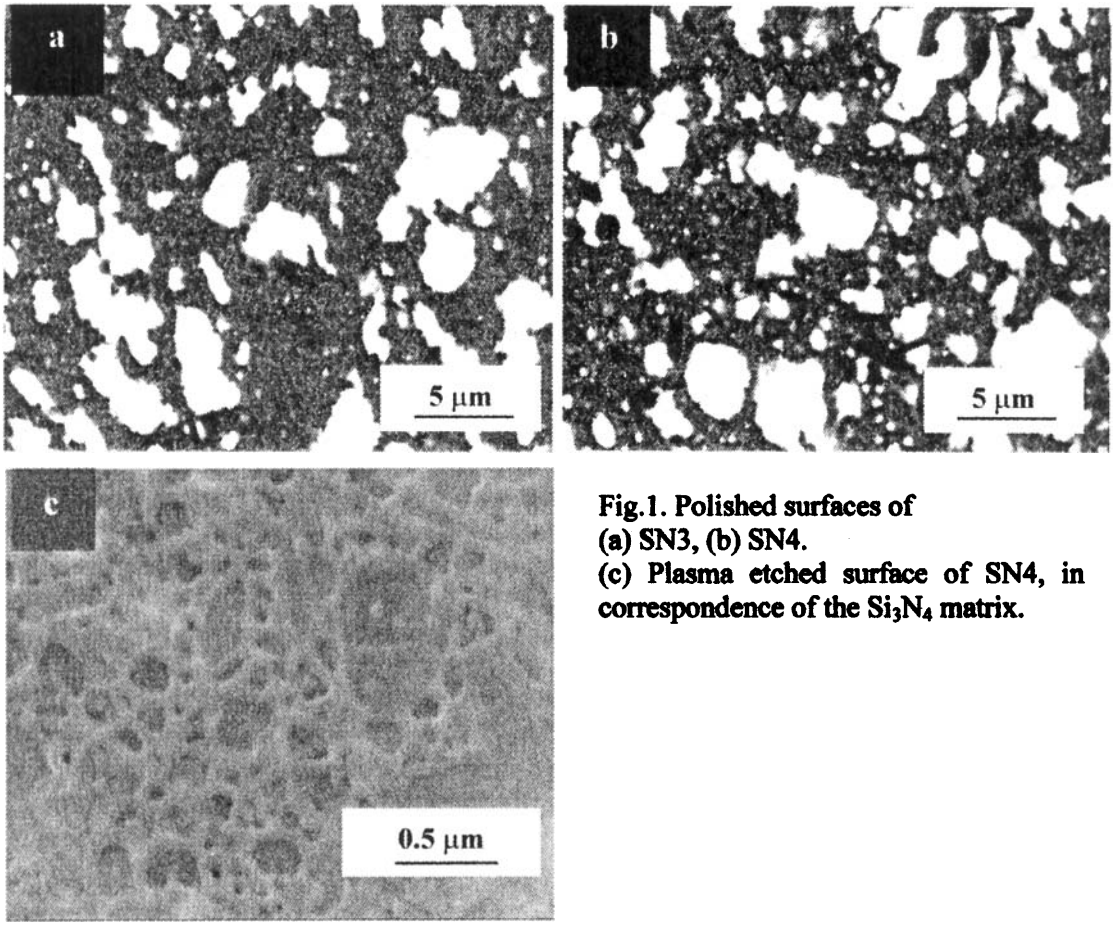

Fig.1. Polished surfaces of
(a) SN3, (b) SN4.
(c) Plasma etched surface of SN4, in correspondence of the Si_3N_4 matrix.

The shape of inclusions is irregular, as their external outline follows the Si_3N_4 grains boundaries. It can be hypothesized that the higher ductility of $MoSi_2$ compared to matrix material favours the constraint and the accommodation of these particles in the spaces available among Si_3N_4 grains during sintering. Moreover, due to the effect of the applied pressure, the shape is slightly elongated with the major axis perpendicular to the direction of the pressure. The mean particle diameter of $MoSi_2$ inclusions is ~ 0.8 μm in both composites.

In Fig. 1c, an image of SN4 after plasma etching is shown, revealing the microstructure of the silicon nitride matrix. Silicon nitride grain size is considerably small (0.18 and 0.20 μm for SN3 and SN4, respectively), see Table I.

Si_3N_4 grains undergo a partial α→β-phase transition, as detected by X-ray spectra: residual amounts of α-Si_3N_4 are in the range of 35-40%. As a result, most of the Si_3N_4 grains are still equiaxed. A low amount of elongated grains is also present with different aspect ratio values (up to ~5). The grains are separated by an intergranular secondary phase typical of liquid-phase sintered systems [5], that is completely glassy, as confirmed by the absence of crystalline phases in addition to silicon nitride and molybdenum disilicide.

Mechanical properties

The results of the mechanical properties measured on the composites are shown in Table II.

Young modulus.

In Fig.2, the data are plotted with the Hashin and Strikman bounds [7] calculated with 440 GPa [1], 311 [5] GPa, 0.28 and 0.15 [1] as Young modulus and Poisson ratio for Si_3N_4 and $MoSi_2$, respectively. The experimental error is estimated to be about 1%. The difference between the bounds and the experimental values of the composites can be attributed to the presence of a glassy phase as no porosity or microcracking was observed in the microstructure.

Hardness

The Vickers hardness of the composites is in good agreement with the values found in literature on similar materials [3]. Being softer than the Si_3N_4 matrix, the introduction of the $MoSi_2$ phase lowers the hardness linearly. An estimate of $MoSi_2$ pure phase hardness is, by linear regression, 12.3 GPa, Fig.3.

Fracture toughness

Two factors are evident from the toughness values: the increase of the K_{Ic} with the introduction of the $MoSi_2$ phase compared to monolithic Si_3N_4 having the same intergranular phase (4.5 $MPa \cdot m^{1/2}$) and the decrease of toughness when the molybdenum content passes from 30 to 40 vol %. The toughening increment in the $MoSi_2$-Si_3N_4 composites was attributed, by Petrovic et al. [3], to the residual stresses caused by the different thermal expansion coefficients of matrix and particles. Another toughening mechanism, often present in ceramic-reinforced composites, comes from crack deflection. Cracks were produced by a Vicker indenter on polished surfaces in order to analyze the crack path, Fig. 4a,b. In S3N, the crack path is quite tortuous so that the toughening contributions can come both from the residual stresses and crack deflection. On the other hand, in SN4, the crack path is almost straight and crosses the $MoSi_2$ particles without any appreciable deviation leaving only the residual stress mechanism to contribute to the toughness increment.

Flexural strength

Good values of flexural strength were measured, especially in the case of sample SN4 with a RT strength of 1130 MPa, while SN3 was weaker.

Fracture origin was investigated on fracture surfaces. EDS analysis revealed that the defects are mainly Al silicates or Al - Y silicates. In the case of sample SN4 the critical flaws are supposed to be much smaller as their presence on the fracture surface is more difficult to ascertain. However, some small defects containing silica were detected on the fracture surface. Molybdenum disilicide does not seem to play any role in such defects, indicating good homogeneity in the dispersion of the second phase.

The good values of strength in the materials under investigation can be attributed to the decrease of matrix grain size and the increase of toughness.

At 1000°C, the flexural strength decreases both for the matrix and the composites. The material SN4, which remains stronger than the matrix, has a remarkable value of about 900 MPa. The strength decrease is lower for the composites (about 20 %) than for the matrix (about 40 %).

At 1300°C, a pronounced decrease is observed for the composites (250-260 MPa, corresponding to a decrease of 70-80 % compared to the initial value) due to grain boundary sliding. The extent of this mechanism depends on the refractoriness and amount of amorphous phase present in the microstructure.

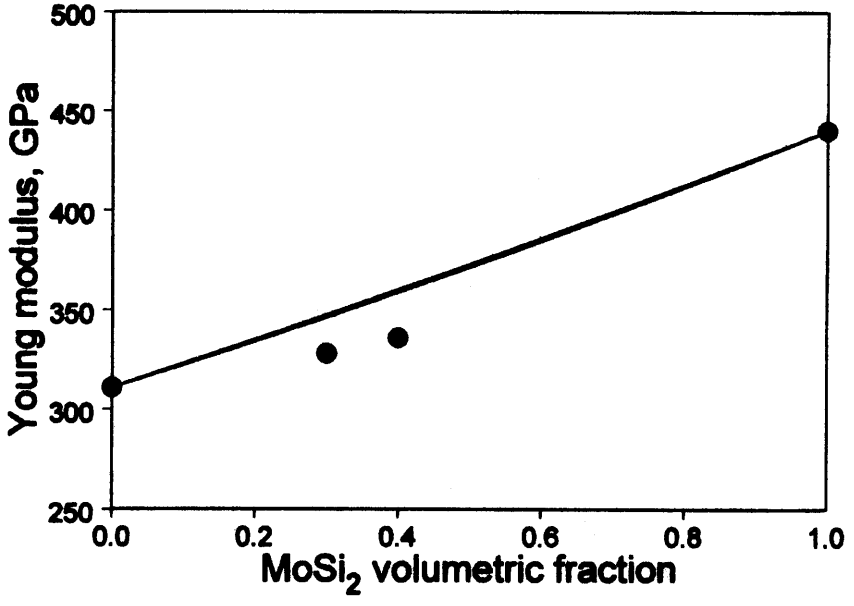

Fig. 2. Young's modulus experimental values compared with Hashin and Shtrikman bounds

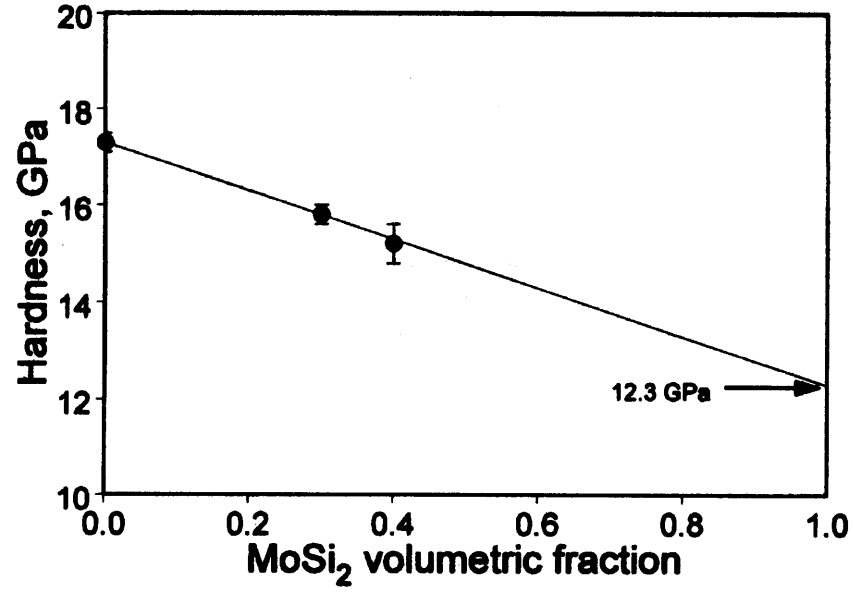

Fig. 3. Mean hardness values as a function of $MoSi_2$ volumetric content.

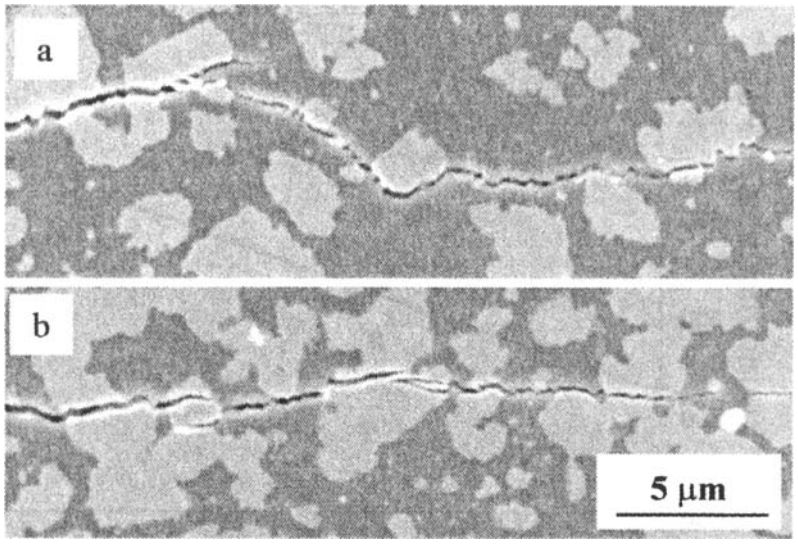

Fig.4. Crack path in (a) SN3, (b) SN4.

Electrical resistivity

The experimental data obtained are shown in Table II. Both composites are good conductors with resistivities of the order 10^{-3} Ω·cm, as a result of interconnectivity of $MoSi_2$ inclusions. In the work of Kao [4] a Si_3N_4 composite containing 30 vol % of $MoSi_2$ exhibits a resistivity two orders of magnitude higher than sample SN3. This difference is related to the mean dimensions of the conductive particles that in the present case are at least one order of magnitude smaller than in the work mentioned. The experimental values confirmed that 30 vol % of finely dispersed $MoSi_2$ is well over the percolation limit for conductivity.

Table I. Microstructural parameters

Sample	$MoSi_2$ Mean grain size (μm)	Si_3N_4 Mean grain size (μm)
SN3	0.82	0.18±0.05
SN4	0.80	0.20±0.04

Table II. Mechanical properties and electrical resistivity

Sample	E (GPa)	Hv (GPa)	K_{Ic} (MPa·$m^{1/2}$)	$\sigma_{(RT)}$ (MPa)	$\sigma_{(1000)}$ (MPa)	$\sigma_{(1300)}$ (MPa)	ρ (Ω·cm 10^{-3})
SN3	328	15.8±0.2	6.0±0.2	948±54	754±91	249±27	2.3±0.3
SN4	336	15.2±0.4	5.2±0.1	1130±44	877±19	261±30	0.8±0.4

CONCLUSIONS

Si_3N_4-$MoSi_2$ composites containing different amounts (30 and 40 vol %) of $MoSi_2$ were produced by hot-pressing and their microstructure and properties were studied. The presence of $MoSi_2$ inhibited the Si_3N_4 grain growth, the development of elongated grains and the $\alpha \rightarrow \beta$ - Si_3N_4 phase transition without retarding densification. As a result, a nearly nanosized matrix was obtained with mean grain size of about 0.2 μm.

The combination of the fine microstructure of the matrix Si_3N_4 with the presence of the $MoSi_2$ particles was beneficial for almost all the mechanical properties, including fracture toughness and mechanical strength. In addition, the composite samples were good conductors with resistivities in the order of 10^{-3} Ω·cm. Electrical conductivity resulted from the contact of $MoSi_2$ inclusions, whose volumetric fraction is over the percolation limit for both the composites produced.

High temperature properties were affected by the type and amount of grain boundary phases, therefore the residual silica in the initial $MoSi_2$ powder has a negative influence on strength above 1000°C.

REFERENCES

[1]Y.-L. Jang, E. J. Lavernia, "Review, Processing of molybdenum disilicide", *Journal of Materials Science Letters*, 29 2557-2571 (1994).

[2]J. J. Petrovic, M. I. Pena and H. H. Kung, "Fabrication and Microstructure of $MoSi_2$ reinforced –Si_3N_4 Matrix composites", *Journal of American Ceramic Society*, **80** [5] 1111-16 (1997).

[3]J. J. Petrovic, M. I. Pena, I. E. Reimanis, M. S. Sandlin, S. D. Conzone, H. H. Kung and D. P. Butt, "Mechanical Behaviour of $MoSi_2$ Reinforced – Si_3N_4 Matrix Composites", *Journal of American Ceramic Society*, **80** [12] 3070-76 (1997).

[4]Ming-yuan Kao, "Properties of silicon nitride-molybdenum disilicide particulate ceramic composites", *Journal of American Ceramic Society*, **76** [11] 2879-83 (1993).

[5]A. Bellosi and G. N. Babini, "Microstructural design of silicon nitride with tailored properties", in *Key Engineering Materials*, pp. 117-122, Vol. 89-91, Trans Tech Publications, Switzerland, 1994.

[6] D. G. Munz, J. L. Jr. Shannon, R. T. Bubsey, "Fracture Toughness Calculation from Maximum Load in Four Point Bend Tests of Chevron Notch Specimens," *International Journal of Fracture*, Vol. 16, pp. R137-R141 (1980).

[7]Z. Hashin, "Elasticity of Ceramic Systems", p. 313, in *Proceedings of the Third International Symposium on Ceramic Microstructure: their Analysis, Significance and Production*, edited by R. M. Fulrath and J. A. Pask, John Wiley & Sons Inc. Publishers, New York, 1968.

This page intentionally left blank

SOLUTION-BASED PROCESSING OF NANOCRYSTALLINE SiC

Chang-An Wang, Michael D. Sacks, Greg A. Staab, and Zhe Cheng
Georgia Institute of Technology, Atlanta, GA 30332-0245

ABSTRACT

SiC-based fibers and powders with ~20 nm crystallite size were prepared by carbothermal reduction of silica/carbon mixtures. The reactant mixtures were prepared by solution-based processing in which tetraethoxysilane (TEOS) was the silica-bearing precursor and phenol-formaldehyde resin was the carbon-bearing precursor. Fine-diameter fibers were prepared by dry spinning mixed sols that had been concentrated to high viscosity.

INTRODUCTION

There has been extensive investigation of the processing, structure, and properties of fine-diameter (~10-20 μm), fine-grained (<0.5 μm) SiC-based fibers prepared from preceramic polymers.[1-4] Fibers with excellent thermomechanical properties have been produced using polycarbosilane (PCS)-based polymers as the main precursor material. However, there are some significant disadvantages in fabricating SiC-based from PCS polymers, including (i) high cost and (ii) use of hazardous synthesis procedures (e.g., Wurtz coupling reactions using alkali metals, high pressure pyrolysis reactions, etc.). Hence, there is an interest in developing alternative processing methods for producing SiC-based fibers.

Solution-based methods have been widely investigated for processing of SiC powders with very fine crystallite sizes.[5-11] These methods involve the following steps: preparation of homogeneous sols from mixtures of silica-bearing and carbon-bearing precursors, consolidation and drying to remove the liquid medium, pyrolysis to decompose the precursors and to form intimate silica/carbon mixtures, and higher temperature heat treatment to form fine-grained SiC by carbothermal reduction reactions. Studies directed toward fabrication of SiC-based fibers from such solution-processing methods are very limited. Hasegawa et al. reported preparation of SiC-based fibers using tetraethoxysilane (TEOS) and phenolic resin as the silica and carbon precursors, respectively.[12,13] However, the fibers produced by their method had large diameters (>70 μm). Much finer diameters are generally required for SiC-based

fibers to have both high tensile strength and good weavability. The present study is focused on solution-processing methods to fabricate nanocrystalline SiC-based fibers with diameters <20 μm.

EXPERIMENTAL

Solution-based processing was used for mixing of silica-bearing and carbon-bearing precursors. The silica precursor was tetraethoxysilane (TEOS, $[Si(OC_2H_5)_4]$, Alfa AESAR, Ward Hill, MA) and the carbon precursor was a phenol-formaldehyde resin ("novolac" type, Georgia Pacific, Atlanta, GA). Ethanol was used as a mutual solvent. The mixed solutions were prepared with C:Si molar ratios in the range of ~3.2-3.5. Boron was incorporated as a dopant in fiber samples using boron triethoxide, $B(OC_2H_5)_3$ (Alfa AESAR, Ward Hill, MA) The boron alkoxide/silicon alkoxide molar ratio was ~0.06. Processing conditions were selected to promote nanometer-scale mixing: (i) Phenolic resins with low molecular weight (M_n <2000) were used. (ii) Sols were processed using acid conditions (HNO_3/TEOS molar ratio of 0.01) and relatively low water content (H_2O/TEOS molar ratios in the range of ~1.5-2.0). For TEOS-based sols, these conditions are known to produce a spinnable material containing nanometer-scale polysilicate species.[14] (iii) The mixed TEOS/phenolic solutions were concentrated by rotary evaporation to form highly viscous sols. The high viscosity was beneficial in minimizing segregation of the silica-rich and carbon-rich components during the subsequent drying stage.

Powders were prepared by drying concentrated sols in a vacuum oven. Fibers were formed by dry spinning of the highly viscous sols. Sol viscosities were measured using a cone-plate viscometer (Model HBT, Brookfield Engineering Laboratories, Stoughton, MA). The concentrated sols were extruded through a three-hole stainless steel spinneret (~40 μm hole diameter) into the ambient atmosphere. Continuous "green" fibers were collected by winding them on a rotating wheel which was placed below the spinneret. (The distance between the face of the spinneret and the winding wheel (i.e., the draw length) was varied in the range of ~0.3-1.1 m.) Fibers were dried in a vacuum oven prior to additional heat treatments. The dried powders and fibers were initially pyrolyzed at temperatures in the range of 1000-1100°C (2-4 h) in flowing argon. This resulted in the removal of volatile decomposition products from the precursor materials and the development of fine-scale mixtures of silica/carbon. The pyrolyzed samples were then heat treated in the range of 1200-1600°C (2 h) in flowing argon in order to carry out the carbothermal reduction reaction to produce SiC. A fiber sample was also subsequently heated treated at 1850°C (0.5 h) in argon to determine if fibers could be sintered to high relative density.

Pyrolyzed and carbothermally-reduced powders were analyzed for carbon content using the LECO combustion method (Sherry Laboratories, Muncie, IN). Powder samples were characterized by X-ray diffraction, XRD (Model PW1800, Philips Analytical, Netherlands) to determine the phases present after heat

treatment. The SiC crystallite sizes were calculated from the broadening of the XRD peaks using the Scherrer equation.[15] The weight loss during carbothermal reduction was determined on powders by thermal gravimetric analysis (TGA, Model STA 409, Netzsch, Exton, PA). Heat-treated fibers were characterized by SEM (Model S-800, Hitachi Ltd., Japan).

RESULTS AND DISCUSSION

Powders

Figure 1 shows XRD patterns for powder samples which were heat treated at the indicated temperatures. The 1250°C sample showed only one very weak and broad diffraction peak (centered at $2\theta \approx 23$ deg) which is attributed to amorphous silica. The initial development of β-SiC was observed in the 1350°C sample. The reaction was essentially complete by 1450°C, as the XRD peak intensities did not increase above this temperature. Figure 2 shows a plot of the β-SiC crystallite sizes (determined from the Scherrer equation) vs. heat treatment temperature. Crystallite sizes remained <25 nm after heat treatment at 1500°C. The small crystallite sizes and the low temperature needed to complete carbothermal reduction are both indicative of the fine scale of mixing of the reactants in the pyrolyzed samples.

Thermal gravimetric analysis (TGA) was used to directly compare the reaction temperature for carbothermal reduction in a (TEOS/phenolic)-based powder sample and an oxygenated polycarbosilane (PCS) fiber sample. (PCS is an Si-C backbone polymer. PCS-based fibers were heat treated in air to incorporate oxygen into the structure.) The oxygenated PCS and (TEOS/phenolic)-based samples were initially pyrolyzed in argon at 1150°C (1 h) and 1100°C (2 h), respectively. As noted earlier, the (TEOS/phenolic)-based sample contains amorphous silica and carbon after the pyrolysis heat treatment. In contrast, the oxygenated PCS decomposes to form some weakly crystalline SiC nanocrystals (~2-5 nm) which are separated by amorphous intergranular regions of free carbon and siliceous-rich/silicon oxycarbide phase(s).[16-18] Figure 3 shows TGA results in which the two samples were heated in argon at the same heating rate. The overall weight loss during carbothermal reduction is considerably smaller for the PCS-derived sample because a significant portion of the PCS had already been converted to SiC during the initial pyrolysis step. However, the carbothermal reduction reaction occurs at ~50°C lower temperature for the (TEOS/phenolic)-based sample, thereby confirming that the silica-rich and carbon-rich regions in the pyrolyzed sample were mixed on a fine scale (i.e., mostly <10 nm).

Compositional analysis (LECO method) showed that there was a large excess of carbon in (TEOS/phenolic)-based powder samples after carbothermal reduction at 1650°C. Samples contained ~60 wt% SiC and ~40 wt% excess carbon. (This indicates that silicon was lost during heat treatment, i.e., during pyrolysis and/or carbothermal reduction. Si loss during pyrolysis could occur if insufficient hydrolysis/condensation of TEOS occurred during processing of the sol. Si loss during carbothermal reduction is attributed to volatilization of SiO.)

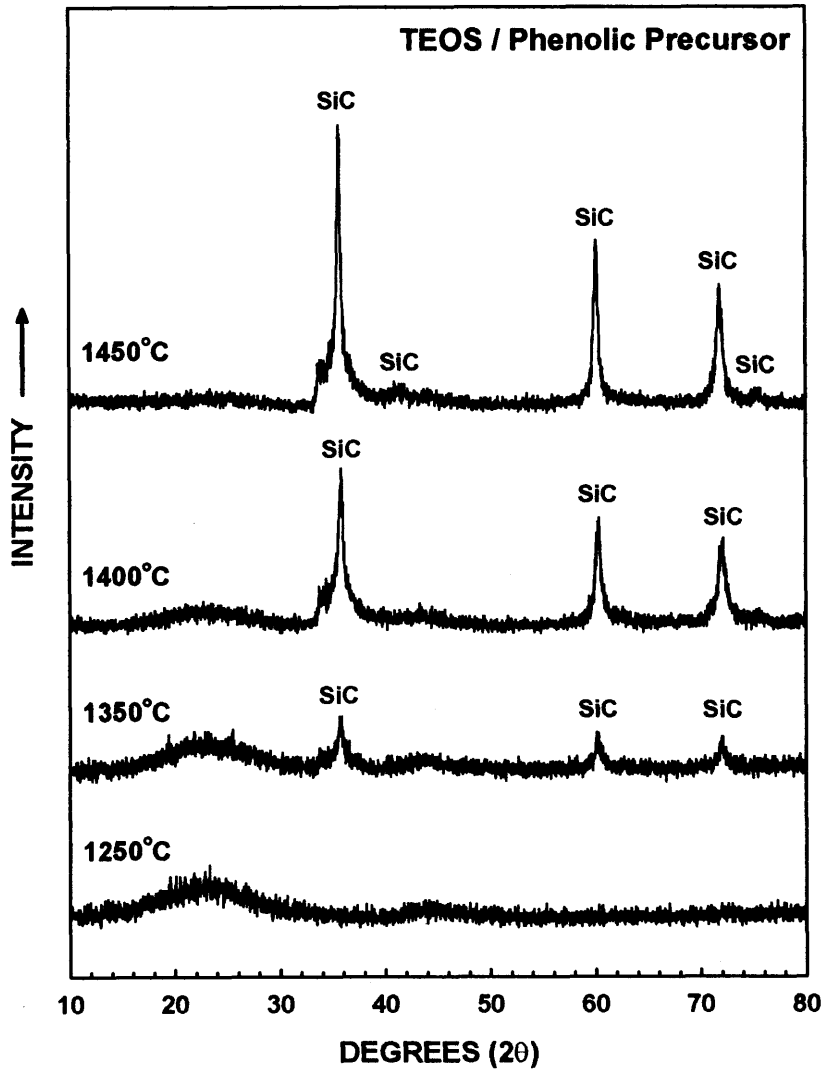

Fig. 1. XRD patterns for samples which were prepared from a (TEOS/phenolic)-based sol, pyrolyzed at 1100°C, and subsequently heat treated at the indicated temperatures.

Fibers

TEOS/phenolic sols exhibited good spinnability after concentration to sufficiently high viscosities. For example, individual filaments could be hand-drawn (using a ~0.3 cm-diameter glass rod) to average lengths in the range of ~53-58 cm when viscosities (measured at 25°C) were in the range of ~800-1300 Pa•s (measured at 1 s^{-1}). Fibers with longer length (average value of ~115 cm) could be hand-drawn

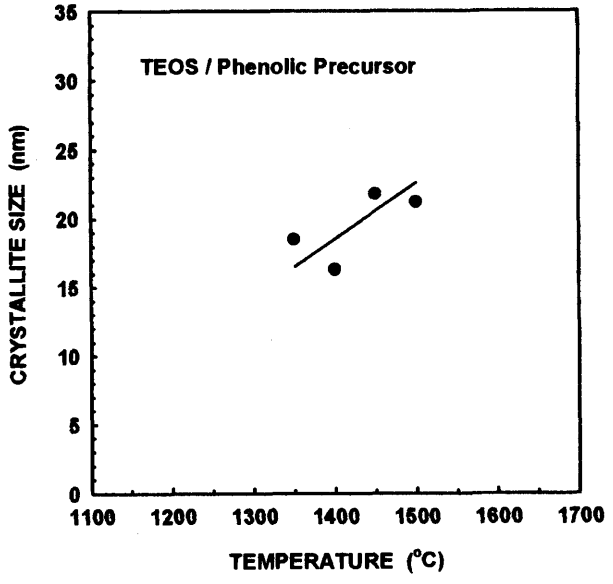

Fig. 2. Plot of crystallite size (determined from XRD line broadening) vs. heat treatment temperature for samples prepared from a (TEOS/phenolic)-based sol.

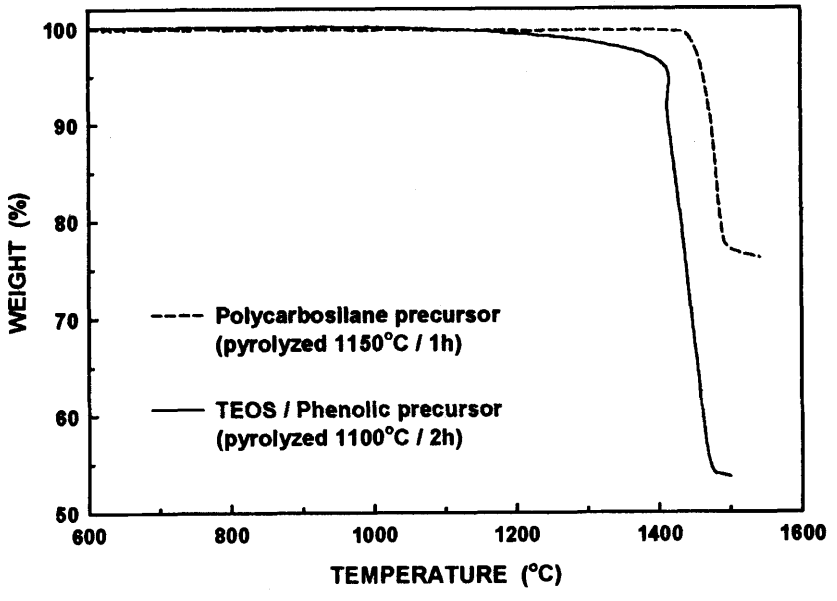

Fig. 3. Plots of weight loss vs. temperature during carbothermal reduction of pyrolyzed samples prepared from PCS-derived fibers and from a (TEOS/phenolic)-based sol.

after further concentration to remove a small additional amount of liquid. (The viscosity at 25°C for this sol exceeded the maximum value (i.e., ~1570 Pa•s at 1 s^{-1}) that could be measured on the viscometer.) However, these solutions were too viscous for fiber spinning via extrusion through the spinneret with 40 μm hole size. Instead, continuous fiber spinning was carried out by heating the spinneret (in the range of ~41-51°C) in order to reduce the sol viscosity. For example, good fiber spinning was achieved at 51°C with a sol viscosity of ~55 Pa•s. (The sol showed approximately Newtonian flow behavior for the range of measured shear rates, 1-40 s^{-1}.)

It was difficult to separate fibers from the bundle that was collected during continuous winding. Sticking between filaments was a problem due to insufficient solvent removal prior to the fibers reaching the winding wheel. This problem was mitigated to some extent by using longer draw lengths (i.e., ~1.1 m). (Further improvement would be expected by larger increases in the draw length and by passing the extruded fibers through a heated column prior to collection on the winding wheel.) Figure 4 shows SEM micrographs of fibers that were pyrolyzed in argon at 1100°C (2 h). The silica/carbon fibers have fine diameters (~15 μm), round cross-sections, and smooth surfaces. The glassy appearance of the fiber cross-section is consistent with the predominantly amorphous character that was observed in the XRD pattern for pyrolyzed powders.

Figure 5A shows an SEM micrograph from an internal fracture surface of a fiber which was heat treated in argon at 1450°C (2 h). A porous fine-grained microstructure is observed. The size of the crystallites appears to be consistent with the values determined from the XRD peak broadening in the powder samples. Some isolated grains with much larger size (~0.5-1.0 μm) were observed on the external surface of the fibers. Grains with similar appearance have also been observed after carbothermal reduction in fibers processed from oxygenated PCS.[19] (In the latter case, the large grains were eliminated by improved control over the removal of the volatiles (SiO and CO) that form during carbothermal reduction.)

Fig. 5B shows an SEM micrograph from an internal fracture surface of a fiber which was heat treated at 1850°C (0.5 h). The microstructure remains porous and fine-grained after this heat treatment. The lack of densification and the slow coarsening of the SiC crystallites are both attributed to slow diffusion rates that result from the large amount of free carbon in the sample. This conclusion is based on previous work with PCS-based fibers in which slower growth of SiC crystallites was observed in samples containing larger amounts of excess carbon.[4]

CONCLUSION

Solution-processing of (TEOS/phenolic resin)-based mixtures was used to produce nanocrystalline SiC-based fibers and powders. The fibers were fabricated by continuous dry spinning of mixed sols that had been concentrated to high viscosity. Heat treatments for drying, pyrolysis, and carbothermal reduction were subsequently

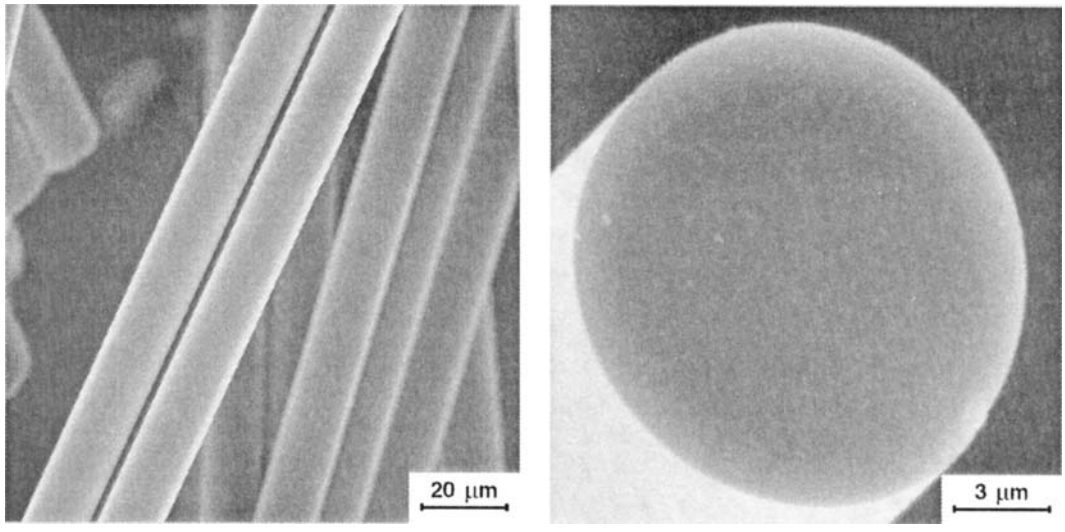

Fig. 4. SEM micrographs of SiC-based fibers, prepared from a (TEOS/phenolic)-based sol, after pyrolysis at 1100°C.

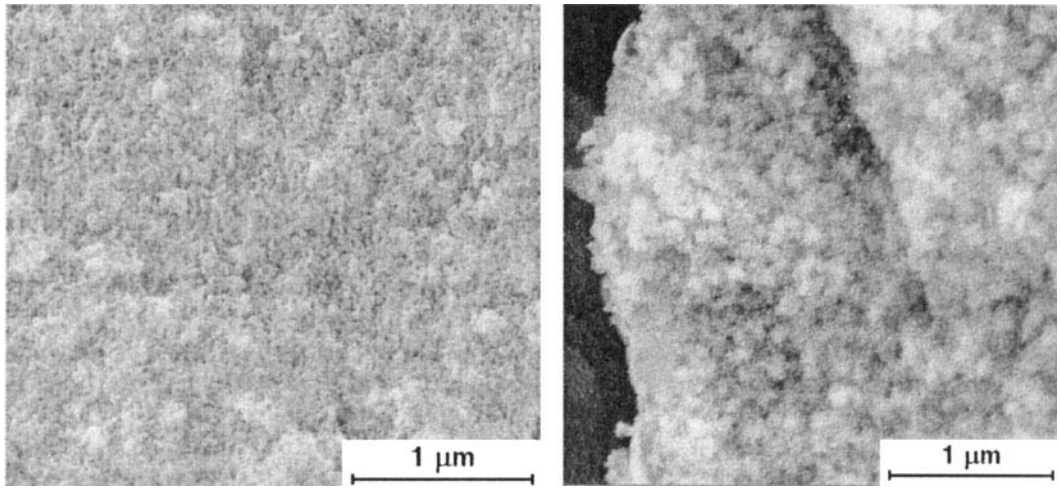

Fig. 5. SEM micrographs of the internal fracture surface of an SiC-based fiber, prepared from a (TEOS/phenolic)-based sol, after (A) carbothermal reduction at 1450°C and (B) heat treatment at 1850°C.

carried out. The resulting SiC-based fibers had fine diameters (~15 μm), round cross-sections, and a porous microstructure that contained extremely fine SiC crystallites (~20 nm) and substantial excess carbon. The fibers remained highly porous after heat treatment at 1850°C, presumably because the large amount of excess carbon inhibited diffusion. To obtain SiC fibers with high relative density, ongoing studies are directed at preparing fibers with chemical compositions closer to that of stoichiometric SiC. Preliminary results have shown that spinnable sols can be produced with substantially lower concentrations of phenolic resin.[20]

ACKNOWLEDGMENT

This work was sponsored by the Air Force Office of Scientific Research, USAF, under grant/contract no. F49620-01-1-0112.

REFERENCES

1. M. Takeda, J. Sakamoto, A. Saeki, and H. Ichikawa, "Mechanical and Structural Analysis of Silicon Carbide Fiber Hi-Nicalon Type S," Ceram. Eng. Sci. Proc., 17 [4] 35-43 1996.
2. J. Lipowitz, J.A. Rabe, G.A. Zank, A. Zangvil, and Y. Xu, "Structure and Properties of Sylramic™ Silicon Carbide Fiber -- a Polycrystalline, Stoichiometric β-SiC Composition," Ceram. Eng. Sci. Proc., 18 [3] 147-157 (1997).
3. K. Kumagawa, H. Yamaoka, M. Shibuya, and T. Yamamura, "Fabrication and Mechanical Properties of New Improved Si-M-C-(O) Tyranno Fibers," Ceram. Eng. Sci. Proc., 19 [3] 65-72 (1998).
4. M.D. Sacks, "Effect of Composition and Heat Treatment Conditions on the Tensile Strength and Creep Resistance of SiC-Based Fibers," J. Eur. Ceram. Soc., 19 2305-2315 (1999).
5. Hans-Peter Martin, R. Ecke, and Eberhard Muller, "Synthesis of Nanocyrstalline Silicon Carbide Powder by Carbothermal Reduction," J. Eur. Ceram. Soc., 18 1737-1742 (1998).
6. H. Tanaka and Y. Kurachi, "Synthesis of β-SiC Powder from Organic Precursor and its Sinterability," Ceram. International 14 109-115 (1988).
7. K. Ono and Y. Kurachi, "Kinetic Studies on β-SiC Formation from Homogeneous Precursors," J. Mater. Sci. 26 388-392 (1991).
8. D. Huang and Y. Ikuhara, "Characterization of β-Silicon Carbide Powders Synthesized by the Carbothermal Reduction of Silicon Carbide Precursors," J. Am. Ceram. Soc. 81 3173-3176 (1998).
9. Y. Sugahara, Y. Takeda, K. Kuroda, and C. Kato, "Carbothermal Reduction Process of Precursors Derived from Alkoxides for Synthesis of Boron-Doped SiC Powder," J. Mater. Sci. Lett., 8 944-946 (1989).
10. Y. Sugahara, Y. Takeda, K. Kuroda, and C. Kato, "The Preparation of Boron-Doped Silicon Carbide Powder by the Carbothermal Reduction of Oxides Derived from the Hydrolyzed MethylTriethoxysilane," J. Non-Cryst. Solids, 100 542-546 (1988).
11. G.C. Wei, C.R. Kennedy, and L.A. Harris, "Synthesis of Sinterable SiC Powders by Carbothermic Reduction of Gel-Derived Precursors and Pyrolysis of Polycarbosilane," Bull. Am. Ceram. Soc., 63 [8] 1054-1061 (1984).

12. I. Hasegawa, T. Nakamura, S. Motojima, and M. Kajiwara, "Silica Gel-Phenolic Resin Hybrid Fibres: New Precursors for Continuous β-Silicon Carbide Fibres," J. Mater. Chem., 5 [1] 193-194 (1995).
13. I. Hasegawa, T. Nakamura, S. Motojima, and M. Kajiwara, "Synthesis of Silicon Carbide Fibers by Sol-Gel Processing," J. Sol-Gel Sci. Tech., 8 577-579 (1997).
14. C.J. Brinker and G.W. Scherer, Sol-Gel Science, Academic Press, Inc., San Deigo, CA, 1990.
15. B.D. Cullity, Elements of X-ray Diffraction, Addison-Wesley Publishing Co., Inc., Reading, MA, 1967.
16. E. Bouillon, D. Mocaer, J.F. Vileneuve, R. Pailler, R. Naislan, M. Monthioux, A. Oberlin, C. Guimon, and G. Pfister, "Composition-Microstructure-Property Relationships in Ceramic Monofilaments Resulting from the Pyrolysis of a Polycarbosilane Precursor at 800 to 1400°C," J. Mater. Sci., 26 1517-1530 (1991).
17. P. Le Costumer, M. Monthioux, and A. Oberlin, "Understanding Nicalon Fibre," J. Eur. Ceram. Soc., 11 95-103 (1993).
18. M. Monthioux and O. Delverdier, "Thermal Behavior of (Organosilicon) Polymer-Derived Ceramics. V: Main Facts and Trends," J. Eur. Ceram. Soc., 16 721-737 (1996).
19. M.D. Sacks, unpublished work.
20. C.A. Wang, G. Staab and M.D. Sacks, unpublished work.

This page intentionally left blank

SOLUTION-BASED PROCESSING OF NANOCRYSTALLINE ZrC

Zeshan Hu, Michael D. Sacks, Greg A. Staab, Chang-An Wang, and Anubhav Jain
Georgia Institute of Technology, Atlanta, GA 30332-0245

ABSTRACT

ZrC-based fibers and powders with ~20 nm crystallite size were prepared by carbothermal reduction of zirconia/carbon mixtures. The reactant mixtures were prepared by solution-based processing in which zirconium 2,4-pentanedionate (ZTP) was the zirconia-bearing precursor and phenol-formaldehyde resin was the carbon-bearing precursor. Fine-diameter fibers were prepared by dry spinning mixed sols that had been concentrated to high viscosity.

INTRODUCTION

ZrC is a potential candidate for ultrahigh temperature applications because of its high melting point (~3600°C), solid-state phase stability, and good thermomechanical properties.[1,2] ZrC also has advantages of lower density and lower cost compared to refractory metals, such as Rh and Ir alloys, which have been more widely investigated for rocket applications.

Investigations directed toward the preparation of fine-grained ZrC powders and fibers are rather limited. However, several studies have shown that ZrC can be synthesized at relatively low temperatures by using solution-based processing methods.[3-6] The initial step in these methods involved preparation of homogeneous mixtures of soluble zirconia-bearing and carbon-bearing precursors. These mixtures were subsequently dried to remove liquids, pyrolyzed to decompose the precursors and to form intimate zirconia/carbon mixtures, and heat treated at higher temperature to form fine-grained ZrC by carbothermal reduction reactions. Sham et al. synthesized ZrC using solution-processed mixtures of Zr n-propoxide (as a zirconia source) and either ethylene glycol or 1,4 benzenediol (as a carbon source).[3] Preiss et al. used chelated derivatives of Zr n-propoxide and various soluble carbon-bearing compounds (including those used by Sham et al.) to form ZrC fibers and films.[4] The fibers were hand-drawn and had diameters of ~50 μm. Kurokawa et al. produced fine-grained, large-diameter (~100 μm) ZrC fibers by feeding cellulose-based solutions into Zr n-butoxide.[5] Hasegawa et al. used mixtures of Zr 2,4,-pentanedionate and phenolic resins to produce ZrC fibers with diameter ≥60 μm.[6]

For applications in ceramic-matrix composites, fibers with much finer diameters are generally required in order to achieve both high tensile strength and good weavability. The present study is focused on using solution-processing methods to fabricate nanocrystalline ZrC-based fibers with diameters $\leq$20 μm.

EXPERIMENTAL

Solution-based processing was used for mixing of zirconia-bearing and carbon-bearing precursors. The zirconia precursor was zirconium 2,4-pentanedionate (ZTP, $[Zr(O_2C_5H_7)_4]$, Alfa AESAR, Ward Hill, MA) and the carbon precursor was a phenol-formaldehyde resin ("novolac" type, Georgia Pacific, Atlanta, GA). A mixture of ethanol and 2,4-pentanedione was used as a mutual solvent. The mixed solutions were prepared with C:Zr molar ratio of 4. Processing conditions were selected to promote nanometer-scale mixing: (i) Phenolic resins with low molecular weight (M_n <2000) were used. (ii) Sols were processed using acid conditions (H_2SO_4/ZTP molar ratio of 0.66) and relatively low water content (H_2O/ZTP molar ratios of 0.45). These conditions restrict ZTP hydrolysis (and subsequent condensation reactions) and thereby limit the growth of zirconia-bearing precipitates. (iii) The mixed ZTP/phenolic solutions were concentrated by rotary evaporation to form highly viscous sols. The high viscosity was beneficial in minimizing segregation of the zirconia-rich and carbon-rich components during the subsequent drying stage.

Powders were prepared by drying concentrated sols in a vacuum oven. Fibers were formed by dry spinning of the highly viscous sols. Sol viscosities were measured using a cone-plate viscometer (Model HBT, Brookfield Engineering Laboratories, Stoughton, MA). The concentrated sols were extruded through a three-hole stainless steel spinneret (~40 μm hole diameter) into the ambient atmosphere. Continuous "green" fibers were collected by winding them on a rotating wheel which was placed below the spinneret. (The distance between the face of the spinneret and the winding wheel (i.e., the draw length) was ~0.4 m). Fibers were dried in a vacuum oven prior to additional heat treatments.

The dried powders and fibers were initially pyrolyzed at temperatures in the range of 1000-1100°C (2 h) in flowing argon. This resulted in the removal of volatile decomposition products from the precursor materials and the development of fine-scale mixtures of zirconia/carbon. The pyrolyzed samples were then heat treated in the range of 1250-1500°C (2 h) in flowing argon in order to carry out the carbothermal reduction reaction to produce ZrC. Pyrolyzed and carbothermally-reduced powders were analyzed for carbon content using the LECO combustion method (Sherry Laboratories, Muncie, IN). Powder samples were characterized by X-ray diffraction, XRD (Model PW1800, Philips Analytical, Netherlands) to determine the phases present after heat treatment. The ZrC and ZrO_2 crystallite sizes were calculated from the broadening of the XRD peaks using the Scherrer equation.[15] Heat-treated fibers were characterized by SEM (Model S-800, Hitachi Ltd., Japan).

RESULTS AND DISCUSSION

Powders

Figure 1 shows XRD patterns for powder samples which were heat treated at the indicated temperatures. The 1100°C sample shows weak and broad diffraction peaks which are due to tetragonal zirconia (t-ZrO_2). The initial development of ZrC was observed in the 1250°C sample. The t-ZrO_2 peaks in this sample showed little change compared to the 1100°C sample. The ZrC peaks were much more intense after the 1350°C heat treatment, while the t-ZrO_2 peak intensities decreased. The carbothermal reduction reaction was essentially complete in the 1450°C sample, as indicated by two observations: (i) the ZrC peak intensities did not increase above this temperature and (ii) there were no ZrO_2 peaks in the XRD pattern. Figure 2 shows plots of the ZrC and t-ZrO_2 crystallite sizes (determined from the Scherrer equation) vs. heat treatment temperature. The fine scale of mixing of the carbon/zirconia reactants in the pyrolyzed samples was indicated by the very small size (~3 nm) of the t-ZrO_2 crystallites. The ZrC crystallites were still relatively small (<25 nm) after heat treatment at 1500°C.

Compositional analysis (LECO method) showed that there was a large excess of carbon in (ZTP/phenolic)-based powder samples after carbothermal reduction at 1500°C. Samples contained ~63 wt% ZrC and ~36 wt% excess carbon. The reason for the high excess carbon content is not known with certainty. However, it is very likely that ZTP hydrolysis was far from complete under the processing conditions used. Thus, it would be expected that a significant amount of carbon in the pyrolyzed samples would be contributed from the partially hydrolyzed ZTP.

Fibers

ZTP/phenolic sols exhibited good spinnability after concentration to sufficiently high viscosities. Continuous fiber spinning was carried out by heating the spinneret in the range of ~47-56°C in order to reduce the sol viscosity. Optimum spinning was observed with spinneret temperatures of ~49-51°C. As indicated in Fig. 3, the heated sols exhibited shear thinning rheological flow behavior. The viscosity at 50°C was ~10 Pa•s at a shear rate of 100 s^{-1}.

It was difficult to separate fibers from the bundle that was collected during continuous winding. Sticking between filaments was a problem due to insufficient solvent removal prior to the fibers reaching the winding wheel. Recent experiments with solution-processed SiC-based fibers indicates that this problem can be mitigated by using longer draw lengths (i.e., >1 m).[7] (Further improvement would be expected by passing the extruded fibers through a heated column prior to collection on the winding wheel.)

Figure 4 shows SEM micrographs of fibers after carbothermal reduction in argon at 1450°C (2 h). The fibers have fine diameters (~20 μm) and relatively smooth

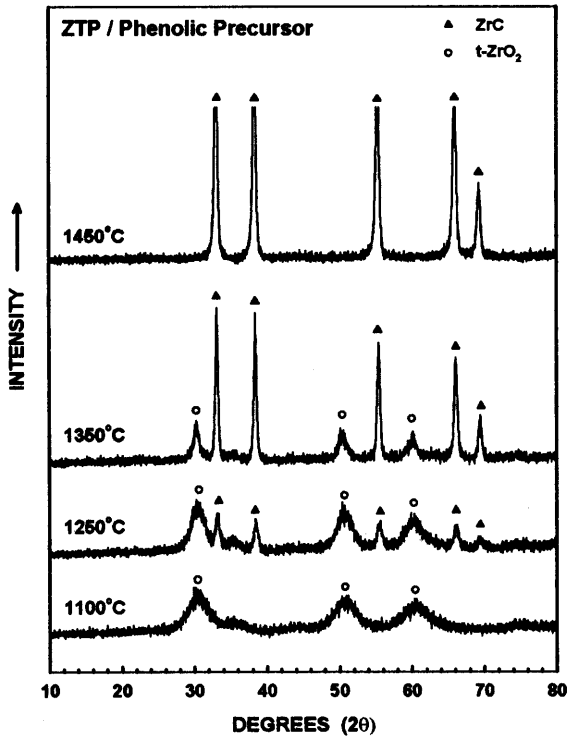

Fig. 1. XRD patterns for samples which were prepared from a (ZTP/phenolic)-based sol heat treated at the indicated temperatures.

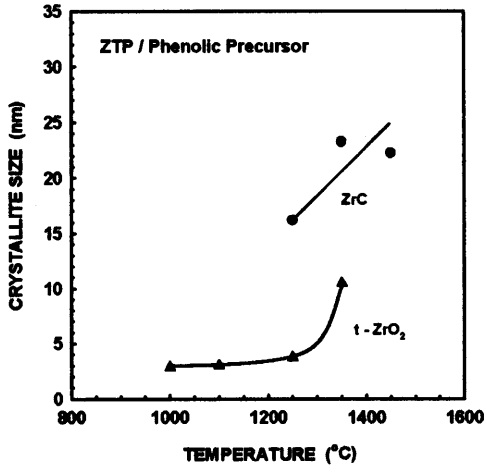

Fig. 2. Plot of the t-ZrO_2 and ZrC crystallite sizes (determined from XRD line broadening) vs. heat treatment temperature for samples prepared from a (ZTP/phenolic)-based sol.

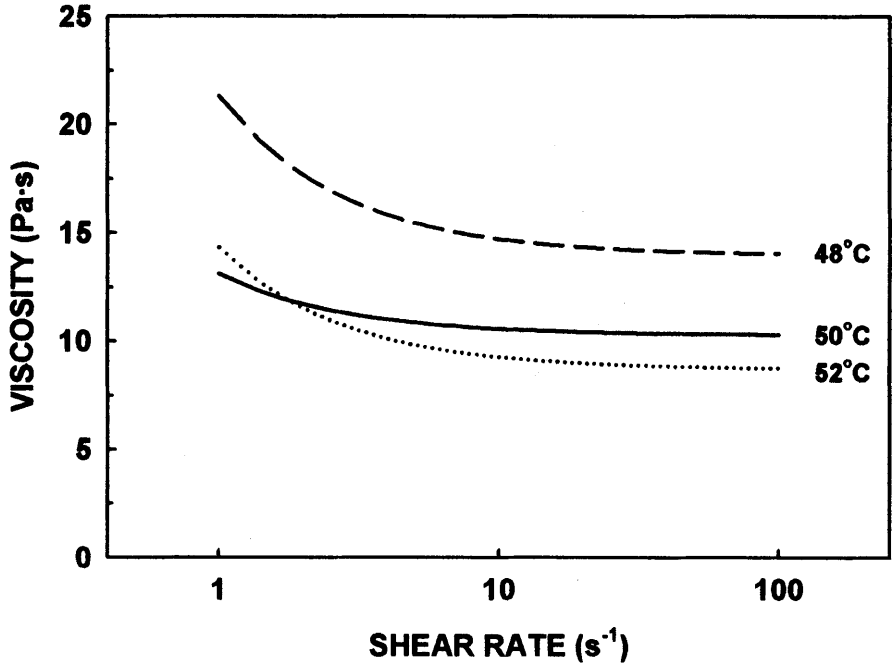

Fig. 3. Plots of viscosity vs. shear rate for a (ZTP/phenolic)-based sol that was used for fiber spinning.

surfaces. A higher magnification micrograph (Fig. 5) shows that the fiber has a porous, extremely fine-grained microstructure. The size of the crystallites appears to be consistent with the values determined from the XRD peak broadening in the powder samples.

CONCLUSION

Solution-processing of (ZTP/phenolic resin)-based mixtures was used to produce nanocrystalline ZrC-based fibers and powders. The fibers were fabricated by continuous dry spinning of mixed sols that had been concentrated to high viscosity. Heat treatments for drying, pyrolysis, and carbothermal reduction were subsequently carried out. The resulting ZrC-based fibers had fine diameters (~20 μm) and relatively smooth surfaces. The fibers were porous and consisted of extremely fine ZrC crystallites (<25 nm), as well as substantial excess carbon. Ongoing studies are directed at preparing fibers with chemical compositions closer to that of stoichiometric ZrC. Preliminary results suggest that spinnable sols can be produced with substantially lower concentrations of phenolic resin.[8]

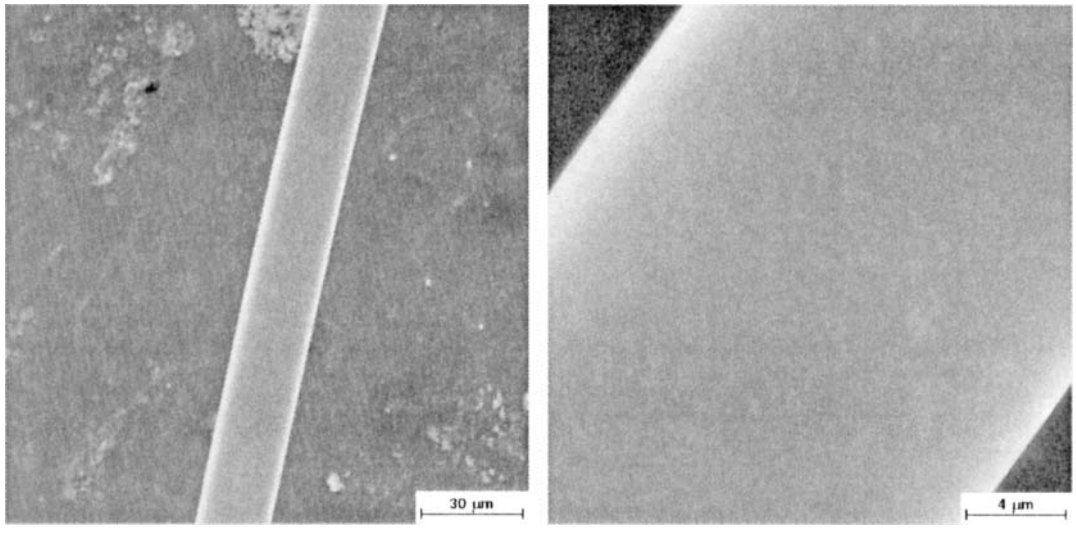

Fig. 4. SEM micrographs of a ZrC-based fiber, prepared from a (ZTP/phenolic)-based sol, after carbothermal reduction at 1450°C.

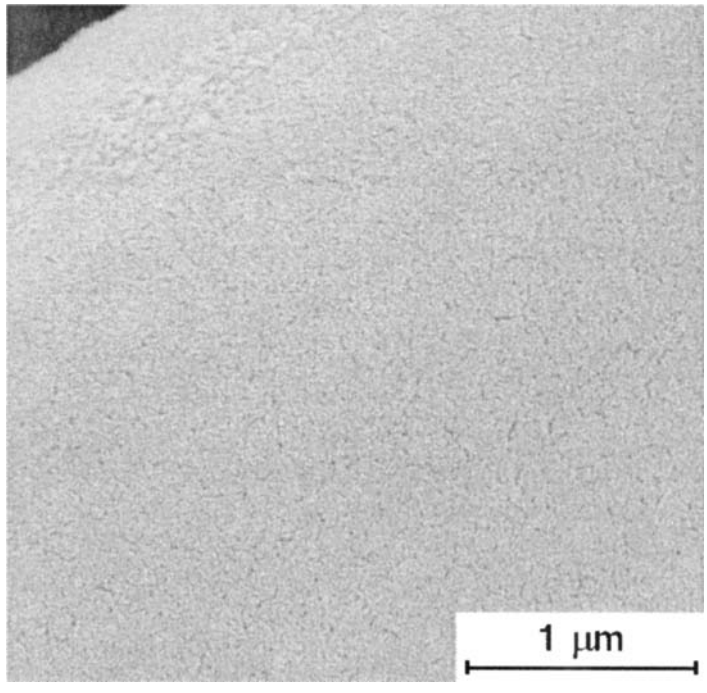

Fig. 5. Higher magnification SEM micrograph of a ZrC-based fiber, prepared from a (ZTP/phenolic)-based sol, after carbothermal reduction at 1450°C.

ACKNOWLEDGMENT

This work was sponsored by the Air Force Office of Scientific Research, USAF, under grant/contract no. F49620-01-1-0112.

REFERENCES

1. L.E. Toth, Transition Metal Carbides and Nitrides, Academic Press, New York, 1971.
2. K. Upadhya, J.-M. Yan, and W.P. Hoffman, "Materials for Ultrahigh Temperature Structural Applications," Bull. Am. Ceram. Soc., 76 51-56 (1997).
3. E.L. Sham, E.M. Farfan-Torres, S. Bruque-Gamez, and J.J. Rodriguez-Jimenez, "Synthesis of ZrC/ZrO_2 by Pyrolysis of Modified Zirconium Alkoxide Precursors," Solid State Ionics, 63-65 45-51 (1993).
4. H. Preiss, E. Schierhorn, and K.W. Brzenzinka, "Synthesis of Polymeric Titanium and Zirconium Precursors and Preparation of Carbide Fibers and Films," J. Mater. Sci., 33 4697-4706 (1998).
5. Y. Kurokawa, S. Kobayashi, M. Suzuki, M. Shimazaki, and M. Takahashi, "Preparation of Refractory Carbide Fibers by Thermal Decomposition of Transition Metal (Ti, Zr, Hf, Nb, Ta) Alkoxide-Cellulose Precursor Gel Fibers," J. Mater. Res., 13 [3] 760-765 (1998).
6. I. Hasegawa, Y. Fukuda, and M. Kajiwara, "Inorganic-Organic Hybrid Route to Synthesis of ZrC and Si-Zr-C Fibres," Ceram. International, 25 523-527 (1999).
7. G.A. Staab and M.D. Sacks, unpublished work.
8. Z. Hu and M.D. Sacks, unpublished work.